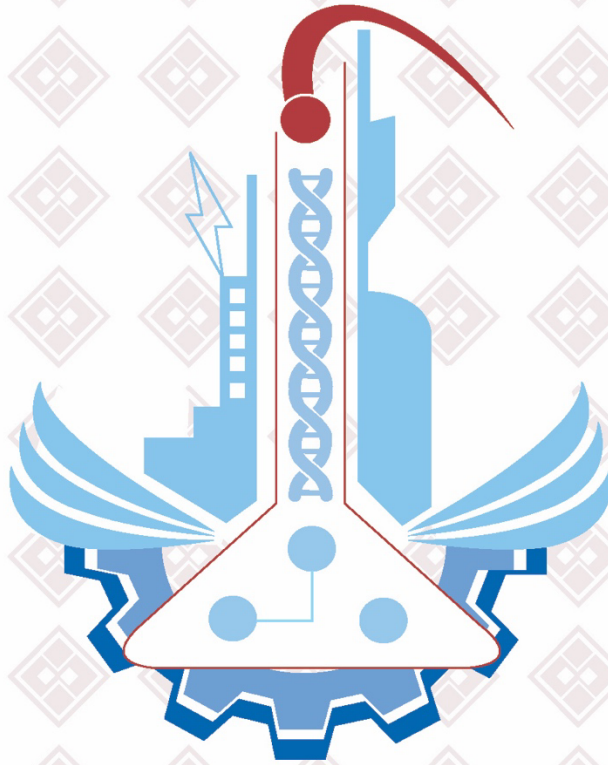


PRINTED ISSN: 1308-9080 / OLINE ISSN: 1308-9099

Volume: 18 / Number: 1 / Year: 2023

# TURKISH JOURNAL OF SCIENCE & TECHNOLOGY





# TURKISH JOURNAL OF SCIENCE AND TECHNOLOGY (TJST)

**Year: 2023      Vol: 18      Number: 1**

**Address:**

Fırat Universitesi  
Fen Bilimleri Enstitüsü  
23119, Elazig - TURKEY

**Tel:** 0 424 212 27 07

**Fax:** 0 424 236 99 55

**e-mail:** [fenbilim@firat.edu.tr](mailto:fenbilim@firat.edu.tr)

**New ISSN**

**Online: 1308-9099**

**Printed: 1308-9080**

**Old ISSN**

**Online: 1306 – 8555**

**Printed: 1306 – 8547**

**Refereed journal. Published twice a year**

*<https://dergipark.org.tr/tr/pub/tjst>*



**TURKISH JOURNAL OF SCIENCE & TECHNOLOGY (TJST)**  
**Published by Firat University**

**Owner**

**Prof. Dr. Fahrettin GÖKTAŞ**  
Rector of Firat University

**Editor in Chef**

**Assist. Prof. Dr. Ferhat UÇAR**  
Firat University, Faculty of Technology  
Department of Software Engineering

**Responsible Director**

**Prof. Dr. Burhan ERGEN**  
Firat University, Faculty of Engineering  
Department of Computer Engineering

**Editor**

**Assoc. Prof. Dr. Nida KATI**  
Firat University, Faculty of Technology  
Department of Metallurgical and Materials Engineering

**ADVISORY BOARD**

**Eyüp BAĞCI**

Firat University, Department of Biology,  
Elazig-Turkey

**Eres SOYLEMEZ**

Middle East Technical University,  
Department of Engineering Science,  
Ankara-Turkey

**Coskun BAYRAK**

UALR Donaghey Collage of Eng. and  
Information Tech. Dept. of Computer  
Science, Little Rock, AR, USA

**Hikmet GECKIL**

Inonu University, Department of Biology,  
Malatya-Turkey

**Metin CALTA**

Firat University, Fisheries Faculty,  
Elazig-Turkey

**Ertan GOKALP**

Karadeniz Technical University,  
Department of Geodesy and  
Photogrametry Engineering, Trabzon-  
Turkey

**Abdulkadir ŞENGÜR**

Firat University, Department of  
Electronics and Computer Education,  
Elazig-Turkey

**Hasan EFEOGLU**

Ataturk University, Department of  
Electrical-Electronics Engineering,  
Erzurum-Turkey

**Yanhui GUO**

St. Thomas University, School of Science  
and Technology, Miami, FL, USA

**İbrahim TURKMEN**

Balıkesir University, Department of  
Geology Engineering, Balıkesir-Turkey

**Deniz UNER**

Middle East Technical University,  
Department of Chemical Engineering,  
Ankara-Turkey

**M.Polat SAKA**

Bahreyn University, Department of Civil  
Engineering, Bahrain

**Siqing XIA**

Tongji Univ, State Key Lab Pollut Control  
& Resource Reuse, Coll Environm Sci &  
Engn, Shanghai 200092, R China

**Zihni DEMIRBAG**

Karadeniz Technical University,  
Department of Biology, Trabzon-Turkey

**Hanifi GULDEMİR**

Firat University, Department of Electronics  
and Computer Education, Elazig-Turkey

**Nilgun GULEC**

Middle East Technical University,  
Department of Geology Engineering,  
Ankara-Turkey

**Erdogan GUNEL**

West Virginia University, Department of  
Statistics, Morgontown, USA

**Sedigheh GHOFRANI**

Islamic Azad University, Electrical  
Engineering Department, Tehran South  
Branch, Iran

**Wang XIBAO**

Tianjin University, The School of  
Materials Science and Engineering, China

**Brain WOERNER**

West Virginia University, Department of  
Computer Sciences & Electrical  
Engineering, Morgontown, WV, USA

**A. Kadri CETIN**

Firat University, Department of Biology,  
Elazig-Turkey

**Yusuf Kağan KADIOĞLU**

Ankara University, Department of Geology  
Engineering, Ankara-Turkey

**Sezgin BAKIRDERE**

Yıldız Technical University, Department of  
Chemistry, Ankara-Turkey.

**Tuncay OREN**

Ottawa Univ, Fac Eng, Inform Technol.  
McLeod Inst Sim.t Sci, Ottawa, ON KIN  
6N5 Canada

**Halil ONDER**

Middle East Technical University,  
Department of Civil Engineering, Ankara-  
Turkey

**Nazmi POLAT**

Ondokuz Mayıs University, Department of  
Biology, Samsun-Turkey

**Mustafa DORUCU**

Firat University, Fisheries Faculty,  
Elazig-Turkey

**Binod Chandra TRIPATHY**

Mathematical Sciences Division, Institute  
of Advanced Study Science and Tech.  
Paschim Boragaon; Guwahati, India

**Eoin CASEY**

University College Dublin, Chemical and  
Bioprocess Engineering, Dublin, Ireland

**Farid El-TANTAWY**

Suez Canal University, Faculty of  
Science, Department of Physics, Ismailia,  
Egypt

**Saleem HASHMI**

International College of Technology,  
Dublin, Ireland

**Sakir ERDOĞDU**

Karadeniz Technical University,  
Department of Civil Engineering, Trabzon-  
Turkey

**Serdar SALMAN**

Marmara University, Metallurgical and  
Materials Engineering, İstanbul-Turkey



**Firat University Turkish Journal of Science & Technology (TJST)**  
**18-1, 2023**

**CONTENTS / İÇİNDEKİLER**

- 1. FRF Based Structural Modification of a Mechanical System by Adding Masses and Utilizing the Grey Wolf Optimization Technique**  
*Bir Mekanik Sistemin Kütle Eklenerek ve Bozkurt Optimizasyon Tekniği Kullanılarak FTF Tabanlı Yapısal Değişikliği*  
**Murat ŞEN, Osman YİĞİD, Orhan ÇAKAR.....** 1-10
- 2. Investigation of electronic and thermal properties of CoCrFe and CoCrFeNi high entropy alloys via extended tight-binding DFT computational method**  
*Geniştirilmiş Sıkı Bağlanma Dft Hesaplama Yöntemi ile Cocrfe ve Cocrfeni Yüksek Entropili Alaşımlarının Elektronik ve Termal Özelliklerinin İncelenmesi*  
**Fatih Ahmet ÇELİK, Sefa KAZANÇ.....** 11-21
- 3. Computational Relationship of the Surface Area and Stiffness of the Spring Constant on Fractional Bagley-Torvik Equation**  
*Kesirli Bagley-Torvik Denklemi Üzerindeki Yay Sabitinin Yüzey Alanı ve Sertliğinin Hesaplamalı İlişkisi*  
**Kazem İyanda FALADE, Abd'gafar Tunde TIAMIYU, Adesina Kamorudeen ADIO, Huzifa Muhammad TAHIR, Umar Muhammad ABUBAKAR, Sahura Muhammad BADAMASİ.....** 23-31
- 4. Anomaly Detection in Yarn Tension Signal Using Independent Component Analysis**  
*Bağımsız Bileşen Analizi Kullanılarak İplik Gerginlik Sinyalinde Anormallik Tespiti*  
**Canan TASTIMUR, Mehmet AGRIKLI, Erhan AKIN.....** 33-43
- 5. The Effects of Hydroxyapatite on the Corrosion Behaviour of AZ Series Mg Alloys**  
*AZ Serisi Mg Alaşımlarında Hidroksiapatitin Korozyon Davranışı Üzerine Etkisi*  
**Yakup SAY.....** 45-57
- 6. Analysis of Views on Digitalization of Design Studios**  
*Tasarım Stüdyolarının Dijitalleştirilmesine Yönelik Görüşlerin Analizi*  
**Nihal Arda AKYILDIZ, Betül BEKTAŞ EKİCİ, Songül KARABATAK, Müslim ALANOĞLU.....** 59-73
- 7. Evaluation of the Effects of Earthquakes on Radon and Total Electron Content Values and Meteorological Changes on the North Anatolian Fault Zone, Türkiye**  
*Depremlerin Radon ve Toplam Elektron İçeriği Değerleri Üzerindeki Etkilerinin ve Meteorolojik Değişimlerin Değerlendirilmesi Kuzey Anadolu Fay Zonu, Türkiye*  
**Dawar Hama Khalid MOHAMMED, Fatih KÜLAHCI, Ahmet SAİT ALALI.....** 75-85
- 8. Assessment of Elenolic Acid Incorporation on Physical Properties of Chitosan Films to be Used as Active Packaging Material**  
*Elenolik Asit Katılmasının Aktif Ambalaj Malzemesi Olarak Kullanılacak Kitosan Filmlerinin Fiziksel Özellikleri Üzerine Etkisinin Değerlendirilmesi*  
**Ayça AYDOĞDU EMİR, Osman UÇKUN.....** 87-95
- 9. Optimization Studies on the Changeable Components of Hydroelectric Power Plants**  
*Hidroelektrik Santrallerin Değişken Bileşenleri Üzerine Optimizasyon Çalışmaları*  
**Muhammed Cihat TUNA, Alp Buğra AYDIN.....** 97-112

<b>10. Threats Detection in IoT Network</b> <i>IoT Ağında Saldırı Algılama</i> <b>Hanan ABU KWAİDER, Erdinç AVAROĞLU.....</b>	<b>113-122</b>
<b>11. Novel Quaternary CuAlZnMg High Temperature Shape Memory Alloy (HTSMA) Fabricated by Minor Batch of Zn and Mg Additions</b> <i>Minör Miktarda Zn ve Mg Katkıları Eklenecek Üretilmiş Yeni Kuaterner CuAlZnMg Yüksek Sıcaklık Şekil Hafızalı Alaşımı (YSSHA)</i> <b>Oktay KARADUMAN, Güneş BAŞBAĞ, İskender ÖZKUL, Canan Aksu CANBAY, Mustafa BOYRAZLI.....</b>	<b>123-130</b>
<b>12. Variation of Electrical Resistivity During Magnetic Field-Induced Martensitic Transformation in Vanadium added NiMnSnB alloys</b> <i>Vanadyum Eklenecek NiMnSnB Alaşımalarında Manyetik Alan Kaynaklı Martensitik Dönüşüm Sırasında Elektrik Direncinin Değişimi</i> <b>Gökhan KIRAT.....</b>	<b>131-138</b>
<b>13. An NCA-based Hybrid CNN Model for Classification of Alzheimer's Disease on Grad-CAM- enhanced Brain MRI Images</b> <i>Grad-CAM ile İyileştirilmiş Beyin MRI Görüntülerinde Alzheimer Hastalığının Sınıflandırılması için NCA tabanlı Hibrit CNN Modeli</i> <b>Feyza ALTUNBEY ÖZBAY, Erdal ÖZBAY.....</b>	<b>139-155</b>
<b>14. Performance Comparison of Biology based Metaheuristics Optimization Algorithms using Unimodal and Multimodal Benchmark Functions</b> <i>Tek Modlu ve Çok Modlu Kıyaslama Fonksiyonlarını Kullanan Biyoloji Tabanlı Metasezgisel Optimizasyon Algoritmalarının Performans Karşılaştırması</i> <b>Fatma BELLİ, Harun BİNGÖL.....</b>	<b>157-167</b>
<b>15. 3-D Printed Dual-Band Frequency Selective Surfaces for Radome Applications</b> <i>Radom Uygulamaları için 3-B Baskılı Çift Bantlı Frekans Seçici Yüzeyler</i> <b>Mete BAKIR.....</b>	<b>169-176</b>
<b>16. Molecular Docking Study on Interaction of Polyvinyl Alcohol (PVA) with Group IA Bacteriocin</b> <i>Polivinil Alkolün (PVA) Grup IA Bakteriyosiniyle Etkileşimi Üzerine Moleküler Docking Çalışması</i> <b>Nihan ÜNLÜ, Arzu ÖZGEN, Canan Aksu CANBAY.....</b>	<b>177-182</b>
<b>17. A Hybrid Model Based on Deep Features and Ensemble Learning for the Diagnosis of COVID-19: DeepFeat-E</b> <i>COVID-19 Teşhisi için Derin Özniteliklere ve Topluluk Öğrenmeye Dayalı Hibrit bir Model: DeepFeat-E</i> <b>Berivan ÖZAYDIN, Ramazan TEKİN.....</b>	<b>183-198</b>
<b>18. The Effect of The Number of Reference Points and Distribution on Coordinate Transformation in Underground Mining Measurements</b> <i>Yeraltı Madencilik Ölçümlerinde Referans Noktası Sayısı ve Dağılımının Koordinat Dönüşümüne Etkisi</i> <b>Levent TAŞÇI, Hacı Sait ARSLAN.....</b>	<b>199-206</b>
<b>19. Electroencephalogram-Based Major Depressive Disorder Classification Using Convolutional Neural Network and Transfer Learning</b> <i>Konvolüsyonel Sinir Ağı ve Transfer Öğrenme Kullanılarak Elektroensefalogram Tabanlı Majör Depresif Bozukluk Sınıflandırması</i> <b>Şüheda KAYA, Burak TAŞÇI.....</b>	<b>207-214</b>



20. **BP19: An Accurate Audio Violence Detection Model Based On One-Dimensional Binary Pattern**  
*BP19: Tek Boyutlu İkili Modele Dayalı Doğru Bir Sesli Şiddet Tespit Modeli*  
Arif Metehan YILDIZ, Tugce KELEŞ, Kubra YILDIRIM, Sengul DOGAN, Turker TUNCER..... 215-222
21. **Effect on Thermal and Structural Properties of Element Content in CuAlBe Shape Memory Alloys Irradiated with a Constant Gamma Radiation Dose**  
*Sabit Gama Radyasyon Dozu ile Işınlanan CuAlBe Şekil Hatırlamalı Alaşımlarda Element İçeriğinin Termal ve Yapısal Özellikleri Üzerine Etkisi*  
Ş. Nevin BALO, Abdulvahap ORHAN..... 223-231
22. **Predicting the Height of Individuals with Machine Learning Methods by Considering Non-Genetic Factors**  
*Genetik Olmayan Faktörler Ele Alınarak Bireylerin Boyunun Makine Öğrenmesi Yöntemleri ile Tahmini*  
Osman ALTAY, Tuğba ÇELİKİTEN, Tuba AKBAŞ, Hüseyin Yasin DÖNMEZ..... 233-241
23. **A Hierarchical Reinforcement Learning Framework for UAV Path Planning in Tactical Environments**  
*Taktik Ortamlarda İHA Güzergahı Planlama Amaçlı Hiyerarşik Pekiştirmeli Öğrenmeye Dayalı bir Çerçeve*  
Mahmut Nedim ALPDEMİR..... 243-259
24. **CDIEA: Chaos and DNA Based Image Encryption Algorithm**  
*CDIEA: Kaos ve DNA Tabanlı Görüntü Şifreleme Algoritması*  
Ali ARI..... 261-273
25. **Deep Transfer Learning-Based Broken Rotor Fault Diagnosis For Induction Motors**  
*Asenkron Motor Kırık Rotor Çubuğu Arızasının Derin Transfer Öğrenme Tabanlı Teşhisi*  
Fırat DİŞLİ, Mehmet GEDİKPINAR, Abdulkadir ŞENGÜR..... 275-290



## FRF Based Structural Modification of a Mechanical System by Adding Masses and Utilizing the Grey Wolf Optimization Technique

Murat ŞEN<sup>1\*</sup>, Osman YİĞİD<sup>2</sup>, Orhan ÇAKAR<sup>3</sup>

<sup>1,2,3</sup> Department of Mechanical Engineering, Engineering Faculty, Firat University, Elazığ, Türkiye  
<sup>\*1</sup> msen@firat.edu.tr, <sup>2</sup> oyigid@firat.edu.tr, <sup>3</sup> cakaro@firat.edu.tr

(Geliş/Received: 25/07/2022;

Kabul/Accepted: 24/01/2023)

**Abstract:** Resonance and anti-resonance frequencies are important parameters that determine the dynamic behavior of mechanical systems. Changes in these parameters, which depend on the system's physical properties such as mass and stiffness, also affect the system's dynamic behavior. Finding the necessary structural modifications to adjust the resonance and anti-resonance frequencies of a system to the desired values is a study area of inverse structural modification. In this study, an inverse structural modification method for one and multi-rank modifications is presented. With the presented method some resonance or anti-resonance frequencies of mechanical systems can be shifted to prescribed values by calculating the necessary modifications. The presented method is based on Sherman-Morrison (SM) formula and uses the frequency response functions (FRF) of the original system directly. For one modification an exact solution is obtained on the other hand for two or more modifications some nonlinear set of equations has to be solved. A meta-heuristic optimization technique known as Grey Wolf Optimizer (GWO) is applied for the solution of the nonlinear equations. The method is applied to a six-degrees-of-freedom mass-spring system. Some resonance and anti-resonance frequencies in the frequency bandwidth of the system are selected as target frequencies. The necessary modification masses are calculated to match these frequencies. After applying the calculated masses to the system the target frequencies are obtained successfully.

**Key words:** Frequency response function, frequency shifting, grey wolf optimization, structural modification.

### Bir Mekanik Sistemin Kütle Eklenerek ve Bozkurt Optimizasyon Tekniği Kullanılarak FTF Tabanlı Yapısal Değişikliği

**Öz:** Rezonans ve ters rezonans frekansları, mekanik sistemlerin dinamik davranışını belirleyen önemli parametrelerdir. Sistemin kütle ve rijitlik gibi fiziksel özelliklerine bağlı olan bu parametrelerin değişimi sistemin dinamik davranışını da değiştirmektedir. Bir sistemin rezonans ve ters rezonans frekanslarını istenilen değerlere ayarlamak için gerekli yapısal değişiklikleri bulmak, ters yapısal değişiklik çalışma alanının konusudur. Bu çalışmada, tek ve çoklu değişiklikler için bir ters yapısal değişiklik yöntemi sunulmuştur. Bu yöntem ile mekanik sistemlerin bazı rezonans ve ters rezonans frekansları gerekli değişiklikler hesaplanarak istenilen değerlere kaydırılabilir. Sunulan yöntem Sherman-Morrison (SM) formülüne dayalı olup doğrudan orijinal sistemin frekans tepki fonksiyonlarını (FTF) kullanmaktadır. Tek bir değişiklik için kesin bir çözüm elde edilebilmektedir diğer yandan iki veya daha fazla değişiklik için bazı doğrusal olmayan denklem takımlarının çözülmesi gerekmektedir. Doğrusal olmayan bu denklemlerin çözümü için bu çalışmada, meta-sezgisel bir optimizasyon tekniği olan bozkurt optimizasyonu kullanılmıştır. Yöntem kütle ve yaylardan oluşan altı serbestlik dereceli bir sisteme uygulanmıştır. Sistemin frekans aralığında bazı rezonans ve ters rezonans frekansları hedef frekanslar olarak seçilmiştir. Bu frekansları yakalamak için gerekli kütle değişiklikleri hesaplanmıştır. Bu değişikliklerin uygulanmasıyla hedeflenen frekanslar başarılı bir şekilde elde edilmiştir.

**Anahtar kelimeler:** Frekans tepki fonksiyonu, frekans kaydırma, bozkurt optimizasyonu, yapısal değişiklik.

#### 1. Introduction

Resonance frequencies (natural frequencies) and anti-resonance frequencies are very important parameters that determine the dynamic behavior of mechanical systems. If a mechanical system is excited with a harmonic force with the same value as any of its natural frequencies, a resonance phenomenon occurs and the structure vibrates at high amplitudes. This situation can cause destructive effects on systems. For all that, at the anti-resonance frequencies, a certain point on the system does not vibrate against the harmonic force applied from a certain location of the system. For this reason, designers should consider these features while designing, manufacturing, and improving dynamic systems.

Resonance frequencies are the general (global) feature of the system. Therefore, they appear in all FRF graphs of the system, except for the nodal points. Anti-resonance frequencies are local features and they may not be seen

\* Corresponding author: [msen@firat.edu.tr](mailto:msen@firat.edu.tr). ORCID: <sup>1</sup> 0000-0002-3063-5635, <sup>2</sup> 0000-0002-1798-1250, <sup>3</sup> 0000-0001-6947-3875

in every FRF. In Figure 1 a point FRF and a transfer FRF are illustrated. It can be said from the graph that the resonance frequencies are seen in both points FRFs (the response and the excitation at the same location) and transfer FRFs (the response and the excitation at different locations), while the anti-resonance frequencies do not necessarily occur in transfer FRFs however they occur after every single resonance frequency in point FRFs.

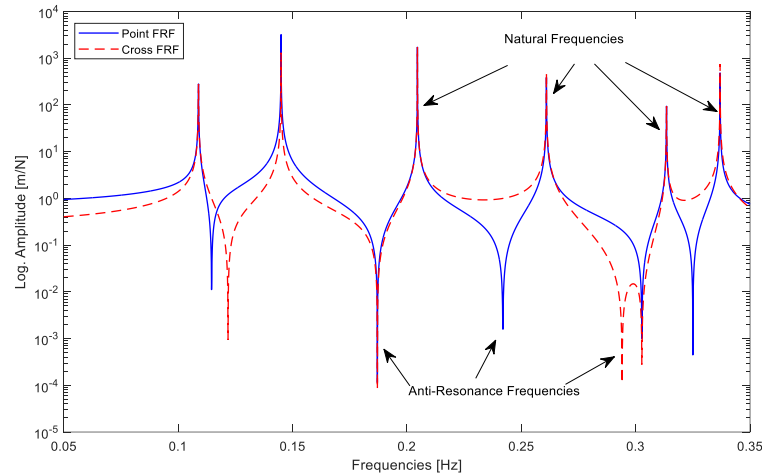


**Figure 1.** Point and cross FRFs of six degrees of freedom mass-spring system

The dynamic properties of a system, such as its natural frequencies, anti-resonance frequencies, and mode shapes depend on the physical properties of the system, such as mass, stiffness, and damping. When these physical properties of the system change, its dynamic behavior also changes. The relationship between the physical parameters and their effects on the dynamic characteristics is examined in the scope of the structural modification. Numerous studies e.g. mass-spring modification [1-4], rotational receptance modification [5], beam modification [6-9], transfer receptance based modification [10], and pole-zero cancellation [11] have been made over the last decades. The process of determining the dynamic properties of the modified system as a result of these structural modifications is called direct structural modification. The process of finding the modifications that must be made in the existing system to provide the desired dynamic properties is called inverse structural modification.

In structural modification applications, the results obtained from the finite element (FE) solution or when the FE model is difficult to form, the results obtained by the experimental modal analysis are used. In addition, FRFs are used directly in many studies [12-16]. FRFs can be obtained from numerical solutions or they can be obtained by measuring over physical structure in experimental applications. Experimental FRFs are preferred by many researchers in structural modification applications [17-18]. Researchers have been trying to find effective methods by continuing their studies for years on direct and inverse structural modifications. Tsuei and Yee [19] have presented a simple and effective method for inverse structural modification that uses FRFs of the system by changing the mass and stiffness values on an undamped system. They continued to work similarly on the damped systems to shift the damped natural frequencies to the desired values [20]. Ouyang and Zhang [21] have carried out structural modifications on two different mass-spring systems that are connected sequentially and complexly. They used two different methods in their work. One of the methods is based on the use of orthogonal similarity transformation and the real symmetric matrix obtained by using the eigenvalues planned to make structural modifications with the mass and stiffness matrices of the system transformed into the upper triangular matrix. In the other method, the new matrix to be created for structural modification is obtained by minimizing the difference between the desired eigenvalues and the isospectral matrices. Since the obtained changes are made in the specified region, it is suitable for structural modifications in the masses and springs in the desired location on the system and can be easily applied to physical systems. Liu et al. [22] presented a method based on the principle of using additional mass-spring systems for an undamped physical system and using FRFs of the system directly. Although the original system has not been changed and there are advantageous aspects of the method, the degree of freedom of the system increases due to the added masses. Mottershead and Ram [23] conducted a study on vibration isolation using the structural modification technique. Ouyang et al. [24] conducted a structural modification study using the FRFs of a dynamic system. They have made some limiting approaches to make the structural modification within the range of changes determined in terms of applicability and cost. Since the method they

proposed resolves the change to be made within a specified range and provides optimum value, it can be easily applied to real physical systems.

In many structural modification studies, it is seen techniques based on Sherman-Morrison (SM) formula [25] are used. The SM is a formula used to calculate the inverse of a modified matrix by using the inverse of the original matrix and the modifications and can be used effectively in structural modification problems based on FRFs. Çakar [26] proposed a method based on SM to calculate the stiffness of a spring to preserve a specified natural frequency value after adding a known mass on any specified location on a cantilever beam. In a different study [27], he used this method to prevent the desired natural frequency of the system from changing after the mass modification. In this study, a single frequency was taken into account and a successful result was obtained with an additional spring added between the structure and the ground in a chosen coordinate. However, as aircraft and spacecraft, it is impossible to make modifications by using grounded springs. Considering this situation, Hüseyinoğlu and Çakar [28] have kept the location of more than one frequency value fixed by adding more than one spring between two generalized coordinates instead of a grounded spring. Later, Çakar [29-30] presented studies including experimental applications related to shifting a certain number of natural frequencies of a system to desired values with mass modification. With the results obtained, it has shown that the proposed method is quite effective in calculating the masses required to shift one and more natural frequencies to desired values. Also, Çakar [31], Şen, and Çakar [32] proposed the same method to shift one and more anti-resonance frequencies to desired values successfully.

In this study, the resonance and anti-resonance frequencies of a six-degrees-of-freedom mass-spring system have been shifted to desired values with mass modifications based on the SM formula without the need for any matrix inversion. With the presented study, it can be said SM based-structural modification method can be used effectively on mechanical systems to solve some vibration problems. An exact solution is obtained for one modification, and for two or more modifications, some nonlinear set of equations is obtained. These nonlinear sets of equations should be solved numerically. There are many methods for solving nonlinear equation sets in literature. Recently, meta-heuristic optimization techniques have been widely used for this purpose e.g. Bee Colony Ant Colony and Particle Swarm [33], Spider [34, 35], and Grey Wolf [36] optimization techniques. In this study, GWO is used to solve the obtained set of nonlinear equations.

This paper is organized as follows: In Section 2, the mathematical formulations where the relevant equations used for numerical simulations are presented. In Section 3, numerical results for shifting both resonance and anti-resonance frequencies are given. The results are tabulated for the number of modifications and different modification coordinates. Finally, Section 4, presents the conclusions of this work.

## 2. Structural Modification Based on SM Formula

The SM is a formula for calculating the inverse of the new matrix resulting from a change to an existing matrix, using the inverse of the original matrix and modification vectors as given in Equation 1.

$$[A^*]^{-1} = [A]^{-1} - \frac{([A]^{-1}\{u\})(\{v\}^T[A]^{-1})}{1+\{v\}^T[A]^{-1}\{u\}} \quad (1)$$

Here,  $[A]$  is a non-singular square matrix. If the inverse of this matrix is available or known, the inverse of the modified  $[A^*]$  matrix resulting from a change to this matrix can be calculated using the inverse of  $[A]$  and the modification vectors. The change is expressed as the product of two vectors as follows.

$$[\Delta] = \{u\}\{v\}^T \quad (2)$$

Also, for a dynamic system, the dynamic stiffness matrix  $[Z]$  and the modified dynamic stiffness matrix  $[Z^*]$  resulting from the modification of  $[AZ]$  can be expressed as follows.

$$[Z^*] = [Z] + [\Delta Z] \quad (1)$$

Here, the modification in dynamic stiffness can be expressed as the product of two vectors as follows.

$$[\Delta Z] = \{u\}\{v\}^T \quad (4)$$

The inverse of the new matrix resulting from a modification in the dynamic stiffness matrix can be expressed in the form of the SM formula as in Equation 5, using the inverse of the original matrix and the modifications.

$$[Z^*]^{-1} = [Z]^{-1} - \frac{([Z]^{-1}\{u\})(\{v\}^T[Z]^{-1})}{1+\{v\}^T[Z]^{-1}\{u\}} \quad (5)$$

Considering the relationship ( $\alpha=Z^{-1}$ ) between the receptance and the dynamic stiffness, the FRFs of a modified system  $[\alpha^*]$  can be calculated by using the FRFs of the original system  $[\alpha]$  and the modifications  $\{u\}$ ,  $\{v\}$  without the need for any matrix inversion as in Equation 6.

$$[\alpha^*] = [\alpha] - \frac{([\alpha]\{u\})(\{v\}^T[\alpha])}{1+\{v\}^T[\alpha]\{u\}} \quad (6)$$

In Equation 6, the receptance type FRF matrix contains all elements in symmetric and square form. However, measuring the entire FRF matrix experimentally is a very laborious task. Therefore, Equation 6 given above can also be expressed with the active (response, excitation, and modification) coordinates only [29]. In this case, for a single mass modification, the following equation can be written for only the active  $p$  (response),  $q$  (excitation), and  $r$  (modification) coordinates for a specified element of the FRF matrix in the frequency range of interest of the modified system [13, 14].

$$\alpha_{pq}^* = \frac{\alpha_{pq} - \omega^2 \delta m (\alpha_{rr} \alpha_{pq} - \alpha_{pr} \alpha_{rq})}{1 - \omega^2 \delta m \alpha_{rr}} \quad (7)$$

Here,  $\delta m$  is the modification mass and  $\omega$  is the frequency in (rad/s). For Equation 7 the  $r^{th}$  elements of the modification vectors,  $\{u\}$  and  $\{v\}$  are  $u_r=1$  and  $v_r=-\omega^2 \delta m$  respectively and other elements are zero.

The resonance frequencies represent the poles of a system, and the anti-resonance frequencies represent zeroes. Based on this statement, if the denominator of Equation 7 is equated to zero, it is expected that peaks will form at these frequencies of the modified system. Therefore, the denominator of Equation 7 must be zero for the corresponding frequency value for the receptance of a modified system by adding a mass to the coordinate  $r$  to have a resonance frequency at a frequency of  $\omega_s$ .

$$1 - \omega^2 \delta m \alpha_{rr} = 0 \quad (8)$$

Using Equation 8, the modification mass that needs to be applied to the  $r^{th}$  coordinate for this modification can be easily calculated with the following equation as an exact solution.

$$\delta m = \frac{1}{\omega^2 \alpha_{rr}} \quad (9)$$

Similarly, if the numerator of Equation 7 is equated to zero, it is expected that reverse peaks will form at the FRFs for these frequencies of the modified system. Therefore, the numerator of Equation 7 must be zero for the corresponding frequency value for the receptance of a modified system by applying a modification mass to the coordinate  $r$  to have an anti-resonance frequency at a frequency  $\omega_s$ .

$$\alpha_{pq} - \omega_s^2 \delta m (\alpha_{rr} \alpha_{pq} - \alpha_{pr} \alpha_{rq}) = 0 \quad (10)$$

By using Equation 10, the required modification mass to be applied to the coordinate  $r$  for this modification can be easily calculated with the following equation as an exact solution.

$$\delta m = \frac{\alpha_{pq}}{\omega_s^2 (\alpha_{rr} \alpha_{pq} - \alpha_{pr} \alpha_{rq})} \quad (p, q \neq r) \quad (11)$$

In case of more than one modification, this formula can be applied sequentially. In this case, if  $n$  number of mass modifications are handled then this formula can be rewritten as follows.

$$[\alpha_a^i] = [\alpha_a^{i-1}] - \frac{-\omega^2 m^{(i)} ([\alpha_a^{i-1}]\{u_i\})(\{v_i\}^T [\alpha_a^{i-1}])}{1 - \omega^2 m^{(i)} \{v_i\}^T [\alpha_a^{i-1}]\{u_i\}} \quad (i = 1, 2, \dots, n) \quad (12)$$

For a single FRF, Equation 12 can be written as follows.

$$\alpha_{pq}^i = \frac{\alpha_{pq}^{i-1} - \omega^2 m^{(i)} (\alpha_{rr}^{i-1} \alpha_{pq}^{i-1} - \alpha_{pr}^{i-1} \alpha_{rq}^{i-1})}{1 - \omega^2 m^{(i)} \alpha_{rr}^{i-1}} \quad (13)$$

If the system under consideration wanted to have  $n$  number of resonance frequencies at the frequencies of  $\omega_{s1}, \omega_{s2}, \dots, \omega_{sn}$ , this can be achieved sequentially with  $n$  mass modifications. For this, the FRFs of the last system obtained after mass modifications must go to infinity at these frequency values. In this case, for  $i=n$  in Equation 13 and the denominator of the equation must be equal to zero for each frequency value. Thus  $n$  number of interconnected nonlinear equations are obtained for  $n$  modifications on the system as follows.

$$\begin{aligned} F_1(m^i) &= 1 - \omega_{s1}^2 m^{(n)} \alpha_{rr}^{n-1}(\omega_{s1}) = 0 \\ F_2(m^i) &= 1 - \omega_{s2}^2 m^{(n)} \alpha_{rr}^{n-1}(\omega_{s2}) = 0 \\ \dots &\dots \dots \dots \dots \dots \dots \dots \\ F_n(m^i) &= 1 - \omega_{sn}^2 m^{(n)} \alpha_{rr}^{n-1}(\omega_{sn}) = 0 \end{aligned} \quad (14)$$

In the same way, to shift  $n$  number of anti-resonance frequencies,  $n$  number of interconnected nonlinear sets of equations can be expressed for  $n$  modifications on the system as follows.

$$\begin{aligned} F_1(m^i) &= \alpha_{pq}^{n-1}(\omega_{s1}) - \omega_{s1}^2 m^{(n)} \left( \alpha_{rr}^{n-1}(\omega_{s1}) \alpha_{pq}^{n-1}(\omega_{s1}) - \alpha_{pr}^{n-1}(\omega_{s1}) \alpha_{rq}^{n-1}(\omega_{s1}) \right) = 0 \\ F_2(m^i) &= \alpha_{pq}^{n-1}(\omega_{s2}) - \omega_{s2}^2 m^{(n)} \left( \alpha_{rr}^{n-1}(\omega_{s2}) \alpha_{pq}^{n-1}(\omega_{s2}) - \alpha_{pr}^{n-1}(\omega_{s2}) \alpha_{rq}^{n-1}(\omega_{s2}) \right) = 0 \\ \dots &\dots \dots \dots \dots \dots \dots \dots \\ F_n(m^i) &= \alpha_{pq}^{n-1}(\omega_{sn}) - \omega_{sn}^2 m^{(n)} \left( \alpha_{rr}^{n-1}(\omega_{sn}) \alpha_{pq}^{n-1}(\omega_{sn}) - \alpha_{pr}^{n-1}(\omega_{sn}) \alpha_{rq}^{n-1}(\omega_{sn}) \right) = 0 \end{aligned} \quad (15)$$

Equations 14-15 contain unknown nested mass values. By solving this set of equations numerically, the necessary modification mass values can be calculated. It should be noted here that each modified FRF needed in Equations 14-15 can be obtained from Equation 13. To solve these equations, the GWO technique was used in this study. This technique is developed and well described in the reference [36] which uses the social hierarchy, encircling prey, hunting, attacking, and searching for prey of the wolves. So, detailed mathematical formulations for this optimization technique are not given in this study.

### 3. Numerical Applications

In this section, the applications for shifting some natural frequencies and some anti-resonance frequencies of a six-degree-of-freedom system consisting of masses and springs, which are frequently used in the literature [29] to the desired values are given respectively.

Numerical applications have been performed on the system given in Figure 2, all masses are considered as 1 kg and all springs are equal to 1 N / m.

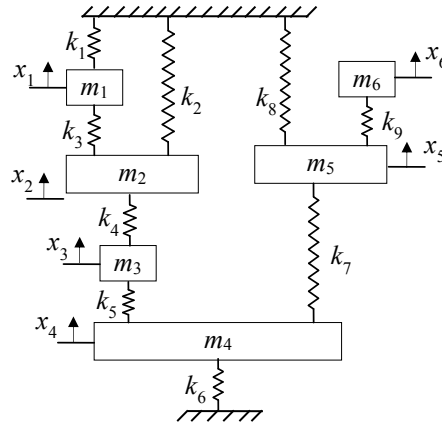
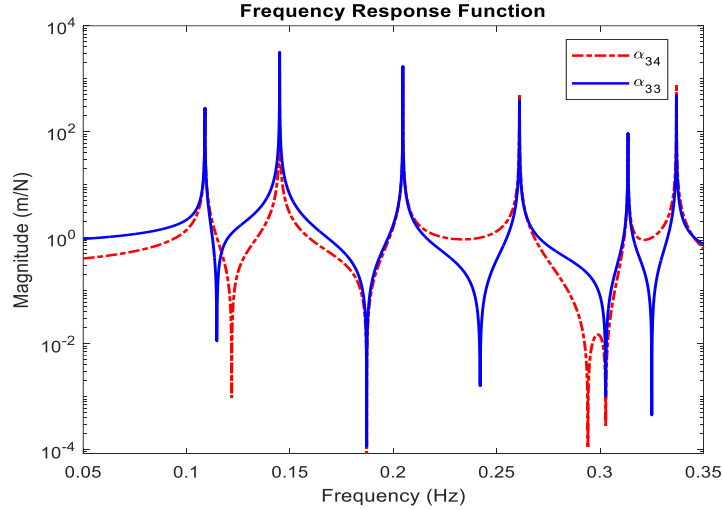


Figure 2. Six degrees of freedom mass-spring system [29]

In the applications, it is aimed to obtain the desired frequencies by making mass modifications on the selected FRFs shown in Figure 3.

The FRFs of the original system were obtained in the 0.0000-0.3500 Hz frequency bandwidth at intervals of 0.0001 Hz and for this system the FRFs of  $\alpha_{33}$  and  $\alpha_{34}$  are illustrated in Figure 3 together.



**Figure 3.** The FRFs of the original system ( $\alpha_{33}$  and  $\alpha_{34}$ ).

In addition, the natural frequencies and eigenvectors of the system are given in Table 1.

**Table 1.** The natural frequencies, anti-resonance frequencies for  $\alpha_{33}$  and eigenvectors of the original system.

Modes	1	2	3	4	5	6
Natural Frequencies (Hz)	0.1089	0.1450	0.2046	0.2610	0.3135	0.3369
Anti-resonance Frequencies $\alpha_{33}$ (Hz)	0.1146	0.1871	0.2420	0.3027	0.3250	-
Eigenvectors	0.0962	-0.4027	0.7451	-0.3310	-0.3761	-0.1496
	0.1473	-0.4712	0.2588	0.2280	0.7068	0.3711
	0.2769	-0.6199	-0.3965	0.4019	-0.2455	-0.4001
	0.2769	-0.2541	-0.3965	-0.5049	-0.2455	0.6216
	0.4242	0.0685	-0.1377	-0.5590	0.4613	-0.5206
	0.7973	0.4027	0.2110	0.3310	-0.1602	0.1496

### 3.1. Mass Modifications for Shifting Natural Frequencies

As mentioned earlier, the proposed method can be used to shift a single natural frequency or a single anti-resonance frequency to a desired value with a single mass modification as an exact solution. The main problem here is to shift more than one natural frequency or anti-resonance frequency to the desired values with multiple mass modifications.

For shifting the natural frequencies to the desired values, the objective functions can be expressed as follows.

$$F_{obj} = |F_i| \quad (i = 1, 2, \dots, n) \quad (16)$$

A number of grey wolves and the iteration were chosen as 50 and 500 respectively. Also, the constraints were chosen for the modification mass values as follows.

$$m_{min} < m_i < m_{max} \quad (i = 1, 2, \dots, n) \quad (17)$$

For all masses lower and upper bounds are chosen as  $m_{min} = -1$  and  $m_{max} = 1$  respectively.



In Table 2, applications of some modifications for desired natural frequencies with some selected coordinates are given. Calculated masses and obtained natural frequencies by using these applied mass values are given for both two and three modification cases.

**Table 2.** The natural frequencies of the system after multi-mass modifications.

Desired Frequencies	Modification Coordinates	Calculated Masses	Natural Frequencies of Modified System					
0.1840 0.3030	1	0.1964	0.1027	0.1262	<b>0.1840</b>	0.2503	<b>0.3030</b>	0.3284
	3	0.8786						
0.1000 0.2000	1	0.1077	0.1043	0.1395	<b>0.1840</b>	0.2366	<b>0.3030</b>	0.3184
	4	0.9162						
0.1000 0.2000	2	0.2174	<b>0.1000</b>	0.1411	<b>0.2000</b>	0.2274	0.2861	0.3187
	5	0.9037						
0.0915 0.2015 0.3015	1	0.0663	<b>0.1000</b>	0.1419	<b>0.2000</b>	0.2571	0.3113	0.3359
	6	0.2759						
0.0915 0.2015 0.3015	1	-0.2709	<b>0.0915</b>	0.1374	<b>0.2015</b>	0.2538	<b>0.3015</b>	0.3317
	4	0.7015						
0.1000 0.2000 0.3000	6	0.5440						
	3	0.2263	<b>0.1000</b>	0.1375	<b>0.2000</b>	0.2329	<b>0.3000</b>	0.3216
0.1000 0.2000 0.3000	5	0.5289						
	6	0.1079						

The desired frequencies in the frequency range and the modification coordinates, are selected randomly. The negative calculated mass value means the mass has to be removed from the system. According to the results in Table 2, the desired resonance frequencies are obtained successfully.

Some FRFs of the modified systems for the applications given in Table 2 are given in Figures 4-5 below.

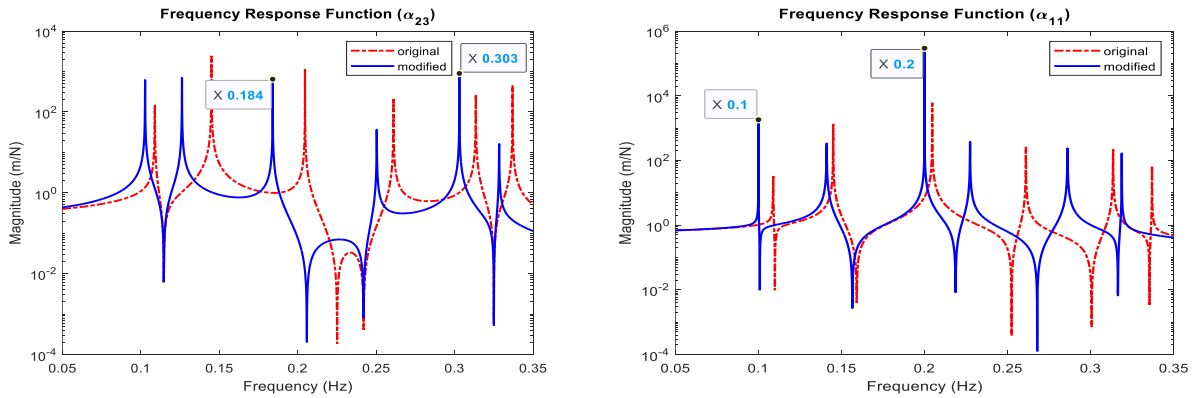


**Figure 4.** The FRFs of the original and the modified system for two desired resonance frequencies

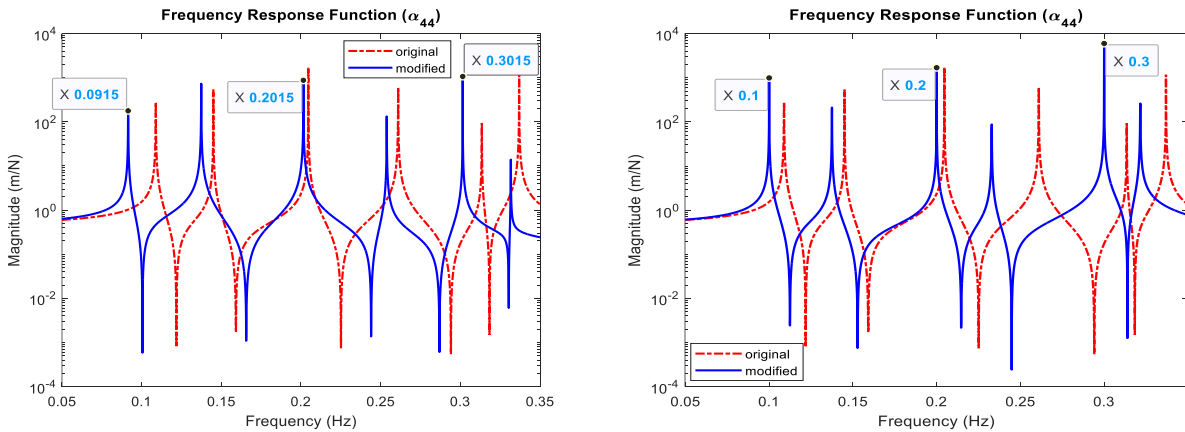


**Figure 5.** The FRFs of the original and the modified system for three desired resonance frequencies

As seen in Figures 4-5, the desired frequencies were obtained successfully after applying the calculated mass values to the system.

### 3.2. Mass Modifications for Shifting Anti-resonance Frequencies

In Table 3, applications of some modifications for desired anti-resonance frequencies with some selected coordinates are given. Calculated masses and obtained anti-resonance frequencies by using these applied mass values are given for both two and three modification cases. The modifications were made for  $\alpha_{33}$  and the modification coordinates were selected randomly.

**Table 3.** The anti-resonance frequencies of the system after multi-mass modifications.

Desired Frequencies	Modification Coordinates	Calculated Masses	Anti-resonance Frequencies of Modified System				
0.1700 0.2200	1	0.2816	0.1077	<b>0.1700</b>	<b>0.2200</b>	0.2943	0.2949
	5	0.6644					
	2	0.6092	0.1140	<b>0.1700</b>	<b>0.2200</b>	0.2627	0.3115
	4	0.3308					
0.1000 0.3000	1	0.0718	<b>0.1000</b>	0.1824	0.2367	<b>0.3000</b>	0.3227
	6	0.3927					
	4	0.0256	<b>0.1000</b>	0.1864	0.2367	<b>0.3000</b>	0.3227
	6	0.3927					
0.1000 0.2000 0.3000	1	-0.1790	<b>0.1000</b>	0.1905	<b>0.2000</b>	0.3127	<b>0.3000</b>
	4	0.0070					
	5	0.4401					
	6	0.3927					
0.1050 0.2050 0.3050	2	-0.0201	<b>0.1050</b>	0.1876	<b>0.2050</b>	0.2606	<b>0.3050</b>
	4	0.3805					
	5	0.8688					

Also, some FRFs of the modified systems for the applications of shifting anti-resonance frequencies given in Table 3 are illustrated in Figure 6 and Figure 7 below.

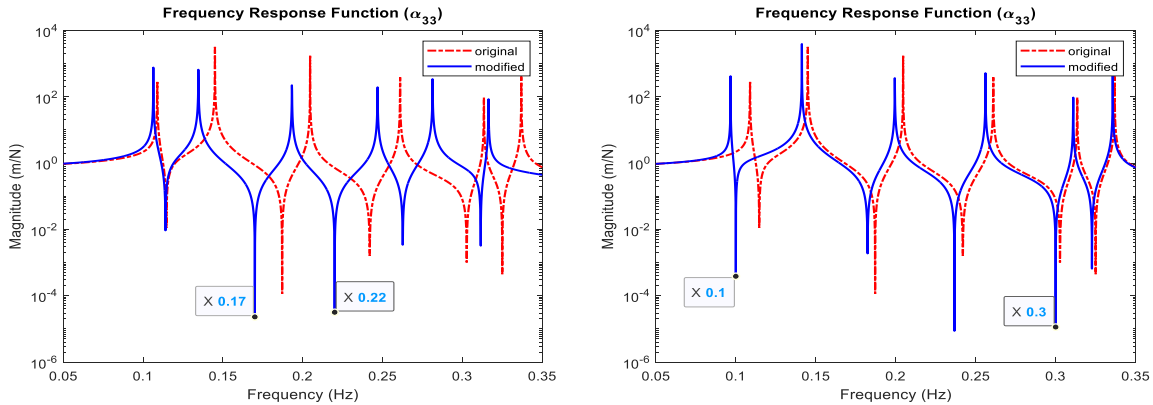


**Figure 6.** The FRFs of the original and the modified system for two desired anti-resonance frequencies

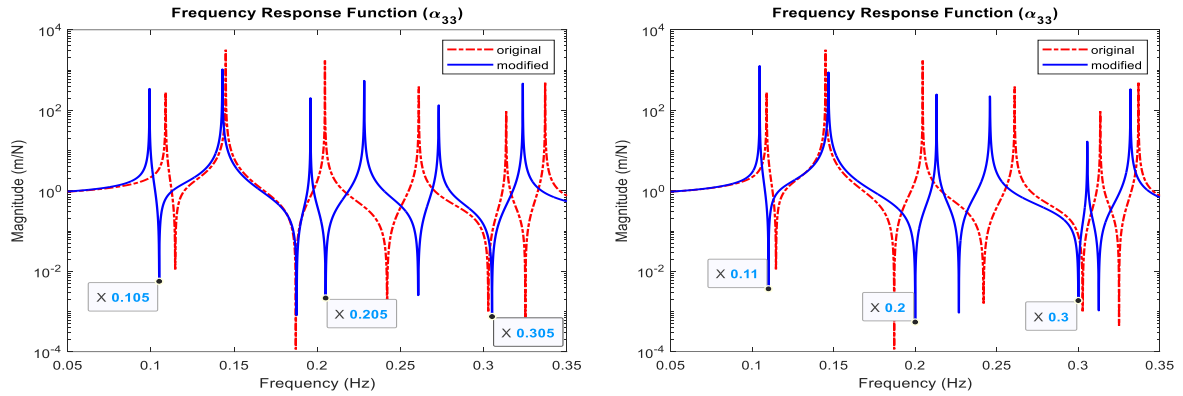


Figure 7. The FRFs of the original and the modified system for three desired anti-resonance frequencies

#### 4. Results and Discussion

In this study, to contribute to the solution of vibration problems, a method is presented for shifting one or more natural frequencies and anti-resonance frequencies of mechanical systems to desired values by making mass modifications in specified coordinates and its validity is proven by some numerical applications. The proposed method in the study is based on the SM formula known from mathematics and calculates the required masses directly using the FRFs of the system. In this respect, it is quite suitable for practical applications as the FRFs can be obtained from real mechanical systems with modal tests. An equation with an exact solution is obtained in the case of a single frequency shifting. In case of shifting more than one frequency, the nonlinear equation sets consisting of equations as many as the number of frequencies to be shifted must be solved numerically. In this study, these nonlinear equation sets are solved by using the GWO technique. The presented method is applied to a six-degrees-of-freedom mass-spring system. The frequency-magnitude FRF graphs are obtained within a bandwidth containing all the resonance frequencies. In this bandwidth, some target frequencies are matched with calculated mass modifications successfully. The results are given with tables and FRF graphs. According to the results gained from the numerical applications, the presented method can be said to be very effective and applicable to physical systems. In this presented study, for multi-rank modifications, the number of modifications and target frequencies are considered the same. In this case, non-linear equation sets combined with equations with the same number of modifications are obtained for both resonance and anti-resonance frequency shifting. But, it can also be possible for a different number of modifications and equations as under-determined or over-determined equation sets. Also, an optimization study of coordinates and modification type as stiffness and/or mass can be used for obtaining more feasible results for future studies.

#### References

- [1] Braun SG, Ram YM. Modal modification of vibrating systems: some problems and their solutions. *Mech Syst Signal Process* 2001; 15(1): 101–119.
- [2] Kyprianou A, Mottershead JE, Ouyang H. Assignment of natural frequencies by an added mass and one or more springs. *Mech Syst Signal Process* 2004; 18(2): 263–289.
- [3] Ram YM. *Dynamic Structural Modification*. The Shock and Vibration Digest 2000; 32(1): 11-17.
- [4] Sivan DD, Ram YM. Mass and stiffness modifications to achieve desired natural frequencies. *Commun Numer Methods Eng*. 1996; 12(9): 531–542.
- [5] Mottershead JE, Kyprianou A, Ouyang H. Structural modification. Part 1: Rotational receptances. *J Sound Vib* 2005; 284(1–2): 249–265.
- [6] Kyprianou A, Mottershead JE, Ouyang H. Structural modification. Part 2: Assignment of natural frequencies and anti-resonances by an added beam *J Sound Vib* 2005; 284(1–2): 267–281.
- [7] Bucher I, Braun S. The Structural modification inverse problem: An exact solution. *Mech Syst Signal Process* 1993; 7(3): 217-238.
- [8] Zhu J, Mottershead JE, Kyprianou A. An inverse method to assign receptances by using classical vibration absorbers. *J Vib Control* 2009; 15(1): 53–84.
- [9] Mottershead JE, Mares C, Friswell MI. An inverse method for the assignment of vibration nodes. *Mech Syst Signal Process* 2001; 15(1): 87-100.

- [10] Sanlitürk KY. An efficient method for linear and nonlinear structural modifications. Proceedings of ESDA 2002: 6th Biennial Conference on Engineering Systems Design and Analysis 2002; İstanbul, Turkey, 028-040.
- [11] Mottershead JE, Lallement G. Vibration nodes, and the cancellation of poles and zeros by unit-rank modifications to structures. *J Sound Vib* 1999; 222(5): 833-851.
- [12] Park YH, Park YS. Structural modification based on measured frequency response functions: an exact eigenproperties reallocation. *J Sound Vib* 2000; 237(3): 411-426.
- [13] Mottershead J. Structural modification for the assignment of zeros using measured receptances. *Journal of Applied Mechanics* 2001; 68(5): 791-798.
- [14] Prells U, Mottershead JE, Friswell MI. On pole-zero placement by unit-rank modification. *Mech Syst Signal Process* 2003; 17(3): 611-633.
- [15] Çakar O, Şanlıtürk KY. Elimination of suspension effects from measured frequency response functions. 9th International Research/Expert Conference, Trends in the Development of Machinery and Associated Technology 2005; Antalya, Turkey.
- [16] Mottershead JE. On the zeros of structural frequency response functions and their sensitivities. *Mech Syst Signal Process* 1998; 12 (5): 591-597.
- [17] Şanlıtürk KY, Çakar O. Noise elimination from measured frequency response functions. *Mech Syst Signal Process* 2005; 19 (3): 615-631.
- [18] Çakar O, Sanlitürk KY. Elimination of transducer mass loading effects from frequency response functions. *Mech Syst Signal Process* 2005; 19(1): 87-104.
- [19] Tsuei YG, Yee EKLA. method for modifying dynamic properties of undamped mechanical systems. *ASME J Dyn Syst Meas Control* 1989; 111: 403-408.
- [20] Yee EKL, Tsuei YG. Method for shifting natural frequencies of damped mechanical systems. *AIAA Journal* 1991; 29(11).
- [21] Ouyang H, Zhang J. Passive modifications for partial assignment of natural frequencies of mass-spring systems. *Mech Syst Signal Process* 2015; 50-51: 214-226.
- [22] Liu Z, Li W, Ouyang H, Wang D. Eigenstructure assignment in vibrating systems based on receptances. *Arch Appl Mech* 2015; 85(6): 713-724.
- [23] Mottershead JE, Ram YM. Inverse eigenvalue problems in vibration absorption: Passive modification and active control. *Mech Syst Signal Process* 2006; 20: 5-44.
- [24] Ouyang H, Richiedei D, Trevisani A, Zanardo G. A convex-constrained modification method based on receptances. *Mech Syst Signal Process* 2012; 27: 397-409.
- [25] Sherman J, Morrison WJ. Adjustment of an inverse matrix corresponding to a change in one element of a given matrix. *Ann Math Stat* 1950; 21 (1): 124-127.
- [26] Çakar O. Bir konsol kirişin belirli bir doğal frekansını değiştirmeksizin kütle ve ay eklenmesi. 14. Ulusal Makine Teorisi Sempozyumu (UMTS 2009); 2009; Kıbrıs; 183-190.
- [27] Çakar O. Mass and stiffness modifications without changing any specified natural frequency of a structure. *J Vib Control* 2011; 17(5): 769-776.
- [28] Huseyinoglu M, Çakar O. Determination of stiffness modifications to keep certain natural frequencies of a system unchanged after mass modifications. *Arch Appl Mech* 2017; 87(10): 1629-1640.
- [29] Çakar O. Bir Sistemin Doğal Frekanslarının Kütle Eklenerek Kaydırılması Üzerine Bir Çalışma. 18. Ulusal Makine Teorisi Sempozyumu (UMTS 2017); 2017; Trabzon, Turkey; 380-386.
- [30] Çakar O. A method for shifting natural frequencies of a dynamic system to desired values with concentrated mass modifications. *J Vibroeng* 2018; 20(1): 1-12.
- [31] Çakar O. Mekanik bir sistemin bir ters rezonans frekansının kütle eklenerek değiştirilmesi. *Fırat Üniversitesi Mühendislik Bilimleri Dergisi* 2018; 30(2): 127-134.
- [32] Şen M, Çakar O. Bir sistemin ters rezonans frekanslarının kütle eklenerek istenilen değerlere kaydırılması. 19. Ulusal Makine Teorisi Sempozyumu (UMTS 2019); 2019; İskenderun, Turkey; 321-328.
- [33] Stojanovi I, Brajevi I, Stanimirovi PS, Kazakovtsev LA, Zdravev Z. Application of heuristic and metaheuristic algorithms in solving constrained weber problem with feasible region bounded by arcs. *Math Probl Eng* 2017: 1-13.
- [34] Cuevas E, Cienfuegos M. A new algorithm inspired in the behavior of the social-spider for constrained optimization. *Expert Systems with Applications* 2014; 41: 412-425.
- [35] Baydoğan C, Alatas B. Sentiment analysis in social networks using social spider optimization algorithm. *Technical Gazette* 2021; 28(6): 1943-1951.
- [36] Mirjalili S, Mirjalili SM, Lewis A. Grey Wolf Optimizer. *Adv Eng Software* 2014; 69: 46-61.

## Investigation of electronic and thermal properties of CoCrFe and CoCrFeNi high entropy alloys via extended tight-binding DFT computational method

Fatih Ahmet ÇELİK<sup>1\*</sup>, Sefa KAZANÇ<sup>2</sup>

<sup>1</sup> Physics Department, Faculty of Arts&Sciences, Bitlis Eren University, Bitlis, Turkey

<sup>2</sup> Mathematics and Science Education, Faculty of Education, Fırat University, Elazığ, Turkey

\*<sup>1</sup>facelik@beu.edu.tr, <sup>2</sup>skazanc@firat.edu.tr

(Geliş/Received: 18/08/2023;

Kabul/Accepted: 30/11/2023)

**Abstract:** In this study, CoCrFe and CoCrFeNi transition high entropy alloys (HEAs) are modelled by extended tight-binding density functional theory (DFT) method. Also, the geometric optimizations, band structures, density of states (DOS), thermodynamic properties and phonon dispersion curves of alloys are investigated to give a detailed information. The results show that the covalent d-d bonding between Fe-Cr is occurred because of strong metallic Cr-Fe interactions. The entropy (S) value increases gradually with the addition of Ni element to the CoCrFe alloy. The heat capacity ( $C_V$ ) increases due to the harmonic effect of the phonons in the range of 0-400 K and then, close to the classic limit at high temperatures with 0.82 J/mol.K and 0.94 J/mol.K for the CoCrFe and the CoCrFeNi. The alloy systems exhibit metallic properties because the DOS of the metals have a nonzero value at the Fermi energy level. Also, the addition of element Ni to the CoCrFe alloy system causes a decrease in phonon frequencies.

**Key words:** Simulation and modelling, metals and alloys, high entropy alloys, DFT method.

### Geniştirilmiş sıkı bağlanma DFT hesaplama yöntemi ile CoCrFe ve CoCrFeNi yüksek entropili alaşımlarının elektronik ve termal özelliklerinin incelenmesi

**Öz:** Bu çalışmada, CoCrFe ve CoCrFeNi yüksek entropili geçiş alaşımlar (HEA), genişletilmiş sıkı bağlanma yoğunluğu fonksiyonel teorisi (DFT) yöntemi ile modellenmiştir. Ayrıca, modellenen alaşımların geometrik optimizasyonları, bant yapıları, durum yoğunlukları (DOS), termodinamik özellikleri ve fonon dağılım eğrileri incelenmiştir. Sonuçlar Fe-Cr arasındaki kovalent d-d bağının, güçlü metalik Cr-Fe etkileşimleri nedeniyle oluştuğunu göstermektedir. CoCrFe alaşımına Ni elementinin eklenmesiyle entropi değeri kademeli olarak artmakla beraber ve 0-400 K aralığında fononların harmonik etkisine bağlı olarak ısı kapasitesi artmakta ve daha sonra CoCrFe için 0,82 J/mol.K ve 0,94 J/mol.K ile yüksek sıcaklıklarda klasik sınıra yaklaşmaktadır. CoCrFeNi. Alaşım sistemleri metalik özellikler sergiler çünkü metallerin DOS'ları Fermi enerji seviyesinde sıfırdan farklı bir değere sahiptir. Ayrıca CoCrFe alaşım sistemine Ni elementinin eklenmesi fonon frekanslarında azalmaya neden olmaktadır.

**Anahtar kelimeler:** Simülasyon ve modelleme, metaller ve alaşımlar, yüksek entropili alaşımlar, DFT yöntemi.

## 1. Introduction

In recent years, high entropy alloys (HEAs) have attracted extensive attentions of researchers because of their remarkable physical characteristics. Especially, HEAs including equiatomic multicomponent enables to develop in material design and engineering technologies [1-6]. Because HEAs with adding more different elements have important mechanical properties such as strength, ductility, corrosion resistance [1-10]. In this context, CoCrFeNi, CoCrFeMnNi, CoFeNi, CoCrNi HEAs have been investigated to understand the mechanical and structural properties of HEAs via experimental analysis [11-15]. Among them, Li et al. [10] introduced the non-equiatomic CoCrFeMnNi HEAs which exhibited excellent strength and ductility. Ji et al. [16] studied the CoCrCuFeNi for understanding the wear resistance properties. Zhang et al. investigated the deformation behaviors of a dual-phase FeCoCrNiMn alloy with transformation-induced plasticity effect [15]. The microstructures and mechanical properties of CoCrFeMnNi HEAs with addition of nitrogen alloying during different heat treatments were systematically studied by Xiong et al [7].

These experimental studies reveal that the addition of Fe and Ni elements to CoCr/CuMn can affect phase formations behavior, electronic properties, and mechanical characteristics of these alloys [1-5]. Although experimental studies are available on HEAs, there have been still needed powerful computational approaches to overcome difficulties arising from experimental studies. Hence, many researchers recently have studied on HEAs to reveal the mechanical properties and microstructure of HEAs by using computational methods. Sharma et al.

\* Corresponding author: facelik@beu.edu.tr. ORCID Number of authors: <sup>1</sup> 0000-0001-7860-5550, <sup>2</sup> 0000-0002-8896-8571

explored the structural phase transformations in AlxCrCoFeNi using classical molecular dynamics (MD) with classical Lennard-Jones pair-potentials [17]. Similarly, Liu reported a MD study which performed to mechanical characteristics and homogeneous plastic inception of CoCrCuFeNi HEAs under uniaxial tension [18]. Besides classical MD studies, density functional theory (DFT) methods are used in model calculations to evaluate physical properties of HEAs [19]. Biermair et al. demonstrated the applicability of a DFT for prediction of the lattice constant and thermodynamic property changes of a paramagnetic HEAs [20]. Moreover, some thermo-physical properties of NiFeCrCo were investigated via first-principles tool by Niu et al [21].

As it appears from quantum mechanical calculations, Cr/Fe interactions are a notable factor for realizing the electronic band structure because of the covalent d-d bonding between Cr and Fe d states [19]. For this purpose, density functional theory (DFT) methods provide an accurate description the different properties of the material's [22-27]. Among these, GFN1-xTB supplies higher accuracy for all combination of periodic table [28]. But there is still a lack of geometric optimization, band structures, phonon spectrum properties and density of states (DOS) by using extended tight-binding DFT with SCC contributions of CoCrFe and CoCrFeNi HEAs alloys. In the current work, we reported a computational exploration of CoCrFe and CoCrFeNi HEAs by using extended tight-binding DFT method. We have calculated the band structures, DOS, phonon spectrum and some thermodynamic parameters of alloys.

## 2. Material and Method

A new extended tight-binding method (GFN1-xTB) provides to enough accuracy for geometry optimizations. The total energy expression comprises electronic (*el*), atom pairwise repulsion (*rep*), dispersion (*disp*), and halogen-bonding (XB) terms [28]:

$$E = E_{el} + E_{rep} + E_{disp} + E_{XB} \quad (1)$$

The electronic energy  $E_{el}$  is given by

$$E_{el} = \sum_i^{occ} n_i \langle \varphi_i | H_0 | \varphi_i \rangle + \frac{1}{2} \sum_{A,B} \sum_{l(A)} \sum_{l'(B)} p_l^A p_{l'}^B \gamma_{AB,ll'} + \frac{1}{3} \sum_A \tau_A q_A^3 - T_{el} S_{el} \quad (2)$$

where  $\varphi_i$  are the valence molecular orbitals with occupation numbers  $n_i$  and  $H_0$  is the zero-order Hamiltonian.  $T_{el} S_{el}$  is the electronic free energy term [28]. GFN1-xTB, based on developed extended tight-binding method, aims to reduce set of physically interpretative parameters to solve the distinct deficiencies of other DFT calculations by making a parameterization in a wide range of elements up to  $Z=86$ . Hence, this method has been recently used for understanding the optimization process of various materials at nano-scale [28]. Using the symmetry properties, firstly, the CoCr crystal structure was built according to  $Pm\bar{3}m$  space group with the following unit cell lattice parameters:  $a = b = c = 2.821 \text{ \AA}$ . Fig. 1 shows the atomic distribution on the lattice points of Cu-%50Cr alloy system containing 128 atoms. Fe and Ni atoms were doped on the crystal lattice by creating a random mixture of elements, respectively. The CoCrFe and CoCrFeNi model systems were created to form crystal phase. The geometric optimizations are performed using the Amsterdam Modeling Suite (AMS) software (version 2020.104) [29-31] with DFTB module based on GFN1-xTB calculations. The maximum force and energy convergence are executed as  $0.001 \text{ Ha/\AA}$  and  $1 \times 10^{-5} \text{ Ha}$  on each atom with  $0.001 \text{ \AA}$  step convergence until the lattice constants and the atomic positions are relaxed during the geometric optimization process. The stress energy per atom during the optimized lattice is set up  $5 \times 10^{-5} \text{ Ha}$ .

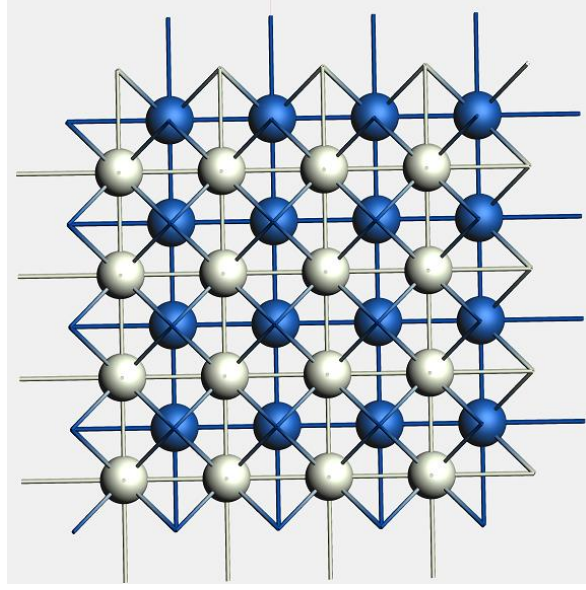


**Figure 1.** Crystal structure of CoCr.

### 3. Results and Discussion

Fig. 2 (a) and Fig. 3 (a) show the evolution of the total energy with respect to the frame number or optimization iteration step for CuCrFe and CuCrFeNi systems, respectively. The total energy for the systems has the maximum value at the beginning of optimization. The energy reaches its minimum with progressing of optimization process. The systems have high stability at final of optimization compared with the beginning structure and also, the energy of CoCrFe is lower than CoCrFeNi during the optimization process. The volumes of systems during the optimization process are shown in Fig. 2 (b) and Fig. 3 (b). The figures show that the volumes of systems linearly increase at the beginning of optimization and then dramatically decrease at certain optimization step. Then, the system volumes reach a stable value after iteration 60. Fig. 2 (c, d) and Fig. 3 (c, d) show the atomic configurations of CuCrFe and CuCrFeNi structures at the beginning and final of optimization. From the figures, we can see that Fe and Cr atoms tend to bond during the optimization. This result can be explicated that covalent d–d bonding between Fe–Cr is evidenced because of strong metallic Cr–Fe interactions. This strong bonding interaction between Cr–Fe for electron exchange and correlation early investigated by Johnson et. al by using DFT [19].

Investigation of electronic and thermal properties of CoCrFe and CoCrFeNi high entropy alloys via extended tight-binding DFT computational method

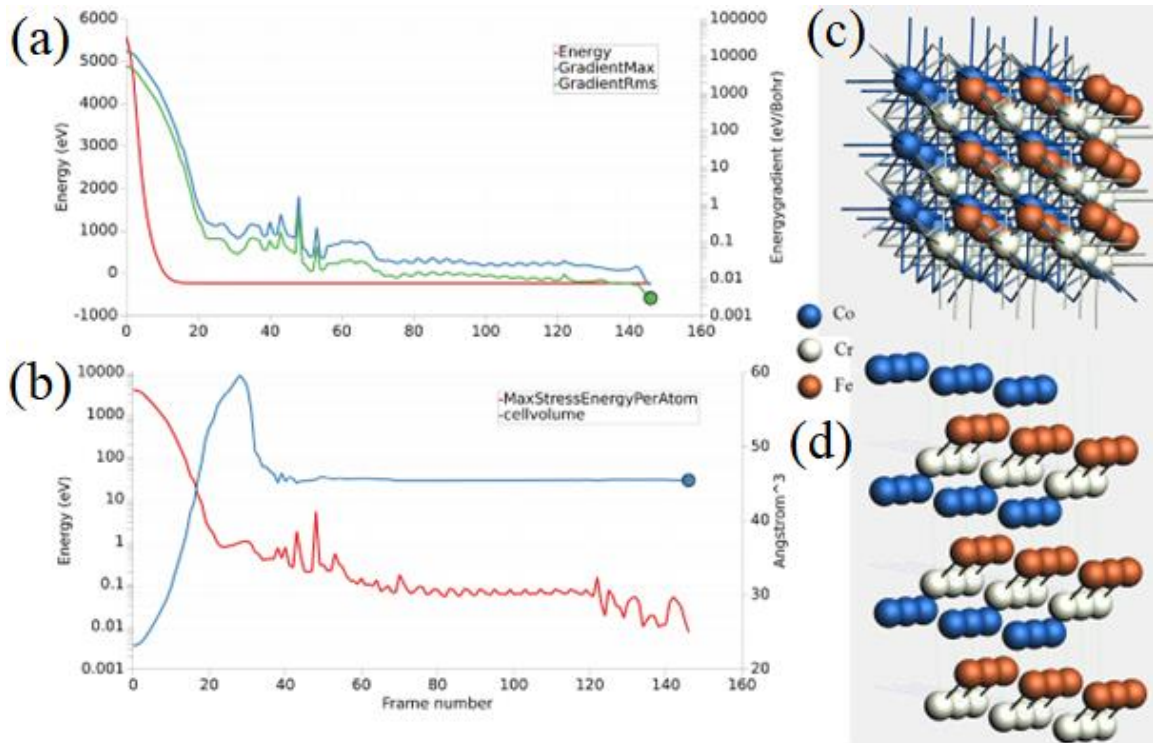


Figure 2. Geometric optimization process of CoCrFe.

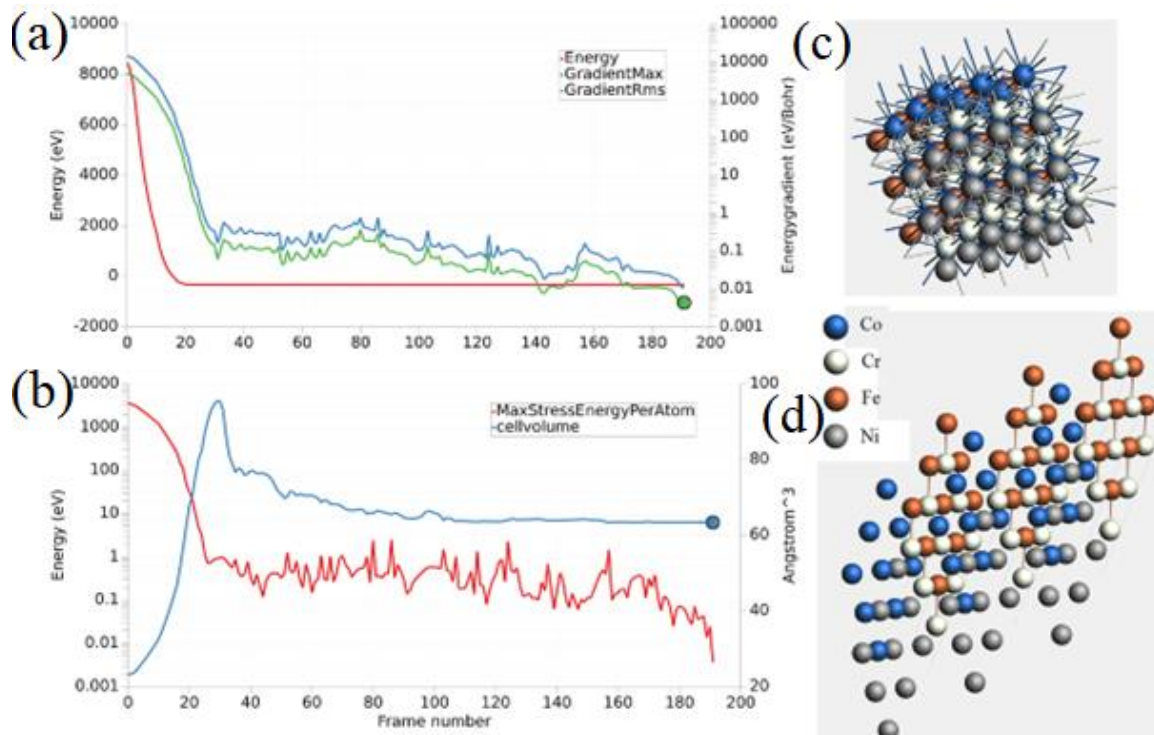
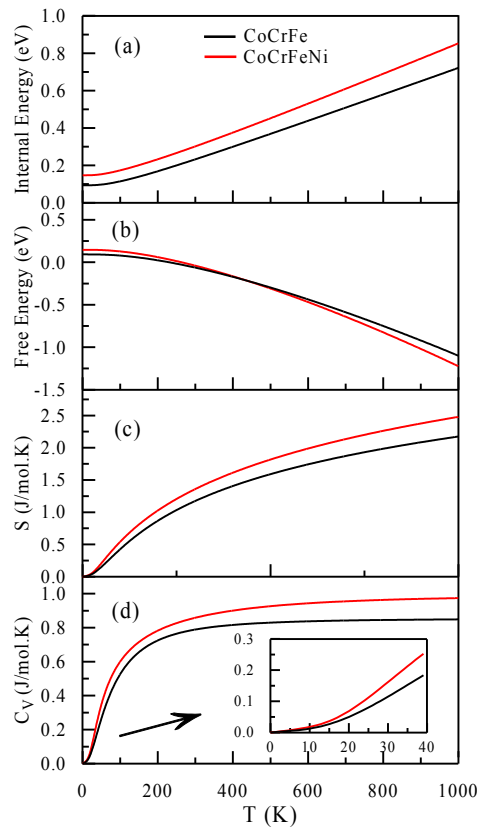


Figure 3. Geometric optimization process of CoCrFeNi.



The variation of thermodynamic parameters obtained from phonon as shown in Fig. 4 (a-d). The internal energies of both alloys increase linearly in the temperature range of 50-1000 K. It is noted that the internal energy of CoCrFe at 0 K is lower than the internal energy of CoCrFeNi. When the variation graph of free energy according to temperature is examined in Fig. 4 (b), it is seen that the free energy is at an almost constant value in both alloy systems up to 50 K, however, it exhibits a linear decrease with the increase in temperature. The entropy values calculated in the low temperature region increase rapidly with the increase in temperature as seen Fig. 4 (c). This increment continues exponentially as the contribution of vibration to entropy (S) increases as the temperature rises [32, 33]. The increase continues exponentially as the contribution of vibration to entropy increases as the temperature continues to rise. It is observed that the entropy value increases gradually with the addition of Ni element to the CoCrFe alloy. From figure, the  $C_V$  increases due to the harmonic effect of the phonons in the range of 0-400 K. The  $T^3$  dependence at low temperatures is detailed in Figure 4 (d). This increase is strongly dependent on temperature. But, when the temperature is higher than 400 K, the  $C_V$  is close to the classic limit in good agreement with Dulong-Petit's law [34] at about 0.82 J/mol.K and 0.94 J/mol.K for the CoCrFe and the CoCrFeNi, respectively.



**Figure 4.** Thermodynamic parameters of model systems (a) internal energy (b) free energy (c) entropy (d) heat capacity.

Fig. 5 and Fig.6 show the band structure of systems. It is clearly observed that there is no band gap formation along the high symmetry lines at the Fermi energy level for both alloys. In other words, the top of the valence band and the bottom of the conduction band overlap. This causes the curve to have a value above zero at the Fermi energy level in the DOS. It could be argued that because the DOS of the metals have a nonzero value at the Fermi energy level, both alloy systems exhibit metallic properties. Since most of the occupied states come from the d states of Co, Cr, Fe and Ni atoms, it could be argued that the d orbitals make the major contribution to DOS in the energy band structure [35]. The  $4s^2 3d^7$ ,  $4s^1 3d^5$ ,  $4s^2 3d^6$  and  $4s^2 3d^8$  orbitals of Co, Cr, Fe and Ni elements are considered as valence states, respectively. These elements tend to form covalent bonds with each other because of their 3d electrons. In Figure 6, a small band gap formation is observed in the energy band structure in the  $A5-\Gamma$ -

A6 high symmetry directions of the CoCrFeNi alloy system. This band gap causes a decrease in DOS. Although band gap is formed in some aspects of the Brillouin zone, there are sufficiently high DOS at the Fermi level to make the CoCrFeNi alloy system metallic [36]. It is clearly observed from the band structure in figure that the p states are filled well above the conduction band because of the addition of Ni element to the CoCrFe alloy system. In addition, it is determined that the s and p states also contribute to the DOS in the valence band and conduction band.

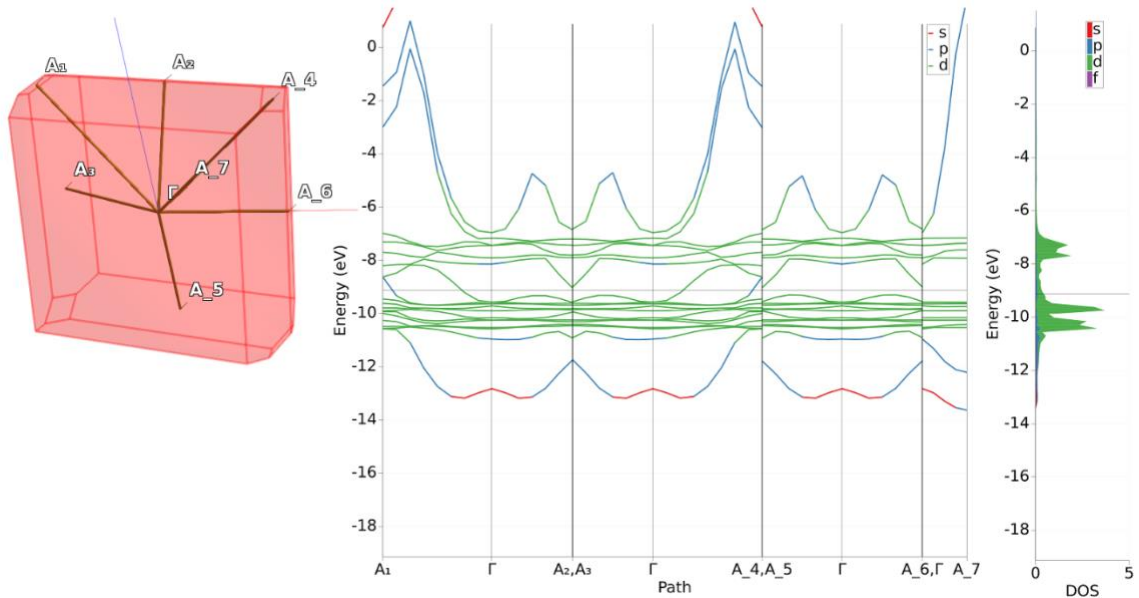


Figure 5. Band structure of CoCrFe.

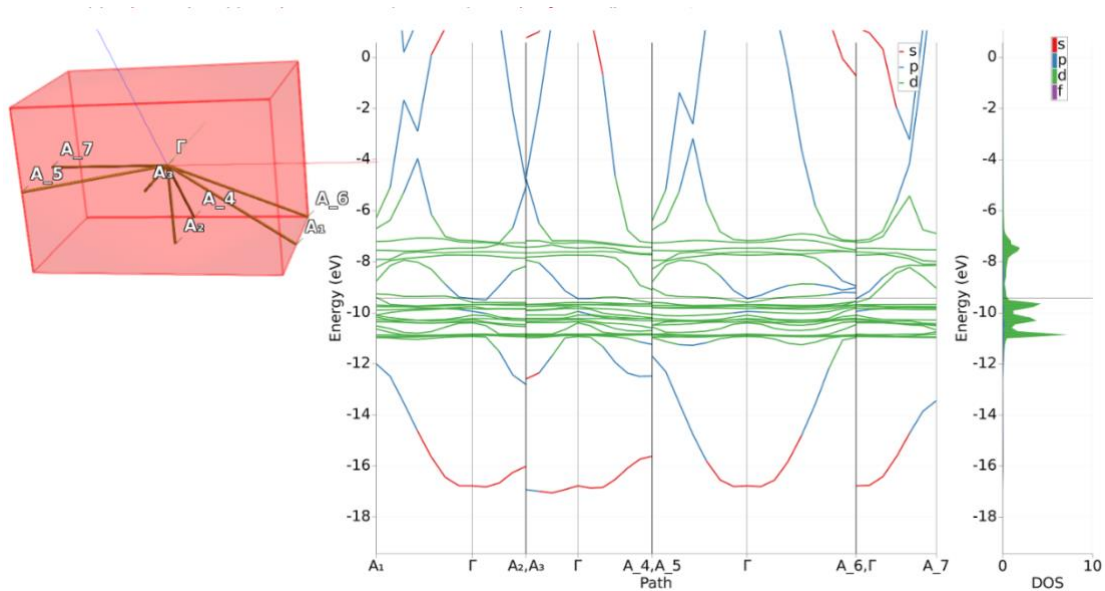
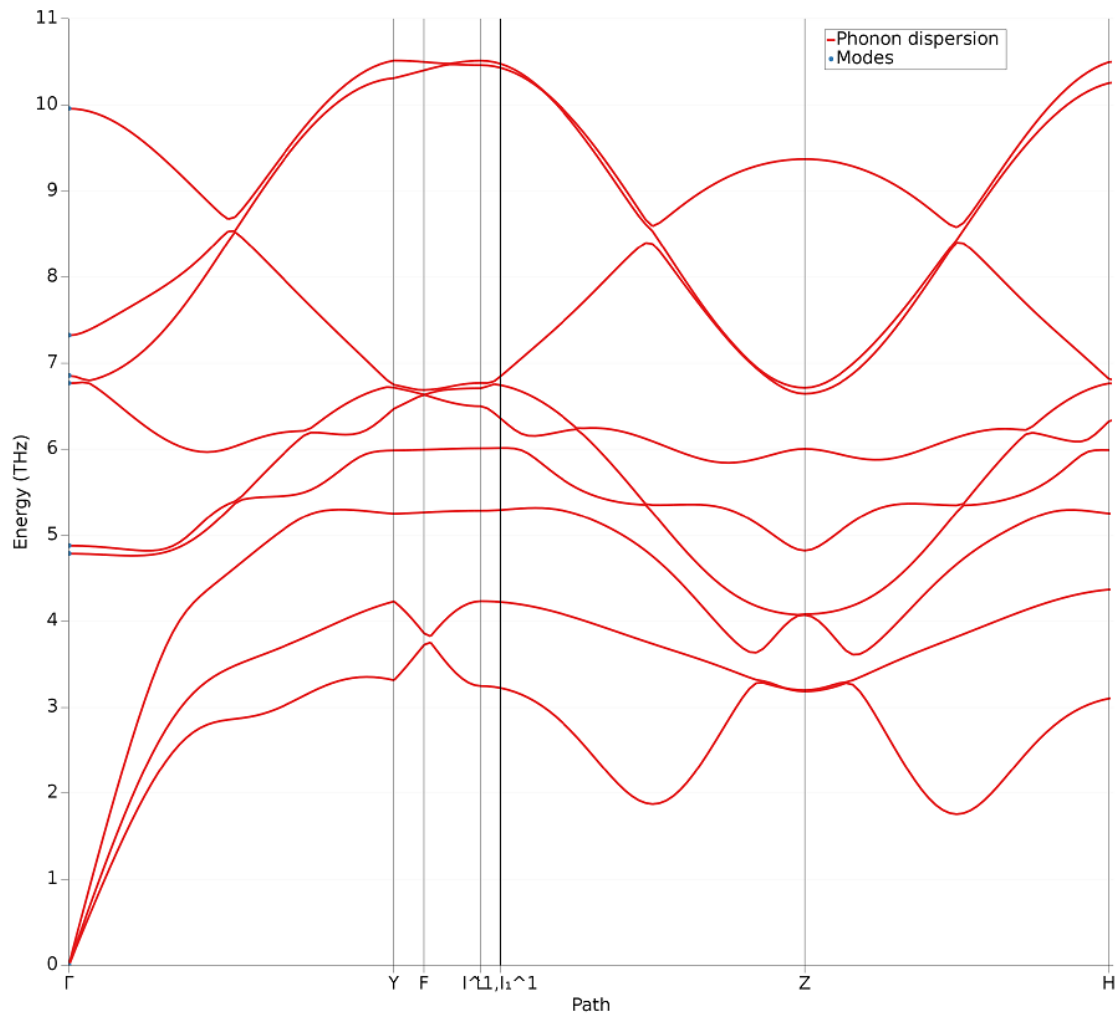


Figure 6. Band structure of CoCrFeNi.

In order to understand the lattice dynamics microscopically, it is required to know the phonon distribution. Phonon properties of solids are very important because they are closely related to various fundamental properties such as thermal expansion, specific heat, electron-phonon interaction, and thermal conduction by lattice [37]. According to the lattice vibration theory, there are  $3n$  number of phonon arms in a crystal with  $n$  number of atoms per unit cell. These phonon arms consist of 3 acoustic arms and  $3n-3$  optical arms [38]. In order to verify the dynamic stability of CoCrFe and CoCrFeNi high entropy alloy systems, phonon dispersion curves were calculated along the path containing the high symmetry points of the Brillouin region, as seen in Fig. 7 and Fig. 8. There are 3 atoms in the primitive unit cell of the  $Pm\bar{3}m$  alloy model with space group symmetry. Thus, it is observed that the phonon spectrum has a total of 9 branches, 3 being acoustic modes and 6 being optical modes. In a stable crystal structure, all phonon frequencies must be positive [39]. It was determined that the phonon frequencies obtained for both alloy systems were positive along the high symmetry directions of the Brillouin region, in other words, no imaginary phonon frequencies were observed. This clearly indicates that both alloy systems are dynamically stable [37, 38, 40].

It is clearly observed in figures that the addition of element Ni to the CoCrFe alloy system causes a decrease in phonon frequencies. It is known that high-frequency phonon modes originate mainly from light atoms, while low-frequency phonon modes originate from heavier atoms [39]. Therefore, it can be argued that the addition of Ni element to the CoCrFe alloy system causes a decrease in phonon frequencies. It is observed that the gaps between the optical and acoustic phonon modes in the phonon distribution curves of both alloy systems are very small or does not exist in some high symmetry directions, and they intersect with each other at more than one Brillouin zone point. It can be argued that this is an indication of the high entropy alloy systems used in the study exhibiting a ductile structure [41]. There are many studies in the literature in which ductility is analyzed by associating it with phonon dispersion [42-46]. However, in Figure 8, the formation of a frequency gap between the optical and acoustic arms in the phonon distribution curve in the  $A5-\Gamma-A6$  high symmetry directions of the CoCrFeNi alloy system is clearly observed. When the energy band structure of the same alloy system is examined in Figure 2, it can be determined that a small band gap is formed in the same high symmetry directions. Although there is a frequency gap in these directions of the Brillouin zone, this does not affect the dynamic stability of the system. In addition, the frequency gap can be directly related to the mass ratio of atoms in the model system. A higher mass ratio indicates a larger frequency interval [37].



**Figure 7.** Phonon curves of CoCrFe.

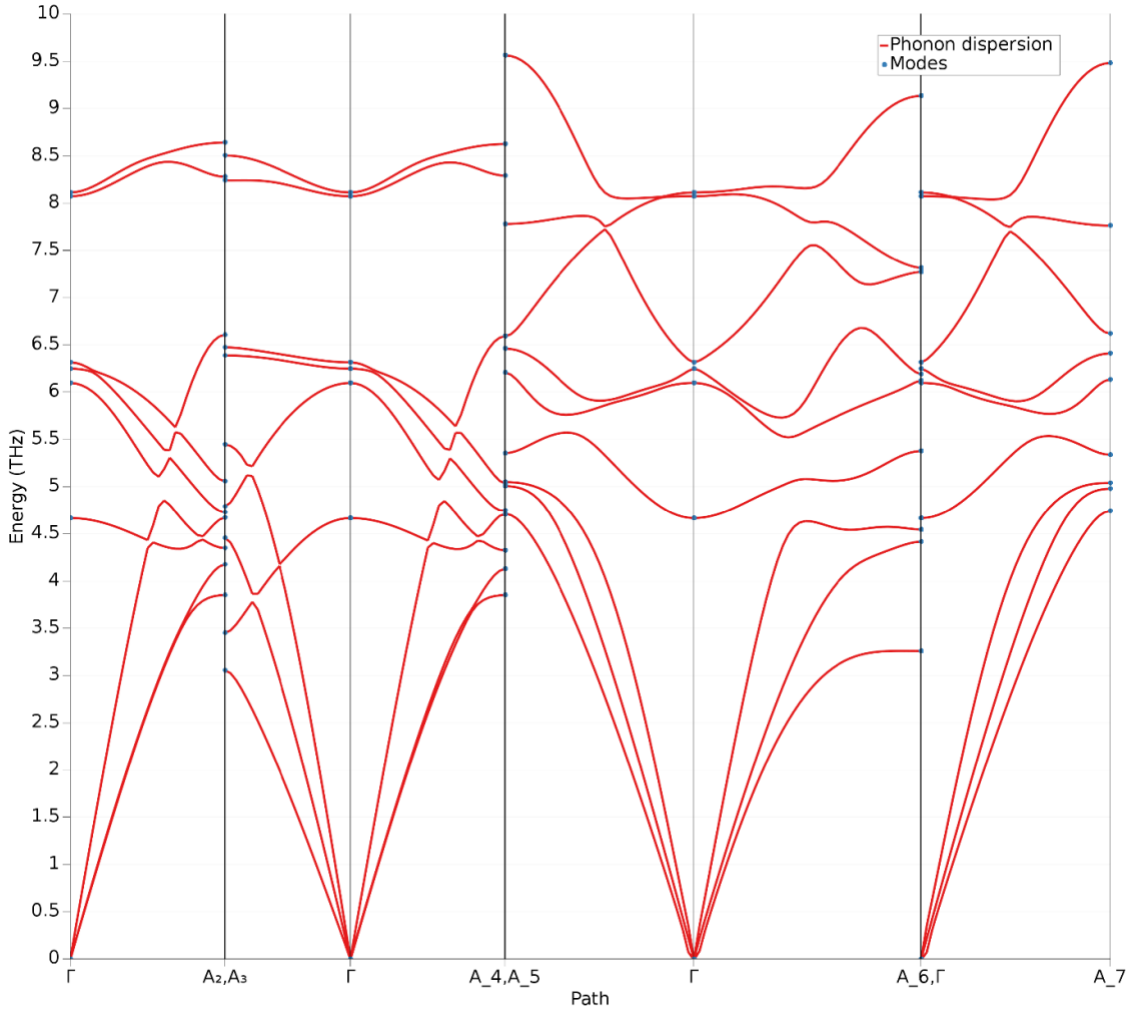


**Figure 8.** Phonon curves of CoCrFeNi.

#### 4. Conclusion

In summary, we have performed tight-binding DFT calculations of CoCrFe and CoCrFeNi HEAs. The geometric optimization, electronic and thermodynamic properties have also been investigated. Fe and Cr atoms tend to bond during the optimization because of strong metallic Cr–Fe interactions. Cv values are obtained as 0.82 J/mol.K and 0.94 J/mol.K for the CoCrFe and the CoCrFeNi. Moreover, there is no band gap formation along the high symmetry lines at the Fermi energy level for both alloys due to exhibit metallic properties of systems. the gaps between the optical and acoustic phonon modes in the phonon distribution curves of both alloy systems are very small and does not exist in some high symmetry directions.

## References

- [1] Zhao S, Li Z, Zhu C, Yang W, Zhang Z, Armstrong DE., Meyers MA. Amorphization in extreme deformation of the CrMnFeCoNi high-entropy alloy. *Sci Adv* 2021; 7(5): eabb3108.
- [2] Yang YC, Liu C, Lin CY, Xia Z. Core effect of local atomic configuration and design principles in AlxCoCrFeNi high-entropy alloys. *Scr Mater* 2020; 178: 181-186.
- [3] Fan AC, Li JH, Tsai MH. On the phase constituents of three CoCrFeNiX (X= Cr, Mo, W) high-entropy alloys after prolonged annealing. *Mater Chem Phys* 2022; 276: 125431.
- [4] Lin Y, Yang T, Lang L, Shan C, Deng H, Hu W, Gao, F. Enhanced radiation tolerance of the Ni-Co-Cr-Fe high-entropy alloy as revealed from primary damage. *Acta Mater* 2020; 196: 133-143.
- [5] Daryoush S, Mirzadeh H, Ataie A. Amorphization, mechano-crystallization, and crystallization kinetics of mechanically alloyed AlFeCuZnTi high-entropy alloys. *Mater Lett* 2022; 307: 131098.
- [6] Fang W, Chang R, Ji P, Zhang X, Liu B, Qu X, Yin F. Transformation induced plasticity effects of a non-equal molar Co-Cr-Fe-Ni high entropy alloy system. *Metals* 2018; 8(5): 369-379
- [7] Xiong F, Fu R, Li Y, Xu B, Qi X. Influences of nitrogen alloying on microstructural evolution and tensile properties of CoCrFeMnNi high-entropy alloy treated by cold-rolling and subsequent annealing. *Mater Sci Eng A* 2020; 787: 139472.
- [8] He F, Wang Z, Wu Q, Niu S, Li J, Wang J, Liu CT. Solid solution island of the Co-Cr-Fe-Ni high entropy alloy system. *Scr Mater* 2017; 131: 42-46.
- [9] Feng R, Zhang C, Gao MC, Pei Z, Zhang F, Chen Y, Liaw PK. High-throughput design of high-performance lightweight high-entropy alloys. *Nat Commun* 2021; 12(1): 1-10.
- [10] Li Z. Interstitial equiatomic CoCrFeMnNi high-entropy alloys: carbon content, microstructure, and compositional homogeneity effects on deformation behavior. *Acta Mater* 2019; 164: 400-412.
- [11] Zhang Z, Jiang Z, Xie Y, Chan SLI, Liang J, Wang J. Multiple deformation mechanisms induced by pre-twinning in CoCrFeNi high entropy alloy. *Scr Mater* 2022; 207: 114266.
- [12] Zaddach AJ, Niu C, Koch CC, Irving DL. Mechanical properties and stacking fault energies of NiFeCrCoMn high-entropy alloy. *Jom* 2013; 65(12): 1780-1789.
- [13] Vaidya M, Karati A, Marshal A, Pradeep KG, Murty BS. Phase evolution and stability of nanocrystalline CoCrFeNi and CoCrFeMnNi high entropy alloys. *J Alloys Compd* 2019; 770: 1004-1015.
- [14] Fang W, Yu H, Chang R, Zhang X, Ji P, Liu B, Yin F. Microstructure and mechanical properties of Cr-rich Co-Cr-Fe-Ni high entropy alloys designed by valence electron concentration. *Mater Chem Phys* 2019; 238: 121897.
- [15] Zhang T, Zhao RD, Wu FF, Lin SB, Jiang SS, Huang YJ, Eckert J. Transformation-enhanced strength and ductility in a FeCoCrNiMn dual phase high-entropy alloy. *Mater Sci Eng A* 2020; 780: 139182.
- [16] Ji, X, Ji C, Cheng J, Shan Y, Tian S. Erosive wear resistance evaluation with the hardness after strain-hardening and its application for a high-entropy alloy. *Wear* 2018; 398: 178-182.
- [17] Sharma A, Deshmukh SA, Liaw PK, Balasubramanian G. Crystallization kinetics in AlxCrCoFeNi (0 ≤ x ≤ 40) high-entropy alloys. *Scr Mater* 2017; 141: 54-57.
- [18] Liu J. Molecular dynamic study of temperature dependence of mechanical properties and plastic inception of CoCrCuFeNi high-entropy alloy. *Phys Lett A* 2020; 384: 126516.
- [19] Johnson DF, Jiang DE, Carter EA. Structure, magnetism, and adhesion at Cr/Fe interfaces from density functional theory. *Surf Sci* 2007; 601(3): 699-705.
- [20] Biermair F, Razumovskiy VI, Ressel G. Influence of alloying on thermodynamic properties of AlCoCrFeNiTi high entropy alloys from DFT calculations. *Comput Mater Sci* 2022; 202: 110952
- [21] Niu C, Zaddach AJ, Koch CC, Irving DL. First principles exploration of near-equiatomic NiFeCrCo high entropy alloys. *J Alloys Compd* 2016; 672: 510-520.
- [22] Kohn W, Sham LJ. Self-Consistent Equations Including Exchange and Correlation Effects. *Phys Rev* 1965; 140: A1133-A1138.
- [23] Galvão BR, Viegas LP, Salahub DR, Lourenço MP. Reliability of semiempirical and DFTB methods for the global optimization of the structures of nanoclusters. *J Mol Model* 2020; 26(11): 1-8.
- [24] Wahiduzzaman M, Oliveira AF, Philipsen P, Zhechkov L, Van Lenthe E, Wittek HA, Heine T. DFTB parameters for the periodic table: Part I, electronic structure. *J Chem Theory Comput* 2013; 9(9): 4006-4017.
- [25] Chopra S. Performance study of the electronic and optical parameters of thermally activated delayed fluorescence nanosized emitters (CCX-I and CCX-II) via DFT, SCC-DFTB and B97-3c approaches. *J Nanostruct Chem* 2020; 10: 115-124.
- [26] Slater JC, Koster GF. Simplified LCAO method for the periodic potential problem. *Phys Rev* 1954; 94(6): 1498.
- [27] Yildiz AK, Celik FA. Atomic concentration effect on thermal properties during solidification of Pt-Rh alloy: A molecular dynamics simulation. *J Cryst Growth* 2017; 463: 194-200.
- [28] Grimme S, Bannwarth C, Shushkov P. A robust and accurate tight-binding quantum chemical method for structures, vibrational frequencies, and noncovalent interactions of large molecular systems parametrized for all spd-block elements (Z= 1-86). *J. Chem Theory Comput* 2017; 13(5): 1989-2009.

- [29] Te Velde GT, Bickelhaupt FM, Baerends EJ, Fonseca Guerra C, van Gisbergen SJ, Snijders JG, Ziegler T. Chemistry with ADF. *J Comput Chem* 2001; 22(9): 931-967.
- [30] Fonseca Guerra C, Snijders JG, Te Velde GT, Baerends EJ. Towards an order-N DFT method. *Theor Chem Acc* 1998; 99(6): 391-403.
- [31] AMS DFTB 2021.1, SCM, Theoretical Chemistry, Vrije Universiteit Amsterdam, The Netherlands, 2013 <http://www.scm.com>.
- [32] Jain E, Pagare G, Dubey S, Sharma R, Sharma Y. High pressure phonon and thermodynamic properties of Ru based intermetallics: A DFT investigation. *J Phys Chem Solids* 2018; 122: 246-254.
- [33] Asadi Y, Nourbakhsh Z. First principle characterization of structural, electronic, mechanical, thermodynamic, linear and nonlinear optical properties of zinc blende InAs, InSb and their InAs<sub>x</sub>Sb<sub>1-x</sub> ternary alloys. *J Phys Chem Solids* 2019; 132: 213-221.
- [34] Arıkan N, İyigör A, Candan A, Uğur Ş, Charifi Z, Baaziz H, Uğur G. Structural, elastic, electronic and phonon properties of scandium-based compounds ScX<sub>3</sub> (X= Ir, Pd, Pt and Rh): An ab initio study. *Comput Mater Sci* 2013; 79: 703-709.
- [35] Rameshkumar S, Jaiganesh G, Jayalakshmi V. Structural, phonon, elastic, thermodynamic and electronic properties of Mg–X (X= La, Nd, Sm) intermetallics: The first principles study. *J Magnets Alloy* 2019; 7(1): 166-185.
- [36] Mukherjee D, Sahoo BD, Joshi KD, Gupta SC. High pressure phase transition in Zr–Ni binary system: A first principle study. *J Alloys Compd* 2015; 648: 951-957.
- [37] Jain E, Pagare G, Dubey S, Sharma R, Sharma, Y. High pressure phonon and thermodynamic properties of Ru based intermetallics: A DFT investigation. *J Phys Chem Solids* 2018; 122: 246-254.
- [38] Yang JW, An L, Zheng JJ. Structure, mechanical and phonon stability of the Th-Sn system from ab initio. *J Nucl Mater* 2021; 556: 153187.
- [39] Zhao Y, Li H, Huang Y. The structure, mechanical, electronic and thermodynamic properties of bcc Zr-Nb alloy: A first principles study. *J Alloys Compd* 2021; 862: 158029.
- [40] Guechi A, Chegaar M, Bouhemadou A, Arab F. Structural, mechanical and phonons properties of binary intermetallic compound BaSn<sub>3</sub> under pressure. *Solid State Commun* 2021; 323: 114110.
- [41] Liu J, Guo X, Lin Q, He Z, An X, Li L, Zhang Y. Excellent ductility and serration feature of metastable CoCrFeNi high-entropy alloy at extremely low temperatures. *Sci China Mater* 2019; 62(6): 853-863.
- [42] Arıkan N, Charifi Z, Baaziz H, Uğur Ş, Ünver H, Uğur G. Electronic structure, phase stability, and vibrational properties of Ir-based intermetallic compound IrX (X= Al, Sc, and Ga). *J Phys Chem Solids* 2015; 77: 126-132.
- [43] Parlinski K, Li ZQ, Kawazoe Y. First-principles determination of the soft mode in cubic ZrO<sub>2</sub>. *Phys Rev Lett* 1997; 78(21): 4063.
- [44] Wang R, Wang S, Wu X, Liu A. First-principles phonon calculations of thermodynamic properties for ductile rare-earth intermetallic compounds. *Intermetallics* 2011; 19(10): 1599-1604.
- [45] Perdew JP, Burke K, Ernzerhof M. Generalized gradient approximation made simple. *Phys. Rev. Lett* 1996; 77(18): 3865.
- [46] Blanco MA, Francisco E, Luana V. GIBBS: isothermal-isobaric thermodynamics of solids from energy curves using a quasi-harmonic Debye model. *Comput Phys Commun* 2004; 158(1): 57-72.





## Computational Relationship of the Surface Area and Stiffness of the Spring Constant on Fractional Bagley-Torvik Equation

Kazeem Iyanda FALADE<sup>1</sup>, Abd'gafar Tunde TIAMIYU<sup>2</sup>, Adesina Kamorudeen ADIO<sup>3</sup>, Huzifa Muhammad TAHIR<sup>4</sup>, Umar Muhammad ABUBAKAR<sup>5</sup>, Sahura Muhammad BADAMASI<sup>6</sup>

<sup>1,4,5,6</sup>Department of Mathematics, Faculty Computing and Mathematical Sciences  
Kano University of Science and Technology, Wudil Kano State Nigeria.

<sup>2</sup>Department of Mathematics, Federal University of Technology Minna Niger State Nigeria.

<sup>3</sup>Department of Basic Sciences, School of Science and Technology, Babcock  
University, Ilesan-Remo, Ogun State Nigeria.

\*<sup>1</sup>faladekazeem2016@kustwudil.edu.ng <sup>2</sup>abdgafartunde@yahoo.com <sup>3</sup>adioa@babcock.edu.ng

<sup>4</sup>huzaimfamtahir1234@gmail.com <sup>5</sup>umabubakar347@gmail.com <sup>6</sup>sahurabadamasi77@gmail.com

(Geliş/Received: August 4, 2022;

Kabul/Accepted: November 26, 2022)

**Abstract:** In this paper, we formulate an efficient algorithm based on a new iterative method for the numerical solution of the Bagley-Torvik equation. The fractional differential equation arises in many areas of applied mathematics including viscoelasticity problems and applied mechanics of the oscillation process. We construct the fractional derivatives via the Caputo-type fractional operator to formulate a three-step algorithm using the MAPLE 18 software package. We further investigate the relationships between the surface area and stiffness of the spring constants of the Bagley-Torvik equation on three case problems and numerical results are presented to demonstrate the efficiency of the proposed algorithm.

**Key words:** Fractional Bagley-Torvik equation, new iterative method, Caputo derivative, Riemann-Liouville fractional integral operator, MAPLE 18 software package

### Kesirli Bagley-Torvik Denklemi Üzerindeki Yay Sabitinin Yüzey Alanı ve Sertliğinin Hesaplamalı İlişkisi

**Öz:** Bu makalede, Bagley-Torvik denkleminin sayısal çözümünü için yeni iteratif yöntemle dayalı etkili bir algoritma formüle ediyoruz. Kesirli diferansiyel denklemler, uygulamalı mekanik ve salınım sürecinin viskoelastisite problemleri dahil olmak üzere, uygulamalı matematiğin birçok alanında ortaya çıkar. MAPLE 18 yazılım paketini kullanarak üç adımlı bir algoritma formüle etmek için Caputo tipi kesirli operatör aracılığıyla kesirli türevler üretiyoruz. Üç durumlu bir problemde Bagley-Torvik denkleminin yay sabitlerinin yüzey alanı ve katılığı arasındaki ilişkileri araştırdık ve önerilen algoritmanın etkinliğini göstermek için sayısal sonuçlar sunuldu.

**Anahtar kelimeler:** Kesirli Bagley-Torvik denklemi, yeni iteratif metod, Caputo, Riemann-Liouville kesirli integral operatörü, Maple 18 yazılım paketi.

### 1. Introduction

Initial value problems (IVPs) and boundary value problems (BVPs) of fractional order occur in the description of many physical processes of stochastic transportation, investigation of liquid filtration in a strongly porous medium, diffusion wave, cellular systems, signal processing, control theory, and oil industries. The analytical and numerical solutions to these fractional differential equations have attracted a lot of attention from researchers over the last decade. The Bagley-Torvik equation was proposed by Bagley and Torvik to describe it is one of the many leading mathematical models of viscoelasticity damped structures with fractional derivatives. Therefore, it is meaningful to investigate the nature of the Bagley-Torvik equation with time delay. In particular, the  $\frac{1}{2}$ -order derivative or  $\frac{3}{2}$ -order derivative describes the frequency-dependent damping materials quite satisfactorily and the Bagley-Torvik equation with  $\frac{1}{2}$ -order derivative or  $\frac{3}{2}$ -order derivative describes the motion of real physical systems, an immersed plate in a Newtonian fluid and a gas in a fluid respectively [1-7].

In this paper, we investigate the relationship between the surface area and stiffness of the spring constants appearing in the Bagley-Torvik equation which arises in the application of fractional calculus of the theory of viscoelasticity and it can also describe the motion of real physical systems, the modeling of the motion of a rigid plate immersed in a viscous fluid, and a gas in a fluid respectively [8, 9,10].

$$MD^2y(x) + SD^{\frac{3}{2}}y(x) + Ky(x) = g(x) \quad 0 < x \leq 1 \quad (1)$$

with initial conditions

$$\begin{cases} y(0) = \Omega \\ y_x(0) = \Phi \end{cases} \quad (2)$$

Where  $y(x)$  represents the displacement of the plate of mass  $M$ ,  $S$  is the surface area,  $K$  is the stiffness of the spring to which the plate is attached,  $\Omega$  and  $\Phi$  are constant parameters,  $D^{\frac{3}{2}}$  is the Caputo fractional derivative of order  $\frac{3}{2}$ , and  $g(x)$  represents the loading force.

Several numerical methods have been proposed for analytically and numerically solutions of this typical equation in area formulation of mathematical model of viscoelastic damped structures with fractional derivative such as [11] who presented a theoretical frame work on basis for the application of fractional calculus to viscoelasticity, [12] studied the fractional calculus in the transient analysis of viscoelastically damped structures, [14] obtained numerical solution of the Bagley-Torvik equation, [14] proposed and applied generalized Taylor collocation method for numerical solutions of the Bagley-Torvik equation, [15] employed discrete spline methods for solving two point fractional Bagley-Torvik equation, [16] applied fractional iteration method to obtain approximate analytical solutions to the Bagley-Torvik equation, [17] proposed and applied Chebyshev wavelet operational matrix of fractional derivative for the numerical solution of Bagley-Torvik equation, [18] employed Adomian decomposition method for analytical solution of the Bagley-Torvik equation, [19] formulated numerical scheme for solving two point fractional Bagley-Torvik equation using Chebyshev collocation method, [20] presented and applied Bessel collocation method for the numerical solution of the Bagley-Torvik equation, [21] applied shifted Chebyshev operational matrix for the numerical solution of the Bagley–Torvik equation and [22] investigated the existence and uniqueness as well as approximations of the solutions for the Bagley-Torvik equation.

We aim to investigate and obtain numerical solutions for the relationship between surface area  $S$  and stiffness of the spring constants  $K$  of equation (1) and coupled with given initial conditions. Although some of the methods stated in our references have done great work in solving the Bagley-Torvik equation, however, there is still a need for a robust, fast, and suitable algorithm using MAPLE 18 software codes command to overcome the complexity of Riemann–Liouville fractional integral and Liouville–Caputo fractional derivative for better simplicity and efficiency.

## 2. The fractional integration and differentiation

The definition of fractional derivatives are defined in many ways such as Riemann-Liouville, Grunwald-Letnikov and Caputo. In the present paper, we consider the Caputo fractional derivative and Riemann–Liouville fractional integral as follow [21]:

### Definition 1

The Riemann–Liouville fractional integral operator  $J^\alpha$ ,  $\alpha > 0$  is defined as follows:

$$J^\alpha f(x) = \frac{1}{\Gamma(\alpha)} \int_0^x (x-s)^{\alpha-1} f(s) ds, \quad \alpha > 0 \quad (3)$$

### Definition 2

The Liouville–Caputo fractional derivative operator  $D^\alpha$  is defined as follows:

$$\begin{cases} D^\alpha f(x) = \frac{1}{\Gamma(m-\alpha)} \int_0^x (x-s)^{m-\alpha-1} f^m(s) ds \\ \text{for } m-1 < \alpha \leq m, \quad m \in \mathbb{N}, \quad x > 0, f(x) \in C_{-1}^m \end{cases} \quad (4)$$

And the Liouville–Caputo derivative (4), we have

$$D^\alpha x^\beta = \begin{cases} 0 & \text{for } \beta \in \mathbb{N}_0 \text{ and } \beta < [\alpha]; \\ \frac{\Gamma(\beta+1)}{\Gamma(\beta+1-\alpha)} x^{\beta-\alpha} & \text{for } \beta \in \mathbb{N}_0 \text{ and } \beta \geq [\alpha]; \\ & \text{or } \beta \notin \mathbb{N}_0 \text{ and } \beta > [\alpha] \end{cases} \quad (5)$$

Here,  $\lceil \alpha \rceil$  and  $\lfloor \alpha \rfloor$  are the ceilings and floor functions respectively, and  $\mathbb{N}_0 = \{0,1,2 \dots\}$ .

### 3. Description of the new iterative method (NIM)

The new iterative method was proposed by Daftardar-Gejji and Jafari [23]. It is an efficient technique for solving linear and nonlinear functional differential equations which arise in a wide area of applications in nonlinear problems without linearization or small perturbation [24, 25]. We consider the basic idea of the new iterative method for the general functional equation of the form:

$$y(x) = f(x) + N(y(x)) \tag{6}$$

where  $N$  Na nonlinear operator from a Banach is space  $B \rightarrow B$  and  $f(x)$  is a known function. Looking for a solution of (6) having the series form:

$$y(x) = \sum_{i=0}^{\infty} y_i(x) \tag{7}$$

The nonlinear operator which is on the right-hand side of (6) can be decomposed as follow:

$$N\left(\sum_{i=0}^{\infty} y_i(x)\right) = N(y_0) + \sum_{i=1}^{\infty} \left\{ N\left(\sum_{j=0}^i y_j\right) - N\left(\sum_{j=0}^{i-1} y_j\right) \right\} \tag{8}$$

Substituting equations (7) and (8) into equation (6); becomes;

$$\sum_{i=0}^{\infty} y_i(x) = f(x) + N(y_0) + \sum_{i=1}^{\infty} \left\{ N\left(\sum_{j=0}^i y_j\right) - N\left(\sum_{j=0}^{i-1} y_j\right) \right\} \tag{9}$$

The recurrence relation is given by:

$$\begin{cases} y_0 = f \\ y_1 = N(y_0) \\ y_{m+1} = N(y_0 + y_1 + \dots + y_m) - N(y_0 + y_1 + \dots + y_{m-1}) \quad m = 1,2,3,\dots \end{cases} \tag{10}$$

Then,

$$N(y_0 + y_1 + \dots + y_m) = N(y_0 + y_1 + \dots + y_{m-1}) \quad m = 1,2,3 \dots \tag{11}$$

and

$$\sum_{i=0}^{\infty} y_i = f + N\left(\sum_{i=0}^{\infty} y_i\right), \tag{12}$$

The  $k$  – term approximate solution of (6) is given by;

$$y = y_0 + y_1 + \dots + y_{k-1}. \tag{13}$$

#### 3.1 Suitable Algorithm

In this section, we formulate three steps algorithm using MAPLE 18 software codes for solving fraction Bagley-Torvik equation (1) coupled with initial conditions given in equation (2). We utilize definition 2 and the new iterative method discussed in the previous section as follows:

```
restart;
Step 1:
withplots:
Digits := ℝ+;
N := ℝ+;
S := ℝ+;
K := ℝ+;
g := g(x);
y[0] := Ω;
dy[0] := Φ;
```

```

Y[0] := (y[0] + dy[0] * x + int(g, x$2));
m := alpha + 1/2;
Step 2:
for n from 0 to N do
f := diff(Y[n], x$2);
G := simplify(1/(Gamma(m - alpha)) * int((x - s)^(m - alpha - 1) * subx(s = x, f), s = 0 ... x), assume = nonnegative);
H := simplify(-int(S * G + K * Y[n], x$2), assume = nonnegative);
Y[n + 1] := expand(H);
end do;
Step 3:
NIA := sum(Y[k], k = 0..N + 1);
for x from 0 by 0.1 to 1 do
NIA[x] := evalf(eval(NIA));
end do;
y[x][2Dplot] := plot([NIA], x = 0 ... 1, color [red], axes = boxed, title
                    = fractional Bagley - Torvik equation IVPs);
y[x][2Dplot] := logplot([NIA], x = 0 ... 1, color [red], axes = boxed, title
                    = fractional Bagley - Torvik equation IVPs);
    
```

#### 4. Numerical experiments

To illustrate the effectiveness of the proposed algorithm, three test cases are considered to examine the relationship between surface area  $S$  and the stiffness of the spring constants  $K$  of equation (1) as follows:

**Case 1. The stiffness of the spring constant  $K$  is greater than surface area  $S$**  [20]

$$D^2 y(x) + \frac{2}{5} D^{\frac{3}{2}} y(x) - \frac{1}{2} y(x) = \frac{x^2}{4} - \frac{x}{4} - \frac{8\sqrt{x}}{5\sqrt{\pi}} - 2, \quad (14)$$

with initial conditions:

$$\begin{cases} y(0) = 0, \\ y_x(0) = 1, \end{cases} \quad (15)$$

The exact solution is

$$y(x) = x(1 - x), \quad (16)$$

```

restart;
Step 1:
withplots:
N := 5;
S := 2/5;
K := 1/2;
g := x^2/4 - x/4 - 8*sqrt(x)/(5*sqrt(pi)) - 2;
y[0] := 0;
dy[0] := 1;
Y[0] := (0 + 1 * x + int(x^2/4 - x/4 - 8*sqrt(x)/(5*sqrt(pi)) - 2, x$2));
    
```

```

m := 3/2 + 1/2;
Step 2:
for n from 0 to N do
f := diff(Y[n], x$2);
G := simplify(1/Gamma(m - alpha) * int((x - s)^(m - alpha - 1) * subx(s = x, f), s = 0 ... x), assume = nonnegative);
H := simplify(-int(2/5 * G - 1/2 * Y[n], x$2), assume = nonnegative);
Y[n + 1] := expand(H);
end do;
Step 3:
NIA := sum(Y[k], k = 0..N + 1);
for x from 0 by 0.1 to 1 do
NIA[x] := evalf(eval(NIA));
end do;
y[x][2Dplot] := plot([NIA], x = 0 ... 1, color [red], axes = boxed, title
= fractional Bagley – Torvik equation IVPs Case 1);
y[x][2Dplot] := logplot([NIA], x = 0 ... 1, color [red], axes = boxed, title
= fractional Bagley – Torvik equation IVPs Case 1);
Output: See Table 1 and Figures 1, 2

```

**Case 2. The surface area  $S$  is greater than the stiffness of the spring constant  $K$**

$$D^2y(x) + \frac{1}{2}D^{\frac{3}{2}}y(x) - \frac{2}{5}y(x) = \frac{x^2}{4} - \frac{x}{4} - \frac{8\sqrt{x}}{5\sqrt{\pi}} - 2, \quad (17)$$

with initial conditions

$$\begin{cases} y(0) = 0, \\ y_x(0) = 1, \end{cases} \quad (18)$$

```

restart:
Step 1:
withplots:
N := 5;
S := 1/2;
K := 2/5;
g := x^2/4 - x/4 - 8*sqrt(x)/(5*sqrt(pi)) - 2;
y[0] := 0;
dy[0] := 1;
Y[0] := (0 + 1 * x + int(x^2/4 - x/4 - 8*sqrt(x)/(5*sqrt(pi)) - 2, x$2));
m := 3/2 + 1/2;
Step 2:
for n from 0 to N do
f := diff(Y[n], x$2);
G := simplify(1/Gamma(m - alpha) * int((x - s)^(m - alpha - 1) * subx(s = x, f), s = 0 ... x), assume
= nonnegative);

```

```

H := simplify(-int(1/2 * G - 2/5 * Y[n], x$2), assume = nonnegative);
Y[n + 1] := expand(H);
end do;
Step 3:
NIA := sum(Y[k], k = 0..N + 1);
for x from 0 by 0.1 to 1 do
NIA[x] := evalf(eval(NIA));
end do;
y[x][2Dplot] := plot([NIA], x = 0 ... 1, color [red], axes = boxed, title
= fractional Bagley - Torvik equation IVPs Case 2);
y[x][2Dplot] := logplot([NIA], x = 0 ... 1, color [red], axes = boxed, title
= fractional Bagley - Torvik equation IVPs Case 2);
Output: See Table 1 and Figures 1, 2.
    
```

**Case 3. The surface area  $S$  is equal to the stiffness of the spring constant  $K$**

$$D^2y(x) + \frac{1}{2}D^{\frac{3}{2}}y(x) - \frac{1}{2}y(x) = \frac{x^2}{4} - \frac{x}{4} - \frac{8\sqrt{x}}{5\sqrt{\pi}} - 2, \quad (19)$$

with initial conditions

$$\begin{cases} y(0) = 0, \\ y_x(0) = 1, \end{cases} \quad (20)$$

```

restart;
Step 1:
withplots:
N := 5;
S := 1/2;
K := 1/2;
g := x^2/4 - x/4 - 8*sqrt(x)/(5*sqrt(pi)) - 2;
y[0] := 0;
dy[0] := 1;
Y[0] := (0 + 1 * x + int(x^2/4 - x/4 - 8*sqrt(x)/(5*sqrt(pi)) - 2, x$2));
m := 3/2 + 1/2;
Step 2:
for n from 0 to N do
f := diff(Y[n], x$2);
G := simplify(1/(Gamma(m - alpha)) * int((x - s)^(m - alpha - 1) * subx(s = x, f), s = 0 ... x), assume
= nonnegative);
H := simplify(-int(1/2 * G - 1/2 * Y[n], x$2), assume = nonnegative);
Y[n + 1] := expand(H);
end do;
Step 3:
NIA := sum(Y[k], k = 0..N + 1);
for x from 0 by 0.1 to 1 do
    
```

```

NIA[x] := evalf(eval(NIA));
end do;
y[x][2Dplot] := plot([NIA], x = 0 ... 1, color[red], axes = boxed, title
= fractional Bagley – Torvik equation IVPs Case 3);
y[x][2Dplot] := logplot([NIA], x = 0 ... 1, color[red], axes = boxed, title
= fractional Bagley – Torvik equation IVPs Case 3);
Output: See Table 1 and Figures 1, 2.
    
```

**Table 1.** Numerical solutions for fractional Bagley-Torvik equation

x	Case 1 $K > S$	Case 2 $S > K$	Case 3 $K = S$
0	0.00000000000000000000	0.00000000000000000000	0.00000000000000000000
0.1	0.09003714575609670000	0.09019689275910890000	0.09021153557133420000
0.2	0.16027451051370710000	0.16111925446865500000	0.16122699444995600000
0.3	0.21085875278105220000	0.21308057719348000000	0.21341687704856900000
0.4	0.24188680735470110000	0.24629374672292200000	0.24703205762285500000
0.5	0.25341043900550710000	0.26091502542611400000	0.26225001775907700000
0.6	0.24543906121089720000	0.25705962169323800000	0.25919177007896000000
0.7	0.21794167866797620000	0.23480976534771500000	0.23793083257874900000
0.8	0.17084825859778810000	0.19421956791560900000	0.19849869251988200000
0.9	0.10405067979332910000	0.13531816759601700000	0.14088834094878100000
1.0	0.01740334450319540000	0.05811182557896970000	0.06505659389962100000

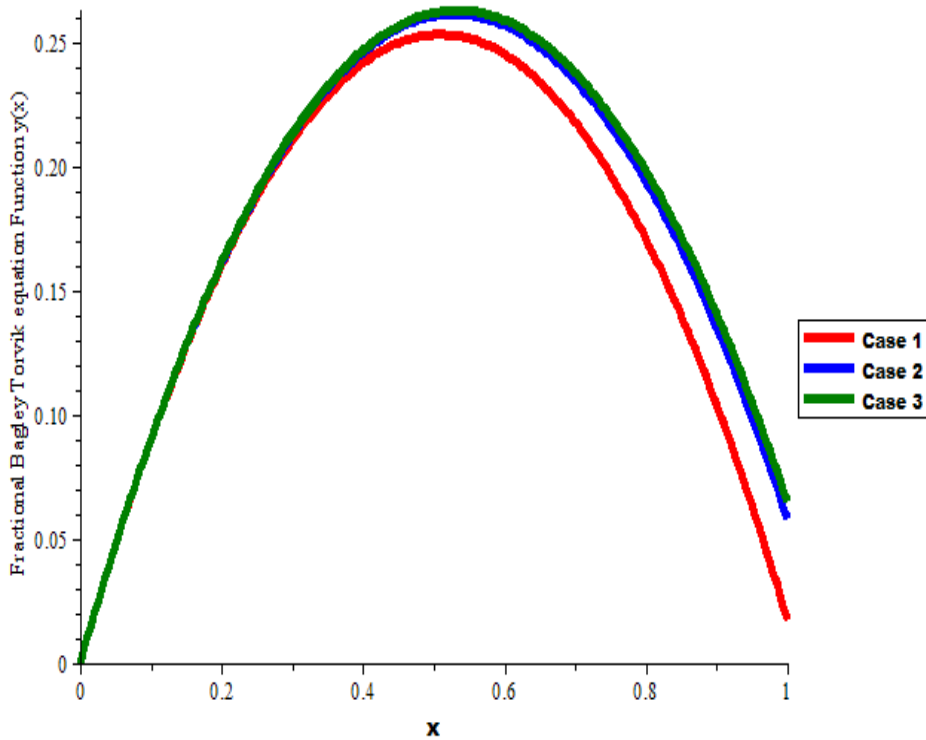


**Figure 1.** Depict the numerical solution  $y(x)$  for the relationship between three cases of the stiffness of the spring constant  $K$  and surface area  $S$  on interval  $0 \leq x \leq 1$  for  $K > S, S > K,$  and  $K = S$

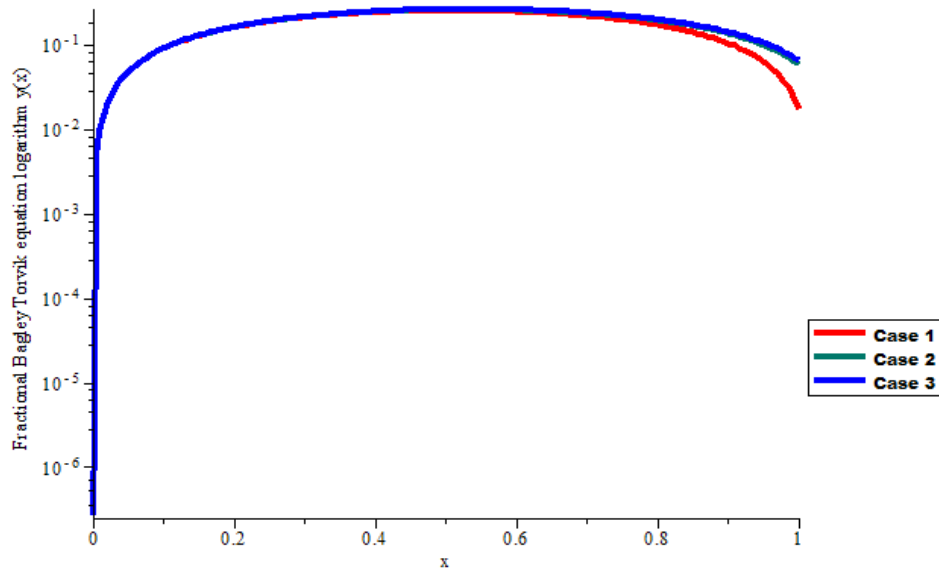


**Figure 2.** Depict the numerical solution  $y(x)$  ( $\log$ ) for the relationship between three cases of stiffness of the spring constant  $K$  and surface area  $S$  on interval  $0 \leq x \leq 1$  for  $K > S, S > K,$  and  $K = S$ .

## 5. Results and Discussion

The surface area  $S$  and stiffness of the spring constants  $K$  of fractional Bagley-Torvik equation are examined and from the numerical solutions obtained, we observed the following:

- i. The proposed algorithm demonstrated a good alternative to the conventional approach to solving the fractional differential equations.
- ii. The peak (maximum) results obtained for all cases within interval  $0.5 \leq x \leq 0.55$ .
- iii. The highest numerical results are obtained when the surface area  $S$  is equal to the stiffness of the spring constants  $K$  (see case 3: Table 1. and Figure 1. Blue).
- iv. The last results have obtained the stiffness of the spring constant  $K$  is greater than surface area  $S$  (see case 1: Table 1. and Figure 1. Red).
- v. Intermediary solutions are obtained when surface area  $S$  is greater than the stiffness of the spring constant  $K$  (see case 2: Table 1. and Figure 1. Green).

## 6. Conclusion

An efficient new iterative algorithm was formulated and applied for the numerical solutions of fractional Bagley-Torvik equation with constant parameters of the surface area  $S$  and stiffness of the spring  $K$ . Numerical results show that the computational cost of the technique has decreased significantly and through the numerical experiments, we observed that the solutions obtained are considered as the sum of finite series  $y(x) = \sum_{i=0}^5 y_i$  converges to exact solutions which demonstrated that new iterative algorithm is a suitable and powerful tool for solving fractional differential equations arising in the calculus of the theory of viscoelasticity.



## References

- [1] Agrawal OP, Kumar P. Comparison of five schemes for fractional differential equations, J. Sabatier et al. (eds.), *Advances in Fractional Calculus: Theoretical Developments and App in Phy and Eng* 2007; 43-60.
- [2] Chen W, Ye L, Sun H. Fractional diffusion equation by the Kansa method, *Comp Math App* 2010;59:1614-1620.
- [3] Jiang CX, Carletta JE, Hartley TT. Implementation of fractional order operators on field programmable gate arrays, J. Sabatier et al. (eds.), *Advances in Fractional Calculus: Theoretical Developments and App in Phy and Eng* 2007; 333-346.
- [4] Kilbas AA, Srivastava HM, Trujillo JJ. *Theory of application of fractional differential equations*, first ed., Belarus, 2006.
- [5] Lakshmikantham V, Vatsala AS. Basic theory of fractional differential equations, *Noon Anal.* 2008;(69): 2677-2682.
- [6] Miller KS, Ross B. *An Introduction to the fractional calculus and differential equations*, John Wiley, New York, 1993.
- [7] Momani S, Noor MN. Numerical methods for fourth-order fractional integrodifferential equations, *App Math and Comp* 2006 (182);754-760.
- [8] Torvik PJ, Bagley RL. On the appearance of the fractional derivative in the behavior of real materials. *J Appl Mech.* 1984; (51): 294-298.
- [9] Azhar AZ, Grzegorz K, Jan A. An investigation of fractional Bagley–Torvik equation, *MDPI Entropy* 2020; (22): 1-13.
- [10] Witkowski K, Kudra G, Wasilewski G, Awrejcewicz J. Modelling and experimental validation of 1-degree-of-freedom impacting oscillator. *Journal of System Control Engineering* 2019; (233): 418–430.
- [11] Bagley RL, Torvik PJ. A theoretical basis for the application of fractional calculus to viscoelasticity, *J Rheol* 1983; (27): 201-210.
- [12] Torvik PJ, Bagley RL. Fractional calculus in the transient analysis of viscoelastically damped structures. *AIAA J* 1985(23): 918-925.
- [13] Diethelm K, Ford NJ, Numerical solution of the Bagley-Torvik equation, *BIT Numerical Mathematics*, 2002; (42): 490-507.
- [14] Çenesiz Y, Keskin Y, Kurnaz A. The solution of the Bagley-Torvik equation with the generalized Taylor collocation method, *J Frankl Inst* 2010;(347), 452-466.
- [15] Zahra WK. Van Daele M. Discrete spline methods for solving two-point fractional Bagley-Torvik equation, *Appl Math Comput* 2017; (296):42-56.
- [16] Mekkaoui T, Hammouch Z. Approximate analytical solutions to the Bagley-Torvik equation by the fractional iteration method, *Ann Univ Craiova Math Comput Sci Ser* 2012; 39 (2): 251-256.
- [17] Mohammadi F. Numerical solution of Bagley-Torvik equation using Chebyshev wavelet operational matrix of fractional derivative, *Int J Adv in Appl Math and Mech* 2014; 2(1): 83-91.
- [18] Ray S. S., Bera R. K. Analytical solution of the Bagley-Torvik equation by Adomian decomposition method, *Appl Math Comput* 2005; 168 (1): 398-410.
- [19] Vijay S, Sushil K. Numerical scheme for solving two-point fractional Bagley-Torvik equation using Chebyshev collocation method, *WSEAS Transactions on Systems* 2018; (17):166-177.
- [20] Uzbas S. Y. Numerical solution of the Bagley-Torvik equation by the Bessel collocation method, *Mathematical Methods in the Applied Sciences* 2013; 36:300-312.
- [21] Tianfu J, Jianhua H and Changqing Y. Numerical solution of the Bagley–Torvik equation using shifted Chebyshev operational matrix, *Advances in Difference Equations* 2020; 3-14.
- [22] Hossein F, Juan J. N. An investigation of fractional Bagley-Torvik equation, *DE GRUYTER Open Math.* 2019, 17: 499–512.
- [23] Daftardar-Gejji. V and Jafari H. An iterative method for solving nonlinear functional equations, *Journal of Mathematical Analysis and Applications* 2006; 316(2): 753–763.
- [24] Falade KI, Tiamiyu AT. Numerical solution of partial differential equations with fractional variable coefficients using new iterative method (NIM), *IJ Mathematical Sciences and Computing*, 2020; 3: 12-21.
- [25] Hemeda AA. New iterative method: an application for solving fractional physical differential equations, *Hindawi Publishing Corporation Abstract and Applied Analysis* 2013; 1-10.



## Anomaly Detection in Yarn Tension Signal Using Independent Component Analysis

Canan TASTIMUR<sup>1\*</sup>, Mehmet AGRIKLI<sup>2</sup>, Erhan AKIN<sup>3</sup>

<sup>1</sup> Department of Computer Engineering, Faculty of Engineering-Architecture, Erzincan Binali Yildirim University, Erzincan, Turkey

<sup>2</sup> Managing Director, Agteks LTD, Istanbul, Turkey

<sup>3</sup> Department of Computer Engineering, Faculty of Engineering, Firat University, Elazig, Turkey

\*<sup>1</sup> ctastimur@erzincan.edu.tr, <sup>2</sup> mehmet.agrikli@agteks.com, <sup>3</sup> eakin@firat.edu.tr

(Geliş/Received: 07/09/2022;

Kabul/Accepted: 24/01/2023)

**Abstract:** Finding patterns in data that defy expected behavior is what anomaly detection entails. In many application fields, these incorrect patterns are referred to as contaminants, abnormalities, exceptions, or outliers. The significance of anomaly detection is that it helps to identify irregularities in data across a range of application domains and turns them into valuable information. When the yarn tension signals are inspected, anomaly states in the signals are seen in situations where it defect for whatever reason. This distinction makes it possible to predict whether the twister is malfunctioning. So, a bigger issue is avoided. The employment of Cluster-Based Algorithms, Statistical Method Algorithms, and other techniques to identify anomalies is common in the literature. The yarn tension signals in the twisting machines have been analyzed in this work using independent component analysis, and the problematic signal locations have been identified. The proposed method has been contrasted with other ways, and it has produced the highest success rate.

**Key words:** Anomaly detection, defect diagnosis, ICA, twister, yarn tension signal.

### Bağımsız Bileşen Analizi Kullanılarak İplik Gerginlik Sinyalinde Anormallik Tespiti

**Öz:** Anormallik tespiti, verilerde beklenen davranışı göstermeyen kalıpların elde edilmesine karşılık gelmektedir. Bu uygun olmayan kalıplar, farklı uygulama etki alanlarında anormallikler, istisnalar, aykırı değerler veya kirleticiler olarak adlandırılır. Anormallik tespitinin önemi, çeşitli uygulama alanlarındaki verilerdeki anormalliklerin önemli bilgilere dönüşmesidir. İplik gerginlik sinyalleri incelendiğinde herhangi bir nedenle arıza yaptığı durumlarda bu sinyallerde anormallik durumları gözlemlenmektedir. Bu farklılıktan yola çıkarak iplik bükme makinesinde, bir arıza olup olmadığı önceden tespit edilebilir. Böylece daha büyük bir sorunun önüne geçilmiş olmaktadır. Anormallikleri tespit etmek için literatürde birçok yöntem kullanılmaktadır: Küme Tabanlı Algoritmalar, İstatistiksel Yöntem Algoritmaları vb. Bu çalışmada, bağımsız bileşen analizi kullanılarak, iplik makinelerinde bulunan iplik gerilim sinyalleri incelenmiş ve hatalı sinyal bölgeleri incelenmiştir. belirlenen. Önerilen yöntem diğer yöntemlerle karşılaştırılmış ve önerilen yöntemle en yüksek başarı oranı elde edilmiştir.

**Anahtar kelimeler:** Anormallik tespiti, arıza teşhisi, BBA, iplik bükme makinesi, iplik gerilim sinyali.

### 1. Introduction

To identify unexpected flaws in the yarn quality control system, the tension signal model in the yarn twisting machine should be examined. However, due to some unidentified noise that alters the wave appearance of the twisted yarn tension signal in various manufacturing locations or production processes, this analysis method is quite challenging [1]. On the spinning machine, a few methods can be used to extract the tension signal from the noise signal. Unknown noises confuse the yarn tension signal. The wave appearance of the tension signals in the yarn twisting machine is generally affected by noise during the yarn twisting operation. Uncertain signals (such as electrical noise, mass change, vibration disturbance, etc.) cause noise irregularity [2]. The tension sensor must be able to distinguish between even the tiniest variations in thread tension and eliminate noise—higher frequency variations—from the signal [3].

The quality control system fails to appropriately identify atypical flaws as a result of noise incidents. For signal processing to correctly categorize all kinds of odd voltages, a strong filter is required. Traditional low-pass filters, however, sometimes fail to successfully suppress noise. In order to reduce noise, the conventional low-pass filter often uses frequency-assigned information. Designing the filter function and multiplying the measurement signal by the filter function is the fundamental technique for the conventional low pass filter. High-frequency

\* Corresponding author: [ctastimur@erzincan.edu.tr](mailto:ctastimur@erzincan.edu.tr). ORCID Number of authors: <sup>1</sup> 0000-0002-3714-6826, <sup>2</sup> 0000-0002-1014-5970, <sup>3</sup> 0000-0001-6476-9255

noise-related components in the signal are reduced using the filter function. However, the typical filter struggles to produce noise in the presence of a low-frequency noise signal. For instance, the mass change of material in the twister machine is seen as noise. This noise is broadcast in the low-frequency region, which is also the region where the primary voltage signal is broadcast. The conventional low-pass filter has a difficult time removing this noise (mass change). Figure 1 depicts how an exemplary yarn twist machine looks.



**Figure 1.** Example of a twister yarn machine [4].

In order to perform Sparse Kernel Principal Component Analysis (SKPCA) for outlier detection, Das et al. [5] proposed a novel method. On five real-world datasets, they examined them, and they found that by employing just 4% of the main components (PCs). A different study [6] advocated for detecting anomalies in hyperspectral data using a selective kernel principal component analysis approach. The kernel principal component analysis (KPCA) step in this approach is the first step in thoroughly mining the high-order correlation between spectral bands. Then, in regional events, high-order statistics are used to determine the local average singularity.

Mei et al. [7] suggested using an independent component analysis (ICA) technique to find anomalies in hyperspectral imaging. Kernel Principal Component Analysis (KPCA) is performed on a feature space in order to whiten the data and fully mine the nonlinear information between spectral bands. Then, ICA examines the projection directions in the KPCA-whitened space to carry out a mutually independent distribution of the calculated data. Applying ICA after random massive reductions was indicated in a different study as a way to reduce EEG signals with artifacts [8]. Zonglin et al. [9] presented a multidimensional traffic anomaly detection system based on ICA. They employed ICA to separate the potentially anomalous component from a particular traffic signal's time and frequency domain properties. Zunic et al. [10] published an original method for locating various forms of abnormalities in GPS data. The connection between detecting a QRS complex in a GPS signal and an ECG signal was given as the explanation. A kernel background cleaning-based technique for anomalous target detection was suggested [11]. The suggested method consists of two levels: kernel-based pure background pixel set extraction and background covariance matrix estimation using the returned pure background pixel set. Johnson et al. [12] employed ICA manipulation and hyperspectral imaging (HSI) anomaly detectors to locate anomalous pixels.

In this study, the yarn tension signal has been carried out by examining the system developed to detect the failures in the twister machine early. By using independent component analysis, noisy components in the yarn tension signal are separated without damaging the main component. Later on, anomaly detection has been made and defective regions in the yarn tension signal have been exposed. Ten different faulty yarn tension signals have been evaluated during the testing phase. The use of the ICA technique enhances the literature by allowing for predictive maintenance of yarn tension signals. When studies for predictive maintenance in textile machines are examined in the literature, this study is a new and unique study in terms of developing a method by examining yarn tension signals. In this study, by investigating the yarn tension levels through an ICA-based method, it is possible to determine whether or not there is an abnormal situation. In our study, the proposed method, as well as other techniques such as PCA, KPCA, SRP, and GRP, have been thoroughly evaluated in terms of precision-recall curve value and AUC value in the experimental results section.

## 2. Anomaly Detection

A simple definition of anomaly detection is a method that makes it possible to find unusual events or patterns in data. These unexpected events or patterns are genuine occurrences that deviate from the data's expected behavior. In the literature, these unanticipated events are referred to as outliers, exceptions, or anomalies. Data sets that do not fit a clearly defined pattern of typical behavior are considered anomalies [13]. Figure 2 shows anomalies in a straightforward 2D dataset. Two observation zones,  $N_1$  and  $N_2$ , which each cover two regions, are present in the data. Far enough from the areas, the  $O_1$ ,  $O_2$ , and  $O_3$  points are oddities. Data irregularities can occur for a number of causes, including malware, credit card fraud, cyberattacks, or terrorist activities.

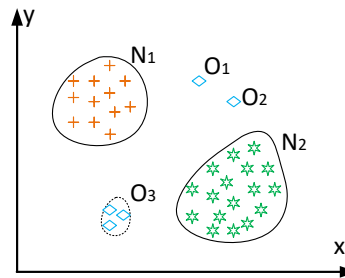


Figure 2. An illustration of an anomaly in a 2-D data set [14].

### 2.1. Difficulties of Anomaly Detection

It can be difficult to distinguish between typical and deviant behavior. Therefore, a neighboring anomalous observation can appear normal. Aggressive opponents frequently make adjustments to make abnormal observations seem normal when anomalies emerge from corrupt activity, making normal behavior even harder to identify. Most datasets do not frequently create clusters like the one in the previous example between normal and anomalous data. A cluster where the data is located may have a normal data anomaly nearby, and a cluster where the normal data is placed may have a normal data anomaly nearby. Anomaly detection becomes quite challenging in this situation.

Data or behaviors that we consider normal may alter over time. Therefore, it is not always easy to define what constitutes normal behavior. An anomaly detection method may not be applicable in all situations. In the medical area, a tiny change in body temperature, for instance, can signal abnormal conduct, whereas a small change in stock prices can signal normal behavior. This makes it impossible to use an anomaly detection method everywhere. It is important to do a rigorous operation to remove the noise in order to discover any noise abnormalities in the day-tastes (noise removal). However, separating noises is an extremely challenging procedure. It might be challenging to filter out and remove noise from data that frequently closely resembles true anomalies. The most common sort of anomaly detection problem is tough to fix as a result of the aforementioned issues. The majority of anomaly detection algorithms in use today can resolve a certain problem formulation. Figure 3 illustrates the aforementioned essential elements of any anomaly detection method.

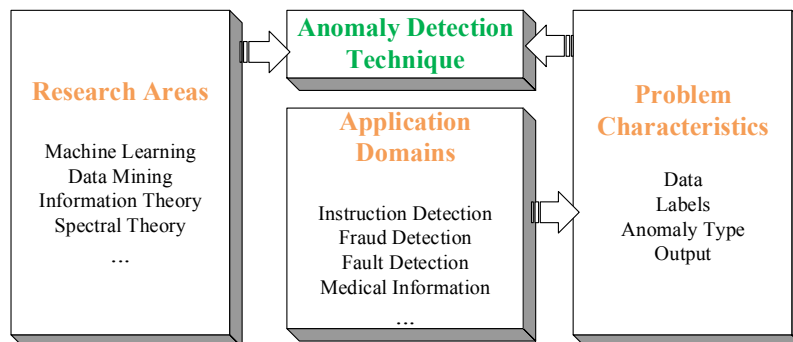


Figure 3. Anomaly detection's most important components

## 2.2. Types of Anomaly

### A. Point Anomaly

If a data sample differs significantly from other normal data, it is considered anomalous data. Because the anomaly detection is dependent on a particular attribute, the cause of this anomaly detection is referred to as a point anomaly. For instance, we can look for irregularities in the amount we charge to our credit cards. For instance, in Figure 2, points  $O_1$  and  $O_2$  are not within the boundaries of the standard regions, nor are the points in the  $O_3$  region, therefore the point anomalies are different from the usual data points.

### B. Contextual Anomaly

A data sample behaves abnormally in a certain environment, which is known as a contextual anomaly or conditional anomaly. The dataset's structure makes it easier to understand the concept of context, which must be stated as part of the formulation of the problem. Three feature sets: environmental attributes, behavioral characteristics, define each data sample. In this illustration, the context is established using contextual attributes. The longitude and latitude of a point, for instance, are contextual elements in spatial databases. In time-series data, the contextual attribute of time reveals the direction of a row inside the overall row. Behavioral traits define a sample's non-contextual properties. Contextual features in spatial databases include, for instance, a position's longitude and latitude. In time-series data, time is a contextual information that specifies a row's position within a full row. Behavioral traits are used to categorize a sample's non-contextual properties. For instance, a behavioral feature in a geographic dataset that describes average precipitation worldwide is the amount of precipitation wherever. The context abnormality in the temperature time series  $t_2$ ,  $t_1$  is identical to the temperature at time  $t_2$ , but takes place in a different setting, therefore it is not regarded as abnormal [14]. Figure 4 is an example of temperature time series with a contextual anomaly.

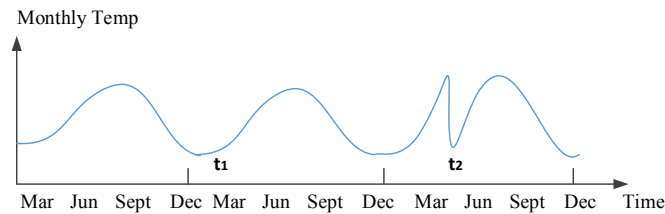


**Figure 4.** A temperature time series with a contextual anomaly.

### C. Collective Anomaly

If the data connected to one another causes unusual behavior in the entire dataset, this is an illustration of a collective anomaly. When combined, certain connected data may create an anomaly, even though these data might not act in a single dataset. An illustration of a human ECG is shown in Figure 5. Because the same low value has been abnormally prevalent for a long period, the highlighted area displays abnormality.

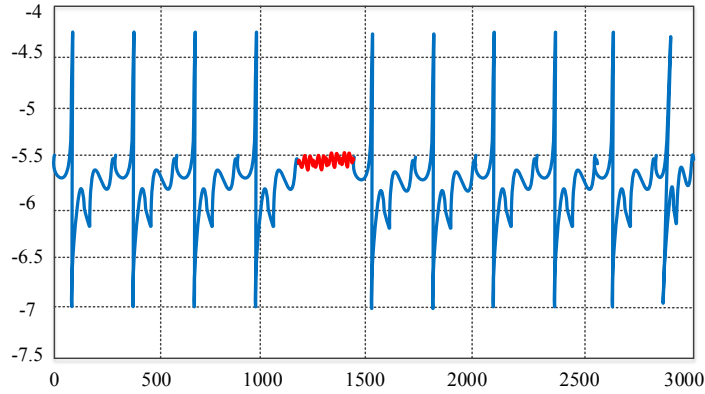


**Figure 5.** An example of collective anomaly [14]

### 3. The Proposed Method

By examining the yarn tension signals in the spinning machine, malfunctions in the twisting machine can be detected early. For some reason, the noisy signal can be added to the main thread tension signal. To analyze the yarn tension signal, the noise must be extracted from the main signal. By detecting anomalies in the signal obtained as a result of this process, it can be determined whether there is a malfunction. The ICA approach is used in the noise separation process.

#### 3.1. Independent Component Analysis (ICA)

In 1988, Herault and Jutten [15] developed ICA for blind source separation (BBS). It's commonly used in voice, and medical signal analysis, as well as image processing [16]. In several scientific and engineering settings [17], an unknown mix matrix is assumed to linearly transform unobservable signals into a collection of observable mixed signals. Figure 6 and equation (1) denote the model.

$$X(t) = AS(t) + N(t) \tag{1}$$

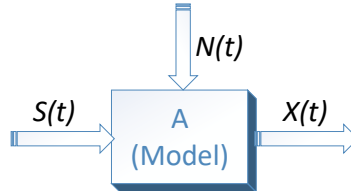


**Figure 6.** Mix system model [17]

In Figure 6,  $S(t)$  denotes unobservable source signals, 'A' means the mixing matrix,  $N(t)$  represents Gaussian white noise, and  $X(t)$  depicts the acquired data. The data variables in the model are assumed to be linear mixes of unseen source signals. They are referred to as the independent components of the observed data since they are non-Gaussian and mutually independent. When traditional approaches fail, ICA can expose these independent components or source signals [17]. It is quite beneficial to perform some pre-processing such as whitening and fixing before using an ICA algorithm [18-20]. With the assumption of the existence of  $M$  independent source signals  $s = [s_1, s_2, s_3, \dots, s_M]^T$  and observations of  $J$  mixture signal is  $x = [x_1, x_2, x_3, \dots, x_J]^T$ . The standard model of ICA is

$$x = A \cdot s \tag{2}$$

In Equation (2),  $A$  is a  $J \times M$  mixing matrix. The ICA's goal is to create a demixing matrix  $W$  that can be used to split the signal source vector into a set of statistically independent sources. Therefore, the independent components can be determined as

$$y = W \cdot x \quad (3)$$

where  $y$  is the estimation of  $s$ . It can be seen from the Equation (2) and (3) that  $y$  is the linear combination of  $s$  [7].

$$y = Wx = WAs = Vs \quad (4)$$

In Equation (4), it is obtained  $V = WA$ . With ICA, it is aimed to find abnormalities in the signal after independent components are detected. In detecting an anomaly, a number of pre-processing steps are applied to the received input signal first. Thanks to this process, the properties of the signal are removed. Then anomaly detection is made and as a result, the time periods with abnormalities can be listed or the abnormalities can be removed from the main signal. Anomaly detection framework shows in Figure 7.

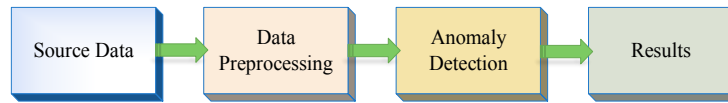


**Figure 7.** Anomaly detection framework

The proposed approach is completely data-driven and does not work based on threshold values. In this study, abnormalities were found by non-parametric Empirical Data Analytics (EDA) estimators, depending on the respective distribution of the data and the association characteristics. The proposed approach is completely data-driven and does not work based on threshold values. In this study, abnormalities were found by non-parametric EDA estimators, depending on the mutual distribution of the data and community characteristics. In the proposed study, potential anomalies were identified first, and these anomalies were divided into non-parametric data clouds. Later, abnormalities in each data cloud were determined. The proposed approach has been tested on ten separate yarn tension signals. Besides, the proposed approach has been compared with many methods such as Principal Component Analysis (PCA), Kernel PCA, Gaussian Random Projection (GRP), and Sparse Random Projection (SRP) to detect the components in the signal, and the highest precision and accuracy rate have been obtained in the proposed approach.

#### 4. Experimental Results

In this study, yarn tension signals are taken as inputs, and the main signal is separated from the noisy components by the ICA method on these signals. Later, abnormalities in the signal have been detected. On the yarn tension signal, PCA, Kernel PCA, ICA, SRP and GRP methods are applied to separate the signal into its components, and the precision-recall curve and AUC (Area Under the Curve) curve of these methods are given below. In figure 8, there are examples of yarn tension signals. Figures of yarn tension and signal applied ICA are given in figure 9.



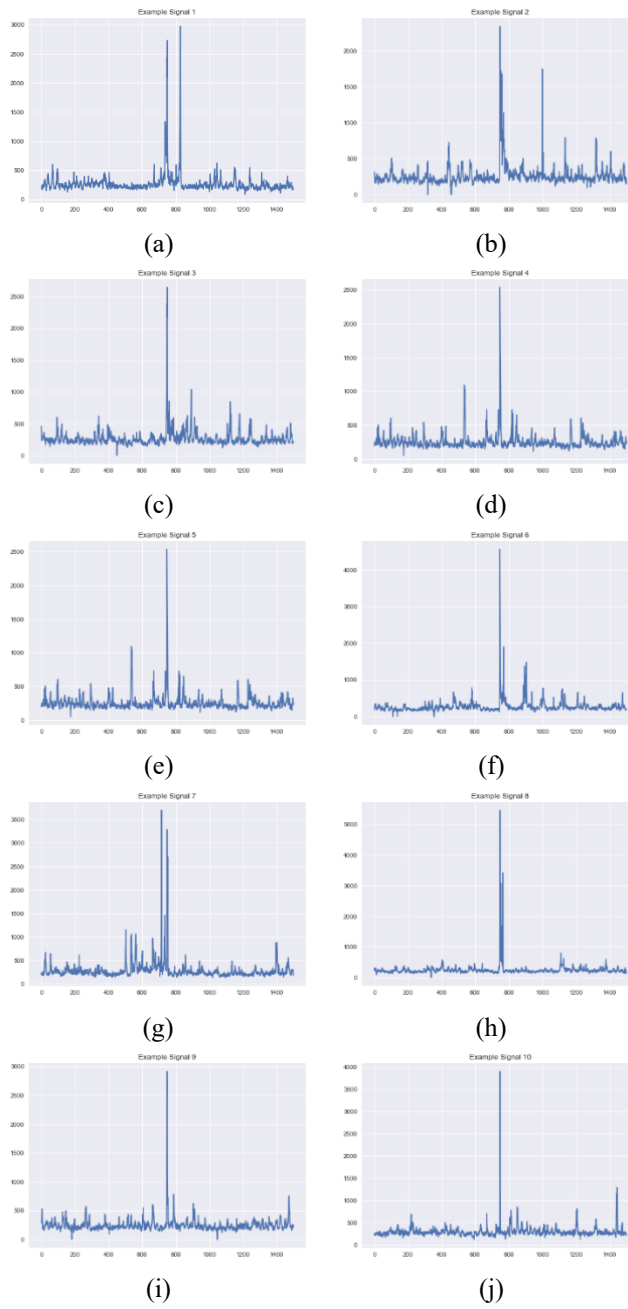


Figure 8. Examples of yarn tension signals.

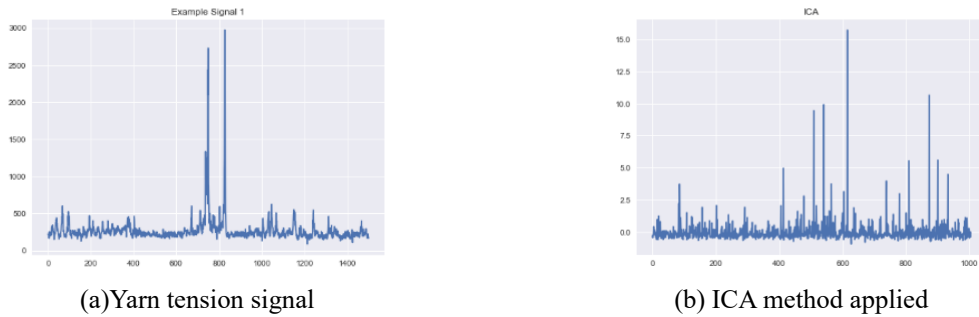
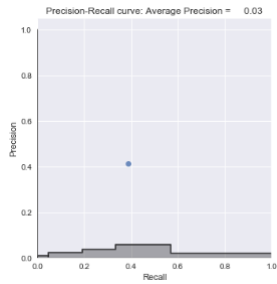
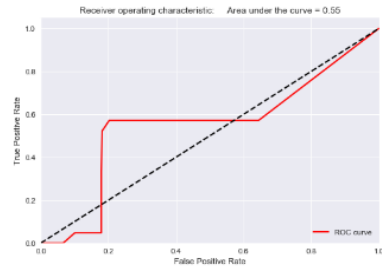


Figure 9. Yarn tension and signal applied ICA

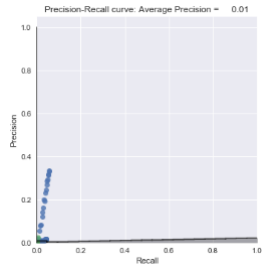
Anomaly Detection in Yarn Tension Signal Using Independent Component Analysis



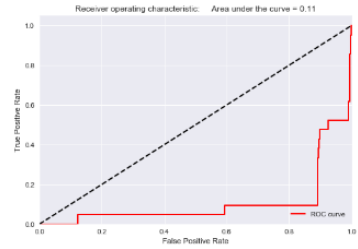
(a) Precision-recall curve of the PCA method



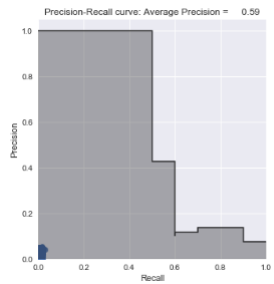
(b) AUC of the PCA method



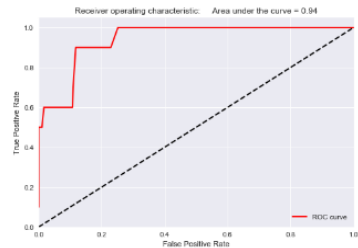
(c) Precision-recall curve of the Kernel PCA method



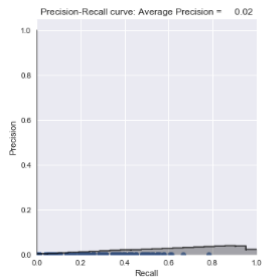
(d) AUC of the Kernel PCA method



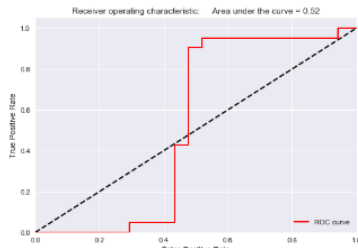
(e) Precision-recall curve of the ICA method



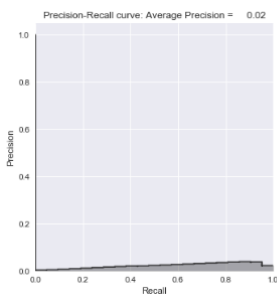
(f) AUC of the ICA method



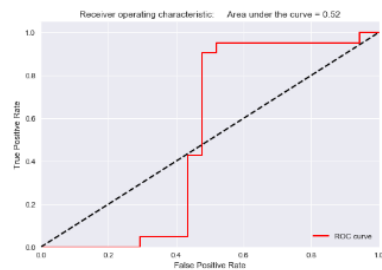
(g) Precision-recall curve of the SRP method



(h) AUC of the SRP method



(i) Precision-recall curve of the GRP method



(j) AUC of the GRP method

**Figure 10.** Precision-recall curves and AUC curves obtained from this study.

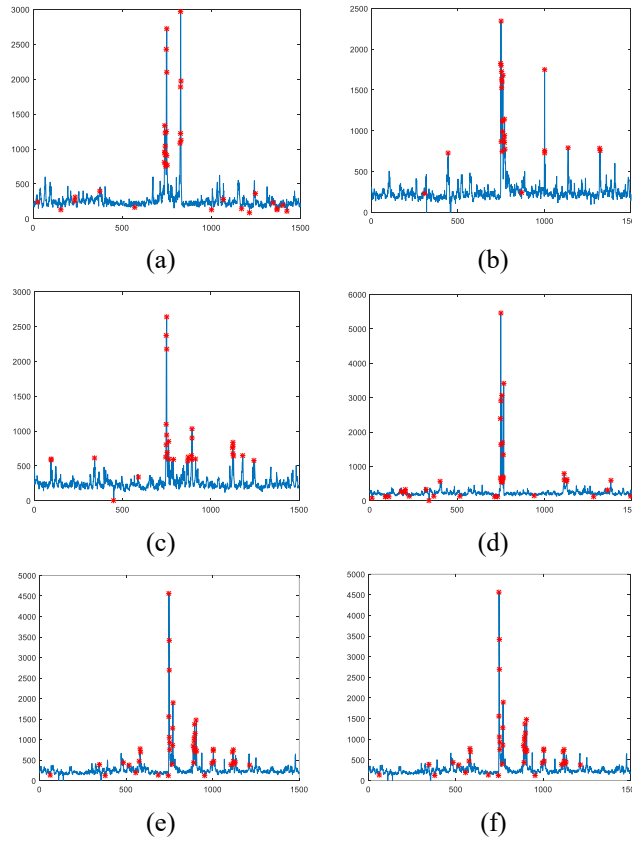


**Figure 11.** Anomaly detection results of example yarn tension signals

**Table 1.** Performance comparison of the proposed and other methods.

Method	Precision-recall curve value	AUC value
PCA	0.03	0.55
Kernel PCA	0.01	0.11
ICA	0.59	0.94
SRP	0.02	0.52
GRP	0.02	0.52

Anomaly detection results of example yarn tension signals are given in Figure 11. The drawback of the PCA method is that it ignores the less significant dimensions while examining the data. The PCA method is also computationally expensive for high-dimensional data. The KPCA method only captures nonlinear structures, although it uses less memory and processing resources than PCA. Size reduction is a task that both RP approaches must do, just like any other technique. Additionally, it provides the benefit of faster working speed. According to PCA, RP approaches do not demand that data be kept in memory. PCA performs best with data that has few dimensions. However, it may be claimed that with RP approaches, the quality degrades during the conversion process. It is considered that ICA multivariate data consists of the linear combination of a number of independent components. In most cases, it is assumed that the number of components equals the number of variables. It has a benefit because of this. When the data in Table 1 are evaluated, it becomes clear that the proposed ICA technique yields the best results. The performance in binary classification issues can be interpreted using the precision-recall curve and the AUC curve. The link between the genuine positive rate value and the positive predictive value is represented by the precision-recall curve. A low recall with high precision on the precision-recall curves denotes strong performance, while a high recall with low precision denotes subpar performance. This kind of analysis of the tables reveals that the suggested approach performs at the highest level. Precision-recall curves and AUC curves obtained from this study are given in Figure 10. On the other hand, this study also made use of the AUC

curve, which is utilized to gauge a classifier's capacity for class distinction. The model performs better at differentiating between positive and negative classes the higher the AUC value. AUC value close to 1 indicates good distinguishability between classes. Figure 10 (f) indicates that the proposed method has the highest AUC.

## 5. Conclusions

The importance of anomaly detection is that the abnormalities in the data in various application areas turn into important information. When the yarn tension signals are examined, in cases where they defect for any reason, anomaly states are observed in these signals. Based on this difference, it can be determined beforehand whether there is a malfunction in the twister. Thus, a larger problem is prevented. Many methods are used in the literature to detect anomalies: cluster-based algorithms, statistical method algorithms, etc. In this study, using independent component analysis, the yarn tension signals in the twister machines have been examined and the defective signal regions have been determined. In this study, yarn tension signals are taken as inputs, and then the main signal is separated from the noisy components by the ICA method on these signals. Abnormalities in the signal have been detected. On the yarn tension signal, PCA, Kernel PCA, ICA, Sparse Random Projection (SRP), and Gaussian Random Projection (GRP) methods have been applied to separate the signal into its components, and results have been compared; it is observed that ICA produces more successful results than other methods.

## References

- [1] Shih-Hsuan C and Lu C. Noise separation of the yarn tension signal on twister using FastICA. *Mechanical systems and signal processing* 2005; 19(6): 1326-1336.
- [2] Hwa Y. QAI–Yarn Quality Control System. User Guide 2003; 25-45.
- [3] Recep E, Mutlu H N and Celik O. Design and Realisation of A Yarn Tension Sensor Using Strain Gauge Type Load Cells. *Uludag University Journal of The Faculty of Engineering* 2019; 24(2): 751-768.
- [4] Two for One Yarn Twisting Machine, <http://www.yarn-winding.com/twisting-machine/yarn-twisting-machine/two-for-one-yarn-twisting-machine.html>, last accessed 2020/04/05.
- [5] Das R, Golatkar A and Awate S. Sparse Kernel PCA for Outlier Detection. In: 2018 17th IEEE International Conference on Machine Learning and Applications (ICMLA), 2018; Florida, USA: IEEE. pp. 152-157.
- [6] Yanfeng G, Liu Y and Zhang Y. A selective kernel PCA algorithm for anomaly detection in hyperspectral imagery. In: 2006 IEEE International Conference on Acoustics Speech and Signal Processing Proceedings, 2006; France: IEEE.
- [7] Mei F, Zhao C, Wang L and Huo H. Anomaly detection in hyperspectral imagery based on kernel ICA feature extraction. In: 2008 Second International Symposium on Intelligent Information Technology Application, 2008; IEEE. pp. 869-873.
- [8] Katsumata S and Kanemoto D. Applying Outlier Detection and Independent Component Analysis for Compressed Sensing EEG Measurement Framework. In: 2019 IEEE Biomedical Circuits and Systems Conference (BioCAS): 2019; IEEE. pp. 1-4.
- [9] Zonglin L, Guangmin H and Xingmiao Y. Multi-dimensional traffic anomaly detection based on ICA. In: 2009 IEEE Symposium on Computers and Communications, 2009; IEEE. pp. 333-336.
- [10] Žunić E, Delalić S, Hodžić K, and Tucaković Z. Innovative GPS Data Anomaly Detection Algorithm inspired by QRS Complex Detection Algorithms in ECG Signals. In: IEEE EUROCON 2019-18th International Conference on Smart Technologies, 2019; IEEE. pp. 1-6.
- [11] Zhang Y, Xu M, Fan Y, Zhang Y, and Dong Y. A Kernel Background Purification Based Anomaly Target Detection Algorithm for Hyperspectral Imagery. In: IGARSS 2019-2019 IEEE International Geoscience and Remote Sensing Symposium, 2019; IEEE. pp. 441-444.
- [12] Johnson R J, Williams J P and Bauer K W. AutoGAD: An improved ICA-based hyperspectral anomaly detection algorithm. *IEEE Transactions on Geoscience and Remote Sensing* 2012; 51(6): 3492-3503.
- [13] A'dan Z'ye Anomaly Detection, Medium, <https://medium.com/@oguzkircicek/adan-z-ye-anomaly-detection-62b54f6bdd63>, last accessed 2020/04/05.
- [14] Chandola V, Banerjee A and Kumar V. Anomaly detection: A survey. *ACM computing surveys (CSUR)* 2009; 41(3): 1-58.
- [15] Jutten C and Herault J. Independent components analysis (INCA) versus principal components analysis. In: Fourth European Signal Processing Conference, 1988; Grenoble, France. pp. 643– 646.
- [16] Zhao C, Wang Y and Mei F. Kernel ICA feature extraction for anomaly detection in hyperspectral imagery. *Chin. J. Electron* 2012; 21(2): 265-269.
- [17] Xu L and Li H Z. An anomaly detection method for spacecraft using ICA technology. In: 2013 International Conference on Advanced Computer Science and Electronics Information (ICACSEI 2013), 2013.
- [18] Vecchio E, Lazzarini B, Boley S. Spacecraft Fault Analysis Using Data Mining Techniques. In: Proc of ISAIRAS Conference, 2005; pp. 5-8.

- [19] Agarwal L and Rajan K S. Integrating Mser into a Fast ICA Approach for Improving Building Detection Accuracy. In: IGARSS 2018-2018 IEEE International Geoscience and Remote Sensing Symposium, 2018; IEEE. pp. 4831-4834.
- [20] Abidi A, Noura I and Bedoui M H. Parallel Implementation on GPU for EEG Artifact Rejection by Combining FastICA and TQWT. In; 2018 IEEE/ACS 15th International Conference on Computer Systems and Applications (AICCSA), 2018; IEEE. pp. 1-8.



## The Effects of Hydroxyapatite on the Corrosion Behaviour of AZ Series Mg Alloys

Yakup SAY<sup>1\*</sup>

<sup>1</sup>Department of Machine and Metallic Technology, Munzur University, Tunceli, Turkey  
\*[yakupsay@gmail.com](mailto:yakupsay@gmail.com)

(Geliş/Received: 03/09/2022;

Kabul/Accepted: 29/10/2022)

**Abstract:** Metallic biomaterials are widely used in the orthopedic and dental applications owing to their advanced biocompatibility and sophisticated mechanical properties. Many studies are carried out to develop new alloys with high specific strength, high corrosion resistance and high biocompatibility as an alternative to present metallic biomaterials. Mg alloys are potential alloys as a biomaterial, especially because they have low density and high biocompatibility. However, especially the corrosion properties of Mg alloys need to be improved. In this study, the surfaces of AZ31, AZ61 and AZ91 alloys, which are promising as biomaterials, were coated with hydroxyapatite with high biocompatibility, and the effects of the bioceramics coatings on corrosion resistance were comprehensively investigated. Crack-free and porous surface morphologies were obtained in all bioceramic coatings and the presence of the coatings on the surfaces was supported by EDS analysis. As a result of the corrosion tests performed in SBF, it was determined that the AZ91 alloy had the highest corrosion resistance among the uncoated samples. The hydroxyapatite bioceramic coatings also improved the corrosion properties of all samples. However, among all samples, the highest corrosion resistance was obtained in the hydroxyapatite coated AZ91 alloy.

**Key words:** Hydroxyapatite; AZ Mg alloys; Sol-gel; Corrosion

### AZ Serisi Mg Alaşımlarında Hidroksiapatitin Korozyon Davranışı Üzerine Etkisi

**Öz:** Metalik biyomalzemeler, özellikle ortopedik uygulamalarda yaygın olarak kullanılmaktadır. Mevcut metalik biyomalzemelere alternatif, yüksek spesifik mukavemete, yüksek korozyon direncine ve yüksek biyouyumluluğa sahip yeni alaşımlar geliştirebilmek için pek çok çalışma yapılmaktadır. Mg alaşımları özellikle düşük yoğunluk ve yüksek biyouyumluluğu ile umut vadeden bir alaşımdır. Ancak özellikle korozyon özelliklerinin geliştirilmesi gerekmektedir. Bu çalışmada biyomalzeme olarak umut vadeden AZ31, AZ61 ve AZ91 alaşımlarının yüzeyleri yüksek biyouyumluluğa sahip hidroksiapatit ile kaplanarak, kaplamaların korozyon direncine etkileri kapsamlı olarak incelenmiştir. Tüm biyoseramik kaplamalarda çatlaksız ve gözenekli yüzey morfolojileri elde edilmiş ve EDS analizleri ile kaplamaların yüzeylerdeki varlığı desteklenmiştir. SBF içerisinde yapılan korozyon testleri sonucunda kaplamasız numuneler arasında en yüksek korozyon dayanımına AZ91 alaşımının sahip olduğu tespit edilmiştir. Hidroksiapatit biyoseramik kaplama, tüm numunelerde de korozyon özelliklerini iyileştirmiştir. Bununla birlikte en yüksek korozyon dayanımı hidroksiapatit kaplı AZ91 alaşımında elde edilmiştir.

**Anahtar kelimeler:** Hidroksiapatit, AZ Mg Alaşımları, Sol-Gel, Korozyon

### 1. Introduction

The basic features that biomaterials should have in order to be used safely in orthopedic applications; biocompatibility, corrosion resistance, wear resistance, mechanical compatibility and osteointegration [1,2]. Metallic biomaterials are widely used in the orthopedic and dental applications owing to their advanced biocompatibility and sophisticated mechanical properties. Commonly used traditional metallic implant materials are low-carbon stainless steel, cobalt, and titanium alloys. These alloys have highly improved mechanical properties compared to body tissues (e.g. bone and tooth). However, the fact that the implant has very high strength values compared to the tissue causes load distribution imbalances between the tissue and the implant. In tissue-implant interaction, this biomechanical incompatibility is called “stress shielding effect” and this is a negative situation that reduces the life of the implant [3,4]. However, the high density values of these alloys cause tissue-implant incompatibility and various complications [5,6]. This causes implant loss and requires a second surgical operation. Therefore, it is very important to develop new biocompatible materials with sufficient strength and low density. Magnesium alloys have high specific strength (strength/density) [3,7-10] and low density values [11,12]. Hence, magnesium alloys are a potential alloy for orthopedic applications due to their low density value, near-bone elastic modulus and biocompatibility [13-17]. However, the biodegradable behavior of magnesium alloys limits the use of these materials. Magnesium has a very low corrosion potential and is more active than most metals

at 25°C. Therefore, it has a particularly high susceptibility to galvanic corrosion [18]. Implant materials used in in-vivo applications are exposed to body fluids containing various anions ( $\text{Cl}^-$ ,  $\text{HCO}_3^-$ ,  $\text{HPO}_4^{2-}$ ), cations ( $\text{Na}^+$ ,  $\text{K}^+$ ,  $\text{Ca}^{+2}$ ,  $\text{Mg}^{+2}$ ) and dissolved oxygen [19, 20]. Therefore, the human body is a highly corrosive environment for metals used as biomaterials. Chloride, in particular, degrades the semi-passive unstable layer formed on the surface of magnesium as a result of various reactions and causes local degradation. Therefore, it is very difficult to use biodegradable metals (such as Mg alloys) as implant materials in in-vivo applications [21]. Therefore, it is necessary to improve the corrosion properties of these alloys, which have low density and low elastic modulus [22, 23]. In order to prevent or reduce corrosion, it is necessary to prevent the diffusion of corrosive media such as water, oxygen, acid to the surface. For this purpose, metallic surfaces are coated with materials that are stable against corrosive environments. However, bioceramic coatings are made not only to improve corrosion resistance, but also to provide metallic implants with bioactivity and antibacterial properties, and to increase biocompatibility, abrasion and creep resistance [24-27].

Different surface modifications are generally preferred in order to improve the interaction of the metallic implant with the tissue and to increase its corrosion resistance and biocompatibility. The most commonly used materials for surface modifications of metallic implants are hydroxyapatite, bioactive glass and glass ceramics [12,28]. Hydroxyapatite (HA), which is a biodegradable or absorbable biocompatible material, is capable of forming strong chemical bonds with natural bone tissue due to its characteristic properties [29-31]. Due to its bone-like structure, HA allows tissue development of the bone and thus provides significant advantages in terms of osteointegration in orthopedic applications [32]. Besides, it improves biocompatibility and corrosion resistance and helps to prevent ion release as a physical barrier. For this reason, it is generally preferred as the surface coating material of metallic implants [33-35]. Surface modifications of metallic implants can be made using different techniques [36-39]. It is possible to obtain homogeneous solutions at low temperatures with the sol-gel method. For this reason, it is a more advantageous and easier method compared to other methods [40,41].

In order to demonstrate a possible alternative usage of AZ series Mg alloys in low load bearing biomedical applications, corrosion resistances of sol-gel derived Hydroxyapatite based bioceramic dip-coating on AZ31, AZ61 and AZ91 alloys are investigated in this work.

## 2. Experimental Procedure

### 2.1. Materials

AZ31, AZ61 and AZ91 Alloys has been used as substrate. AZ series samples were cut in the sizes of 10x20x5 mm. Firstly, the substrates were sand blasted by  $\text{SiO}_2$  particles before the coating process in order to improve adhesion of the coating. Sand blasted process with  $\text{SiO}_2$  particles (90  $\mu\text{m}$ ) at 6 bar pressure was applied onto surfaces. Finally, they were ultrasonically cleaned in distilled water, acetone, and ethanol in order to remove the contaminants and made ready for the coating process.

### 2.2. Surface Coating

Substrates were coated by sol gel dipcoating technique. The dipping sol fort the coatings were prepared by usingh HA powder with a approximately 10  $\mu\text{m}$  and to ease gelation and sinterability  $\text{P}_2\text{O}_5$ ,  $\text{KH}_2\text{PO}_4$  and  $\text{NaCO}_3$  inorganic materials as additives were added. Before sol gel process commercial pure hydroxyapatite (HA) and  $\text{NaCO}_3$  powders were dried in incubator at 80 °C to avoid agglomeration. The prepared sol was ultrasonically homogenized until a homogenous gel was obtained. After the gel was formed, the substrates were dipped into the gel and dip-coated at an immersion rate of 5 mm/s. Coated samples were kept under room conditions and then they were subjected to the pre-drying in the furnace and later subjected to sintering process at 500 °C (3 °C/min) for 120 min in a vacuum environment.

### 2.3. Corrosion Tests

The corrosion tests were performed by potentiodynamic polarization technique (PDP) in GAMRY PCI14/750 (USA) corrosion test unit in order to examine the effect of the coatings on corrosion resistance of AZ alloys. In corrosion tests, Ringer solution was used as the electrolyte and the temperature of the corrosion cell was fixed to the body temperature (37 °C). All the analyses were performed by using the three electrodes technique. Saturated silver/silver chloride ( $\text{Ag}/\text{AgCl}$ ), platinum wire (Pt), and the already prepared corrosion samples were used as reference electrode (RE), counter electrode (CE), and working electrode (WE), respectively. A minimum of 2 tests



were performed for each sample group until the steady state was determined. Open circuit potential measurements (OCP) and potentiodynamic polarization measurements (PDS) were carried out at the scanning rates of 1 mV/s.

## 2.4. Surface Analyses

Microstructural characterization studies and film thickness of the coated samples were examined by using scanning electron microscopes (SEM, Jeol JSM-6335F) with attachment energy dispersive spectroscopy (EDS). Improving the image quality for before microstructural observations, samples were coated with Au-Pd alloy. However, coating thicknesses were measured using SEM that views taken from the cross section of the samples and mean coating thickness values were then determined.

## 3. Results and Discussion

In order to improve osseointegration in bioceramic coatings, it is desired that the coating has biocompatible and homogeneous surfaces and low crack content [42]. Fig. 1 shows the SEM views of HA coated AZ alloy substrates, before and after corrosion. SEM analyses showed that a porous surface morphology was obtained at low crack intensity and the corrosion caused formation of dimple in the coatings (Fig. 1).

SEM images of surfaces before corrosion show the presence of locally agglomerated regions in bioceramic coatings. Agglomeration intensity on AZ61/HA sample surfaces increased compared to AZ31/HA group samples. SEM images show that the most agglomerated structure is in AZ91/HA coatings. It is thought that the agglomeration intensity on the surfaces is related to the coating thicknesses. SEM images and coating thickness measurements of the cross-sections of HA coated samples are given in Figure 2. While the average thickness value was measured as 3,25  $\mu\text{m}$  in the AZ31 alloy, this value was measured as 6,68  $\mu\text{m}$  and 7,78  $\mu\text{m}$  in the AZ61 and AZ91 alloys, respectively. These results show that the increase in the agglomeration intensity may be related to the increase in the coating thickness. In similar studies, it is clear that there is a relationship between coating thickness and agglomeration [43].

The damage and pits caused by corrosion on the sample surfaces is clearly seen in the SEM images (Fig. 1). Magnesium and its alloys have very low corrosion resistance in high  $\text{Cl}^-$  environments [44]. Because unlike the protective passive layer formed in metals such as aluminum or stainless steel, an unstable semi-passive magnesium hydroxide layer is formed in magnesium and its alloys. The formation of metal-hydroxyl-chloride complex compounds with the penetration of  $\text{Cl}^-$  ions into the hydroxide film causes the formation of pits and an increase in the corrosion rate [45]. Furthermore,  $\text{Cl}^-$  ions cause pitting corrosion in Magnesium alloys [46]. Although the damages in bioceramic coatings after corrosion is close to each other, it would be more sensible to evaluate the corrosion resistance properties of the samples together with the OCP and PDS analysis results.

EDS analysis results obtained from the surfaces of HA coated AZ alloys are presented in Table 1 and EDS analysis results from cross-sections are presented in Figure 3. Ca, P, O and Mg were detected on all bioceramic coated surfaces. It is thought that the differences in the amount of Mg are affected by the form and distribution of the porosity in the coatings. In addition, differences were determined in the amount of Ca, P and Ca/P ratio. As it is known, the Ca/P ratio in the HA structure is expected to be 1.62 [47]. However, the EDS analysis results show that this ratio was only achieved in the AZ61/HA sample. For this reason, local EDS analyzes were performed on the bioceramic coated sample surfaces and the Ca/P ratio was confirmed in all coatings (Figure 4). The local EDS analysis results given in Figure 4 show that the Ca/P ratio is 1,62 in agglomerated structures and the Mg content is quite low (2,86% wt). The fact that the Mg content in the general surface EDS analysis results given in Table 1 is higher than the local EDS results (Figure 4) is thought to be due to the porous structure of the coating.

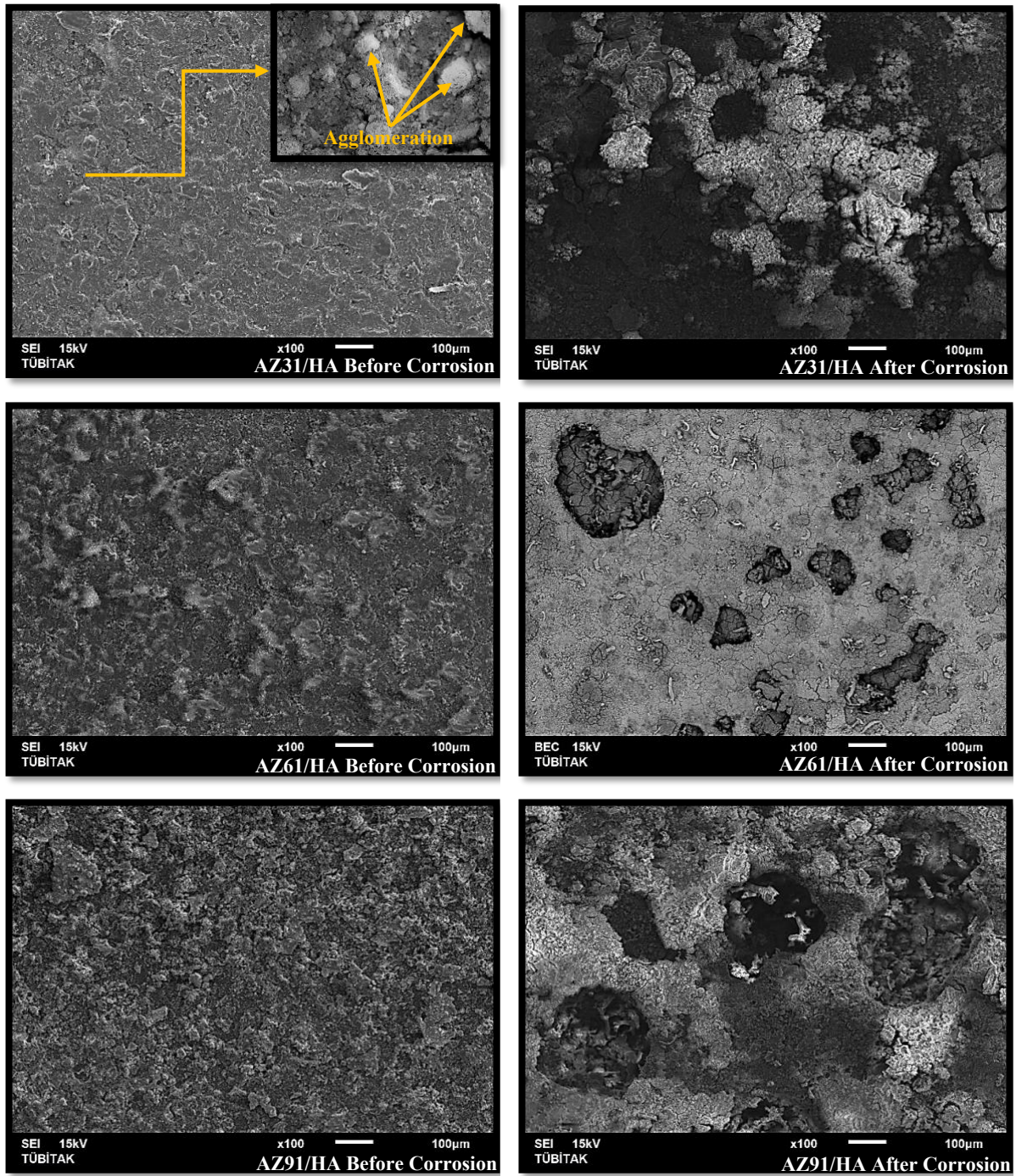
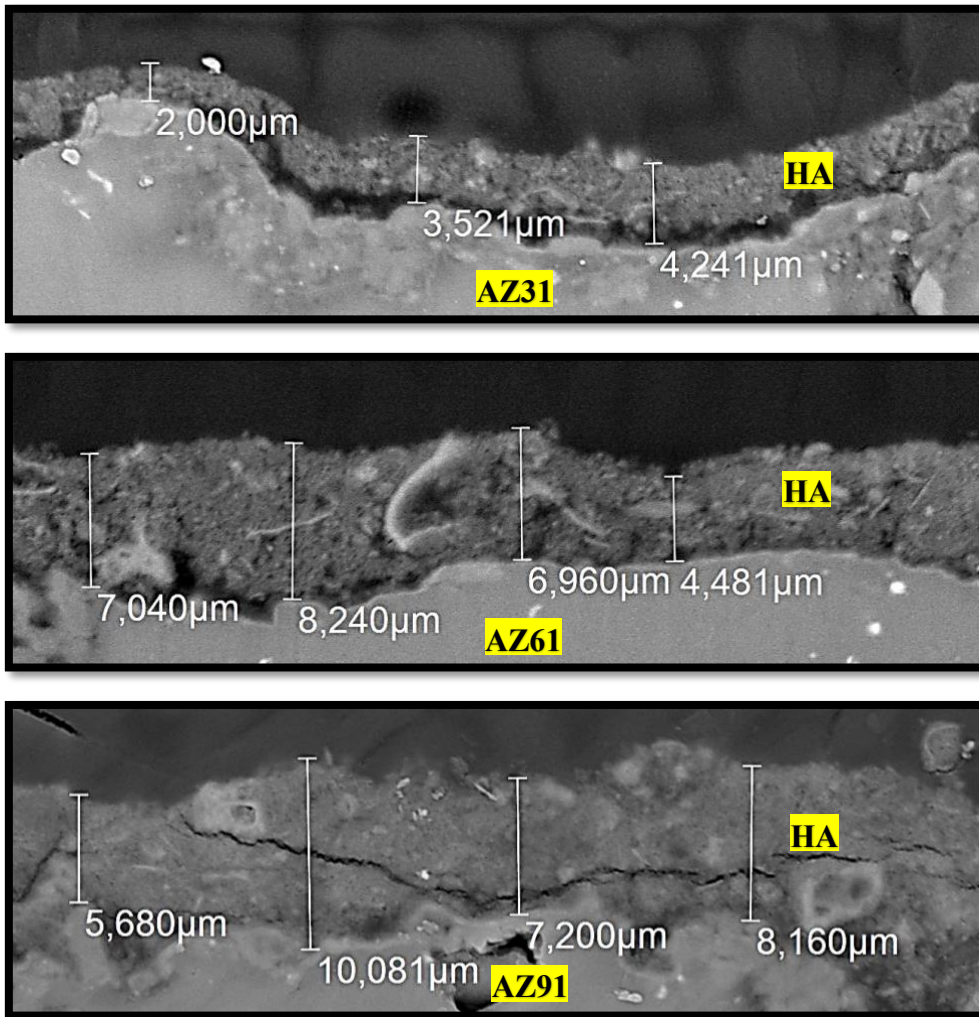


Figure 1. SEM views of coated surfaces before corrosion and after corrosion

Table 1. HA coated AZ Alloy surfaces EDS analysis results.

Sample	Element (wt. %)						Ca/P Rate
	Mg	Al	Zn	Ca	P	O	
AZ31/HA	45,49	-	-	11,80	8,59	34,12	1,3737
AZ61/HA	30,13	-	-	18,92	11,69	39,26	1,6185
AZ91/HA	31,85	-	-	16,06	10,45	42,44	1,5368



**Figure 2.** Cross-sectional images and coating thickness measurements of bioceramic coatings

Yakup SAY

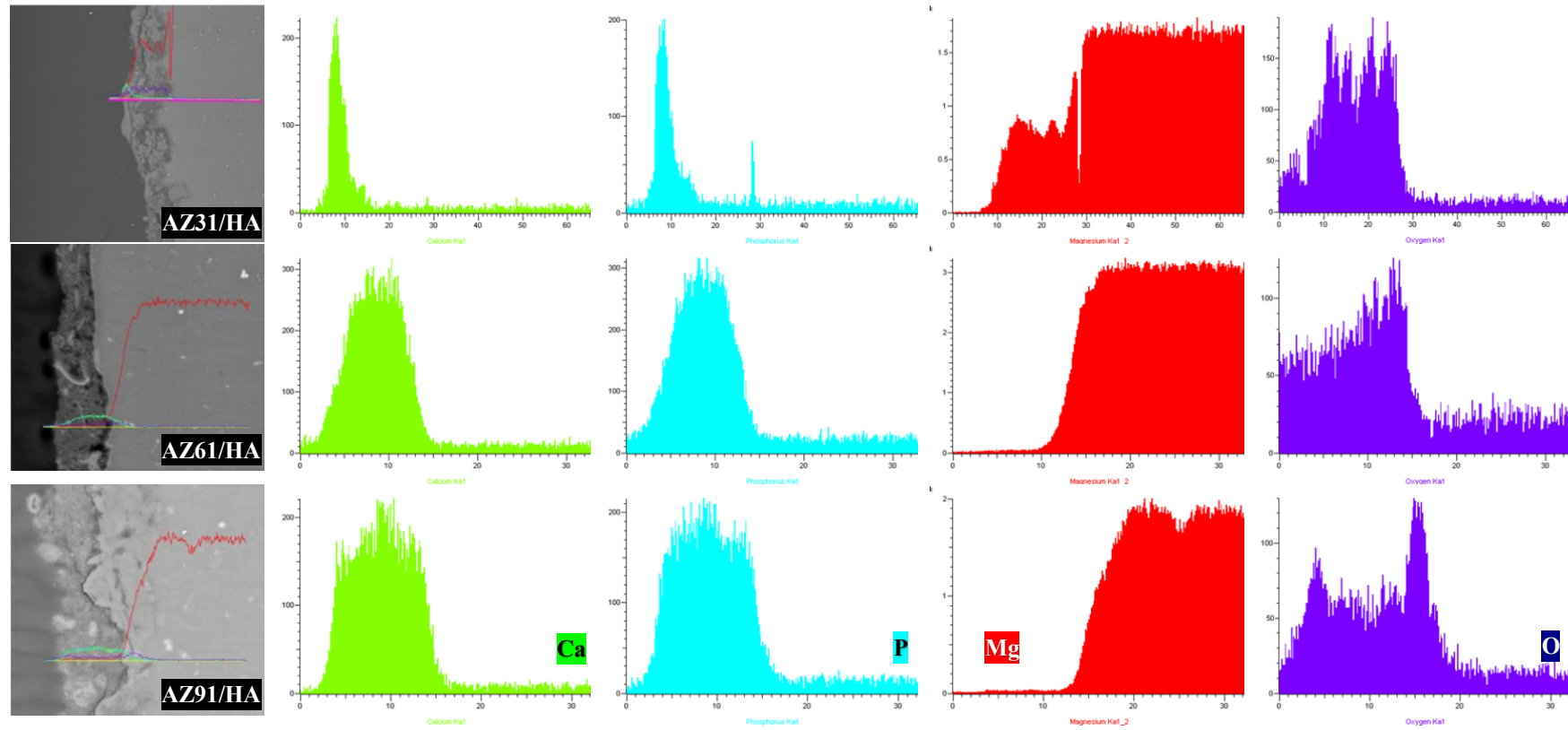
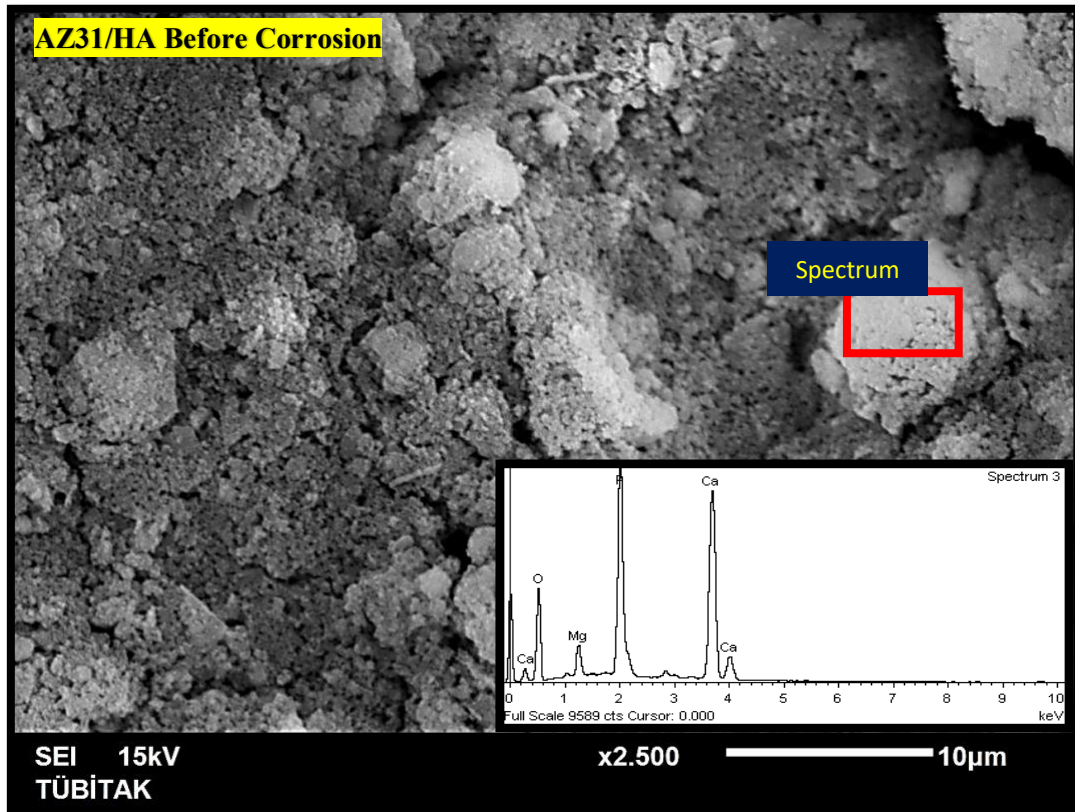


**Figure 3.** Cross-Sectional EDS analyzes of HA coated AZ series alloys

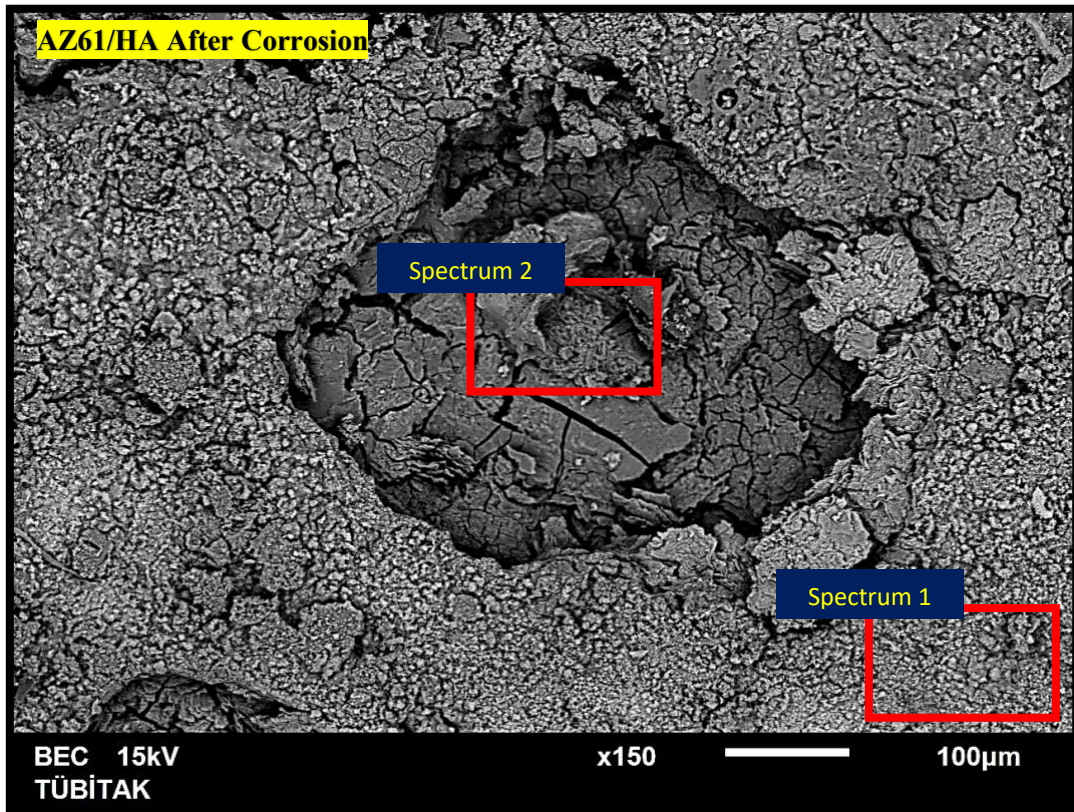


Element (wt. %)						Ca/P Rate
Mg	Al	Zn	Ca	P	O	
2,86	-	-	35,32	21,20	40,62	1,6257

**Figure 4.** Local EDS analysis results on HA coated AZ31 alloy surface before corrosion

In Figure 5, the EDS analysis results obtained from the inner and outer regions of the pits formed after corrosion on the bioceramic coated surfaces are given. While the Ca-P structure was clearly detected in the outer region of the pit (Spectrum 1), Ca-P could not be detected in the pit region (Spectrum 2). The high rate of Cl<sup>-</sup> (16,69 wt. %) detected in the pit region shows that the Cl<sup>-</sup> ions in the Ringer solution are highly effective in corrosion. Similar results were obtained in the line EDS analyzes performed on the pits (Fig. 6). While Ca-P dominates the structure throughout the coating, the inside of the pit is almost entirely composed of Mg-Cl-O. These results show that the coating is completely destroyed, especially in the region where the pits are formed, and the corrosion reaches the substrate. It is thought that the porous structure of the coating reduces the corrosion resistance and causes localized corrosion on the bioceramic coated sample surfaces. These pores are regions where the electrolyte remains static. The increase in the concentration of Cl<sup>-</sup> ions in these regions causes the formation of localized regions where the solubility of the oxide film and the surface conductivity increase. In other words, these porosities may have acted as preferential corrosion sites.

Areas where passive Mg(OH)<sub>2</sub> and MgO layers on magnesium alloys surfaces are destroyed are susceptible to pitting. Cl<sup>-</sup> ions penetrate these areas and activate the area [48,49]. However, ions in the body (especially Cl<sup>-</sup>) cause the environment to become aggressive in terms of corrosion. Especially cracked and porous surface morphologies are areas where the electrolyte is static and cause local areas of high corrosion sensitivity [50]. The accumulation of Cl<sup>-</sup> ions in these regions causes the disruption of the magnesium hydroxide layer and ultimately the degradation of magnesium [21].



Spectrum	Element (wt. %)				
	Mg	Ca	P	Cl	O
Spectrum 1	20,38	19,22	15,77	-	44,63
Spectrum 2	31,88	-	-	16,69	51,43

Figure 5. Local EDS analysis results on HA coated AZ31 alloy surface after corrosion

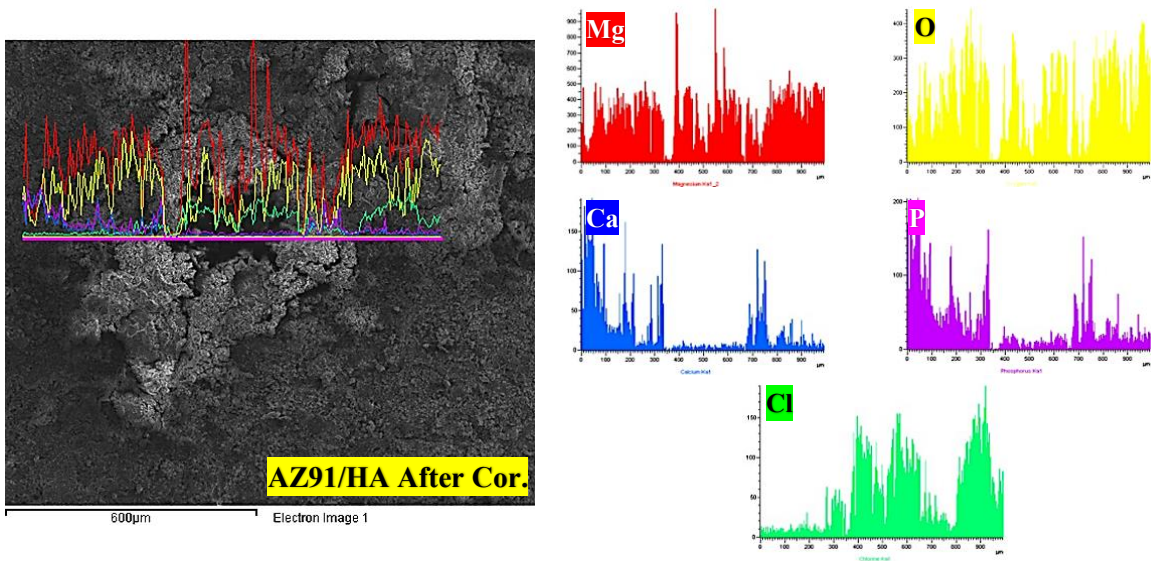


Figure 6. Pitting formation in HA coated AZ91 alloy

OCP analysis results of uncoated and HA coated samples are given in Figure 7. It was observed that  $E_{OCP}$  values increased with time in all uncoated and HA coated samples. In addition, it was observed that there was no significant change in  $E_{OCP}$  values after an immersion period of approximately 30 minutes in all curves. OCP analysis results of HA coated samples showed that the time to reach stable state was shorter for AZ61/HA sample compared to AZ31/HA and AZ91/HA samples. However, only OCP analyzes are not sufficient to evaluate corrosion properties. Therefore, the corrosion properties were interpreted together with the PDS curves obtained by potentiodynamic analysis.

In Figure 8, the potentiodynamic (PDS) polarization curves of uncoated and AZ alloys coated with HA bioceramic in Ringer solution and at body temperature are presented comparatively. The potentiodynamic polarization method is a very useful method in the determination of the quality and stability of the coating by electrochemical techniques to examine the corrosion that occurs starting from the coated surface. The samples were over-polarized in the anodic direction with the PDS method. The samples were first exposed to free corrosion for a certain period of time. Then, by increasing the potential, corrosion differentiations were determined. Some corrosion parameters ( $E_{ocp}$ ,  $E_{corr}$ ,  $I_{corr}$ ,  $\beta_A$  and  $\beta_C$ , Corrosion Rate) calculated from these curves for different coating groups are given in Table 2.

In the PDS curves, it is observed that the potential increases and the current decreases regularly in the cathodic region for all coatings. However, in all samples, it is observed that the corrosion current density increases significantly in the anodic region. This indicates that the Ringer solution has a significant corrosive effect on the samples and an activation-controlled corrosion mechanism occurs in all coatings. Therefore, it is decisive to compare the  $I_{corr}$  values in determining the corrosion behavior. When uncoated AZ alloys are compared with each other,  $I_{corr}$  values of AZ31, AZ61 and AZ91 alloys were measured as 3480, 621 and 97,2 nA/cm<sup>2</sup>, respectively. These results show that the sample with the highest corrosion resistance on uncoated surfaces is AZ91 alloy. However, it was determined that there was a significant decrease in  $I_{corr}$  values in all samples after the alloy surfaces were coated with HA.  $I_{corr}$  values for AZ31/HA, AZ61/HA and AZ91/HA alloys were measured as 947, 159 and 32,40 nA/cm<sup>2</sup>, respectively. This decrease in  $I_{corr}$  values after the surfaces were coated with HA indicates that the corrosion resistance properties of all samples were improved with HA bioceramic coatings. The results show that the  $I_{corr}$  value of the AZ31 alloy, which was 3480 nA/cm<sup>2</sup> before coating, decreased to 947 nA/cm<sup>2</sup> after coating, thus a decrease of 72%. Similarly, these decreases were calculated as 74% and 66% for AZ61 and AZ91 alloys, respectively. In addition, while the corrosion rate values of uncoated AZ31, AZ61 and AZ91 alloys were measured as 2940 – 525,3 and 80,89 mpy, respectively, these values were measured as 788,1 – 134,9 and 28,04 mpy, after the HA bioceramic coatings on the sample surfaces. These results show that a significant increase in corrosion resistance (73%, 74% and 65%, respectively) was achieved in all sample groups with HA bioceramic coatings.

**Table 2.** Corrosion parameters obtained as a result of corrosion tests

Sample	$E_{ocp}$ (mV)	$E_{corr}$ (mV)	$I_{corr}$ (nA/cm <sup>2</sup> )	$\beta_a$ (mV/dec.)	$\beta_c$ (mV/dec.)	Corrosion Rate (mpy)
AZ31	-1460	-1360	3480	382,1	892,4	2940
AZ61	-1463	-1350	621	69,9	332,2	525,3
AZ91	-1440	-1230	97,2	48,2	243,5	80,89
AZ31/HA	-1462	-1355	947	155,1	311,3	788,1
AZ61/HA	-1506	-1252	159	78,50	277,9	134,4
AZ91/HA	-1476	-1114	32,40	37	236,9	28,04

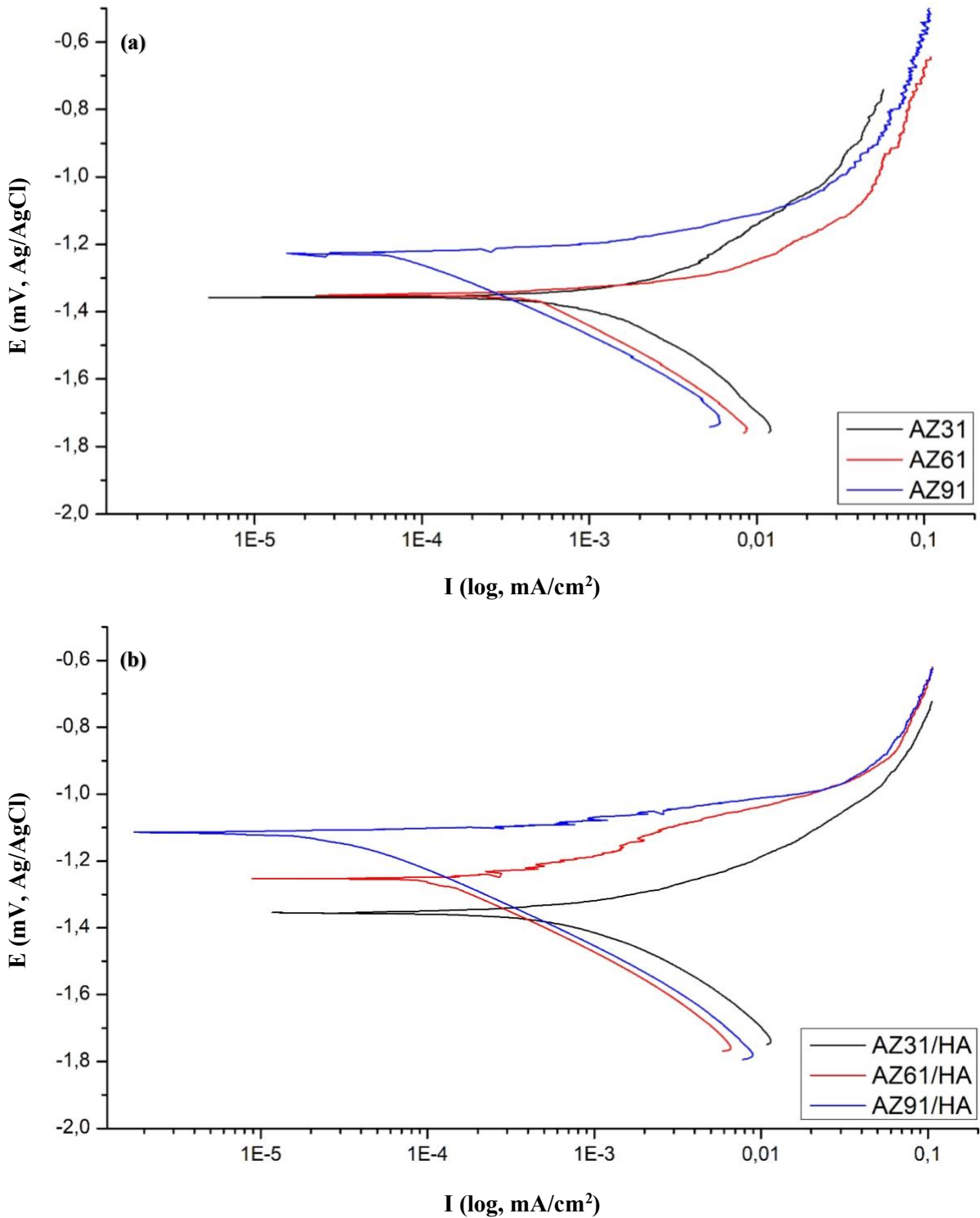


**Figure 8.** PDS analysis results of uncoated (a) and HA coated (b) samples

As the corrosion potential value increases positively and the current density value decreases, the corrosion rate decreases [51]. In addition, when the potential approaches zero, it means that passivation has started in the surfaces [52]. Compared to the uncoated sample,  $E_{\text{corr}}$  values were observed to be more noble in all bioceramic coatings. Therefore, the surface reactivity of AZ alloys after coating decreased significantly. The results show that AZ91/HA is the best sample in terms of corrosion resistance among all samples.



In theory, the current flowing through the unit anode surface area gives the corrosion rate [51]. Corrosion rates in uncoated AZ31, AZ61 and AZ91 samples were measured as 2940 – 525,3 and 80,89 mpy, respectively. The corrosion rate decreased in all samples after coating and was measured as 788,1 – 134,4 and 28,04 mpy for AZ31/HA, AZ61/HA and AZ91/HA, respectively. In orthopedic applications, long-term implant materials, at 37 °C solution, 0,5 mm annual degradation rate is desired and this value corresponds to approximately 19,7 mpy [53]. These results, it was determined that the closest result to this desired value was obtained with AZ91/HA (28,04 mpy).

#### 4. Conclusions

The general results obtained as a result of the study are summarized below;

- Crack-free and porous surface morphologies were obtained in all HA bioceramic coatings.
- Coating thickness values of AZ31, AZ61 and AZ91 alloys were measured as 3,25 – 6,68 and 7,78  $\mu\text{m}$ , respectively.
  - Agglomerated structures were detected in the coatings and it was determined that the agglomeration intensity increased with the increase of the coating thickness.
  - Pit formation was observed in the coatings after corrosion.
  - It has been determined that AZ91 alloy exhibits the highest corrosion resistance on uncoated metallic sample surfaces.
    - The results show that the Icorr value of the AZ31 alloy, which was 3480 nA/cm<sup>2</sup> before coating, decreased to 947 nA/cm<sup>2</sup> after coating, thus a decrease of 72%. Similarly, these decreases were calculated as 74% and 66% for AZ61 and AZ91 alloys, respectively.
    - After HA bioceramic coating, the corrosion rate of AZ31, AZ61 and AZ91 alloys decreased and corrosion resistance increased.
    - It was determined that the sample with the highest corrosion resistance and the lowest corrosion rate among all sample groups was the AZ91/HA sample.

#### References

- [1] Hornberger H, Virtanen S, Boccaccini AR. Biomedical coatings on magnesium alloys—a review. *Acta Biomater* 2012; 8(7): 2442-2455.
- [2] Manivasagam G, Dhinasekaran D, Rajamanickam A. Biomedical implants: corrosion and its prevention-a review. *Recent Patents on Corrosion Science* 2010; 2(1): 40-54.
- [3] James MI, Wu G, Zhao Y, McKenzie DR, Bilek MM, Chu PK. Electrochemical corrosion behavior of biodegradable Mg–Y–RE and Mg–Zn–Zr alloys in Ringer’s solution and simulated body fluid. *J Corros Sci Eng* 2015; 91: 160-184.
- [4] Razavi M., Fathi M. H., Meratian M. Microstructure, mechanical properties and bio-corrosion evaluation of biodegradable AZ91-FA nanocomposites for biomedical applications. *Mater Sci Eng A* 2010; 527(26): 6938-6944.
- [5] Hiromoto S, Tomozawa M, Maruyama N. Fatigue property of a bioabsorbable magnesium alloy with a hydroxyapatite coating formed by a chemical solution deposition. *J Mech Behav Biomed Mater* 2013; 25: 1-10.
- [6] Rončević IŠ, Grubač Z, Metikoš-Huković M. Electrodeposition of hydroxyapatite coating on AZ91D alloy for biodegradable implant application. *Int J Electrochem Sci* 2014; 9: 5907-5923.
- [7] Hu J, Wang C, Ren WC, Zhang S, Liu F. Microstructure evolution and corrosion mechanism of dicalcium phosphate dihydrate coating on magnesium alloy in simulated body fluid. *Mater Chem Phys* 2010; 119(1-2): 294-298.
- [8] Wang H, Guan S, Wang Y, Liu H, Wang H, Wang L, Reb C, Zhu S, Chen K. In vivo degradation behavior of Ca-deficient hydroxyapatite coated Mg–Zn–Ca alloy for bone implant application. *Colloids Surf B* 2011; 88(1): 254-259.
- [9] Wang MJ, Chao SC, Yen SK. Electrolytic calcium phosphate/zirconia composite coating on AZ91D magnesium alloy for enhancing corrosion resistance and bioactivity. *J Corros Sci Eng* 2016; 104: 47-60.
- [10] Xiong Y, Lu C, Wang C, Song R. Degradation behavior of n-MAO/EPD bio-ceramic composite coatings on magnesium alloy in simulated body fluid. *J Alloys Compd* 2015; 625: 258-265.
- [11] Fintová S, Kunz L. Fatigue properties of magnesium alloy AZ91 processed by severe plastic deformation. *J Mech Behav Biomed Mater* 2015; 42: 219-228.
- [12] Wang HX, Guan SK, Wang X, Ren CX, Wang LG. In vitro degradation and mechanical integrity of Mg–Zn–Ca alloy coated with Ca-deficient hydroxyapatite by the pulse electrodeposition process. *Acta Biomater* 2010; 6(5): 1743-1748.
- [13] Gopi D, Murugan N, Ramya S, Kavitha L. Electrodeposition of a porous strontium-substituted hydroxyapatite/zinc oxide duplex layer on AZ91 magnesium alloy for orthopedic applications. *J Mater Chem B* 2014; 2(34): 5531-5540.

- [14] Li N, Zheng Y. Novel magnesium alloys developed for biomedical application: a review. *J Mater Sci Technol* 2013; 29(6): 489-502.
- [15] Liu GY, Tang SW, Chuan W, Jin HU, Li DC. Formation characteristic of Ca-P coatings on magnesium alloy surface. *Trans Nonferrous Met Soc Chin* 2013; 23(8): 2294-2299.
- [16] Liu GY, Hu J, Ding ZK, Wang C. Formation mechanism of calcium phosphate coating on micro-arc oxidized magnesium. *Mater Chem Phys* 2011; 130(3): 1118-24.
- [17] Zhang Y, Wei M. Controlling the biodegradation rate of magnesium using sol-gel and apatite coatings. *Int J Mod Phys B* 2009; 23(06n07):1897-1903.
- [18] Gray J, Luan B. Protective coatings on magnesium and its alloys - a critical review. *J Alloys Compd* 2002; 336(1-2): 88-113.
- [19] Ratner BD, Hoffman A.S, Schoen FJ, Lemons JE. *Biomaterials science: an introduction to materials in medicine*. San Diego, California 2004; 162-4.
- [20] Kamachimudali U, Sridhar TM, Raj B. Corrosion of bio implants. *Sadhana* 2003; 28(3): 601-637.
- [21] Gerengi H, Kaya E, Cabrini M. Magnezyumun (% 99.95) Biyobozunur Malzeme Olarak Kullanilma Potansiyeli. *İleri Teknoloji Bilimleri Dergisi* 2017; 6(2): 1-17.
- [22] Agarwal S, Curtin J, Duffy B, Jaiswal S. Biodegradable magnesium alloys for orthopaedic applications: A review on corrosion, biocompatibility and surface modifications. *Mater Sci Eng C* 2016; 68: 948-963.
- [23] Atrens A, Liu M, Abidin NIZ. Corrosion mechanism applicable to biodegradable magnesium implants. *Mat Sci Eng B* 2011; 176(20): 1609-36.
- [24] Arnould C, Denayer J, Planckaert M, Delhalle J, Mekhalif Z. Bilayers coating on titanium surface: the impact on the hydroxyapatite initiation. *J Colloid Interface Sci* 2010; 341(1): 75-82.
- [25] Chang YY, Huang HL, Chen HJ, Lai CH, Wen CY. Antibacterial properties and cytocompatibility of tantalum oxide coatings. *Surf Coat Technol* 2014; 259: 193-198.
- [26] Hiromoto S, Inoue M, Taguchi T, Yamane M, Ohtsu N. In vitro and in vivo biocompatibility and corrosion behaviour of a bioabsorbable magnesium alloy coated with octacalcium phosphate and hydroxyapatite. *Acta Biomater* 2015; 11: 520-530.
- [27] Surmeneva MA, Tyurin AI, Mukhametkaliyev TM, Pirozhkova TS, Shuvarin IA, Syrtanov MS, Surmenev RA. Enhancement of the mechanical properties of AZ31 magnesium alloy via nanostructured hydroxyapatite thin films fabricated via radio-frequency magnetron sputtering. *J Mech Behav Biomed Mater* 2015; 46: 127-136.
- [28] Hiromoto S, Tomozawa M. Hydroxyapatite coating of AZ31 magnesium alloy by a solution treatment and its corrosion behavior in NaCl solution. *Surf Coat Technol* 2011; 205(19): 4711-19.
- [29] Kiahosseini SR, Afshar A, Larijani MM, Yousefpour M. Structural and corrosion characterization of hydroxyapatite/zirconium nitride-coated AZ91 magnesium alloy by ion beam sputtering. *Appl Surf Sci Adv* 2017; 401: 172-180.
- [30] Pang X, Zhitomirsky I. Electrodeposition of hydroxyapatite-silver-chitosan nanocomposite coatings. *Surf Coat Technol* 2008; 202(16): 3815-21.
- [31] Tomozawa M, Hiromoto S, Harada Y. Microstructure of hydroxyapatite-coated magnesium prepared in aqueous solution. *Surf Coat Technol* 2010; 204(20): 3243-47.
- [32] Chen Q, Thouas GA. *Metallic implant biomaterials*. *Mater Sci Eng R* 2015; 87: 1-57.
- [33] Bakhsheshi-Rad HR, Hamzah E, Ismail AF, Sharer Z, Abdul-Kadir MR, Daroonparvar M, Saud SN, Medraj, M. Synthesis and corrosion behavior of a hybrid bioceramic-biopolymer coating on biodegradable Mg alloy for orthopaedic implants. *J Alloys Compd* 2015; 648: 1067-71.
- [34] Rajendran A, Barik RC, Natarajan D, Kiran MS, Pattanayak DK. Synthesis, phase stability of hydroxyapatite-silver composite with antimicrobial activity and cytocompatibility. *Ceram Int* 2014; 40(7): 10831-38.
- [35] Tan L, Yu X, Wan P, Yang K. Biodegradable Materials for Bone Repairs: A Review. *J Mater Sci Technol* 2013; 29: 503-513.
- [36] Barranco V, Carmona N, Galván JC, Grobelny M, Kwiatkowski L, Villegas MA. Electrochemical study of tailored sol-gel thin films as pre-treatment prior to organic coating for AZ91 magnesium alloy. *Prog Org Coat* 2010; 68(4): 347-355.
- [37] Gu XN, Li N, Zhou WR, Zheng YF, Zhao X, Cai QZ, Ruan L. Corrosion resistance and surface biocompatibility of a microarc oxidation coating on a Mg-Ca alloy. *Acta Biomater* 2011; 7(4): 1880-1889.
- [38] Kannan MB. Electrochemical deposition of calcium phosphates on magnesium and its alloys for improved biodegradation performance: A review. *Surf Coat Technol* 2016; 301: 36-41.
- [39] Liu GY, Hu J, Ding ZK, Wang C. Bioactive calcium phosphate coating formed on micro-arc oxidized magnesium by chemical deposition. *App Surf Sci* 2011; 257(6): 2051-57.
- [40] Ma J, Thompson M, Zhao N, Zhu D. Similarities and differences in coatings for magnesium-based stents and orthopaedic implants. *J Orthop Transl* 2014; 2(3): 118-130.
- [41] Wang D, Bierwagen GP. Sol-gel coatings on metals for corrosion protection. *Prog Org Coat* 2009; 64(4): 327-338.
- [42] Yoshida K, Tanagawa M, Kamada K, Hatada R, Baba K, Inoi T, Atsuta M. Silica coatings formed on noble dental casting alloy by the sol-gel dipping process. *J Biomed Mater* 1999; 46(2): 221-227.

- [43] Bakhsheshi-Rad HR, Hamzah E, Shuang CP, Berto F. Preparation of poly ( $\epsilon$ -caprolactone)-hydroxyapatite composite coating for improvement of corrosion performance of biodegradable magnesium. *Mater Des Process Commun* 2020; 2(4): 170
- [44] Gozuacik NK, Altay M, Baydogan M. Micro Arc Oxidation of AZ91 Magnesium Alloy–Effect of Organic Compounds in the Electrolyte. In *Defect and Diffusion Forum Trans Tech Pub Ltd.* 2014; 353: 217-222.
- [45] Wang L, Zhang BP, Shinohara T. Corrosion behavior of AZ91 magnesium alloy in dilute NaCl solutions. *Mater Des* 2010; 31(2): 857-863.
- [46] Perez N. *Electrochemistry and corrosion science.* Boston, MA: Springer Us. 2004.
- [47] Wang H, Lee JK, Moursi A, Lannutti JJ. Ca/P ratio effects on the degradation of hydroxyapatite in vitro. *J Biomed Mater Res Part A* 2003; 67(2): 599-608.
- [48] Pe PAS. *Fundamentals of corrosion: Mechanisms, causes, and preventative methods.* CRC Press, 2009.
- [49] Song GL. *Corrosion of magnesium alloys.* Elsevier, 2011.
- [50] Tahmasebifar A, Kayhan SM, Evis Z, Tezcaner A, Çinici H, Koc M. Mechanical, electrochemical and biocompatibility evaluation of AZ91D magnesium alloy as a biomaterial. *J Alloys Compd* 2016; 687: 906-919.
- [51] Callister WD, Rethwisch DG. *Materialwissenschaften und Werkstofftechnik: Eine Einführung.* John Wiley & Sons, 2012.
- [52] El Abedin SZ, Welz-Biermann U, Endres F. A study on the electrodeposition of tantalum on NiTi alloy in an ionic liquid and corrosion behaviour of the coated alloy. *Electrochem Commun* 2005; 7(9): 941-946.
- [53] Erinc M, Sillekens WH, Mannens RGTM, Werkhoven RJ. *Applicability of existing magnesium alloys as biomedical implant materials.* TNO Industrie en Techniek, 2009.



## Analysis of Views on Digitalization of Design Studios

Nihal Arda AKYILDIZ<sup>1\*</sup>, Betül BEKTAŞ EKİCİ<sup>2</sup>, Songül KARABATAK<sup>3</sup>, Müslim ALANOĞLU<sup>4</sup>

<sup>1</sup> Department of Architecture, Faculty of Architecture, Balıkesir University, Balıkesir, Türkiye

<sup>2</sup> Department of Architecture, Faculty of Architecture, Fırat University, Elazığ, Türkiye

<sup>3</sup> Department of Educational Administration, Faculty of Education, Fırat University, Elazığ, Türkiye

<sup>4</sup> Department of Education Programs and Teaching, Faculty of Education, Fırat University, Elazığ, Türkiye

\*<sup>1</sup> nihalaradaa@hotmail.com, <sup>2</sup> bbektas@firat.edu.tr, <sup>3</sup> s\_halici@hotmail.com, <sup>4</sup> muslimalanoglu@gmail.com

(Geliş/Received: 13/09/2022;

Kabul/Accepted: 11/12/2022)

**Abstract:** Design studios, one of the most important components of architectural education had to move to digital environments urgently and independent of space with the Covid-19 pandemic. This study aims to evaluate whether design studios can be digitized according to the views of students and instructors in two different architecture schools (Fırat and Balıkesir University) by considering this compulsory experience. The views of 71 students and 5 academicians were taken with a purposeful sampling method. Content and descriptive analyses were performed on the views collected from the participants. As a result, the biggest problem in moving design studios to a digital environment is the disappearance of physical environments in which collaboration, idea sharing, and discussions will occur. In addition, the advantages of online education continued their attraction for some students in the digitalization of design studios. In terms of instructors, games, simulations, modeling, and virtual reality can be used for successful digital studio applications and the infrastructures of these applications can be improved with support from mobile devices.

**Key words:** Design studio, digital design studio, face-to-face education, architecture education

## Tasarım Stüdyolarının Dijitalleştirilmesine Yönelik Görüşlerin Analizi

**Öz:** Mimarlık eğitiminin en önemli bileşenlerinden biri olan tasarım stüdyoları, Covid-19 pandemisi ile acilen ve mekandan bağımsız dijital ortamlara geçmek zorunda kalmıştır. Bu çalışma, bu zorunlu deneyimin dikkate alınarak iki farklı mimarlık okulunda (Fırat ve Balıkesir Üniversitesi) öğrenci ve öğretim elemanlarının görüşlerine göre tasarım stüdyolarının dijital bir ortama dönüştürülüp dönüştürülemediğini değerlendirmeyi amaçlamaktadır. Amaçlı örnekleme yöntemi ile 71 öğrenci ve 5 akademisyenin görüşleri alınmıştır. Katılımcılardan toplanan görüşler üzerinde içerik ve betimsel analizler yapılmıştır. Sonuç olarak tasarım stüdyolarının dijital ortama taşınmasındaki en büyük sorun, işbirliğinin, fikir paylaşımının ve tartışmaların yaşanacağı fiziksel ortamların ortadan kalkmasıdır. Bunun yanı sıra online eğitimin getirdiği avantajlar tasarım stüdyolarının dijitalleşmesinde bazı öğrenciler için cazibesini sürdürmektedir. Öğitmenler açısından başarılı dijital stüdyo uygulamaları için oyunlar, simülasyonlar, modelleme ve sanal gerçeklik kullanılabilir ve bu uygulamaların altyapıları mobil cihazlardan destek alınarak geliştirilebilir.

**Anahtar kelimeler:** Tasarım stüdyosu, dijital tasarım stüdyosu, yüzyüze eğitim, mimarlık eğitimi

### 1. Introduction

Architecture, which meets the needs of shelter and coming together since the existence of humanity, is one of the oldest known professions. In addition to reflecting the culture and philosophy of the period in which they existed, architecture and its products have important clues that can help us to understand the social values, habits, and technological knowledge level of the societies in the geography they existed. From this point of view, *the art of building constructions*, which can be expressed quite technically, is important in terms of the continuity/sustainability of social structure and social life habits. With this aspect, unlike the organizational use of

\* Corresponding author: [bbektas@firat.edu.tr](mailto:bbektas@firat.edu.tr). ORCID Number of authors: <sup>1</sup> 0000-0003-1948-188X, <sup>2</sup> 0000-0003-0142-0587, <sup>3</sup> 0000-0002-1303-2429, <sup>4</sup> 0000-0003-1828-4593.

“innovation”, the act of “creativity”, which is the most important argument in designing space, takes reference from the knowledge of the social structure and mediates the reflection of creativity at the personal level from a psychological point of view [1, 2].

Although architectural education requires having information about structure systems, construction methods, and structural materials to produce a *product of design* with theoretical and practical training [3], it is considered an art in many areas [4, 5]. Therefore, different from basic engineering sciences; architects, who are the performers of the profession by giving life to works that have symbolic values with different aesthetic and beauty criteria, are considered artists [6]. *Function-revealing the final form*, which is considered the essence of architectural works, shows a parallel course with knowledge and quality of education. In this aspect, architecture, which includes the stage of creativity, has a process in which the act of creating does not occur at a fixed point in time, but instead manifests itself as an act that spreads over time and changes the flow [2, 7].

In addition to providing art and aesthetic education, the curriculum of architecture is prepared by taking into account the acquisition of engineering competencies. Although sometimes there are small differences in details and practices, architecture education is realized almost everywhere in the world with education programs that have design studios in the center. In this context, the main setup of the education program is built on the fact that design studios, which are the essence of architecture, are supported and complemented by other courses [8]. Although many parameters are required for these courses, “*studio spaces*” constitute the main backbone of design studios. Design guidance carried out by the master-apprentice method contributes to training students through a studio environment in all national/international schools. In this sense, architectural design studios are considered spaces where irrational creativity and subjective knowledge dominate [9].

Studio pedagogy, which has been developed as a tool to solve uncertain problems and to train students with technical disciplines, is commonly used in disciplines of fine arts [10]. The most common method followed in educational studies carried out in studio environments in architectural schools is the method called problem-based learning which was put forward at the end of the 1960s [11]. The design studio is also known as the core of architectural pedagogy, which advocates “learning by doing”. It is generally accepted that besides theoretical subjects, students’ works are carried out by making and breaking, retrying, using different principles/elements and most importantly being curious within the framework of these theories contribute to developing learning styles and creative souls [12]. Students also have important missions such as having an all-around approach to problems resulting from the needs program of the design problem given each academic term, understanding the needs of the society to develop the most suitable design suggestions, and completing the natural environment as function-appearance. Today, design spaces that make creativity and rationality possible simultaneously and encourage these have special importance for engineering [9]. Design studios, which are considered the basis of architectural education, provide a creative learning environment and offer opportunities such as getting a multi-functional interactive area and providing transformable personal space and a sustainable completing design process [13]. Getting studio education and acquiring creative learning is much more important for first-year design students with its significance in shaping especially engineering ideology and thinking ways. Design studios, due to reasons such as a natural design environment, an interactive discussion environment, and private and personal areas are accepted as the most important and most effective design areas in this respect [13].

While studios enable students to internalize and transform new information with the active participation of students, they also enable educators to build a strong relationship with their participation levels [9, 14]. For this reason, the most important factors that distinguish studios from other course environments are “one-to-one interaction with the instructors” and “feedback from the instructor” [15]. In general, they are both a learning environment and also social spaces in which students have the chance to study with their peers and continue the act of learning outside the classroom hours -when instructors are not present- and also places where the art of learning is encouraged [16]. Courses held in these places with the participation of students who are in the same or different years of study enable learning design processes, supporting learning with interactive and motivational activities and increasing the quality of the end product with critical discussions. Design activities carried out in groups or collectively in the studio are effective in instilling a sense of belonging and responsibility in addition to the ability to work in a team [17].

Studio environment, which plays an important role in the socialization of students at different levels from the beginning to end of architectural education, as well as in increasing the level of discussion and professional etiquette, became digitized in architecture schools in the whole world with Covid-19 pandemic and practices that took place underwent important transformations. The pandemic process eliminated the traditional “studio culture” in almost all architecture schools. This has caused the formation of distance education models as an alternative to

usual teaching methods and also the emergence of unprecedented pedagogical problems [18]. Although some of these problems are partly solved with technological means, problems are experienced by first-year students getting used to architecture formation since they have not yet experienced a design studio environment. In addition to this, it is also thought that this new experience will cause some potential problems in the future education process of second, third, and fourth-year students who are used to getting design education in the studio, and it may affect their professional lives in the long run.

In architecture formation, the face-to-face teaching model, which is the traditional model, and the distance education model, which has been experienced globally with the pandemic process, has attracted the attention of many researchers. In line with studies conducted in the literature on face-to-face education and distance education models, the results including the potential and difficulties of both education models have been summarized in Table 1.

**Table 1.** Research findings regarding learning with face-to-face and distance education.

Importance of face-to-face education	Value of distance education	Reference
	Many problems and difficulties are experienced in design courses	[19]
	There are many difficulties for students in addition to a few positive aspects	[20]
	Students are disappointed and students with low living standards are more negatively influenced	[21]
Face-to-face courses are more preferred by students	The interest and positive perspectives on courses are decreased and even not preferred	[22]
It should be used in design education	It provides suitable opportunities for computer-assisted design courses	[23]
	In addition to the new potentials it includes, it is necessary to focus on new challenges	[24]
	There are also gaps in practices in addition to motivation and socialization	[25]
Studio based courses are more efficient than distance education	Lessons can be recorded, provides ease in Project delivery, encourages participation in seminars, effective education, and knowledge transfer in schools with sufficient infrastructure	[26]
	Level of satisfaction is associated with age, length/skill of computer use	[27]
Mutual dialogue has better results in making use of the educators' potential	Provides efficiency through good opportunities, a knowledge that is not limited to course books is reflected in learning	[28, 29]
Success is higher in face-to-face groups		[30]
	It contributes to educational activities	[31]
Educators' focusing on technical topics makes the education insufficient	It provides a flexible area of learning independent of space and time	[32]
	There is a need for a mixed system integrating virtual + face-to-face education	[32]
	Increasing internet opportunities supported by following courses regularly	[33]
	Developing technology and increasing mobile internet use supports adaptation to courses	[34]
Students prefer face-to-face education instead of the online education model		[35]
	Distance education is insufficient in art teaching and it should be improved	[36]
The processes in design education should be supported		[37]
	It provides equal opportunity-in terms of economic means- for a quality education	[38]

It is preferred in a technical art course		[39]
The limits of the studio are exceeded with virtual practices,	It provides the opportunity to answer students' needs actively and dynamically; however, the lack of traditional education is felt	[40]
In addition to the benefits to educators and students, a mixed system can also provide benefits for design education		
It contributes to students' mental health and socialization In addition to in-class cooperation, it also develops the experience of learning from peers	Financial costs are decreased, equal opportunities are provided, and innovative software that provides flexibility	[29, 41, 42]
	Lessons have become boring, it prevents socializing, the connection between student-instructor has become weaker	[43]
	It supports schools in answering changing student needs, increasing quality, supporting students, and accessing information	[44]
A mixed model created with the traditional method can be used in the future, too	More than half of the students are satisfied with online teaching	[45]

The studies in Table 1 compare face-to-face and distance education in architectural formation with the advantages and disadvantages of both models. Design studios, which are at the core of architectural education, are physical environments where students can produce simulations in the presence of an educator and where social and cultural interactions take place [46]. Distant design studio activities, which have been experienced with the pandemic process and the closures, have created some disruptions in the design education of both instructors and students. However, no studies were found that examined how design studios can be digitized to minimize these disruptions from the perspectives of both students and instructors.

Studio design is important in terms of increasing the value in learning, contributions to the originality of design, and study skills of students with institutional and practical contexts in addition to imagination. This way, students get the chance to produce their designs by optimizing the balance in artistic, rational, and pragmatic thinking [47]. In addition to the social and physical infrastructure it provides, the studio environment is also supported with materials/equipment that can be a reference to students' studies, inspire them, and help them to create original products. For this purpose, students gain the tradition of working together with study groups by using sketches/discussing with the help of physical models/prototypes on their desks and the magazines/publications in the environment [48]. In studio environments where the act of design is carried out traditionally, contrary to customs, factors such as the instructor and students not getting together, not seeing the designed works at the same time, not being able to make the improvements they want, and not having the chance to discuss have made the process difficult for both sides [49].

Based on these, it is important how the competence that students receiving distance education during the pandemic process should experience and gain is affected during the pandemic process. For this reason, the present study aims to make evaluations about what studio means for architecture faculty students, to address distance education of design studios from the perspectives of students and instructors, and to evaluate whether studios can be digitized in future practices. In this sense, it is important to find out the aspects which are accepted and rejected by students in practices carried out with distance education in studio culture which has existed for centuries as a successful method in providing art infrastructure the foundations of which are in the architecture profession and to determine the precautions to be taken to solve these insufficiencies in the distance education process. In parallel with these, the present study examines how important studios, which enable the master-apprentice training method that form the basis of design, are and how design studios can be transferred to digital platforms with the pandemic process. With this purpose answers were sought to the following questions:

1. What does a design studio mean to architecture faculty students?
2. Can design studios be digitized according to the views of students?
3. How can design studios be digitized effectively according to the views of instructors?



## 2. Method

### 2.1. Study Model

The present study, which aims to show the importance of studios for architecture education and how they can be transferred to digital platforms, has been conducted with phenomenology design, one of the qualitative research designs. Phenomenology is a method that focuses on evaluating experiences [50, 51]. It focuses on phenomena that we are aware of, but do not have an in-depth and detailed understanding about. The phenomena that will be discussed in studies can be events in the world we live, experiences, perceptions, orientations, concepts, and situations. Due to the nature of qualitative studies, phenomenology studies may not give definite and generalizable studies. However, they may present explanations and experiences that better describe and help to understand a phenomenon [52]. This study discusses design studios as a phenomenon and examines studio design experiences from the eyes of students and instructors.

### 2.2. Study Group

A purposeful sampling method was used in line with the purpose of the study. Purposeful sampling is a type of sampling that is selected based on the information about the population and the purpose of the study [53]. The present study made use of maximum variation sampling by using data source (participant) variation. This type of sampling is used to increase variation if the views of a large number of participants are to be taken [54]. In this context, the views of instructors and students studying at the faculties of architecture in universities where the researchers were working [Firat University (FU) and Balıkesir University (BU)] were examined. Demographic information of students whose views were taken is presented in Table 2.

**Table 2.** Demographic information of participants

Student Code	University	Gender	Grade	Student Code	University	Gender	Grade
S1	BU	Female	1	S37	BU	Male	4
S2	BU	Male	1	S38	BU	Male	4
S3	BU	Female	1	S39	BU	Male	4
S4	BU	Female	1	S40	BU	Female	4
S5	BU	Female	1	S41	FU	Female	4
S6	BU	Female	1	S42	FU	Male	4
S7	BU	Female	1	S43	FU	Female	4
S8	BU	Female	1	S44	FU	Female	4
S9	BU	Male	1	S45	FU	Male	4
S10	BU	Male	1	S46	FU	Female	4
S11	BU	Male	1	S47	FU	Male	4
S12	BU	Female	1	S48	FU	Female	1
S13	BU	Male	1	S49	FU	Female	1
S14	BU	Female	1	S50	FU	Female	1
S15	BU	Female	1	S51	FU	Female	1
S16	BU	Male	1	S52	FU	Female	1
S17	BU	Female	1	S53	FU	Male	1
S18	BU	Female	1	S54	FU	Female	2
S19	BU	Female	1	S55	FU	Female	2
S20	BU	Male	1	S56	FU	Female	2
S21	BU	Male	2	S57	FU	Female	2
S22	BU	Female	2	S58	FU	Female	3
S23	BU	Female	2	S59	FU	Female	3
S24	BU	Female	2	S60	FU	Male	3
S25	BU	Female	2	S61	FU	Male	3
S26	BU	Female	2	S62	FU	Male	3
S27	BU	Female	2	S63	FU	Female	3
S28	BU	Female	2	S64	FU	Male	3
S29	BU	Male	2	S65	FU	Male	3
S30	BU	Male	2	S66	FU	Female	3
S31	BU	Female	2	S67	FU	Male	4
S32	BU	Female	2	S68	FU	Male	4
S33	BU	Male	3	S69	FU	Male	4
S34	BU	Female	3	S70	FU	Male	4
S35	BU	Male	3	S71	FU	Male	4
S36	BU	Male	4				

According to Table 2, 30 of the students are male, while 41 are female; 40 are studying at Balikesir University, while 31 are studying at Firat University; 26 of the students are in their first year, while 16 are in their second year, 12 are in their third year and 17 are in their fourth year. It can be said that variation was achieved in terms of the year of study. In addition to these, three of the instructors in the study are female, while one is male; three are working at Firat University, and two are working at Balikesir University.

### 2.3. Data Collection

Interviews, one of the most preferred techniques to collect data in qualitative studies [55] are the leading data collection tools in phenomenology studies. Researchers conduct interviews to find out the experiences of cases and the meanings of these experiences [52]. Since the study data were collected during the pandemic process, an open-ended question form was used as a data collection tool to find out the views of students. Views of instructors were taken through face-to-face interviews.

The form which was prepared to find out the views of students consists of two parts including students' personal information and questions examining the importance of design studios and their transferability to digital environments from students' perspectives. The data collection form prepared to find out the views of instructors consisted of personal information of instructors and one question on their views about how design studios can be transferred effectively to the digital environment.

While preparing the data collection tool, a form consisting of five questions was prepared by the researchers working in the faculty of architecture in line with the purpose of the study. These questions were then discussed in an online meeting by all the researchers and the questions were revised. The survey questions prepared were answered by 10 students in the architecture faculty and then their views were taken about the comprehensibility and number of survey questions. The students stated that the questions in the interview form would be filled in mostly with smartphones and they recommended for the questions to be short and comprehensible and the number of questions to be as few as possible so that they could be filled in easier. Their recommendations were taken into account and the draft survey form was revised. Later, two experts in the field were told about the aim of the study, and they were asked to examine the questions to be asked to students and instructors. The suitability of survey questions in terms of content was discussed again and the survey forms were finalized. Open-ended questions in the survey form prepared for the students are as follows:

1. What does a design studio mean to you?
2. Do you think that design studios can be digitized?
  - a. Yes, they can be. Because ...
  - b. No, they can't be. Because ...

The open-ended questions in the survey form prepared for the instructors are as follows:

1. Design studios are very important environments for architectural education. In your opinion, how can design studios that need to be used in case of an urgent training need or during training be effectively transferred to a digital environment?

With the 06.08.2021 dated and 18/6 numbered ethics committee approval and permission to conduct the study, a data collection tool was sent to students studying at Firat University and Balikesir University through Google forms, and the students were asked to write down their thoughts. Instructors' views were taken through face-to-face interviews.

### 2.4. Data Analysis

Before analyzing the research data, the views were turned into electronic forms from the survey system. Content analysis and descriptive analysis were then used to analyze the qualitative data. To do this, first, the electronic forms including the views of students were coded starting from S1 to S71, while the forms including the views of instructors were coded starting from A1 to A5.

Content analysis was used to analyze the views about what design studios mean and about whether they can be digitized. In phenomenology studies, data analysis is for finding out experiences and their meanings and there is an effort to conceptualize data and find out themes to describe the phenomenon [52]. In addition, the main aim

of content analysis is to reach concepts and correlations that can explain the data collected. For this purpose, similar data were brought together within the framework of specific concepts and themes, organized, and interpreted in a way that readers can understand.

For content analysis, the steps recommended by Yildirim and Simsek were followed (1) coding the data, (2) finding the themes, (3) organizing the codes and themes, and (4) defining and interpreting the findings [52]. Electronic forms were transferred to Maxqda qualitative data analysis program for content analysis. Next, students' views were coded. The codes formed were then brought together under common categories. Categories were also brought together and main themes were formed.

After the data were analyzed, two experts, one from the education management department who knew and used the Maxqda program and one from the architecture department, were included in the data analysis process. They were told how the coding was performed and they were asked to analyze it again. Miles and Huberman's reliability formula "Reliability = Consensus/ (Agreement + Disagreement)" was used for the reliability of the analyses [56]. As a result of the analysis, Miles and Huberman's reliability formula value was found as .92 for the first research question, .99 for the first theme of the second research question, and .94 for the second theme. These values showed that the interview data were reliable. Direct quotations were included to reflect students' views.

The descriptive analysis method was used to analyze the data obtained from the third research question of how design studios could be digitized effectively. In the descriptive analysis, the aim is to organize and interpret and present the data obtained from interviews. A cause-and-effect relationship is built between the findings and if necessary, comparisons are made between cases [52]. It also tries to reflect the educational benefits of explanations made by researchers [57]. In qualitative analysis, the data are organized and described for readers under specific themes. Therefore, descriptions are enriched with direct quotations from participant views. These quotations also increase the reliability of the study.

### 3. Findings

#### 3.1. What do design studios mean to architecture faculty students?

In this part of the study which aims to show how important the design studio environment is for architecture education, the "What is a Design Studio?" theme was formed as a result of the analysis of data obtained from views to answer the question "What does design studio mean to you?". Categories and codes of the theme are shown in Figure 1.



Figure 1. What is a design studio?

As seen in Figure 1, there are four categories under the “**What is a Design Studio?**” theme: *The environment for effective communication* (f = 59), *the environment in which abstract information is embodied* (f = 49), *the effective and motivating environment* (f = 28), *the environment where skills and abilities are developed* (f = 15). Under the category of *the environment for effective communication*, there are make critiques (f = 4), providing feedback (f = 1), argument (f = 10), information exchange (f = 4), sharing ideas (f = 11), helping each other (f = 5), communicating (f = 9), brainstorming (f = 2), and working together (f = 13). Under the category of *the environment in which abstract information is embodied*, there are embodiment of ideas (f = 7), making an application (f = 6), producing (f = 4), designing (f = 25), providing experience (f = 2), development (f = 2), and learning (f = 3).

Under the category of *the effective and motivating environment*, there are efficient working environment (f = 2), do exciting work (f = 2), increase motivation (f = 2), comfortable working environment (f = 10), customized design environment (f = 5), effective workshop/lab environment (f = 4), and inspiring environment (f = 3). Under the category of *the environment where skills and abilities are developed*, there are ability development (f = 1), enable abstract thinking (f = 1), expand the imagination (f = 3), skill development (f = 2), developing visual intelligence (f = 1), and generating innovative ideas (f = 7).

According to the analysis of data obtained from the views, design studios are defined as effective and motivating environments in which students develop their knowledge, skills, and talents by working together and in which they turn the abstract information they have learned into projects and designs.

Some of the attention-getting views of students who participated in the study are presented below by staying true to their essence.

*“Design studio enables the information we are taught to keep more place in our memory and enables our visual intelligence to develop; it enables us to conduct our designs more meaningfully by learning their aims and by communicating with our friends and teachers”* (S15; developing visual intelligence, developing skills and abilities; sharing ideas, providing an opportunity for effective communication).

*“I think that design studios should be working environments which enable students to transfer their imagination to their designs in a free and creative way and which have the required means. The design studio is an area in which we try to turn feelings and emotions into space”* (S30; turning dreams into the design –free design, making abstract information concrete).

*“Design studios are classrooms in which applied project courses are taught and communication is realized most effectively. They are workshops in which we can advance projects in line with the critics taken. In short, I can call design studios workshops in which students, who are designer candidates, look for solutions to design problems through trial-and-error method individually or in groups, interact with the studio executive while searching for solutions, and learn about how to make designs”* (S63; designing, making abstract information concrete, criticizing-communicating, providing effective communication).

*“Design studios are environments which enable students to keep their minds more alive and to be productive with the advantage of being together and which enables students to exchange ideas with each other and to discuss”* (S66; sharing ideas-discussion, providing an opportunity for effective communication).

### 3.2. Can design studios be digitized?

For the second research question of the study, the students attending architecture faculty were asked “*Do you think that design studios can be digitized? Yes, they can be. Because.... and No, they can’ be. Because....*”. The views of students who answered as *Yes, they can be. Because....* (n=6) were grouped under the theme “**Can Be Digitized**” and the views of students who answered as *No, they can’ be. Because ...* (n=65) were grouped under the theme “**Cannot Be Digitized**”. The results regarding the categories and codes of the “**Can Be Digitized**” theme were created through the analysis of views regarding the explanation *Yes, they can be. Because....* can be seen in Figure 2.

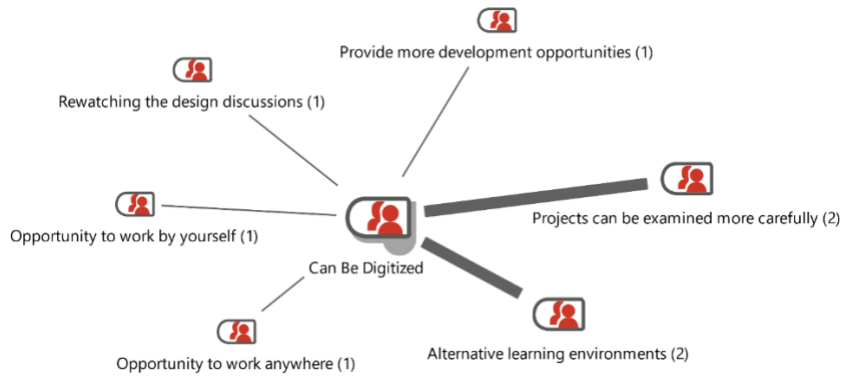


**Figure 2.** Design studios' digitizable theme

As can be seen in Figure 2, the students (n=6) who stated that design studios can be digitized are in their first-year (n=2; S9, S11), third-year (n=2; S64, S65), and fourth-year (n=2; S68, S70). Six categories were found in the **Can Be Digitized** theme: alternative learning environments (f = 2), provide more development opportunities (f = 1), opportunity to work anywhere (f = 1), opportunity to work by yourself (f = 1), projects can be examined more carefully (f = 2), and rewatching the design discussions (f = 1). It can be seen that the codes obtained as a result of the analysis of views point to the advantages provided by distance education rather than the benefits digitizing design studios will bring.

Some of the attention-getting views of students who participated in the study are presented below by staying true to their essence.

*“Design is a concept that contains originality and a concept with which individuals exhibit their ideas. Therefore, it is not very important for the design to be working in a studio or not, it is possible to work anywhere”* (S11; opportunity to work anywhere).

*“We have the opportunity to examine all projects made in online education together and to see them closely. We have the opportunity to rewatch what we discuss in our designs”* (S70; rewatching the design discussions).

*“I can learn with distance education, too”* (S9; opportunity to work by yourself).

The results regarding the categories and codes of the **“Cannot Be Digitized”** theme were created through the analysis of views regarding the explanation *No, they cannot be. Because....* can be seen in Figure 3.

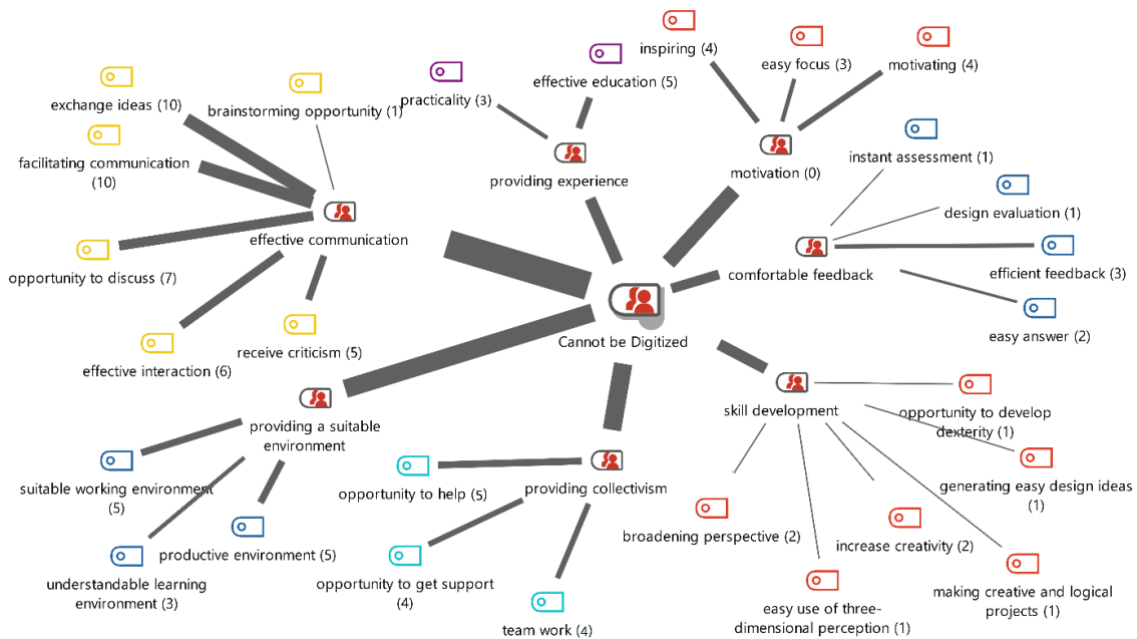


**Figure 3.** Design studios cannot be digitized theme

As can be seen in Figure 3, the majority of the students (n=65) expressed the view that design studios cannot be digitized. As a result of the categorization of views, seven *categories* were found under the theme **Cannot Be Digitized**. Students mostly stated that design studios cannot be digitized because design studios provide effective communication [*effective communication* (f = 39)]. According to this category, the students stated that they brainstormed (f = 1), interacted effectively (f = 6) and exchanged ideas (f = 10), received criticism easily (f = 5), had the opportunity to discuss (f = 7) and communicated easily (f = 10).

The students stated that in design studio environment they could get support from their friends (f = 4), they could help each other (f = 5) and work in teams (f = 4) and therefore had the opportunity to work collectively [*providing collectivism* (f = 13)]. While design studios provide students with an easy to understand course environment (f = 3), a suitable (f = 5) and effective working environment (f = 5) [*providing a suitable environment* (f = 13)], they also help them to get motivated (f = 4), to focus easily (f = 3) and to be inspired (f = 4) [*motivation* (f = 11)].

It can also be seen that design studios are environments where students receive effective education (f = 5) and practice (f = 3) [*providing experience* (f = 8)]. Thanks to this environment, students develop skills [*skill development* (f = 8)], they can make creative and logical projects (f = 1), they develop hand skills (f = 1), produce creative ideas (f = 2), widen their perspectives (f = 2), they can use three dimensional perception easily (f = 1) and produce design ideas more easily (f = 1).

It can also be seen that design studios provide effective feedback (f = 3), instant evaluations (f = 1) and design evaluations (f = 1) and answers can be taken quickly and easily [*comfortable feedback* (f = 7)].

Some of the attention-getting views of students who stated that design studios can be digitized are presented below by staying true to their essence.

*“Design studios provide a better environment, information, and the opportunity to work in a community. When I try to make designs in my room at home, the comfort of the house brings laziness and sometimes I lose seriousness”* (S3; more comprehensible course environment, suitable environment, opportunity to work in a community, collectivism).

*“I think that I can understand what instructors tell better face-to-face and I can solve more quickly and more effectively when I have a problem, making designs with other people in the same environment will give me more enthusiasm and inspiration and making designs by discussing with these people will have a better influence on my design”* (S17; inspires, motivation; provides the opportunity to discuss, effective communication).

*“We have the opportunity to present our designs and projects concretely by using the experiences of our instructors in the studio environment. We have the opportunity to realize the mistakes we make and fix them more quickly. We also have the opportunity to work more effectively as a group with our friends”* (S24; group work, collectivism).

*“Anything you want can be learned with distant education. I think that architecture is not one of these. With distance education, my perspective is as much as my instructors tell me and as much as I can think; however, in the face-to-face environment, I have friends that can expand my perspective. I attribute an individual’s developing architecture perspective to discussions made”* (S40; expands perspectives, skill development, provides the opportunity to discuss, effective communication).

*“I think that there is a lot we can learn by discussing with friends and we have a hard-working environment and we motivate each other. I would like to communicate closely with our instructors in my project courses that I received online, I think that I could not make enough use of my instructors’ knowledge and I feel sad; maybe our instructors would want different things from us in the courses that we would learn in the studio, or we would have the chance to make up for our shortcomings immediately. Distance education is different; of course, it has its benefits; however, I believe that studio environment is very important in architecture education”* (S57; motivation, the possibility to discuss, easier communication).

*“In the studio environment, our communication with our instructors may be healthier. I can ask my questions about what I do not understand more quickly and the feedback may be easier. Listening to the critics of our friends may be more useful than resting at home. Finally, discussing a subject with our friends and getting their ideas carries us forward, and we can get more accurate results. For these reasons, courses are better taught in a studio environment”* (S63; easier communication, effective feedback).

### 3.3. How can design studios be digitized effectively?

In the analysis of views regarding the third research question which discussed how design studios can be digitized effectively;

A1 encoded instructor made suggestions such as “If we have to experience distance education again; the project design process should be supported with new methods. This can be realized through the field of virtual internet, which is used effectively by the new generation; for example, the use of virtual media tools such as metaverse and virtual game classes should be allowed in design courses. Making use of such applications will keep students interested and make it possible to teach project courses like a game” and suggested that design courses and design studios could be realized in three-dimensional virtual environments new generations are interested in and tend to use.

A2 encoded instructor made suggestions such as “Maybe courses can be much more effective if they are supported with virtual glasses and with *virtual space applications* with which spaces can be navigated. Virtual courses in which different platforms are used should be taught in a fun way and virtual environments in which students socialize with each other should be created. Maybe by using *avatars*... Why not?” and stated that virtual space applications can be developed by using virtual reality glasses and designs can be made in these environments through avatars.

A3 encoded instructor stated “...although I do not agree with the view that online education can be very successful in a field like architecture since it has a formation that students have not experienced before, I think that it can be an alternative method that can be used instead of discontinuing education in extraordinary situations such as earthquakes and the pandemic that we have experienced in the recent past. It will be possible to establish special units to develop distance education curricula and teaching techniques in faculties. These units should create a curriculum that should be taught based on design education with innovative approaches that increase the motivation of students to classes in a way that students can understand and be interested in and present these in 3D visualization infrastructures such as games, simulation modeling, and virtual reality. Here not only students but also instructors need support because there are still instructors who have difficulties in using the computer and drawing programs” and stated that the reason why higher education institutions were not effective in distance education was the fact that instructors and students did not have the required experience and formation. For the solution to this problem, they recommend creating the infrastructure of applications such as games, simulation modelling, and virtual reality to increase the motivation of students.

Similarly, A3 encoded instructor made suggestions such as “... advanced technological methods, 3D programs, virtual reality applications, etc. should be developed and first educators should be trained about these. In addition, during this process, educators should be encouraged to minimize rote-based/monologue approach and assessments/exams based on researching/reading should be increased” and stated that advanced technological methods, 3D programs, and virtual reality applications can be used in design studios.

As can be understood from A3 encoded instructor’s statement “although I think that equality in education, I mean, providing students infrastructure support such as computer, etc. is not very realistic, I believe that the process can be supported with phone applications that can be developed for architecture formation that can be used with mobile phones which are the devices every student can access most easily”, instructor A3 stated that design courses can be digitized through mobile applications.

## 4. Conclusion and Discussion

The present study aims to research the importance of design studios in architecture education and their transferability to digital environments. According to the results found in the study, it can be stated that the greatest advantage of the studio environment for students is the fact that it creates an effective area of communication in which cooperation, idea sharing, and discussions can take place. Studies conducted on studio environments [9], [13, 14] have also emphasized that they are environments that support students’ design skills. Studios are environments that contribute to design, production, and learning activities and they provide important benefits to design education. When a general conclusion is made from the results of studies, for students studio spaces can be defined as “effective and motivating environments in which knowledge, skills, and talents are developed by working together, and knowledge taught abstractly are turned into projects and designs”.

When the answers to the second question of the study were examined, it was found that there were fewer students who thought that design studios can be digitized than those who thought that they cannot be digitized. This result supports the results of a study that found that undergraduate and postgraduate students in Turkey preferred the face-to-face education model instead of distance education [22, 35]. Two students expressed their views on why design studios could be digitized in the first year, two in the third year, and two in the fourth year.

When the opinions of these students were examined, it was seen that they did not state a definite recommendation or justification for the transfer of the original structure or usage purposes of the design studios to the digital environment. Students generally focused on the idea that the activities included in face-to-face education can also be carried out in online environments. However, there are also research results showing that students prefer distance education instead of face-to-face education [25, 28, 38, 58]. When the results are examined, it is seen that general conclusions were made such as distance education makes use of advances in technology, provides equality in accessing education, reduces educational costs, and allows the opportunity to rewatch the courses recorded. In other words, it can be understood that students focus on the advantages of distance education.

Another result of the study is that practical and designing courses that should take place in design studios cannot be digitized completely. Similar to the results of the present study, it is stated in studies that discuss design studios in distance education that it is not preferable for studio environments to be digitized since students encounter many difficulties [20, 21, 25] and especially the processes of cooperation, interaction, and peer learning are interrupted [30, 41] and student motivation is negatively affected. Based on this, it is thought that first-year students could not evaluate the difference between the traditional/digital applications of studios since they do not have previous design studio experiences.

In the present study, when students' views about the transferability of design studios to digital environments are examined, in general, they stated that design studios cannot be digitized since they allow effective interaction. According to the results of this study, design studios are environments in which students exchange ideas, discuss, brainstorm, criticize studies and interact comfortably. In addition to allowing students to interact together, design studios also allow for individual or group work during the design process. Similarly, there are also results that distance education, which is used as an alternative to a traditional design studio, eliminates communication and interaction canals which make significant contributions to motivation during the design process [43]. Design studios can be defined as places that enable students to get instant and efficient feedback and evaluate one another's designs, and allow them to learn from instructors or friends when they need help. In addition, by making use of the positive and supportive contribution of studio space to learning, students who work in design studios also can develop design skills, gain experience and make effective-correct decisions.

The students stated that in addition to providing a collective study environment, design studios also provided easy to understand, comfortable, and effective environment. Thanks to this environment, students can prepare creative and rational projects, develop their skills, imagination, and perspectives and make effective designs. Other studies stated that the physical components of design studios and the education provided in this environment support and develop individuals' creativity [59, 60]. The results of the present study also show that students who work together can inspire each other by being influenced by their friends' projects and designs. These benefits and advantages of design studios provide students with being motivated and to focus more comfortably on designs or projects they will carry out due to the environment they are in.

Based on the views of the instructors in the study, it can be understood that design studio formation applied during the distant education period needs solutions that will minimize the problems experienced. In this sense, it can be seen that virtual reality practices have been discussed for inclusion in the education model and are the topic of many studies [11, 18] were also suggested by the instructors in our study, and also an idea came out that infrastructures of applications such as game and simulation modeling can also be created.

It is thought that in environments where virtual space applications can be developed with virtual reality glasses three-dimensional virtual environments that allow for designs through avatars can be designed and supporting the digitalization of design courses with mobile applications will contribute to improving the conditions of distance education of design when it is not possible to be physically together.

While the present study concluded that design studios cannot be digitized completely, it sets forth that a hybrid method can be used. Improving the existing formation can be possible by including the positive characteristics of distance education, which is also included in design education and which we were not prepared for, in education programs. Based on this, by using the thoughts of students who stated that design studios can be digitized, it can be stated that jury and final examinations of design projects can be carried out in a digital environment and thus students can listen to the criticism of instructors or friends. This situation will allow criticism, brainstorming, or interaction in design studios to reach more students and will prevent misunderstanding based on the revisions between the teacher and the student.

Based on the views of instructors, for effective digitalization of design studios, practices such as a game, simulation, 3D modeling and virtual reality can be used to digitize design studios effectively in universities. Infrastructures for these applications should be prepared and mobile support should be provided in the applications



to be used. However, it is also very important to provide students and instructors with the required training to operate these infrastructures effectively and to use applications.

### References

- [1] Sternberg RJ, Lubart TI. The concept of creativity: prospects and paradigms. In Handbook of creativity. In R. J. Sternberg (Ed.), Cambridge: Cambridge University Press, 1999.
- [2] Sidawi B. Correction: the impact of social interaction and communications on innovation in the architectural design studio. *Buildings* 2012; 2(3):203-217.
- [3] Piplani P, Brar TS. Traditional building knowledge: contemporary relevance for architecture education in India. *Int J Des Educ* 2020; 14(2): 89-109.
- [4] Peters OR, Olabode, O. Comparative analysis between art and architecture. *Online Journal of Art and Design*, 2018; 6(2):15-32.
- [5] Al-Saidi AZM. Artistic skills and scientific abilities in architectural education. *Journal of Design Studio* 2020; 2(2): 143-152.
- [6] Mizia M. Architecture as an art of understanding. *Pol Rev* 2014; 59(4): 81-92.
- [7] Ord DY, Harris JJ. The elusive definition of creativity. *J Creat Behav* 1992; 26(3): 186-198.
- [8] Doheim RM, Yusof N. Creativity in architecture design studio assessing students' and instructors' perception. *J Cleaner Prod* 2020; 249: 1-24.
- [9] Ramaraj A. Art of facilitating 'problem-driven outcomes' in an architectural design studio. *New Trends and Issues Proceedings on Human & Social Sciences* 2017; 4(11): 93-106.
- [10] Del Rosario Z, Aggarwal R, Coffey C, Sadler A, Matsumoto S, Wood A, Ruvolo P, Woodard CJ. Crafting a virtual studio: some models and implementations. In: 2021 ASEE Virtual Annual Conference; 26-29 July 2021; Virtual conference.
- [11] Maghool SAH, (Iradj) Moeini SH, Arefazar Y. An educational application based on virtual reality technology for learning architectural details: challenges and benefits. *International Journal of Architectural Research ArchNet-IJAR* 2018; 12(3): 246-272.
- [12] Boucharenc CG. Research on basic design education: an international survey. *Int J Technol Des Educ* 2006; 16 (1):1-30.
- [13] Ismail, AS, Mohidin HHB, Bauzi NBN. Sustainable architectural design studio towards the development of creative learning environment. *Adv Sci Lett* 2017; 23(9): 9259-9264.
- [14] Le Cornu R, Peters J. Towards constructivist classrooms: the role of the reflective teacher. *Journal of Educational Enquiry* 2005; 6(1): 50-64.
- [15] Alnusairat S, Al Maani D, Al-Jokhadar, A. Architecture students' satisfaction with and perceptions of online design studios during covid-19 lockdown: the case of Jordan universities. *International Journal of Architectural Research ArchNet-IJAR* 2020; 15(1): 219-236.
- [16] P. L. O. Lueth. The architectural design studio as a learning environment: a qualitative exploration of architecture design student learning experiences in design studios from first-through fourth-year. PhD. Iowa State University, Ames, Iowa, USA, 2008.
- [17] Akincitürk N, Erbil Y, Yücel Ç. Cooperative learning in an architectural design studio. *Uludağ University Journal of Faculty of Engineering and Architecture* 2011; 16(2): 35-43.
- [18] Iranmanesh A, Onur Z. Mandatory virtual design studio for all: exploring the transformations of architectural education amidst the global pandemic. *Int J Art Des Educ*, 2021; 40(1): 251-267.
- [19] Al-Ayash A, Hussein MF. Distance education technology tools in interior design during covid-19 pandemic (UOP & UOG students as a case study). *PalArch's Journal of Archaeology of Egypt / Egyptology* 2020; 17(7): 13184-13202.
- [20] Ahmad L, Sosa M, Musfy K. Interior design teaching methodology during the global covid-19 pandemic. *Interiority* 2020; 3(2): 163-184.
- [21] Aristovnik A, Keržič D, Ravšelj D, Tomaževič N, Umek L. Impacts of the covid-19 pandemic on life of higher education students: a global perspective. *Sustainability* 2020; 12(20): 1-34.
- [22] Bircan H, Eleroglu H, Arslan R, Ersoy M. Cumhuriyet üniversitesi öğrencilerinin uzaktan eğitimde sunulan derslere yönelik bakış açısı. *Eurasian Journal of Researches in Social and Economics (EJRSE)* 2018; 5(12): 91-100.
- [23] Bingol B. Landscape architecture students' views on emergency remote teaching system in the covid-19 process: the case of Burdur Mehmet Akif Ersoy University, Turkey. *Eur J Sci Technol* 2020; 20: 890-

897.

- [24] Ceylan S, Şahin P, Seçmen S, Somer ME, Süher KH. An evaluation of online architectural design studios during covid-19 outbreak. *International Journal of Architectural Research ArchNet-IJAR* 2020; 15(1): 203-218.
- [25] Dilmac S. Students' opinions about the distance education to art and design courses in the pandemic process. *World Journal of Education* 2020; 10(3): 113-126.
- [26] Elrawy S, Abouelmagd D. Architectural and urban education in Egypt in the post covid-19 pandemic. *European Journal of Sustainable Development* 2021; 10(2): 91-112.
- [27] Eygu H, Karaman S. A study on the satisfaction perceptions of the distance education students. *Kırıkkale University Journal of Social Sciences* 2015; 3(1): 35-59.
- [28] Gautam P. Advantages and disadvantages of online learning. Available: <https://elearningindustry.com/advantages-and-disadvantages-online-learning>. Accessed: March 20, 2022.
- [29] Allu ELA, Allu-Kangkum ELA. Covid-19 and sustainable architectural education: challenges and perceptions on online learning. *IJRDO-Journal of Education Research* 2021; 6(2): 7-13.
- [30] Gursul F, Keser H. The effects of online and face to face problem based learning environments in mathematics education on student's academic achievement. *Procd Soc Behv*, 2009; 1(1): 2817-2824.
- [31] Horzum MB. Michael Graham Moore: eğitim teknolojisi alanına önemli katkılar sağlayan kişi. *Sakarya University Journal of Education* 2013; 3(1): 113-119.
- [32] Masdéu M, Fuses J. Reconceptualizing the design studio in architectural education: distance learning and blended learning as transformation factors. *International Journal of Architectural Research ArchNet-IJAR* 2017; 11(2): 6-23.
- [33] Metin AE, Karaman A, Aksoy Sastim Y. Student perspectives on distance education and the assessment of the efficiency of distance education english courses: Banaz Vocational College. *Karabük University Journal of Institute of Social Sciences* 2017; 7(2): 640-652.
- [34] Moore M, Kearsley G. *Distance education: A systems view of online learning*. 3<sup>rd</sup> ed. California: CENGAGE learning, 2011.
- [35] Oz Ceviz N, Tektas N, Basmacı G, Tektas M. University students' perspective on distance education during the covid-19 pandemic period: the case of Turkey. *Ulakbilge - Journal of Social Sciences* 2020; 52: 1322-1335.
- [36] Purbo OW. Online teaching and experience art & culture during coronavirus and beyond. 2020. Available: <https://lms.onnocenter.or.id/pustaka/docs/art/OWP-20201003-Experience-art-and-culture-during-covid19-lockdown.pdf>. Accessed: June 19, 2022.
- [37] Reimers A, Schleicher A. *A frame work to guide an education response to the Covid - 19 pandemic of 2020*. Paris: OECD Publishing, 2020.
- [38] Qureshi JA. Advancement in massive open online courses (MOOCs) to revolutionize disruptive technology in education: a case of Pakistan. *Journal of Education and Educational Development* 2019; 6(2): 219-234.
- [39] Sakarya K. Suggestions of distance education models for interior design education. *Journal of Cukurova University Institute of Social Sciences* 2019; 28(2): 388-401.
- [40] Sidawi B. The use of e-learning system in learning about architecture: obstacles and opportunities. In: 2015 Fifth International Conference on e-Learning; 18-20 October 2015; (econfer). pp 117-124.
- [41] Schwarz M, Scherrer A, Hohmann C, Heiberg J, Brugger A, Nuñez-Jimenez A. Covid-19 and the academy: it is time for going digital. *Energy Res Social Sci* 2020;68:101684.
- [42] Milovanović A, Kostic M, Zoric A, Dordevic A, Pesic M, Bugarski J, Todorovic D, Sokolovic N, Josifovski A. Transferring Covid-19 challenges into learning potentials: online workshops in architectural education. *Sustainability* 2020; 12(17): 1-22.
- [43] Sen O, Kizilcalioglu G. Determining the views of university students and academics on distance education during the covid-19 pandemic. *International Journal of 3d Printing Technologies And Digital Industry* 2020; 4(3): 239-252.
- [44] Toquero CM. Challenges and opportunities for higher education amid the Covid-19 Pandemic: the Philippine context. *Pedagogical Research* 2020; 5(4): 1-5.
- [45] Varma A, Jaffri MS. Covid-19 responsive teaching of undergraduate architecture programs in India: learnings for post-pandemic education. *International Journal of Architectural Research ArchNet-IJAR*

- 2020; 15(1): 189-202.
- [46] Jones MA, Bubb S. Student voice to improve schools: perspectives from students, teachers and leaders in 'perfect' conditions. *Improving Schools* 2021; 24(3): 233-244.
- [47] Ibrahim NLN, Utaberta N. Learning in architecture design studio. *Procd Soc Behv* 2012; 60: 30-35.
- [48] Vyas D, van der Veer G, Nijholt, A. Creative practices in the design studio culture: Collaboration and communication. *Cognit Technol Work* 2013; 15(4): 415-443.
- [49] Bittencourt II, Costa E, Silva M, Soares E. A computational model for developing semantic web-based educational systems. *Knowledge-Based Syst* 2009; 22(4): 302-315.
- [50] Jasper MA. Issues in phenomenology for researchers of nursing. *Journal of Advanced Nursing*, 1994; 19(2): 309-314.
- [51] Miller S. Analysis of phenomenological data generated with children as research participants. *Nurse Researcher* 2003; 10(4): 68-82.
- [52] Yıldırım A, Simsek H. *Qualitative research methods in the social sciences*. 5<sup>th</sup> ed. Ankara: Seckin Publishing, 2006.
- [53] Christensen LB, Johnson B, Turner LA. *Research Methods, Design, and Analysis*. 12<sup>th</sup> ed. Pearson Education Limited, 2014.
- [54] Patton MQ. *Qualitative Research & Evaluation Methods: Integrating Theory and Practice*. 4<sup>th</sup> ed. Sage Publications, 2014.
- [55] Creswell JW. *Qualitative inquiry and research design: Choosing among five approaches*. Sage Publications, 2013.
- [56] Miles MB, Huberman AM. *Qualitative data analysis: An expanded sourcebook*. California: Sage Publications, 1994.
- [57] Gliner JA, Morgan GA, Leech NL. *Research methods in applied settings: An integrated approach to design and analysis*. New York: Routledge, 2011.
- [58] Dumbauld B. 13 Great Benefits of Online Learning. <https://www.indiaeducation.net/onlineeducation/articles/10-benefits-of-online-learning.html>, Accessed: 20 February 2020.
- [59] Paker Kahvecioglu N. Architectural design studio organization and creativity, A| Z - ITU Journal of the Faculty of Architecture 2007; 4(2): 6-26.
- [60] Cantürk Akyıldız E. Design studio a learning environment: experience of Maltepe university design studio 1. *The Turkish Online Journal of Design Art and Communication* 2020; 10(4): 389-407.



## Evaluation of the Effects of Earthquakes on Radon and Total Electron Content Values and Meteorological Changes on the North Anatolian Fault Zone, Türkiye

Dawar Hama Khalid MOHAMMED<sup>1\*</sup>, Fatih KÜLAHCI<sup>2</sup>, Ahmet SAİT ALALI<sup>3</sup>

<sup>1</sup> Department of Physics, College of Science, University of Halabja, Iraq

<sup>2</sup> Nuclear Physics Division, Department of Physics, Science Faculty, Firat University, Elazığ, Türkiye

<sup>3</sup> Solid Physics Division, Department of Physics, Science Faculty, Yıldız Technical University, İstanbul Türkiye

\*<sup>1</sup> dawarhawrami18@gmail.com

(Geliş/Received: 17/10/2022;

Kabul/Accepted: 08/02/2023)

**Abstract:** A cross-correlation analysis is proposed to analyse the relationships of soil Radon-222 gas, Ionospheric Total Electron Content (TEC), and some meteorological variables with earthquakes from the North Anatolian Fault Zone, Türkiye, one of the most active fault lines in the World. Statistically important results are obtained for Earthquake-Rn gas changes and Seismo-Ionospheric Coupling. In addition, we think that this study will be an important step for further studies on earthquake precursors.

**Key words:** Radon; Earthquake; TEC; Meteorology; Cross-correlation; Prediction; Precursor

### Depremlerin Radon ve Toplam Elektron İçeriği Değerleri Üzerindeki Etkilerinin ve Meteorolojik Değişimlerin Değerlendirilmesi Kuzey Anadolu Fay Zonu, Türkiye

**Özet:** Bir çapraz-korelasyon analizi, toprak Radon-222 gazı, İyonosferik Toplam Elektron İçeriği (TEİ) ve bazı meteorolojik değişkenlerin, Türkiye'nin en aktif faylarından biri olan Kuzey Anadolu Fay Zonu, Türkiye'deki depremlerle ilişkisini analiz etmek için önerildi. Deprem-Rn gaz değişimleri ve Sismo-İyonosferik Bağlantısı için istatistiksel olarak önemli sonuçlar elde edildi. Ayrıca, bu çalışmanın deprem tahmini konusunda yapılacak daha sonraki çalışmalar için önemli bir adım olacağını düşünmekteyiz.

**Anahtar kelimeler:** Radon; Deprem; TEC; Meteoroloji; Çapraz Korelasyon; Kestirim; Öngörü.

#### 1. Introduction:

Rn-222 is generated due to the nuclear decay of Radium (<sup>226</sup>Ra) and Uranium (<sup>238</sup>U) [1]. Radon gas (<sup>222</sup>Rn) has the longest half-life (3.82 days) compared with daughters' [2], Rn has omnipresent occurrences is chemically uncertain is radioactive gas tasteless, colourless, odourless gas [1], [3]. Rn gas travels over large distances on the surface of the Earth through different methods. Such as diffusion, convection, or advection [4]. The soil with a lower and medium permeability, diffusion takes priority, but for soils with higher permeability, convection transport takes precedence [5]. Radon is also affected by tectonic plate activities, and meteorological parameters, for example, temperature, pressure and wind speed, precipitation, and humidity. The radon is also affected by seasonal variations. The impact of these parameters on Rn-222 emission dynamics ranges between several hours and several days [6]–[12].

TEC is an important parameter in the investigation of changes in the ionosphere. It observation provides a direct connection between seismo-ionospheric coupling and causes for understanding their relation. The ionosphere is a layer in the air atmosphere located at an altitude between 50 to 1000 km, with charged particles containing ions and electrons [13]. The TEC is defined as the total electron density between two points in a cylindrical tube with a cross-section of 1 m<sup>2</sup>. The unit for measuring it is defined as (TECU), with 1 TECU equalling 10<sup>16</sup> electrons per square meter [14]–[15]. The global positioning system is used extensively for ionosphere investigation [17]–[20].

Many researchers have noted that Rn-222 levels increase from a few hours to several weeks before earthquakes occur [6], [21]–[31]. Rn variations have been predicted as a valuable method as earthquake precursors in a different place in the world and confirmed [28], [32]–[38]. Examined worldwide land, water, and air radon analysis and confirmed that radon is a reliable predictor of the prediction of earthquakes in the future [39], [40].

\* Corresponding author: [dawarhawrami18@gmail.com](mailto:dawarhawrami18@gmail.com). ORCID Number of authors: <sup>1</sup> [0000-0003-2947-427X](https://orcid.org/0000-0003-2947-427X), <sup>2</sup> [0000-0001-6566-4308](https://orcid.org/0000-0001-6566-4308), <sup>3</sup> [0000-0002-7750-5571](https://orcid.org/0000-0002-7750-5571)

The purpose of this research is to determine a correlation between concentration of radon gas, the total electron density in the ionosphere, and variations with seismic activities, by considering meteorological parameters (underground and air atmospheric temperature with air pressure). Investigating all parameters together is innovation in this field on the North Anatolian Fault Zone, Türkiye.

## 2. Data Sources and Method of Analysis

One of the main areas for the slip of continents that form the neo-tectonic evolution of Türkiye and the East Mediterranean region is the North Anatolian Fault Zone (NAFZ, see **Error! Reference source not found.**). The seismic activity of the region is heavy and poses a high risk to heavily populated areas. The NAFZ, is situated within 1500 km of the triple junction Karliova in eastern Anatolia to the Marmara Sea.

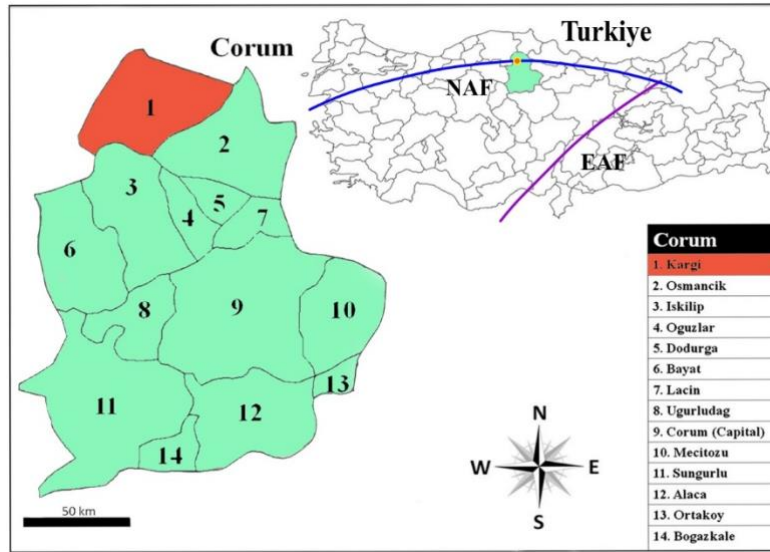


Figure 1 Study area Kargı Çorum province Türkiye

The study area is the district of Kargı is located (106 km) in the north of the Çorum province (39°54'20" N, 34°04'28" E) in the North-central Anatolia, Türkiye [42]. The location is shown in Figure 1. Çorum has a warm dry-summer continental climate with moderates to cool wet springs and light rain in the fall and spring. The hottest times in Çorum province are in July and August. The average daily temperature in these months is (21 °C). The coldest days of the year are experienced in January nearly (-4 °C). Annual rainfall is an average of (444 mm per square meter). The monthly average sunbathing hours are 200 h (Turkish State Meteorological Service, n.d.).

A cross-correlation method is a common approach for determining how closely or correlated two series are. To determine the degree of similarity the function lag correlation is used [43], [44]. Also in the literature, the cross-correlation plot as an essential method in identifying the relations between non-stationary time series, such as soil radon, and the effect meteorological data on it is used [45].

### 2.1. Earthquake, TEC, and radon gas measurements

During the observation period Dec 2008 to Dec 2009, the seismic activity in the Çorum -Kargı area obtained from the Boğaziçi Kandilli Observatory. During the observation period, 90 earthquakes are recorded with a magnitude between (3 to 4.4  $M_L$ ) the Richter scale (<http://www.koeri.boun.edu.tr/scripts/lasteq.asp>).

In this study, TEC was collected through IONOLAB (ionospheric research laboratory-Türkiye) (<http://www.ionolab.org/index.php?page=index&language=en>), in this laboratory, the online TEC measurement is provided in near real-time. The nearest station from the study area to measure TEC for the period (16 Dec 2008 to 31 Dec 2009) in the study area is Ankara TEC station. The TEC data are provided every 2.5 min daily for a station in the period days.

Radon gas ( $^{222}\text{Rn}$ ) concentration data for the period Dec 2008-Dec 2009 in the Çorum -Kargı area was donated by the Ministry of Interior Disaster and Emergency Management Presidency (AFAD) (<https://en.afad.gov.tr/>).

Monitoring radon gas measurement was operated online. Data is transferred to the centre from all online stations. In this study, the Alpha Meter 611 detector (factory-made by Alpha Nuclear Company, Canada) was used to measurement radon gas (<sup>222</sup>Rn). Soil radon gas was continually deliberated every 15 minutes by alpha meter detector.

### 3. Results and Discussions

In this study, an investigation of the relation between the soil radon gas concentration, meteorological parameters, and total electron content TEC with earthquakes and the cross-correlation between Rn concentrations with total electron content variation is provided. In addition, critical and statistically significant information for future Rn behaviour provides.

The earthquake data TEC and radon gas, in addition to the meteorological data, have been divided into three groups. Each group contains about 4 months of data, and the impact of earthquakes on these data will be discussed to find the cross-correlation between <sup>222</sup>Rn concentration and TEC data.

#### 3.1. First group

The first group starts on (Dec 16, 2008, to Mar 31, 2009), numerous micro-earthquakes occurred with magnitude (3 to 4.3), with total electron content and <sup>222</sup>Rn gas concentration between (70 to 140 kBq.m<sup>-3</sup>), atmosphere, pressure and underground (5, 10, 20, and 50 cm) temperature for the same period are shown in Error! R eference source not found..

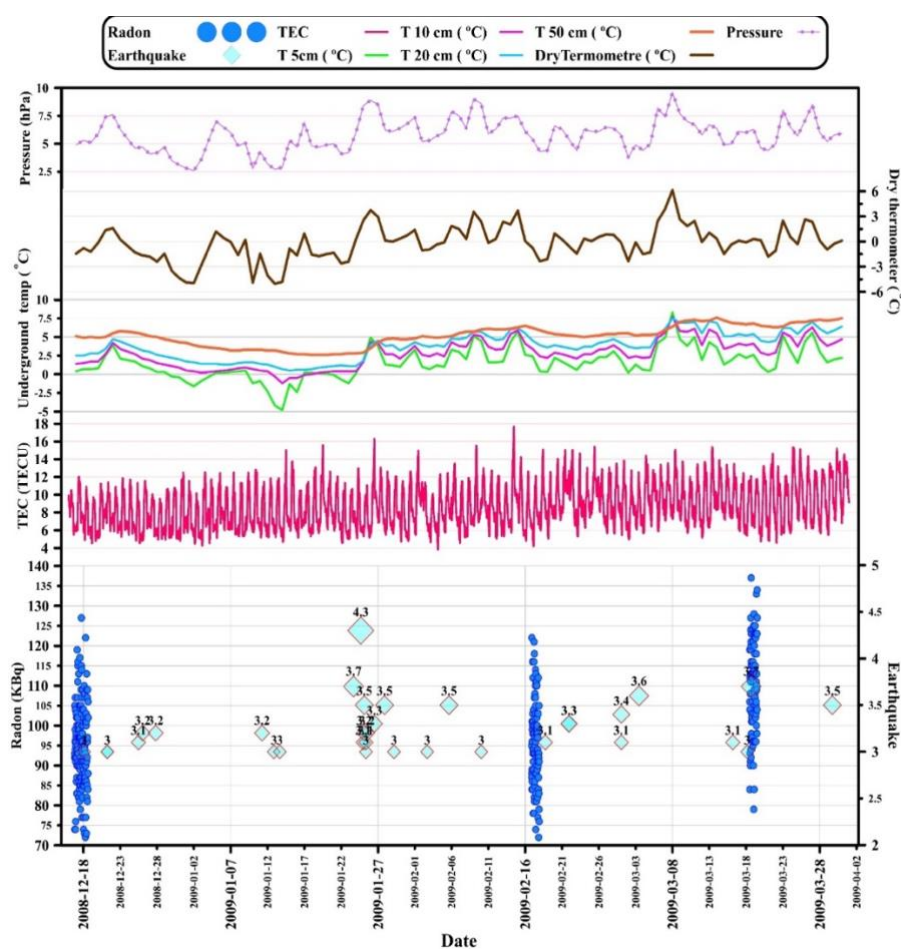


Figure 2. Radon, TEC, Temp of soil (5, 10, 20, and 50 cm) and Pressure with Earthquakes for the first group

During the observation time, there is no abnormal change in the pressure and total underground and atmospheric temperature. Otherwise, the total electron content for some days recorded a high magnitude value. To find the correlation between the parameters we divide the first group into the same small groups based on the availability of all parameters at the same time. The first group A graph is shown in the figure below Error! Reference source not found..

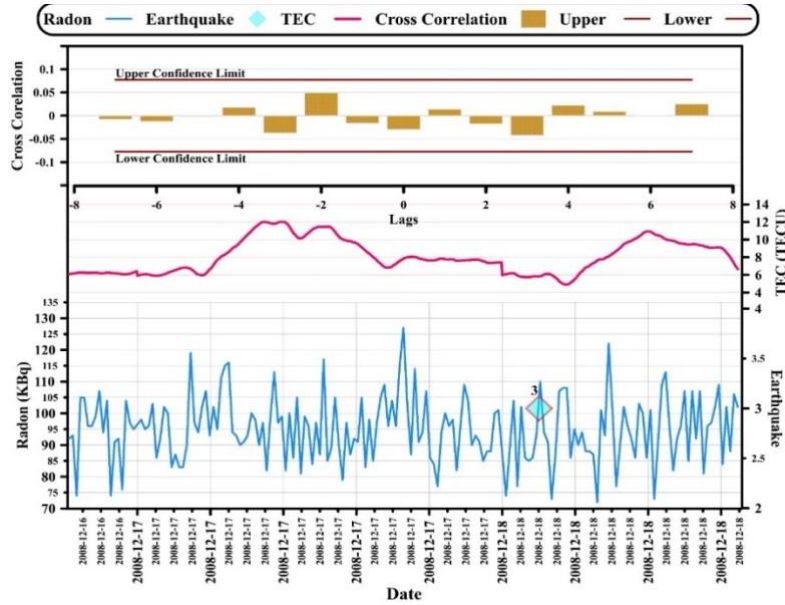


Figure 3 First group A cross-correlation for the data

We can see in Error! Reference source not found. that the radon gas concentration one day before the earthquake with magnitude (3 M<sub>L</sub>) recorded a small anomaly reaching approximately (127 kBq.m<sup>-3</sup>), but the total electron content for the same period slowly start to decrease. Soil and atmosphere temperature differences and air pressure are nearly stable. Therefore, the cross-correlation between Rn gas and TEC would not record the anomaly path through the confidence bound.

For Error! Reference source not found. (first group B) exactly when the earthquake with a magnitude (3.7 M<sub>L</sub>) occurs release gases due to the pressure of tectonic plates causing for emanation process and the radon gas concentration increase up to (137 kBq.m<sup>-3</sup>), but in contrast, the TEC gradually decrease. The cross-correlation for this variation did not show any anomaly between them.



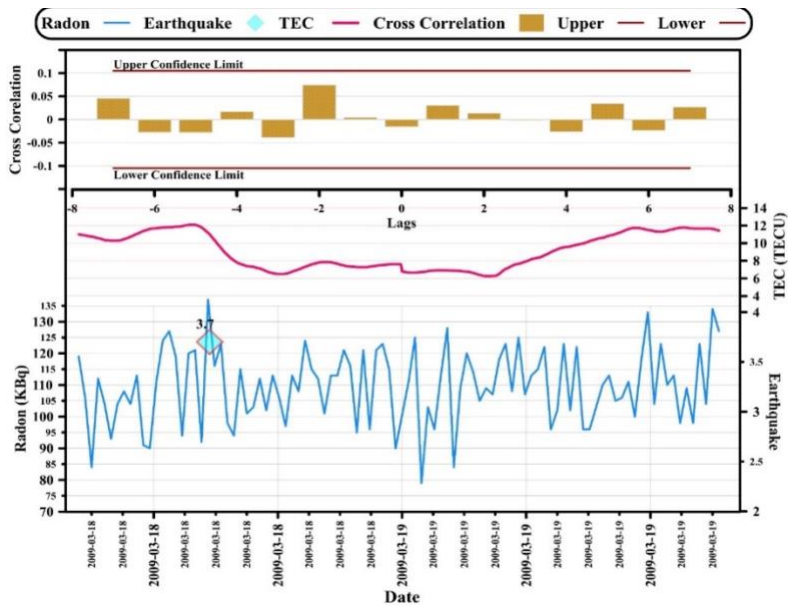


Figure 4 First group B cross-correlation for the data

### 3.2. Second group

The second group starts on (Apr 1, 2009, to Aug 31, 2009); many micro-earthquakes occurred with a magnitude (3 - 4.4  $M_L$ ), with TEC and radon gas concentrations varying between (60 to 270  $\text{kBq.m}^{-3}$ ). Air atmosphere and underground soil temperature record almost (8 °C) increment in the temperature this unique change for both underground and air is not helpful for transferee radon gas upward by the convection process. All data for the same period are shown in Error! Reference source not found..

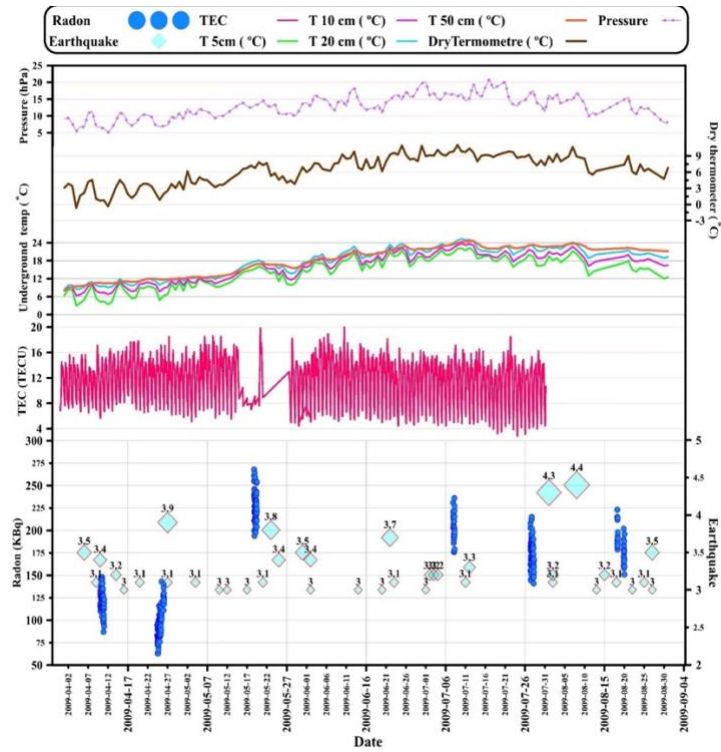
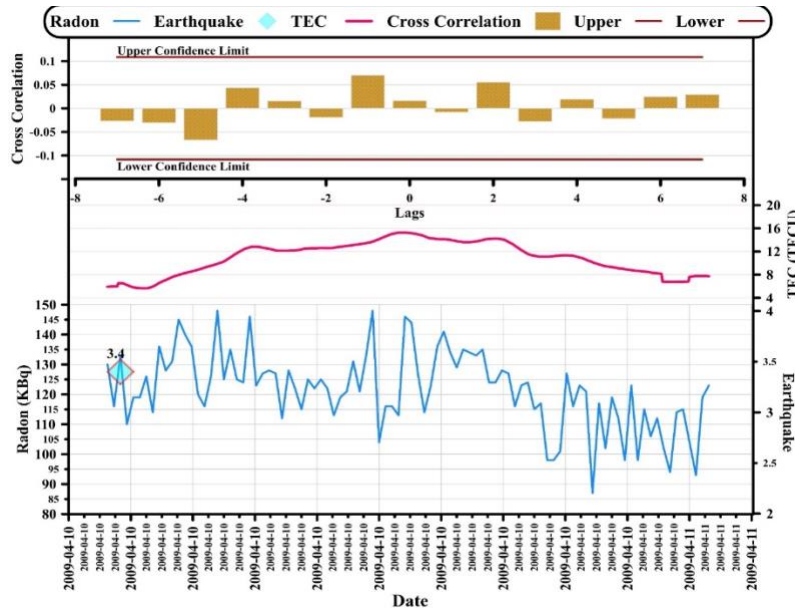


Figure 5. Radon, TEC, Temp of soil (5, 10, 20, and 50 cm), and Pressure with Earthquakes for the second group

We see from the figure above that the increase in the temperature causes the increase in pressure because the variation in the temperature is directly proportional to the variation in the air atmosphere pressure. There are some missing data in the total electron concentration data the reason behind this is some technical issue in the IONOLAB (Hacettepe University, Electrical and Electronics Engineering Department). To deal with the relation between parameters in the second group we magnify apportion of the data when we have all available data (earthquake, Rn, and TEC) for the same period. So, the relations are shown in Error! Reference source not found. (second group A).



**Figure 6** Second group A cross-correlation for the data

As may be seen in the figure above, the effect of an earthquake with a magnitude 3.4 on the relation between  $^{222}\text{Rn}$  data and TEC can be seen on the same day after the earthquake occurred. The pressure is produced in the tectonic plates by the effect of earthquakes caused for moving the radon gas in the soil pores toward the earth's surface and then into the air. This movement of radon gas is the main cause of the ionization of the air atmosphere as well as the increment in the total electron content. This relationship is confirmed in the study [12], [46]. In addition, the cross-correlation between radon gas and TEC did not record any anomaly.

### 3.3. Third group

The third group starts from (Sep 1, 2009, to Dec 31, 2009), and (11 micro-earthquakes) occurred with a magnitude (3 – 3.6 M<sub>L</sub>), with TEC and radon concentrations for the same period of time are presented in **Error! Reference source not found.**

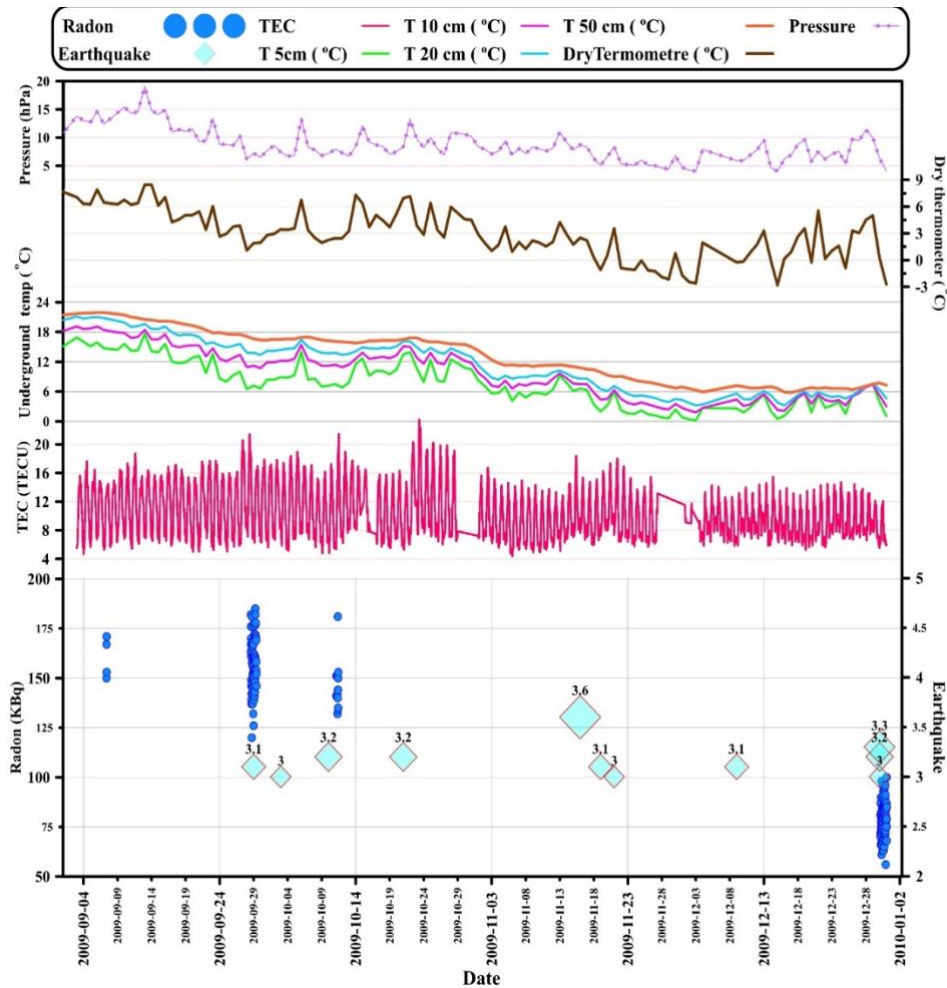


**Figure 7.** Radon, TEC, Temp of soil (5, 10, 20, and 50 cm) and Pressure with Earthquakes for the Third group

From the **Error! Reference source not found.**, we can see the variation of meteorological data especially the average underground temperature and air atmosphere temperature due to seasonal change starting to decrease gradually, and we can see the effect of this change on the radon gas emission from soil to the atmosphere, the maximum radon gas concentration reaches only (100 kBq.m<sup>-3</sup>) on the end of 2009. The process of Rn gas movement by the convection is slowed down in this case. The missing data in the TEC can be seen in the graph, the cause is a technical issue in the IONOLAB.

The third group graph has two subgroups (third group A and third group B). In the third group A, the cross-correlation between the parameters is shown in **Error! Reference source not found.** and an earthquake with a magnitude of (3.1 M<sub>L</sub>) is recorded. The reason the earthquake epicentre in the Marmara, and it is very far from the Çorum station in our study area the effect of the earthquake on the radon gas concentration cannot be seen. In contrast, the TEC magnitude starts to decrease one day before the earthquake, and after the earthquake occurs steadily increases to the previous magnitude. The reason for the changing in the TEC is the radon gas diffusion and emission reduced under decompression and raises during compressing earth tectonic plates. So, when the radon gas as a main source of ionization in the atmosphere decreases directly to make an impact on the TEC magnitude. There is no strong correlation between TEC and radon emanation.

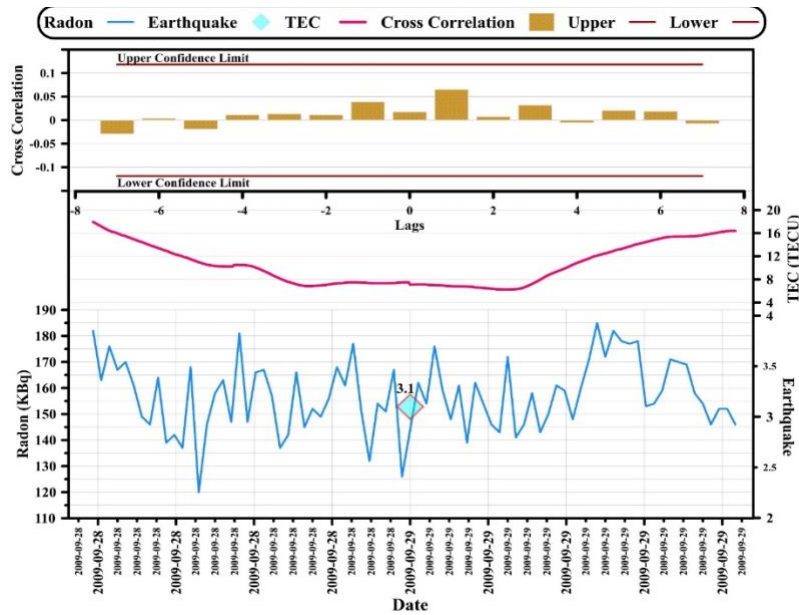


Figure 8 Third group A cross-correlation for the data

In Error! Reference source not found. (Third group B graph) there are three earthquakes' magnitudes (3.3, 3.2, and 3 M<sub>L</sub>), and the total radon concentration variation in response to seismic activity is (45 kBq.m<sup>-3</sup>), this variation is normal because radioactive materials such as Rn and parents disintegrate randomly. Therefore, the low influence of seismic activity on the radon gas is due to the epicentre distance from Çorum station and the depth of the focus. In another hand, earthquakes in the epicentre affect air ionization. The TEC start to fall in the mid-day on (Dec 31, 2009) this response is incongruous with total electron daily variation and directly related to changes in the radon concentration in the epicentre area transferred to the atmosphere. The cross correlation between the parameters is stay between the confidence bounds.

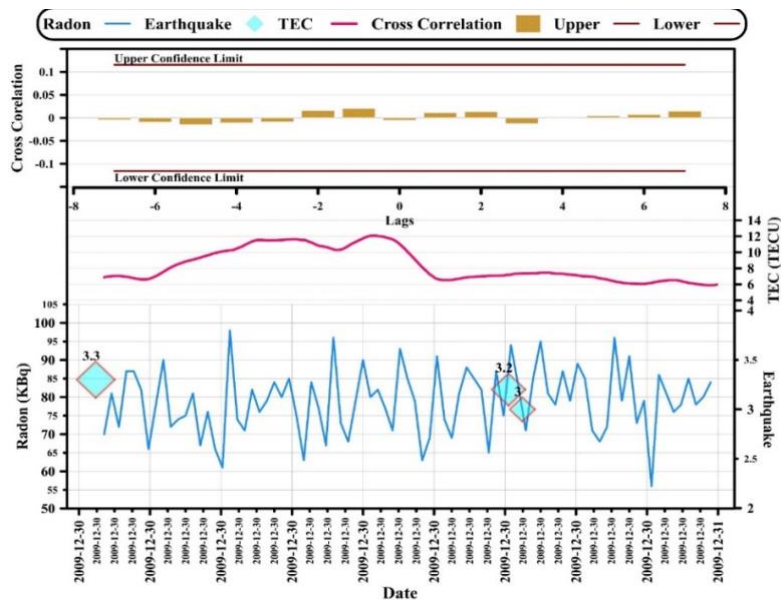


Figure 9 Third group B cross-correlation for the data

#### 4. Conclusions

The relations between Earthquake-TEC-Rn were tried to be explained through find the cross-correlation between Rn emanations with total electron condition under the effect of seismic activity. Seismo-Ionospheric Coupling studies have a critical place in earthquake predictions. In this study, we examined a triple change relation under the effect of microearthquakes.

A significant number of scientists has studied the changes caused by earthquakes in the ionosphere. However, we could not find any studies that examined for finding the correlation between the three variables outside of our research group. We think this research will be an important step to fill a critical gap in this area. The important results we have achieved can be listed as follows:

1. There is no significant correlation between TEC-Rn under the influence of microearthquakes.
2. The meteorological data especially air atmosphere pressure has a very low effect on the TEC-Rn anomalies.
3. The earthquake's epicentre distance and focal depth are inversely proportional to radon gas concentration.
4. We recommend for researchers in the future studies further develop, and work on the external magnetic effects such as (geomagnetic activity, disturbance time storm, and solar flux) on the ionospheric TEC distributions.

#### Acknowledgments

We would like to thank AFAD (Ministry of Interior Disaster and Emergency Management's Presidency, (<https://en.afad.gov.tr/>) for Radon data, IONOLAB (Hacettepe University Department of Electrical and Electronics Engineering) (<http://www.ionolab.org/index.php?page=index&language=en>) for TEC data, Boğaziçi Kandilli Observatory (<http://www.koeri.boun.edu.tr/scripts/lasteq.asp>) for earthquake data.

#### References

- [1] Baskaran M. Radon: A Tracer for Geological, Geophysical and Geochemical Studies. Cham: Springer International Publishing, 2016.
- [2] Tanner AB. Physical and chemical controls on distribution of radium-226 and radon-222 in ground water near Great Salt Lake, Utah," Natural radiation environment, 1964; 253–276.
- [3] Külahcı F, Şen Z. On the Correction of Spatial and Statistical Uncertainties in Systematic Measurements of 222Rn for Earthquake Prediction, Surv Geophys, 2014; 35(2): 449–478.
- [4] Nazaroff WW, Moed BA, Sextro RG. Soil as a Source of Indoor Radon, Generation, Migration, and Entry, Radon and its decay products in indoor W.W. Nazaroff, A.V. Nero Jr., 1988; 19(21): 57–112.
- [5] Sextro RG, Moed BA, Nazaroff WW, Revzan KL, Nero AV. Investigations of Soil as a Source of Indoor Radon, 1987;10–29.
- [6] Walia V, Su TC, Fu CC, Yang TF. Spatial variations of radon and helium concentrations in soil-gas across the Shan-Chiao fault, Northern Taiwan, Radiat Meas, 2005; 40(2–6): 513–516.
- [7] Sundal AV, Valen V, Soldal O, Strand T. The influence of meteorological parameters on soil radon levels in permeable glacial sediments, Science of the Total Environment, 2008; 389 (2–3): 418–428.
- [8] Cigolini C, et al. Radon surveys and real-time monitoring at Stromboli volcano: Influence of soil temperature, atmospheric pressure and tidal forces on 222Rn degassing, Journal of Volcanology and Geothermal Research, 2009; 184 (3–4): 381–388.
- [9] Sahoo M, Katlamudi J P, Shaji KS, Murali K, Udaya Lakshmi G. Influence of meteorological parameters on the soil radon (Rn222) emanation in Kutch, Gujarat, India, Environ Monit Assess 2018; 190 (3): 1–20.
- [10] Chowdhury S, Barman C, Deb A, Raha S, Ghose D. Study of variation of soil radon exhalation rate with meteorological parameters in Bakreswar–Tantloi geothermal region of West Bengal and Jharkhand, India, J Radioanal Nucl Chem 2019; 319 (1): 3–32.
- [11] Fujiyoshi R, et al. Meteorological parameters contributing to variability in 222Rn activity concentrations in soil gas at a site in Sapporo, Japan, Science of the Total Environment 2006; 370 (1): 224–234.
- [12] Muhammad A, Külahcı F, Akram P. Modeling radon time series on the North Anatolian Fault Zone, Türkiye: Fourier transforms and Monte Carlo simulations, Natural Hazards 2020; 104 (1): 979–996.
- [13] Pulinetz S, Boyarchuk K. Ionospheric precursors of earthquakes. Springer Science & Business Media, 2004.
- [14] Xia C, Wang Q, Yu T, Xu G, Yang S. Variations of ionospheric total electron content before three strong earthquakes in the Qinghai-Tibet region, Advances in Space Research 2011; 47 (3): 506–514.

- [15] Nayir H, Arikan F, Arikan O, Erol CB. GPS/TEC Estimation with IONOLAB Method, in 2007 3rd International Conference on Recent Advances in Space Technologies, Jun. 2007, pp. 29–34.
- [16] Muhammad A, Külahcı F, Salh H, Hama Rashid PA. Long Short Term Memory networks (LSTM)-Monte-Carlo simulation of soil ionization using radon, *J Atmos Sol Terr Phys* 2021; 221:105688.
- [17] Liu JY, Tsai HF, Jung TK. Total electron content obtained by using the global positioning system, *Terr Atmos Oceanic Sci* 1996; 7(1): 107–117.
- [18] Liu JY, Chen YI, Chen CH, Hattori K. Temporal and spatial precursors in the ionospheric global positioning system (GPS) total electron content observed before the 26 December 2004 M9.3 Sumatra-Andaman Earthquake, *J Geophys Res Space Phys* 2010; 115(A9): p. n/a-n/a.
- [19] Arikan F. Regularized estimation of vertical total electron content from Global Positioning System data, *J Geophys Res* 2003; 108 (A12): 1469.
- [20] Sezen U, Arikan F, Arikan O, Ugurlu O, Sadeghimorad A. Online, automatic, near-real time estimation of GPS-TEC: IONOLAB-TEC, *Space Weather* 2013; 11(5): 297–305.
- [21] Okabe S. Time variation of the atmospheric radon content near the ground surface with relation to some geophysical phenomena, University of Kyoto, 1956; Series A 28 (2): 99-115 [Online] Available: <http://hdl.handle.net/2433/257395>.
- [22] King CY. Episodic radon changes in subsurface soil gas along active faults and possible relation to earthquakes, *J Geophys Res* 1980; 85 (B6):3065–3078.
- [23] Birchard G, WF Libby. Soil radon concentration changes preceding and following four magnitude 4.2-4.7 earthquakes on the San Jacinto Fault in Southern California, *J Geophys Res* 1980; 85 (B6): 3100–3106.
- [24] Shapiro MH, Melvin JD, Tombrello TA, Mendenhall MH, Larson BP, Whitcomb JH. Relationship of the 1979 southern California radon anomaly to a possible regional strain event, *J Geophys Res* 1981; 86 (B3): 1725–1730.
- [25] Rastogi BK, Chadha RK, Raju IP. Seismicity near Bhatsa reservoir, Maharashtra, India, *Physics of the Earth and Planetary Interiors* 1986; 44(2): 179–199.
- [26] Zmazek B, Todorovski L, Džeroski S, Vaupotič J, Kobal I. Application of decision trees to the analysis of soil radon data for earthquake prediction, *Applied Radiation and Isotopes* 2003; 58 (6): 697–706.
- [27] Hartmann J, Levy JK. Hydrogeological and gasgeochemical earthquake precursors - A review for application, *Natural Hazards* 2005; 34(3), 279–304.
- [28] Walia V, Virk HS, Bajwa BS. Radon precursory signals for some earthquakes of magnitude > 5 occurred in N-W Himalaya: An overview, *Pure Appl Geophys* 2006; 163 (4): 711–721.
- [29] S. Singh, H. P. Jaishi, R. P. Tiwari, and R. C. Tiwari. A study of variation in soil gas concentration associated with earthquakes near Indo-Burma Subduction zone, *Geoenvironmental Disasters* 2016; 3(1): 1–8.
- [30] Yang TF, et al. Variations of soil radon and thoron concentrations in a fault zone and prospective earthquakes in SW Taiwan, *Radiat Meas* 2005; 40(2–6): 496–502.
- [31] Kamyşlıoğlu M, Kulalı F. A new study area for chaotic time series analyses applications: Lesvos island, *Arabian Journal of Geosciences*, 2021; 14(20): 1–6.
- [32] Virk HS, Walia V. Helium/radon precursory signals of Chamoli Earthquake, India, *Radiat Meas* 2001; 34(1–6):379–384.
- [33] Ramola RC, Prasad Y, Prasad G, Kumar S, Choubey VM. Soil-gas radon as seismotectonic indicator in Garhwal Himalaya, *Applied Radiation and Isotopes* 2008; 66(10):1523–1530.
- [34] Ramola RC. Relation between spring water radon anomalies and seismic activity in Garhwal Himalaya, *Acta Geophysica* 2010; 58(5): 814–827.
- [35] Jaishi HP, Singh S, Tiwari RP, and R. C. Tiwari, “Analysis of soil radon data in earthquake precursory studies,” *Annals of Geophysics*, 2014; 57( 5): 0544.
- [36] Jaishi S, Singh RP, Tiwari, and R. C. Tiwari, Correlation of radon anomalies with seismic events along Mat fault in Serchhip District, Mizoram, India, *Applied Radiation and Isotopes* 2014; 86:79–84.
- [37] Deb A, Gazi M, Barman C. Anomalous soil radon fluctuations – Signal of earthquakes in Nepal and Eastern India regions, *Journal of Earth System Science* 2016; 125(8):1657–1665.
- [38] Riggio A, Santulin M. Earthquake forecasting: A review of radon as seismic precursor, *Bollettino di Geofisica Teorica ed Applicata* 2015; 56(2): 95–114.
- [39] Baskaran M. Radon: A Tracer for Geological, Geophysical and Geochemical Studies, vol. 367. Springer, 2016.
- [40] Muhammad A. Monte Carlo Simulations Of Radon-Seismoionospheric Trilogly In Some Parts On The North Anatolian Fault Zone, Ph.D, Fırat University, 2022.
- [41] Karasartova D, et al., Bacterial and protozoal pathogens found in ticks collected from humans in Corum province of Turkey, *PLoS Negl Trop Dis* 2018; 12 (4): e0006395.
- [42] Turkish State Meteorological Service, Kütükçü Alibey Caddesi No:4 06120 Kalaba, Keçiören/ANKARA.

- [43] Gubner JA. Probability and random processes for electrical and computer engineers. Cambridge University Press, 2006.
- [44] Bracewell R. Pentagram notation for cross correlation. The Fourier transform and its applications, New York: McGraw-Hill, 1965; 46, 243.
- [45] Sahoo SK, Katlamudi M, Shaji JP, Murali Krishna KS, Udaya Lakshmi G. Influence of meteorological parameters on the soil radon (Rn222) emanation in Kutch, Gujarat, India, Environ Monit Assess 2018; 190 (3): 1–20.
- [46] Mohammed DHK, Külahcı F, Muhammed A. Determination of possible responses of Radon-222, magnetic effects, and total electron content to earthquakes on the North Anatolian Fault Zone, Turkiye: an ARIMA and Monte Carlo Simulation, Natural Hazards 2021;108 (3), 2493–2512.





## Assessment of Elenolic Acid Incorporation on Physical Properties of Chitosan Films to be Used as Active Packaging Material

Ayça AYDOĞDU EMİR<sup>1\*</sup>, Osman UÇKUN<sup>2</sup>

<sup>1</sup> Department of Food Technology, Faculty of Canakkale Applied Sciences, Canakkale 18 Mart University, Canakkale, Turkey

<sup>2</sup> Department of Food Technology, Faculty of Canakkale Applied Sciences, Canakkale 18 Mart University, Canakkale, Turkey

\*<sup>1</sup> ayca.aydogdu@comu.edu.tr, <sup>2</sup> uckunosman95@gmail.com

(Geliş/Received: 11/10/2022;

Kabul/Accepted: 08/02/2023)

**Abstract:** There is growing interest in biodegradable active packaging materials to extend shelf lives of food by retarding deteriorative reactions. The objective of this study was to fabricate active packaging films made from elenolic acid and chitosan. Elenolic acid is one of the phenolic compounds of olive leaves. Different amount of elenolic acid (%2.5 and %5 w/v) was incorporated into chitosan films (%1 and 2% w/v). The physical properties (density, moisture content, solubility, water vapor permeability, opacity, and color), total phenolic content and antioxidant activity were investigated. While elenolic acid addition did not affect the moisture content of chitosan films and the density, opacity, a\* and b\* values increased significantly ( $p \leq 0.05$ ). Elenolic acid incorporation reduced the water vapor permeability of chitosan films by 25%. Correlated to total phenolic content of the films, antioxidant activity of films reached up to % 85. Elenolic acid added chitosan films exhibited good water vapor barrier properties, opacity and antioxidant activity indicating that they could be developed as biodegradable active food packaging material for the food industry.

**Key words:** Elenolic acid, chitosan, active package, antioxidant activity, water vapor permeability.

### Elenolik Asit Katılmasının Aktif Ambalaj Malzemesi Olarak Kullanılacak Kitosan Filmlerinin Fiziksel Özellikleri Üzerine Etkisinin Değerlendirilmesi

**Öz:** Bozunma reaksiyonlarını geciktirerek gıdaların raf ömrünü uzatmak için biyolojik olarak parçalanabilen aktif ambalaj malzemelerine artan bir ilgi vardır. Bu çalışmanın amacı, elenolik asit ve kitosandan yapılan aktif ambalaj filmleri üretmektir. Elenolik asit, zeytin yapraklarının fenolik bileşiklerinden biridir. Kitosan filmlere (%1 ve %2 w/v) farklı miktarlarda elenolik asit (%2.5 ve %5 w/v) eklenmiştir. Filmlerin fiziksel özellikleri (yoğunluk, nem içeriği, çözünürlük, su buharı geçirgenliği, opaklık ve renk), toplam fenolik içerik ve antioksidan aktivite araştırılmıştır. Elenolik asit ilavesi kitosan filmlerin nem içeriğini etkilemezken yoğunluk, opaklık, a\* ve b\* değerleri önemli ölçüde artmıştır ( $p \leq 0.05$ ). Elenolik asit eklenmesi, kitosan filmlerinin su buharı geçirgenliğini %25 oranında azaltmıştır. Toplam fenolik içeriği ile ilişkili olarak, filmlerin antioksidan aktivitesi %85'e kadar çıkmıştır. Elenolik asit katılı kitosan filmler, iyi su buharı bariyer özellikleri, opaklık ve antioksidan aktivite sergileyerek, gıda endüstrisi için biyolojik olarak parçalanabilen aktif gıda ambalaj malzemesi olarak geliştirilebileceğini göstermektedir.

**Anahtar kelimeler:** Elenolik asit, kitosan, aktif paket, antioksan aktivite, su buharı geçirgenliği.

#### 1. Giriş

Due to rising consumer awareness of sustainability and health concern for using plastic food packaging, the growing interest in the development of biopolymer-based packages has increased. In general, to produce edible and biodegradable films, biopolymers include polysaccharides, protein and lipids [1]. Moreover, to extend the shelf life of foods and maintain food quality, active packaging systems are developed. One of the main reasons of food deterioration is oxidation and to improve the quality of oxidation sensitive foods, antioxidant incorporated food packaging technology is an effective alternative [2]. The common synthetic antioxidants that are commonly used in food industry are butylated hydroxyanisole (BHA), butylated hydroxytoluene (BHT), propyl gallate (PG), and tert-butyl hydroquinone (TBHQ). However, due to growing health concern, there is great demand to replace synthetic antioxidants with natural ones. In general, tocopherol, plant extracts, and essential oils from herbs and spices are widely used natural antioxidants [3]. Olive leaves are significant waste in olive oil production. Olive leaves are rich source of phenolic compounds so olive leaf extracts are good candidates for active packaging

\* Corresponding author: ayca.aydogdu@comu.edu.tr, <sup>1</sup> 0000-0003-3877-9200, <sup>2</sup> 0000-0001-9454-3695

designs [4]. Oleuropein is the main component of olive leaf extract, and it is a complex phenolic compound olive tree leaves [5]. Elenolic acid is the form of chemical hydrolysis of oleoside methylester, oleuropein and ligstroside and it is naturally found in olive oil linked to tyrosol and hydroxytyrosol [6]. The studies of Briante et al. (2002) [7] and Thiealman et al. [8] showed the antioxidant and antimicrobial activities of elenolic acid derivatives. In this study, elenolic acid was used as active compound to produce biodegradable active packaging material. Chitosan is one of the most commonly used biopolymer due to its non-toxicity, biodegradability, biocompatibility. Chitosan is a cationic polysaccharide obtained by deacetylation of chitin and consists of  $\beta$ -(1-4)-2-acetamido- $\alpha$ -glucose and  $\beta$ -(1-4)-2-amino- $\alpha$ -glucose units [9]. Compared to other biopolymers used for edible films, chitosan shows excellent film forming characteristics such as mechanical performance and good barrier properties [10]. Moreover, owing to its antimicrobial activity, chitosan is great option to produce antimicrobial packaging [9] [11]. To improve antimicrobial activity of chitosan films, several phenolic compounds [12], [13] and essential oils [14][15] were incorporated. In contrast to antimicrobial activity, chitosan does not show significant antioxidant activity. Therefore, it is important to enhance of antioxidant activity of chitosan films to be used for biopolymer-based antioxidant packages. Thus, in several studies, extracted phenolic compounds such as tea polyphenols [9], onion skin [16], apple peel [12], black soybean seed coat [17] were incorporated into chitosan films and significant increase in antioxidant activity was observed. To the best of our knowledge, no study in the literature examines the use of elenolic acid for active packaging materials. The objective of this study is to develop environmentally friendly, biodegradable films from chitosan incorporated elenolic acid to be used as active packaging material. Within this scope, total phenolic content, antioxidant activity and physical properties, including density, moisture content, water solubility, water vapor permeability, opacity and color of the films were investigated.

## 2. Materials and Methods

### 2.1 Materials

Chitosan was bought from Sigma-Aldrich Chemie GmbH (Darmstadt, Germany) and elenolic acid powder was provided from Kale Naturel Ltd. Şti. The other chemicals (Glycerol ( $\geq 99\%$ ), 2,2-Diphenyl-1-picrylhydrazyl, Folin-Ciocalteu reagent, sodium carbonate) were purchased from Sigma-Aldrich Chemie GmbH (Darmstadt, Germany).

### 2.2 Methods

#### 2.2.1 Film preparation

1% and 2% (w/v) chitosan solutions were prepared by dissolving 1 g and 2 g of chitosan in 100 ml of acetic acid solution (1% v/v). 0.5% (w/v) glycerol was added to the prepared solution as a plasticizer and the mixture was stirred for 2 hours with a magnetic stirrer. %5 and %2.5 (w/v) elenolic acid was dissolved by ethanol/water (80/20) solution. Then, to remove insoluble particles, the slurry was centrifuged (Nüve, NF 800, Turkey) at 3500 rpm for 10 minutes. Chitosan and elenolic acid solutions were mixed to get chitosan/elenolic acid ratio as 1:1, 1:0.5, 2:1, 2:0.5. Solutions of 15 ml were poured into LDPE petri plates and dried at room temperature (25°C, 50%RH) for 24 h. For conditioning, the films were stored in a desiccator (52%, 20°C) before analysis. The films were labelled as Ch1Ele1, Ch1Ele0.5, Ch2Ele1, Ch2Ele0.5. Control films were 1% and 2% chitosan films named as Ch1 and Ch2, respectively.

#### 2.2.2 Thickness of films

To measure thickness values of films, a hand-held micrometer (Dial thickness gauge No. 7301, Mitutoyo Co. Ltd., Tokyo, Japan) was used. Six measurements from three films were done.

#### 2.2.3. Density, moisture content and solubility of films

The films were cut into pieces (2 cm  $\times$  2 cm), and their initial weight was recorded ( $W_1$ ). Films were dried until the samples reached a constant weight ( $W_2$ ) by placing them inside an oven set to 105 °C. Density was calculated from the Eq. 1;

$$\text{Density} = \frac{W_2}{\text{Area} \times \text{Thickness}} \quad (1)$$

Moisture content (% , wet basis) was found from the Eq. 2;

$$\text{Moisture content (\%)} = \frac{W_1 - W_2}{W_1} \times 100 \quad (2)$$

The dried films ( $W_2$ ) were immersed in 30 ml of distilled water at room temperature and kept there for 24 h. Then, the undissolved remnants were dried in a 105°C oven for 24 h, and the final weight was recorded ( $W_3$ ). Solubility was calculated by Eq. 3;

$$\text{Solubility (\%)} = \frac{W_2 - W_3}{W_2} \times 100 \quad (3)$$

#### 2.2.4. Opacity of films

Light transmittance of the films was measured with a UV–visible spectrophotometer (UV-1800, Shimadzu, Kyoto, Japan). Opacity values were calculated from the method described by (Aydogdu et al., 2018) [1] with Eq. 4 ;

$$\text{Opacity} = \frac{A_{600}}{x} \quad (4)$$

where  $A_{600}$  is the absorbance at 600 nm and  $x$  is the film thickness (mm). Three pieces were taken from each film for measurement; three replicates were measured for each formulation.

#### 2.2.5. Color of films

To investigate color of the films, a color reader Chroma Meter CR400 (Konica Minolta, Inc., Japan) was used. The values were expressed in the CIE  $L^*$ (lightness),  $a^*$ (redness- greenness),  $b^*$  (yellowness-blueness) color space by the help of Eq. 5;

$$\Delta E = \sqrt{(L_0^* - L^*)^2 + (a_0^* - a^*)^2 + (b_0^* - b^*)^2} \quad (5)$$

where  $L_0^*$ ,  $a_0^*$  and  $b_0^*$  are the color measurements of control films.

#### 2.2.6. Water vapor permeability of films (WVP)

WVP of chitosan/elenolic acid films was measured with the modified version of ASTM E-96 described by (Aydogdu et al., 2018) [1]. The custom-built test cups are cylindrical polyacetal (Delrin) with a 40 mm internal diameter. To provide the films to 100% RH, 35 mL of distilled water were filled into cups. The cups were placed in a desiccator at 25-30 % RH by using silica gel. The cups were weighed at 2 h intervals. The Water vapor transmission rate (WVTR) was calculated from the regression analysis of weight loss data vs. time. Then the WVP values were calculated by using Eq. 6;

$$\text{WVP} = \frac{\text{WVTR} \times \Delta x}{S \times (R_1 - R_2)} \quad (6)$$

where  $x$  is the thickness of the films (m),  $S$  is the saturated water vapor pressure (Pa) at measured temperature,  $R_1$  and  $R_2$  are the relative humidity inside the cups and desiccator, relatively. The measurements were performed in duplicate.

#### 2.2.7. Total phenolic content of films

Total phenolic contents of films were determined by the modified Folin–Ciocalteu method [18]. Briefly, about 0.1 g sample was dissolved in 10 ml ethanol/water (80/20) to extract phenolic compounds of films. Diluted 1 ml of sample was mixed with 0.2 N Folin-Ciocalteu reagent and kept in dark for 5 min and then, 2 ml of 75 g/L sodium carbonate solution was added. After standing for 1 hour in dark at room temperature, the absorbance at 760 nm was measured by a spectrophotometer (UV 1800, Shimadzu, Columbia, USA) and total phenolic content (TPC) was calculated as follows;

$$\text{TPC (mg GAE/g film)} = \frac{C \times V \times D}{W_s} \quad (7)$$

where  $C$  is the concentration corresponding to the measured absorbance value from the calibration curve (mg/L),  $V$  is the volume of the solution (L),  $D$  is the dilution rate, and  $W_s$  is the weight of the film (g).

### 2.2.8. DPPH radical-scavenging activity

The modified method described by Aydogdu et al. 2019 [19] was applied to determine the DPPH radical-scavenging activity. Firstly, about 0.1 g film was dissolved in 10 ml ethanol/water (80/20). After the removal of undissolved parts, solutions at 100  $\mu$ l were mixed with 3.9 mL DPPH<sup>•</sup> radical solution and kept in dark place for 1 h to complete reaction between DPPH solution and phenolic compounds. Absorbance value of samples was measured at 517 nm by a spectrophotometer (UV 1800, Shimadzu, Columbia, USA). The antioxidant activity (%AA) of the films were defined by Eq. 8 ;

$$\text{DPPH scavenging activity (\%)} = \frac{A_{\text{control}} - A_{\text{film}}}{A_{\text{control}}} \times 100 \quad (8)$$

where  $A_{\text{control}}$  and  $A_{\text{film}}$  are the absorbance values of the DPPH solution without and with the presence of the sample solutions.

### 2.2.9 Statistical analysis

All experiments were performed in duplicate. Analysis of variance (ANOVA) was applied by MINITAB (version 16, State College, PA, USA). If significant differences were found, Tukey's Multiple Comparison Test was used for comparisons ( $p \leq 0.05$ ).

## 3. Results and Discussion

### 3.1 Moisture content, density and solubility

Thickness, moisture content, water solubility and density of the films are shown in Table 1. Thickness values were within the range 0.072–0.084 mm. The fact that there was no significant difference between the samples ( $p > 0.05$ ) represented that elenolic acid addition did not affect the average thickness. The density values (Table 1) lay within the range 1.28–1.48  $\text{g/cm}^3$  with no statistically significant difference between the formulations ( $P > 0.05$ ). However, it is obviously seen that elenolic acid addition increase the density of chitosan films, significantly. Similar density range (1.132–1.231) were observed with the addition of tea polyphenols into chitosan films [9]. Moisture content of films were in the range of 14.75–18.65% and no significant difference was observed by the addition of elenolic acid. Similarly, Kocakulak et al. 2019 [20] found no difference in moisture content of chickpea flour films with gallic acid addition. Although elenolic acid incorporation did not affect solubility of Ch1 film, Ch2's solubility decreased significantly. Interaction between elenolic acid and the polysaccharide chain of chitosan decreased the available amino and hydroxyl groups of chitosan to interact with water. This resulted in significant decrease in the solubility of chitosan films [21]. Similar decrease in solubility of chitosan films after apple peel polyphenol incorporation observed in the study of Riaz et al.2018 [13] and the reason was stated that phenolic compounds might interact with chitosan molecules with hydrogen bonding and this might decrease the interactions between water molecules and chitosan.

Table 1. Physical properties of films

Film	Moisture Content (%)	Thickness (mm)	Solubility (%)	Density ( $\text{g/cm}^3$ )
Ch1Ele1	15.94 $\pm$ 0.25 <sup>a</sup>	0.081 $\pm$ 0.004 <sup>a</sup>	33.79 $\pm$ 1.01 <sup>a</sup>	1.33 $\pm$ 0.31 <sup>a</sup>
Ch1Ele0.5	18.65 $\pm$ 1.66 <sup>a</sup>	0.072 $\pm$ 0.003 <sup>a</sup>	32.13 $\pm$ 0.31 <sup>a</sup>	1.48 $\pm$ 0.29 <sup>a</sup>
Ch2Ele1	15.73 $\pm$ 1.08 <sup>a</sup>	0.084 $\pm$ 0.005 <sup>a</sup>	22.62 $\pm$ 1.38 <sup>b</sup>	1.38 $\pm$ 0.12 <sup>a</sup>
Ch2Ele0.5	14.75 $\pm$ 0.14 <sup>a</sup>	0.083 $\pm$ 0.003 <sup>a</sup>	20.59 $\pm$ 1.69 <sup>b</sup>	1.28 $\pm$ 0.47 <sup>a</sup>
Ch1	18.45 $\pm$ 0.28 <sup>a</sup>	0.072 $\pm$ 0.006 <sup>a</sup>	33.46 $\pm$ 3.36 <sup>a</sup>	0.70 $\pm$ 0.09 <sup>b</sup>
Ch2	17.85 $\pm$ 0.39 <sup>a</sup>	0.078 $\pm$ 0.003 <sup>a</sup>	33.35 $\pm$ 2.32 <sup>a</sup>	0.56 $\pm$ 0.03 <sup>b</sup>

Different letters in the same column show the significant difference between samples by Tukey's test ( $p \leq 0.05$ ).

### 3.2 Color and opacity

Color properties are directly related to film appearance (Fig. 1). The values of  $L^*$ ,  $a^*$ ,  $b^*$ , and  $\Delta E^*$  were shown in Table 2. As can be seen, elenolic acid addition resulted in darker films and decreased  $L^*$  values of chitosan films. Moreover,  $a^*$  and  $b^*$  values of chitosan films increased significantly with addition of elenolic acid. This is indication of tendency towards redness and yellowness, respectively. The nature color of elenolic acid powder is brownish so elenolic acid incorporated films had lower  $L^*$  and higher  $a^*$  and  $b^*$  values. There are several studies representing phenolic acid addition resulted in films having high  $a^*$  and  $b^*$  values [22], [10]. When elenolic acid amount in films increased, significant increase in the total color difference ( $\Delta E^*$ ) was observed that is indication of more colored films. In general, the overall color change of films could be distinguished by the naked eye ( $\Delta E > 5$ ) [23]. Thus, the color change of chitosan/elenolic acid films was obviously visible (Figure 1).

Packages are the only way of presenting foods to consumers; the opacity of films is crucial parameter for consumer acceptance. On the other hand, higher opacity value might be desired to pack foods that could easily oxidized due to light catalyzation. Opaque packaging materials could provide against to light [24]. Opacity values of films were shown in Table 2. While opacity of chitosan films was about  $1.3\text{-}1.9\text{ A mm}^{-1}$ , the opacity values of elenolic acid incorporated films ranged between  $5.49\pm 1.02$  and  $6.45\pm 0.98\text{ A mm}^{-1}$ . Opacity value of commercial polyethylene packaging films were found as  $4.26\text{ A mm}^{-1}$  [25] so it can be stated that chitosan/elenolic acid films can be used as packaging material to provide protection against to light. Incorporation of elenolic acid could cause light scattering and reflection so opacity values increased [26]. This resulted in significant protection to packed foods from light that accelerates nutrient losses, oxidation and discoloration [13]. Similar increase in opacity values was observed in studies about phenolic acid incorporated films; extracts from grape skins [27], red cabbage [28], green tea extract [29] etc.

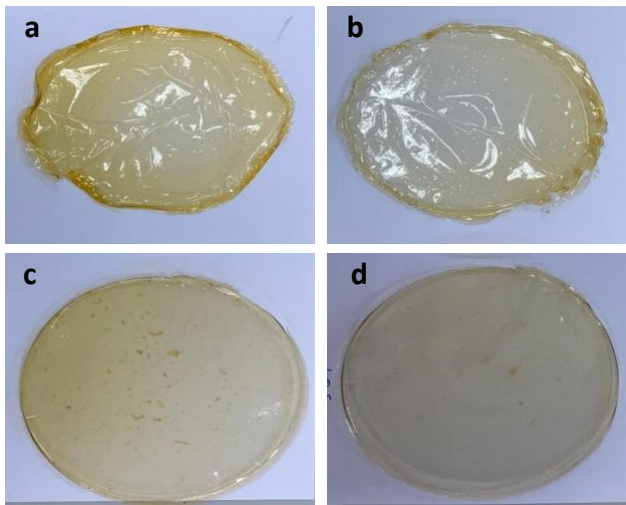


Figure 1. Images of films; a: Ch1Ele1, b: Ch1Ele0.5, c: Ch2Ele1, d: Ch2Ele0.5.

Table 2. Opacity and color parameters of films

Film	Opacity ( $\text{A mm}^{-1}$ )	$L^*$	$a^*$	$b^*$	$\Delta E^*$
Ch1Ele1	5.49±1.02 <sup>a</sup>	85.81±1.58 <sup>b</sup>	2.79±0.05 <sup>a</sup>	23.92±1.06 <sup>a</sup>	23.66±1.21 <sup>a</sup>
Ch1Ele0.5	6.45±0.98 <sup>a</sup>	87.35±1.01 <sup>b</sup>	2.41±0.29 <sup>a</sup>	14.45±1.24 <sup>b</sup>	14.16±0.75 <sup>b</sup>
Ch2Ele1	6.41±0.69 <sup>a</sup>	85.01±0.85 <sup>b</sup>	2.57±0.09 <sup>a</sup>	23.14±0.86 <sup>a</sup>	22.72±1.73 <sup>a</sup>
Ch2Ele0.5	5.94±0.63 <sup>a</sup>	86.57±0.41 <sup>b</sup>	2.38±0.11 <sup>a</sup>	16.44±1.21 <sup>b</sup>	15.89±0.99 <sup>b</sup>
Ch1	1.98±0.24 <sup>b</sup>	91.82±0.69 <sup>a</sup>	0.48±0.08 <sup>b</sup>	1.15±0.03 <sup>c</sup>	-
Ch2	1.34±0.12 <sup>b</sup>	91.89±0.22 <sup>a</sup>	0.54±0.11 <sup>b</sup>	1.58±0.12 <sup>c</sup>	-

Different letters in the same column show the significant difference between samples by Tukey's test ( $p \leq 0.05$ ).

### 3.3 Total phenolic content and antioxidant activity

The main phenolic compounds of olive leaves and fruits are oleuropein, hydroxytyrosol, tyrosol, coumaric acid, ferulic acid, luteolin, rutin etc. [8]. Oleuropein could be hydrolyzed to elenolic acid, hydroxytyrosol, and oleuropein aglycone [5]. In this study, elenolic acid was added into chitosan films as phenolic compounds. The total phenolic content and antioxidant activity values of chitosan and elenolic acid/chitosan films were presented in Table 3. As can be seen from Table 2, Ch2Ele1 films had the highest total phenolic content with 9.32±0.35 mg GAE/g film followed by Ch1Ele1 films having 7.65±0.09 mg GAE/g film. Films having higher amounts of elenolic acid showed higher total phenolic content. It is known that phenolic compounds are the main source of antioxidant activity. Ch1Ele1, Ch1Ele0.5 and Ch2Ele1 showed the highest antioxidant activity (about %85). As stated before, chitosan shows antioxidant activity and also proved in this study, but pure chitosan films could not affective as active packaging material. However, incorporating elenolic acid, chitosan films could be good candidates for active packaging materials owing to having high antioxidant activity.

### 3.4 Water vapor permeability (WVP)

Control of moisture transfer between the environment and food which affects the shelf lives of food is the one of the main functions of packaging due to role of water content on deteriorative reactions [30]. The WVP values of chitosan and elenolic acid/chitosan films were shown in Table 3. It was observed that regardless of the elenolic acid content, the incorporation of elenolic acid resulted in significant decrease in WVP values ( $p \leq 0.05$ ). While WVP of chitosan films ranged 3.66-3.82×10<sup>-10</sup> g m<sup>-1</sup> s<sup>-1</sup> Pa<sup>-1</sup>, the WVPs of Ch\_Ele films lied within the narrow range of 2.92-2.82×10<sup>-10</sup>. It is obvious that elenolic acid addition enhanced the water vapor barrier property of chitosan films. One of the reason behind the decrease in WVP of films might the interactions between chitosan and elenolic acid which could decrease the available hydrophilic groups in chitosan and reduce the interactions with water [9]. The other possible reason could be related to higher density of elenolic acid/chitosan films than control chitosan films (Table 1). Elenolic acid incorporation resulted in a dense network so due to the lower space in chitosan matrix, diffusion rate of water through the chitosan films decreased [9]. Thus, WVP of chitosan films enhanced by the addition of elenolic acid. Similar trend was observed phenolic compounds incorporated chitosan films. In study of Kadam et al. 2021 [31] pine needles and in the study of Wang et al. 2022 [16] onion skin phenolic compounds integrated to chitosan films, significant decrease in WVP was observed.

Table 3. Total phenolic content, antioxidant activity and water vapor permeability of the films

Film	TPC (mg GAE/g film)	DPPH activity (% inhibition)	WVP x 10 <sup>10</sup> (g m <sup>-1</sup> s <sup>-1</sup> Pa <sup>-1</sup> )
Ch1Ele1	7.65±0.09 <sup>b</sup>	84.90±1.83 <sup>a</sup>	2.86±0.06 <sup>b</sup>
Ch1Ele0.5	4.59±0.30 <sup>d</sup>	83.11±2.71 <sup>a</sup>	2.91±0.05 <sup>b</sup>
Ch2Ele1	9.32±0.35 <sup>a</sup>	85.26±1.15 <sup>a</sup>	2.92±0.06 <sup>b</sup>
Ch2Ele0.5	5.34±0.67 <sup>c</sup>	65.95±2.99 <sup>b</sup>	2.82±0.05 <sup>b</sup>
Ch1	1.22±0.07 <sup>f</sup>	26.71±1.18 <sup>c</sup>	3.82±0.06 <sup>a</sup>
Ch2	1.84±0.08 <sup>f</sup>	25.92±1.09 <sup>c</sup>	3.66±0.02 <sup>a</sup>

Different letters in the same column show the significant difference between samples by Tukey's test ( $p \leq 0.05$ ).

#### 4. Conclusion

In this study, elenolic acid, component of olive leaf, was used as an active compound to enhance the functional characteristics of chitosan films as an alternative to synthetic antioxidants. Although incorporation of elenolic acid did not affect the density and moisture content of the chitosan films, %2 chitosan films containing different amount of elenolic acid showed lower solubility values which is a desirable property to pack foods having high moisture content. With the addition of elenolic acid, opacity of chitosan films was significantly increased so they can be used to pack light sensitive foods. Due to the nature color of elenolic acid powder, as the elenolic acid amount into films increased, tendency towards redness and yellowness observed. Independent of the elenolic concentrations, elenolic acid addition decreased WVP of chitosan films that is evidence of enhanced water barrier property of the films. Thus, during the shelf life, controlling moisture transfer could be possible. Incorporation of elenolic acid increased total phenolic content and antioxidant activity (almost %85) of chitosan films significantly. Results suggested that elenolic acid added chitosan films could be used as promising alternative to synthetic packaging materials and could also have ability to extend shelf lives of foods. As a future study, the real package system can be design by using elenolic acid incorporated chitosan films and shelf-life extension can be investigated.

#### Acknowledgment

The research was supported by the Research Fund of the Çanakkale Onsekiz Mart University with Project Number FBA-2021-3573. Ayca Aydogdu Emir: conceptualization, supervision, methodology, investigation, writing—original draft; Osman Uçkun: methodology, investigation, writing—original draft, visualization.

#### References

- [1] Aydogdu Emir A, Kirtil E, Sumnu G, Oztop MH, and Aydogdu Y. Utilization of lentil flour as a biopolymer source for the development of edible films. *J Appl Polym Sci* 2018; 135 (23): 46356.
- [2] Pereira de Abreu DA, Cruz JM, Paseiro Losada P. Active and Intelligent Packaging for the Food Industry. *Food Rev Int* 2012; 28 (2): pp. 146–187.
- [3] Gómez-Estaca J, López-de-Dicastillo C, Hernández-Muñoz P, Catalá R, and Gavara R. Advances in antioxidant active food packaging. *Trends Food Sci Technol* 2014; 35 (1) :42–51.
- [4] Kontogianni VG and Gerathanassis IP. Phenolic compounds and antioxidant activity of olive leaf extracts. *Nat Prod Res* 2012; 26 (2):186–189.
- [5] Mourtzinis I, Salta F, Yannakopoulou K, Chiou A and Karathanos VT. Encapsulation of olive leaf extract in  $\beta$ -cyclodextrin. *J Agric Food Chem* 2007; 55 (20): 8088–8094.

- [6] Rovellini P. Elenolic acid in virgin olive oil: A liquid chromatography-mass spectrometry method. *Riv Ital delle Sostanze Grasse* 2008; 85 (1):21–31.
- [7] Briante R, Patumi M, Terenziani S, Bismuto E, Febbraio F and Nucci R. *Olea europaea* L. leaf extract and derivatives: Antioxidant properties. *J Agric Food Chem* 2002; 50 (17): 4934–4940.
- [8] Thielmann J, Kohnen S and Hauser C. Antimicrobial activity of *Olea europaea* Linné extracts and their applicability as natural food preservative agents. *Int J Food Microbiol* 2017; 251: 48–66.
- [9] Wang L, Dong Y, Men H, Tong J, and Zhou J. Preparation and characterization of active films based on chitosan incorporated tea polyphenols. *Food Hydrocoll* 2013; 32 (1): 35–41.
- [10] Kurek M, Elez I, Tran M, Šč M, Dragovi V, and Gali K. Development and evaluation of a novel antioxidant and pH indicator film based on chitosan and food waste sources of antioxidants. *Food Hydrocoll* 2018; 84: 238–246.
- [11] Yao X, Hu H, Qin Y, and Liu J. Development of antioxidant, antimicrobial and ammonia-sensitive films based on quaternary ammonium chitosan, polyvinyl alcohol and betalains-rich cactus pears (*Opuntia ficus-indica*) extract. *Food Hydrocoll* 2020;106.
- [12] Sun L, Sun J, Chen L, Niu P, Yang X, and Guo Y. Preparation and characterization of chitosan film incorporated with thinned young apple polyphenols as an active packaging material. *Carbohydr Polym* 2017;163: 81–91.
- [13] Riaz A et al. Preparation and characterization of chitosan-based antimicrobial active food packaging film incorporated with apple peel polyphenols. *Int J Biol Macromol* 2018;114: 547–555.
- [14] Sánchez-gonzález L, González-martínez C, Chiralt A, and Cháfer M. Physical and antimicrobial properties of chitosan – tea tree essential oil composite films. *J Food Eng* 2010; 98 (4): 443–452.
- [15] Perdonés A, Sánchez-gonzález L, Chiralt A, and Vargas M. Effect of chitosan – lemon essential oil coatings on storage-keeping quality of strawberry. *Postharvest Biol Technol* 2012; 70: 32–41.
- [16] Wang C et al. Preparation and characterization of chitosan-based antioxidant composite films containing onion skin ethanolic extracts. *J Food Meas Charact* 2022;16 (1): 598–609.
- [17] Wang X, Yong H, Gao L, Li L, Jin M, and Liu J. Preparation and characterization of antioxidant and pH-sensitive films based on chitosan and black soybean seed coat extract. *Food Hydrocoll* 2018; 89: 56–66.
- [18] Wang H, Hao L, Wang P, Chen M, Jiang S, and Jiang S. Release kinetics and antibacterial activity of curcumin loaded zein fibers. *Food Hydrocoll* 2017; 63: 437–446.
- [19] Aydogdu A, Yildiz E, Aydogdu Y, Sumnu G, Sahin S, and Ayhan Z. Enhancing oxidative stability of walnuts by using gallic acid loaded lentil flour based electrospun nanofibers as active packaging material. *Food Hydrocoll* 2019; 95: 245–255.
- [20] Kocakulak S, Sumnu G, and Sahin S. Chickpea flour-based bio films containing gallic acid to be used as active edible films. *J Appl Polym Sci* 2019; 47704: 1–9.
- [21] Rambabu K, Bharath G, Banat F, Loke P, and Hernández H. Mango leaf extract incorporated chitosan antioxidant film for active food packaging. *Int J Biol Macromol* 2019; 126: 1234–1243.
- [22] Shivangi S, Dorairaj D, Negi PS, and Shetty NP. Development and characterisation of a pectin-based edible film that contains mulberry leaf extract and its bio-active components. *Food Hydrocoll* 2021;121:107046.
- [23] Yildiz E, Sumnu G and Kahyaoglu LN. Monitoring freshness of chicken breast by using natural halochromic curcumin loaded chitosan/PEO nanofibers as an intelligent package. *Int J Biol Macromol* 2021; 170: 437–446.
- [24] Kirtil E, Aydogdu A, Svitova T, and Radke CJ. Assessment of the performance of several novel approaches to improve physical properties of guar gum based biopolymer films. *Food Packag Shelf Life* 2019; 29:100687.
- [25] Guerrero P, Nur Hanani ZA, Kerry JP, and De La Caba K. Characterization of soy protein-based films prepared with acids and oils by compression. *J Food Eng* 2011; 107 (1): 41–49.



- [26] Wu C. et al. Preparation of an intelligent film based on chitosan/oxidized chitin nanocrystals incorporating black rice bran anthocyanins for seafood spoilage monitoring. *Carbohydr Polym* 2019; 222: 115006.
- [27] Ma Q and Wang L. Preparation of a visual pH-sensing film based on tara gum incorporating cellulose and extracts from grape skins. *Sensors Actuators B Chem* 2016; 235: 401–407.
- [28] Liang T, Sun G, Cao L, Li J, and Wang L. A pH and NH<sub>3</sub> sensing intelligent film based on *Artemisia sphaerocephala* Krasch . gum and red cabbage anthocyanins anchored by carboxymethyl cellulose sodium added as a host complex. *Food Hydrocoll* 2019; 87: 858–868.
- [29] Siripatrawan U and Harte BR. Physical properties and antioxidant activity of an active film from chitosan incorporated with green tea extract. *Food Hydrocoll* 2010; 24 (8): 770–775.
- [30] Aydogdu A, Radke CK, Bezci S, and Kirtil E. Characterization of curcumin incorporated guar gum/orange oil antimicrobial emulsion films. *Int J Biol Macromol* 2020; 148: 110–120.
- [31] Kadam AA, Singh S, and Gaikwad KK. Chitosan based antioxidant films incorporated with pine needles (*Cedrus deodara*) extract for active food packaging applications. *Food Control* 2020; 124:107877.



## Optimization Studies on the Changeable Components of Hydroelectric Power Plants

Muhammed Cihat TUNA<sup>1</sup>, Alp Buğra AYDIN<sup>2\*</sup>

<sup>1</sup> İnşaat Mühendisliği, Mühendislik Fakültesi, Fırat Üniversitesi, Elazığ, Türkiye

<sup>2</sup> İnşaat Mühendisliği, Teknoloji Fakültesi, Fırat Üniversitesi, Elazığ, Türkiye

<sup>1</sup> mctuna@firat.edu.tr, <sup>2\*</sup> baydin@firat.edu.tr

(Geliş/Received: 20/10/2022;

Kabul/Accepted: 26/12/2023)

**Abstract:** The design flow rate, the dimensions of the transmission structure and the penstock size have a large impact on the cost of run-of-river type hydroelectric power plants. Equipment costs constitute a large part of the total budget of the plant. Optimum sizing, which maximizes the use of hydraulic potential, does not fit together with optimum sizing, which is necessary to obtain economic benefit from its investment. The main design parameters can be selected with the help of an optimization study in terms of both economic benefit and hydraulic potential. In this study, an easy to implement model, aimed at determining the costs associated with the different components in the structural organization of a hydroelectric power plant, is developed by a feasibility study to overcome the difficulties in practice. Gokcekoy HEPP, built in Turkey, was selected as the system. Annual energy production values were calculated by taking into account the current energy market conditions in Turkey. In addition, real situation studies were carried out regarding design flow rate selection, forced pipe diameter optimization and transmission channel sizing.

**Key words:** Hydroelectric power plants, optimization, investment cost, changeable components.

### Hidroelektrik Santrallerin Değişken Bileşenleri Üzerine Optimizasyon Çalışmaları

**Öz:** Nehir tipi hidroelektrik santrallerin maliyeti üzerinde tasarım debisi, iletim kanalı ve tünelin boyutları ile cebri boru boyutunun büyük bir etkisi vardır. Ekipman maliyetleri santralin toplam bütçesinin büyük bir kısmını oluşturmaktadır. Yatırımından ekonomik faydanın elde edilmesi için gerekli olan optimum boyutlandırma ile hidrolik potansiyelin kullanımını en üst düzeye çıkaran optimum boyutlandırma birbirine uymamaktadır. Ana tasarım parametreleri hem ekonomik fayda hem de hidrolik potansiyel açısından bir optimizasyon çalışması yardımıyla seçilebilir. Bu çalışmada, ortaya çıkan zorluğu gidermek için, hidroelektrik santrali üzerindeki ekonomik bir uygulanabilirlik çalışmasıyla, bir hidroelektrik santralinin yapısal organizasyonunda yer alan farklı unsurların maliyetinin belirlenmesi için kullanımı kolay bir yaklaşım geliştirilmiştir. Ayrıca tasarım debisi seçimi, cebri boru çap optimizasyonu ve iletim kanalı boyutlandırılmasına ait durum çalışmaları yapılmıştır.

**Anahtar kelimeler:** Hidroelektrik santraller, optimizasyon, yatırım maliyeti, değişken bileşenler

#### 1. Introduction

Hydroelectric energy is a renewable energy source which is relatively inexpensive, reliable, sustainable and that can be produced without toxic waste and with greenhouse gas emissions that are significantly lower than fossil fuel energy plants [1-6]. The world's technically feasible hydropotential is 14,370 TWh / year. This value is almost equal to our global electricity demand. [7,8]. According to the report published by the International Hydroelectric Association in 2019 [9]; In 2018, it was stated that approximately 22 GW installed capacity was added to the hydroelectric projects worldwide and thus the total capacity increased to 1292 GW. In the same report, it was stated that the electricity generated from hydroelectric power plants in 2018 was approximately 4,200 terawatt hours (TWh) [9]. Figure 1 shows that the installed capacity of hydroelectric power plants increases day by day in the world.

\* Corresponding author: [baydin@firat.edu.tr](mailto:baydin@firat.edu.tr). ORCID Number of authors: <sup>1</sup> 0000-0001-9005-1968, <sup>2</sup> 0000-00001-5267-1429

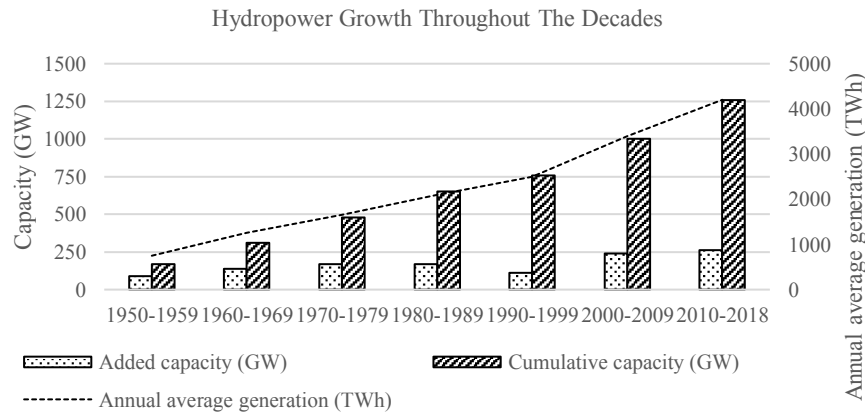


**Figure 1.** Change of the installed power of hydroelectric power plant in the world by years, adapted from [9]

A good economic analysis is necessary for the energy resource with such great potential to the benefit of the national economy. The decision to develop a hydroelectric project is made for economic reasons. However, factors such as environmental, cultural and physical features of the region and the costs and availability of technological and engineering solutions should be thoroughly examined. Initial investment costs of hydroelectric power plant installation are quite high. In contrast, operational and maintenance costs are low. This means that most of the overall budget of the project will be spent during the development phase. In relation to that it is important to balance the installation costs with the amount and speed and the energy outcome to assess if the project is worth to realize and, if the answer is yes, to plan the next budget. The applicability of each hydroelectric project is site-specific and depends on local characteristics. The amount of power generated depends on the water flow, the hydraulic head and the efficiency of the electromechanical equipment.

The maximum electricity that a river basin can produce technologically is defined as a hydroelectric potential. Losses are excluded when determining the hydroelectric potential. The economic potential of a river basin is defined as annual energy that can be developed at competitive costs compared to other energy sources. The economic potential shows the economic optimization of electricity production of a river basin [7,10-12].

Optimization of run-of-river hydroelectric power plant design has been investigated in various studies. Topics covered in these research are:

- (I) Determination of optimum plant capacities of power plants [13-26].
- (II) Development of special equations that adequately represent the economic performance and power generation of power plants [18, 22, 27-35]
- (III) Determination of effective optimization that can be solved quickly for optimum plant design [18, 19, 21-24, 26, 36-40]
- (IV) Determination of the effect of flow processes total productivity of the power plant [41-68]
- (V) Investigation of the design and performance of turbines [6, 53, 69-76].

The purpose of this study is to optimize variable components to maximize the generated energy and to minimize the initial investment cost of a hydroelectric project. In scope of this study, an easy-to-use approach was developed to determine the cost of different elements of the structural organization of a hydroelectric power plant and to determine its impact on the total cost. In this context, a real case study was carried out using hydrological and economic data of Gökçeköy HEPP project built in Turkey. The results of this study are not only theoretical but can be used by applying the local unit costs of that region to a hydroelectric power plant to be built anywhere in the world. In addition, the results of this study will not be only theoretical, in contrary to some studies in the literature, but will provide the advantage of being used in real practice.

## 2. Optimization Methodology

The primary objective in the optimization study is to determine the appropriate plant conformation that minimizes or maximizes the value of some operation or economic parameters [23]. The purpose of this article is to develop an optimization to achieve maximum power in return for minimum capital investment. The layout of a typical run-of-river project that has been considered is as shown in Figure 2.

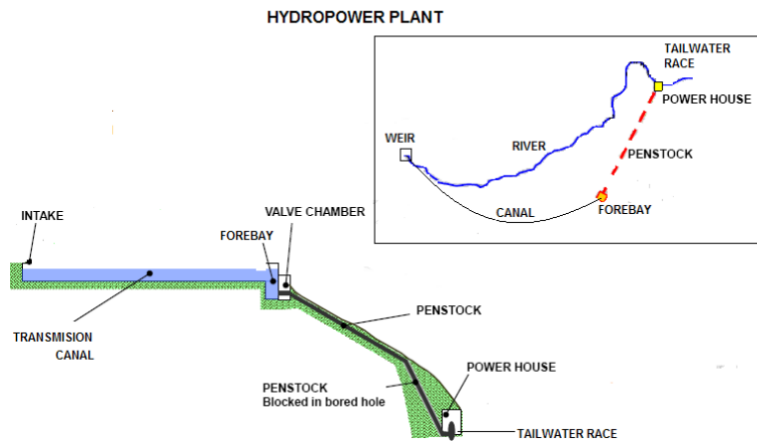


Fig. 2. General scheme of a hydropower plant.

## 2.1 Important parameters in the optimization study

The design flow rate, the dimensions of the transmission canal or tunnel and the penstock dimension are the three most important optimization parameters on the cost of river-type hydroelectric power plants. The design flow rate affects both energy and power capacity. For this reason, hydroelectric plants have a significant impact on the cost. A reduced design flow rate leads to reduced power capacity and initial investment cost. The percentage of decrease in installed power is almost identical to the percentage of decrease in the design flow rate. However, the percentage of increase in the cost-benefit ratio is not as significant as the decrease in power capacity. Consequently, a too small the design flow rate prevents the optimal utilization of hydroelectric potential, on the other hand a too high the design flow rate may render the project financially unfeasible.

The second important parameter is the selection of channel types and dimensions, which are also related to the design flow. Canals are usually excavated and follow the contours of the existing land. Increasing channel excavation and dimensions significantly increases the cost rate. The cost of the channel is based on the total volume of rock and soil excavated.

The third important parameter is the penstock. The penstock that carry pressured water are usually made of steel. The penstock of a hydropower project, which serves to transmit water with optimum hydraulic losses to create the head, are included in the optimization study. The cost of penstock depends on the approximate weight of the penstock.

Easily fictionalized, simple-designed and well-worked structures are crucial to minimize costs in terms of optimal design in a hydraulic project.

## 2.2 Transmission structure optimization

It is necessary to be careful in sizing as the conditions of construction of the channels that will transmit water to hydroelectric plants affect both initial investment costs and operating expenses. When the slope is selected small in this type of transmission channels, the speed decreases and the wet cross-sectional area increases. Thus the channel construction costs increase. However, energy losses are reduced since the load losses occurring along the channel will be low. In open channels, when the slope is selected large, the speed will increase and the wet section area will decrease, so the construction costs will decrease. However, the energy loss will increase as the load loss along the channel will be high. This will increase operating costs. Therefore, there is an optimum channel size and slope in the channels that act as transmission in hydroelectric plants. The aim is to dimension the transmission structure in the most economical way under the most favorable conditions.

## 2.3 Economic dimensioning

In the most economical section, the construction and operation costs of the channels are asked to be reduced to a minimum. Usually a portion for air is left on top of the water flow line in the canals [77]. In practice, the sizing

process is completed by adding an air portion in accordance with the water depth after the channel dimensions are selected according to the most appropriate hydraulic section. With the subsequent addition of air portion, the concept of economic cross-section is eliminated, construction and operation costs increase and deeper channel cross-sections are obtained.

In order to reduce the size of the canal, the flow rate needs to be increased. However, by increasing the flow rate and hence the severing power, erosions will be encountered in the canal inner walls and at the base. For this reason, coatings are used in the canals to prevent the caving in the walls and the base of the canal. Channel coating thickness is selected between 10-25 cm. It is already a structural necessity to coat the transmission channels that carry water to hydroelectric facilities. Because it is not desirable to have any foreign matter in the pressurized water supplied to the turbines by means of penstock, especially in high slope plants.

Generally, the [incline of slope](#) is chosen according to the structure of the land. b/h ratio is selected between 3 and 6. It is more suitable to select b/h ratio as 3 for the canal to have a suitable size. This way, z=1 and b/h=3. With the depth h, the base width b, the bevel slope z and the flow cross-section A in the trapezoid canals, the following relation could be provided;

$$A = \frac{h^2}{[b/(h+z)]} \quad (1)$$

$$A_{grs} = 4h^2 \text{ is obtained from this relation. With } Q = V.A \text{ } R = \frac{A}{b + 2h\sqrt{1+z^2}}, \text{ and replacing } A = 4h^2$$

and  $b = 3h$ , then  $R = 0,68.h$

Taking the coating thickness e into consideration for the coated canals;

$$Q = V.A \longrightarrow A_{net} = 4(h-e)^2 \text{ and } R = 0,68.(h-e)$$

Replacing these values in the Manning formula, the following relation is obtained

$$V = k.R^{2/3} J^{1/2} \longrightarrow J = \frac{v^2}{k^2.[0.68(h-e)]^{4/3}} \quad (2)$$

k: smoothness coefficient, taken as 60 for concrete; e: coating thickness

For the canal cost;

$$M_k = U.e.L.f_b.a.100 \quad (3)$$

$M_k$ : canal cost per meter (USD);  $U = b + 2h\sqrt{1+z^2}$  U: wetted perimeter ; $f_b$ : unit price of concrete (USD);  
The canal cost share per annum;

$$M_i = A_{brt}.L.f_h.a/100 \quad (4)$$

$M_i$ : Canal cost per annum (USD);  $A_{grs}$ : gross area ( $m^2$ );  $f_h$ : Unit price for 1  $m^3$  of excavation; a: depreciation coefficient; The annual cost of the energy loss due to the slope is;

$$M_e = 8.Q.J.L.T.f_e \quad (5)$$

$M_e$ : cost of energy loss per annum (USD); Q : flow rate ( $m^3/s$ )

T : annual number of operation hours of the plant (hr); L: canal length (m);  $f_e$ : electricity price (USD/KWH)

Thus the annual cost of the canal is obtained as;

$$M = M_i + M_e$$

The total canal cost is then;

$$M_t = M_k + M_i + M_e$$

Cost studies performed at different flow rates are given in tables below. The cost analyses carried out at different flow rates are provided in the tables below. The annual amount of canal excavation is provided in Table 1, the annual amount of canal concrete coating was provided in Table 2 and the energy losses and the total cost are provided in Table 3. The change in the total canal cost with respect to varying operation flow rates and canal heights are displayed in Figure 2.

**Table 1.** Amount of canal excavation per annum (k:60, e:0.15)

Q	h	$A_{grs}$	$A_{net}$	a/100	$f_h$	L	$M_i$
(m <sup>3</sup> /s)	(m)	$A_g=4.h^2$	$A_n=4(h-e)^2$	0.08	(\$/m <sup>3</sup> )	(m)	(\$)
3	0.9	3.24	2.25	0.08	25.5	5000	33048.00
	1.0	4.00	2.89	0.08	25.5	5000	40800.00
	1.1	4.84	3.61	0.08	25.5	5000	49368.00
	1.2	5.76	4.41	0.08	25.5	5000	58752.00
	1.3	6.76	5.29	0.08	25.5	5000	68952.00
5	0.8	2.56	1.69	0.08	25.5	5000	26112.00
	0.9	3.24	2.25	0.08	25.5	5000	33048.00
	1.0	4.00	2.89	0.08	25.5	5000	40800.00
	1.1	4.84	3.61	0.08	25.5	5000	49368.00
	1.2	5.76	4.41	0.08	25.5	5000	58752.00
	1.3	6.76	5.29	0.08	25.5	5000	68952.00
	1.4	7.84	6.25	0.08	25.5	5000	79968.00
	1.5	9.00	7.29	0.08	25.5	5000	91800.00
7	1.0	4.00	2.89	0.08	25.5	5000	40800.00
	1.1	4.84	3.61	0.08	25.5	5000	49368.00
	1.2	5.76	4.41	0.08	25.5	5000	58752.00
	1.3	6.76	5.29	0.08	25.5	5000	68952.00
	1.4	7.84	6.25	0.08	25.5	5000	79968.00
	1.5	9.00	7.29	0.08	25.5	5000	91800.00
	1.6	10.24	8.41	0.08	25.5	5000	104448.00
10	1.2	5.76	4.41	0.08	25.5	5000	58752.00
	1.3	6.76	5.29	0.08	25.5	5000	68952.00
	1.4	7.84	6.25	0.08	25.5	5000	79968.00
	1.5	9.00	7.29	0.08	25.5	5000	91800.00
	1.6	10.24	8.41	0.08	25.5	5000	104448.00
	1.7	11.56	9.61	0.08	25.5	5000	117912.00
	1.8	12.96	10.89	0.08	25.5	5000	132192.00
15	1.5	9.00	7.29	0.08	25.5	5000	91800.00
	1.6	10.24	8.41	0.08	25.5	5000	104448.00
	1.7	11.56	9.61	0.08	25.5	5000	117912.00
	1.8	12.96	10.89	0.08	25.5	5000	132192.00
	1.9	14.44	12.25	0.08	25.5	5000	147288.00
	2.0	16.00	13.69	0.08	25.5	5000	163200.00
2.1	17.64	15.21	0.08	25.5	5000	179928.00	

**Table 2.** Amount of canal concrete cost per annum (k:60)

Q	h	e	A <sub>net</sub>	V	f <sub>b</sub>	L	J	M <sub>k</sub>
(m <sup>3</sup> /s)	(m)	0.15	A <sub>n</sub> =4(h-e) <sup>2</sup>	Q/A <sub>n</sub>	(\$/m <sup>3</sup> )	(m)	$\frac{v^2}{k^2 \cdot [0.68(h-e)]^{4/3}}$	(\$)
3	0.9	0.15	2.25	1.33	66.6	5000	0.001065637	20859.12
	1.0	0.15	2.89	1.04	66.6	5000	0.000546663	23176.80
	1.1	0.15	3.61	0.83	66.6	5000	0.000302072	25494.48
	1.2	0.15	4.41	0.68	66.6	5000	0.000177137	27812.16
	1.3	0.15	5.29	0.57	66.6	5000	0.000109046	30129.84
5	0.8	0.15	1.69	2.96	66.6	5000	0.006349531	18541.44
	0.9	0.15	2.25	2.22	66.6	5000	0.002960103	20859.12
	1.0	0.15	2.89	1.73	66.6	5000	0.001518509	23176.80
	1.1	0.15	3.61	1.39	66.6	5000	0.000839090	25494.48
	1.2	0.15	4.41	1.13	66.6	5000	0.000492046	27812.16
	1.3	0.15	5.29	0.95	66.6	5000	0.000302905	30129.84
	1.4	0.15	6.25	0.80	66.6	5000	0.000194172	32447.52
7	1.0	0.15	2.89	2.42	66.6	5000	0.002976278	23176.80
	1.1	0.15	3.61	1.94	66.6	5000	0.001644617	25494.48
	1.2	0.15	4.41	1.59	66.6	5000	0.000964411	27812.16
	1.3	0.15	5.29	1.32	66.6	5000	0.000593695	30129.84
	1.4	0.15	6.25	1.12	66.6	5000	0.000380578	32447.52
	1.5	0.15	7.29	0.96	66.6	5000	0.000252461	34765.20
	1.6	0.15	8.41	0.83	66.6	5000	0.000172460	37082.88
10	1.2	0.15	4.41	2.27	66.6	5000	0.001968186	27812.16
	1.3	0.15	5.29	1.89	66.6	5000	0.001211622	30129.84
	1.4	0.15	6.25	1.60	66.6	5000	0.000776690	32447.52
	1.5	0.15	7.29	1.37	66.6	5000	0.000515227	34765.20
	1.6	0.15	8.41	1.19	66.6	5000	0.000351960	37082.88
	1.7	0.15	9.61	1.04	66.6	5000	0.000246621	39400.56
15	1.2	0.15	4.41	2.27	66.6	5000	0.001968186	27812.16
	1.3	0.15	5.29	1.89	66.6	5000	0.001211622	30129.84
	1.4	0.15	6.25	1.60	66.6	5000	0.000776690	32447.52
	1.5	0.15	7.29	1.37	66.6	5000	0.000515227	34765.20
	1.6	0.15	8.41	1.19	66.6	5000	0.000351960	37082.88
	1.7	0.15	9.61	1.04	66.6	5000	0.000246621	39400.56
15	1.5	0.15	7.29	2.06	66.6	5000	0.001159261	34765.20
	1.6	0.15	8.41	1.78	66.6	5000	0.000791910	37082.88
	1.7	0.15	9.61	1.56	66.6	5000	0.000554897	39400.56
	1.8	0.15	10.89	1.38	66.6	5000	0.000397566	41718.24
	1.9	0.15	12.25	1.22	66.6	5000	0.000290489	44035.92
	2.0	0.15	13.69	1.10	66.6	5000	0.000215985	46353.60
2.1	0.15	15.21	0.99	66.6	5000	0.000163116	48671.28	



**Table 3.** Canal energy loss and total cost analysis

Q	h	T	V	$f_e$	L	J	$M_e$	$M_t$
(m <sup>3</sup> /s)	(m)	(hours)	Q/A <sub>n</sub>	\$/kwh	(m)	$\frac{v^2}{k^2[0.68(h-e)]^{4/3}}$	(\$)	(\$)
3	0.9	2500	1.33	0.04	5000	0.001065637	12787.65	67833.30
	1.0	2500	1.04	0.04	5000	0.000546663	6559.96	71680.20
	1.1	2500	0.83	0.04	5000	0.000302072	3624.87	79611.37
	1.2	2500	0.68	0.04	5000	0.000177137	2125.64	89770.09
	1.3	2500	0.57	0.04	5000	0.000109046	1308.55	101402.62
5	0.8	2500	2.96	0.04	5000	0.006349531	126990.63	172753.38
	0.9	2500	2.22	0.04	5000	0.002960103	59202.07	114247.73
	1.0	2500	1.73	0.04	5000	0.001518509	30370.19	95490.43
	1.1	2500	1.39	0.04	5000	0.000839090	16781.80	92768.31
	1.2	2500	1.13	0.04	5000	0.000492046	9840.93	97485.38
	1.3	2500	0.95	0.04	5000	0.000302905	6058.11	106152.18
	1.4	2500	0.80	0.04	5000	0.000194172	3883.45	117218.82
7	1.5	2500	0.69	0.04	5000	0.000128807	2576.14	129944.50
	1.0	2500	2.42	0.04	5000	0.002976278	83335.80	148456.04
	1.1	2500	1.94	0.04	5000	0.001644617	46049.27	122035.77
	1.2	2500	1.59	0.04	5000	0.000964411	27003.51	114647.96
	1.3	2500	1.32	0.04	5000	0.000593695	16623.45	116717.52
	1.4	2500	1.12	0.04	5000	0.000380578	10656.18	123991.56
	1.5	2500	0.96	0.04	5000	0.000252461	7068.91	134437.27
10	1.6	2500	0.83	0.04	5000	0.000172460	4828.89	147021.91
	1.2	2500	2.27	0.04	5000	0.001968186	78727.43	166371.88
	1.3	2500	1.89	0.04	5000	0.001211622	48464.87	148558.94
	1.4	2500	1.60	0.04	5000	0.000776690	31067.59	144402.96
	1.5	2500	1.37	0.04	5000	0.000515227	20609.08	147977.44
	1.6	2500	1.19	0.04	5000	0.000351960	14078.39	156271.42
15	1.7	2500	1.04	0.04	5000	0.000246621	9864.83	167674.20
	1.8	2500	0.92	0.04	5000	0.000176696	7067.84	181285.23
	1.5	2500	2.06	0.04	5000	0.001159261	69555.65	209195.05
	1.6	2500	1.78	0.04	5000	0.000791910	47514.57	189707.60
	1.7	2500	1.56	0.04	5000	0.000554897	33293.80	191103.17
	1.8	2500	1.38	0.04	5000	0.000397566	23853.96	198071.35
15	1.9	2500	1.22	0.04	5000	0.000290489	17429.32	208846.42
	2.0	2500	1.10	0.04	5000	0.000215985	12959.12	222367.60
	2.1	2500	0.99	0.04	5000	0.000163116	9786.96	237978.50

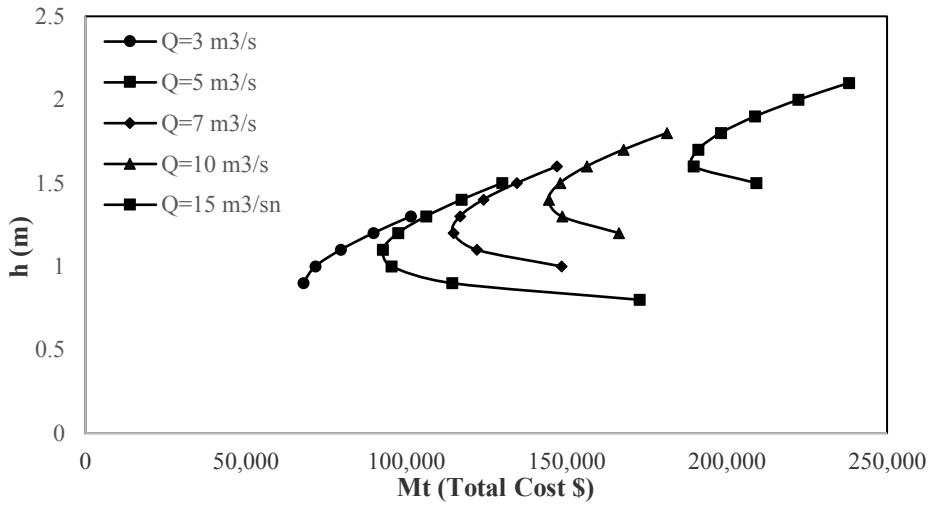


Figure 2. Variation in the canal total cost

### 2.4 Penstock optimization

Penstock costs account for approximately 1/3 of the total installation cost of hydroelectric plants. This structure, which is one of the most expensive items, should be chosen carefully. Penstock optimization should minimize the total cost by taking into account the costs incurred due to load losses. In practice the estimate of an associated cost of the head losses involves predicting both an interest rate and the project life that allows the expected cash flows to be converted to a present worth.

For the best power in the Penstock design, it is necessary to determine a suitable penstock slope and determine the maximum power per unit length. To offer an economic solution, head loss flow rate and site slope must be considered. The penstock length will increase as the slope decreases. Accordingly, head losses will increase. Thus, a larger gross head would be required to provide the same power from the power plant. If penstock is selected on a small diameter, a system that is cheap but has more load losses will be installed. In addition, if penstock is selected on a large diameter, a system that is expensive but has less load losses will be installed. Penstock price typically varies directly proportionally to the length and to the second power of the diameter. For this reason, a good optimization is required. A case study for Penstock optimization is given in Table 4 and Figure 3.

Table 4. Optimization of the penstock

Diameter D	Friction loss	Net Head	Velocity	Overpressure	Wall thickness	Concrete cover	Min. Wall thickness	Average wall thickness	Cost	Annual cost	Lost energy friction	Balance sheet of the annual energy loss	Total annual cost
(m)	(m)	(m)	(m/s)	(m)	(mm)	(mm)	(mm)	(mm)	(\$)	(\$)	(kWh)	(\$)	(\$)
1	11.82	88.18	10.19	97.35	8.95	2.00	6.50	8.72	343067.1	37737.4	6437743.6	386264.6	424002.0
1.2	4.47	95.53	7.07	67.60	9.78	2.00	7.00	9.39	443348.3	48768.3	2434634.1	146078.0	194846.4
1.4	1.96	98.04	5.20	49.67	10.64	2.00	7.50	10.07	554185.3	60960.4	1070000.9	64200.1	125160.4
1.5	1.36	98.64	4.53	43.26	11.08	2.00	7.75	10.42	613562.3	67491.9	740594.2	44435.7	111927.5
1.6	0.96	99.04	3.98	38.03	11.55	2.00	8.00	10.77	675578.3	74313.6	524920.8	31495.2	105808.9
<b>1.7</b>	<b>0.70</b>	<b>99.30</b>	<b>3.52</b>	<b>33.68</b>	<b>12.02</b>	<b>2.00</b>	<b>8.25</b>	<b>11.14</b>	<b>740233.3</b>	<b>81425.7</b>	<b>379903.0</b>	<b>22794.2</b>	<b>104219.8</b>
1.8	0.51	99.49	3.14	30.04	12.51	2.00	8.50	11.50	807527.2	88828.0	280078.9	16804.7	105632.7
1.9	0.39	99.61	2.82	26.97	13.00	2.00	8.75	11.88	877460.1	96520.6	209917.1	12595.0	109115.6
2	0.29	99.71	2.55	24.34	13.50	2.00	9.00	12.25	950032.0	104503.5	159676.3	9580.6	114084.1

Effective discharge= 4.50 m<sup>3</sup>/s  
 Design flow= 9.50 m<sup>3</sup>/s  
 The length of penstock= 375 m  
 Gross head= 100 m

Note= Effective discharge were taken into account of the friction calculation.  
 g= 9.81 m/s  
 T<sub>c</sub>= 8 sec  
 σ<sub>y</sub>= 1.4 kg/cm<sup>2</sup>

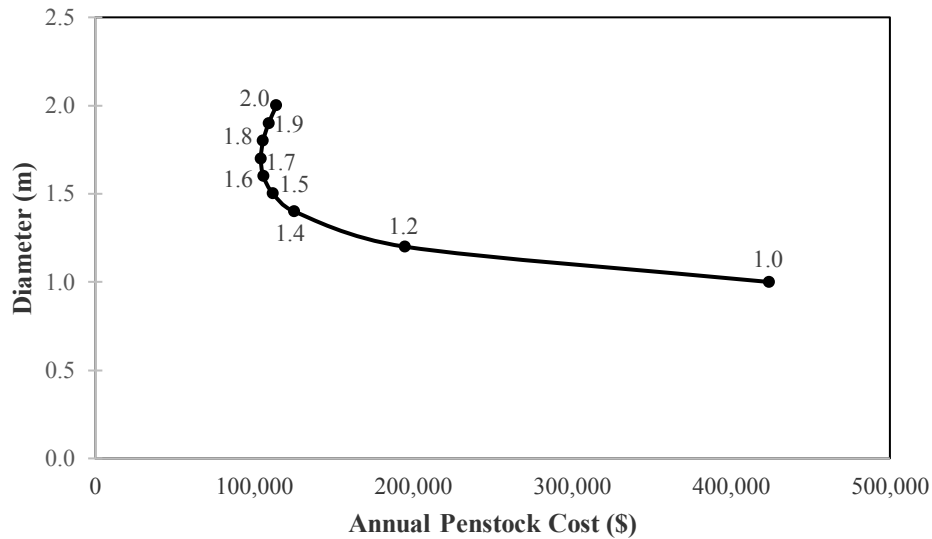


Figure 3. Change in Diameter versus Annual Cost

## 2.5 Design flow rate and installed power optimization

Operation works have been repeated based on the selected discharge values for energy optimization, and the discharge value which has made the utilization ratio 95% which has been calculated as firm. In order to dimension such hydroelectric power plants in the world in a healthy way, the flow rate values of at least 25 years should be known in hourly periods on the stream where the power plant will be built. Because rivers have irregular flow regimes depending on the climatic conditions of the countries. When the distribution of hourly flow rate values measured by 25-year period is made according to months, the flow rate which is present in the river at 95% of the all time is taken as the design flow rate. The ratio of time in this design flow rate can be selected in desired amount considering the development status of the countries and other economic reasons. The energy generated by this flow rate is taken into account as firm energy. Following this stage, for the optimization of power, the optimum discharge has been determined by taking into account the project values of various plants that would have been effective in the cost of power structures depending on the selected discharges. Based on this design discharge, the transmission canal dimensions, the penstock diameter and the power central size have been selected; and based on these data, the net heads have been determined from the hydraulics calculations. Together with the net head corresponding to each of the selected discharges, the installed power and the annual production have been calculated. The operational works have been carried out based on the 7.00, 7.25, 7.50, 7.75, 8.00, 8.25, 8.50, 8.75, 9.00, 9.25, 9.50, 9.75, 10.00, 10.25, 10.50, 10.75, and 11.00 m<sup>3</sup>/s discharges values. The total cost, the annual income and the annual expense rates pertaining to each discharge and installed power have been specified. Then, the profitability and marginal profitability calculations have been done, and the optional system whose marginal profitability is closest to 1, and which has a design discharge of 9.50 m<sup>3</sup>/s has produced the best outcome. The calculation details are given in Table 5 and Figure 4.

**Table 5.** Power Optimization

Q (m <sup>3</sup> /s)	H <sub>net</sub> (m)	Installed power (kW)	Produced energy-firm (GWh/year)	Produced energy-second (GWh/year)	The annual energy produced (GWh/year)	Annual income (\$)	Total cost (\$)	Annual expense (\$)	Annual net income (\$)	Income / expenditure	The difference comes (\$)	The difference expense (\$)	Marginal profitability
7.00	95.67	5.928	37.14	10.76	47.91	2.583.930	18.903.334	1.670.944	<b>912.986</b>	1.546	377.700	82.028	4.605
7.25	95.70	6.141	37.17	11.52	48.69	2.610.253	18.993.523	1.681.122	<b>929.131</b>	1.553	26.323	10.178	2.586
7.50	95.73	6.355	37.19	12.20	49.38	2.633.782	19.083.530	1.691.285	<b>942.497</b>	1.557	23.529	10.163	2.315
7.75	95.76	6.569	37.21	12.80	50.01	2.654.925	19.173.364	1.701.433	<b>953.492</b>	1.560	21.143	10.148	2.083
8.00	95.78	6.782	37.22	13.34	50.57	2.673.664	19.263.035	1.711.567	<b>962.097</b>	1.562	18.739	10.134	1.849
8.25	95.81	6.996	37.24	13.82	51.06	2.690.440	19.352.549	1.721.688	<b>968.752</b>	1.563	16.775	10.121	1.657
8.50	95.83	7.210	37.25	14.26	51.51	2.705.613	19.441.914	1.731.796	<b>973.816</b>	1.562	15.173	10.108	1.501
8.75	95.85	7.424	37.26	14.66	51.92	2.719.443	19.531.137	1.741.893	<b>977.550</b>	1.561	13.830	10.096	1.370
9.00	95.87	7.637	37.27	15.03	52.30	2.732.183	19.620.224	1.751.977	<b>980.206</b>	1.559	12.741	10.085	1.263
9.25	95.89	7.851	37.28	15.37	52.65	2.743.928	19.709.180	1.762.051	<b>981.877</b>	1.557	11.744	10.074	1.166
<b>9.50</b>	<b>95.91</b>	<b>8.065</b>	<b>37.29</b>	<b>15.68</b>	<b>52.97</b>	<b>2.754.777</b>	<b>19.798.012</b>	<b>1.772.114</b>	<b>982.663</b>	<b>1.555</b>	<b>10.850</b>	<b>10.063</b>	<b>1.078</b>
9.75	95.93	8.279	37.30	15.97	53.26	2.764.724	19.886.723	1.782.167	<b>982.557</b>	1.551	9.947	10.053	0.989
10.00	95.95	8.493	37.30	16.23	53.54	2.773.979	19.975.320	1.792.210	<b>981.769</b>	1.548	9.255	10.043	0.922
10.25	95.97	8.707	37.31	16.48	53.79	2.782.603	20.063.805	1.802.244	<b>980.360</b>	1.544	8.625	10.034	0.860
10.50	95.98	8.921	37.32	16.72	54.03	2.790.624	20.152.184	1.812.268	<b>978.356</b>	1.540	8.021	10.025	0.800
10.75	96.00	9.134	37.32	16.93	54.25	2.798.042	20.240.460	1.822.284	<b>975.757</b>	1.535	7.417	10.016	0.741
11.00	96.01	9.348	37.33	17.13	54.46	2.804.885	20.328.637	1.832.292	<b>972.593</b>	1.531	6.843	10.008	0.684

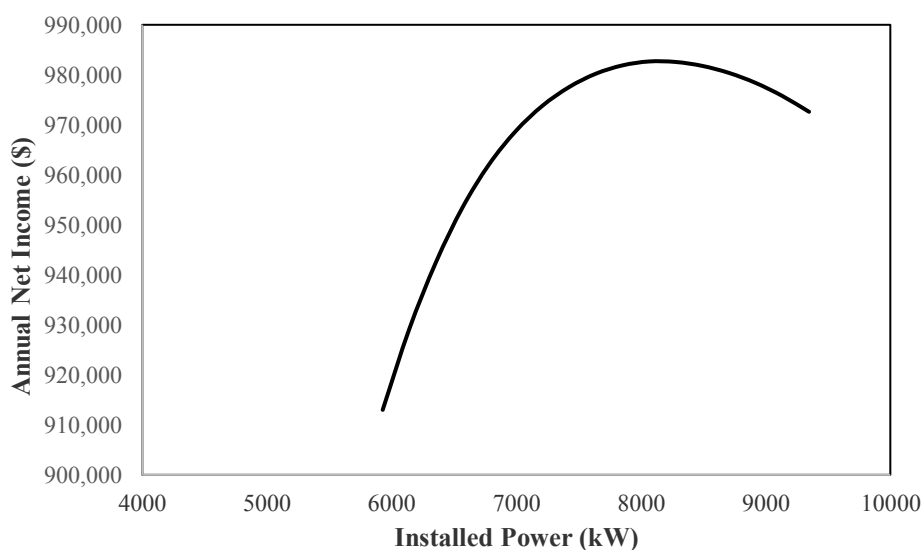


**Figure 4.** HEPP installed power optimization curve

### 3. Conclusions

In hydroelectric projects, maximum energy with minimum cost producing is the primary goal. Within the context of the present paper we have developed an easy to use approach for the definition of the cost of different parameters which take part in the structural organization of a hydropower plant. Approaches which have been developed for the cost analysis of different elements are based on a series of unitary prices which can be applied to its corresponding counterparts in any country, so that its use is not limited to any particular place.

It is crucial for the design personnel to thoroughly consider each and every part component individually since the optimization of the replaceable elements in the hydropower plant projects significantly affects the operational costs. We can specifically conclude the following for the selection of the design flow rate, canal and the penstock optimization;

The maximum flow rate used by the turbine is the design flow. For run-of-river projects, the design flow rate depends on the current flow in the field and is generally close to the flow rate that is equaled or exceeded about 30% of the time

In the event of the selection of the design flow rate to be less than that value, the flow potential of the river is not completely utilized and the profitability of the project has been decreased. In the event of the selection of the design flow rate to be less than that value, the size of the transmission structure (canal) gets larger, the penstock diameter increases and the turbine capital costs increase. In the calculations that have been carried out in this study, the maximum utility principles have been considered in hydropower plants while performing the analysis. In order to make a financially correct investment, it is necessary to consider at the design flow determination of hydroelectric power plants together not only hydrological data but also economic data.

The determination of suitable canal sizing is the most significant element in the planning and design of the canals. Parameters such as the type of the canal coating, the maximum speed at which siltation is prevented, the canal base slope, the maximum speed at which erosions would be prevented, the bevel slope and the air portion would be considered in the determination of the optimum cross-section during that process. In conclusion, it can be deduced that;

- As the canal slope increased, the capital investment costs would decrease due to the increased flow rates and decreased cross-sections. However, the operational costs would increase as a result of the increased flow rates and increased loss in load.
- As the slope increased, in addition to increases in the operational costs, the capital investment costs were decreased. Therefore, a suitable  $h_{opt}$  value existed for each flow rate.
- Increased canal height to obtain the most suitable hydraulic cross-section also increased the costs.

In order for an open canal project to be economically feasible, the topographical conditions, the equivalence of the fill-cleave amounts along the canal excavation path, the duration of construction and the most suitable and economical cross-section need to be determined in addition to the above mentioned criteria. The open canals should be built as less steep terrain as possible and steep slopes with a risk of land slip should be prevented. Canal constructions in cleavages should be preferred over the canals in the fills since they are cheap, secure and safe in terms of water leakage. The shape and the project of the canal should be constructed as much suitable for obtaining the aimed conditions minimizing the capital investment costs and the operational costs.

The penstocks, which are among the most significant components of hydroelectric power plants, also constitute a significant portion of the plant costs. Especially the optimization of the penstock diameter is very important. Selection of the diameter to be lower than the optimum value decreases the cross section and the capital investment costs, however, as a result of the increase in the flow rate of water in the canal, the friction and energy losses would increase and the energy capacity of the plant would decrease. In the case of the selection of the diameter to be larger than the optimum value, the cross-section would increase and the frictional losses would decrease, however the capital investment costs would increase. Because of this reason, there is an optimum value between the design flow rate and the penstock diameter and this optimum value, maximizing the net profit, was aimed to be determined in this study. Additionally, the route that the penstock follows is also important. Especially the geological analyses should be thoroughly carried out. The penstock should never be constructed in an area where land slips occur, along the slope back fills, in clay or similarly weak soil lands. Usually, mountain ridges pointed by the topography would be firm grounds. If firm grounds could not be identified, shaft or tunnel systems should be preferred. Penstocks should take the shortest path to the plant. Increasing the length of the penstock increases both the cost and the high slope losses. High slope losses mean energy losses. The path should be selected to have minimum bends and turns with the least amount of excavation and the curve locations should be selected

to be on rocks or very firm grounds. Penstocks may be constructed as single or multiple structures. This is determined as a result of the feasibility computations. Although a single penstock appears to be more feasible, care should be taken when selecting large diameter penstocks. Penstocks that have been designed taking into consideration all of these factors would increase the profitability of the hydroelectric power plant.

The results of this study enable performing the optimizations for the maximization of the delivered energy and the minimization of the initial investment cost of a hydropower project within a short duration of time, without a detailed study. For run off river type of projects, a prefeasibility report can be obtained in a short while in comparison to the conventional feasibility studies. Moreover, the developed method can be edited all the time by changing some variables and thus different alternatives can be compared easily without extensive calculation which is really helpful for the designers.

### References

- [1] Jacobson Mark Z, Delucchi Mark A. Providing all global energy with wind, water, and solar power, Part I: Technologies, energy resources, quantities and areas of infrastructure, and materials. *Energy policy* 2011; 39(3): 1154-1169.
- [2] Berga L. The role of hydropower in climate change mitigation and adaptation: a review. *Engineering* 2016; 2(3): 313-318.
- [3] Dursun B, Gokcol C. The role of hydroelectric power and contribution of small hydropower plants for sustainable development in Turkey. *Renewable Energy* 2011; 36(4): 1227-1235.
- [4] Demarty M, Bastien J. GHG emissions from hydroelectric reservoirs in tropical and equatorial regions: Review of 20 years of CH<sub>4</sub> emission measurements. *Energy Policy* 2011; 39(7): 4197-4206.
- [5] Mao G, Wang S, Tenq Q, Zuo J, Tan X., Wang H, Liu Z. The sustainable future of hydropower: a critical analysis of cooling units via the Theory of Inventive Problem Solving and Life Cycle Assessment methods. *J. Clean. Prod.* 2017; 142 (4): 2446–2453.
- [6] Yildiz V, Vrugt JA. A toolbox for the optimal design of run-of-river hydropower plants. *Environmental modelling & software* 2019; 111: 134-152.
- [7] Mutlu R. Feasibility Study Of A Hydropower Project: Case Study Of Niksar HEPP, Turkey. vol, 5, 265-288, 2010.
- [8] Bartle A. Hydropower potential and development activities. *Energy policy* 2002; 30(14): 1231-1239.
- [9] International Hydroelectric Association: Hydropower status report; sector trends and insights, 2019.
- [10] Küçükbeycan M. RETScreen decision support system for prefeasibility analysis of small hydropower projects. MSc, Middle East Technical University, Ankara, Turkey, 2008.
- [11] Lehner B, Czisch G, Vassolo S. The impact of global change on the hydropower potential of Europe: a model-based analysis. *Energy Policy* 2005; 33(7): 839-855.
- [12] Eurelectric, Study on the importance of harnessing the hydropower resources of the world, Union of the Electric Industry (Eurelectric), Hydro Power and other Renewable Energies Study Committee, Brussels, 1997.
- [13] Sharma DP, Verma GL, Bahadur AK. Selecting installed capacity for a run-of-river plant. *Journal of International Water Power & Dam Construction* 1980; 32: 23–26.
- [14] Sharma MG, Das D, Sharma J. Selection of optimum capacity for run-of-river plant. *Journal of Dam Engineering* 2002; 23: 97–117.
- [15] Gingold PR. The optimum size of small run-of-river plants. *Journal of International Water Power & Dam Construction* 1981; 33: 26–39.

- [16] Fahlbuch F. Optimum capacity of a run-of-river plant. *Journal of International Water Power & Dam Construction* 1983; 35: 25–37.
- [17] Fahlbuch F. Optimum capacity and tunnel diameter of run-of-river plants. *Journal of International Water Power & Dam Construction* 1986; 38: 42–55.
- [18] Deppo LD, Datei C, Fiorotto V, Rinaldo A. Capacity and type of units for small run-of-river plants. *Journal of International Water Power & Dam Construction* 1984; 36: 31–47.
- [19] Najmaï M, Movaghar A. Optimal design of run-of-river power plants. *Water Resour. Res.* 1992; 28: 991–997.
- [20] Voros NG, Kiranoudis CT, Maroulis ZB. Short-cut design of small hydroelectric plants. *Renew. Energy* 2000; 19: 545–563.
- [21] Montanari R. Criteria for the economic planning of a low power hydroelectric plant. *Renew. Energy* 2003; 28: 2129–2145.
- [22] Hosseini SMH, Forouzbakhsh F, Rahimpour M. Determination of the optimal installation capacity of small hydro-power plants through the use of technical, economic and reliability indices. *Energy Pol.* 2005; 33: 1948–1956.
- [23] Anagnostopoulos JS, Papantonis DE. Optimal sizing of a run-of-river small hydropower plant. *Energy Convers. Manag.* 2007; 48: 2663–2670.
- [24] Haddad OB, Moradi-Jalal M, Mariño MA. Design operation optimization of run-of-river power plants. *Proc. Inst. Civ. Eng. Water Manage.* 2011; 164: 463–475.
- [25] Santolin A, Cavazzini G, Pavesi G, Ardizzon G, Rossetti A. Techno-economical method for the capacity sizing of a small hydropower plant. *Energy Convers. Manag.* 2011; 52: 2533–2541.
- [26] Basso S, Botter G. Streamflow variability and optimal capacity of run-of-river hydropower plants. *Water Resour. Res.* 2012; 48: 463–475.
- [27] Voros NG, Kiranoudis CT, Maroulis ZB. Short-cut design of small hydroelectric plants. *Renew. Energy* 2000; 19: 545–563.
- [28] Motwani KH, Jain SV, Patel RN. Cost analysis of pump as turbine for pico hydropower plants – a case study. *Procedia Engineering* 2013; 51: 721–726.
- [29] Nouni MR, Mullick SC, Kandpal TC. Techno-economics of micro-hydro projects for decentralized power supply in India. *Energy Pol.* 2006; 34 (10): 1161–1174.
- [30] Liu Y, Ye L, Benoit I, Liu X, Cheng Y, Morel G, Fu C. Economic performance evaluation method for hydroelectric generating units. *Energy Convers. Manag.* 2003; 44: 797–808.
- [31] Karlis AD, Papadopoulos DP. A systematic assessment of the technical feasibility and economic viability of small hydroelectric system installations. *Renew. Energy* 2000; 20: 253–262.
- [32] Aslan, Y., Arslan, O., Yasar, C., 2008. A sensitivity analysis for the design of small-scale hydropower plant: kayabogazi case study. *Renew. Energy* 33, 791–801.
- [33] Niadas IA, Mentzelopoulos P. Probabilistic flow duration curves for small hydro plant design and performance evaluation. *Water Resour. Manag.* 2008; 22: 509–523
- [34] Brealey RA, Myers SC. *Principle of Corporate Finance*, seventh ed. (New York), 2002.

- [35] Kaldellis JK, Vlachou DS, Korbakis G. Techno-economic evaluation of small hydro power plants in Greece: a complete sensitivity analysis. *Energy Pol.* 2005; 33: 1969–1985.
- [36] Fleten SE, Kristoffersen TK. Short-term hydropower production planning by stochastic programming. *Comput. Oper. Res.* 2008; 35 (8): 2656–2671.
- [37] Finardi EC, Silva EL, Sagastizabal C. Solving the unit commitment problem of hydropower plants via Lagrangian Relaxation and Sequential Quadratic Programming. *Comput. Appl. Math.* 2005; 24 (3): 317–341.
- [38] Lopes de Almeida JPPG, Lejeune AGH, Sá Marques JAA, Cunha MC. OPAH a model for optimal design of multipurpose small hydropower plants. *Adv. Eng. Software* 2006; 37: 236–247.
- [39] Yoo JH. Maximization of hydropower generation through the application of a linear programming model. *J. Hydrol.* 2009; 376 (1–2): 182–187.
- [40] Baños R, Manzano-Agugliaro F, Montoya FG, Gil C, Alcayde A, Gómez J. Optimization methods applied to renewable and sustainable energy: a review. *Renew. Sustain. Energy Rev.* 2011; 15 (4): 1753–1766.
- [41] Gibson NR. The Gibson Method and Apparatus for Measuring the Flow of Water in Closed Conduits. ASME Power Division, 1923; pp. 343–392.
- [42] Troskolanski A. 1960. Hydrometry. Pergamon Press Ltd. US Energy Information Administration, 2016. Monthly Energy Review 1960; Table 1.3 and 10.1.
- [43] IEC. 41, International Standard: Field Acceptance Tests to Determine the Hydraulic Performance of Hydraulic Turbines, Storage Pumps and Pump-turbines 1991.
- [44] Khosrowpanah S, Fiuzat A, Albertson M. Experimental study of cross flow turbine. *J. Hydraul. Eng.* 1988; 114 (3): 299–314.
- [45] Desai VR, Aziz NM. An experimental investigation of cross-flow turbine efficiency. *J. Fluid Eng.* 1994; 116 (3): 545–550
- [46] Williams AA. The turbine performance of centrifugal pumps: a comparison of prediction methods. *Proc. Inst. Mech. Eng. Part A: Journal Power Energy* 1994; 208: 59.
- [47] Ye L, Weidong L, Zhaohui L, Malik OP, Hope GS. An integral criterion appraising the overall quality of a computer-based hydro turbine generating system. *IEEE Trans. Energy Convers.* 1995; 10 (2): 376–381.
- [48] Liu X. Application of ultrasonic flow measurement technologies on the testing of hydroelectric generating units in China. *J Hydro Power Plant Automat supplement edition*, 2000.
- [49] Adamkowski A, Janicki W, Kubiak J, Urquiza G, Sierra F., Fernández DJM. Water turbine efficiency measurements using the gibson method based on special instrumentation installed inside pipelines. In: 6th International Conference on Innovation in Hydraulic Efficiency Measurements, Portland, Oregon, USA, 2006. pp. 1–12.
- [50] Ye-xiang X, Feng-qin H, Jing-lin Z, Takashi K. Numerical prediction of dynamic performance of Pelton turbine. *Journal of Hydrodynamics, Ser. B* 2007; 19 (3): 356–364.
- [51] Wallace AR, Whittington HW. Performance prediction of standardized impulse turbines for micro-hydro, Sutton. *Int. Water Power Dam Constr Elsevier B.V., U.K.*, <https://www.sciencedirect.com/science/article/pii/S1364032114009769>, 2008.
- [52] Derakhshan S, Nourbakhs A. Experimental study of characteristic curves of centrifugal pumps working as turbines in different specific speeds. *Exp. Therm. Fluid Sci.* 2008; 32: 800–807



- [53] Singh P, Nestmann F. Experimental optimization of a free vortex propeller runner for micro-hydro application. *Exp. Therm. Fluid Sci.* 2009; 33: 991–1002.
- [54] Alexander KV, Giddens EP, Fuller AM. Radial- and mixed-flow turbines for low head microhydro systems. *Renew. Energy* 2009; 34: 1885–1894.
- [55] Yassi Y, Hashemloo S. Improvement of the efficiency of the agnew micro-hydro turbine at part loads due to installing guide vanes mechanism. *Energy Convers. Manag.* 2010; 51: 1970–1975.
- [56] Akinori F, Watanabe S, Matsushita D, Okuma K. Development of ducted Darrieus turbine for low head hydropower utilization. *Curr. Appl. Phys.* 2010; 10: pp. 128–132.
- [57] Anagnostopoulos JS, Dimitris EP. A fast Lagrangian simulation method for flow analysis and runner design in Pelton turbines. *J. Hydrodyn.* 2012; 24 (6): 930–941.
- [58] Shimokawa K, Furukawa A, Okuma K, Matsushita D, Watanabe S. Experimental study on simplification of Darrieus-type hydro turbine with inlet nozzle for extra-low head hydropower utilization. *Renew. Energy* 2012; 41: 376–382
- [59] Ramos HM, Simão M, Borga A. Experiments and CFD analyses for a new reaction micro hydro propeller with five blades. *J. Energy Eng.* 2013; 139: 109–117
- [60] Bozorgi A, Javidpour E, Riasi A, Nourbakhsh A. Numerical and experimental study of using axial pump as turbine in pico-hydropower plants. *Renew. Energy* 2013; 53: 258–264.
- [61] Khurana S, Kumar V, Kumar A. The effect of nozzle angle on erosion and the performance of turgo impulse turbines. *Int. J. Hydropower Dams* 2013; 20: pp. 97–101.
- [62] Williamson SJ, Stark BH, Booker JD. Performance of a low-head pico-hydro turgo turbine. *Appl. Energy* 2013; 102: 1114–1126.
- [63] Williamson SJ, Stark BH, Booker JD. Low head pico hydro turbine selection using a multi-criteria analysis. *Renew. Energy* 2014; 61: pp. 43–50.
- [64] Laghari JA, Mokhlis H, Bakar AHA, Mohammad H. A comprehensive overview of new designs in the hydraulic, electrical equipments and controllers of mini hydro power plants making it cost effective technology. *Renew. Sustain. Energy Rev.* 2013; 20: 279–293.
- [65] Pimnapat I, Patib T, Bhumkittipich K. Performance study of micro hydro turbine and PV for electricity generator, case study: bunnasopit School, y Nan province, Thailand, 10th eco-energy and materials science and engineering (EMSES2012). *Energy Proc.* 2013; 34. 235–242.
- [66] Cobb BR, Sharp KV. Impulse (Turgo and Pelton) turbine performance characteristics and their impact on pico-hydro installations. *Renew. Energy* 2013; 50: 959–964.
- [67] Yaakob OB, Ahmed YM, Elbatran AH, Shabara HM. A review on micro hydro gravitational vortex power and turbine systems. *Jurnal Teknologi (Sci Eng)* 2014; 69 (7): 1–7.
- [68] Elbatran AH, Yaakob OB, Ahmed YM, Shabara HM. Operation, performance and economic analysis of low head micro-hydropower turbines for rural and remote areas: a review. *Renew. Sustain. Energy Rev.* 2015; 43: 40–50.
- [69] Heitz LF. *Hydrologic Analysis Programs for Programmable Calculators and Digital Computers for Use in Hydropower Studies.* University of Idaho Water Resources Research Institute, pp. 127 Report No: 198207, 1982.
- [70] US Army Corps of Engineers (USACE). *Hydropower Engineering and Design, Engineering Manual 1110-2-1701.* US Army Corps of Engineers, Washington, DC., 1985.

- [71] Vogel RM, Fennessey NM. Flow duration curves II: a review of applications in water resources planning. *J. Am. Water Resour. Assoc.* 1995; 31: pp. 1029–1039.
- [72] Hobbs BF, Mittelstadt RL, Lund JR. Energy and water, chapter 31. In: Mays, L.W. (Ed.), *Water Resources Handbook, International Edition*. McGraw-Hill, New York. 1996.
- [73] Borges CLT, Pinto RJ. Small hydro power plants energy availability modeling for generation reliability evaluation. *IEEE Trans. Power Syst.* 2008; 23 (3): 1125–1135.
- [74] Niadas IA, Mentzelopoulos P. Probabilistic flow duration curves for small hydro plant design and performance evaluation. *Water Resour. Manag.* 2008; 22: 509–523
- [75] Peña R, Medina A, Anaya-Lara O, McDonald JR. Capacity estimation of a minihydro plant based on time series forecasting. *Renew. Energy* 2009; 34: 1204–1209
- [76] Heitz LF, Khosrowpanah SH. Prediction of Flow Duration Curves for Use in Hydropower Analysis at Ungaged Sites in Kosrae. FSM, University of Guam/WERI Technical, pp. 28 Report No. 137 under printing, 2012.
- [77] Erkek C, Ağırlioğlu N. *Su Kaynakları Mühendisliği*, Beta Basım Yayın, 1986.
- [78] Masoudinia F. Retscreen--Small Hydro Project Software. In 2013 International Conference on Communication Systems and Network Technologies April 2013; pp. 858-861 IEEE.

## Threats Detection in IoT Network

Hanan ABU KWAİDER <sup>1\*</sup>, Erdiñç AVAROĐLU <sup>2</sup>

<sup>1</sup> Msc. Department of Computer Engineering, Mersin University, Mersin, TURKEY

<sup>2</sup> Associated Professor, Department of Computer Engineering, Mersin University, Mersin, TURKEY

\*<sup>1</sup> hanan.abukwaider@gmail.com, <sup>2</sup> eavaroglu@mersin.edu.tr

(Geliş/Received: 31/10/2022;

Kabul/Accepted: 08/02/2023)

**Abstract:** The recent growth in Internet of Things (IoT) deployment has increased the rapidness of integration and extended the reach of the internet from computers, tablets, and phones to countless devices in our physical world. This growth makes our life more convenient and industries more efficient. However, at the same time, it brought numerous challenges in terms of security and expanded the area of cyber-attacks, especially the DoS and DDoS attacks. Moreover, since many IoT devices run custom or outdated operating systems, and most do not have enough resources to run typical intrusion detection systems, it was necessary to search for alternative solutions. Therefore, many researchers have joined the race to develop new lightweight intrusion detection methods. In this study, we have investigated the detection of different DoS attacks on the IoT network using machine learning techniques. The studied attacks are TCP Syn-Flood Attack, UDP Flood Attack, HTTP Slowloris GET Attack, Apache Range Header DoS, and Port Scan attack. We have proposed a new dataset, namely HEIoT21, which was generated in a real smart home environment using a collective of IoT devices and non-IoT devices connected to a wireless network. The proposed dataset included normal and anomaly data, and using the CiCflowmeter application, we extracted 82 network features from the proposed dataset. The dataset was labeled and categorized into binary-class and multi-class. Our dataset underwent multiple feature selection methods to keep only enough features to produce a good detection accuracy; for that, we have used Anova F-value Feature Selection, Random Forest importance feature selection, and Sequential Forward Feature Selection. The feature selection techniques produced three new sub-datasets, which were evaluated using multiple machine learning algorithms like Logistic Regression (LR), J48 Decision Tree (DT), Naïve Bayes, and Artificial Neural Network (ANN). A comparison study was conducted on the result obtained from applying the different machine learning algorithms on the derived sub-datasets, which led to the finding that the most suitable feature selection technique for the proposed dataset was Anova F-value and the best-fit machine learning algorithm for the proposed dataset was The Decision Tree which produced an accuracy result of 99.92% for binary classification and 99.94% for multi-class classification.

In the end, our study was compared with other studies in the field of IoT intrusion detection, and we found that the result obtained through this study was higher than most others. Therefore, the proposed dataset could be of great use to those who want to work on the analysis and detection of the existing network security threats. Also, this study can be considered a cornerstone for a proper lightweight intrusion detection system, where the datasets can be expanded to include other types of attacks, new detection rules can be added, and an alert mechanism can be integrated to become a complete detection system.

**Key words:** Internet of things, IoT, machine learning, network security, attack detection.

### IoT Ağında Saldırı Algılama

**Öz:** Nesnelerin İnterneti (IoT) dağıtımındaki son büyüme, entegrasyonun hızını artırdı ve internetin erişimini bilgisayarlardan, tabletlerden ve telefonlardan fiziksel dünyamızdaki sayısız cihaza genişletti. Bu gelişme hayatımızı daha rahat ve endüstrileri daha verimli hale getiriyor. Ancak güvenlik açısından da sayısız zorluğu getirdi ve başta DoS ve DDoS saldırıları olmak üzere siber saldırıların alanını genişletti. Dahası, birçok IoT cihazı özel veya yeni olmayan işletim sistemleri çalıştırdığından ve çoğu tipik Saldırı Tespit Sistemleri çalıştırmak için yeterli kaynağa sahip olmadığından, alternatif çözümlere bulmaya çalışmalıydı. Bu nedenle, birçok araştırmacı yeni hafif saldırı tespit yöntemleri ortaya atmak için yarışa katıldı. Bu çalışmada, makine öğrenimi teknikleri kullanılarak IoT ağında farklı DoS saldırılarının tespiti araştırıldı. Üzerinde çalışılmış saldırıları, TCP Syn-Flood saldırı, UDP Flood saldırı, HTTP Slowloris GET saldırı, Apache Range Header DoS ve Port Scan saldırısıdır. Bir kablosuz ağa bağlı IoT cihazları ve IoT olmayan cihazlar kullanılarak gerçek bir akıllı ev ortamında oluşturulan HEIoT21 adlı yeni bir veri seti önerdik. Önerilen veri seti normal ve anomali verilerini içeriyordu, ve CiCflowmeter uygulamasını kullanarak, önerilen veri setinden 82 ağ özelliği çıkardık. Veri seti, ikili sınıf ve çoklu sınıf olarak etiketlendi ve kategorilere ayrıldı. Sınırlı IoT kaynakları sorununu çözmek için hafif bir saldırı tespit yöntemine ihtiyaç duyulduğundan.

Veri kümemizin, iyi bir tespit doğruluğu oluşturmak için yeterli olan çok az özelliğe sahip olması gerekiyordu; Bunun için üç Özellik Seçimi tekniği kullandık, Anova F-değeri özellik seçimi, Rastgele Orman önemi öznetelik seçimi ve Ardışık İleri Yönde özellik seçimi. Özellik seçimi teknikleri, Lojistik Regresyon (LR), J48 Karar Ağacı (DT), Naive Bayes ve Yapay Sinir Ağları (YSA) gibi çoklu Makine öğrenimi

algoritmaları kullanılarak değerlendirilen üç yeni alt veri kümesi oluşturdu. Türetilmiş alt veri kümesi üzerinde farklı makine öğrenimi algoritmalarının uygulanmasından elde edilen sonuç üzerinde bir karşılaştırma çalışması yapılmış ve önerilen veri

\* Corresponding author: [hanan.abukwaider@gmail.com](mailto:hanan.abukwaider@gmail.com). ORCID Number of authors: <sup>1</sup> 0000-0003-3887-2819, <sup>2</sup> 0000-0003-1976-2526

kümesi için en elverişli özellik seçim tekniğinin Anova a F değeri olduğu bulgusuna yol açmıştır. Önerilen veri kümesi için en uygun makine öğrenimi algoritması, ikili sınıflandırma için %99,92 ve çok sınıflı sınıflandırma için %99.94 doğruluk sonucu oluşturan an Karar Ağacı olmuştur.

Sonuç olarak, çalışmamız IoT saldırı tespiti alanında yapılan diğer çalışmalarla karşılaştırıldı ve bu çalışma ile elde edilen sonucun diğerlerinin çoğundan daha yüksek olduğunu gördük. Bu nedenle, önerilen veri kümesi, mevcut ağ güvenliği tehditlerinin analizi ve tespiti üzerinde çalışmak isteyenler için çok faydalı olabilir. Ayrıca, bu çalışma, veri kümelerinin diğer saldırı türlerini içerecek şekilde genişletilebildiği, yeni tespit kurallarının eklenebildiği ve eksiksiz bir tespit sistemi haline gelmek için bir uyarı mekanizmasının entegre edilebildiği, uygun bir hafif saldırı tespit sistemi için bir mihenk taşı olarak kabul edilebilir.

**Anahtar kelimeler:** Nesnelerin İnterneti, IoT, makine öğrenimi, ağ güvenliği, saldırı tespiti.

## 1. Introduction:

The security risks accompanied by the increasing demand and growth of the Internet of Things (IoT) are increasing. Some statistics mentioned that the number of IoT-connected devices is expected to grow from 15 billion in 2015 to around 75 billion devices in 2025 [1]. These numbers are raising many concerns as the area of the attacks is expanding, and the aim to access sensitive information without authorization has been troubling; Figure 1 presents IoT-connected devices worldwide.

In 2020, McAfee company reported that cybercriminals used the COVID-19 pandemic to increase the cyber-threat categories like mobile malware, IoT malware, and PowerShell malware. Moreover, McAfee has detected around 375 cyber threats per minute within the first quarter of 2020. Furthermore, as the disease spreads, critical systems such as medical IoT devices and healthcare networks become more susceptible to cyber-attacks [2].

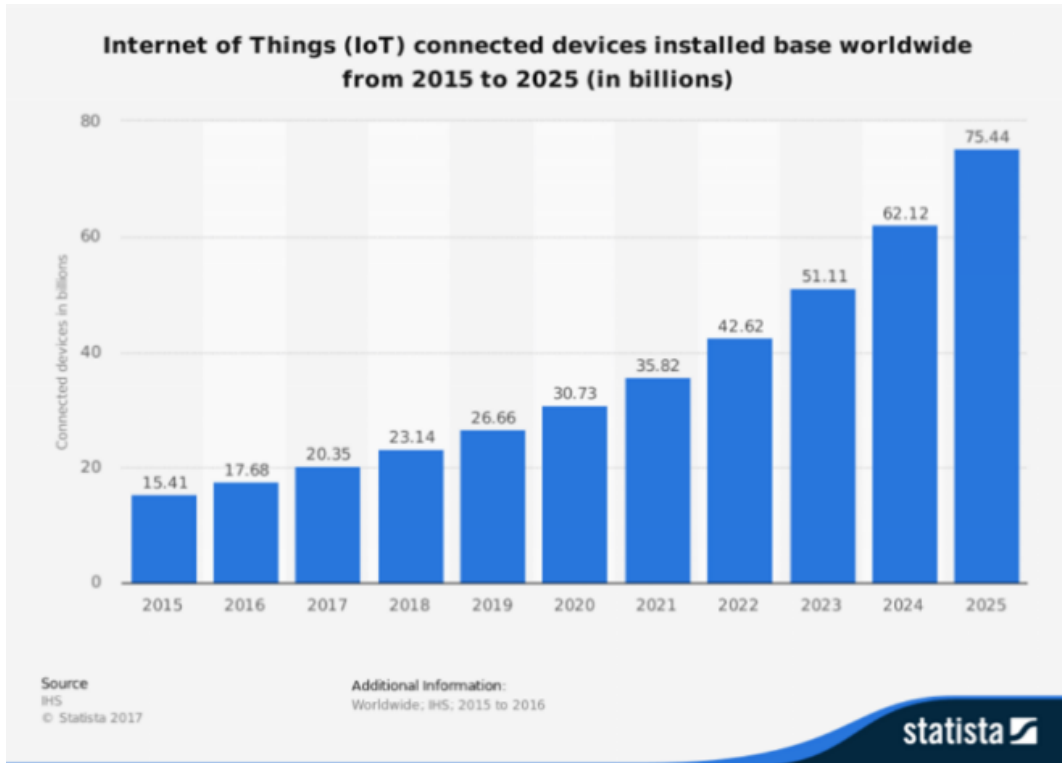


**Figure 1.** The number of IoT connected devices by the year

Following these facts, cybersecurity has become vital in today's research area. The need to build a detection method for IoT attacks has led many researchers to invest more time in this area, and for that purpose, many have used machine learning to achieve this goal.

In this study, the work will focus on detecting multiple IoT attacks by analyzing the packet flow in the network and extracting the needed metrics for the detection. The dataset used in this study is HEIoT21, a dataset created in a real smart home wireless environment containing normal and anomaly data with different attacks. The dataset underwent multiple feature selection methods to keep only the best features for classification. The newly created sub-datasets generated from applying the feature selections will be used as input for several machine learning algorithms to predict the probability that the IoT device is under attack or not. The result of the used algorithms will then be compared to determine the most suitable classification algorithm for the IoT network attack detection within the scope of the input. Thus, the contribution to knowledge obtained by this study is as follows:

- Building a new dataset in a smart home environment and making it available for public use to benefit other researchers [3].
- Implement and perform a performance evaluation of the used feature selection methods and the machine learning classification algorithms in terms of detecting the attacks.
- Create a comparison study between the results obtained in this study and others in the same field.

The rest of this study is structured as follows. Section two showcases a review of some related work in this field, section three discusses the methods and material used, section four presents the results obtained from this study, and finally, section five concludes the paper and shares ideas about future work.

## 2. Literature Summary

Since IoT network security has become an urgent matter that needs to be handled, multiple researchers have joined the race to tackle this issue either by studying the design challenges and the taxonomy of the security attacks from the network side or by using machine learning to find solutions to the current problem and against the attacks.

Teng Xu, James B. Wendt and Miodrag Potkonjak in [4] have done a brief survey on IoT challenges focusing on the security issues, they have also discussed the potential of hardware-based IoT security approaches and concluded by presenting several use case studies that advocate the use of stable PUFs (Physical Unclonable Functions) and digital PUFs for several IoT security protocols.

The authors in [5] have proposed the use of SDN gateway as a distributed means of monitoring the traffic originating from and directed to IoT based devices. The gateway can then both detect anomalous behavior and perform an appropriate response (blocking, forwarding, or applying Quality of Service), they have successfully detected and blocked TCP and ICMP flood based attacks using the proposed gateway.

Farahnakian and Heikkonen [6] proposed a Deep Auto-Encoder-based Intrusion Detection System (DAE-IDS), and they used the KDD-CUP 99 dataset to evaluate their proposed scheme. Their schema resulted in an accuracy of 96.53% on binary classification.

Also, in [7] for DoS attack detection, Moukhafi proposed a novel hybrid genetic algorithm and support vector machine with the particle swarm optimization-based scheme. The authors used the KDD99 dataset and PSO for feature selection and got an accuracy of 96.38% on multi-class classification.

In [8], the authors used KDD CUP 99 dataset to implement their model for detecting and classifying IoT attacks using SVM and Bayesian. They achieved an accuracy of 91.50% on multi-class classification. The dataset went through feature reduction before applying the classification.

Moreover, in [9], the authors proposed a deep learning-based intrusion detection system for DDoS attacks based on three models: convolutional neural networks, deep neural networks, and recurrent neural networks. For each model, the performance was studied within two classification types (binary and multi-class) using two new real traffic datasets: the CIC-DDoS2019 dataset and the TON\_IoT dataset. For the first dataset, they achieved an accuracy of 95.90% and 99.95% on multi-class classification and binary classification, respectively. For the second dataset, they achieved an accuracy of 98.94% for multi-class classification.

Furthermore, in [10], S. Latif, Z. Zou, Z. Idrees, and J. Ahmad proposed a novel lightweight random neural network (RaNN)- based prediction model capable of predicting different cybersecurity attacks. They used several evaluation parameters such as accuracy, in which they achieved 99.20% on multi-class classification, precision, recall, and F1 score, and applied their model in a dataset named DS2OS.

Also, in [11], the authors have proposed an anomalous activity detection system for IoT networks based on flow and control flags features using a feed-forward neural network. The model has been evaluated using BoT-IoT, IoT network intrusion, MQTT-IoT-IDS2020, MQTTset, IoT-23, and IoT-DS2 datasets for binary and multi-

class classification. The authors have achieved an accuracy of 99.97% and 99.99% for multi-class and binary classification, respectively.

In [12], the authors created a new dataset, IoTID20, consisting of two IoT devices and other interconnected devices such as laptops and smartphones in a typical smart home environment. Their dataset consisted of both normal and anomaly data. They removed the highly correlated features, and they used Shapira-Wilk to keep the high-ranking features only. Seven supervised machine learning algorithms were used for classification, and it was evaluated using the accuracy and F1 score. They got a high accuracy of 100% for both binary and multi-class classification.

### 3. Materials and Methods

This study was conducted in an IoT-based smart home environment, which provided a realistic setting for collecting and analyzing data on IoT devices and their vulnerabilities to different types of intrusions.

The first step in the study was to produce a dataset by collecting both normal and anomaly data from the network. This data was collected from various IoT devices such as smart cameras, smart appliances, and other connected devices. The collected data went through a pre-processing step to ensure that it was in the appropriate format for analysis. The data was then cleaned, and any irrelevant or redundant information was removed.

The next step was to perform feature selection, which involved identifying the most relevant features that would be used in the analysis. This step is crucial in reducing the dimensionality of the data and eliminating any irrelevant features that could negatively affect the results.

After the dataset was prepared, it was used to evaluate the results using multiple machine learning techniques. The results from these techniques were compared and analyzed to find the best-fitting machine learning algorithm for our dataset.

#### 3.1. Proposed Dataset

For this research, we have proposed a new dataset called HEIoT21. The dataset was generated in a smart home environment; the environment consisted of a collection of real IoT devices and other non-IoT devices, such as laptops and mobiles, all connected to a Wifi router. The used IoT devices were WD MY Cloud running a plex server, Mi Home Security Camera 360°, Raspberry Pi 4 running an Apache server, and Lix smart lamp, Figure 2 shows the ecosystem of the HEIoT21 dataset.

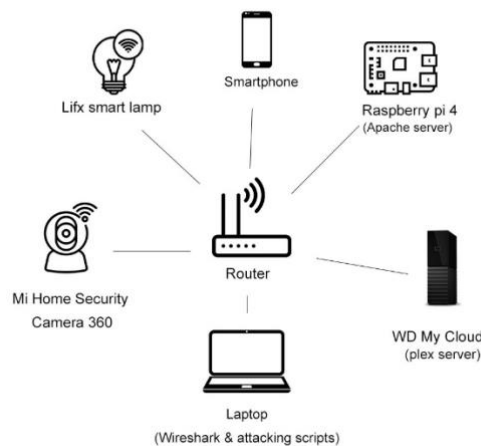


**Figure 2.** The ecosystem of the HEIoT21

The data was gathered in an interval of 7 days discontinuously. The dataset consists of normal and anomaly data; the normal data was collected by continuously sniffing the network packets of all the wireless network devices using Wireshark and without any attacks. For every 48 hours, the data will be saved as a Pcap file.

For the attack data, we used a laptop running Kali Linux to launch attacks on the IoT devices using the command line, and on the same laptop, we used Wireshark to collect the network packets and then save them as Pcap files as well.

The different types of attacks on the proposed dataset were generated as follows;

**TCP SYN Flood Attack:** This attack was generated using hping3 network tool by running the corresponding commands using the Kali Linux laptop.

The attacks were generated in two different modes; the first one was to send packets from a generated spoofed IP address to a victim IP address in order to cloak the original source and evade detection, with a packet of 460 bytes and a 64-byte TCP window size, the attack was generated in Flood mode, i.e., the packets will be sent as fast as possible. For the second mode, the packets were sent from a particular source IP Address with the same packet size and window size settings.

We have used the TCP SYN flood attack against two IoT devices; WD MY Cloud running a Plex server, and Raspberry Pi 4, running Apache Server.

**UDP Flood Attack:** For this attack also hping3 tool was used, but this time in UDP mode instead of TCP. The packets were sent from a spoofed IP address to hide the actual source and evade detection, the packet size was 120 bytes, and a window of 32 was used.

This attack was used against Lifx smart lamp and Mi Home Security Camera 360°.

**HTTP-Slowloris Attack:** This attack was generated using the SlowHTTPTest tool. This tool was used from the Kali Linux command line and can simulate DoS attacks. For the attack generation, we have used the following configurations; the request type was set to GET, the mode was set to slow-header with a different number of connections for each run between 1500 to 3500 connections, the interval between packets was set to 10s, and the connection rate was set to 200 connection per seconds.

We have used this attack against websites running using an apache server on Raspberry Pi 4.

**Port Scan:** This attack scans all the network ports, looking for a specific port. It was generated using the Nmap tool against the WD My Cloud, Lifx Lamp, and Raspberry Pi 4.

The data generated from the above attacks were saved in separate Pcap files for each attack type, then an application named CICFlowMeter was used to extract network features and save the results as CSV files. CICFlowMeter extracts 82 features, and we added to them another two features for labeling, a -label- field that has two values (normal and attack), a -category- field that categorize the data according to the attack type ( Normal, TCP Syn Flood, Apache Killer, Port Scan, UDP Flood and HTTP Slowloris GET). The CSV files were labelled separately and combined into a final CSV file using a Python script. The final CSV file was named HEIoT21, representing our dataset.

The HEIoT21 dataset has 125365 instances after being cleaned, 36346 instances for normal data, and 89019 instances for the different attacks. Table 1 shows the attack and normal data of the proposed dataset.

**Table 1.** The attack and normal instances in the HEIoT21 dataset

<b>Label Distribution</b>	
Normal	<b>36346</b>
Attack	<b>89019</b>
<b>Category Distribution</b>	
Normal	<b>36346</b>
UDP Flood	<b>53601</b>
TCP Syn Flood	<b>15009</b>
HTTP <u>Slowloris</u> GET	<b>9217</b>
Port Scan	<b>4136</b>
Apache Killer	<b>7056</b>

Figure 3 and Figure 4 represent the distribution of instances in the HEIoT21.

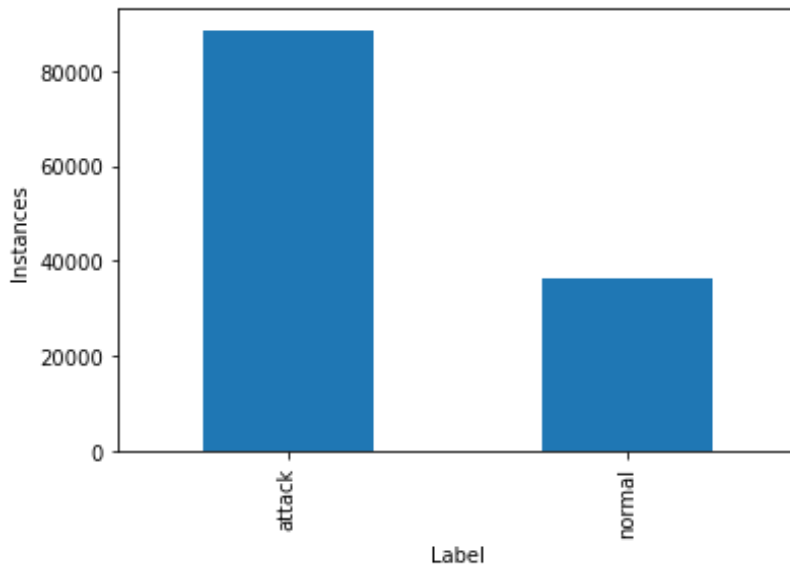


**Figure 3.** Distribution of instances by label

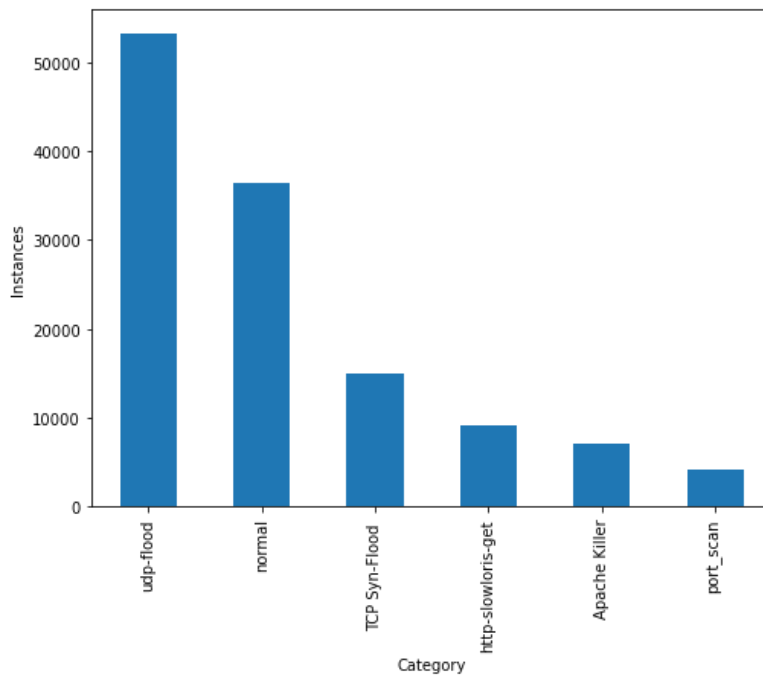


**Figure 4.** Distribution of instances by category

The dataset passed through different steps of pre-processing before using it for classifications. The steps were as follows

- Removing all NaN values and object type values since they are not useful for classification.
- Using StandardScaler to scale the data and convert the 'label' field into binary 1=normal, 0=attack.
- Converting the 'category' field into numerical as follows 5=udp-flood, 4=port\_scan, 3=normal, 2=HTTP-Slowloris-get, 1=TCP Syn-Flood and 0= Apache Killer



- To avoid the overfitting caused by the high number of features, we used three different feature selection methods.
  - **ANOVA f-Value**; was used to select 20 features based on their highest score, and from those features, we removed the highly correlated ones, leaving a new sub-dataset consisting of 14 features instead of 84.
  - **Random Forest**; was used to select the top 20 features based on their highest score value. Then from those features we removed the highly correlated ones, creating a new sub-dataset made up of 17 features instead of 84.
  - **Forward Feature Selection**: used to select the top 20 features based on the best ROC\_AUC score. The highly correlated features were then removed leaving a new sub-dataset made up of 20 features.
  - The previous process resulted in 3 different sub-datasets, which were used for modelling.

### 3.2. Dataset Modelling and Evaluation

Classification is a machine learning technique that assigns specific instances to a pre-defined category [13]. Classification takes a dataset as an input and uses machine learning algorithms to categorize instances to their best-fit label or category [13].

For this research, we have used J48 Decision Tree, Logistic Regression, Gaussian Naïve Bayes, and Neural Networks using Keras as supervised classification algorithms.

For classification, we have split the three sub-datasets derived from the original HEoIT21 after applying the feature selection techniques into training and testing datasets. The model was first trained for both binary and multi-class classification, and then was tested against the test datasets. Then the performance of each classification algorithm was evaluated using the performance measures such as Accuracy, Precision and F-Score.

Moreover, to diagnose the performance of our model, we have plotted the learning curve of the training sample for label classification against the accuracy using our classification algorithms as an estimator once at a time. The learning curve showed that in order to get a high classification accuracy, we need at least a minimum amount of forty thousand (40,000) instances, we plotted the same curve for multi-class classification and it showed that a minimum amount of (20,000) instances is needed to get a high accuracy rate. Figure 5 shows the learning and validation curve for DT of the training set against the predictive accuracy.

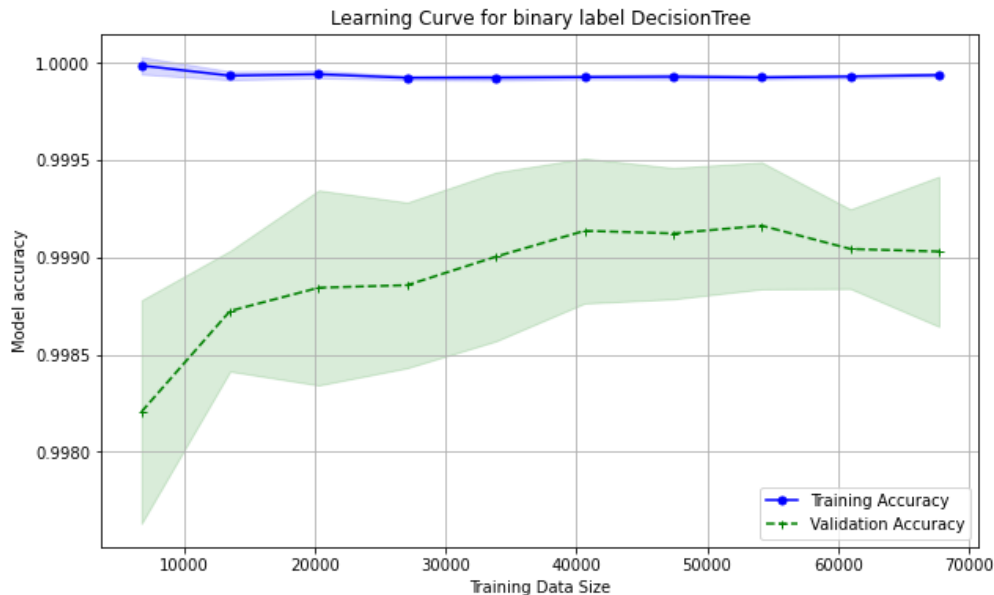


**Figure 3.** The learning and validation curve for DT of the training set against the predictive accuracy

#### 4. Results and Discussions

We have concluded from the work done in this research that the features of the dataset play a massive role in the performance of the detection model, and the best feature selection technique for our proposed dataset was ANOVA F-Value which has generated a high accuracy rate for all the selected algorithms and in both multi-class and binary classification. Figure 6 shows a comparison of the evaluation accuracy for binary classification.

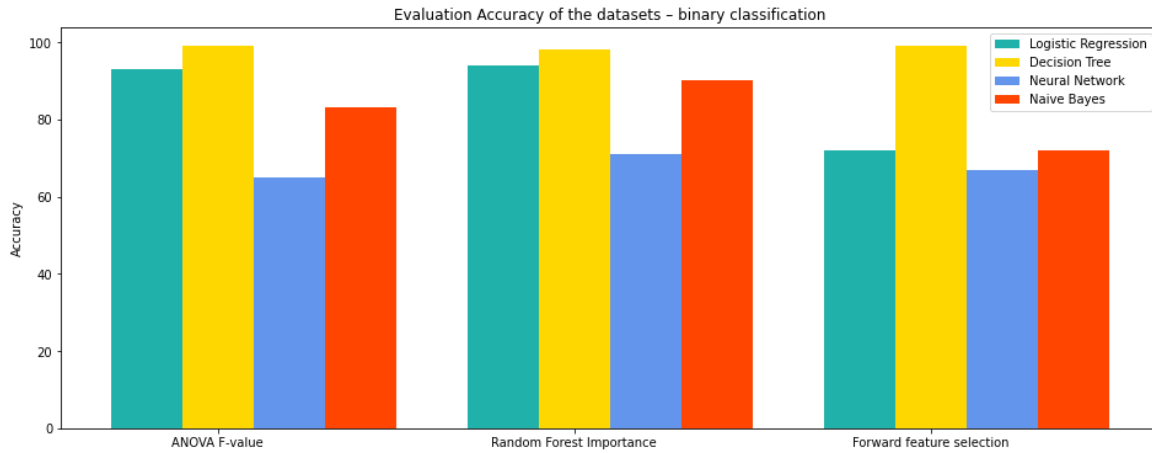


**Figure 4.** Comparison between the evaluation accuracy - binary classification

Also, from all the used classification algorithms (Decision Tree, Gaussian Naïve Bayes, Logistic Regression, and Neural Network), Decision Tree has performed the best on the three sub-datasets with an accuracy of 99.92% and 99.94% for both binary and multi-class classification, respectively. Figure 7 shows a comparison between the evaluation accuracy for multi-class classification and confirms that Decision Tree has performed the best.

We have compared the results obtained in this research with other related studies in the same field as IoT network security and intrusion detection; Table 2 shows this comparison. Our results were higher than most other studies, and our proposed dataset might be promising for future work and studies.

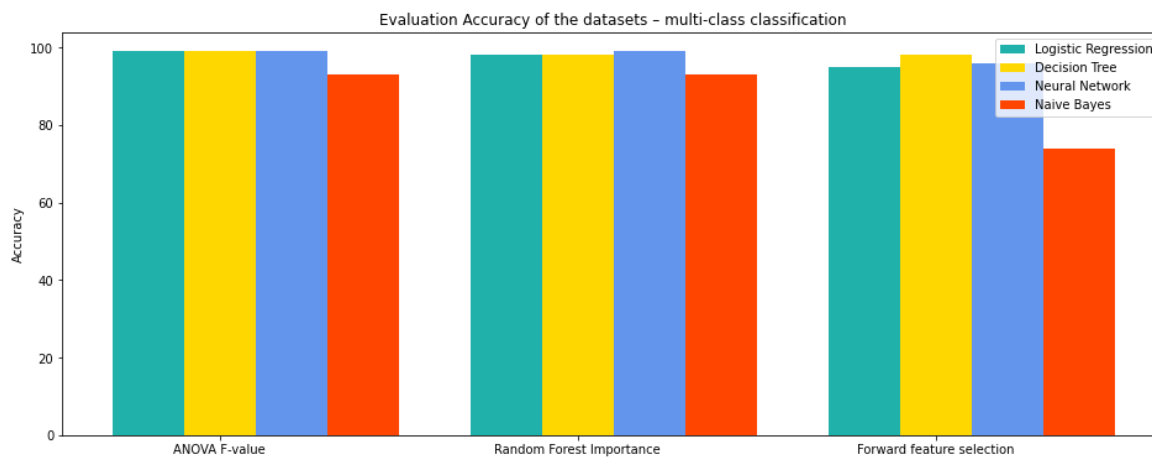


**Figure 5.** Evaluation accuracy comparison - multi-class

**Table 2.** Result comparison with other studies

<b>Research</b>	<b>Dataset</b>	<b>Classification type</b>	<b>Model</b>	<b>Accuracy</b>
Farahnakian and Heikkonen [6]	<b>KDD CUP 99</b>	Binary	Deep Auto-Encoder	96.53%
M. Moukhafi, K. El Yassini and S. Bri [7]	<b>KDD 99</b>	Multi-class	hybrid genetic algorithm and support vector machine	96.38%
Khalvati [8]	<b>KDD CUP 99</b>	Multi-class	SVM and Bayesian	91.50%
Ferrag, Mohamed Amine & Shu, Lei & Hamouda, Djallel & Choo, Raymond [9]	<b>CIC-DDoS2019 dataset</b>	Multi-class Binary	CNN CNN	95.90% 99.95%
Ferrag, Mohamed Amine & Shu, Lei & Hamouda, Djallel & Choo, Raymond [10]	<b>TON_IoT dataset</b>	Multi-class	RNN	98.94%
S. Latif, Z. Zou, Z. Idrees and J. Ahmad [11]	<b>DS2OS</b>	Multi-class	lightweight RaNN	99.20%
Imtiaz Ullah, Qusay H. Mahmoud [12]	<b>BoT-IoT, IoT network intrusion, MQTT-IoT-IDS2020, MQTTset, IoT-23, and IoT-DS2</b>	Multi-class Binary	feed-forward neural network	99.97% 99.99%
Imtiaz Ullah, Qusay H. Mahmoud [13]	<b>IoTID20</b>	Multi-class Binary	DT DT	100% 100%
Our Study	<b>HEIoT21</b>	Binary Multi-class	DT DT	99.92% 99.94%

## 5. Conclusion

In conclusion, this study was successful in achieving its two primary goals in a comprehensive manner. The first goal was to create a new IoT dataset that was composed of data obtained from real devices in different scenarios, rather than using simulated data. This dataset was collected in a real smart home environment, making it highly relevant and useful for researchers in the field as it provides a realistic representation of IoT devices and the attacks they are vulnerable to. This dataset will be helpful in training and testing other intrusion detection models and it will also be useful for researchers in the field of IoT security to better understand the behavior of real-world IoT devices.

The second goal was to identify the most effective model for detecting different types of intrusions within the scope of our dataset. This was accomplished by evaluating multiple models and selecting the one that achieved the highest accuracy rate. The chosen model was able to detect various types of intrusions with a high level of accuracy, reaching 99.9%.

In the future, the dataset will be expanded and updated to include a wider range of attack types, this will make the dataset more comprehensive and will help in detecting new and emerging attacks. Additionally, an alert mechanism will be integrated to create a more robust and efficient attack detection system. Overall, this study has made significant contributions to the field of IoT security by providing a realistic dataset and an effective intrusion detection model, and it will be of great use to researchers and practitioners in the area.

## References

- [1] Butun I, Österberg P, Song H. Security of the Internet of Things: vulnerabilities, attacks and counter measures. *IEEE Commun Surv Tutor* 2019; 616-644.
- [2] Alotaibi B, Alotaibi M. A stacked deep learning approach for IoT cyber attack detection. *J Sens* 2020.
- [3] Abu Kwaider H. HEIoT2021. [Online]. Available: <https://drive.google.com/file/d/1WAHorikhN9fw9T1YpOkH6DwvnbwdjiHC/view?usp=sharing>. 2021.
- [4] Xu T, Potkonjak M, Wendt J. Security of IoT systems: design challenges and opportunities. *ACM International Conference on Computer-Aided Design* 2014; IEEE. pp. 417-423.
- [5] Bull P, Austin R, Popov E, Sharma M, Watson R. Flow based security for IoT devices using an SDN gateway. *IEEE 4th International Conference on Future Internet of Things and Cloud* 2016; IEEE. pp. 157-163.
- [6] Farahnakian F, Heikkonen JA. Deep auto-encoder based approach for intrusion detection system. *20th International Conference on Advanced Communication Technology* 2018; pp. 178-183.
- [7] Moukhafi M, El Yassini K, Bri S. A novel hybrid GA and SVM with PSO feature selection for intrusion detection system. *Int J Adv Sci Eng Technol* 2018; 4(5): 129-134.
- [8] Khalvati L, Keshtgary M, Rikhtegar N. Intrusion detection based on a novel hybrid learning approach. *J AI Data Mining* 2018; 6(1): 157-162.
- [9] Ferrag M, Shu L, Hamouda D, Choo R. Deep learning-based intrusion detection for distributed denial of service attack in agriculture 4.0. *Electronics* 2021; 10(11): 1257.
- [10] Latif S, Zou Z, Idrees Z, Ahmad J. A novel attack detection scheme for the industrial Internet of Things using a lightweight random neural network. *IEEE Access* 2020; (8): 89337- 89350.
- [11] Ullah I, Mahmoud Q. An anomaly detection model for IoT networks based on flow and flag features using a feed-forward neural network. *IEEE 19th Annual Consumer Communications & Networking Conference* 2022; pp. 363-368.
- [12] Ullah I, Mahmoud Q. A scheme for generating a dataset for anomalous activity detection in IoT networks. *Advances in Artificial Intelligence: 33rd Canadian Conference on Artificial Intelligence, Canadian AI 2020, Ottawa, ON, Canada, 13–15 May 2020, Proceedings*; pp. 508–520.
- [13] Lopez Alma D, Mohan Asha P, Nair S. Network traffic behavioral analytics for detection of DDoS attacks. *SMU Data Science Review* 2019; 2(1): Article 14.

## Novel Quaternary CuAlZnMg High Temperature Shape Memory Alloy (HTSMA) Fabricated by Minor Batch of Zn and Mg Additions

Oktay KARADUMAN<sup>1</sup>, Güneş BAŞBAĞ<sup>2</sup>, İskender ÖZKUL<sup>3</sup>, Canan Aksu CANBAY<sup>4\*</sup>, Mustafa BOYRAZLI<sup>5</sup>

<sup>1</sup> Munzur University, Rare Earth Elements Application and Research Center, Tunceli 62000, Turkey

<sup>2,5</sup> Department of Metallurgical and Materials Engineering, Engineering Faculty, Firat University, Elazığ, Turkey

<sup>3</sup> Department of Mechanical Engineering, Faculty of Engineering, Mersin University

<sup>4</sup> Department of Physics, Faculty of Science, Firat University, 23119 Elazığ

\*<sup>4</sup> caksu@firat.edu.tr, <sup>1</sup> oktaykaraduman@munzur.edu.tr

(Geliş/Received: 10/11/2022;

Kabul/Accepted: 15/02/2023)

**Abstract:** Shape memory alloys (SMAs) constitute the second largest commercial smart material class after piezoelectric materials. Different SMA alloy systems or SMAs with miscellaneous functionalities and characteristic properties have been designed for using in different applications until today. High temperature shape memory alloys (HTSMAs) are also widely desired to be used in various smart materials applications. HTSMAs with different functional and characteristic properties are muchly demanded for different tasks to be done by these alloys or devices designed by these alloys. A common and practical way to fabricate SMAs or HTSMAs with different shape memory effect (SME) and other properties is to fabricate them with different alloying compositions and add different additive elements. In this work, a quaternary CuAlZnMg HTSMA with an unprecedented composition consisting minor amount of zinc and magnesium additives was produced by arc melting method. As a result of applying post-homogenization in high  $\beta$ -phase temperature region and immediate quenching, the microstructural mechanism of a SME property was formed in the produced alloy. After then, to examine SME characteristics of the CuAlZnMg alloy some differential thermal analysis (DTA), microstructural (XRD) and magnetization (VSM) characterization tests were carried out. The DTA results showed that the alloy is a HTSMA exhibiting reverse martensitic transformations at temperature range between 167 °C and 489 °C. The XRD pattern obtained at room temperature revealed the martensite phases formed in the alloy, which phases are the base mechanism of the reversible martensitic transformation (the SME property) of the alloy. The VSM test showed that the alloy exhibit a diamagnetic property with a weak ferromagnetic coercivity contribution.

**Key words:** CuAlZnMg, High temperature shape memory alloy (HTSMA), Shape memory effect, Martensitic transformation, Enthalpy, DTA, XRD, VSM.

### Minör Miktarda Zn ve Mg Katkıları Eklenerek Üretilmiş Yeni Kuaterner CuAlZnMg Yüksek Sıcaklık Şekil Hafızalı Alaşımı (YSSHA)

**Öz:** Şekil hafızalı alaşımlar (SHA), piezoelektrik malzemelerden sonra ikinci en büyük ticari akıllı malzeme sınıfını oluşturmaktadır. Farklı SMA alaşım sistemleri ya da farklı işlevlere ve karakteristik özelliklere sahip SMA'lar bugüne kadar farklı uygulamalarda kullanılmak üzere tasarlanmıştır. Yüksek sıcaklık şekil hafızalı alaşımlar (YSSHA) da farklı fonksiyonel ve karakteristik özelliklere sahip akıllı malzeme uygulamalarında yaygın olarak kullanılmaktadır. Bu alaşımlar veya bu alaşımlar ile tasarlanan cihazların farklı işlevleri için bu alaşımların farklı fonksiyon ve karakteristik özelliklere sahip olmaları çok talep edilmektedir. Farklı şekil hafıza etkisine (ŞHE) ve diğer özelliklere sahip SHA ya da YSSHA'ları üretmenin yaygın ve kolay bir yolu farklı alaşım kompozisyonları ile ve farklı katkı elementleri ilave ederek üretmektir. Bu çalışmada, ark eritme yöntemi ile az miktarda çinko ve magnezyum katkı maddelerinden oluşan benzersiz bir kompozisyona sahip dördü CuAlZnMg YSSHA üretilmiştir. Yüksek  $\beta$ -faz sıcaklık bölgesinde homojenleştirme ve hemen sonrasında hızlı söndürme işlemi uygulanması sonucunda alaşımda ŞHE özelliğinin mikroyapısal mekanizması oluşturulmuştur. Daha sonra, CuAlZnMg alaşımının ŞHE özelliklerini incelemek için diferansiyel termal analiz (DTA), mikroyapısal (XRD) ve magnetik karakterizasyon (VSM) gibi bazı karakterizasyon testleri yapılmıştır. DTA sonuçları, alaşımın 167 °C ve 489 °C sıcaklık aralığında ters martensitik dönüşümler gösteren YSSHA olduğunu göstermiştir. Oda sıcaklığında elde edilen XRD desenleri, alaşımın tersinir martensitik dönüşümlerinin (ŞHE etkisi özelliğinin) temel mekanizmasını oluşturan alaşımdaki oluşmuş martensitik fazları ortaya çıkarmıştır. VSM testi alaşımın diyamanyetik özellik ve yanısıra buna ek olarak zayıf bir ferromanyetik koersivite sergilediğini göstermiştir.

**Anahtar kelimeler:** CuAlZnMg, Yüksek sıcaklık şekil hafızalı alaşım (YSSHA), Şekil hafıza etkisi, Martensitik dönüşüm, Entalpi, DTA, XRD, VSM.

### 1. Introduction

\* Corresponding author: caksu@firat.edu.tr. ORCID Numbers of Authors: <sup>1</sup> 0000-0002-6947-7590, <sup>2</sup> 0000-0001-6766-1741, <sup>3</sup> 0000-0003-4255-0564, <sup>4</sup> 0000-0002-5151-4576, <sup>5</sup> 0000-0002-2340-6703

In terms of technological developments in the world investment and development of new materials is of great importance. These developments should not only be aimed at obtaining materials, and also these demands can be to reduce the cost of these versatile smart alloys or to increase their performance and change their properties [1–3]. Shape memory alloys (SMAs) are crystallographically designed smart materials that can make large distortions like martensitic phase transformation in a temperature interval region or high elastic behavior at a higher temperature region which can be triggered by application of external effects such as heat or mechanical force, and can backtrack to their original shape when external forces are removed [4,5]. These exceptional behaviors of SMAs based on martensitic phase transformation are defined as their unique properties of shape memory effect (SME) and superelasticity (SE) [5–7]. These versatile alloys have already been utilized for their SME, SE and some other properties in numerous applications including actuator, automotive, aerospace, medical, robotics, micro/nano electromechanical systems (M/NEMS) and photodetectors [6,8–19].

Martensitic phase transformations are solid-to-solid phase transitions that can occur isothermally and atomically a non-diffusional manner in SMAs between their two solid phases called as martensite (M) or product phase (at low temperature) and austenite (A) or parent phase (at high temperature) [5,8]. For a certain SMA that is commercial or ready to use in an application, one of the main characteristic parameters are its transformation or working (operation) temperatures which are the start and finish temperatures ( $M_f < M_s < A_s < A_f$ ) and hysteresis gap ( $A_s - M_f$ ) of phase transition reactions resulting martensite from austenite (direct transformation;  $A \rightarrow M$ ) upon cooling the alloy or austenite from martensite (reverse transformation;  $M \rightarrow A$ ) upon heating the alloy [5,8]. SMAs can show superelastic behavior at temperatures above their austenite finish temperature ( $A_f$ ) until a higher temperature ( $M_d$ ) at which the martensite cannot be stress induced above this point [6,20].

SMAs are generally classified as; Cu-based, Fe-based and NiTi alloys [5,21]. Among these, NiTi alloys with superior shape memory properties are the most commercially used SMAs in industry and technological applications, but they are expensive and the production-processing processes are more difficult. This led researchers to pay attention to the second largest SMAs group; the Cu-based SMAs, which are regarded as the closest alternative to NiTi SMAs in terms of good SME and SE properties [7,22,23]. The most-known Cu-based SMAs such as Cu-Al-Ni, Cu-Zn-Al, Cu-Al-Mn alloy systems have been substantially studied until today. The main reasons for the selection of Cu-based SMA systems are the low costs, easy fabrication and also much higher heat and electrical conductivity of these alloy systems as compared to NiTi ones. But, Cu-based SMAs have some drawbacks that are tried to be improved such as thermal instabilities, martensite stabilization and brittle nature and weak mechanical properties (low cold workability) stemmed from mainly their microstructural properties such as the large grain sizes, accumulation of secondary phases or impurities along the grain boundaries, high degree of order and also high elastic anisotropy in the  $\beta$ -phase [7,23–25]. A common and simple way to modify microstructure and reduce the grain size for improving these drawbacks and also to change characteristic martensitic transformation temperatures, SME, SE or other properties is to add some ternary, quaternary or more extra additive elements such as Ti, V, Co, Mn, Zr, Ce, Fe, Ni, B, Be, Mg, Sn or C [7,18,19,22–24,26–35]. SMAs are ultra sensitive to the compositional changes, their properties can change dramatically by even very little changes in the alloying composition. For example it was shown in a previous work [35] that the characteristic transformation temperatures of a CuAlMn SMA were decreased approximately 40–50 °C by a quaternary 1.69 (at%) amount of magnesium addition which also caused formation of uniformly distributed spot-like Mg precipitations in the alloy due to the low solubility of Mg in Cu-matrix. In another work [36], the transformation temperatures of a CuAlMn SMA were reduced as nearly minimum 15 °C and maximum 30 °C by the addition of a 0.5 (wt%) magnesium content, and the strain recovery and superelasticity abilities were changed, too.

Although there are many studies been done on ternary CuZnAl SMAs [5,23,37–39] and some also on CuAlZn SMAs [27,40], there is no any Mg incorporated quaternary CuAlZnMg SMA work in the available literature. In this work, a CuAlZnMg SMA with a minor batch of Zn and Mg additives was produced by arc melting method. The characteristic microstructural properties, martensitic transformation temperatures and thermodynamical parameters related to the shape memory properties of the alloy were investigated by differential calorimetry tests and structural measurements, and apart from these the magnetic properties of the alloy were tested by making vibrating sample magnetometer (VSM) measurement, too.

## 2. Experimental Details

In this study, the arc melting method was used to produce the quaternary CuAlZnMg alloy with an unprecedented composition of 74.79Cu-21.38Al-3.50Zn-0.34Mg (at%). At the beginning, the high purity (99.9%) of Cu, Al, Zn and Mg alloying elements powders were mixed, then the obtained mixture was pelletized under pressure. Then these pellets were melted together in a arc melter under argon atmosphere and the as-cast ingot

alloy was obtained. Then the ingot was cut into small sized test samples (~4x4x2 mm and ~30-60 mg) proper for characterization measurements. Then in order to improve homogenization, these alloy samples were all heat-treated at 900 °C for 1 h in a furnace. At the end of this homogenization process, without waiting a pronto rapid cooling was made by quenching the alloy samples in iced-brine water solution. This traditional quenching method for this quick cooling of the alloy samples from  $\beta(A2)$  phase (to around 0 °C) surpasses the formation of  $\alpha$  and  $\gamma_2$  precipitation phases under eutectoid point and thus directly lead the formation of martensite phases in the alloy that will be the crystallographic base mechanism of shape memory effect property of the alloy. The chemical composition of the alloy was determined in room conditions by using a Zeiss Evo MA10 model EDS (energy dispersive X-ray spectrum). The SEM image and EDS result of the alloy are given in Fig.1.a and b, respectively. The diffraction planes of the martensite phases formed in the fabricated CuAlZnMg alloy were determined by performing structural X-ray diffraction (XRD) test using a Rigaku RadB-DMAX II diffractometer with  $CuK\alpha$  radiation at room temperature. The DTA measurements were performed as taking three consecutive times of DTA heating/cooling cycles via using a Shimadzu DTG-60AH instrument between room temperature and 900 °C at a same single heating/cooling rate of 25 °C/min to observe the phase transitions occurred in the alloy in this temperature interval. The magnetic properties of the alloy were investigated by performing vibrating sample magnetometer (VSM) measurement by using a Quantum Design Physical Properties Measurement System (PPMS) with VSM under a magnetic field of  $\pm 3$  T at room temperature.

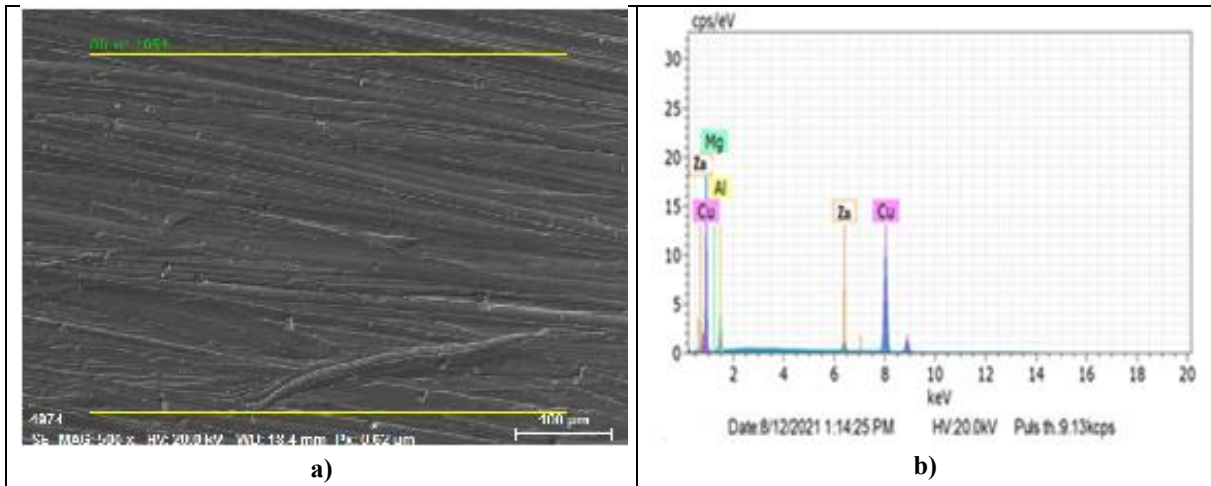
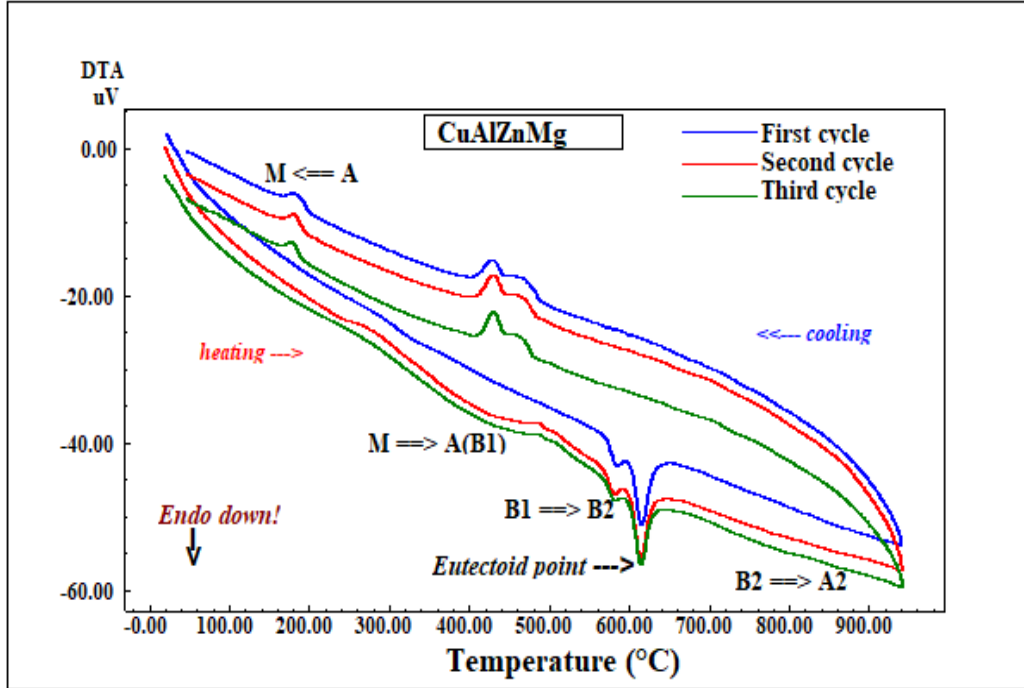


Fig.-1. a) The SEM image and b) EDS spectra of the CuAlZnMg alloy at room temperature.

### 3. Results and Discussions

The DTA curves of the first, second and third heating/cooling cycles of the produced CuAlZnMg alloy each taken at the same single 25 °C/min of heating/cooling rate are given together in Fig.2. The emerged downside endothermic peaks and their corresponding upside exothermic counterparts observed on this DTA curves indicated the common multi-stage phase transitions behavior of Cu-based SMAs. Such that, this thermo-responsive events, which are all multi-stepped solid-to-solid phase transition reactions occurred either on heating and cooling the CuAlZnMg alloy, are caused by the heat induced structural and geometric changes in the crystal lattice of the alloy. As seen, from the far left of the downside heating segments of these DTA curves to their far right ends such multi-stage phase transitions arrays occurred as; martensite  $\beta_1'$  (with  $\gamma_1'$ )  $\rightarrow$  austenite  $\beta_1(L2_1)$   $\rightarrow$  metastable  $\beta_2(B2)$   $\rightarrow$  eutectoid dissolution of hypoeutectoid precipitations ( $\alpha$  and  $\gamma_2$ )  $\rightarrow$  ordered  $\beta_2(B2)$   $\rightarrow$  disordered  $\beta(A2)$  on the each heating segments of the curves representing heating the CuAlZnMg alloy, and this phase transition array proceeded reversely way-back on cooling the alloy (as seen on the up-side cooling segments of the DTA curves), too [22,31,41–43]. To determine the characteristic reverse ( $M \rightarrow A$ ) and direct ( $A \rightarrow M$ ) martensitic transformation temperatures and some other transformational thermodynamic parameters of the CuAlZnMg alloy, the  $M \rightarrow A$  and  $A \rightarrow M$  phase transition peaks observed on the third cycling DTA curve were analyzed by DTA peak analysis program which applies tangent differentiation method automatically on a choosen peak area bordered manually and directly give as a data set of values of those transformational parameters. The determined parameter values of transformation temperatures and the values of some other related thermodynamic parameters hysteresis gap ( $A_s - M_f$ ),  $A_{max}$  temperature, equilibrium temperature ( $T_0$ ), enthalpy change ( $\Delta H_{M \rightarrow A}$ ) and entropy change ( $\Delta S_{M \rightarrow A}$ ) are

given in Table 1. Here, the the equilibrium temperature,  $T_0$  (calculated by using  $T_0=(A_f+M_s)/2$  formula [7]) is the temperature at where the Gibbs free energy differences of two interconvertible solid (M and A) phases are equal therefore there is no any driving force to lead a martensitic transformation. Then, the entropy change amount,  $\Delta S_{M \rightarrow A}$  was found by using  $\Delta S_{M \rightarrow A}=\Delta H_{M \rightarrow A}/T_0$  formula [7,44]. As seen, the produced CuAlZnMg alloy is a high temperature shape memory alloy (HTSMA) [1,20,31,45] due to that it showed a reversible martensitic transformation at a temperature range (or simply an  $A_f$  temperature) far above 100 °C.



**Fig.-2:** The sequential cycling DTA curves of the CuAlZnMg HTSMA each taken at the same 25 °C/min of heating/cooling rate.

**Table-1:** The characteristic martensitic transformation temperatures and other transformational thermodynamic parameters values of the alloy determined by making the tangent peak analyses on the third cycle DTA curve.

$A_s$ (°C)	$A_f$ (°C)	$A_{max}$ (°C)	$M_s$ (°C)	$M_f$ (°C)	$A_s - M_f$ (°C)	$T_0$ (°C)	$\Delta H_{M \rightarrow A}$ (j/g)	$\Delta S_{M \rightarrow A}$ (j/g)
316.69	489.30	382.11	190.31	167.08	149.61	339.81	14.16	0.042

Due to the some martensite stabilization, the endothermic peaks of the reverse transformation from martensite to austenite ( $M \rightarrow A$ ) phase observed on the down curve segments of heating the alloy were seen as abnormally too extended (i.e.  $A_f - A_s = 172.6$  °C) and therefore as seen in Table 1 the  $A_f$  temperature was found to be substantially elevated by the effect of minor Mg content. Some local stabilized martensite regions, which were formed by the heat effect of the first and second DTA cycles and residually remained, were needed more energies to be forced to transform to austenite and this extended this transformation till being fully completed. On the other hand the exothermic direct ( $A \rightarrow M$ ) transformation peaks observed on cooling the alloy are seen very stable. The enthalpy change ( $\Delta H_{M \rightarrow A}$ ) value of the reverse transformation seen in Table 1 is very huge (14.16 j/gr) as compared to those (generally changing between ~1-12 j/gr) of other Cu-based SMAs [22,26,38,44,46,47], which indicates a martensitic transformation occurring by proceeding from difficult heat transmission pathways [22,42,44] and also a powerful shape memory effect property the produced CuAlZnMg alloy has.

The average valence or conduction electron number per atom ( $e/a$ ) ratio of the Cu-based SMAs generally takes values between 1.45 and 1.51 to exhibit good shape memory effect [5,22]. The  $e/a$  ratio of the CuAlZnMg HTSMA was calculated as 1.466 and this value, been found indeed in the interval of 1.45- 1.51, theoretically



indicates that a nearly high volume dominance of  $\beta 1'$  (18R) over the co-existent  $\gamma 1'$ (2H) type martensite phase with lower volume [42,48]. This theoretical expectation was confirmed by the microstructural XRD test result of the CuAlZnMg alloy given below.

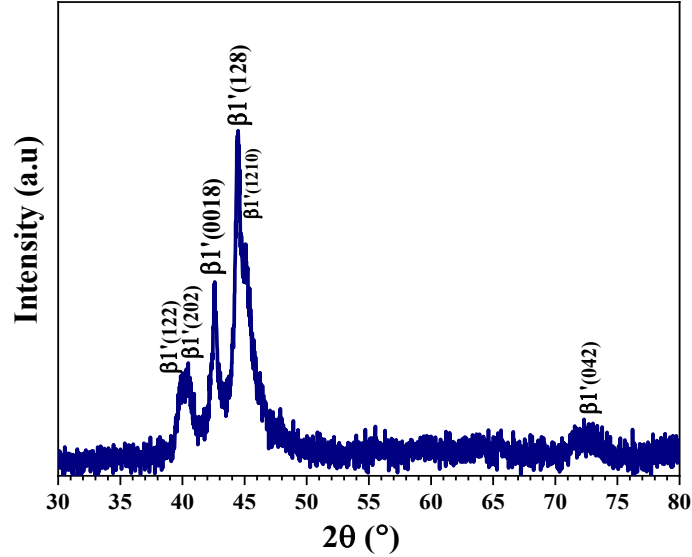


**Fig.-3:** The XRD pattern of the CuAlZnMg HTSMA obtained at room temperature.

The XRD pattern of the CuAlZnMg HTSMA obtained at room temperature is given in Fig.3. The main or the highest intensity peak is  $\beta 1'$ (128) martensite peak and the others are  $\beta 1'$  martensite peaks of (122), (202), (0018),(1210) and (042) according to the reference works of [37,38,42,49]. The alloy has a polycrystalline structure. The crystallographic base mechanism of  $\beta 1'$  martensitic structure for the produced CuAlZnMg alloy to show a shape memory effect was found to be well formed in the alloy and this confirms the theoretical prediction made over the  $c/a$  ratio of this alloy mentioned above.

The magnetic hysteresis loop of the CuAlZnMg alloy in the form of magnetization ( $M_s$ ) versus magnetic field strength ( $H$ ) graph obtained by vibrating sample magnometry (VSM) test at room temperature (300 °K) is given in Fig.4. Here, magnetization ( $M_s$ ) is magnetic moment per unit mass (emu/g). The VSM test showed a diamagnetic characteristic which stemmed from the main copper and minor zinc contents in the CuAlZnMg alloy [50–52]. A small inset graphic also inserted in Fig.4 shows the magnetic forcing hysteresis profile (coercivity) of the alloy between  $\pm 200$  Oe magnetic field strength values and this means that the alloy has a very weak ferromagnetic property in addition to its diamagnetic property [7,50–54].

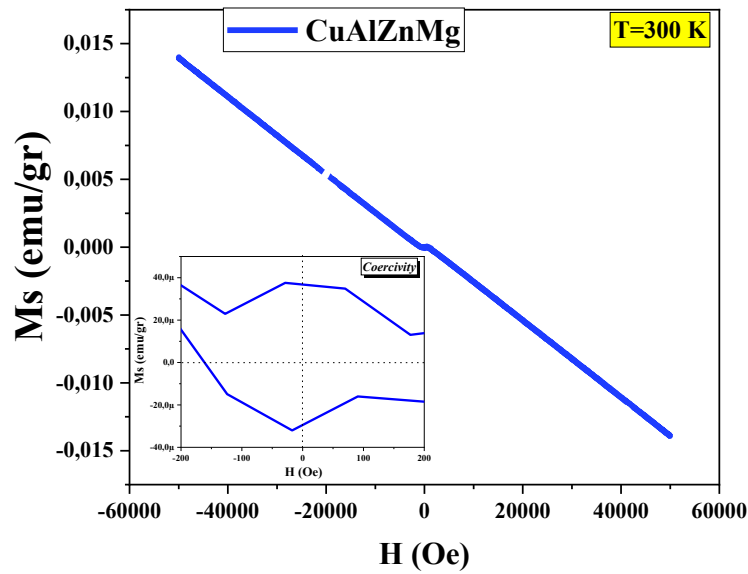


Fig.-4: Vibrating sample magnetometer (VSM) curve of CuAlZnMg HTSMA at room temperature.

#### 4. Conclusions:

In this study, the novel CuAlZnMg high temperature shape memory alloy was successfully produced by arc melting method. The DTA results showed that the alloy is a HTSMA exhibiting reversible martensitic transformations at a temperature range between 167 °C and 489 °C. The partial martensite stabilization remained from the prior DTA heating-cooling processes led the reverse martensitic transformation to be extended and thus the  $A_f$  temperature of the alloy was found to be increased. The average conduction electron ratio ( $e/a$ ) of the alloy was found as 1.466 which indicates the martensite phases should have formed in the alloy to show a shape memory behavior. The existence of martensite phases was revealed by XRD pattern of the alloy obtained at room temperature, which phases are the base mechanism of the reversible martensitic transformation (the SME property) of the alloy. The VSM test showed that the alloy has a diamagnetic nature with a weak ferromagnetic coercivity contribution. In conclusion, the novel CuAlZnMg high temperature shape memory alloy with good shape memory effect property was produced and may be useful in related HTSMA applications and further research on HTSMAs.

#### Acknowledgements

This research study is one of the doctoral thesis studies carried out Güneş BAŞBAĞ (the first author) in Metallurgical and Materials Engineering Department, Engineering Faculty of Firat University, and was presented only as an oral presentation at the MSNG2022 conference. In this study, G.B. formed the idea, carried out experiments and wrote the article; O.K. wrote & edited the article, performed experiments, analyses, calculations and graphs, and interpreted the results; İ.Ö. carried out the experiments and interpreted the results; M.B. formed the idea and interpreted the results; and C.A.C. formed the idea, carried out the experiments, interpreted the results and edited.

#### References

- [1] Ma J, Karaman I, Noebe RD. High temperature shape memory alloys. *Int Mater Rev* 2010; 55: 257–315.
- [2] Canbay CA. The production of copper based shape memory alloys and investigation of the structural, thermal and electrical properties of alloys. PhD. Firat University, Elazig, Türkiye, 2010.
- [3] Mallik US, Sampath V. Influence of quaternary alloying additions on transformation temperatures and shape memory properties of Cu-Al-Mn shape memory alloy. *J Alloys Compd* 2009; 469: 156–63.
- [4] Naresh C, Bose PSC, Rao CSP. Shape memory alloys: a state of art review. *IOP Conf Ser Mater Sci Eng* 2016; 149: 012054.
- [5] Otsuka K, Wayman CM. *Shape memory materials*. Cambridge University Press: 1999.
- [6] Mohd Jani J, Leary M, Subic A, Gibson MA. A review of shape memory alloy research, applications and opportunities. *Mater Des* 2014; 56: 1078–113.

- [7] Özkul İ, Karaduman O, Şimşek T, Şimşek T, Canbay CA, Ibrahim PA, et al. Experimental investigation of the effects of different quaternary elements (Ti, V, Nb, Ga, and Hf) on the thermal and magnetic properties of CuAlNi shape memory alloy. *J Mater Res* 2022; 37.
- [8] Canbay CA, Karaduman O. The photo response properties of shape memory alloy thin film based photodiode. *J Mol Struct* 2021; 1235: 130263.
- [9] Lambrecht F, Aseguinolaza I, Chernenko V, Kohl M. Integrated SMA-based NEMS actuator for optical switching. In: IEEE 29th 2016 International Conference on Micro Electro Mechanical Systems (MEMS) Conference; 24-28 Jan. 2016; Shanghai, China. New York, NY, USA: IEEE. p. 79–82.
- [10] Stachiv I, Alarcon E, Lamac M. Shape memory alloys and polymers for mems/nems applications: Review on recent findings and challenges in design, preparation, and characterization. *Metals (Basel)* 2021; 11: 1–28.
- [11] Costanza G, Tata ME. Shape Memory Alloys for Aerospace, Recent Developments, and New Applications: A Short Review. *Materials* 2020; 13(8): 1856.
- [12] Hu K, Rabenoroosa K, Ouisse M. A Review of SMA-Based Actuators for Bidirectional Rotational Motion: Application to Origami Robots. *Front Robot AI* 2021; 8: 678486.
- [13] Nespoli A, Passaretti F, Szentmiklósi L, Maróti B, Placidi E, Cassetta M, et al. Biomedical NiTi and  $\beta$ -Ti Alloys: From Composition, Microstructure and Thermo-Mechanics to Application. *Metals (Basel)* 2022; 12: 406.
- [14] Riccio A, Sellitto A, Ameduri S, Concilio A, Arena M. Shape memory alloys (SMA) for automotive applications and challenges. In: Concilio A, Antonucci V, Auricchio F, Lecce L, Sacco E, editors. *Shape Memory Alloy Engineering (Second Edition)*. Oxford, UK: Butterworth-Heinemann, 2021. pp. 785–808.
- [15] Rokaya D, Bohara S, Srimanepong V, Kongkiatkamon S, Khurshid Z, Heboyan A, et al. Metallic Biomaterials for Medical and Dental Prosthetic Applications. In: Jana S, Jana S, editors. *Functional Biomaterials*, Singapore: Springer, 2022, pp. 503–22.
- [16] Fu YQ, Luo JK, Huang WM, Flewitt AJ, Milne WI. Thin film shape memory alloys for optical sensing applications. *J Phys Conf Ser* 2007; 76(1): pp. 012032
- [17] Karaduman O., Aksu Canbay C. Photo-electrical Characterization of New CuAlNi/n-Si/Al Schottky Photodiode Fabricated by Coating Thin-Film Smart Material. *Turk J Sci Technol* 2022; 17(2): pp.329-341.
- [18] Karaduman O, Canbay CA. Shape Memory Alloy Layered CuAlFeMn/n-Si/Al Photodiode with a High Photo-responsivity Merit and Negative Capacitance. *J Mater Electron Device* 2022; 1(1): pp.28-35.
- [19] Karaduman O, Canbay CA. The Photosensitive Properties of a new Photodiode consisting Thin Film CuAlMnNi Shape Memory Alloy Layer Contact. *J Mater Electron Device* 2022; 1(1): pp.7–16.
- [20] López-Ferreño I, Gómez-Cortés JF, Breczewski T, Ruiz-Larrea I, N6 ML, San Juan JM. High-temperature shape memory alloys based on the Cu-Al-Ni system: Design and thermomechanical characterization. *J of Mater Res and Tech* 2020; 9: pp.9972–84.
- [21] Nnamchi P, Younes A, González S. A review on shape memory metallic alloys and their critical stress for twinning. *Intermetallics* 2019; 105: pp.61–78.
- [22] Canbay CA, Karaduman O, Ünlü N, Baiz SA, Özkul İ. Heat treatment and quenching media effects on the thermodynamical, thermoelastical and structural characteristics of a new Cu-based quaternary shape memory alloy. *Compos B Eng* 2019; 174: pp.106940.
- [23] Dasgupta R. A look into Cu-based shape memory alloys: Present scenario and future prospects. *J Mater Res* 2014; 29: pp.1681–98.
- [24] Mazzer EM, da Silva MR, Gargarella P. Revisiting Cu-based shape memory alloys: Recent developments and new perspectives. *J Mater Res* 2022; 37: pp.162–82.
- [25] Al-Humairi SNS. Cu-Based Shape Memory Alloys: Modified Structures and Their Related Properties. In: Al-Naib B, Vikraman D, Karuppasamy K, editors. *Recent Advancements in the Metallurgical Engineering and Electrodeposition*. London UK: IntechOpen, 2020. p. 25.
- [26] Karaduman O, Canbay CA. Investigation of CuAlNi Shape Memory Alloy Doped with Graphene. *J Mater Electron Device* 2021; 3: pp.8–14.
- [27] Canbay CA, Başbağ G, Karaduman O, Boyrazlı M. Magnesium Effect on Characteristic Properties of Cu-based Smart Materials. *J Mater Electron Device* 2021; 2: pp.19–23.
- [28] Canbay CA, Karaduman O, Ünlü N, Özkul İ. Study on Basic Characteristics of CuAlBe Shape Memory Alloy. *Brazilian J Phys* 2021; 51: pp.13–8.
- [29] Canbay CA, Karaduman O, Ünlü N, Özkul İ. An exploratory research of calorimetric and structural shape memory effect characteristics of Cu–Al–Sn alloy. *Physica B Condens Matter* 2020; 580: pp.411932.
- [30] Canbay CA, Karaduman O, Ünlü N, Özkul İ, Çiçek MA. Energetic Behavior Study in Phase Transformations of High Temperature Cu–Al–X (X: Mn, Te, Sn, Hf) Shape Memory Alloys. *Trans Indian Inst Met* 2021; 74(10): pp.2447-2458.
- [31] Karaduman O, Özkul İ, Altın S, Altın E, Bağlayan, Canbay CA. New Cu–Al based quaternary and quinary high temperature shape memory alloy composition systems. *AIP Conf Proc* 2018; 2042(1): p.020030.
- [32] Canbay CA, Çiçek MA, Karaduman O, Özkul İ, Şekerçi M. Investigation of Thermoelastical Martensitic Transformations and Structure in New Composition of CuAlMnTi Shape Memory Alloy. *J of Mater and Elec Dev* 2019; 1(1): pp.60–64.
- [33] Yang J, Wang QZ, Yin FX, Cui CX, Ji PG, Li B. Effects of grain refinement on the structure and properties of a CuAlMn shape memory alloy. *Mater Sci and Eng A* 2016; 664: pp.215–20.

- [34] Sutou Y, Omori T, Okamoto T, Kainuma R, Ishida K. Effect of grain refinement on the mechanical and shape memory properties of Cu-Al-Mn base alloys. *J Phys IV* 2001; 11(PR8): pp.185-190.
- [35] Canbay CA, Karagoz Z. The effect of quaternary element on the thermodynamic parameters and structure of CuAlMn shape memory alloys. *Appl Phys A Mater Sci Process* 2013; 113: pp.19–25.
- [36] Mallik US, Sampath V. Influence of quaternary alloying additions on transformation temperatures and shape memory properties of Cu–Al–Mn shape memory alloy. *J Alloys Compd* 2009; 469: pp.156–63.
- [37] Wu S-K, Chan W-J, Chang S-H. Damping Characteristics of Inherent and Intrinsic Internal Friction of Cu-Zn-Al Shape Memory Alloys. *Metals (Basel)* 2017; 7: pp.397.
- [38] Karaduman O, Canbay CA, Ünlü N, Özkul S. Structural and thermodynamical study of Cu-Zn-Al shape memory alloys with new compositions produced by hot isostatic press (HIP). *AIP Conf Proc* 2019; 2178(1): p.030040.
- [39] Alkan S, Wu Y, Ojha A, Sehitoglu H. Transformation stress of shape memory alloy CuZnAl: Non-Schmid behavior. *Acta Mater* 2018; 149: pp.220–34.
- [40] Gomidželović L, Požega E, Kostov A, Vuković N, Krstić V, Živković D, et al. Thermodynamics and characterization of shape memory Cu-Al-Zn alloys. *Trans Nonferrous Met Soc China (English Edition)* 2015; 25: pp.2630–6.
- [41] Chentouf SM, Bouabdallah M, Gachon J-C, Patoor E, Sari A. Microstructural and thermodynamic study of hypoeutectoidal Cu–Al–Ni shape memory alloys. *J Alloys Compd* 2009; 470(1-2): pp.507-514.
- [42] Canbay CA, Karaduman O, Özkul İ. Investigation of varied quenching media effects on the thermodynamical and structural features of a thermally aged CuAlFeMn HTSMA. *Physica B Condens Matter* 2019; 557: pp.117–25.
- [43] Pérez-Landazábal JI, Recarte V, Sánchez-Alarcos V. Influence on the martensitic transformation of the  $\beta$  phase decomposition process in a Cu-Al-Ni shape memory alloy. *J. Phys. Condens. Matter* 2005; 17(26): pp.4223–36.
- [44] Canbay CA, Karaduman O, Özkul İ, Ünlü N. Modifying Thermal and Structural Characteristics of CuAlFeMn Shape Memory Alloy and a Hypothetical Analysis to Optimize Surface-Diffusion Annealing Temperature. *J Mater Eng Perform* 2020; 29: pp.7993–8005.
- [45] Karaduman O, Özkul İ, Canbay CA. Shape memory effect characterization of a ternary CuAlNi high temperature SMA ribbons produced by melt spinning method. *Ad Eng Sci* 2021; 1: pp.26–33.
- [46] Guilemany JM, Fernández J, Franch R, Benedetti A, Adorno AT. A New Cu-Based SMA with Extremely High Martensitic Transformation Temperatures. *J Phys IV* 1995; 05: pp. C2-361-C2-365.
- [47] Mañosa L, Planes A, Ortín J, Martínez B. Entropy change of martensitic transformations in Cu-based shape-memory alloys. *Phys Rev B* 1993; 48: pp.3611–9.
- [48] Sari U, Aksoy I. Electron microscopy study of 2H and 18R martensites in Cu-11.92 wt% Al-3.78 wt% Ni shape memory alloy. *J Alloys Compd* 2006; 417: pp.138–42.
- [49] Suzuki T, Kojima R, Fujii Y, Nagasawa A. Reverse transformation behaviour of the stabilized martensite in Cu□Zn□Al alloy. *Acta Metall* 1989; 37: pp.163–8.
- [50] Ma J, Liu C, Chen K. Assembling non-ferromagnetic materials to ferromagnetic architectures using metal-semiconductor interfaces. *Sci Rep* 2016; 6(1): pp.1-11.
- [51] Jiraskova Y, Bursik J, Janos P, Lunacek J, Chrobak A, Zivotsky O. Effect of iron impurities on magnetic properties of nanosized CeO<sub>2</sub> and Ce-based compounds. *Metals (Basel)* 2019; 9(2): pp.222.
- [52] Başbağ G, Karaduman O, Özkul İ, Canbay CA, Boyrazlı M. Thermo-structural Shape Memory Effect Characterization of Novel CuAlCoMg HTSMA with Ternary Co and Quaternary Mg Additions. *J Mater Electron Device* 2022; 2: pp.34–9.
- [53] Castañeda EJG, Castro REB, Briseño AC, Arguijo BF, Castillo AAT, Rodríguez AS, et al. Effect of quenching and normalizing on the microstructure and magnetocaloric effect of a Cu–11Al–9Zn alloy with 6.5 wt % Ni–2.5 wt % Fe. *Magnetochemistry* 2019; 5(3): pp.48.
- [54] Başbağ G, Karaduman O, Özkul İ, Boyrazlı M, Canbay CA. Yeni CuAlCrMg Yüksek Sıcaklık Şekil Hafızalı Alaşımının (YSSHA) Termal, Yapısal ve Manyetik Karakterizasyonu. *Fırat Üni Fen Bil. Dergisi* 2022; 34: pp.161–70.

## Variation of Electrical Resistivity During Magnetic Field-Induced Martensitic Transformation in Vanadium added NiMnSnB alloys

Gökhan KIRAT<sup>1\*</sup>,

<sup>1</sup> Scientific and Technological Research Center, İnönü University, Malatya, Türkiye

\*<sup>1</sup> gokhan.kirat@inonu.edu.tr

(Geliş/Received: 23/11/2022;

Kabul/Accepted: 10/02/2023)

**Abstract:** In this study, the structural and electrical properties of  $Ni_{49-x}V_xMn_{37}Sn_{12}B_2$  ( $x = 0, 1, 2,$  and  $3$ ) ferromagnetic shape memory alloys were investigated. According to XRD analyzes at room temperature, the  $x=0$  sample was in the martensite phase, the  $x=1$  and  $2$  samples were in the mixture phase, and the  $x=3$  sample was in the austenite phase. The resistivity analyses depend on temperature showed that all samples exhibited martensitic transformation and the phase transformation temperature decreased with V doping. Magnetoresistance (MR) values were calculated using  $\rho$ -T curves performed under  $0$  T and  $1$  T magnetic fields. The observed negative MR is consistent with Kataoka's s-d model.  $A_s$ - $A_f$  interval was determined and M-H measurements were made at constant temperatures determined in this interval. The results were attributed to the magnetic field-induced phase transformation (MFIPT). In order to examine the effects of MFIPT on the electrical resistivity, the resistivity depend on magnetic field was measured using the same thermal process. The overlapping of the curves in the high magnetic field revealed that the resistivity decreased due to the MFIPT as well as the MR.

**Key words:** Magnetoresistivity, martensitic transformation, magnetic field induced structural transformation.

### Vanadyum Eklenmiş NiMnSnB Alaşımlarında Manyetik Alan Kaynaklı Martensitik Dönüşüm Sırasında Elektrik Direncinin Değişimi

**Öz:** Bu çalışmada  $Ni_{49-x}V_xMn_{37}Sn_{12}B_2$  ( $x = 0, 1, 2,$  and  $3$ ) ferromanyetik şekil hatırlamalı alaşımların yapısal ve elektriksel özellikleri incelenmiştir. Oda sıcaklığındaki XRD analizine göre  $x=0$  numunesi martensit fazında,  $x=1$  ve  $2$  numunesi karışım fazında ve  $x=3$  numunesi östenit fazındadır. Sıcaklığa bağlı öz direnç analizleri bütün numunelerin martensitik dönüşüm sergilediğini ve faz dönüşüm sıcaklığının V katkılanmasıyla azaldığını göstermiştir.  $0$  T ve  $1$  T manyetik alan altında gerçekleştirilen  $\rho$ -T eğrileri kullanılarak manyetodirenç (MR) değerleri hesaplanmıştır. Gözlemlenen negatif MR, Kataoka'nın s-d modeli ile uyumludur.  $A_s$ - $A_f$  aralığı belirlenmiştir ve bu aralıkta belirlenen sabit sıcaklıklarda M-H ölçümleri yapılmıştır. Sonuçlar manyetik alan kaynaklı faz dönüşümüne atfedilmiştir (MFIPT). MFIPT'in elektrik öz direnci üzerindeki etkilerini incelemek için, aynı termal süreç kullanılarak manyetik alana bağlı öz direnç ölçülmüştür. Yüksek manyetik alanda eğrilerin üst üste binmesi, MR'in yanı sıra MFIPT'e bağlı olarak direncin azaldığını ortaya koymuştur.

**Anahtar kelimeler:** Manyetodirenç, martensitik dönüşüm, manyetik alan kaynaklı yapısal dönüşüm.

#### 1. Introduction

The martensitic transformation (MT) is a first-order structural phase transition in the solid state without any diffusion. During the MT, the high temperature phase, which is called austenite, transforms into the low temperature phase, which is called martensite [1]. Shape memory effect (SME) is an important property of some alloy groups that exhibit martensitic transformation. The most important characteristic feature of shape memory alloys (SMA) is that they regain their original shape when they transform to the austenite phase after being deformed by stress in the martensite phase [2]. In addition, SMA have useful mechanical properties such as excellent corrosion resistance and superelasticity [3]. Therefore, in recent years, SMA have been the subject of many scientific studies and also they have been using extensively in the a lot of industrial applications. Some instances of these applications are stents, eyeglass frames, sensitive thermal sensors, microactuators, electronic devices, magnetic field sensors, valves and medical devices [4].

In the conventional SMA, shape recovery is usually triggered by heat, whereas in ferromagnetic shape memory alloys (FSMA) it can be controlled by magnetic field as well as heat [4]. The obtained higher strain depends on the applied magnetic field compared to traditional actuator materials like piezoelectric and magnetostrictive materials increases the interest in FSMA. For example, while a strain of  $<0.2\%$  can be obtained under approximately  $60$  MPa stress and  $0.3$  T magnetic field in

\* Corresponding author: gokhan.kirat@inonu.edu.tr ORCID Number of author: <sup>1</sup> 0000-0001-7357-2921

magnetostrictive Terphenol-D material, up to 10% magnetic field-induced strain can be obtained in FSMA [5]. Two different magnetic field induced strain (MFIS) mechanisms can occur in the FSMA as a result of applying an external magnetic field. The first is the magnetic field-induced martensitic twin variant reorientation (MIR), and the second is the magnetic field-induced structural phase transformation. The former mechanism, MIR is the rearrangement of the microstructure without a change in the crystalline structure as a result of twin boundary motion triggered by the external magnetic field (Fig 1.a.). If the magnetocrystalline anisotropy energy (MAE) of a martensite variant is larger than the energy required for twin boundary motion, MAE acts as a driving force for MIR. The MAE is determined from the difference between the magnetizations along the easy and hard axes of the ferromagnetic single martensite variant (Fig 1.b.). Another possible mechanism for inducing MFIS is magnetic field-induced structural phase transformation (MFIPT). In this mechanism, the crystal structure transforms from martensite to austenite by increasing the external magnetic field at a certain temperature where both phases (austenite and martensite) should coexist (Fig 1.c.) [6]. The difference in Zeeman energies of the present phases is the driving force for MFIPT and the difference must be higher than the energy required to move the phase boundaries (Fig 1.d.). If the external magnetic field is shown by  $\mu_0 H$  and the magnetization difference between the transformation phases is given by  $\Delta M$ , Zeeman energy can be expressed as  $E_{zeeman} = \mu_0 H \Delta M$  [7].

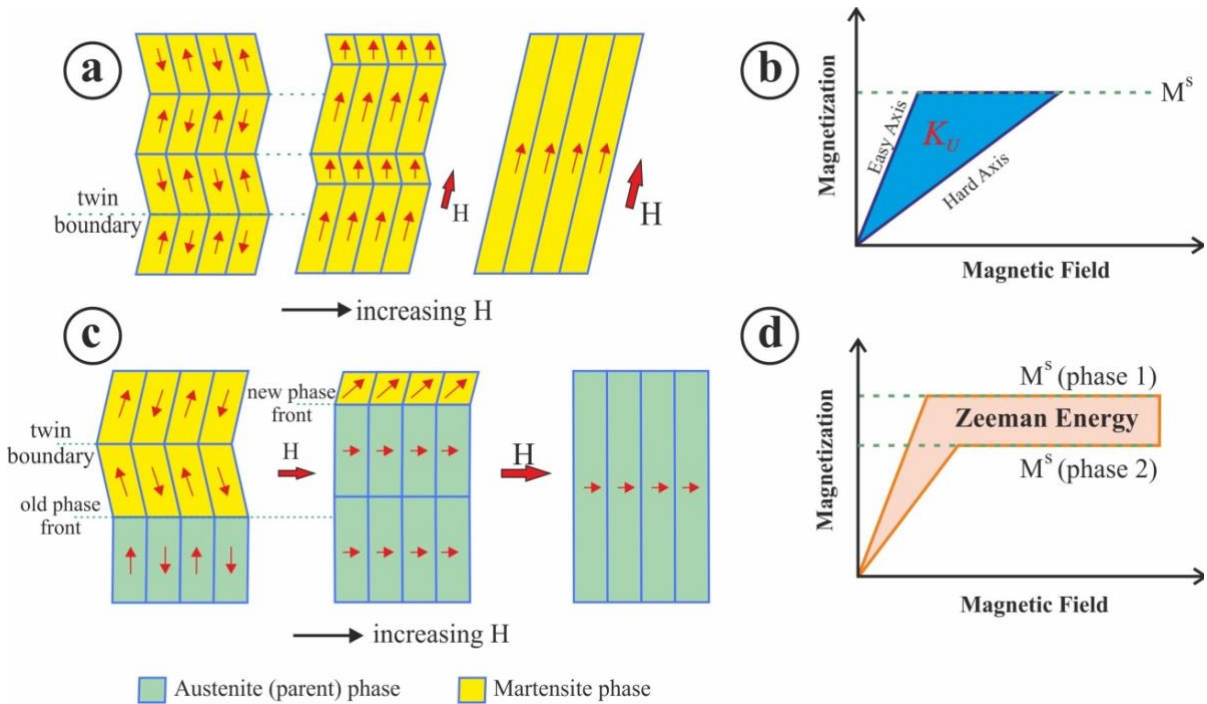


**Figure 1.** (a) Effect of increasing external magnetic field on MIR (b) MAE( $K_u$ ) responsible for MIR (c) Effect of increasing external magnetic field on MFIPT (d) Zeeman energy difference between austenite and martensite phases responsible for MFIPT [5, 6]

In recent years, researchers have carried out a lot of notable research about MFIPT. In most of these studies, they have aimed to explain the MFIPT mechanism by determining the magnetic moment of the material during the field-induced structural phase transformation. In addition, various transition metal doping are made to improve the magnetic properties of Ni-Mn based alloys. In this study, it is desired to reach high magnetic moment value by adding Vanadium to the NiMnSn alloy system. The goals of the current study are (i) to investigate the magnetoresistance properties of vanadium (V) doped NiMnSn alloys and (ii) to determine the resistance variation due to the magnetic field change during MFIPT.

## 2. Experimental

$Ni_{49-x}V_xMn_{37}Sn_{12}B_2$  ( $x = 0, 1, 2, \text{ and } 3$ ) (at. %) ferromagnetic shape memory Heusler alloys were produced as ingots form by arc-melting furnace using pure Ni, V, Mn, Sn and B (purities higher than 99.99%) powders. The melting process was carried out by creating plasma in an argon atmosphere and flowing a current of  $\sim 150$  A throughout the samples. In order to obtain homogeneous samples, the melting process was repeated several times by turning the samples. The fabricated samples were heat treated at  $900$  °C for 48 h to ensure homogenization, and then quenched in ice-water. To prevent the oxidation during heat treatment, the samples were placed in the vacuumed quartz tube. The samples were marked as V0 ( $x=0$ ), V1 ( $x=1$ ), V2 ( $x=2$ ) and V3 ( $x=3$ ), respectively. The crystal structures at room temperature (RT) were determined with the “Rigaku Miniflex

600” computer-controlled X-ray diffractometer using CuK $\alpha$  ( $\lambda=1.5405 \text{ \AA}$ ) radiation. The electrical resistivity measurements were performed with the AC Transport attachment of the Quantum Design PPMS device. Martensitic transformation temperatures were determined by means of temperature-dependent resistivity measurements. Then, magnetoresistivity measurements were carried out at different temperatures determined between the austenite start ( $A_s$ ) and austenite finish ( $A_f$ ) temperatures of each sample. It should be noted that the temperature was kept constant during these measurements and the samples were cooled until they completely transform to the martensite phase before each measurement. Magnetic field-dependent magnetization (M-H) curves were determined by the vibrating sample magnetometer (VSM) with using the same thermal process.

### 3. Results and Discussions

As discussed above, a first-order structural phase transition occurs between the austenite and martensite phases during MT. While the austenite phase usually has a cubic  $L2_1$  crystal structure, the martensite phase may have monoclinic  $10M$  and  $14M$ , orthorhombic  $4O$  or unmodulated double tetragonal  $L1_0$  crystal structures depending on the composition and temperature [8–11]. XRD patterns of the V0, V1, V2 and V3 samples at RT are shown in Fig. 1. Peaks of monoclinic  $10M$  and orthorhombic  $4O$  crystal structures were obtained in the V0 sample, whereas no peaks from the cubic structure were detected. Based on this result, it can be expected that the sample in the martensite phase at RT. In addition to the peaks of  $10M$  and  $4O$ , the V1 sample has cubic (220) peaks due to the presence of the austenite phase. Except for the cubic (220), (222), (400) and (422) peaks, only the (221) peak of the  $4O$  phase was observed in the V2 sample. Therefore, it can be expected that the ratio of the austenite phase in the V2 sample at room temperature is higher than in the V1 sample. The detection of only the peaks of the cubic structure in the V3 sample shows that the sample is completely in the austenite phase at RT. The lattice parameters of all samples refined by the least-squares method and the final compositions of the samples analyzed by the Energy Dispersive X-Ray Analysis(EDX) method were listed in Table 1.

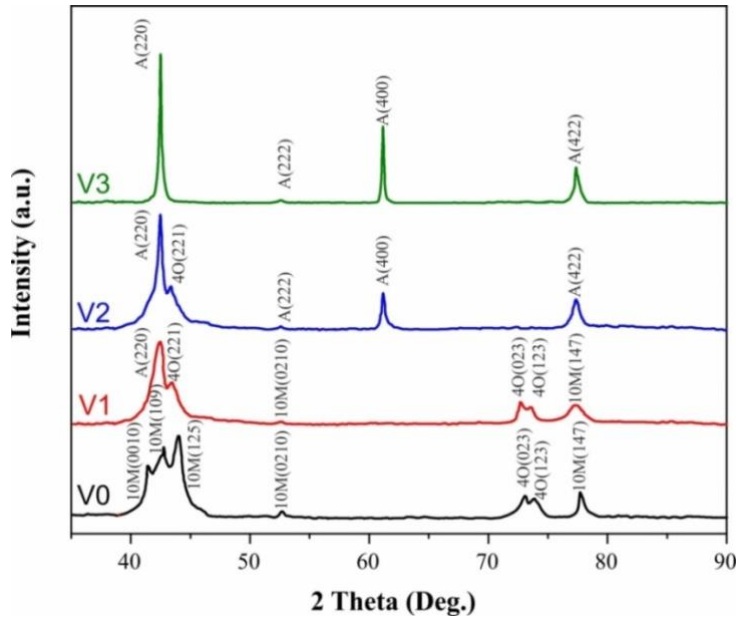


**Figure 2.** XRD patterns of V0, V1, V2 and V3 samples at room temperature

**Table 1.** Crystal structures, lattice parameters and final composition (determined by EDX) at RT of the V0, V1, V2 and V3 samples.

Sample	Nominal composition (at. %)	Final composition (at. %)	Crystal structure	Lattice parameters		
				a(nm)	b(nm)	c(nm)
V0	Ni <sub>49</sub> Mn <sub>37</sub> Sn <sub>12</sub> B <sub>2</sub>	Ni <sub>49.2</sub> Mn <sub>36.1</sub> Sn <sub>14.7</sub> +B <sub>y</sub>	10M	0.4337	0.5660	2.1968
			4O	0.4431	0.5702	0.8795
V1	Ni <sub>48</sub> V <sub>1</sub> Mn <sub>37</sub> Sn <sub>12</sub> B <sub>2</sub>	Ni <sub>48.1</sub> V <sub>1.2</sub> Mn <sub>36.3</sub> Sn <sub>14.4</sub> +B <sub>y</sub>	4O	0.4424	0.5693	0.8786
			L <sub>21</sub>	0.6014	0.6014	0.6014
V2	Ni <sub>47</sub> V <sub>2</sub> Mn <sub>37</sub> Sn <sub>12</sub> B <sub>2</sub>	Ni <sub>47.1</sub> V <sub>2.1</sub> Mn <sub>36.2</sub> Sn <sub>14.6</sub> +B <sub>y</sub>	L <sub>21</sub>	0.6011	0.6011	0.6011
V3	Ni <sub>46</sub> V <sub>3</sub> Mn <sub>37</sub> Sn <sub>12</sub> B <sub>2</sub>	Ni <sub>46.0</sub> V <sub>3.6</sub> Mn <sub>36.4</sub> Sn <sub>14.0</sub> +B <sub>y</sub>	L <sub>21</sub>	0.6010	0.6010	0.6010

Since Heusler alloys are one of the rare examples of ferromagnetic alloys whose resistance exceeds the critical Mooij value, investigation of their magneto-transport properties provides interesting results [12]. According to Mooij's rule, the resistivity should decrease with increasing temperature when the resistivity of the alloy exceeds  $150\mu\Omega\text{cm}$ , regardless of the scattering mechanism of the charge carriers. The resistivity of Heusler alloys is can suitable to this rule, while it can be similar to metallic behavior, depending on the composition of the alloy [13–16].

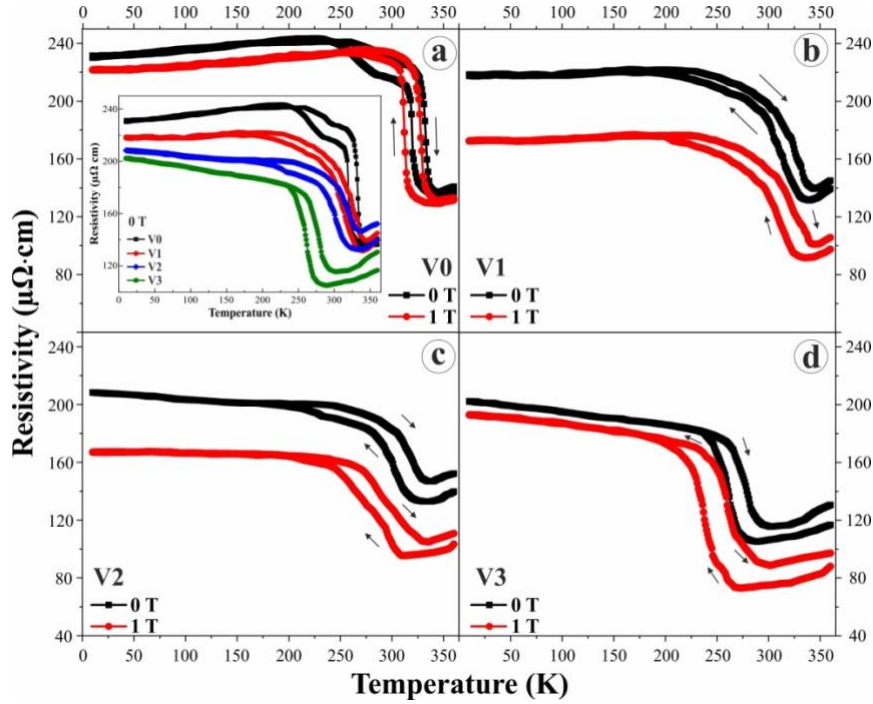


**Figure 3.**  $\rho$ -T curves of (a)V0, (b)V1, (c)V2 and (d)V2 at 0T and 1T

The resistivity vs temperature curves of  $\text{Ni}_{49-x}\text{V}_x\text{Mn}_{37}\text{Sn}_{12}\text{B}_2$  ( $x = 0, 1, 2,$  and  $3$ ) alloys are given in Figure 3. Resistivity measurements were performed both without a magnetic field and under 1 T external magnetic field. One of the ways to the characterization of martensitic transformation is the sudden resistance changes obtained in the temperature-dependent resistance curve. The abrupt changes due to MT have been clearly detected in the resistivity curves of all samples. This jumplike difference between the resistances of martensite and austenite phases can originate owing to two reasons. (i) A sudden change in the density of states at the fermi energy level (ii) a change in the order parameter of the crystal structure. In the studies carried out to calculate the normal hall effect coefficient, no jump in the state density of the fermi energy level was observed around the martensitic transformation temperature. Therefore, it can be expect that the dominant mechanism in the resistance change during MT is the variation in the structural order parameter [17]. Evidently, both the phase transition temperatures (table 2) and the resistivity values (inset of Fig.3.a) decreased by increasing the amount of V. In addition, a more gradual phase transition was observed with increasing doping amount. It is clearly seen that especially in V0 and V1 samples, the temperature dependence of the martensite phase is relatively weak which is typical behavior of high resistivity metals. This is because scattering by phonons and magnetic heterogeneities is negligible and scattering originating from increasing disorder is more dominant in the scattering mechanism [17]. The resistivity of martensite phase of V0 and V1 samples, during cooling, firstly increased slightly and then started to decrease around 225 K and 175 K, respectively. The increase in resistivity in this temperature range ( $T < 225\text{K}$  for V0,  $T < 175\text{K}$  for V1) has been attributed to scattering by magnetic inhomogeneities [18]. The resistivity value in the martensite phase of V2 and V3 samples increased continuously with decreasing temperature in accordance with Mooij's rule.  $\rho$ -T measurements performed under an external magnetic field of 1 T revealed that both the phase transition temperature and the resistivity value decreased. The shift in phase transformation temperatures with application of a magnetic field is described by the Clausius-Clapeyron equation[19];

$$\frac{\Delta H}{\Delta T} = -\frac{Q}{T_M \Delta M}, \quad \Delta S = -\frac{Q}{T_M} \quad (1)$$

where Q indicates the evolved heat of transformation,  $T_M$  represents MT temperatures and  $\Delta M$  shows the magnetization difference between austenite and martensite phases.



**Table 2:** Martensite start ( $M_s$ ), martensite finish ( $M_f$ ), austenite start ( $A_s$ ) and austenite finish ( $A_f$ ), of the V0, V1, V2 and V3 samples.

Sample	Mag. Field	$M_s$ (K)	$M_f$ (K)	$A_s$ (K)	$A_f$ (K)
V0	0 T	325.5	307.6	325.0	342.1
	1 T	315.8	304.3	320.1	333.0
V1	0 T	324.5	276.8	295.0	340.5
	1 T	316.9	271.9	291.2	332.4
V2	0 T	319.6	274.1	292.9	331.4
	1 T	307.8	236.6	262.8	324.5
V3	0 T	276.8	249.5	262.9	291.8
	1 T	250.5	225.3	245.7	274.1

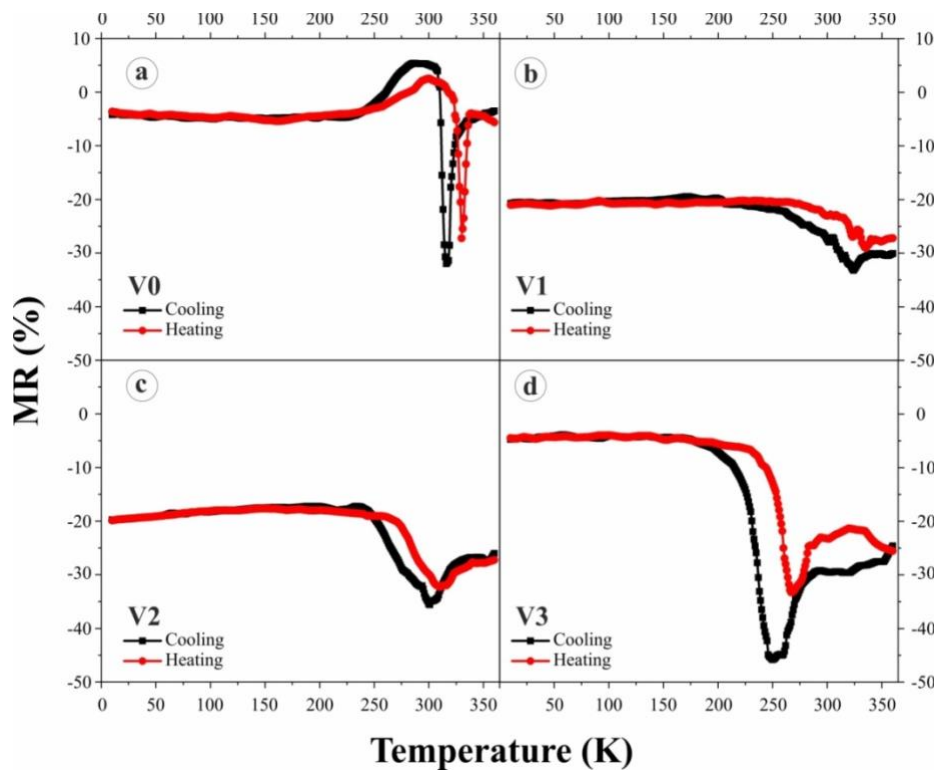


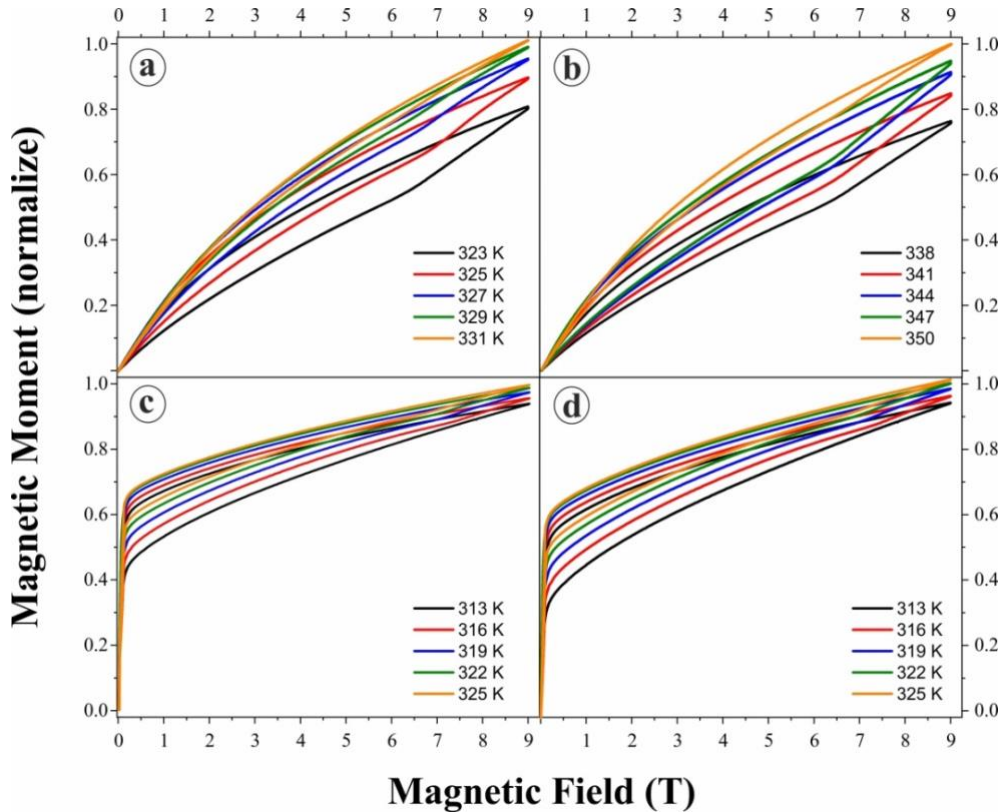
**Figure 4.** Magnetoresistivity curves of (a)V0, (b)V1, (c)V2 and (d)V2 during cooling and heating  
Figure 4 shows temperature dependence magnetoresistivity (MR) in the magnetic field of 1 T which is calculated from;

$$MR(\%) = \frac{[\rho(H) - \rho(0)]}{\rho(H)} 100(\%) \quad (2)$$

equation. MR has a negative value for all alloys. The negative MR generated by the application of the magnetic field in ferromagnetic materials was explained by Kataoka using the s-d model. This model is based on the principle that s-conduction electrons are scattered by localized d spins. In addition, the MR increased with increasing V doping and the highest MR values in the magnetic field of 1 T are -31.7%, -33.2%, -35.2% and -45.6%, respectively. The resistivity of the martensite phase increases because of scattering from various orientations of the twin boundaries and residual resistivity. With the application of the magnetic field, the MT temperature shifts to a lower temperature. Also, the structural transition to the martensite phase, which has the lower symmetry, is accompanied by modulation, which increases the scattering of conduction electrons. Coexistence of all these effects leads to higher negative MR [20, 21]. Moreover, MR values obtained in the cooling process

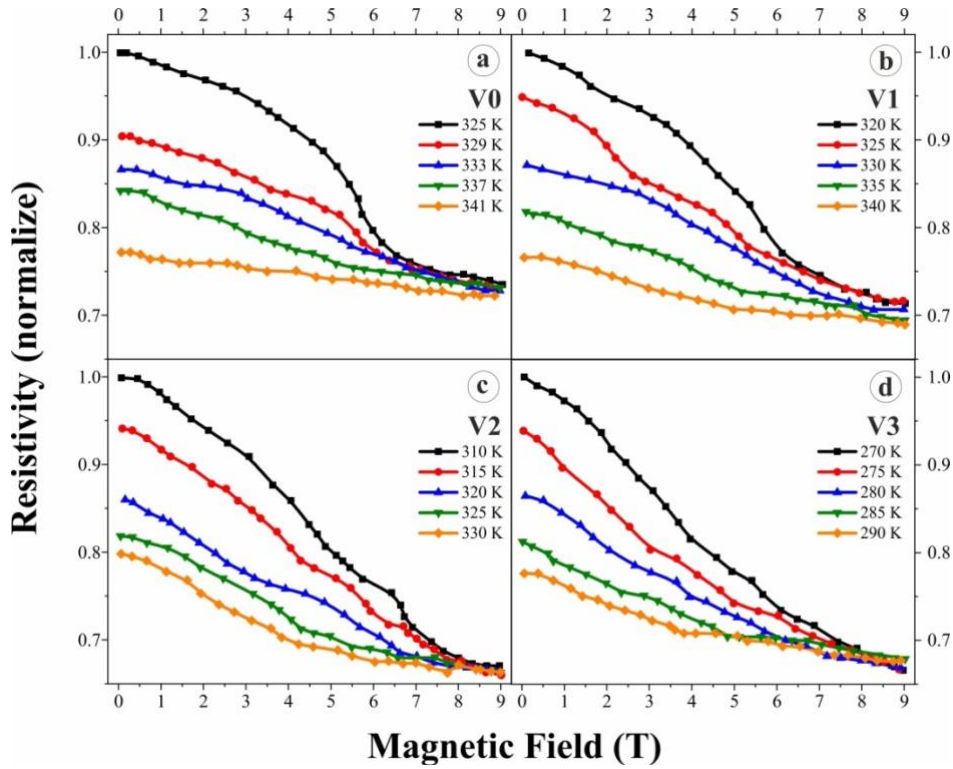
are higher than in the heating process. The obtained MR values in the current study exhibit very successful results when compared with the literature [2, 22, 23].

Figure 5 shows the thermomagnetization curves at 5 different temperatures in the  $A_s$ - $A_f$  range determined from Table 2 for each sample. Before each measurement, the samples were cooled until they were completely transformed into the martensite phase. Metamagnetic behavior attributed to magnetic field-induced structural transformation was detected in all samples. Martensite and austenite phases coexist in the  $A_s$ - $A_f$  range and with increasing temperature, the martensite ratio decreases while the austenite ratio increases. With the application of a magnetic field to the sample in this temperature region, the magnetization of the austenite phase, which has stronger ferromagnetic interactions, increases suddenly, whereas the magnetization of the weak magnetic martensite phase increases more slowly. Simultaneously, structural transformation occurs from martensite to the austenite phase with the rising magnetic field. When a critical magnetic field level is reached, the sample completely transforms into the austenite phase and after that, the sample remains in the austenite phase even if the magnetic field is reduced. Consequently, a hysteresis occurs between the curves obtained by increasing and decreasing the magnetic field. The hysteresis as a result of metamagnetic behavior have been provide clear evidence for MFIPT [23–29].



**Figure 5.** (color online) M-H curves of (a)V0, (b)V1, (c)V2 and (d)V2 at different temperatures determined in the range of  $A_s$  and  $A_f$

In order to determine the change in electrical resistance during MFIPT, the same thermal process as the thermomagnetization analyzes was applied, and resistance measurements depending on the magnetic field were carried out. The results are given in figure 6. It should be noted that each measurement was carried out at a constant temperature and beforehand the samples were cooled until they transform into the martensite phase. In these measurements carried out at a constant temperature, it is clearly seen that the resistivity decreases as the temperature increases when focusing on the resistivity values at 0 T magnetic field. This is the opposite of what is expected from the metallic behavior and it is owing to the higher proportion of the martensite phase, which has higher resistivity, at low temperatures. The resistivity decreased with increasing magnetic field and the curves overlapped at approximately 8-9 T magnetic field. The negative magnetoresistance behavior of ferromagnetic Heusler alloys was discussed above. Although the decrease in resistivity with an increasing magnetic field can be partially explained by the MR effect, MR is insufficient to explaining the difference between the resistance values at 0 T and the overlapping of the curves at the high magnetic field. The transition from the higher resistive martensite phase to the lower resistive austenite phase can explain the reduction in resistivity with an increasing magnetic field. Moreover, the structural transformation can account for the overlapping of the curves in a high magnetic field. Therefore, it can be anticipated that the resistivity behavior depending on the magnetic field from Figure 6 is a result of the structural phase transformation as well as the MR. Additionally, these results are in accordance with the M-H curves shown in Fig. 5.



**Figure 6.**  $\rho$ -H curves of (a)V0, (b)V1, (c)V2 and (d)V2 at different temperatures determined in the range of  $A_s$  and  $A_f$

#### 4. Conclusion

In the present study, the structural and electrical properties of  $Ni_{49-x}V_xMn_{37}Sn_{12}B_2$  ( $x = 0, 1, 2, \text{ and } 3$ ) alloys produced by the arc melting were investigated in detail. XRD patterns showed that the V0 sample has the 4O and 10M structures coexist at RT. V1 has L2<sub>1</sub> cubic structure in addition to 4O and 10M. The martensite content decreased in the V2 sample and only cubic L2<sub>1</sub> structure was detected in the V3. The all samples exhibited martensitic transformation around RT. The phase transition temperature and electrical resistivity value decreased with doping. MT temperatures shifted to lower temperatures by applying an external magnetic field, which the Clausius-Clapeyron equation explains. The magnetoresistivity was calculated using equation 2 and it was determined that increasing the magnetic field decreases the resistivity. It was confirmed that the samples exhibited MFIPT by M-H measurements performed at the determined constant temperatures in the  $A_s$ - $A_f$  interval. Electrical resistivity analyzes were carried out during MFIPT using the same thermal process as the M-H measurements. In the measurements made at different temperatures, the resistivity decreased with increasing magnetic field and the curves overlapped in the high field. These obtained curves reveal the variation characteristic of electrical resistance during MFIPT.

#### References

- [1] Pérez-Landazábal JI, Recarte V, Sánchez-Alarcos V, Gómez-Polo, C, Kustov S, Cesari E. Magnetic field induced martensitic transformation linked to the arrested austenite in a Ni-Mn-In-Co shape memory alloy. *J Appl Phys* 2011; 109(9), 093515-093521.
- [2] Han ZD, Wang DH, Zhang CL, Xuan HC, Zhang JR, Gu BX, Du YW. The phase transitions, magnetocaloric effect, and magnetoresistance in Co doped Ni-Mn-Sb ferromagnetic shape memory alloys. *J Appl Phy* 2008; 104(5), 053906-0539012.
- [3] Desroches R, Smith B. Shape memory alloys in seismic resistant design and retrofit: A critical review of their potential and limitations. *J Earthq Eng* 2004; 8, 415-429.
- [4] Kirat G. Exchange Bias Effect in NiMnSbB Ferromagnetic Shape Memory Alloys Depending on Mn Content. *Adu J Sci* 2021; 11, 444-455.
- [5] Karaca HE, Karaman I, Basaran B, Lagoudas DC, Chumlyakov YI, Maier HJ. On the stress-assisted magnetic-field-induced phase transformation in Ni<sub>2</sub>MnGa ferromagnetic shape memory alloys. *Acta Mater* 2007; 55, 4253-4269.

- [6] Karaca HE, Karaman I, Basaran B, Ren Y, Chumlyakov I, Maier HJ. Magnetic Field-Induced Phase Transformation in NiMnCoIn Magnetic Shape-Memory Alloys — A New Actuation Mechanism with Large Work Output. *Adv Funct Mater* 2009; 19, 983–998.
- [7] Zhang H, Zhang X, Qian M, Yao Z, Wei L, Geng L. Increasing working temperature span in Ni-Mn-Sn-Co alloys via introducing pores. *J Magn Magn Mater* 2000; 500, 166359-166362.
- [8] Zheng H, Wang W, Xue S, Zhai Q, Frenzel J, Luo Z. Composition-dependent crystal structure and martensitic transformation in Heusler Ni-Mn-Sn alloys, *Acta Mater* 2013; 61, 4648–4656.
- [9] Kirat G, Aksan MA. Influence of the Cu substitution on magnetic properties of Ni–Mn–Sn–B shape memory ribbons. *Appl Phys A-Mater* 2021; 127, 1–9.
- [10] Pons J, Chernenko VA, Santamarta R, Cesari E. Crystal structure of martensitic phases in Ni-Mn-Ga shape memory alloys, *Acta Mater* 2000; 48, 3027–3038.
- [11] Deltell A, Escoda L, Saurina J, Suñol J. Martensitic Transformation in Ni-Mn-Sn-Co Heusler Alloys. *Metals* 2015; 5, 695–705.
- [12] Titov IS, Zhukov AP, Gonzalez J, Kazakov AP, Dubenko IS, Granovskii AB, Pathak AK, Perov NS, Prudnikov VN, Ali N. Hall effect in a martensitic transformation in Ni-Co-Mn-In Heusler alloys. *JETP Lett* 2011, 92, 666–670.
- [13] Guha S, Datta S, Panda SK, Kar M. Critical Behavior and Magnetocaloric Effect in Co<sub>2</sub>CrAl Heusler Alloy. *Physica Status Solidi (B): Basic Res* 2022; 259, 2100533-2100541.
- [14] Blinov M, Aryal A, Pandey S, Dubenko I, Talapatra S, Prudnikov V, Lähderanta E, Stadler S, Buchelnikov V, Sokolovskiy V, Zagrebin M, Granovsky A, Ali N. Effects of magnetic and structural phase transitions on the normal and anomalous Hall effects in Ni-Mn-In-B Heusler alloys. *Phys Rev B* 2020; 101, 94423-94429.
- [15] Pandey S, Blinov M, Aryal A, Dubenko I, Prudnikov V, Lähderanta E, Granovsky A, Kazachkova N, Stadler S, Ali N. Drastic violation of the basic correlation between the Hall effect and resistivity in the Heusler alloy Ni<sub>45</sub>Cr<sub>5</sub>Mn<sub>37</sub>In<sub>13</sub>. *J Magn Magn Mater* 2019; 481, 25–28.
- [16] Sivaprakash P, Arumugam S, Esakki Muthu S, Raj Kumar DM, Saravanan C, Rama Rao NV, Uwatoko Y, Thiyagarajan R. Correlation of magnetocaloric effect through magnetic and electrical resistivity on Si doped Ni–Mn–In Heusler melt spun ribbon. *Intermetal* 2021; 137, 107285-107293.
- [17] Zhukov AP, Prudnikov VN, Dubenko IS, Granovskii AB, Kazakov AP. Determination of the normal and anomalous hall effect coefficients in ferromagnetic Ni<sub>50</sub>Mn<sub>35</sub>In<sub>15-x</sub>Si<sub>x</sub> Heusler alloys at the martensitic transformation. *J Exp Theor Phys+* 2012; 115, 805–814.
- [18] Prudnikov VN, Kazakov AP, Titov IS, Perov NS, Granovskii AB, Dubenko IS, Pathak AK, Ali N, Zhukov AP, Gonzalez J. Hall effect in a martensitic transformation in Ni-Co-Mn-In Heusler alloys. *JETP Lett* 2010; 92, 666–670.
- [19] Pasquale M, Sasso CP, Lewis LH, Giudici L, Lograsso T, Schlagel D, Magnetostructural transition and magnetocaloric effect in Ni<sub>55</sub>Mn<sub>20</sub>Ga<sub>25</sub> single crystals. *Phys Rev B* 2005; 72, 1–5.
- [20] Singh S, Biswas C. Magnetoresistance origin in martensitic and austenitic phases of Ni<sub>2</sub>Mn<sub>1+x</sub>Sn<sub>1-x</sub>, *Appl Phys Lett* 2021; 98, 212101-212104.
- [21] Biswas C, Rawat R, Barman SR. Large negative magnetoresistance in a ferromagnetic shape memory alloy: Ni<sub>2+x</sub>Mn<sub>1-x</sub>Ga. *Appl Phys Lett* 2005; 86, 1–3.
- [22] Xuan HC, Zheng YX, Ma SC, Cao QQ, Wang DH, Du YW. The martensitic transformation, magnetocaloric effect, and magnetoresistance in high-Mn content Mn<sub>47+x</sub>Ni<sub>43-x</sub>Sn<sub>10</sub> ferromagnetic shape memory alloys. *J Appl Phys* 2010; 108, 1–5.
- [23] Kirat G, Kizilaslan O, Aksan MA. Magnetoresistance properties of magnetic Ni-Mn-Sn-B shape memory ribbons and magnetic field sensor aspects operating at room temperature. *J Magn Magn Mater.* 2019; 477, 366–371.
- [24] Kirat G, Aksan MA, Aydogdu Y. Magnetic field induced martensitic transition in Fe doped Ni-Mn-Sn-B shape memory ribbons. *Intermetall* 2019; 111, 106493-106503.
- [25] Sakon T, Sasaki K, Numakura D, Abe M, Nojiri H, Adachi Y, Kanomata T. Magnetic Field-Induced Transition in Co-Doped Ni<sub>41</sub>Co<sub>9</sub>Mn<sub>31.5</sub>Ga<sub>18.5</sub> Heusler Alloy. *Mater Trans* 2013; 54, 9-13.
- [26] Kainuma R, Imano Y, Ito W, Sutou Y, Morito H, Okamoto S, Kitakami O, Oikawa K, Fujita A, Kanomata T, Ishida K. Magnetic-field-induced shape recovery by reverse phase transformation. *Nature* 2006; 439, 957–960.
- [27] Liu J, Scheerbaum N, Hinz D, Gutfleisch O. Magnetostructural transformation in Ni-Mn-In-Co ribbons. *Appl Phys Lett* 2008; 92, 35–38.
- [28] Chen Z, Cong D, Li S, Zhang Y, Li S, Cao Y, Li S, Song C, Ren Y, Wang Y. External-field-induced phase transformation and associated properties in a Ni<sub>50</sub>Mn<sub>34</sub>Fe<sub>3</sub>In<sub>13</sub> metamagnetic shape memory wire. *Metals* 2021; 11, 1–14.
- [29] Brown PJ, Gandy AP, Ishida K, Kainuma R, Kanomata T, Neumann KU, Oikawa K, Ouladdiaf B, Ziebeck KRA. The magnetic and structural properties of the magnetic shape memory compound Ni<sub>2</sub>Mn<sub>1.44</sub>Sn<sub>0.56</sub>. *J Phys-Condens Mat* 2006; 18, 2249–2259.

## An NCA-based Hybrid CNN Model for Classification of Alzheimer's Disease on Grad-CAM-enhanced Brain MRI Images

Feyza ALTUNBEY ÖZBAY<sup>1\*</sup>, Erdal ÖZBAY<sup>2</sup>

<sup>1</sup> Software Engineering Department, Faculty of Engineering, Firat University, 23119, Elazığ, Türkiye

<sup>2</sup> Computer Engineering Department, Faculty of Engineering, Firat University, 23119, Elazığ, Türkiye

\*<sup>1</sup> [faltunbey@firat.edu.tr](mailto:faltunbey@firat.edu.tr), <sup>2</sup> [erdalozbay@firat.edu.tr](mailto:erdalozbay@firat.edu.tr)

(Geliş/Received: 30/11/2022;

Kabul/Accepted: 06/01/2023)

**Abstract:** Alzheimer's, one of the most prevalent varieties of dementia, is a fatal neurological disease for which there is presently no known cure. Early diagnosis of such diseases and classification with computer-aided systems are of great importance in determining the most appropriate treatment. Imaging the soft tissue of the brain with Magnetic Resonance Imaging (MRI) and revealing specific findings is the most effective method of Alzheimer's diagnosis. A few recent studies using Deep Learning (DL) to diagnose Alzheimer's Disease (AD) with brain MRI scans have shown promising results. However, the fundamental issue with DL architectures like CNN is the amount of training data that is required. In this study, a hybrid CNN method based on Neighborhood Component Analysis (NCA) is proposed, which aims to classify AD over brain MRI with Machine Learning (ML) algorithms. According to the classification results, DenseNet201, EfficientNet-B0, and AlexNet pre-trained CNN architectures, which are 3 architectures that give the best results as feature extractors, were used as hybrids among 10 different DL architectures. By means of these CNN architectures, the features trained on the dataset and the features obtained by Gradient-weighted Class Activation Mapping (Grad-CAM) are concatenated. The NCA method has been used to optimize all concatenated features. After the stage, the optimized features have been classified with KNN, Ensemble, and SVM algorithms. The proposed hybrid model achieved 99.83% accuracy, 99.88% sensitivity, 99.92% specificity, 99.83% precision, 99.85% F1-measure, and 99.78% Matthews Correlation Coefficient (MCC) results using the Ensemble classifier for the 4-class classification of AD.

**Key words:** Classification, Alzheimer's disease, Grad-CAM, MRI, NCA.

### Grad-CAM ile İyileştirilmiş Beyin MRI Görüntülerinde Alzheimer Hastalığının Sınıflandırılması için NCA tabanlı Hibrit CNN Modeli

**Öz:** Demansın en yaygın türlerinden biri olan Alzheimer, şu anda bilinen bir tedavisi olmayan ölümcül bir nörolojik hastalıktır. Bu tür hastalıkların erken teşhisi ve bilgisayar destekli sistemlerle sınıflandırılması en uygun tedavinin belirlenmesinde büyük önem taşımaktadır. Manyetik Rezonans Görüntüleme (MRI) ile beyin yumuşak dokusunun görüntülenmesi ve spesifik bulguların ortaya çıkarılması Alzheimer teşhisinde en etkili yöntemdir. Beyin MRI taramaları ile Alzheimer Hastalığını (AD) teşhis etmek için Derin Öğrenmeyi (DL) kullanan birkaç yeni çalışma umut verici sonuçlar vermiştir. Ancak, CNN gibi DL mimarileriyle ilgili temel sorun, gereken eğitim verisi miktarıdır. Bu çalışmada, Makine Öğrenimi (ML) algoritmaları ile beyin MRI üzerinden AD'yi sınıflandırmayı amaçlayan Komşuluk Bileşen Analizi (NCA) tabanlı hibrit bir CNN yöntemi önerilmiştir. Sınıflandırma sonuçlarına göre, özellik çıkarıcı olarak en iyi sonuçları veren 3 mimari olan DenseNet201, EfficientNet-B0 ve AlexNet ön-egitimli CNN mimarileri, 10 farklı DL mimarisi arasından hibrit olarak kullanılmıştır. Bu CNN mimarileri sayesinde, veri seti üzerinde eğitilen öznetelikler ile Gradient-weighted Class Activation Mapping (Grad-CAM) ile elde edilen öznetelikler birleştirilmiştir. NCA yöntemi, tüm birleştirilmiş özellikleri optimize etmek için kullanılmıştır. Bu aşamadan sonra optimize edilen öznetelikler KNN, Ensemble ve SVM algoritmaları ile sınıflandırılmıştır. Önerilen hibrit model, AD'nin 4-sınıflı sınıflandırması için Ensemble sınıflandırıcısını kullanarak %99,83 doğruluk, %99,88 duyarlılık, %99,92 özgüllük, %99,83 kesinlik, %99,85 F1-ölçütü ve %99,78 Matthews Korelasyon Katsayısı (MCC) sonuçlarına ulaşmıştır.

**Anahtar kelimeler:** Sınıflandırma, Alzheimer hastalığı, Grad-CAM, MRI, NCA.

#### 1. Introduction

Dementia, which is frequently encountered especially in the elderly population, is a general name given to many diseases in which forgetfulness is at the forefront and may occur due to different diseases. Alzheimer's disease (AD) consists of an average of 70% of dementia cases [1]. There is presently no cure for the neurodegenerative disease Alzheimer's, one of the most prevalent types of dementia, which results in the loss of brain cells and a decline in mental abilities [2]. As people age, signs of this disease, which impairs cognition,

\* Corresponding author: [faltunbey@firat.edu.tr](mailto:faltunbey@firat.edu.tr). ORCID Number of authors: <sup>1</sup> 0000-0003-0629-6888, <sup>2</sup> 0000-0002-9004-4802

memory, and behavioral abilities, become more pronounced [3]. Due to the fact that it is a progressive disease, early symptoms of Alzheimer’s are usually seen as forgetting recent events, but within a few years, individuals may have difficulty performing their daily activities alone [4].

By 2050, it is anticipated that there would be almost twice as many cases of different types of dementia [5]. Since there is no definitive treatment that stops or slows the progression of the disease, it is vital to provide a solid diagnosis with accurate methods [6]. A brain biopsy is required for definitive diagnosis, but this method is not preferred because it is an invasive procedure [7]. In this regard, Magnetic Resonance Imaging (MRI) is widely used to analyze clinical and neuroimaging findings since it offers more insightful data on cerebral cortical atrophy, even though Computed Tomography (CT) may be favored for illness diagnosis. Since MRI reveals the involvement caused by the loss of volume in some parts of the brain of sick people, it can diagnose the disease at a rate of 90%. However, the inability to detect this volume loss at the onset of AD may lead to underdiagnosis and overlook of the disease [8].

Brain imaging findings are used to analyze the degree of AD in clinically evaluated patients while focusing on features such as medial temporoparietal and temporal lobe atrophy [9]. The volume of the hippocampus, entorhinal cortex (inferior surface of the parahippocampal gyrus), cingulate gyrus, and parietal lobe decreases with medial temporal lobe atrophy, but the parahippocampal fissure enlarges [10]. Early symptoms include parietal atrophy and enlargement of the parietooccipital and posterior cingulate sulcus. As a result, the precuneus’ volume increases [11].

Some medical tests are performed for the diagnosis of AD, which results in a large amount of variable heterogeneous data. Due to the nature of these tests, manually analyzing data can be tiring. It is possible for radiologists to make mistakes when interpreting radiological images. In this case, misdiagnosis and treatment of patients become inevitable [12]. Machine Learning (ML) and Deep Learning (DL) applications minimize the occurrence of such errors in medical imaging and especially Computer-Aided Diagnosis (CAD) and allow doctors to increase their experience by easing the workload [13].

Today, deep CNN approaches attract the attention of researchers in the field of computer vision due to their performance in applications such as recognition, detection, classification, and segmentation. In these applications, besides determining the presence or absence of a disease, classification of diseases can also be performed [14]. Feature extraction and visualization in DL applications are important steps that determine the effectiveness of the CAD method. Different features are revealed by texture analysis in images. However, these features alone may be insufficient to determine the accuracy of the model. CNN models are capable of extracting features in a hierarchical fashion, from low to high [15].

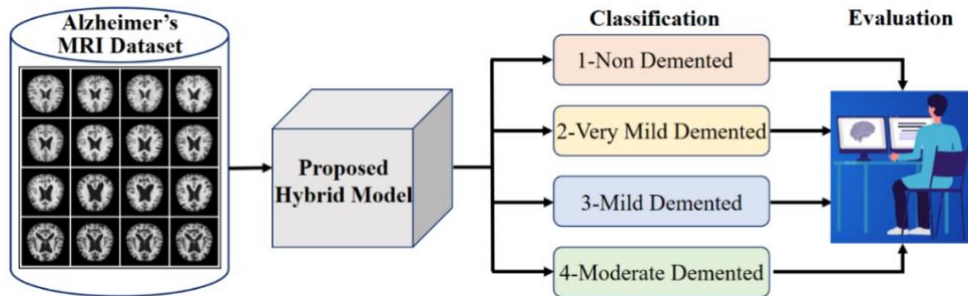


**Figure 1.** The workflow of the proposed hybrid model

This study aimed to classify the diagnosis of AD according to the stage of dementia, which is a challenging task for specialists since the pixel intensities of the brain MRI images of individuals can be similar. In this respect, brain MRI images were classified with a hybrid model based on DL. Firstly, the features extracted with 10 different CNN architectures were classified with 3 different classifiers. The results obtained here were evaluated comparatively and a hybrid model was created by combining the features obtained from the 3 architectures that gave the highest results using these 10 architectures, and the features obtained using Gradient-weighted Class Activation Mapping (Grad-CAM), a method that reveals distinctive texture features. Then, the best features were selected among the features with the Neighborhood Component Analysis (NCA) method, and these features were classified by KNN, Ensemble, and SVM classifiers. While 98.3% accuracy was achieved with the DenseNet201 + Ensemble model, 97.9% accuracy was achieved with the EfficientNet-B0 + Ensemble model, and 97.1% accuracy was achieved with the AlexNet + Ensemble model, and 99.83% accuracy was achieved with the proposed hybrid model + Ensemble. The workflow of the proposed hybrid model is shown in Fig 1. Unintentional manual

errors can be prevented by reducing the workload of doctors with the proposed method in the diagnosis of AD. Moreover, this method eliminates the need for specialists for preliminary diagnosis.

The significant contributions of this study are as follows:

- We propose a deep CNN that can classify 4-classes of disease stages in AD.
- The proposed hybrid model demonstrates superior performance for AD diagnosis from an imbalanced dataset and a small number of features.
- The manual feature extraction task of radiologists is eliminated with the developed hybrid CNN model.

The highlights of this study are as follows:

- 4-class brain MRI images are classified using 10 CNN architectures.
- The model proposed in this study aims to improve classification performance in AD diagnosis.
- Different feature maps of the 3 best CNN architectures are concatenated with Grad-CAM features.
- Thanks to this method, different features of the same images obtained in three different architectures are brought together.
- NCA dimension reduction is applied to the feature map to improve model performance.
- Obtained feature map is classified over 3 different ML classifiers.
- High-accuracy classification has been made for 4-class dementia stages of AD.
- As a result, in the proposed method, feature extraction, feature combining, dimension reduction and classification of the obtained feature map in three different classifiers were performed.

The rest of the article is as follows: Section 2 covers related works in the field of diagnosis of AD. A full description of the proposed methodology is given in section 3. The experimental results obtained from our proposed hybrid CNN model and their comparison with existing methods are given in section 4. In section 5, the proposed method is thoroughly explored and contrasted with existing studies in the literature. Finally, section 6 describes the final result emphasizing the developed method.

## 2. Related Works

In this section, information about the current studies in the literature closest to the method proposed in our article for the detection of AD is given.

Hemant et al. proposed two new neural networks, Modified Counter Propagation Neural Network (MCPN) and Modified Kohonen Neural Network (MKNN), to achieve a high convergence rate and accuracy. Changes have been made to the training methodologies of traditional CPN and Kohonen networks for the design of these networks. They used a dataset of 540 MRI images to evaluate the performance of the proposed method. When the test results were examined, it was seen that the two proposed new methods, MKNN and MCPN, were 95% and 98% accurate, respectively [16].

Liu et al. used Densenet as a model for the Alzheimer's dataset, which consists of three classes. Softmax was employed as the classification layer in this investigation, and the accuracy rate was 88.9% [17].

Ahmed et al. used visual features from the hippocampal area, the region most affected by AD, to automatically classify AD from MRI images. Using Circulars Harmonic Functions from the hippocampal region, they extracted two types of features: visual local identifiers and the amount of BOS pixels in this area. In addition, a late fusion was used to achieve successful results. They used two datasets, ADNI and Bordeaux, to evaluate the effectiveness of their proposed method. In these two datasets, the accuracy values obtained for AD and Normal Control (NC) subjects are 87% and 85%. In the ADNI dataset, the accuracy values obtained for MCI vs. NC and MCI vs. AD were 78.22% and 72.23%, respectively, in subjects with Mild Cognitive Impairment (MCI) [18].

In this study, the gray matter section of T1-weighted MR images from cognitively normal older people with pathologically confirmed AD was classified using linear support vector machines [19].

In addition, Farooq et al. tested the performance of their proposed method for detecting AD with brain MRI images consisting of 4 classes. The researchers divided the MRI images in the dataset into 4 different groups in order to detect the disease more easily. They also applied some preprocessing to their data. Researchers used Googlenet, Resnet18, and Resnet152 architectures in their proposed method, and the highest accuracy rate was 98.88% with GoogleNet architecture [20].

Jongkreangkrai et al. combined the hippocampus and amygdala volumes and entorhinal cortex thickness in their proposed method to diagnose AD. Hippocampus, amygdala, and entorhinal cortex thickness in both cerebral hemispheres were measured using T1-weighted MR images of 100 Alzheimer's patients and 100 healthy individuals. Next, 5 different combinations of these features were used to compare the performance of the SVM algorithm for the classification of AD [21].

Moradi et al. proposed a two-step method for estimating conversion from mild cognitive impairment to AD from MRI images. In the first step of the method, they performed a feature selection process for the selection of Alzheimer's-related voxels in MRI images. They then used ML algorithms to predict the transition from mild cognitive impairment to AD [22].

In a different study, an automated-based method using 3D-CNN and SVM was proposed for AD. The researchers compared it with the 2D-CNN structure to test the effectiveness of the proposed method. An accuracy rate of 96.82% was obtained with this method for the automatic diagnosis of AD [23].

In a different study, the effect of measurements of cortical thickness on the detection of AD was investigated. For this purpose, the effectiveness of the suggested method was assessed on 19 patients and 17 healthy people [24].

Cheng et al. proposed a two-step Multi-Domain Transfer Learning method for AD. In the first step of the method, multi-domain transfer feature selection was made. In this step, the most relevant features for the diagnosis of AD were selected from the multi-domain data. In the second step of the method, they performed multi-domain transfer classification for the early diagnosis of AD. They evaluated the performance of their suggested technique using MRI images from 807 participants in the ADNI dataset [25].

Sarraf and Tofghi proposed a method using one of the CNN architectures, LeNet5, for AD using brain MRI. The accuracy value obtained with this method using cloud computing is 96.85% [26].

Billones et al. proposed a method using CNN for the detection of AD and MCI. In this method, they used 16-layer VGGNet. They obtained an accuracy of 91.85% from their method, which they tested on 20 randomly selected MRI images from each subject [27].

Khagi and Kwon proposed a CNN-based model for the diagnosis of AD. The researchers used brain MRI and PET images, consisting of 3 classes of 122 images, to test the effectiveness of their proposed method. This CNN-based method, which combines characteristic information, has an accuracy of 96% [28].

In a different study, a model combining sparse autoencoders and convolutional neural networks is proposed for the diagnosis of AD. In the proposed method, sparse autoencoders are first trained on randomly selected 3D brain MRI images. In this way, they learned filters for convolution operations. Then, a 3D CNN design was made with the learned filters [29]. Similarly, in a different study proposed for the diagnosis of AD, a 3D-CNN model that can learn AD-related features is proposed. This method is designed on a pre-trained 3D convolutional autoencoder. Researchers evaluated the effectiveness of the method in the ADNI and CADDementia datasets [30].

Alzheimer's was diagnosed in another study using SVM, IVM, and RELM algorithms on a 2-class MRI dataset [31]. The RELM algorithm gave better results than other algorithms with a 76.61% accuracy rate using 10 times cross-entropy. In this method proposed by Lama et al., the accuracy rates obtained with SVM and IVM algorithms are 75.33% and 60.2%, respectively.

Hon and Khan, on the other hand, proposed a model for Alzheimer's detection using VGG and Inception V4 architectures. They initialized these architectures using pre-trained weights from large benchmark datasets. Image entropy is used instead of randomly selecting training slices. The experimental evaluation of the proposed method was made on the OASIS dataset and the Inception V4 architecture achieved 96.25% accuracy [32].

Oh et al. proposed a method using autoencoder and 3D-CNN to detect AD. In the proposed method, data preprocessing (reorganization, normalization, smoothing), segmentation, and feature extraction steps are performed respectively. The researchers tested the performance of their proposed method on the ADNI dataset and obtained an accuracy value of 84.5% [33].

In their study, Eroglu et al. proposed a hybrid architecture using MRI in Darknet53, InceptionV3, and Resnet101 models to classify different levels of AD. In the proposed architecture, Alzheimer's brain MR images were classified with SVM and KNN classifiers, and they achieved 99.1% accuracy [34].

In comparison to other research in the literature, the hybrid model we proposed in this study produced better outcomes. The model we proposed allowed for the combination of various features of the same image by employing three different architectures as its foundation, extracting features, and merging these features. The developed model was then applied to create quicker and more successful results using the NCA approach. In order to determine which ML classifiers the proposed model would perform better in, three distinct classifiers were utilized.

### 3. Materials and Methods

This section describe the proposed hybrid model, analyzes the dataset of the study and Grad-CAM Heatmap visualization, the DL architectures used for feature extraction, and the NCA approach used for feature selection.



### 3.1. Proposed Hybrid Model

A combination of the best 3 architectures DenseNet201, EfficientNet-B0 and AlexNet architectures from 10 pre-trained CNN architectures was used for the proposed hybrid method. A total of 6400×3000 features were obtained, 1000 features from the FC layer of each architecture. In addition to the original dataset, feature extraction with these 3 architectures was also applied to the Grad-CAM visualization results that highlight the tissue features of each brain MR image. Then, this feature matrix with the size of 6400×6000 is reduced by the NCA feature selection method. While the feature numbers of the optimized features in this step remained the same, the total number of features was reduced to 400. Thus, the feature matrix of 6400×400 size, selected among the most ideal features, was classified separately in the ML classifiers KNN, Ensemble, and SVM. The workflow of this proposed hybrid model is illustrated in Fig 2.

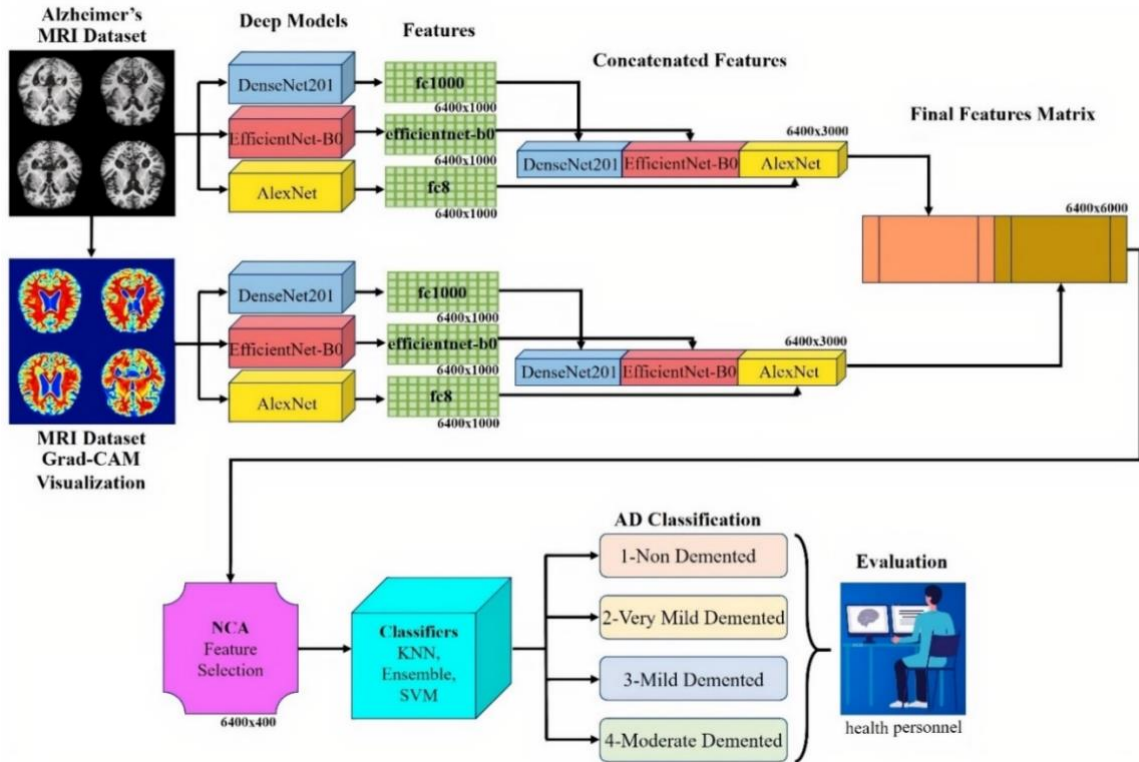


**Figure 2.** The flow chart of the proposed hybrid method

Using the proposed hybrid model, AD was classified in 4-levels in KNN, Ensemble, and SVM classifiers, and these images were presented to the expert.

### 3.2. Brain MRI Dataset Description

The dataset consists of 6400 brain MRI images in total, which were evaluated in 4 different stages of AD: Non Demented, Very Mild Demented, Mild Demented, and Moderate Demented. Data was collected from various web sources, each with a verified tag. The dataset is a publicly available dataset divided into two subfolders, test and train [35]. In Table 1, the data numbers for each folder are listed. The images in the dataset are in .jpg format. Since they are 8-bit deep, the images have been converted to 24-bit.

**Table 1.** Image counts of the brain MRI dataset

Dataset	Non Demented	Very Mild Demented	Mild Demented	Moderate Demented	Total
Train	2560	1792	717	52	5121
Test	640	448	179	12	1279
Total	3200	2240	896	64	6400

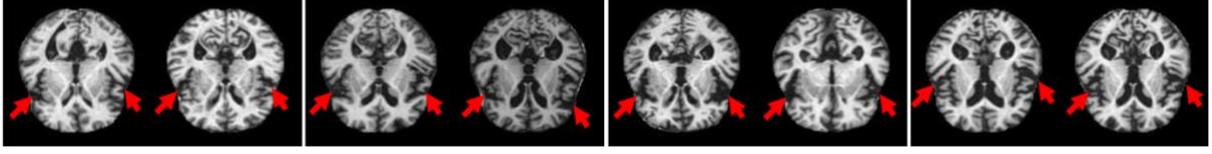


**Figure 3.** Samples of the brain MRI dataset

Fig 3 presents samples of the four classes in the dataset in groups of two. In the samples of the brain MRI dataset, atrophy of the temporal lobe of the brain and subarachnoid spaces are shown in groups of 2 at 4 stages with red arrows.

### 3.3. Grad-CAM Visualization

Grad-CAM is a well-liked method for displaying the search space of a CNN model. Grad-CAM can provide a unique visualization for each class that is present in the image because it is class-specific. Grad-CAM is the process of finding particular objects using a model that was trained using whole-image labels instead of explicit position annotations which can be used for weakly-supervised localization. Grad-CAM can be used to shed more light on a model's shortcomings, such as the reasons why a model failed [36].

The class activation mapping (CAM) method has been generalized as Grad-CAM. The gradients of the classification score with respect to the finished convolutional feature map are used in the Grad-CAM interpretability technique. The portions of a picture that have a significant value on the Grad-CAM map are those that have the most effects on the network score for that class [37].

The pioneering innovations of Grad-CAM and the main advantages of using it for this study are listed as follows:

- Based on a specified input image, a trained CNN, and a selected class of interest, Grad-CAM is a popular method for producing a class-specific Heatmap.
- Grad-CAM can be computed on any CNN architecture as long as the layers are differentiable.
- Weakly supervised segmentation and localization have both been accomplished using Grad-CAM.

Deeper representations in a CNN are said to capture higher-level visual structures, according to a number of earlier works [38]. Grad-CAM assigns appropriate values to each neuron for a given decision of interest using the gradient data entering the last convolutional layer of the CNN [39]. Our method combines feature maps from several DL architectures with results from Grad-CAM in order to explain output layer decisions.

According to task-specific computations of Grad-CAM as given in Eq. 1. First of all, the gradient of the score for the  $c$  class must be calculated,  $y^c$  (before the softmax), with respect to the feature map activations  $A^k$  of a convolutional layer in order to create the class-discriminative localization map Grad-CAM  $L_{Grad-CAM}^c \in \mathbb{R}^{u \times v}$  of width  $u$  and height  $v$  for any class  $c$ , i.e.  $\frac{\partial y^c}{\partial A^k}$ . These gradients flowing back are global-average-pooled throughout the width and height dimensions to produce the neuron significance weights  $\alpha_k^c$  (indexed by  $i$  and  $j$ , respectively):

$$\alpha_k^c = \overbrace{\frac{1}{Z} \sum_i \sum_j}^{\text{global average pooling}} \underbrace{\frac{\partial y^c}{\partial A_{ij}^k}}_{\text{gradients via backprop}} \quad (1)$$

Up until the last convolution layer to which the gradients are being propagated, the actual computation for computing  $\alpha_k^c$  while backpropagation gradients with respect to activations. Which consist of the weight matrices and gradient with regard to activation functions' successive matrix products. As a result, this weight  $\alpha_k^c$  denotes a partial linearization of the deep network downstream from  $A$  and captures the "importance" of feature map  $k$  for a target class  $c$ . In Eq. 2 to get, we combine forwarding activation maps in a weighted manner with a ReLU.

$$L_{Grad-CAM}^c = ReLU \left( \underbrace{\sum_k \alpha_k^c A^k}_{\text{linear combination}} \right) \quad (2)$$

In the final convolutional layers of GoogleNet, this produces a coarse Heatmap that is the same size as the convolutional feature maps. Since we are only interested in characteristics that positively affect the class of interest, we apply a ReLU to the linear combination of maps. i.e., pixels whose intensity should be increased to improve  $y^c$ . Negative pixels are probably part of other image types. Localization maps frequently highlight classes other than the one intended and perform less well in terms of localization without this ReLU. In the samples of the brain MRI dataset, atrophy of the temporal lobe of the brain and subarachnoid spaces are shown in groups of 2 at 4 stages within red and blue tones using Grad-CAM. 2 samples of 4 stages are shown in Fig 4. In general, a CNN image classification class score does not have to be  $y^c$ . Any distinguishable activation, such as words from a caption or a response to a query, is possible. The first group stage to the fourth group stage with red-blue coloration distinguishes the disease by temporal lobe atrophy and subsequent dilatations in the subarachnoid spaces.

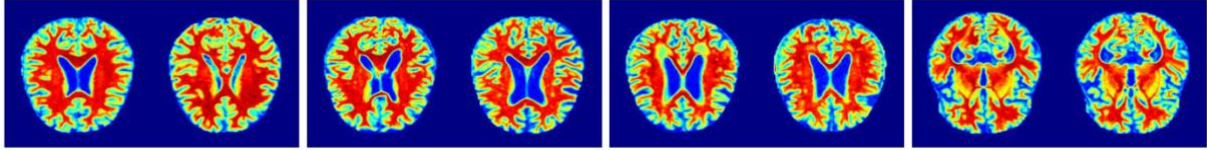


Figure 4. Samples from Grad-CAM results of brain MRI dataset

### 3.4. Pre-trained CNN Architectures

Table 2. Brain MRI dataset classification results (accuracy %) of 10 CNN architectures

Models	KNN	Models	Ensemble	Models	SVM
DenseNet201	98.5	DenseNet201	98.3	EfficientNet-B0	94.5
EfficientNet-B0	98.4	EfficientNet-B0	97.9	AlexNet	93.1
AlexNet	97.9	MobileNetV2	97.2	DenseNet201	92.9
MobileNetV2	97.9	AlexNet	97.1	ResNet101	90.3
ShuffleNet	97.4	ShuffleNet	96.6	ShuffleNet	89.5
VGG19	96.4	VGG19	96.0	MobileNetV2	89.3
DarkNet53	96.3	DarkNet53	95.7	DarkNet53	88.7
ResNet101	95.7	ResNet101	94.9	VGG19	88.0
InceptionV3	94.0	InceptionV3	93.3	InceptionV3	86.3
GoogleNet	91.0	GoogleNet	89.7	GoogleNet	83.2

According to the order given in Table 2, DenseNet201 [40], EfficientNet-B0 [41], and AlexNet [42] architectures, which show high performance using KNN, Ensemble, and SVM classifiers, were preferred for feature concatenation.

The underlying principle is to move the filters over the image to generate the features of the inputs. These filters applied to the inputs or to each convolution layer may differ in each model [43]. Eq. 3 is used to determine the size of the output image after the convolution layer's image filtering.

$$o = ((i - k) + 2p)/s + 1 \quad (3)$$

here,  $o$ ,  $i$ , and  $k$  represent output, input, and filter size, respectively.  $p$  and  $s$  represent padding and step count, respectively. The convolution operation is performed with Eq. 4.

$$S(i, j) = (I * K)(i, j) = \sum_m \sum_n I(m, n)K(i - m, j - n) \quad (4)$$

here,  $I$ ,  $S$ , and  $K$  represent input, output, and kernel, respectively.

The activation function is another component of CNN models. Here, many activation functions may be preferred. The following Eq. 5-7 provide the most popular activation functions [44].

$$ReLU: f(x) = \begin{cases} 0, & x < 0 \\ x, & x \geq 0 \end{cases}, f(x)' = \begin{cases} 0, & x < 0 \\ 1, & x \geq 0 \end{cases} \quad (5)$$

$$\text{Sigmoid: } f(x) = \frac{1}{1 + e^{-x}}, f(x)' = f(x)(1 - f(x)) \quad (6)$$

$$\text{Tanh: } \tanh(x) = \frac{2}{1 + e^{-2x}} - 1, f(x)' = 1 - f(x)^2 \quad (7)$$

Normalization is another feature of CNN models. The effectiveness of the architecture may be impacted by this procedure. Eq. 8-10 are described the normalizing procedure [45].

$$Y_i = \frac{X_i - \mu_\beta}{\sqrt{\sigma_\beta^2 + \epsilon}} \quad (8)$$

$$\sigma_\beta = \frac{1}{M} \sum_{i=1}^M (X_i - \mu_\beta)^2 \quad (9)$$

$$\mu_\beta = \frac{1}{M} \sum_{i=1}^M X_i \quad (10)$$

here,  $Y_i$  is the value following normalization.  $\sigma_\beta$  is the standard deviation.  $\mu_\beta$  represents the average value,  $M$  represents the number of input.

### 3.5. NCA-Feature Selection

The non-parametric method of NCA is used to select features. The main aim is to increase the accuracy of regression and classification algorithms' predictions. The basic formulations of the algorithm are listed as follows;

Assuming  $T = \{(x_1, y_1), \dots, (x_i, y_i), \dots, (x_N, y_N)\}$  is the set of training samples,  $x_i$  represents the  $d$ -dimensional feature vector,  $y_i \in \{1, \dots, C\}$  its associated class label, and  $N$  the number of instances. The purpose is to find a weighting vector  $w$  that allows for feature subset selection and nearest neighbor classification optimization. The weighted distance between two samples  $x_i$  and  $x_j$  is expressed in terms of the weighting vector  $w$  as shown in Eq. 11:

$$d_w(x_i, x_j) = \sum_{r=1}^d w_r^2 |x_{ir} - x_{jr}|, \quad (11)$$

where  $w_r$  denotes the weight of the  $r$ th feature. Optimizing its leave-one-out classification accuracy on the training set  $T$  is a simple and efficient method for closest neighbor classification success. Since the actual leave-one-out accuracy used to select the nearest neighbor as a classification reference point is a non-differentiable function, a probability distribution is utilized as an efficient approximation. The probability that  $x_i$  selects  $x_j$  as its reference point is given by Eq. 12;

$$p_{ij} = \begin{cases} \frac{\kappa(d_w(x_i, x_j))}{\sum_{k \neq i} \kappa(d_w(x_i, x_k))}, & \text{if } i \neq j \\ 0, & \text{if } i = j \end{cases} \quad (12)$$

The kernel width  $\sigma$  is an input parameter that controls the likelihood of specific points being chosen as the reference point when kernel function  $\kappa(z) = \exp(-z/\sigma)$  is applied. In specifically, only the query sample's closest neighbor can be chosen as its reference point, if  $\sigma \rightarrow 0$ . While all the points aside from the question point have the same chance of getting chosen, if  $\sigma \rightarrow +\infty$ . According to the definition above, the likelihood that query point  $x_i$  will be successfully categorized is given in Eq. 13:

$$p_i = \sum_j y_{ij} p_{ij} \quad (13)$$

here  $y_{ij} = 1$  if and only if  $y_i = y_j$  and otherwise  $y_{ij} = 0$ . Thus, the approximate leave-one-out classification accuracy is represented by Eq. 14:

$$\xi(w) = \frac{1}{N} \sum_i p_i = \frac{1}{N} \sum_i \sum_j y_{ij} p_{ij} \quad (14)$$

$\xi(w)$  is represents the true genuine leave-one-out classification accuracy while  $\sigma \rightarrow 0$ . We also include a regularization term to do feature selection and reduce overfitting, and as a result, we get the objective function shown in Eq. 15:

$$\xi(w) = \sum_i \sum_j y_{ij} p_{ij} - \lambda \sum_{r=1}^d w_r^2 \quad (15)$$

where the cross-validation method can be used to adjust the regularization parameter  $\lambda > 0$ . The coefficient  $1/N$  in Eq. 14 is ignored, as it just indicates that the parameter  $\lambda$  changes in accordance with the equation, leaving the final solution vector unchanged. The derivative with respect to  $w_r$  of the object function  $\xi(w)$  can be calculated in Eq. 16 because it is differentiable:

$$\begin{aligned} \frac{\partial \xi(w)}{\partial w_r} &= \sum_i \sum_j y_{ij} \left[ \frac{2}{\sigma} p_{ij} \left( \sum_{k \neq i} p_{ik} |x_{ir} - x_{kr}| - |x_{ir} - x_{jr}| \right) w_r \right] - 2\lambda w_r \\ &= \frac{2}{\sigma} \sum_i \left( p_i \sum_{k \neq i} p_{ik} |x_{ir} - x_{kr}| - \sum_j y_{ij} p_{ij} |x_{ir} - x_{jr}| \right) w_r - 2\lambda w_r \\ &= 2 \left( \frac{1}{\sigma} \sum_i \left( p_i \sum_{j \neq i} p_{ij} |x_{ir} - x_{jr}| - \sum_j y_{ij} p_{ij} |x_{ir} - x_{jr}| \right) - \lambda \right) w_r \end{aligned} \quad (16)$$

The relevant gradient ascent update equation can be acquired by using the aforementioned derivative. The suggested approach is known as NCA-FS [46]. It should be observed that we skipped the line search procedure in the iteration to determine the step length  $\alpha$ . The evaluation of the goal function necessitates expensive calculation, which is the fundamental cause.

#### 4. Experimental Results

The features obtained using DenseNet201, EfficientNet-B0 and AlexNet architectures were concatenated and classified by KNN, Ensemble and SVM ML algorithms. Moreover, in order to emphasize the contribution of Grad-CAM visualization, which is a part of the proposed hybrid model, to the experimental results, the feature extraction classification results of the hybrid model without Grad-CAM are included. Finally, the experimental results, confusion matrices, and performance metrics obtained from the proposed hybrid model are given.

**Table 3.** Parameter values used in training

Environment	Max Epoch	Learning Rate	Mini batch size	Optimization
Matlab R2021b	5	1e-4	32	Sgdm

All applications were executed in MATLAB R2021b environment and on a machine includes a GTX 1080 graphics card and 16 GB of RAM. In order to compare the outcomes reliably, the same parameters were applied during the training of these pre-trained deep architectures. The learning parameters are illustrated in Table 3.

Default values are used in these ML classifiers. CNN models convert different sizes of input images to a standard size. The input image sizes of DenseNet201, EfficientNet-B0, and AlexNet CNN architectures are 224×224, 224×224, and 227×227, respectively. The dimensions of the input images of the architectures used were adjusted to the dimensions specified before the training.

The initial value of the KNN classifier, which is one of the preferred classifiers in the study, is fine KNN. The number of neighbors is given as 1. The distance measure was chosen as Euclidean. The 5-fold is determined in the KNN algorithm. The Ensemble classifier is another algorithm used in the study. The kernel function of this classifier is a subset of KNN. Another classifier in the study is the SVM classifier. Cubic SVM is the kernel function. The core scale value is automatically selected and the cost matrix is the default. As in KNN, the 5-fold is also determined in SVM. In the confusion matrix, it represents the 1st class Non Demented stage, the 2nd class Very Mild Demented stage, the 3rd class Mild Demented stage, and the 4th class Moderate Demented stage.

#### 4.1. Performance metrics

In this study, six different performance evaluation criteria are used to evaluate and compare the proposed method: accuracy, sensitivity, specificity, precision, F1-measure, and Matthews Correlation Coefficient (MCC). These TP, TN, FP, and FN metrics in Table 4 represent true positive, true negative, false positive, and false negative, respectively.

**Table 4.** Statistical performance metrics of the CNN architectures

		Predicted Class	
		Positive	Negative
True Class	Positive	True Positive ( <i>TP</i> )	False Negative ( <i>FN</i> )
	Negative	False Positive ( <i>FP</i> )	True Negative ( <i>TN</i> )

$$Accuracy = \frac{TP + TN}{TP + TN + FP + FN} \quad (17)$$

$$Sensitivity = \frac{TP}{TP + FN} \quad (18)$$

$$Specificity = \frac{TN}{TN + FP} \quad (19)$$

$$Precision = \frac{TP}{TP + FP} \quad (20)$$

$$F1 - measure = \frac{2 TP}{2 TP + FP + FN} \quad (21)$$

$$MCC = \frac{(TP * TN) - (FP * FN)}{\sqrt{((TP + FP) * (TP + FN) * (TN + FP) * (TN + FN))}} \quad (22)$$

#### 4.2. DenseNet201

The fc1000 layer of the DenseNet201 architecture was used to extract features from images in the Alzheimer's brain MRI dataset. These obtained features were classified through KNN, Ensemble, and SVM algorithms. Table 5 illustrates every confusion matrix produced by the classifier algorithms.

Each of the KNN, Ensemble, and SVM algorithms separately classified the features extracted from the DenseNet201 model. The accuracy values obtained from the KNN, Ensemble, and SVM algorithms are 98.5%, 98.3%, and 92.9%, respectively. When the results are examined, it is seen that the KNN algorithm is more successful than other algorithms in classifying the features extracted from the DenseNet201 model. The KNN

algorithms accurately predicted 3161 of 3200 Non Demented images, 2201 of 2240 Very Mild Demented images, 878 of 896 Mild Demented images, and 62 of 64 Moderate Demented images. Thus, the DenseNet201 architecture predicted 6302 correctly and 98 incorrectly out of a total of 6400 images. In this architecture, although the accuracy value of the Ensemble classifier is more successful than the SVM classifier, these two architectures lagged behind the KNN classifier.

**Table 5.** Confusion matrix obtained from DenseNet201, EfficientNet-B0, and AlexNet

DenseNet201+KNN (98.5%)					DenseNet201+Ensemble (98.3%)					DenseNet201+SVM (92.9%)							
True class	1	3161	26	12	1	True class	1	3160	27	12	1	True class	1	3050	121	29	
	2	30	2201	9	2		32	2197	11	2	161		2056	23			
	3	3	14	878	1		3	5	15	875	1		3	37	65	794	
	4	1	1		62		4	2	1		61		4	2	14	1	47
		1	2	3	4			1	2	3	4			1	2	3	4
Predicted class					Predicted class					Predicted class							
EfficientNet+KNN (98.4%)					EfficientNet+Ensemble (97.9%)					EfficientNet+SVM (94.5%)							
True class	1	3150	45	5	True class	1	3141	47	11	1	True class	1	3077	113	9	1	
	2	28	2203	9		2	37	2191	12	2		121	2101	18			
	3	6	10	879		1	3	10	12	873		1	3	39	40	816	1
	4					64	4			1		63	4		7		57
		1	2	3	4			1	2	3	4			1	2	3	4
Predicted class					Predicted class					Predicted class							
AlexNet+KNN (97.9%)					AlexNet+Ensemble (97.1%)					AlexNet+SVM (93.1%)							
True class	1	3146	44	9	1	True class	1	3129	55	15	1	True class	1	3057	123	20	
	2	35	2192	12	1		2	48	2171	18	3		2	153	2064	23	
	3	17	16	863			3	23	21	851	1		3	46	69	781	
	4		1		63		4		1	1	62		4	2	5	1	56
		1	2	3	4			1	2	3	4			1	2	3	4
Predicted class					Predicted class					Predicted class							

### 4.3. EfficientNet-B0

The efficientnet-b0|model|dense|Matmul layer of the EfficientNet-B0 architecture was used to extract features from images in the Alzheimer’s brain MRI dataset. These obtained features were classified through KNN, Ensemble, and SVM algorithms. Table 5 illustrates every confusion matrix produced by the classifier algorithms.

Each of the KNN, Ensemble, and SVM algorithms separately classified the features extracted from the EfficientNet-B0 model. The accuracy values obtained from the KNN, Ensemble, and SVM algorithms are 98.4%, 97.9%, and 94.5%, respectively. When the results are examined, it is seen that the KNN algorithm is more successful than other algorithms in classifying the features extracted from the EfficientNet-B0 model. The KNN algorithms accurately predicted 3150 of 3200 Non Demented images, 2203 of 2240 Very Mild Demented images, 879 of 896 Mild Demented images, and 64 of 64 Moderate Demented images. Thus, the EfficientNet-B0 architecture predicted 6296 correctly and 104 incorrectly out of a total of 6400 images. In this architecture, although the accuracy value of the Ensemble classifier is more successful than the SVM classifier, these two architectures lagged behind the KNN classifier.

### 4.4. AlexNet

The fc8 layer of the AlexNet architecture was used to extract features from images in the Alzheimer’s brain MRI dataset. These obtained features were classified through KNN, Ensemble, and SVM algorithms. Table 5 illustrates every confusion matrix produced by the classifier algorithms.

Each of the KNN, Ensemble, and SVM algorithms separately classified the features extracted from the AlexNet model. The accuracy values obtained from the KNN, Ensemble, and SVM algorithms are 97.9%, 97.1%, and 93.1%, respectively. When the results are examined, it is seen that the KNN algorithm is more successful than other algorithms in classifying the features extracted from the AlexNet model. The KNN algorithms accurately predicted 3146 of 3200 Non Demented images, 2192 of 2240 Very Mild Demented images, 863 of 896 Mild Demented images, and 63 of 64 Moderate Demented images. Thus, the AlexNet architecture predicted 6264 correctly and 136 incorrectly out of a total of 6400 images. In this architecture, although the accuracy value of the

Ensemble classifier is more successful than the SVM classifier, these two architectures lagged behind the KNN classifier.

**4.5. Proposed NCA-Based Hybrid Model**

Features from DenseNet201, EfficientNet-B0, and AlexNet architectures are concatenated without Grad-CAM. Thus, a feature matrix with a total size of 6400×3000 was produced. NCA feature selection was used to optimize this matrix and the matrix size was reduced to 6400×400. Then the reduced features were classified with KNN, Ensemble, and SVM classifiers. Table 6 shows the confusion matrices from this process obtained proposed hybrid model without Grad-CAM. Fig 5 shows best result AUC curves for each class of AD with the proposed hybrid model + KNN classifiers.

**Table 6.** Confusion matrix obtained from the proposed hybrid model

Hybrid model+KNN (99.5%)					Hybrid model+Ensemble(99.4%)					Hybrid model+SVM (97.5%)							
True class	1	3193	4	2	1	True class	1	3188	9	2	1	True class	1	3155	34	11	
	2	12	2226	2			2	12	2226	2			2	58	2173	9	
	3	2	5	889			3	5	5	886			3	13	30	853	
	4	1			63		4	1	1		62		4	2	5		57
		1	2	3	4			1	2	3	4			1	2	3	4
		Predicted class						Predicted class						Predicted class			

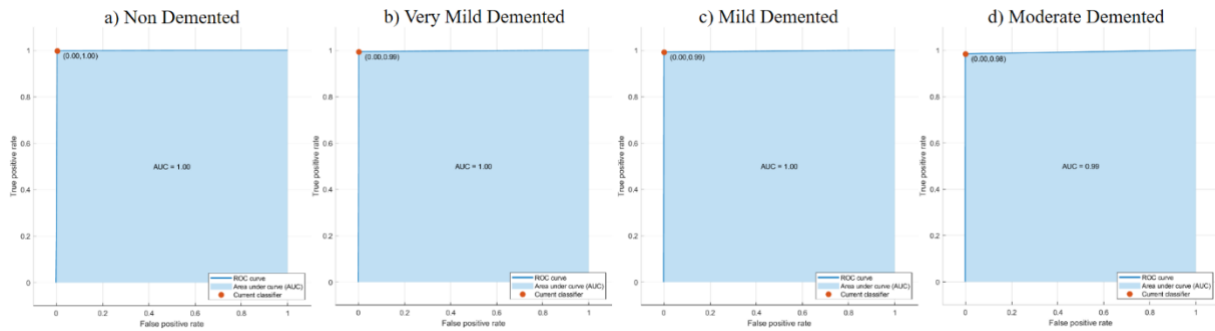


**Figure 5.** Hybrid model + KNN AUC curves of four class AD.

In the proposed hybrid model, in addition to 6400×3000 features obtained from DenseNet201, EfficientNet-B0, and AlexNet architectures, Grad-CAM visualization results obtained from each image of the dataset are given for feature extraction to these architectures. Thus, a total of 6400×6000 size feature matrix was created by adding the 6400×3000 size feature matrix obtained from Grad-CAM to the 6400×3000 size feature matrix obtained from the original dataset. To optimize this matrix, NCA feature selection was used again and the matrix size was reduced to 6400×400. Then the reduced features were classified with KNN, Ensemble, and SVM. Table 7 shows the confusion matrices from this process obtained proposed hybrid model using Grad-CAM. Fig 6 shows best result AUC curves for each class of AD with the proposed hybrid model + Ensemble classifiers.

**Table 7.** Confusion matrix obtained from the proposed hybrid model using Grad-CAM

Hybrid model+Ensemble(99.83%)					Hybrid model+KNN (99.7%)					Hybrid model+SVM (97.5%)							
True class	1	3195	5			True class	1	3191	8	1		True class	1	3154	41	5	
	2	4	2236				2	4	2234	2			2	62	2171	7	
	3	2	1	893			3	1	1	894			3	22	20	854	
	4				64		4				64		4		2	2	
		1	2	3	4			1	2	3	4			1	2	3	4
		Predicted class						Predicted class						Predicted class			



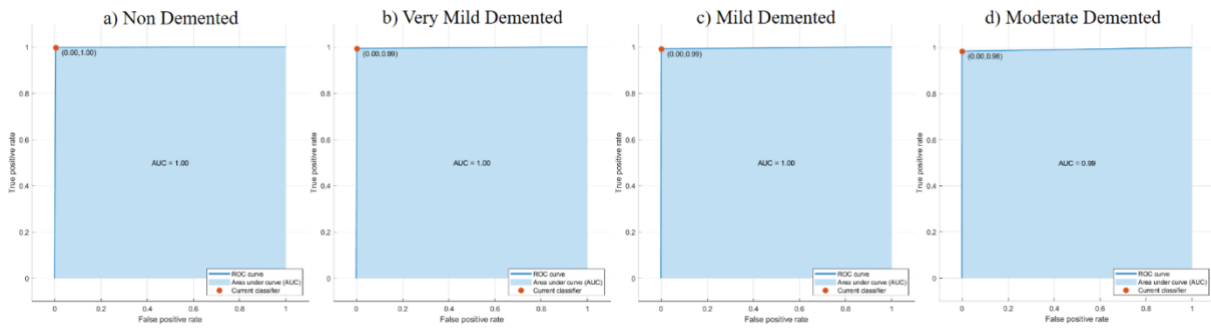


**Figure 6.** Hybrid model + Ensemble AUC curves of four class AD using Grad-CAM.

When the experimental results in Table 6 are examined, the accuracy values obtained from the KNN, Ensemble, and SVM classifiers are 99.5%, 99.4%, and 97.5%, respectively. KNN classifier was more successful than Ensemble and SVM in this hybrid model made on the original dataset without Grad-CAM. This KNN classifier algorithm accurately predicted 3193 of 3200 Non Demented images, 2226 of 2240 Very Mild Demented images, 889 of 896 Mild Demented images, and 63 of 64 Moderate Demented images. Thus, the NCA-based hybrid model without Grad-CAM predicted 6371 correctly and 29 incorrectly out of a total of 6400 images.

When the experimental results in Table 7 are examined, the accuracy values obtained from Ensemble, KNN, and SVM classifiers are 99.83%, 99.7%, and 97.5%, respectively. In this proposed hybrid model, implemented using Grad-CAM with the original dataset, the Ensemble classifier was more successful than KNN and SVM. This Ensemble classifier algorithm accurately predicted 3195 of 3200 Non Demented images, 2236 of 2240 Very Mild Demented images, 893 of 896 Mild Demented images, and 64 of 64 Moderate Demented images. Thus, the NCA-based hybrid model with Grad-CAM predicted 6388 correctly and 12 incorrectly out of a total of 6400 images.

The overall performance rate of the proposed hybrid model 99.83% accuracy, 99.88% sensitivity, 99.92% specificity, 99.83% precision, 99.85% F1-measure, and 99.78% MCC results using the Ensemble classifier for the 4-class classification of AD. Table 8 provides an evaluation of the proposed hybrid model + Ensemble performance using Grad-CAM visualization.

**Table 8.** The 4-class performance results of the proposed hybrid model + Grad-CAM + Ensemble(%)

AD	Stage	Accuracy	Sensitivity	Specificity	Precision	F1	MCC
<b>Proposed hybrid model + Grad-CAM + Ensemble</b>	NonDemented	99.84	99.81	99.84	99.84	99.82	99.65
	VeryMildDemented	99.82	99.73	99.90	99.82	99.77	99.65
	MildDemented	99.66	1	99.94	99.66	99.83	99.80
	ModerateDemented	1	1	1	1	1	1
	Overall	99.83	99.88	99.92	99.83	99.85	99.78

## 5. Discussion

The neurodegenerative brain disorder AD gets worse over time. Increased Amyloid- $\beta$  level causes oxidative damage in brain cells. In this case, the cognitive decline seen in AD has been associated with it. AD is highly correlated with the age factor and its incidence is higher in advancing ages. In the future, Alzheimer’s patient numbers are anticipated to rise, particularly in industrialized nations, as the percentage of elderly people in the population grows [47]. The prevention or delay of the disease’s progression, as well as the ease of the disease’s monitoring depend on an early diagnosis of Alzheimer’s. Imaging techniques are one of the most used ways to diagnose AD [48, 49]. Imaging techniques can also disable other factors of this disease. Specific findings on MRI are used to diagnose AD [50]. Although it is not used frequently today, there are many works using MR methods for the diagnosis and follow-up of AD. These are; Diffusion Tensor Imaging (DTI), functional MRI, and Magnetic Resonance Spectroscopy (MRS) [51-53]. In AD, brain MRI shows temporoparietal lobe atrophy predominantly in the mesial temporal region. With disease progression, more atrophy affects areas close to the temporal region. Mesial temporal lobe atrophy causes a reduction in the hippocampus and parahippocampus volume and enlargement of the parahippocampal fissure. Parietal atrophy occurs in the early stages of the disease.

Today, artificial intelligence and machine learning techniques are used by many researchers in different subjects such as biomedical image processing, text, and voice analysis [54-56]. In this study, a method is proposed

to diagnose AD, which negatively affects the quality of life, according to the severity of dementia using Alzheimer's MRIs. Early diagnosis of the disease may be delayed due to the difficulty of interpreting Alzheimer's MRIs. These delays in the diagnosis of the disease cause delays in treatment as well as cause irreversible problems. In this study, AD was divided into 4 different classes using a ML-based model on brain MRI images. In the first step of the proposed method, feature extraction was performed from brain MRI images using DenseNet201, EfficientNet-B0, and AlexNet CNN architectures. Then, Grad-CAM visualization was applied to the entire AD MRI dataset, which clearly revealed the enlargement of the parahippocampal fissure due to the reduction in the volume of the hippocampus and parahippocampus. The same 3 CNN architectures were applied to the obtained Grad-CAM images for feature extraction. Next, all the features from these 3 different architectures applied to both the AD MRI dataset and the Grad-CAM visualization were combined. The NCA approach was used to optimize all of these combined features. Then, these concatenated features were classified by KNN, Ensemble, and SVM ML algorithms. When Table 9 is examined, it is seen that the method proposed in this study is the most successful. CNN architectures used in this hybrid model, which uses DL CNN and ML methods together, have achieved more successful results than other methods in the literature.

**Table 9.** Accuracy (%) rates from different models

<b>Models / Classifiers</b>	<b>KNN</b>	<b>Ensemble</b>	<b>SVM</b>
DenseNet201	98.5%	98.3%	92.9%
EfficientNet-B0	98.4%	97.9%	94.5%
AlexNet	97.9%	97.1%	93.1%
Proposed hybrid method without Grad-CAM	99.5%	99.4%	97.5%
Proposed hybrid method using Grad-CAM	<b>99.7%</b>	<b>99.83%</b>	<b>97.5%</b>

Information on all available studies related to our study on AD are listed in Table 10. In Table 10, it is seen that the hybrid model proposed in this study gives higher results than other studies in the literature. According to the performance evaluation metrics in Table 4, the proposed model is an effective and usable method for AD diagnosis. Due to the disease's significant morbidity, accurate diagnosis is crucial. Thanks to this study, 4-stages of AD were diagnosed with high success using AD brain MRI images. According to the experimental results obtained, this method will contribute to the medical literature. The limitations of the proposed method are the lack of clinical data from patients.

**Table 10.** Comparison of similar studies in the literature

<b>Study</b>	<b>Models/Methods</b>	<b>Accuracy (%)</b>	<b>Year</b>
Lama et. al [31]	RELM	76.61	2017
Ahmed et. al [18]	SVM	78.22	2015
Oh et. al [33]	CNN	84.5	2019
Liu et. al [17]	DenseNet	88.9	2020
Klöppel et. al [19]	SVM	89.2	2008
Billones et. al [27]	VGGNet	91.85	2016
Hemanth et. al [16]	MKNN, MCPN	95, 98	2014
Khagi and Kwon [28]	CNN	96	2020
Hon and Khan [32]	VGG, Inception V4	96.25	2017
Feng et. al [23]	CNN+SVM	96.82	2020
Sarraf ve Tofighi [26]	LeNet5	96.85	2016
Farooq et. al [20]	GoogLeNet+ResNet18+ResNet152	98.88	2017
Eroglu et. al [34]	Darknet53+InceptionV3+Resnet101	99.1	2022
Odusami et. al [57]	ResNet18 + DenseNet201	98.86	2022
Razzak et. al [58]	PartialNet	99.26	2022
<b>The proposed hybrid model without Grad-CAM</b>	Densenet201+EfficientNet+AlexNet	<b>99.5</b>	2022
<b>The proposed hybrid model using Grad-CAM</b>	Densenet201+EfficientNet+AlexNet	<b>99.83</b>	2022

## 6. Conclusion

AD is a cause of dementia that is frequently seen in elderly individuals and negatively affects the families of the patients. Early diagnosis of Alzheimer's not only prevents the progression of the disease but also plays an important role in increasing the quality of life of patients. This disease is very difficult to diagnose, as the pixel density and images are similar in brain MRI of different individuals. The method in this study was proposed to diagnose AD using four-stage brain MRIs. The proposed method is a hybrid model using Grad-CAM to classify brain MRIs. The accuracy value obtained in this hybrid method using Grad-CAM to diagnose AD is 99.83%. The results obtained in this study were compared with the results of different studies on the subject in the literature. According to the comparison results, the proposed method is quite successful. The success of the results obtained with the proposed method shows that this method can facilitate the diagnosis of AD by experts and can alleviate their workload in this regard.

## References

- [1] Miller-Thomas, M. M., Sipe, A. L., Benzinger, T. L., McConathy, J., Connolly, S., & Schwetye, K. E. Multimodality review of amyloid-related diseases of the central nervous system. *Radiographics* 2016; 36(4): 1147.
- [2] Qiu, C., Kivipelto, M., & Von Strauss, E. Epidemiology of Alzheimer's disease: occurrence, determinants, and strategies toward intervention. *Dialogues Clin Neurosci*, 2022.
- [3] Jalbert, J. J., Daiello, L. A., & Lapane, K. L. Dementia of the Alzheimer type. *Epidemiol Rev* 2008; 30(1): 15-34.
- [4] Altieri, M., Garramone, F., & Santangelo, G. Functional autonomy in dementia of the Alzheimer's type, mild cognitive impairment, and healthy aging: a meta-analysis. *J Neurol Sci* 2021; 42(5): 1773-1783.
- [5] Fargo, K., & Bleiler, L. Alzheimer's association report: 2014 Alzheimers disease facts and figures. *Alzheimers Dement* 2014; 10(2): e47-e92.
- [6] Bron, E. E., Smits, M., Van Der Flier, W. M., Vrenken, H., Barkhof, F., Scheltens, P., ... & Alzheimer's Disease Neuroimaging Initiative. Standardized evaluation of algorithms for computer-aided diagnosis of dementia based on structural MRI: the CADDementia challenge. *NeuroImage* 2015; 111: 562-579.
- [7] Zuliani, G., Trentini, A., Rosta, V., Guerrini, R., Pacifico, S., Bonazzi, S., ... & Cervellati, C. Increased blood BACE1 activity as a potential common pathogenic factor of vascular dementia and late onset Alzheimer's disease. *Sci Rep* 2020; 10(1): 1-8.
- [8] Norfray, J. F., & Provenzale, J. M. Alzheimer's disease: neuropathologic findings and recent advances in imaging. *Am J Roentgenol* 2004; 182(1): 3-13.
- [9] Başkaya, O., Kandemir, M., Tepe, M. S., Acar, M., Ünal, G., Yalçın, Z. B., & Ünay, D. Inter-hemispheric atrophy better correlates with expert ratings than hemispheric cortical atrophy. In 2012 20th Signal Processing and Communications Applications Conference (SIU), April 2012; (pp. 1-4). IEEE.
- [10] Patel, K. P., Wymer, D. T., Bhatia, V. K., Duara, R., & Rajadhyaksha, C. D. Multimodality imaging of dementia: clinical importance and role of integrated anatomic and molecular imaging. *Radiographics* 2020; 40(1): 200.
- [11] Lehmann, M., Koedam, E. L., Barnes, J., Bartlett, J. W., Ryan, N. S., Pijnenburg, Y. A., ... & Fox, N. C. Posterior cerebral atrophy in the absence of medial temporal lobe atrophy in pathologically-confirmed Alzheimer's disease. *Neurobiol Aging* 2012; 33(3): 627-e1.
- [12] Sahiner, B., Chan, H. P., Petrick, N., Wei, D., Helvie, M. A., Adler, D. D., & Goodsitt, M. M. Classification of mass and normal breast tissue: a convolution neural network classifier with spatial domain and texture images. *IEEE Trans Med Imaging* 1996; 15(5): 598-610.
- [13] Adem, K. Diagnosis of breast cancer with Stacked autoencoder and Subspace kNN. *Phys. A: Stat. Mech. Appl.* 2020; 551: 124591.
- [14] Liu, M., Li, F., Yan, H., Wang, K., Ma, Y., Shen, L., ... & Alzheimer's Disease Neuroimaging Initiative. A multi-model deep convolutional neural network for automatic hippocampus segmentation and classification in Alzheimer's disease. *Neuroimage* 2020; 208: 116459.
- [15] Suriya, M., Chandran, V., & Sumithra, M. G. Enhanced deep convolutional neural network for malarial parasite classification. *Int J Comput Appl* 2019; 1-10.
- [16] Hemanth, D. J., Vijila, C. K. S., Selvakumar, A. I., & Anitha, J. Performance improved iteration-free artificial neural networks for abnormal magnetic resonance brain image classification. *Neurocomputing* 2014; 130: 98-107.
- [17] Liu M, Li F, Yan H, et al. A multi-model deep convolutional neural network for automatic hippocampus segmentation and classification in Alzheimer's disease. *NeuroImage* 2020; 208: 116459.
- [18] Ben Ahmed, O., Benois-Pineau, J., Allard, M., Ben Amar, C., & Catheline, G. Classification of Alzheimer's disease subjects from MRI using hippocampal visual features. *Multimed Tools Appl* 2015; 74(4): 1249-1266.
- [19] Klöppel, S., Stonnington, C. M., Chu, C., Draganski, B., Scahill, R. I., Rohrer, J. D., ... & Frackowiak, R. S. Automatic classification of MR scans in Alzheimer's disease. *Brain* 2008; 131(3): 681-689.
- [20] Farooq A, Anwar S, Awais M, Rehman S. A deep CNN based multi-class classification of Alzheimer's disease using MRI. Paper presented at the 2017 IEEE International Conference on Imaging Systems and Techniques (IST); 2017.

- [21] Jongkreangkrai, C., Vichianin, Y., Tocharoenchai, C., Arimura, H., & Alzheimer's Disease Neuroimaging Initiative. Computer-aided classification of Alzheimer's disease based on support vector machine with combination of cerebral image features in MRI. In *Journal of physics: conference series*, March, 2016; 694(1): 012036.
- [22] Moradi, E., Pepe, A., Gaser, C., Huttunen, H., Tohka, J., & Alzheimer's Disease Neuroimaging Initiative. Machine learning framework for early MRI-based Alzheimer's conversion prediction in MCI subjects. *Neuroimage* 2015; 104: 398-412.
- [23] Feng W, Halm-Lutterodt NV, Tang H, et al. Automated MRIbased deep learning model for detection of Alzheimer's disease process. *Int J Neural Syst* 2020; 30(06): 2050032.
- [24] Lerch, J. P., Pruessner, J., Zijdenbos, A. P., Collins, D. L., Teipel, S. J., Hampel, H., & Evans, A. C. Automated cortical thickness measurements from MRI can accurately separate Alzheimer's patients from normal elderly controls. *Neurobiol Aging* 2008; 29(1): 23-30.
- [25] Cheng, B., Liu, M., Shen, D., Li, Z., & Zhang, D. Multi-domain transfer learning for early diagnosis of Alzheimer's disease. *Neuroinformatics* 2017; 15(2): 115-132.
- [26] Sarraf S, Tofighi G. Deep learning-based pipeline to recognize Alzheimer's disease using fMRI data. Paper presented at the 2016 Future Technologies Conference (FTC); 2016.
- [27] Billones, C. D., Demetria, O. J. L. D., Hostallero, D. E. D., & Naval, P. C. DemNet: a convolutional neural network for the detection of Alzheimer's disease and mild cognitive impairment. In 2016 IEEE region 10 conference (TENCON), November, 2016; pp. 3724-3727. IEEE.
- [28] Khagi B, Kwon GR. 3D CNN design for the classification of Alzheimer's disease using brain MRI and PET. *IEEE Access* 2020; 8:217830-217847.
- [29] Payan, A., & Montana, G. Predicting Alzheimer's disease: a neuroimaging study with 3D convolutional neural networks 2015; arXiv preprint arXiv:1502.02506.
- [30] Hosseini-Asl, E., Gimel'farb, G., & El-Baz, A. Alzheimer's disease diagnostics by a deeply supervised adaptable 3D convolutional network 2016; arXiv preprint arXiv:1607.00556.
- [31] Lama RK, Gwak J, Park J-S, Lee S-W. Diagnosis of Alzheimer's disease based on structural MRI images using a regularized extreme learning machine and PCA features. *J Healthc Eng* 2017; 5485080.
- [32] Hon, M., & Khan, N. M. Towards Alzheimer's disease classification through transfer learning. In 2017 IEEE International conference on bioinformatics and biomedicine (BIBM), November, 2017; pp. 1166-1169. IEEE.
- [33] Oh K, Chung Y-C, Kim KW, Kim W-S, Oh I-S. Classification and visualization of Alzheimer's disease using volumetric convolutional neural network and transfer learning. *Sci Rep* 2019; 9(1): 1-16.
- [34] Eroglu, Y., Yildirim, M., & Cinar, A. mRMR-based hybrid convolutional neural network model for classification of Alzheimer's disease on brain magnetic resonance images. *Int J Imaging Syst Technol* 2022; 32(2): 517-527.
- [35] Sarvesh D. Alzheimer's Dataset: Available from: <https://www.kaggle.com/datasets/tourist55/alzheimers-dataset-4-class-of-images>, 2019.
- [36] Selvaraju, R. R., Cogswell, M., Das, A., Vedantam, R., Parikh, D., & Batra, D. Grad-cam: Visual explanations from deep networks via gradient-based localization. In *Proceedings of the IEEE international conference on computer vision*, 2017; pp. 618-626.
- [37] Selvaraju, R. R., Das, A., Vedantam, R., Cogswell, M., Parikh, D., & Batra, D. Grad-CAM: Why did you say that?, 2016; arXiv preprint arXiv:1611.07450.
- [38] Y. Bengio, A. Courville, and P. Vincent. Representation learning: A review and new perspectives. *IEEE transactions on pattern analysis and machine intelligence* 2013; 35(8):1798–1828.
- [39] Mahendran, A., & Vedaldi, A. Visualizing deep convolutional neural networks using natural pre-images. *Int J Comput Vis*. 2016; 120(3): 233-255.
- [40] Yu, X., Zeng, N., Liu, S., & Zhang, Y. D. Utilization of DenseNet201 for diagnosis of breast abnormality. *Mach Vis Appl* 2019; 30(7): 1135-1144.
- [41] Tan, M., & Le, Q. Efficientnet: Rethinking model scaling for convolutional neural networks. In *International conference on machine learning*, May, 2019; pp. 6105-6114.
- [42] Zahangir Alom, M., Taha, T. M., Yakopcic, C., Westberg, S., Sidike, P., Shamima Nasrin, M., ... & Asari, V. K. The history began from AlexNet: a comprehensive survey on deep learning approaches, 2018; arXiv e-prints, arXiv:1803.
- [43] Jin, M., & Deng, W. Predication of different stages of Alzheimer's disease using neighborhood component analysis and ensemble decision tree. *J Neurosci Methods* 2018; 302, 35-41.
- [44] Banerjee, C., Mukherjee, T., & Pasilio Jr, E. An empirical study on generalizations of the ReLU activation function. In *Proceedings of the 2019 ACM Southeast Conference*, April, 2019; pp. 164-167.
- [45] Özbay, E., Çinar, A., & Özbay, F. A. 3D Human Activity Classification with 3D Zernike Moment Based Convolutional, LSTM-Deep Neural Networks. *Trait du Signal* 2021; 38(2): 269-280.
- [46] Yang, W., Wang, K., & Zuo, W. Neighborhood component feature selection for high-dimensional data. *J Comput* 2012; 7(1): 161-168.
- [47] Carr, D. B., Goate, A., Phil, D., & Morris, J. C. Current concepts in the pathogenesis of Alzheimer's disease. *The American journal of medicine* 1997; 103(3): 3S-10S.
- [48] Abuhmed, T., El-Sappagh, S., & Alonso, J. M. Robust hybrid deep learning models for Alzheimer's progression detection. *Knowl.-Based Syst.* 2021; 213: 106688.

- [49] El-Sappagh, S., Saleh, H., Sahal, R., Abuhmed, T., Islam, S. R., Ali, F., & Amer, E. Alzheimer's disease progression detection model based on an early fusion of cost-effective multimodal data. *Future Gener Comput Syst* 2021; 115: 680-699.
- [50] McKhann, G. M., Knopman, D. S., Chertkow, H., Hyman, B. T., Jack Jr, C. R., Kawas, C. H., ... & Phelps, C. H. The diagnosis of dementia due to Alzheimer's disease: Recommendations from the National Institute on Aging-Alzheimer's Association workgroups on diagnostic guidelines for Alzheimer's disease. *Alzheimer's & dementia* 2011; 7(3): 263-269.
- [51] Hirni, D. I., Kivisaari, S. L., Monsch, A. U., & Taylor, K. I. Distinct neuroanatomical bases of episodic and semantic memory performance in Alzheimer's disease. *Neuropsychologia* 2013; 51(5): 930-937.
- [52] Petrella, J. R., Wang, L., Krishnan, S., Slavin, M. J., Prince, S. E., Tran, T. T. T., & Doraiswamy, P. M. Cortical deactivation in mild cognitive impairment: high-field-strength functional MR imaging. *Radiology* 2007; 245(1): 224-235.
- [53] Zhu, X., Schuff, N., Kornak, J., Soher, B., Yaffe, K., Kramer, J. H., ... & Weiner, M. W. Effects of Alzheimer disease on fronto-parietal brain N-acetyl aspartate and myo-inositol using magnetic resonance spectroscopic imaging. *Alzheimer Dis Assoc Disord* 2006; 20(2): 77.
- [54] Özbay, E. An active deep learning method for diabetic retinopathy detection in segmented fundus images using artificial bee colony algorithm. *Artif Intell Rev* 2023; 56: 3291-3318.
- [55] Özbay, E. Transformatör-Tabanlı Evrişimli Sinir Ağı Modeli Kullanarak Twitter Verisinde Saldırganlık Tespiti. *Konya Mühendislik Bilimleri Dergisi* 2022; 10(4): 986-1001.
- [56] Özbay, F. A., & Özbay, E. A new approach for gender detection from voice data: Feature selection with optimization methods. *J Fac Eng Archit Gazi Univ* 2023; 38(2): 1179-1192.
- [57] Odusami, M., Maskeliūnas, R., & Damaševičius, R. An Intelligent System for Early Recognition of Alzheimer's Disease Using Neuroimaging Sensors 2022; 22(3): 740.
- [58] Razzak, I., Naz, S., Ashraf, A., Khalifa, F., Bouadjenek, M. R., & Mumtaz, S. Mutliresolutional ensemble PartialNet for Alzheimer detection using magnetic resonance imaging data. *Int J Intell Syst* 2022; 37(10): 6613-6630.



## Performance Comparison of Biology based Metaheuristics Optimization Algorithms using Unimodal and Multimodal Benchmark Functions

Fatma BELLI<sup>1</sup>, Harun BINGOL<sup>1\*</sup>

<sup>1</sup>Software Engineering, Faculty of Engineering and Natural Sciences, Malatya Turgut Ozal University, Malatya, Turkey  
<sup>1</sup>fatmacubukcu@outlook.com, <sup>1\*</sup>harun.bingol@ozal.edu.tr

(Geliş/Received: 05/12/2022;

Kabul/Accepted: 25/02/2023)

**Abstract:** Optimization is used in almost every aspect of our lives today and makes our lives easier. Optimization is generally studied as classical and heuristic optimization techniques. Classical optimization methods are not effective in real-world engineering problems. These methods, by their nature, require a mathematical model. Metaheuristic optimization methods have started to be used frequently today in the solution of these problems when a mathematical model cannot be created or a solution cannot be produced in an effective time even if it is created. These methods, by their nature, cannot produce effective results in all engineering problems. Therefore, new metaheuristic optimization methods are constantly being researched. In this study, quality test functions have been used to compare the performances of five algorithms that have been developed in recent years and produce effective results. The results obtained from these functions are shared in this study. It has been observed that the Artificial Hummingbird Optimization Algorithm (AHA) gives better results than other metaheuristic algorithms.

**Keywords:** AHA, optimization, artificial intelligence, metaheuristic optimization

### Tek Modlu ve Çok Modlu Kıyaslama Fonksiyonlarını Kullanan Biyoloji Tabanlı Metasezgisel Optimizasyon Algoritmalarının Performans Karşılaştırması

**Öz:** Optimizasyon günümüzde hayatımızın hemen her alanında kullanılmakta ve hayatımızı kolaylaştırmaktadır. Optimizasyon genellikle klasik ve sezgisel optimizasyon teknikleri olarak incelenmektedir. Klasik optimizasyon yöntemleri gerçek dünya mühendislik problemlerinde etkili değildir. Bu yöntemler doğaları gereği matematiksel bir modele ihtiyaç duyarlar. Matematiksel modelin oluşturulamadığı yada oluşturulsa bile etkili bir zamanda çözüm üretilmeyeceği anlarda bu problemlerin çözümünde metasezgisel optimizasyon yöntemleri günümüzde sıklıkla kullanılmaya başlamıştır. Bu yöntemler tüm mühendislik problemlerinde etkili sonuçları doğaları gereği üretmezler. Bundan dolayı sürekli olarak yeni metasezgisel optimizasyon yöntemleri araştırılmaktadır. Bu çalışmada da son yıllarda geliştirilen ve etkili sonuçlar üreten beş adet algoritmanın başarımlarını karşılaştırmak amacıyla kalite test fonksiyonları kullanılmıştır. Bu fonksiyonlardan elde edilen sonuçlar bu çalışmada paylaşılmıştır. Yapay Sinek Kuşu Optimizasyon Algoritması'nın (YSA) diğer metasezgisel algoritmalarından daha iyi sonuçlar verdiği gözlemlenmiştir.

**Anahtar kelimeler:** YSA, optimizasyon, yapay zeka, metasezgisel optimizasyon

#### 1. Introduction

Optimization literally means best improvement. It is the task of obtaining the best solution from all the solutions of the problem within certain limits. Optimization problem is the solution of unknown parameter values can be defined as any problem involving the presence of in such a way as to meet the constraints of the problem [1,2]. In addition to using optimization techniques to speed up decision-making and improve decision quality, it is also used to solve problems in the real world in a way that is efficient, accurate, and timely [3,4].

The element that affects the performance of the optimization is called the decision variable. The objective function is formed by the analytical display of the decision element on the objective. The values of the decision variables affect what the value of the objective function will be. Some restrictions need to be met in this process. Any solution in the solution space that satisfies the constraints of the problem is called a feasible solution. Optimum solution refers to the best solution among suitable solutions according to the determined purpose.

We can examine the methods used in the optimization process under two main headings. These are Deterministic (mathematical modeling) and Stochastic (random) [5]. Stochastic methods are examined under two sub-headings as heuristic and metaheuristic. In the deterministic method, it is tried to reach the result within the

tolerances. This method takes a long time to solve large-scale problems and no exact solution can be found. Heuristic methods also produce problem-specific solutions and do not guarantee the optimum solution. But it is faster than analytical methods. Metaheuristic methods, on the other hand, obtain a solution by adapting certain algorithms to the problem to be solved. In this study, we tested using benchmark functions that AHA, which is one of the biological-based metaheuristic algorithms based on swarm intelligence, gives faster results and performs better against the gray wolf optimization (GWO), whale algorithm (WHO), dragonfly algorithm (DA), ant lion algorithm (ALO). All of these algorithms are biology-based algorithms inspired by nature.

The organization of this article is as follows. In the first chapter, general information about optimization methods is given. In the second part, information about the working principle of the AHA optimization algorithm is given. In the third chapter, information about the working principle of the GWO algorithm is given. In the fourth chapter, information about the working principle of the WHO optimization algorithm is given. In the fifth chapter, information about the working principle of the DA optimization algorithm is given. In the sixth chapter, information about the working principle of the ALO optimization algorithm is given. In the seventh chapter, the mathematical expressions of the quality test functions used in the experiments and the experimental results are given. Finally, the results obtained in the eighth chapter are interpreted and the study is summarized.

## 2. AHA Algorithm

The artificial hummingbird algorithm (AHA) is inspired by hummingbirds, considered the smallest birds in the world. This algorithm was designed by Seyedali Mirjalili, Weiguo Zhao, Liying Wang in 2021. AHA is a biological-based metaheuristic algorithm based on swarm intelligence.

The artificial hummingbird algorithm (AHA) is designed by modeling hummingbirds' special flight skills and intelligent foraging strategies. This algorithm was created by modeling strategies such as guided foraging, regional foraging, foraging on the migration route, and axial, cross and omnidirectional flight skills. To guide hummingbirds in the algorithm, a visitation chart has been created that mimics hummingbirds' extraordinary memory abilities [6].

### 2.1. Main Components of AHA

The AHA algorithm has 3 basic components. These are as follows;

**Food sources:** A hummingbird frequently assesses the properties of the sources, such as the nectar quality and content of flowers, the nectar fill rate, and the most recent visit. In the AHA, the nectar filling rate of each food source is represented by the function fitness value, and it is assumed that each food source has the same number and kind of flowers. A food source is a solution vector. The rate of nectar replenishment from the food source increases in direct proportion to fitness value.

**Hummingbirds:** Every hummingbird has a specific food source that it may eat from, and both the hummingbird and its food source are in the same location. A hummingbird can remember where this specific food source is and how quickly it fills up on nectar. It may also communicate this knowledge to other hummingbirds in the community. Each hummingbird can recall how long it has been since it last visited a particular food source.

**Visit table:** The visits chart tracks the frequency with which various hummingbirds visit each food source and displays the amount of time since the same hummingbird last visited a certain food source. A hummingbird will prioritize visits to a food source that receives a lot of visits from that hummingbird. Among the food sources with the same greatest visitation level, a hummingbird prefers to visit the one with the highest ratio of nectar filling in order to get more nectar. Each hummingbird can use the visit chart to locate its preferred food source. Every iteration often involves updating the visit table.

The mathematical expression of the components of the AHA in the algorithm is shown in Table 1. The following algorithm  $i$ .location of food source,  $j$ .food source,  $X_i(t)$  candidate food source,  $V_i$  regional foraging,  $X_{wor}$  worst nectar rate.



**Table 1.** Pseudo Code Artificial Hummingbird Algorithm [6]

<pre> <b>Input:</b> <math>n, d, f, \text{Max\_It}, \text{Up}</math> <b>Output:</b> Glo-min, Glo-minimizer <b>Initialization</b> <b>For</b> ith h-bird from 1 to <math>n</math>, <b>Do</b>   <b>if</b> <math>i \neq j</math>   <b>End For</b>   <b>Then</b> <math>V\_tbl_{ij} = 1</math>,   <b>Else</b> <math>V\_tbl_{ij} = \text{null}</math>,   <b>End If</b> <b>End For</b> <b>End For</b> <b>While</b> <math>t \leq \text{Max\_It}</math> <b>Do</b>   <b>For</b> ith h-bird from 1 to <math>n</math>, <b>Do</b>   <b>If</b> <math>\text{rand} \leq 0.5</math> <b>Then</b>   <b>If</b> <math>r &lt; 1/3</math> <b>Then</b>   <math>D^{(i)} = \begin{cases} 1, &amp; \text{if } i = \text{randi}([1, d]) \\ 0, &amp; \text{else} \end{cases} \quad i = 1, \dots, d</math>   <b>Else If</b> <math>r &gt; 2/3</math> <b>Then</b>   <math>D^{(i)} = \begin{cases} 1, &amp; \text{if } i = P(j), j \in [1, k], P = \text{randperm}(k), k \in [2, \lceil r_1 \cdot (d - 2) + 1 \rceil] \\ 0, &amp; \text{else} \end{cases}</math>   <b>Else</b> <math>D^{(i)} = 1 \quad i = 1, \dots, d</math>   <b>End If</b>   <b>End If</b>   <math>V_i(t+1) = x_{i, \text{tar}}(t) + a \cdot D \cdot (x_i(t) - x_{i, \text{tar}}(t))</math>   <b>If</b>   <math>f(V_i(t+1)) &lt; f(x_i(t))</math>   <b>Then</b>   <math>x_i(t+1) = V_i(t+1)</math>   <b>For</b> jth fd_src from 1 to <math>n</math> (<math>j \neq \text{tar}, i</math>), <b>Do</b>   <math>V\_tbl(i, j) = V\_tbl(i, j) + 1</math>,   <b>End for</b>   <math>V\_tbl(i, \text{tar}) = 0</math>,   <b>For</b> jth fd_src from 1 to <math>n</math> (<math>j \neq \text{tar}, i</math>), <b>Do</b>   <math>V\_tbl(j, i) = \max(V\_tbl(j, l)) + 1</math>   <math>l \in n</math> and <math>l \neq j</math>   <b>End For</b> </pre>	<pre> <b>Else</b> <b>For</b> jth fd_src from 1 to <math>n</math> (<math>j \neq \text{tar}, i</math>), <b>Do</b>   <math>V\_tbl(i, j) = V\_tbl(i, j) + 1</math>, <b>End For</b>   <math>V\_tbl(i, \text{tar}) = 0</math>, <b>End</b> <b>Else</b> <math>V_i(t+1) = x_i(t) + b \cdot D \cdot x_i(t)</math> <b>If</b> <math>f(V_i(t+1)) &lt; f(x_i(t))</math> <b>Then</b> <math>x_i(t+1) = V_i(t+1)</math> <b>For</b> jth fd_src from 1 to <math>n</math> (<math>j \neq i</math>), <b>Do</b>   <math>V\_tbl(i, j) = V\_tbl(i, j) + 1</math>, <b>End For</b> <b>For</b> jth fd_src from 1 to <math>n</math>, <b>Do</b>   <math>V\_tbl(i, j) = \max(V\_tbl(j, l)) + 1</math>   <math>l \in n</math> and <math>l \neq j</math> <b>End For</b> <b>Else</b> <b>For</b> jth fd_src from 1 to <math>n</math> (<math>j \neq i</math>), <b>Do</b>   <math>V\_tbl(i, j) = V\_tbl(i, j) + 1</math>, <b>End For</b> <b>End If</b> <b>End If</b> <b>End For</b> <b>If</b> <math>\text{mod}(t, 2n) == 0</math>, <b>Then</b>   <math>x_{\text{wor}}(t+1) = \text{Low} + r \cdot (\text{Up} - \text{Low})</math> <b>For</b> jth fd_src from 1 to <math>n</math> (<math>j \neq \text{wor}</math>), <b>Do</b>   <math>V\_tbl(\text{wor}, j) = V\_tbl(\text{wor}, j) + 1</math>, <b>End For</b> <b>For</b> jth fd_src from 1 to <math>n</math>, <b>Do</b>   <math>\text{Visit\_table}(j, \text{wor}) = \max(V\_tbl(j, l)) + 1</math>   <math>l \in n</math> and <math>l \neq j</math> <b>End For</b> <b>End If</b> <b>End While</b> </pre>
---	---

### 3. GWO Algorithm

Gray wolf Optimization (GWO) gray wolves; It was inspired by the fact that they lived in packs and hunted together, forming a strong social hierarchy [7].

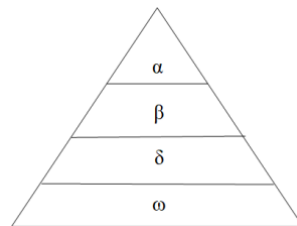


**Figure 1.** Hierarchy in gray wolves [7]

The hierarchical structure of the gray wolf algorithm is shown in Figure 1. Alpha is the leader in Gray Wolf Optimization. Alpha; It is responsible for making decisions such as hunting, sleeping place, and time to get up and communicating these decisions to the swarm. Beta is at the second level in the hierarchy. The beta assists the alpha in decision making or other swarm-related activities. The wolf at the third level is the delta. While Delta takes orders from alpha and beta, he gives orders to those below him in the hierarchy pyramid. Scouts, lookouts, elders, hunters and rangers make up the delta. In the hierarchy pyramid, omega is at the lowest level and omega receives orders from wolves at the higher level [8].

GWO simulates the hunting strategies of gray wolves apart from the social hierarchy of wolves. In GWO, in order to model the social hierarchy mathematically, the best individual is taken as alpha ( $\alpha$ ), second individual as beta ( $\beta$ ), and third individual as delta ( $\delta$ ). It is expected that the remaining solutions are omega ( $\omega$ ) [8].

### 3.1. Components of the GWO Algorithm

The GWO algorithm was developed, inspired by the hunting and feeding behavior of gray wolves living in packs. The hunting behavior of wolves is shown in Figure 2.

**Encircling prey:** Gray wolves have the ability to find and surround their prey. . Hunting behavior of gray wolves; chasing, encircling the prey, and attacking the prey. [9]

**Hunting:** Although beta and delta sometimes take place in hunting, it usually takes place as a result of alpha's guidance. To model this mathematically, it is assumed that alpha, beta, and delta are better solutions than others for locating prey. For this reason, new locations of search agents, including omega, are updated according to the three best solutions.

**Search for prey (exploration):** When the A value is greater than 1 in the gray wolf algorithm, a better prey search is provided by moving away from its prey and thereby improving the global research ability of the gray wolf optimization algorithm.

**Attacking prey (exploitation):** The basic exploitation phase of the gray wolf algorithm is just like in the real world, these wolves first attack their prey and then eat it until it is finished. This corresponds to the exploitation phase of the algorithm. Flowchart of gray wolf algorithm Figure 3 is also shown.



Figure 2. Hunting in gray wolves [7]

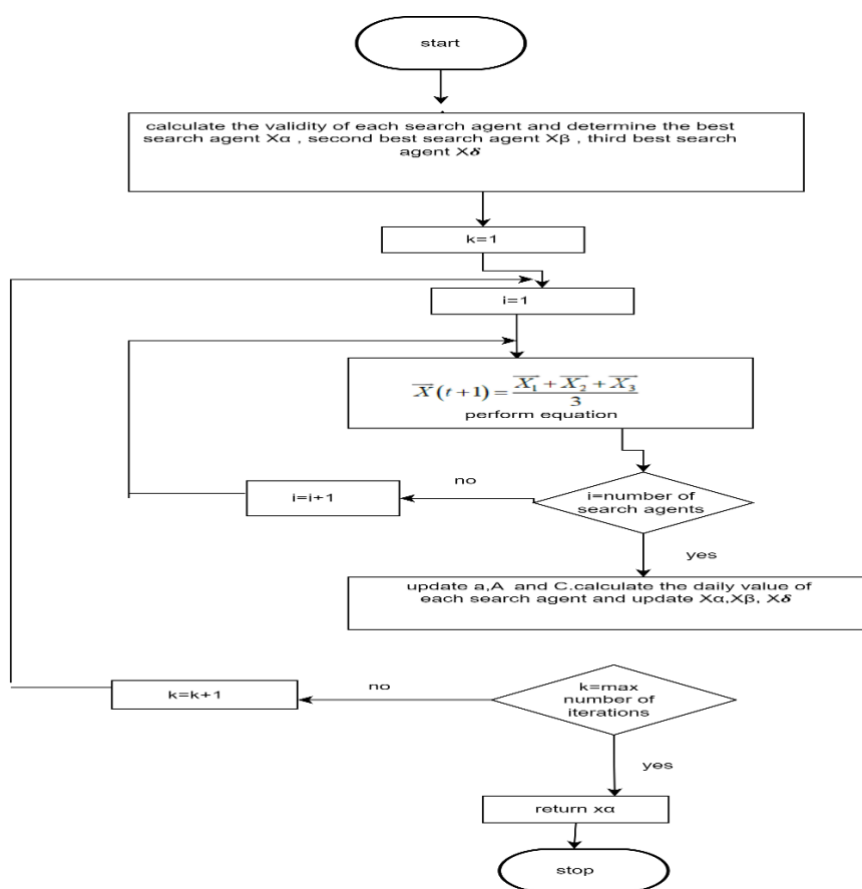


**Figure 3.** Flow Chart of the Gray Wolf Algorithm

#### 4. WOA Algorithm

Humpback whales are the largest of the whale species. Humpback whales have a great hunting method for finding small and krill fish. WOA was developed inspired by this hunting behavior of humpback whales [10]. The distinctive bubble behavior of humpback whales, which often graze on shoals of tiny fish, allows them to breathe underwater and produce bubble clouds. As seen in Figure 4, these huge, interconnecting air bubble masses are quite successful at rallying victims. The whale then starts to ascend towards the surface in the newly generated bubbles. It continues to bubble as it ascends, and as it gets closer to its intended prey, the bubble circle gets smaller and the target gets smaller. This behavior allows the hunter to remain hidden from the prey while also locating the prey, immobilizing it, and taking it by surprise [11].

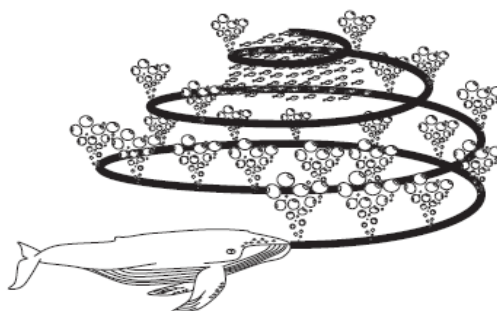


**Figure 4.** Bubble Hunting of Humpback Whales [10]

#### 4.1. WOA Components

The three components of the whale optimization algorithm's hunting strategy are circling the prey, approaching the prey, and looking for prey [12].

**Encircling prey:** Since the optimum solution to optimization issues is unknown, the algorithm's best result or a point very close to it is taken to be the ideal answer. According to the best solution value found, the positions of the other solutions are updated.

**Don't move towards the prey:** This stage is modeled in two parts as constricting the circle around the prey and spiral movement. Humpback whales in nature perform the constricting containment mechanism and the spiral movement at the same time. That is, a humpback whale can choose a constricting motion or a spiraling motion when updating its position relative to the best humpback whale. Therefore, WOA uses these two behaviors with a 50 percent probability.

**Search for prey (exploration):** The global solution determines the new positions of the solution candidates around a randomly chosen solution candidate instead of calculating the best known solution candidate.

The flowchart of the whale algorithm is shown Figure 5. In the flowchart  $X^*$  is the best available position vector,  $\vec{X}$  the location vector of the relevant search agent,  $\vec{A}$  and  $\vec{C}$  coefficient vector,  $r$  [0 1] takes a random value in the range,  $a$  decreases linearly from 2 to 0 during the iteration.  $D$  where  $p$  is the distance between *whale* and *prey*, spiral motion.

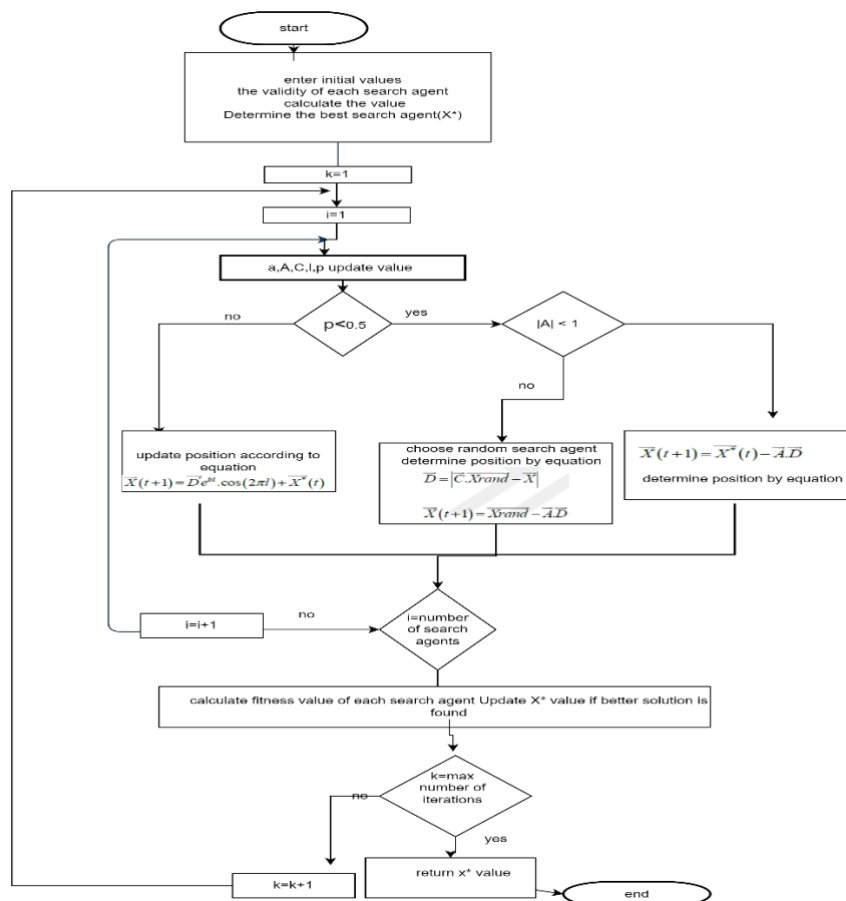


Figure 5. Flowchart of Whale Optimization Algorithm

### 5. ALO Algorithm

Ant lions construct their cone-shaped traps by constructing a circular trail to the ant colonies. They then wait for the ants to fall into the trap by burrowing themselves into the bottom of the cone, which serves as the trap's pointy end. The ant lions begin tossing sand as soon as the ants enter the trap to keep them from escaping and to help them fall to the bottom of the trap. Finally, they swallow the ants, which they slide to the bottom of the trap, with their large jaws. After each hunting job developed in this way, ant lions prepare their traps for a new hunt. The hunting tactic of the ant lion is shown in Figure 6 [13].



Figure 6. Ant lion hunting [12]

#### 5.1. Components of the ALO

The ALO algorithm replicates the five essential phases of hunting: ant random wander, trap setting, ant capture in a trap, prey capture, and trap rebuilding [14]. The flow diagram of the ALO algorithm is given in Figure 7.

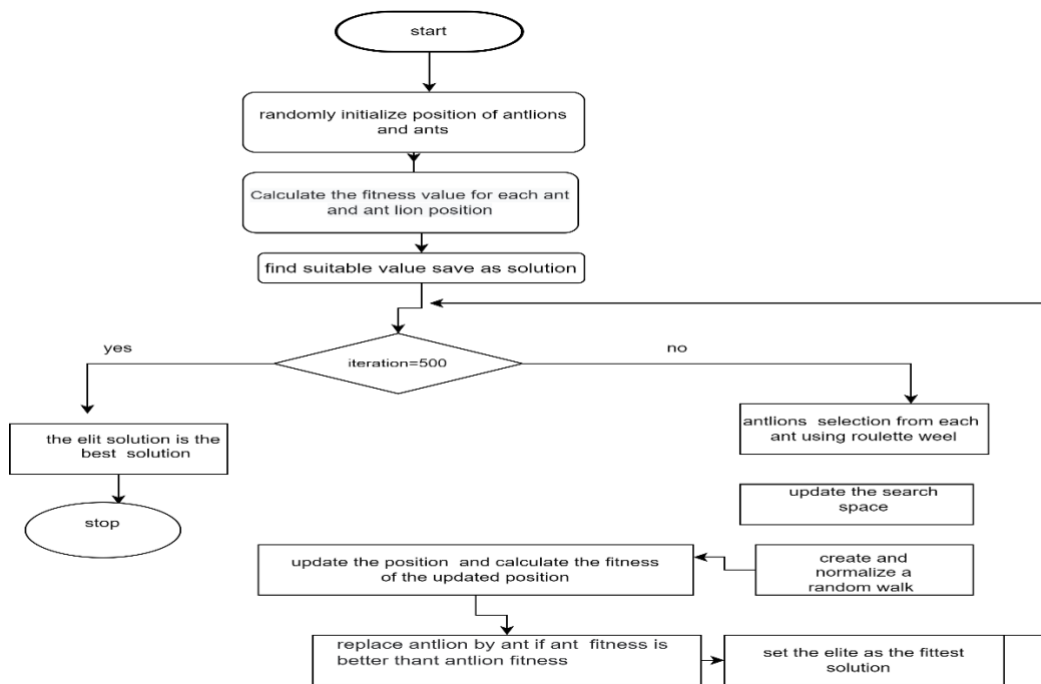


Figure 7. Flowchart of Ant Lion Algorithm

## 6. DA Algorithm

The main inspiration for the creation of the dragonfly algorithm is the static and dynamic swarming behavior of dragonflies. These two characteristics resemble the two primary stages of optimization where metaheuristics are employed: research and exploitation. The primary goal of the exploration phase is to see how dragonflies organize into smaller swarms and fly over various places in a static swarm. The exploitation phase benefits from dragonfly static swarms because they fly in larger flocks and in a single direction [15].

### 6.1. Components of the DA

According to Reynold, the swarming behavior of dragonflies falls within three basic principles.

- a- **Separation**; means to avoid collision with other people in the neighbourhood.
- b- **Alignment**; shows the speed compatibility with other individuals in the neighborhood.
- c- **Cohesion**; refers to the tendency of individuals towards the center of the neighborhood mass.
- d- **Attraction for food**; the main purpose of any swarm is to survive and therefore individuals must tend towards their food source.
- e- **Enemy**; the flock can be disturbed by outside enemies. These components are shown in Figure 8. The flow diagram of the dragonfly algorithm is shown in Figure 9.

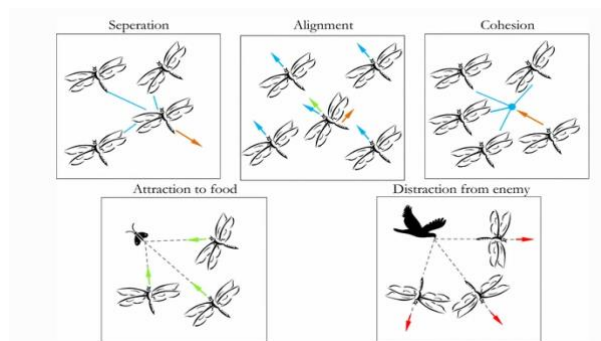


**Figure 8.** Modeling the behavior of dragonflies ((a) Separation, (b) alignment, (c) cohesion, (d) attraction for food, (e) escape from the enemy) [16]

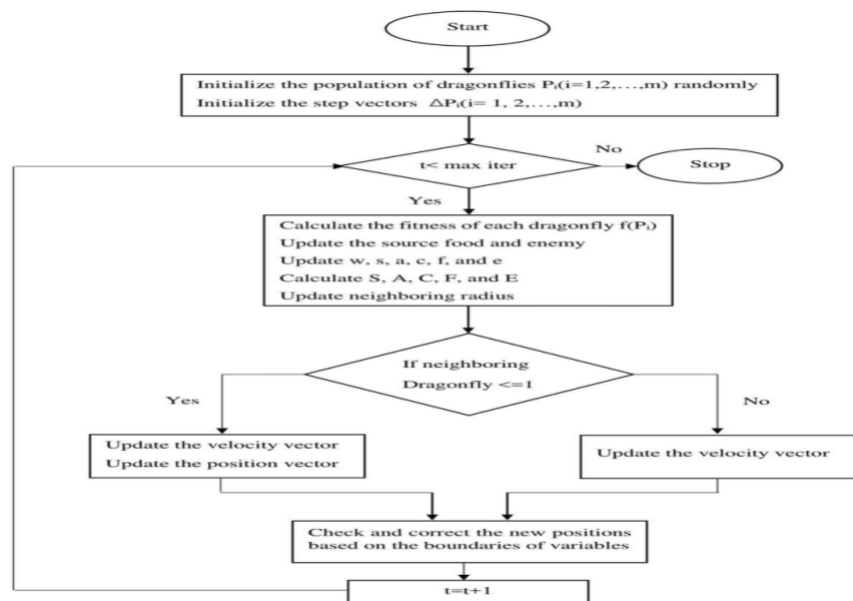


**Figure 9.** Flow diagram of the DA

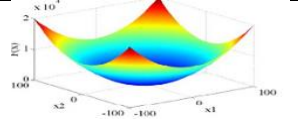
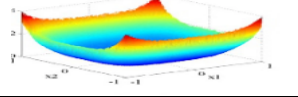
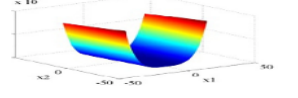
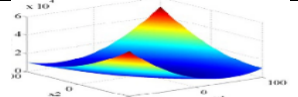
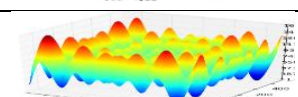
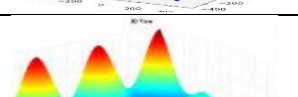
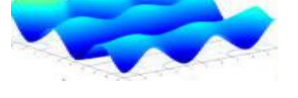
In the flowchart of the dragonfly algorithm Separation behavior  $S_i$ , Alignment behavior  $A_i$ , Association behavior  $C_i$ , Food source  $FI$ , Distracting enemy  $E_i$ , Position of dragonflies  $X_i$ , Direction of dragonflies movement

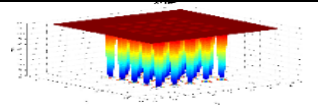
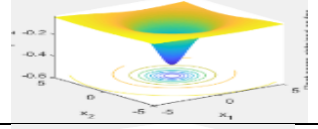
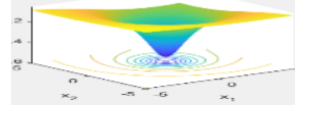
**7. Benchmark Functions and Experimental Results**

All of the experiments were carried out on a Windows 10 operating system computer with Intel i5 processor, 4 GB graphics card, and 16 GB RAM. All algorithms were run under equal conditions. The number of candidate solutions was determined as 10 and the number of iterations was determined as 100. During the experiments, each algorithm was run independently 10 times. During the experiments, the best performance of the algorithms as "min", the worst performance as "max", the mean values "mean" and the standard deviation "std" are shown in Table 3.

The performance of metaheuristic optimization algorithms has been tested in 10 unimodal and multimodal quality test functions. The mathematical expression, size, low-up, and 3-D graphics of these functions are given in Table 2. The performances of metaheuristic algorithms are shown in Table 3.

**Table 2.** Benchmark function that we used in our study

	Mathematical expression	Function	Size	Low-Up	3-D Graphic
f1	$\sum_{i=1}^n X_i^n$	Sphere	30	[-100, 100]	
f2	$\sum_{i=1}^n iX_i^4 + random[0,1]$	Quartic	30	[-1.28, 1.28]	
f3	$\sum_{i=1}^{n-1} [100(X_{i+1} - X_i^2) + (X_i - 1)^2]$	Rosenbrock	30	[-30, 30]	
f4	$\sum_{i=1}^n (\sum_{j=1}^i X_j)^2$	Schwefel1.2	30	[-100, 100]	
f5	$\sum_{i=1}^n -X_i \sin(\sqrt{ x_i })$	Schwefel	30	[-500, 500]	
f6	$\frac{\pi}{\mu} \left\{ (10 \sin(\pi y_1)) + \sum_{i=1}^{n-1} (y_{i-1})^2 [1 + 10 \sin^2(\pi y_{i+1}) + (y_n - 1)^2] \right\}$ $+ \sum_{i=1}^n \mu(X_i, 10, 100, 4)$ $+ \frac{X_i + 1}{4} \mu(X_i, a, k, m)$ $= \begin{cases} k(X_i - a)^m & X_i > a \\ 0 & -a < X_i < a \\ k(-X_i - a)^m & X_i < -a \end{cases}$	Penalized	30	[-50, 50]	
f7	$\sum_{i=1}^{11} [a_i - \frac{X_i (b_i^2 + b_i X_2)}{b_i^2 + b_i X_3 + X_4}]^2$	Kowalik	4	[-5, 5]	

f8	$\frac{1}{500} + \sum_{j=1}^{25} \frac{1}{j + \sum_{i=1}^2 (X_i - a_i)^6}$	Foxholes	2	[-65536, 65536]	
F9	$\sum_{i=1}^5 [(X - a_i)(X - a_i)^T + c_i]^{-1}$	Shekel5	4	[0, 10]	
f10	$\sum_{i=1}^{10} [(X - a_i)(X - a_i)^T + c_i]^{-1}$	Shekel10	4	[0, 10]	

**Table 3.** Performance ranking of each algorithm for each function

		AHA	DA	WOA	ALO	GWO
<b>f1</b>	Min	9.12E-152	1.1907609	1.35E-82	0.0000966	3.86E-25
	Max	1.73E-138	9.844576	2.84E-70	0.00047257	8.91E-23
	Mean	2.53E-139	5.07500656	3.45E-71	0.000315656	2.20E-23
	Std	5.4949E-139	3.377311435	8.86385E-71	0.000149881	3.07612E-23
<b>f2</b>	Min	0.0001003	0.10041	0.00014927	0.071756	0.0004015
	Max	0.76047	0.76356	0.017281	0.27236	0.0038547
	Mean	0.120642553	0.475331	0.00293937	0.1680026	0.001711651
	Std	0.264469479	0.238954597	0.005207293	0.062277744	0.001037898
<b>f3</b>	Min	2.62052	10.8272623	27.4626	21.359	26.0935
	Max	2.73431	48.8701355	28.7498	2041.9985	28.7489
	Mean	2.660833	20.97074773	27.82521	461.82734	27.51782
	Std	0.035851183	12.11520826	0.362612421	685.0012458	1.119730584
<b>f4</b>	Min	2.71E-139	4984.86	23598.49	99.67	2.17E-03
	Max	8.82E-126	86499.82	68700.99	3274.40	4.34E-01
	Mean	8.83E-127	23052.09	47879.37	2256.25	7.97E-02
	Std	2.7897E-126	24303.27	14954.70	885.64	0.137797611
<b>f5</b>	Min	-7204.36	-65337.08	-120688.57	-7585.36	-7650.84
	Max	-5562.74	-6762.20	-8307.41	-5117.15	-5150.69
	Mean	-6558.14	-50808.21	-21278.14	-6355.05	-6203.37
	Std	570.53	16281660.96	34971.94	846.92	735.62
<b>f6</b>	Min	0.00010648	1.60612	0.0054591	4.7364	0.022058
	Max	0.79688	9.9621	0.15795	22.2252	0.090913
	Mean	0.08077894	3.9121777	0.02751851	10.70978	0.0448123
	Std	0.251620616	2.623666763	0.046326745	5.217910697	0.019629011
<b>f7</b>	Min	0.0003404	0.00065729	0.00032828	0.0003111	0.0003075
	Max	0.0012634	0.0016555	0.0022519	0.0012446	0.020363
	Mean	0.000603179	0.001035532	0.001099359	0.000896353	0.004451198
	Std	0.00028031	0.000344255	0.000861785	0.000261617	0.008390604
<b>f8</b>	Min	0.998	0.998	0.998	0.998	0.998
	Max	10.001	1.992	10.7632	5.9288	12.6705
	Mean	2.380002	1.3956	5.79437	1.88829	4.81292
	Std	2.759779274	0.513299393	4.492096588	1.574072941	4.645515959
<b>f9</b>	Min	-10.15	-10.15	-10.15	-10.15	-26.30
	Max	-5.04	-5.05	-2.62	-2.6305	-10.15
	Mean	-7.47	-7.11	-7.76	-6.11858	-11.76
	Std	2.56	5.18	2.95	2.94	5.10
<b>f10</b>	Min	-10.5303	-10.5364	-10.53	-10.5364	-10.5358
	Max	-5.1253	-5.1285	-2.42	-1.8595	-10.5333
	Mean	-8.29517	-8.38704	-6.20	-5.53283	-10.53457
	Std	2.728681234	2.77428543	3.170572096	3.623704507	0.000938142



## 8. Conclusion

Various optimization algorithms have been created by inspiring different living things in nature. These are used in solving today's complex engineering problems. In previous studies, AHA's performance has been tested against many algorithms such as Particle swarm algorithm, Salp swarm algorithm, Differential convolution algorithm, Butterfly algorithm, Shade algorithm, which are the first optimization algorithms of AHA, and it has been proven that it gives faster results than the analyzed algorithms and provides the best convergence to the global optimum [6]. In this study, we tested the performance of AHA with current optimization algorithms. We observed that AHA is faster and gives more successful results. In f5, f7, and f9 functions, AHA generally achieved a worse min value than other algorithms. AHA algorithm obtained similar min values with other algorithms in f8 and f10 functions. In addition, the AHA algorithm obtained better results than other algorithms in f1, f2, f3, f4, and f6 functions. In the future, it is planned to test the performance of the metaheuristic algorithms examined in this study on limited real-world problems.

## References

- [1] Murty KG. Optimization models for decision making: Volume. University of Michigan, Ann Arbor, USA, 2003.
- [2] Baydoğan C. Sentiment Analysis in Social Networks Using Social Spider Optimization Algorithm. *Tehnički vjesnik* 2021; 28(6): 1943-1951.
- [3] Winston WL. Operations research: applications and algorithms. Cengage Learning, USA, 2022.
- [4] Baydoğan C, Alatas B. Metaheuristic ant lion and moth flame optimization-based novel approach for automatic detection of hate speech in online social networks. *IEEE Access* 2021; 9, 110047-110062.
- [5] Ehlers S. A procedure to optimize ship side structures for crashworthiness. *Proceedings of the Institution of Mechanical Engineers, Part M: Journal of Engineering for the Maritime Environment* 2010; 224(1): 1-11.
- [6] Zhao W, Wang L, Mirjalili S. Artificial hummingbird algorithm: A new bio-inspired optimizer with its engineering applications. *Comput. Methods Appl Mech Eng* 2022; 388, 114194.
- [7] Mirjalili S, Mirjalili SM, Lewis A. Grey wolf optimizer. *Adv Eng Software* 2014; 69: 46-61.
- [8] Asghari K, Masdari M, Gharehchopogh, FS, Saneifard R. A chaotic and hybrid gray wolf-whale algorithm for solving continuous optimization problems. *Prog Artif Intell* 2021; 10(3): 349-374.
- [9] Şenel FA, Gökçe F, Yüksel AS, Yiğit T. A novel hybrid PSO–GWO algorithm for optimization problems. *Eng Comput* 2019; 35(4): 1359-1373.
- [10] Mirjalili S, Lewis A. The whale optimization algorithm. *Adv Eng Software* 2016; 95: 51-67.
- [11] Gharehchopogh FS, Gholizadeh H. A comprehensive survey: Whale Optimization Algorithm and its applications. *Swarm Evol Comput* 2019; 48: 1-24.
- [12] Deepa R, Venkataraman R. Enhancing Whale Optimization Algorithm with Levy Flight for coverage optimization in wireless sensor networks. *Computers & Electrical Engineering* 2021; 94, 107359.
- [13] Kılıç H, Yüzgeç U. Improved antlion optimization algorithm via tournament selection and its application to parallel machine scheduling. *Comput Ind Eng* 2019; 132: 166-186.
- [14] Yue X, Zhang H. A novel industrial image contrast enhancement technique based on an improved ant lion optimizer. *Arabian J Sci Eng* 2021; 46(4): 3235-3246.
- [15] Acı Çİ, Gülcan H. A modified dragonfly optimization algorithm for single-and multiobjective problems using Brownian motion. *Comput Intell Neurosci* 2019; 2019, 6871298: 1-17.
- [16] Mirjalili S. Dragonfly algorithm: a new meta-heuristic optimization technique for solving single-objective, discrete, and multi-objective problems. *Neural Comput Appl* 2016; 27: 1053-1073.



## 3-D Printed Dual-Band Frequency Selective Surfaces for Radome Applications

Mete BAKIR<sup>1,2\*</sup>

<sup>1</sup> Makine Mühendisliği, Mühendislik ve Doğa Bilimleri Fakültesi, Ankara Yıldırım Beyazıt Üniversitesi, Ankara, Türkiye

<sup>2</sup> Malzeme Mühendisliği, Türk Havacılık ve Uzay Sanayii, Ankara, Türkiye

\*<sup>1</sup> mete.bakir@aybu.edu.tr, <sup>2</sup> mete.bakir@tai.com.tr

(Geliş/Received: 15/12/2022;

Kabul/Accepted: 21/02/2023)

**Abstract:** In this study, dual-band frequency selective surface (FSS) structures are designed by using 3-D printing technology for antenna radome applications. Four different configurations are studied to find the best alternative for FSS substrate not only for electromagnetic (EM) responses but also for its mechanical properties suitable for radomes. To ease the manufacturing process, a conductive paint is also studied instead of copper microstrip lines. In addition, graphite is also used for the comparison. Different 3-D printed configurations, various thickness values and three different materials for conductive part are examined and compared to find the most efficient radome structure.

**Key words:** 3-D Printer, Additive Manufacturing, Radome, Conductive paint, FSS.

### Radom Uygulamaları için 3-B Baskılı Çift Bantlı Frekans Seçici Yüzeyler

**Öz:** Bu çalışmada anten radom uygulamaları için 3 boyutlu baskı teknolojisi kullanılarak çift bantlı frekans seçici yüzey (FSY) yapıları tasarlanmıştır. Sadece elektromanyetik (EM) tepkiler için değil, aynı zamanda radomlara uygun mekanik özellikleri için de FSY substratı için en iyi adayı bulmak üzere dört farklı konfigürasyon üzerinde çalışılmıştır. Üretim sürecini kolaylaştırmak için bakır mikroşerit hatların yerine iletken bir boya üzerinde de çalışılmıştır. Ayrıca karşılaştırma için grafit de kullanılır. En verimli radom yapısını bulmak için farklı 3-D baskılı konfigürasyonlar, çeşitli kalınlık değerleri ve iletken kısım için üç farklı malzeme karşılaştırılmıştır.

**Anahtar kelimeler:** 3-B yazıcılar, eklemeli imalat, radom, iletken boya, FSY.

#### 1. Introduction

With the developing technology, the production and manufacturing of materials have been improved with the help of 3-D printing technology in the material science area. As in Fused Filament Fabrication (FFF), Fused Deposition Modeling (FDM), Selective Laser Sintering (SLS), and PolyJetting, 3-D printing technology is based on layered production and additive manufacturing. The main advantage of 3-D printers is that very complex structures that cannot be manufactured in CNC machines can be designed and produced easily and in a very short time. 3-D printer technology has been started to be used in several areas from agriculture to the aerospace industry. 3-D printed materials also attract the scientific world and engineering industry in the electromagnetic field.

In this study, the application of 3-D printed materials in designing FSS structures was investigated. Frequency-selective surfaces (FSS) are composed of periodic resonators providing filtering functions for EM waves at any desired frequency band [1]. These periodic cell structures can be used as low-pass, high-pass, band-pass, and band-stop filtering operations. FSS structure is generally composed of metallic periodic resonators placed on a dielectric layer. For our purpose, a dual-band FSS structure providing band-pass response was designed and analyzed on a 3D-printed substrate layer on a radome. With the increasing need in the communication field, electromagnetic interference has become a significant problem, particularly in hospitals, government buildings, military facilities and so on where high sensitivity is needed. Such demand yielded a growing interest in using artificial materials to obtain more efficient results that cannot be obtained from natural materials.

Through a literature review, it is observed that there are some studies on FSS design using 3-D printing technology with various purposes. In a study, Deepika et al. studied FSS printed with acrylonitrile butadiene styrene plastic material using 3-D printers for radar applications [2]. In another study, Singh et al. developed a

\* Corresponding author: [mete.bakir@tai.com.tr](mailto:mete.bakir@tai.com.tr). ORCID Number of authors: <sup>1,2</sup> 0000-0002-5044-3104

circular loop FSS structure with the help of 3-D printers by using ABS material and circular loop shape structures [3]. In another study, Alvarez et al. investigated a 3-D conformal bandpass FSS operating at 26-40 GHz [4]. In addition, Izquierdo et al. developed a 3D folded dipole FSS structure for electromagnetic structure control [5]. Moreover, there are studies on the use of 3D technology in a lot of electromagnetic applications including radome structures for various antenna types and frequency bands [6-8]. This technology is also studied on different antenna parts such as the ground plane. Such applications are usually called electromagnetic band gap (EBG) structures [9].

In general, the FSS structure is designed and manufactured on planar surfaces using an FR-4 type substrate as the dielectric layer, and copper is generally used for the resonator structure. However, this approach is challenging and expensive if FSS structures will be placed on a curved surface or any non-planar zones. For this purpose, conductive paint and graphite were also examined and the obtained performances are compared by taking copper as the reference. This study focuses on designing an efficient dual-band FSS structure with the help of 3-D printed materials by optimizing conductor type, thickness, and raster orientation of substrate providing band-pass behavior at two frequency bands.

## 2. Materials and Methods

### 2.1. Manufacturing 3-D printed samples and Electromagnetic Characterization

For the plastic material of the samples, PLA (Polylactic Acid) filament (MICROZEY PLA, with 1.75 mm diameter) was used. Four samples were printed with different raster orientations as shown in Figure-1 below. The manufactured products have high tensile strength and impact resistance, fast printing ability, and provide very sufficient surface quality. As seen in the figure, the samples have four different configurations of raster orientations. It is well known that raster orientations significantly affect the mechanical strength of the structures.

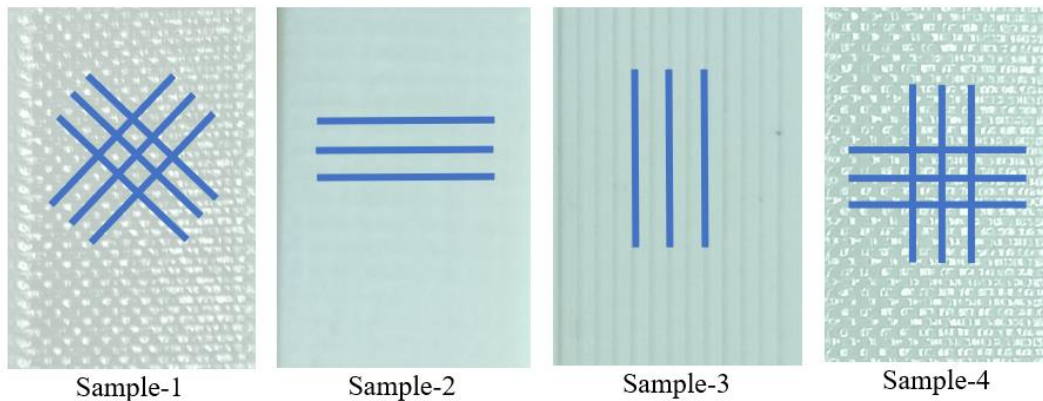


**Figure 1.** 3-D Printed Samples with different configurations

As seen in the figure, each manufactured sample has different raster orientations while their other properties are kept the same. All samples have 30.0% filler density with 200 °C printing temperature while their raster orientations are 45° Grid for Sample-1, Horizontal Lines for Sample-2, Vertical lines for Sample-3 and 90° Grid for Sample-4.

FSS structures are normally produced on printed circuit boards using FR-4 material as the dielectric substrate. Without exception, all electromagnetic simulation programs have libraries providing electromagnetic properties of well-known and most commonly used dielectric materials. To define the produced samples in the computer environment, their electromagnetic properties have to be determined. Some of the methods for this purpose are free space, dielectric probe method, and waveguide measurement setup. The waveguide measurement system was preferred in this study since it requires samples with smaller dimensions compared to the other methods. The samples shown in Figure-1 have rectangular shapes in the dimensions that can fit waveguide sample holder operating at 12-18 GHz. The waveguide measurement setup contains a 2-port vector network analyzer (VNA), two waveguides with two adaptors and a sample holder to place the samples as shown in Figure 2.

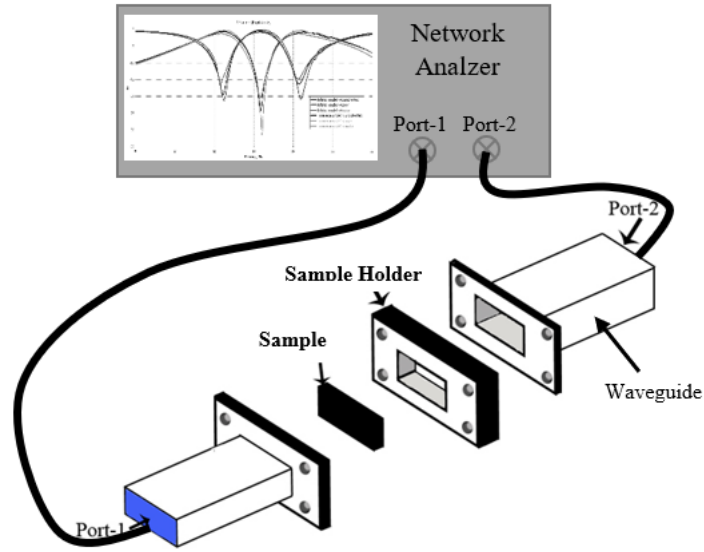


**Figure 2.** Waveguide test setup used to find electromagnetic characteristics of the samples.

With this test method, scattering parameters (S-parameters) providing reflection and transmission information between ports are obtained. Complex electrical permittivity “ $\epsilon$ ” and magnetic permeability “ $\mu$ ” values with respect to frequency can be determined by using the obtained S-parameters. One of the most commonly used method is Nicholson Ross Weir (NRW) method which is used in this setup. NRW method was found by scientists; Nicholson, Ross and Weir in their studies [10,11]. In this method, complex “ $\epsilon$ ” and “ $\mu$ ” values can be found as follows;

$$\mu_r^* = \frac{2\pi}{\Lambda\sqrt{k_0^2 - k_c^2}} \left( \frac{1+\Gamma}{1-\Gamma} \right) \quad (1)$$

$$\epsilon_r^* = \frac{1}{\mu_r^* k_0^2} \left( \frac{4\pi}{\Lambda^2} + k_c^2 \right) \quad (2)$$

Here,

$$\Gamma = X \pm \sqrt{X^2 - 1} \quad (3)$$

$$X = \frac{S_{11}^2 - S_{21}^2 + 1}{2S_{11}} \quad (4)$$

$$T = \frac{S_{11} + S_{21} - \Gamma}{1 - (S_{11} + S_{21})\Gamma} \quad (5)$$

$$\frac{1}{\Lambda^2} = - \left[ \frac{1}{2\pi L} \ln (T) \right]^2 \quad (6)$$

After obtaining EM properties of the 3-D printed samples, they were transferred into the electromagnetic simulation program in computer environment. All different combinations with different conductive materials are tested as a substrate for designing the FSS unit cell structure.

## 2.2. Dual-band FSS Unit Cell Design and Simulation

In this study, we have used diamond shape FSS structure to obtain band-pass behavior. In order to achieve dual-band behavior, the same structure with different sizes were placed in a single cell as shown in Figure-3.

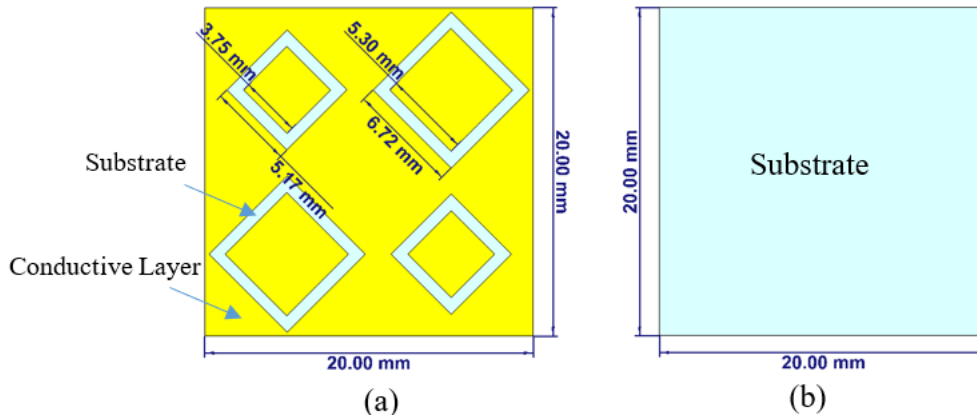


**Figure 3.** Front (a) and back (b) side of the dual band FSS cell structure.

FSS structures are composed of conductive and dielectric layers. In order to design and manufacture an FSS structure, a conductive material must be used on top of the substrate. Most FSS applications in literature and industry are based on planar surfaces. However, there is a need to integrate these periodic structures on non-planar surfaces such as radomes. Therefore, a conductive material with sufficient reflection behavior is needed since conventional methods will be hard and expensive to apply on curved surfaces. At this point, conductive paint has become a very reliable candidate for replacing copper in this type of structure. In general, metal-based pigments (copper, aluminum, zinc, silver etc.) are found in conductive paint products while there are other and different formulations providing conductivity. These types of paints are widely used in different industries including aerospace and automotive. By reviewing related literature and commercial products, the most suitable conductive paint candidate was determined. During this selection, particularly surface resistance value stated in the technical datasheet of the products was taken into consideration. The conductive paint selected for this study is a copper-based product having two component, 3-part binder, and 1.6 g/cm<sup>3</sup> specific gravity value. In terms of surface resistance, the paint has 0.3  $\Omega$ /sq value after final curing period. For comparison, graphite was also used for the replacement of copper and the results for all cases are obtained using CST Microwave Studio.

## 3. Results and Discussion

The results will be discussed for four main cases depending on the material used for the dielectric layer of FSS. In this context, Sample-1 was used as the substrate in the first case while Sample-2, Sample-3, and Sample-4 were used for the second and third cases. Each case includes the use of copper, conductive paint, and graphite as the resonator layer (conductive layer) of FSS. Substrates built by using 3D printed samples were used and compared for all cases in order to achieve maximum efficiency for radome applications. The obtained results for the first case are given in the following figure (Figure 4). As seen in the figure, using 3D-printed samples as the substrate, we have successfully obtained band-pass behavior at two separate frequency bands. The figure provides the reflection and transmission behavior for Sample-1 with different conducting layers including copper, conductive paint, and graphite. It can be clearly seen that copper provides the best solution but conductive paint and graphite also provide very close behavior. For a better understanding, it should be noted that 0 dB for reflection refers to 100% reflection while -10dB corresponds to 10% reflection. On the other hand, 0dB for transmission refers to 100% transmission of the signal sent from one port to the other while -10dB corresponds to that 10% of the signal is transmitted to the other port. In this context, signals are transmitted more than 95% at around  $f=12.5$  GHz and  $f=16.3$  GHz while the reflection behavior also supports this filtering property.

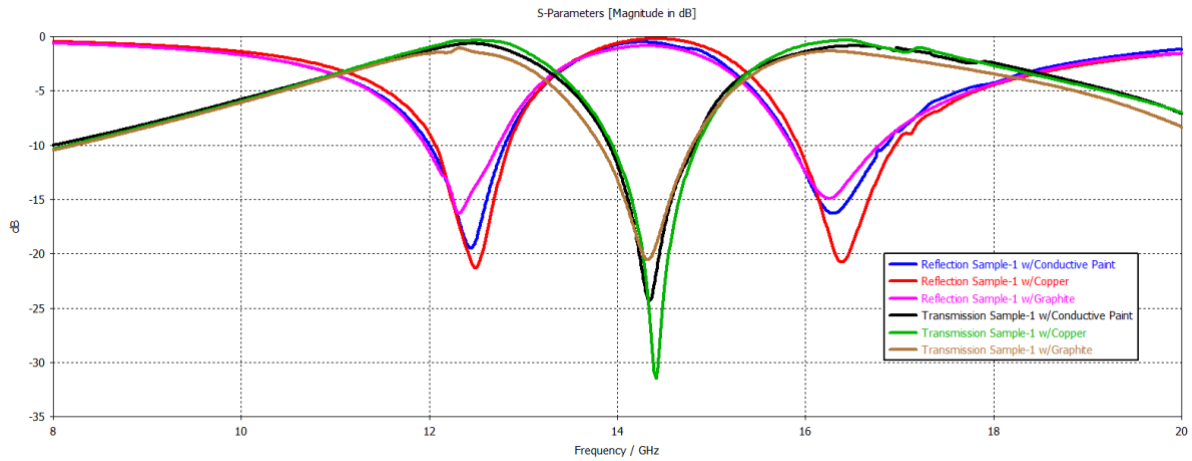


**Figure 4.** Reflection and Transmission behavior of FSS with Sample-1 as the substrate

For the second case, if we change the substrate from Sample-1 to Sample-2, the following transmission and reflection behavior is obtained (Figure 5). As seen in the figure, using conductive paint slightly shifted the filtering band to lower frequencies but it should be noted that the FSS cell structure can be adjusted to work at any frequency range. Therefore, this shift can be adjusted depending on the need. Overall, behavior is very close to the copper case especially at the 1<sup>st</sup> band pass part.

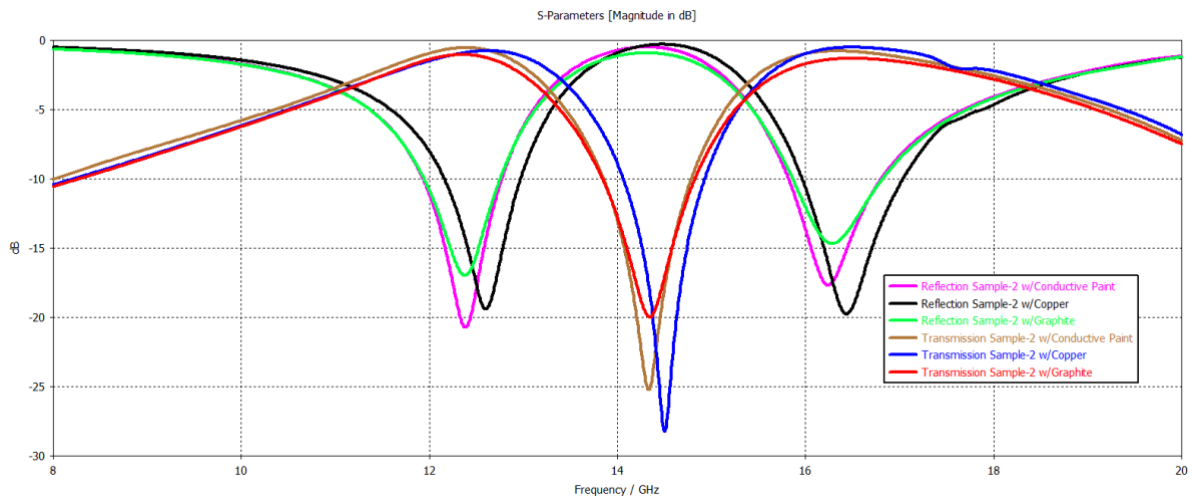


**Figure 5.** Reflection and Transmission behavior of FSS with Sample-2 as the substrate

For the third case, the substrate layer changed to Sample-3 with vertical lines and the obtained reflection and transmission behaviors are drawn in the figure below (Figure 6). There are some oscillations on the curves due to the vertical raster orientations. Since the signals sent from the ports are also vertically polarized, this distortion can be explained by this co-polar behavior.

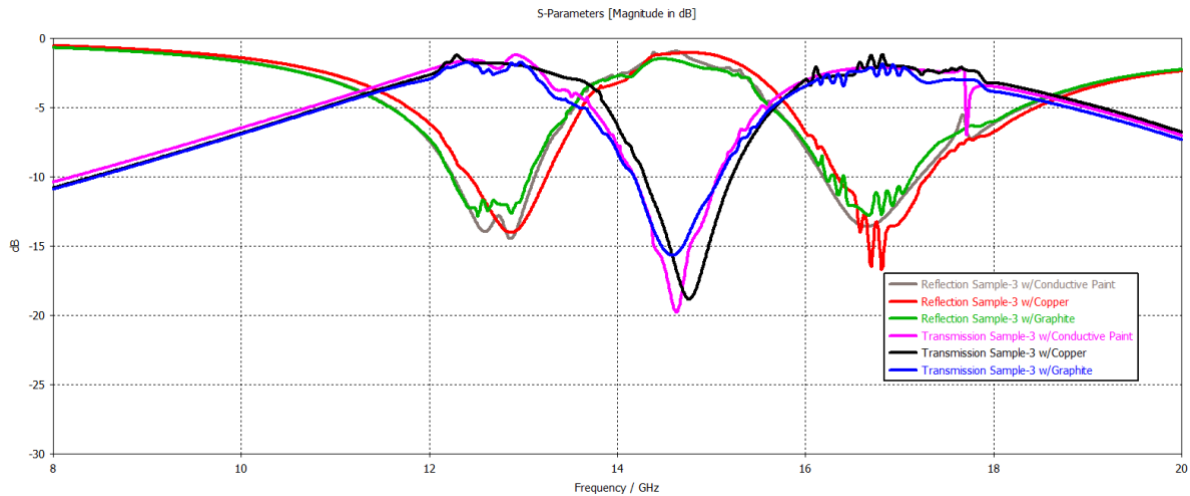


**Figure 6.** Reflection and Transmission behavior of FSS with Sample-3 as the substrate

For the last case, the dielectric substrate of the proposed dual-band FSS structure was changed to Sample-4 with  $90^\circ$  grid configuration. The obtained transmission and reflection values are plotted in Figure 7 below. Unlike the Sample 1 which also has a grid configuration, Sample-5 yields some small oscillation at the band-pass filtering points. This oscillation is a slightly higher for conductive paint but the overall behavior remains the same. The oscillation can also be explained by the grid angle and the polarization of the incoming wave sent by the ports as in the previous case. The structure will provide band-pass behavior at the corresponding frequencies.

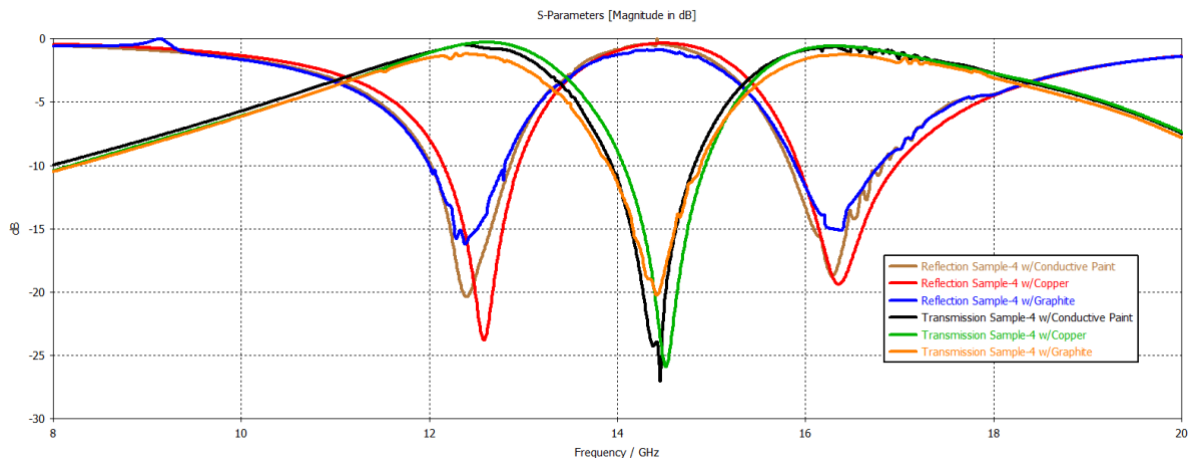


**Figure 7.** Reflection and Transmission behavior of FSS with Sample-3 as the substrate

For a better understanding the effect of resonator size, e-field distributions for low band ( $f=12.5$  GHz) and high band ( $f=16.4$  GHz) were plotted for the first case (Sample-1) with copper conductive layer (Figure 8). Plotting was only made for one case and for one conductive material only since that would be sufficient to show the corresponding effect. As seen in the figure, larger structures are active for the low band while smaller structures become active at the high band which is an expected results due to the wavelengths.



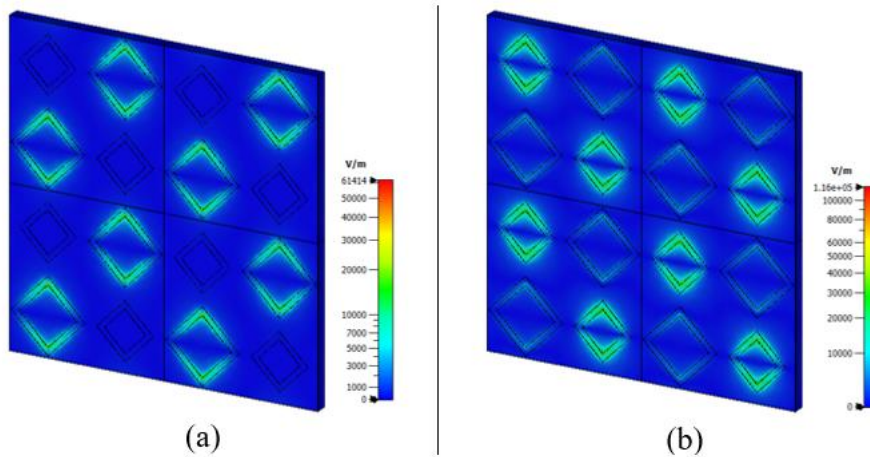


**Figure 8.** E-field distribution for  $f=12.5$  GHz and  $f=16.4$  GHz

In order to clarify the comparison among the different samples used for the substrate and the materials used for the conductive layer, maximum transmission and minimum reflection responses of all cases for two separate filtering bands are tabulated below (Table-1).

**Table 1.** Maximum transmission and minimum reflection values of the designed structure

Sample	Configuration	1 <sup>st</sup> Frequency Band						2 <sup>nd</sup> Frequency Band					
		Max. Transmission (dB)			Min. Reflection (dB)			Max. Transmission (dB)			Min. Reflection (dB)		
		Copper	C. Paint	Graphite	Copper	C. Paint	Graphite	Copper	C. Paint	Graphite	Copper	C. Paint	Graphite
#1	45° Grid	-0.37	-0.64	-1.06	-21.23	-19.45	-16.27	-0.34	-0.86	-1.34	-20.72	-16.27	-14.89
#2	Horizontal Lines	-0.74	-0.51	-1.02	-19.33	-20.74	-16.96	-0.49	-0.75	-1.29	-19.75	-17.66	-14.66
#3	Vertical Lines	-1.18	-1.19	-1.70	-14.01	-14.46	-12.85	-1.14	-2.11	-1.84	-16.72	-13.57	-12.75
#4	90° Grid	-0.29	-0.49	-1.15	-23.78	-20.38	-16.23	-0.59	-0.63	-1.26	-19.35	-18.72	-15.13

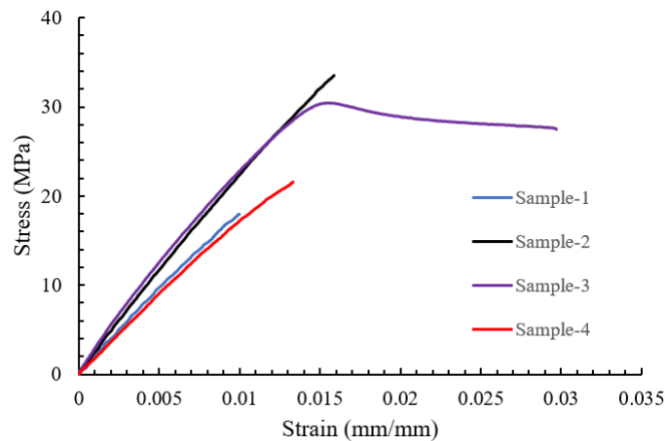


**Figure 9** Mechanical test results for tensile loading configuration

Figure 9 shows the tensile test results for four different sample configurations. Sample-1, with a 45° grid layout, demonstrates 18.0 MPa of tensile strength and 1.0 % of strain that yields a 2.0 MPa of Young’s Modulus. As well, Sample-2, having a horizontal line configuration, shows 33.5 MPa of tensile strength and 1.5 % of strain with 2.4 MPa of Young’s Modulus. It is clear that the single preferential orientation of filaments positively affects the mechanical performance. Sample-3, with a vertical layout, yields 30.4 MPa of tensile strength and 3.0 % of strain, corresponding to 2.7 MPa of Young’s Modulus. By comparing Sample-2 and Sample-3, it is worthwhile to underline that selective orientation along the stress direction improves the plastic deformation capacity, observed

as a higher strain. Sample-4, having 90° grid layout, demonstrates 21.6 MPa of tensile strength and 1.3 % of strain that yields a 1.8 MPa of Young's Modulus. Overall, in line with the electromagnetic analysis, different raster orientations for the plastic substrate differ in mechanical properties due in part to stress distribution along filament position and structural variety to bulk material configuration.

#### 4. Conclusion

In conclusion, a dual-band, diamond shape frequency selective surface was designed using 3-D printed substrates. Different raster orientations along with different conductive layers including copper, conductive paint and graphite were examined. The mechanical properties of the samples were also found. Overall, it can be said that Sample-1 and Sample-4 provide the best filtering behavior for all conductive layer types we have used. Although copper provides smoother and better transmission and reflection behavior, conductive paint will provide the ability to manufacture non-planar radomes more easily at lower cost. This combination can be considered as a good candidate, particularly for more complex radome shapes.

#### References

- [1] Munk BA. Frequency selective surfaces: theory and design. New York: Wiley; 2005.
- [2] Deepika S, Rana P.Y. A 3-D printed square loop frequency selective surface for harmonic radar applications. *J Electromagn Waves Appl* 2020; 34(3): 396-406.
- [3] Deepika S, Abhinav J, Rana PY. Development of Circular Loop Frequency selective surface using 3-D printing technique. *Prog Electromagn Res M Pier M* 2020; 90: 195-203.
- [4] Alvarez HF, Cadman DA, Goulas A, de Cos Gomez ME, Engstrom DS, Vardaxoglou JC, Zhang S. 3D conformal bandpass millimeter-wave frequency selective surface with improved fields of view. *Sci Rep* 2021; 11: 12846.
- [5] Sanz-Izquierdo B, Parker EA. 3-D Printing of Elements in Frequency Selective Array. *IEEE Trans Antennas Propag* 2014; 62(12): 6060.
- [6] Sudhendra C, Madhu AR, Mahesh A, Pillai ACR. FSS Radomes for Antenna RCS Reduction. *Int J Adv Eng Technol* 2013; 6(4):1464-1473.
- [7] Omar AA, Shen Z. Thin 3-D bandpass frequency-selective structure based on folded substrate for conformal radome applications. *IEEE Trans Antennas Propag* 2019; 67(1); 282-290.
- [8] Park CS et al. Analysis of curved frequency selective surface for radome using characteristic basis function method. *EuCAP* 2016: 2-5.
- [9] Jun S, Sanz-Izquierdo B. A CPW-fed Antenna on 3D Printed EBG Substrate. *LAPC* 2015:1-5.
- [10] Nicolson AM, Ross GF. Measurement of the intrinsic properties of materials by time-domain techniques. *IEEE Trans Instrum Meas* 1970; 19: 377–382.
- [11] Weir WB. Automatic measurement of complex dielectric constant and permeability at microwave frequencies. *Proc IEEE* 1974; 62: 33–36.

## Molecular Docking Study on Interaction of Polyvinyl Alcohol (PVA) with Group IA Bacteriocin

Nihan ÜNLÜ<sup>1\*</sup>, Arzu ÖZGEN<sup>2</sup>, Canan Aksu CANBAY<sup>3</sup>

<sup>1</sup> Department of Medical Services and Techniques, Vocational School of Health Sciences, Istanbul Gelisim University, Istanbul, Turkey

<sup>2</sup> Department of Medical Services and Techniques, Vocational School of Health Sciences, Istanbul Gelisim University, Istanbul, Turkey

<sup>3</sup> Department of Physics, Faculty of Science, Firat University, 23119 Elazig

\*<sup>1</sup> nunlu@gelisim.edu.tr, <sup>2</sup> aozgen@gelisim.edu.tr, <sup>3</sup> caksu@firat.edu.tr

(Geliş/Received: 26/12/2023;

Kabul/Accepted: 11/03/2023)

**Abstract:** PVA with the molecular formula  $(C_2H_4O)_n$  is a polymer prepared from polyvinyl acetates by replacing acetate groups with hydroxyl groups. It is a synthetic polymer with low surface tension, flexible and soft, water-soluble and cross-linkable thanks to the hydroxyl groups in its structure, biodegradable and non-toxic due to the carbon bonds in its chain. Bacteriocins are compounds of a protein nature that are ribosomally synthesized by bacteria and suitable for use as a filler in polymer matrices, especially in food packaging systems, and drug design because they are natural antimicrobial compounds sensitive to various enzymes and do not disrupt the physicochemical structure of foods while inhibiting pathogenic microorganisms. Considering their biochemical properties, they are generally divided into 4 different classes. The fact that Nisin and PVA have a structure that can serve a common purpose and have superior properties made us wonder about the interaction and bonding modes between these two. Molecular docking work is important because it prevents time, energy, and economic consumption and prepares the ground for the synthesis of new and advanced materials that are likely to be obtained in the laboratory environment. Therefore, in this study, Nisin bacteriocin (in Group IA) was chosen as the target, and a single monomer of the PVA polymer was chosen as the ligand, and the interaction between them was simulated by molecular docking method. A rational depiction of ligand-protein binding interactions was made.

**Key words:** Polyvinyl alcohol, molecular docking, nisin.

## Polivinil Alkolün (PVA) Grup IA Bakteriyosiniyle Etkileşimi Üzerine Moleküler Docking Çalışması

**Öz:**  $(C_2H_4O)_n$  moleküler formülüne sahip PVA, asetat gruplarının hidroksil gruplarıyla değiştirilmesiyle polivinil asetatlardan hazırlanan bir polimerdir. Düşük yüzey gerilimli, esnek ve yumuşak, yapısındaki hidroksil grupları sayesinde suda çözünür ve çapraz bağlanabilir, zincirindeki karbon bağları sayesinde biyolojik olarak parçalanabilen ve toksik olmayan sentetik bir polimerdir. Bakteriyosinler, bakteriler tarafından ribozomal olarak sentezlenen, çeşitli enzimlere duyarlı doğal antimikrobiyal bileşikler olmaları ve patojenik mikroorganizmaları inhibe ederken gıdaların fizikokimyasal yapısını bozmamaları nedeniyle özellikle gıda paketlenme sistemlerinde ve ilaç tasarımında polimer matrislerde dolgu maddesi olarak kullanıma uygun, protein niteliğindeki bileşiklerdir. Biyokimyasal özelliklerine göre genel olarak 4 farklı sınıfa ayrılırlar. Nisin ve PVA'nın ortak bir amaca hizmet edebilecek yapıya ve üstün özelliklere sahip olmaları, bu ikisi arasındaki etkileşim ve bağlanma modlarını merak etmemize neden oldu. Moleküler yerleştirme çalışması, zaman, enerji ve ekonomik tüketimin önüne geçmesi ve laboratuvar ortamında elde edilmesi muhtemel yeni ve ileri malzemelerin sentezine zemin hazırlaması nedeniyle önemlidir. Bu nedenle bu çalışmada hedef olarak Nisin bakteriyosini (Grup IA'da), ligand olarak da PVA polimerinin tek bir monomeri seçilmiş ve aralarındaki etkileşim moleküler yerleştirme yöntemi ile simüle edilmiştir. Ligand-protein bağlanma etkileşimlerinin rasyonel bir tasviri yapılmıştır.

**Anahtar kelimeler:** Polivinil alkol, moleküler yerleştirme, nisin.

### 1. Introduction

Access to food is decreasing day by day due to reasons such as global warming, the gradual decrease of arable land and the increasing human population. When microbial factors such as aflatoxins and food spoilage that threaten human and animal health as a result of not keeping the harvested agricultural products under proper storage conditions are added to all these problems, the result is more frightening. Therefore, importance is given to the production of antibacterial packaging in order to prevent food loss and to prevent packaging wastes that pose a danger to nature. For this reason, manufacturers have turned to advantageous packaging materials with barrier and protective properties to meet the need for fresh and minimally processed food. For this reason,

\* Corresponding author: nunlu@gelisim.edu.tr. ORCID Number of authors: <sup>1</sup> 0000-0001-5023-6888, <sup>2</sup> 0000-0003-2104-6019, <sup>3</sup> 0000-0002-5151-4576

manufacturers have turned to advantageous packaging materials with barrier and protective properties to meet the need for fresh and minimally processed food.

Bacteriocins are natural antimicrobial compounds synthesized by the same or different bacterial groups, in protein structure, and sensitive to various enzymes [1]. While bacteriocins inhibit pathogenic and spoilage microorganisms, they do not disrupt the physicochemical structure of foods [2]. Bacteriocins, also called antimicrobial peptides or proteins, vary in molecular mass, disulfide and monosulfide (lanthionine) bonds, the spectrum of action, genetic origin, and biochemical properties. The most well-studied group of peptides are bacteriocins produced by lactic acid bacteria (LAB) due to their potential for use in food preservation. Klaenhammer classified these bacteriocins into 4 groups based on their molecular weight, heat sensitivity, enzymatic sensitivity, presence of post-translationally modified amino acids, and mechanism of effect [3, 4]. These are given in Table 1.

**Table 1.** Classification of bacteriocins [3, 4].

BACTERIOCINS			
Group I	Group II	Group III	Group IV
Group IA; <i>Nisin</i> , <i>Lactocin S</i> ,...	Group IIA; <i>Pediocin PA-I</i> , <i>Sakacin A</i> ,...	<i>Helveticin J</i> , <i>Lacticin A</i> ,...	<i>Plantaricin S</i> , <i>Leuconocin S</i> ,...
Group IB; <i>Cinnamycin</i> , <i>Duramycin</i> ,...	Group IIB; <i>Lactacin F</i> , <i>Lactococcin G</i> ,...		
	Group IIC; <i>Acidocin B</i> , <i>Enterocin P</i> ,...		

Group IA bacteriocins are hydrophobic polypeptides that have a net positive charge [5]. Nisin, one of the important bacteriocins in this group, is produced by a group of Gram-positive bacteria belonging to *Lactococcus* and *Streptococcus* species. Nisin is known as a lantibiotic synthesized from mRNA and the translated peptide contains several unusual amino acids due to post-translational modifications [6]. Among the lantibiotics, nisin has the unique function of being used as a food preservative because it is non-toxic. Since it is in a polypeptide structure, the residues left in the food are digested. Many natural and genetically modified variants of Nisin have been identified and studied for their unique antimicrobial properties. Nisin is FDA (the Food and Drug Administration) approved and is generally considered a safe peptide with recognized potential for clinical use. Recently, the application of Nisin has spread to biomedical fields [7]. Nisin has been reported to have additional biological activities beyond its antimicrobial activities. For example, Nisin has beneficial properties in biomedical applications including bacterial infections, cancer, oral diseases, and more [8, 9].

Antimicrobial properties are given to plastic packaging by various modifications of the respective natural-based substances. Recently, bacteriocins and other biologically derived antimicrobials are among the highly interesting materials in packaging systems. Of particular interest is its use in packaging materials. Nisin, which inhibits Gram-positive foodborne pathogens and spoilage microbes, is one of the bacteriocins suitable for use in reliable packaging systems. Among the widely studied bacteriocins, Nisin is the only protein generally recognized as safe and approved by the US Food and Drug Administration [10, 11]. For this reason, some commercially produced Nisin species are often added to food products as preservatives. However, since the use of Nisin is limited by its structural instability resulting from loss of activity due to interactions with food and cell matrices, its incorporation into polymers is more advantageous to overcome this instability.

Polymers are high molecular weight substances or macromolecules that are formed as a result of the combination of simple molecules called monomers with chemical bonds. Polyvinyl alcohol, whose structural formula is given in Fig.1, is a highly used polymer in medical applications due to its biocompatibility, biodegradability, non-toxicity, good mechanical properties, and adhesiveness. In this respect, PVA has proven to be a promising candidate for medical applications such as biomedicine and pharmaceuticals. Commercially

available synthetic polymer poly(vinyl alcohol) (PVA) is also frequently used in packaging applications for food, cosmetics, and pharmaceutical products due to its superior properties [12, 13].

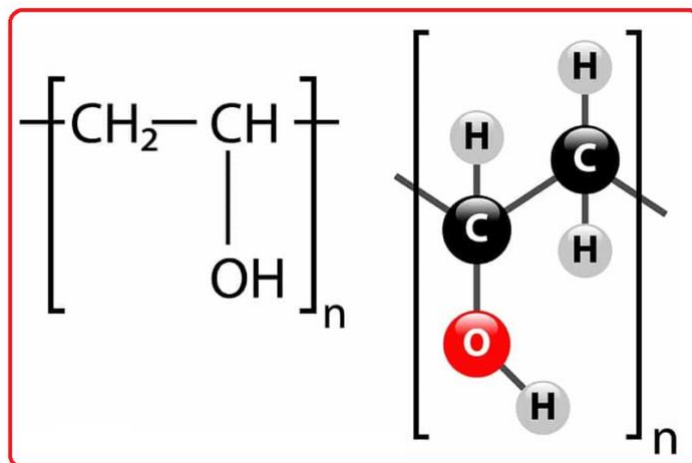


**Figure 1.** The structural formula of PVA [14].

To our knowledge, there has not been a study examining PVA-Nisin interactions before. Since both substances are suitable for use in similar applications, we examined the interactions between them in this study. The interaction of a monomer of PVA polymer as a ligand and Nisin bacteriocin as a protein was investigated by the Molecular Docking method. The placement of the PVA monomer in certain regions of the protein structure was simulated with certain score algorithms, taking into account many factors such as the electro negativities of the atoms, their position to each other, and the conformation of the molecule. This work lays the groundwork for the modification of the structure with the correct estimation of the binding modes and creates a strategic infrastructure for the synthesis of materials that are likely to be more effective.

## 2. Materials and Methods

Nisin's (PDB ID: 1WCO) structure was obtained from The Protein Data Bank (PDB, <https://www.rcsb.org/>). The pdb file of the 2DDE protein was prepared using chain A and transferred to AutoDockTools (ADT ver.1.5.6). Water molecules of the structures were removed and the pdbqt files of the proteins were saved. The chemical structure of the PVA (PubChem CID: 11199) ligand was obtained from the National Library of Medicine (<https://www.ncbi.nlm.nih.gov/>). Torsions of the ligand were examined and then the files of the ligand were saved as pdbqt format by AutodockTools (ADT ver.1.5.6).

The molecular docking study was performed using Autodock 4.1 [15]. Each docking was performed according to standard Autodock steps [16]. The most suitable possible binding modes obtained as a result of the Molecular Docking processes were determined with Autodock 4.1, and their analyzes and visuals were obtained with the Biovia Discovery Studio Visualizer 2021 program.

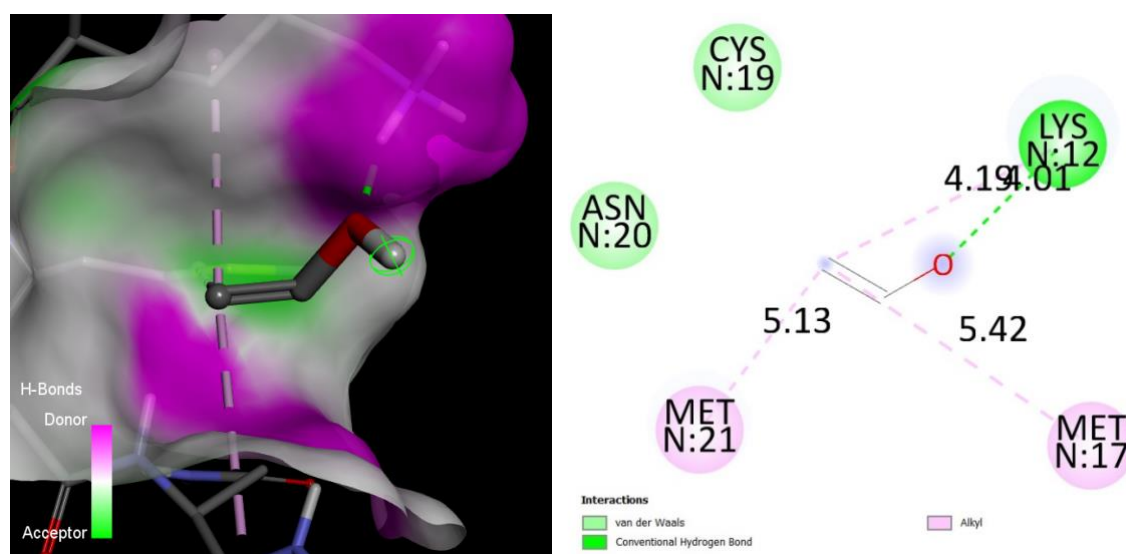
## 3. Results and Discussion

The molecular docking analysis was performed and evaluated following the literature as described in the material method [17]. Molecular docking results on Nisin a polycyclic antibacterial peptide, and monomer of PVA are shown in Table 2. The most stable structures of the ligand with Nisin were determined according to the binding energy and the interaction of the molecule with the active site. Considering the binding energy, it can be said that the studied compound showed significant binding affinity to Nisin.

**Table 2.** Molecular docking analysis of Nisin and the monomer of PVA.

Protein	Ligand	Binding Energy/ $\Delta G$ (kcal/mol)	Inhibition Constant/ $K_i$ (mM)	Bonds	Length ( $\text{\AA}$ )
Nisin	$C_2H_4O$	-1.46	59.34	LYS-12-O	4.01
				LYS-12-C	4.19
				MET-17-C	5.42
				MET-21-C	5.13

The hydrogen bonds at the most suitable binding site analyzed are given in Fig.2. In the figure, it is shown in 2D that the amino acid Lysine (LYS-12) forms a conventional hydrogen bond with the oxygen element. Alkyl bonds are formed between the carbon element and the amino acids Lysine (LYS-12), Methionine (MET-21), and MET-17. In addition, the van der Waals bond, which is a weak interaction between the Asparagine (ASN-20) and Cysteine (CYS-19) amino acids of the Nisin protein and the ligand, formed.

**Figure 2.** 2D interaction of the ligand with the amino acids of the Nisin binding site.

In Fig.3, the binding sites in the protein pocket are simulated. Shown in red is oxygen, dark gray is carbon, light gray is hydrogen, yellow is sulfur, and blue is nitrogen. As can be seen in the figure, the ligand is located in the surface space of the Nisin receptor with good complementarity.

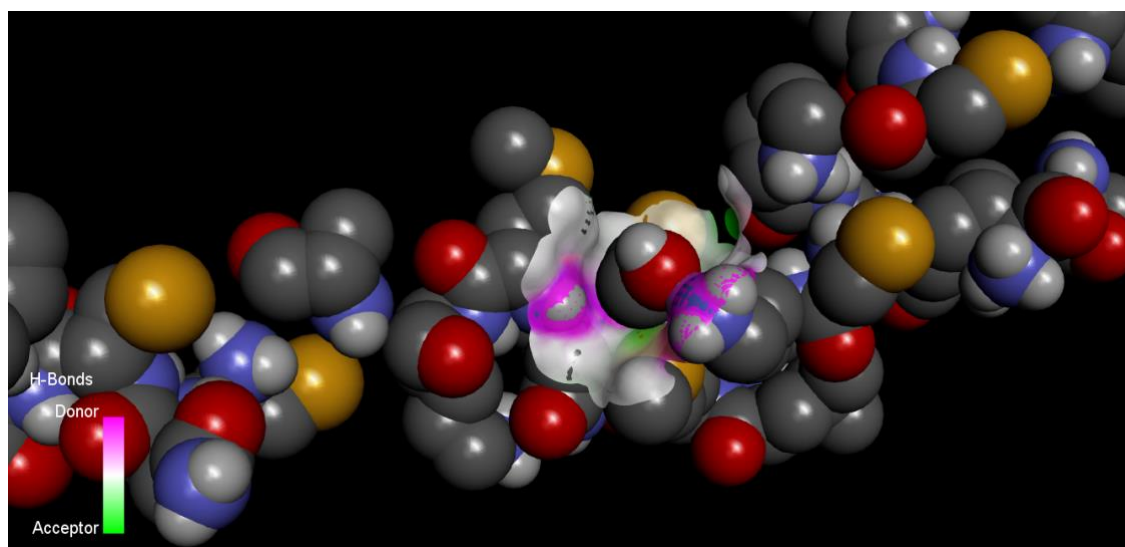


**Figure 3.** The binding sites in the pocket of protein (1WCO).

#### 4. Conclusion

Nisin, a polycyclic antibacterial peptide produced by *Lactococcus lactis* bacteria, is suitable for use as a food preservative [18]. On the other hand, PVA is a synthetic polymer preferred in many fields such as pharmacology, biomedicine, biotechnology, and food chemistry, thanks to its superior properties such as its chemical structure, thermal stability in a wide temperature range, non-toxicity, and compatibility with living tissue [19, 20]. The fact that the usage areas of Nisin and PVA are compatible with each other and that there has not been a study examining the interaction between these two as a result of our research has led us to this study. As a result of our molecular docking study, the presence of binding energy of -1.46 kcal/mol was determined between the C<sub>2</sub>H<sub>4</sub>O monomer of PVA selected as the ligand and the Nisin protein selected as the receptor. Considering the hydrogen bonds formed between the amino acids LYS-12, MET-17, and MET-21 of Nisin, which has 34 amino acid residues, and the PVA monomer, it can be mentioned that there is an interaction between them [21]. As a result, this study can serve as a template for materials to be produced for use in appropriate fields, especially in the food industry.

#### Acknowledgment

This work was presented at the MSNG2022 Conference, Gazi University, Ankara, Turkey, Sep 22-24, 2022.

#### References

- [1] Kuleasan H, Çakmakçı M. L. Bakteriyosinlerin özellikleri, gıda mikrobiyolojisinde kullanım alanları ve ileri dönemlerdeki kullanım potansiyelleri. *Gıda*, 2003; 28.2.
- [2] Settanni, Luca, and Aldo Corsetti. Application of Bacteriocins in Vegetable Food Biopreservation. *Int J Food Microbiol*, 2008; 122(2): 123-138.
- [3] Klaenhammer, Todd R. Bacteriocins of Lactic Acid Bacteria. *Biochimie*, 1988; 70(3); 337-349.
- [4] Klaenhammer, Todd R. Genetics of Bacteriocins Produced by Lactic Acid Bacteria. *FEMS Microbiol Rev*, 1993; 12(1): 39-85.
- [5] Twomey, Denis, et al. Lantibiotics Produced by Lactic Acid Bacteria: Structure, Function and Applications. *Antonie Van Leeuwenhoek*, 2002; 82: 165-185.
- [6] Shin, J. M., et al. Biomedical Applications of Nisin. *J Appl Microbiol*, 2016; 102(6): 1449-1465.
- [7] Hill, Colin, Paul D. Cotter, and R. P. Ross. Bacteriocins: Developing Innate Immunity for Food. *Nat Rev Microbiol*, 2005; 3(10): 777-788.
- [8] Asaduzzaman, Sikder M., and Kenji Sonomoto. Lantibiotics: Diverse Activities and Unique Modes of Action. *J Biosci Bioeng*, 2009; 107(5): 475-487.
- [9] Benmechernene, Zineb, et al. Recent Patents on Bacteriocins: Food and Biomedical Applications. *Recent Patents on DNA & Gene Sequences*, 2013; 7(1): 66.

- [10] Ercolini, Danilo, et al. Development of Spoilage Microbiota in Beef Stored in Nisin Activated Packaging. *Food Microbiol*, 2010; 20(1): 137-143.
- [11] Imran, Muhammad, et al. Microstructure and Physico-Chemical Evaluation of Nano-Emulsion-Based Antimicrobial Peptides Embedded in Bioactive Packaging Films. *Food Hydrocolloids*, 2012; 29(2): 407-419.
- [12] Teodorescu, Mirela, Maria Bercea, and Simona Morariu. Biomaterials of Poly(Vinyl Alcohol) and Natural Polymers. *Polym Rev*, 2018; 58(2): 247-287.
- [13] Teodorescu, Mirela, Maria Bercea, and Simona Morariu. Biomaterials of PVA and PVP in Medical and Pharmaceutical Applications: Perspectives and Challenges. *Biotechnol Adv*, 2019; 37(1): 109-131.
- [14] Ginhong. Polyvinyl Alcohol (PVA) Solutions. Huffpost. <https://ginhong.com/wp-content/uploads/2019/06/Polyvinyl-Alcohol-.jpg>
- [15] Morris, Garrett M., Ruth Huey, and Arthur J. Olson. Using AutoDock for Ligand-Receptor Docking. *Curr Protoc Bioinformatics*, 2008; 24(1): 8-14.
- [16] Huey, Ruth, Garrett M. Morris, and Stefano Forli. Using AutoDock 4 and AutoDock vina with AutoDockTools: a tutorial. The Scripps Research Institute Molecular Graphics Laboratory, 2012; 10550(92037), 1000.
- [17] Elokely, Khaled M., and Robert J. Ooerksen. Docking Challenge: Protein Sampling and Molecular Docking Performance. *J Chem Inf Model*, 2013; 53(8): 1934-1945.
- [18] And, H. Chen, and D. G. Hoover. "Bacteriocins and their food applications. *Compr Rev Food Sci Food Saf*, 2003; 2(3): 82-100.
- [19] Wang, Yuhong, and You-Lo Hsieh. Crosslinking of Polyvinyl Alcohol (PVA) Fibrous Membranes with Glutaraldehyde and PEG Diacylchloride. *J Appl Polym Sci*, 2010; 116(6): 3249-3255.
- [20] Chaouat, Marc, et al. A Novel Cross-Linked Poly(Vinyl Alcohol) (PVA) for Vascular Grafts. *Adv Funct Mater*, 2008; 18(19): 2855-2861.
- [21] Hurst, A. Nisin and other inhibitory substances from lactic acid bacteria. *Antimicrobials in foods* 1983. pp. 327-351.



## A Hybrid Model Based on Deep Features and Ensemble Learning for the Diagnosis of COVID-19: DeepFeat-E

Berivan ÖZAYDIN<sup>1</sup>, Ramazan TEKİN<sup>\*2</sup>

<sup>1</sup>Electrical and Electronics Engineering, Graduate Education Institute, Batman University

<sup>2</sup>Computer Engineering, Faculty of Engineering and Architecture, Batman University

<sup>1</sup>berzaydin@gmail.com, <sup>\*2</sup>ramazan.tekin@batman.edu.tr

(Geliş/Received: 17/01/2023;

Kabul/Accepted: 15/03/2023)

**Abstract:** COVID-19, which has been declared a pandemic disease, has affected the lives of millions of people and caused a major epidemic. Despite the development of vaccines and vaccination to prevent the transmission of the disease, COVID-19 case rates fluctuate worldwide. Therefore, rapid and reliable diagnosis of COVID-19 disease is of critical importance. For this purpose, a hybrid model based on transfer learning methods and ensemble classifiers is proposed in this study. In this hybrid approach, called DeepFeat-E, the diagnosis process is performed by using deep features obtained from transfer learning models and ensemble classifiers consisting of classical machine learning methods. To test the proposed approach, a dataset of 21,165 X-ray images including 10,192 Normal, 6012 Lung Opacity, 1345 Viral Pneumonia and 3616 COVID-19 were used. With the proposed approach, the highest accuracy was achieved with the deep features of the DenseNet201 transfer learning model and the Stacking ensemble learning method. Accordingly, the test accuracy was 90.17%, 94.99% and 94.93% for four, three and two class applications, respectively. According to the results obtained in this study, it is seen that the proposed hybrid system can be used quickly and reliably in the diagnosis of COVID-19 and lower respiratory tract infections.

**Key words:** COVID-19, Deep Features, Transfer Learning, Ensemble Classifier.

### COVID-19 Teşhisi için Derin Özniteliklere ve Topluluk Öğrenmeye Dayalı Hibrit bir Model: DeepFeat-E

**Öz:** Pandemi hastalığı olarak ilan edilen COVID-19, milyonlarca insanın hayatını etkilemiş ve büyük bir salgına neden olmuştur. Hastalığın bulaşmasını önlemek amacıyla aşılarda geliştirilmesine ve aşılamaya yapılmasına rağmen dünya genelinde COVID-19 vaka oranları dalgalı bir seyir göstermektedir. Dolayısıyla COVID-19 hastalığının hızlı ve güvenilir teşhisi kritik bir öneme sahiptir. Bu amaçla, bu çalışmada transfer öğrenme yöntemlerine ve topluluk sınıflandırıcılara dayalı hibrit bir model önerilmiştir. DeepFeat-E olarak isimlendirilen bu hibrit yaklaşımda, transfer öğrenme modellerinden elde edilen derin öznitelikler ile klasik makine öğrenme yöntemlerinden oluşan topluluk sınıflandırıcılar kullanılarak teşhis işlemi gerçekleştirilmektedir. Önerilen yaklaşımı test etmek için 10.192 Normal, 6012 Akciğer Opaklığı, 1345 Viral Pnömoni ve 3616 COVID-19 toplamda 21.165 X-ray görüntüsünden oluşan veri seti kullanılmıştır. Önerilen yaklaşım ile en yüksek başarı DenseNet201 transfer öğrenme modeline ait derin öznitelikler ve İstifleme topluluk öğrenme yöntemiyle elde edildiği görülmüştür. Buna göre dört, üç ve iki sınıflı uygulamalarda sırasıyla test doğruluğu 90,17%, 94,99% ve 94,93% olarak elde edilmiştir. Bu çalışma kapsamında elde edilen sonuçlara göre, önerilen hibrit sistemin COVID-19 ve alt solunum yolu enfeksiyonlarının teşhisinde hızlı ve güvenilir bir şekilde kullanılabileceğini görülmektedir.

**Anahtar Kelimeler:** COVID-19, Derin Öznitelikler, Transfer Öğrenme, Topluluk Sınıflandırıcı.

#### 1. Introduction

COVID-19, the new virus of the coronavirus family called severe acute, affects millions of people worldwide. The World Health Organization (WHO) declared the outbreak caused by this virus, which causes severe acute respiratory syndrome, a global pandemic in March 2020. The first case of COVID-19 was registered in Wuhan, China [1,2]. This severe acute respiratory syndrome coronavirus (Sars-Cov-2) has caused approximately 6.2 million deaths and over 500 million cases of infection worldwide [3]. This puts a serious burden on healthcare workers. Despite advances in health and technology, the impact of the virus still persists and new cases and deaths continue.

The first symptoms of COVID-19 are often similar to the common cold or flu. This makes it difficult to detect the first stage of COVID-19 cases [4]. Due to the long incubation period, people with the virus continue their routine daily lives and interact with other people until they realize that they have the virus. As a result, this leads to more infections, making COVID-19 more contagious [5]. Most people have mild to moderate symptoms and do not require hospitalization. However, if acute respiratory distress progresses too far, it can cause cytokine

\* Corresponding Author: ramazan.tekin@batman.edu.tr. ORCID Number of authors: 1 0000-0001-8935-6684, 2 0000-0003-4325-6922

respiratory syndrome and consequences such as multiple organ failure and death can occur [6]. This virus can be very dangerous, especially in people with chronic diseases such as diabetes, cardiovascular disease and asthma. In addition, due to the large size of the number of cases, it also creates serious problems in the country's economies [6].

The presymptomatic infection rate of Covid-19, the duration of viral transmission and the variability of characteristics in different countries make the COVID-19 pandemic more unpredictable and difficult to control [3]. Being able to contain Covid-19 depends on carriers being identified and quarantined, as well as being tested frequently. Rapid and accurate detection of the COVID-19 disease is critical to slowing the spread of the virus and saving the lives of vulnerable groups. Specialized vaccines have been developed to reduce the rates of COVID-19 infection. However, waves or fluctuations of infection are still experienced due to the difficulty of accessing vaccines in many poor countries and the lack of adequate vaccination.

COVID-19 can be detected by polymerase chain reaction (PCR) testing by taking throat and nose samples from patients [6]. However, since these test kits are not reliable enough, alternative rapid methods are needed to detect COVID-19 and other lower respiratory diseases. Today, artificial intelligence and especially deep learning methods are reliably used to diagnose COVID-19 and other lower respiratory diseases [7]. In addition, artificial intelligence systems can be successfully applied in a wide range of fields from lip-reading applications [8] to document language [9] and gesture recognition [10], epileptic seizures [11] and heart disease detection [12]. Similarly, artificial intelligence systems based on cough sounds [13,14] and especially chest images (X-Ray and CT scan) are widely used in COVID-19 diagnosis [15,16].

For this purpose, in this study, a hybrid artificial intelligence system named DeepFeat-E is proposed for COVID-19 diagnosis. The proposed system is based on deep features extracted from a given pre-trained Transfer Learning (TL) model. Using these features of the training data set, the best five Machine Learning (ML) methods are selected and used as classifiers in ensemble learning algorithms. In order to reduce the computational cost, the deep features were reduced by the Extra Tree Classifier (EAS) method before using them. Then, the reduced features were applied to the five best ML methods selected according to the 10-fold cross validation result. The final decisions of these classifiers are obtained using Stacking, Soft and Hard voting ensemble learning methods. The performance of the proposed hybrid model is analyzed using a large open access dataset of 21,165 chest X-Ray images, including 10,192 Normal, 6012 Lung Opacity, 1345 Viral Pneumonia and 3616 COVID-19 images. In the first application, TL models were applied directly to the dataset for comparison purposes. In the other three applications, separate applications were carried out with three different ensemble learning methods within the scope of the proposed hybrid system. In each application, two-class (COVID-19 and Normal), three-class (COVID-19, Viral-Pneumonia and Normal) and four-class (COVID-19, Lung-Opacity, Viral-Pneumonia and Normal) applications were performed separately.

## 2. Related Work

In this section, we present the current deep learning architecture studies on COVID-19 diagnosis, especially the studies based on the ensemble classification method. Researchers generally preferred transfer methods or improved (Fine-Tuning) transfer methods with their own small size datasets [17]. Using pre-trained models of these approaches reduces the need for labeled datasets for their training and the physical resources required during training [18]. There are quite a number of studies on COVID-19 diagnosis in the literature. Below, studies that include deep learning-based methods, especially ensemble learning methods, which is one of the focal points of this study, are presented.

Chowdhury et al. [19] proposed an EfficientNet-based an ensemble of deep convolutional neural networks (CNN) named ECOVNet to detect COVID-19 using a dataset of 16493 X-Ray images. This method has a CNN architecture embedded in a pre-trained EfficientNet. Using the proposed model, snapshots of several training predictions are entered into the ensemble classifier. In the study, X-Ray images containing COVID-19, normal and pneumonia samples were used and the highest three-class accuracy was %97.

In another study, Mahmud et al. [20] proposed a CNN-based architecture called CovXNet. In this study, the predictions of different forms of this architecture called CovXNet were evaluated together with the stacking ensemble classifier method. In the applications performed in the study, %97.4, %89.6 and %90.2 accuracy was obtained for two-class (COVID/Normal), three-class (COVID, Viral and bacterial pneumonia) and multi-class (COVID, normal, Viral and bacterial pneumonia), respectively.

In another study, Karim et al. [21] trained DenseNet, ResNet and VGGNet architectures and obtained snapshots of these models during the training. They proposed a framework called DeepCOVIDexplainer, which uses Softmax class posterior averaging (SCPA) and prediction maximization (PM) to integrate these models into

ensemble classifiers. Tang et al. [22] proposed a hybrid model based on deep learning and ensemble learning called EDL-COVID. The EDL-COVID model uses multiple snapshots of the architecture named COVID-Net, which was developed for COVID-19 detection. It evaluates these snapshots in an ensemble classifier based on the weighted average method. In the study, X-Ray images containing examples of COVID-19, normal and pneumonia were used and the test accuracy was %95 for three classes.

Banerjee et al. [23] developed a model with ensemble structure by taking snapshots of the network from local minimum points in a single training process of a model with DenseNet-201 architecture. They used Blending method as an ensemble classifier and Random Forest (RF) method as a meta-model. Two different datasets with three categories (COVID-19, Pneumonia, and Normal) were used in the study, one consisting of a large number of X-Ray images and the other a low number of X-Ray images. The accuracy values of the proposed model for the three classes in large and small datasets were %94.55 and %98.13, respectively.

Gour and Jain [24] proposed a new stacked convolutional neural network model based on Xception and Vgg19. In the proposed approach, they tried to predict diagnosis with softmax classifier and Stacking ensemble learning methods, using sub-models obtained from VGG19 and Xception models during training. In the study, CT (Computerized Tomography) images with two categories (COVID-19 and No-Findings) and X-Ray images with three categories (COVID-19, Pneumonia and Normal) were used and %98.30 and %97.27 accuracy was achieved respectively.

In the diagnosis of COVID-19, it is seen that models based on transfer learning or original convolutional architectures are used extensively in the literature, as well as ensemble classifier-based studies. Apostolopoulos and Mpesiana [25] examined some deep architectures such as VGG, Inception, MobilNet on X-ray images. In the study, a dataset consisting of X-Ray images with the categories of COVID-19, pneumonia and normal was used. Among the Transfer Learning models, the highest accuracy was obtained in the VGG19 model with %93.48 and %98.75 for 3 classes and 2 classes, respectively.

Ozturk et al. [26] proposed a new model called CovidDarkNet for automatic COVID-19 detection using raw X-ray images for Covid-19 diagnosis. The CovidDarkNet model, which is used as a classifier for the YOLO (You Only Look Once) real-time object detection system, includes 17 convolutional layers. The method proposed in this study was applied to datasets with two classes (COVID and No-Findings) and three classes (COVID, No-Findings, Pneumonia). It was reported that %98.08 and %87.02 classification accuracy was obtained for 2 classes and 3 classes, respectively.

Khan et al. [27] proposed a deep convolutional neural network model called CoroNet based on Xception architecture for the diagnosis of COVID-19 from X-ray images. The proposed model is based on the Xception architecture pre-trained on the ImageNet dataset. With the proposed model, %89.5, %94.59 and %99 accuracy was achieved on 4, 3 and 2 class datasets, respectively.

Huang and Liao [28] performed Covid-19 diagnosis using InceptionV3, ResNet50V2, Xception, DenseNet121, MobileNetV2, EfficientNet and EfficientNetV2 transfer methods. In this study, they also proposed a new architecture called LightEfficientNetV2. The applications were performed on 2 different datasets consisting of X-Rays and CT images with three classes. The three-class highest accuracy in X-Ray and CT images was obtained in the LightEfficientNetV2 model with %98.33 and %97.48, respectively [28]. Similarly, Ahamed et al. [15] developed a modified ResNet50V2 architecture for COVID-19 detection with datasets consisting of X-Ray and CT images. The datasets used in the study include four classes: COVID-19, Normal, viral pneumonia and bacterial pneumonia. Using the proposed model, an accuracy of %96.45, %97.24 and %98.95 was obtained for X-Ray images with four (COVID-19/Normal/Bacterial pneumonia/Viral pneumonia), three (COVID-19/Normal/Bacterial pneumonia) and two (COVID-19/Viral pneumonia) classes, respectively. In CT images, %99.01 and %99.99 accuracy was obtained in images with three (COVID-19/Normal/Pneumonia) and two (Normal/COVID-19) classes, respectively.

Islam et al. [29] proposed a new convolutional neural network model called Cov-RADNet for the diagnosis of COVID-19 from CT and X-ray images. The first dataset used in this study consists of X-ray images with four categories: COVID-19, viral pneumonia, lung-opacity, and normal. The other dataset, CT, contains images with COVID-19 and non-COVID categories. The prediction accuracy of their proposed model was %97, %99.5 and %99.72 for four classes (COVID-19, Viral Pneumonia, Lung-Plaque and Normal), three classes (COVID-19, Viral Pneumonia, Normal) and two classes (COVID-19 and non-COVID), respectively. In CT images, the prediction accuracy was %99.25.

### 3. The Proposed Method

In the hybrid system called DeepFeat-E proposed in this study, deep features obtained from pre-trained Transfer Learning models are entered into classical ML methods and COVID-19 disease diagnosis is performed

with the help of ensemble classifiers. The proposed system generally consists of four basic stages as shown in Figure 1. The dataset used in the study is a very large dataset containing a total of 21,135 chest X-Ray images in four categories (Normal, Lung Opacity, Viral Pneumonia and COVID-19), and this dataset was selected as the best COVID-19 dataset by the Kaggle committee [19].

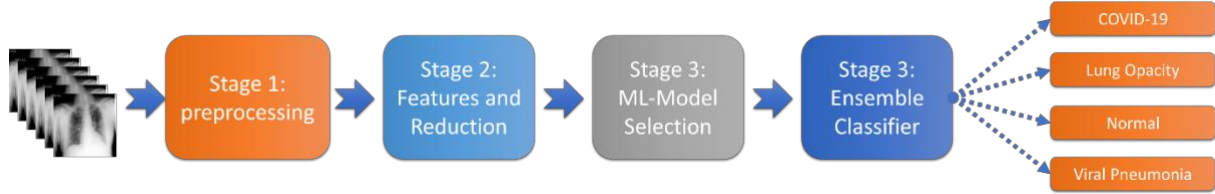


Figure 1. Stages of the proposed hybrid system.

**Stage 1 (Preprocess):** In the first stage, the preprocessing stage, after all images are brought to a standard size (224x224x3); Data augmentation is performed by methods such as rotation, scaling, horizontal/vertical translation, horizontal flip, brightness adjustment. Then, %80 of the data set is divided into two as training and %20 as testing, and the next stage is passed.

**Stage 2 (Features and Reduction):** In the second stage, the deep features of the training and test images obtained separately from the valid pre-trained TL method are reduced and transferred to the next stage. This step is performed separately for each TL model.

**Stage 3 (ML-Model Selection):** In the third stage, the best five ML methods are selected by using the reduced deep features of the training dataset. The selection process is performed according to the AUC metric after 10 cross validations. Then, the five best ML models selected are transferred to the next stage for use in the ensemble classifier.

**Stage 4 (Ensemble Classifier):** In the fourth stage, which is the final stage, predictions are made with the current ensemble learning method using the best five ML models. For each of the Stacking, Soft Voting and Hard Voting ensemble learning methods used in the study, this stage was carried out separately with four-class, three-class and two-class data sets.

In this study, all applications were implemented using Python programming language and Tensorflow, Keras and scikit-learn packages. A personal computer with AMD Ryzen 7 5800H (16 CPU, ~3.2GHz) processor, Nvidia GeForce RTX 3050 GPU (4GB GDDR6, ~1.5GHz) and 16GB RAM was used for models and analysis.

### 3.1. Datasets

The dataset used in this study consists of X-Ray images collected by a group of researchers from different countries (Qatar, Bangladesh, Pakistan, etc.) with four categories: COVID, Viral Pneumonia, Non-COVID Lung Opacity and Normal [19,30]. The dataset "COVID-19 Radiography Database" used in the study can be downloaded from Kaggle's website.

**Table 1.** Number of images in training and test dataset.

Datasets	COVID-19	Lung-Opacity	Normal	Viral-Pneumonia
<b>Total</b>	3616	6012	10192	1345
<b>Train</b>	2893	4809	8154	1076
<b>Test</b>	723	1203	2038	269

The dataset is updated periodically by the working group and the latest version used in this study contains 10,192 Normal, 6012 Lung Opacity (Non-COVID lung infection), 1345 Viral Pneumonia and 3616 chest X-Ray images of COVID-19 [30]. Table 1 shows the distribution of training and test datasets. Contrary to similar studies in the literature, the number of images for each category in the dataset is not equalized. However, data augmentation techniques such as rotation, scaling, horizontal/vertical shift, horizontal rotation, etc. were applied to prevent overlearning and to ensure that the models produce stable results. Examples of the images in the dataset are given in Figure 2.

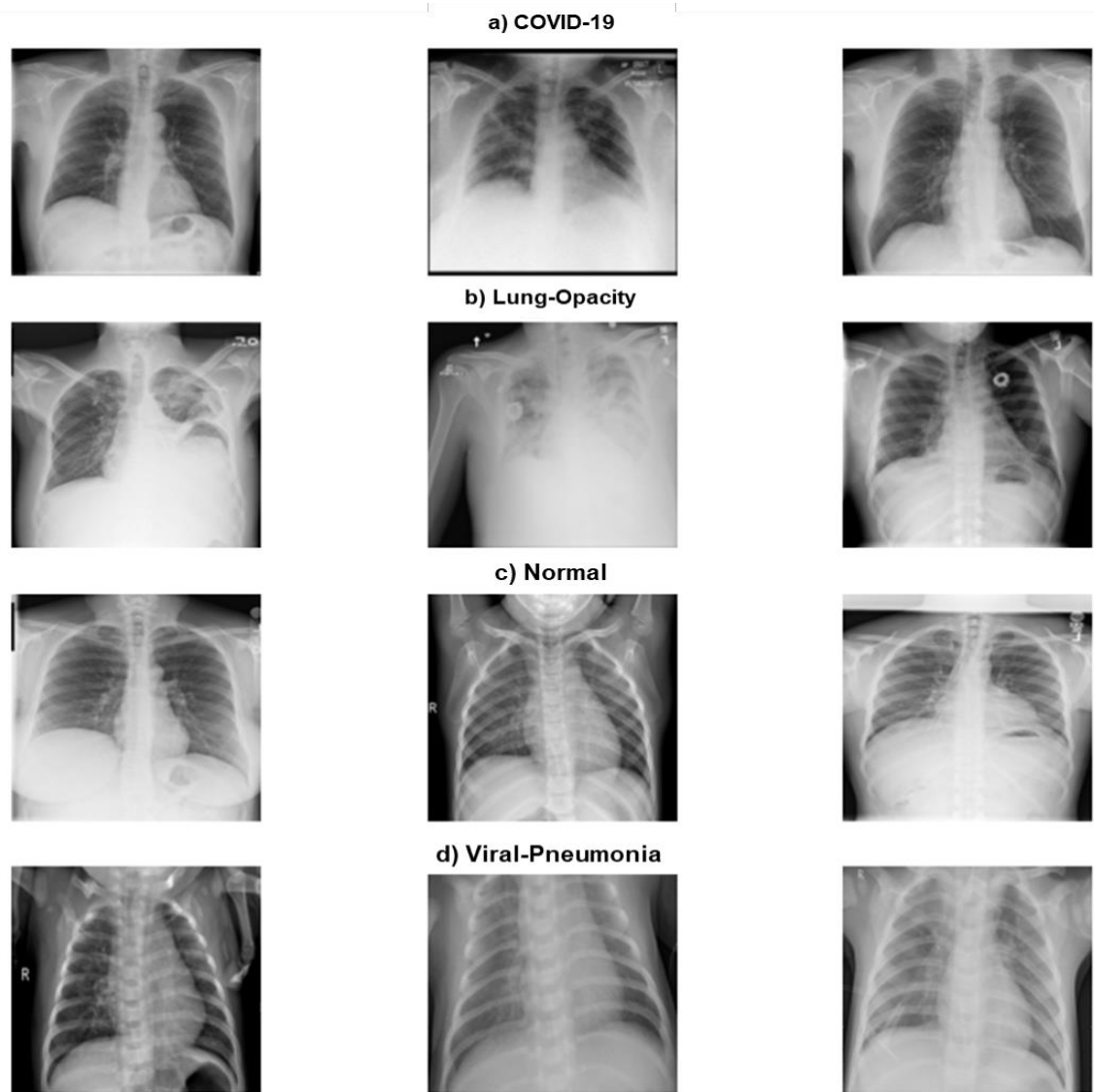


**Figure 2.** Example images. a) COVID-19, b) Lung-Opacity, c) Normal/Healthy, d) Viral-Pneumonia.

### 3.2. Proposed Hybrid System

Within the scope of the study, applications were carried out for a total of four different systems in which pre-trained TL architectures were used directly without community learning and three different ensemble learning techniques were used. In the ensemble learning systems, the deep features obtained from pre-trained TL architectures were analyzed by Stacking, Soft and Hard Voting ensemble methods by entering the five best ML models selected. For each TL model, datasets with two (COVID-19 and Normal), three (COVID-19, Viral Pneumonia and Normal) and four (COVID-19, Viral Pneumonia, Normal, and Lung-Opacity) classes were created and analyzed separately. The pre-trained TL models used in the study are listed in Table 2 and the applications were performed separately for each of them. Since these models are known general TL models, detailed explanations are not given under a separate heading. Detailed information about these models can be accessed through the references given next to the relevant model in the table. In the proposed system, the five best ML (S.ML) methods selected for the ensemble classifier are different for each TL, and the selected methods of the four-class applications are listed in Table 2 by ordering them according to the UAC value. In this table, the number of parameters (Prm), the number of deep features before reduction (BR.Fet.) and after reduction (AR.Fet.) are presented for each TL.

**Table 2.** Used TL methods and deep features.

#	TL Model	S.ML Methods	Prm	BR.Fet.	AR.Fet.
1	Xception [31]	[lr, lda, xgb, lgbm, gb]	20,869,676	2048	550
2	NASNet [32]	[lr, lda, xgb, lgbm, gb]	84,932,950	4032	1163
3	MobileNet [33]	[xgb, lgbm, lr, lda, gb]	3,232,964	1024	263
4	DenseNet169 [34]	[xgb, lda, lgbm, gb, lr]	12,649,540	1664	398
5	DenseNet201 [34]	[xgb, lgbm, lda, gb, rf]	18,329,668	1920	461
6	VGG16 [35]	[xgb, lgbm, lr, lda, gb]	14,716,740	512	189
7	InceptionV3 [36]	[xgb, lr, lgbm, lda, gb]	21,810,980	2048	520
8	ResNet50V2 [37]	[xgb, lgbm, lr, lda, gb]	23,572,996	2048	508
9	ResNet101V2 [37]	[xgb, lgbm, lr, lda, gb]	42,634,756	2048	521

In the first model without ensemble learning, the training and test datasets were applied directly to the TL models in order to compare the performance of the proposed ensemble classifier model. The TL models were used without retraining (pre-trained) with their current configurations and weights. The block diagram of the hybrid system named DeepFeat-E based on the ensemble learning methods proposed in this study is presented in Figure 3. As shown in the *Feature Selection* block, the deep features obtained from each of the pre-trained TL models were reduced by trying various feature selection methods (principal component analysis, linear discriminant analysis and extra tree classifier). Since the most successful results were obtained with the Extra Tree Classifier, after the reduction with this feature selection method, diagnosis was tried to be estimated with Stacking, Soft Voting and Hard Voting ensemble learning techniques, respectively. In ensemble learning models, as shown in the *Model Selection* block, the top 5 methods with the best performance (according to UAC) according to 10 cross-validation results are selected among 14 different known ML methods. Although the priority order of the selected ML methods varies for each TL model, it is generally seen that lr (Logistic Regression), lda (Linear Discriminant Analysis), xgb (eXtreme Gradient Boosting), lgbm (Light Gradient Boosting Machine), gb (Gradient Boosting), rf (Random Forest) ML models were selected. Then, these five best ML methods selected were used as classifiers as seen in the *Ensemble Learning* block. The top five ML models for each TL are presented in Table 2.

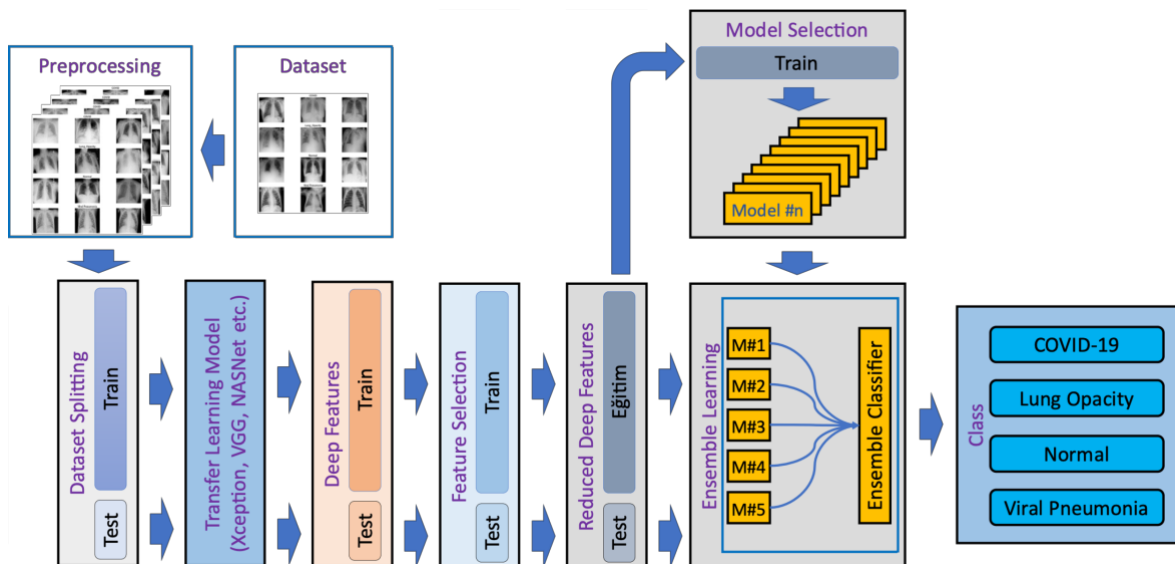


**Figure 3.** Block diagram structure of the proposed system.

### 3.3. Transfer Learning (TL) Methods

TL models are used to solve complex problems in various fields. In terms of machine learning, TL is the use of architectures and trained models designed for a specific problem by pre-training or retraining them on a different problem [38]. Since there is no need for retraining in new problems for which it is desired to use TL models, it saves both resources and time [39]. In this study, 9 TL models listed in Table 2 were used.

### 3.4. Feature Selection with Extra Tree Classifier (ETC)

ETC (Extra Trees Classifier) feature selection method was used to extract appropriate features from the deep features obtained from transfer deep learning methods [40]. Feature reduction is a data preprocessing process that enables the selection of important features that will make the maximum contribution to the estimation method, especially in high-dimensional data. Elimination of unimportant features makes the problem simpler, reducing the computational cost of models and increasing model accuracy [41].

ETC is a decision-based method that provides a common framework between feature selection and classification. It is very similar to the Random Forest classifier due to its characteristics such as generating many subtrees and selecting random subsets. A random partitioning is performed at the parent node and then at the child nodes up to the leaf. The predictions of all trees are then combined to determine the majority decision. During the creation of the forest for feature selection, the Gini importance value is calculated for each attribute. For feature selection, the features are sorted in descending order according to their Gini importance, and as many features as desired can be selected among the top attributes.

$$Gini = 1 - \sum_{i=0}^{c-1} p_i(t)^2 \quad (1)$$

where  $p_i(t)$  is the frequency of class  $i$  at node  $t$ , and  $c$  is the number of unique classes at this node.

### 3.5. Ensemble Learning Methods

Ensemble learning techniques aim to increase success by using multiple decision makers (classifiers) instead of a single decision maker in the decision-making phase. For classification, after 10 cross-validations according to the training set from a group of classical ML models, the best five were selected according to the AUC metric and used in the ensemble classifiers. The Deep features obtained from TL methods were entered into these classifiers and classified using Stacking and Voting (Soft and Hard) ensemble learning techniques. In the voting method, Hard Voting and Soft Voting techniques, which are based on majority vote and the average of class prediction probabilities, respectively, are used to predict class labels.

#### 3.5.1. Voting Ensemble Learning Methods

The mainstay of voting ensemble learning methods is to combine the predictions of different ML methods to obtain a common ensemble decision. In this way, it is predicted that better performance can be obtained by balancing the wrong predictions caused by a single model. Suppose that for a sample  $x$ , we want to predict the class among  $k$  classes  $\{s_1, s_2, s_3, \dots, s_k\}$ , with  $n$  separate classifiers  $\{h_1, h_2, h_3, \dots, h_n\}$  [42]. In the Hard Voting method, the prediction result of the majority of the classifiers that make up the ensemble for a given sample is considered to be the class of the sample. Accordingly, the predicted class of sample  $x$  according to the hard voting method is expressed as follows [42],

$$H(x) = s_{\underset{j}{\operatorname{argmax}} \sum_{i=1}^n h_i^j(x)} \quad (2)$$

In the soft voting method, the class prediction is made by averaging the weighted probabilistic predictions. The class with the highest average is considered as the prediction of the ensemble. Accordingly, the predicted class of sample  $x$  according to the soft voting method is expressed as follows [42],

$$H(x) = s_{\underset{j}{\operatorname{argmax}} \sum_{i=1}^n w_i h_i^j(x)} \quad (3)$$

where  $w_i$  represents the weight of the  $h_i$  classifier in the ensemble.

### 3.5.2. Stacking Ensemble Learning

The stacking ensemble learning method was developed by Wolpert [43] and is a two-step method. In the first stage, predictions are generated by different classifiers using the same data set (training) and in the second stage, these predictions are processed by a meta-classifier to obtain the ensemble prediction. The aim here is for the ensemble classifier to obtain predictions with higher accuracy [43].

### 3.6. Performance Evaluation

In this study, 10-fold cross-validation was used for performance evaluation. Accuracy (Acc.), Precision (Pre.), Sensitivity (Sen.), f1-score (f1-sc.) and AUC (area under the ROC) metrics were used to evaluate the performance of both TL models and ensemble learning classifiers [44]. These metrics are obtained in the light of the data in the confusion matrix in Table 3.

**Table 3.** Representation of the Confusion Matrix

		Predicted Label	
		True Positive (TP)	False Negative (FN)
True Label	False Positive (FP)		True Negative (TN)
	True Positive (TP)		False Negative (FN)

Accuracy is calculated as the ratio of correctly predicted samples to the total number of samples in the model.

$$Accuracy = \frac{TP + TN}{TP + FP + FN + TN} * 100 \quad (4)$$

Sensitivity is the generic name given to the metric that indicates how many of the samples we should have predicted as positive we predicted as positive.

$$Sensitivity = \frac{TP}{TP + FN} * 100 \quad (5)$$

Precision is the metric that allows us to check how many of the values we predict as positive are actually positive.

$$Precision = \frac{TP}{TP + FP} * 100 \quad (6)$$

The f1-score is the harmonic mean of sensitivity and precision measures. The f1-score reveals realistic results including all error costs in the case of non-uniformly distributed data sets, or data sets with unknown distribution.

$$f1 - score = 2 * \frac{TP}{2TP + FN + FP} * 100 \quad (7)$$

## 4. Experimental Results

In order to compare the performance of the proposed system, firstly, direct classification was performed with the TL model without using an ensemble classifier. The other three applications were performed with Stacking, Soft and Hard Voting ensemble classifiers and making a total of four separate applications. The nine TL models used within the scope of the study were tested separately in each application. In addition, in each of these four



applications, two-class (COVID-19 and Normal), three-class (COVID-19, Viral-Pneumonia and Normal) and four-class (COVID-19, Lung-Opacity, Viral-Pneumonia and Normal) applications were performed. Performance measures for the applications are presented separately in tables.

For this purpose, the performance analysis of the four-, three- and two-class applications for the training and test datasets are presented separately. Table 4 shows the accuracy of the TL models without ensemble classifiers for the training and test datasets. Table 5 presents the accuracies obtained for the test dataset using deep features and the proposed ensemble classifier system. The highest accuracies for training and test datasets in four-class applications when the ensemble classifier is not used are %84.83 (Precision: %85.67, Sensitivity: %83.49, f1-score: %84.49) and %85.09 (Precision: %87.18, Sensitivity: %82.05, f1-score: %84.14) obtained with MobileNet. The lowest estimation accuracy was obtained with the VGG16 TL model as %63.17 and %63.17 for the training and test data sets, respectively. In the other application group, the tri-class applications, the highest accuracies were obtained with the DenseNet201 model as %91.26 (Precision: %92.29, Sensitivity: %87.60, f1-score: %89.69) and with the MobileNet as %90.53 (Precision: %93.10, Sensitivity: %84.39, f1-score: %88.09). Similarly, the lowest prediction accuracy was obtained as 73.07% and 72.42% for the training and test data sets in the VGG16 BL model, respectively. In the last application group, two-class applications, the highest accuracies for both training and test datasets were obtained with MobileNet as %90.98 (Precision: %90.10, Sensitivity: %85.94, f1-score: %87.73) and %91.53 (Precision: %92.35, Sensitivity: %85.38, f1-score: %88.12), respectively. The lowest prediction accuracy was obtained in the VGG16 TL model, as %78.52 and %78.93 for the training and test datasets, as in the previous four and three-class applications.

**Table 4.** Training and test accuracies of TL models.

Model	Train (%)			Test (%)		
	4-class	3-class	2-class	4-class	3-class	2-class
Xception	80.86	87.72	87.43	80.6	88.06	88.09
NASNet	80.74	88.04	87.9	79.09	87.73	87.91
MobileNet	<b>84.83</b>	90.99	<b>90.98</b>	<b>85.09</b>	<b>90.53</b>	<b>91.53</b>
DenseNet169	84.33	90.75	89.9	84.88	90.2	90.55
DenseNet201	83.75	<b>91.26</b>	90.74	82.45	90.47	91.09
VGG16	63.17	73.07	78.52	63.17	72.42	78.93
InceptionV3	81.22	88.12	88.19	80.75	86.34	86.82
ResNet50V2	84.37	90.4	90.52	84.17	89.64	90.7
ResNet101V2	83.41	90.29	89.29	83.7	88.95	89.86

According to the proposed hybrid model named DeepFeat-E, in four-class applications with deep features and ensemble classifiers, the highest accuracy of %90.17 (Precision: %92.29, Sensitivity: %89.65, f1-score: %90.88) for the Stacking method was obtained with the DenseNet201 TL model. For Soft and Hard voting methods, the highest accuracy values were obtained with DenseNet169 Transfer Learning model as %88.45 (Precision: %90.84, Sensitivity: %87.05, f1-score: %88.72) and %87.93 (Precision: %90.15, Sensitivity: %86.35, f1-score: %88.03), respectively. On the other hand, the lowest accuracy values were obtained with the Xception TL model for Stacking, Soft and Hard Voting as %82.35, %81.53 and %80.75, respectively. In the other group of applications with three classes, the highest accuracy for the Stacking method was %94.99 (Precision: %95.99, Sensitivity: %91.65, f1-score: %93.68) with the DenseNet201 TL model, and for the Soft and Hard voting methods as %93.17 (Precision: %95.00, Sensitivity: %88.70, f1-score: %91.55) and %92.91 (Precision: %94.59, Sensitivity: %88.34, f1-score: %91.17) with the DenseNet169 TL model, respectively. On the other hand, the lowest accuracy values were obtained in the Xception TL model as %89.84 for the Stacking method, and for Soft and Hard Voting as %88.52 and %88.29, respectively, in the InceptionV3 TL model. In the last group of applications, two-class applications, the highest accuracy in the Stacking method and Soft and Hard voting methods is %94.82 (Precision: %94.43, Sensitivity: %91.99, f1-score: %93.12), %94.21 (Precision: %94.93, Sensitivity: %89.96, f1-score: %92.09) and %94.17 (Precision: %95.13, Sensitivity: %89.71, f1-score: %92.00) was obtained with the DenseNet201 TL model. On the other hand, the lowest accuracy values were obtained with

the InceptionV3 TL model as %90.15, %89.68 and %89.46 for Stacking, Soft and Hard Voting methods, respectively.

**Table 5.** Test accuracy values of ensemble classifiers.

Model	Stacking Method (%)			Soft Voting (%)			Hard Voting (%)		
	4-class	3-class	2-class	4-class	3-class	2-class	4-class	3-class	2-class
Xception	82.35	89.84	90.88	81.53	89.15	90.51	80.75	88.49	90.33
NASNet	84.08	90.7	91.42	81.74	89.05	91.31	81.72	88.55	90.59
MobileNet	88.09	93.67	93.08	86.16	91.95	92.72	85.64	91.45	92.83
DenseNet169	89.63	94.52	93.05	<b>88.45</b>	<b>93.17</b>	93.56	<b>87.93</b>	<b>92.91</b>	93.52
DenseNet201	<b>90.17</b>	<b>94.99</b>	<b>94.82</b>	87.81	92.97	<b>94.21</b>	87.24	92.35	<b>94.17</b>
VGG16	87.15	94.09	92.61	84.08	90.83	92.14	84.03	90.37	91.82
InceptionV3	83.13	90.1	90.15	82.07	88.52	89.68	81.29	88.29	89.46
ResNet50	88.33	93.27	93.63	86.51	91.42	92.47	85.99	91.09	92.58
ResNet101	86.96	92.51	93.12	84.74	90.37	92.65	84.57	90.1	92.43

Table 6 shows the improvement amounts by listing the differences between the accuracy values obtained directly with TL models without using ensemble classifiers (Test column in Table 4) and the accuracy values obtained with the proposed hybrid system (Table 5). Figure 4(a, b and c) shows the improvement of the proposed system for each of the Stacking, Soft and Hard voting ensemble classifiers respectively. The amount of improvement in the TL models used in each graph is presented by grouping according to the different number of classes performed. Accordingly, in the proposed system, ensemble classifiers achieved higher prediction accuracy than TL models in all applications and significantly increased the accuracy of TL models.

**Table 6.** Amount of improvement in test accuracies of the proposed hybrid system.

Model	Stacking Method (%)			Soft Voting (%)			Hard Voting (%)		
	4-class	3-class	2-class	4-class	3-class	2-class	4-class	3-class	2 sinif
Xception	1.75	1.78	2.79	0.92	1.09	2.43	0.14	0.43	2.24
NASNet	4.98	2.97	3.51	2.65	1.32	3.4	2.62	0.82	2.68
MobileNet	3	3.13	1.56	1.06	1.42	1.19	0.54	0.92	1.3
DenseNet169	4.75	4.32	2.5	<b>3.57</b>	<b>2.97</b>	3.01	<b>3.05</b>	<b>2.71</b>	2.97
DenseNet201	<b>7.73</b>	<b>4.52</b>	<b>3.73</b>	5.36	2.51	<b>3.11</b>	4.8	1.88	<b>3.08</b>
VGG16	23.98	21.68	13.69	20.91	18.41	13.22	20.86	17.95	12.89
InceptionV3	2.39	3.76	3.33	1.32	2.18	2.86	0.54	1.95	2.64
ResNet50	4.16	3.63	2.93	2.34	1.78	1.77	1.82	1.45	1.88
ResNet101	3.26	3.56	3.26	1.04	1.42	2.79	0.87	1.15	2.57

As stated before, the highest estimation accuracy in four, three and two-class applications was obtained with the hybrid model named DeepFeat-E. Accordingly, the accuracy values are 90.17%, 94.99% and 94.82% when the stacking ensemble classifier is used with the deep features obtained from the DenseNet201 TL model. As seen in Table 6 and Figure 4(a), the proposed system for DenseNet201 improves the accuracies of the TL model by +7.73, +4.52 and 3.73 points, respectively. Moreover, when all TL models are considered, it is seen that the highest accuracy improvements in four, three and two class applications are realized in the VGG16 TL model by +23.98,

+21.68 and +13.69 points, respectively, with the stacking ensemble learning method. In addition, the VGG16 TL model is also significantly improved in soft and hard voting techniques (Figure 4(b and c)).

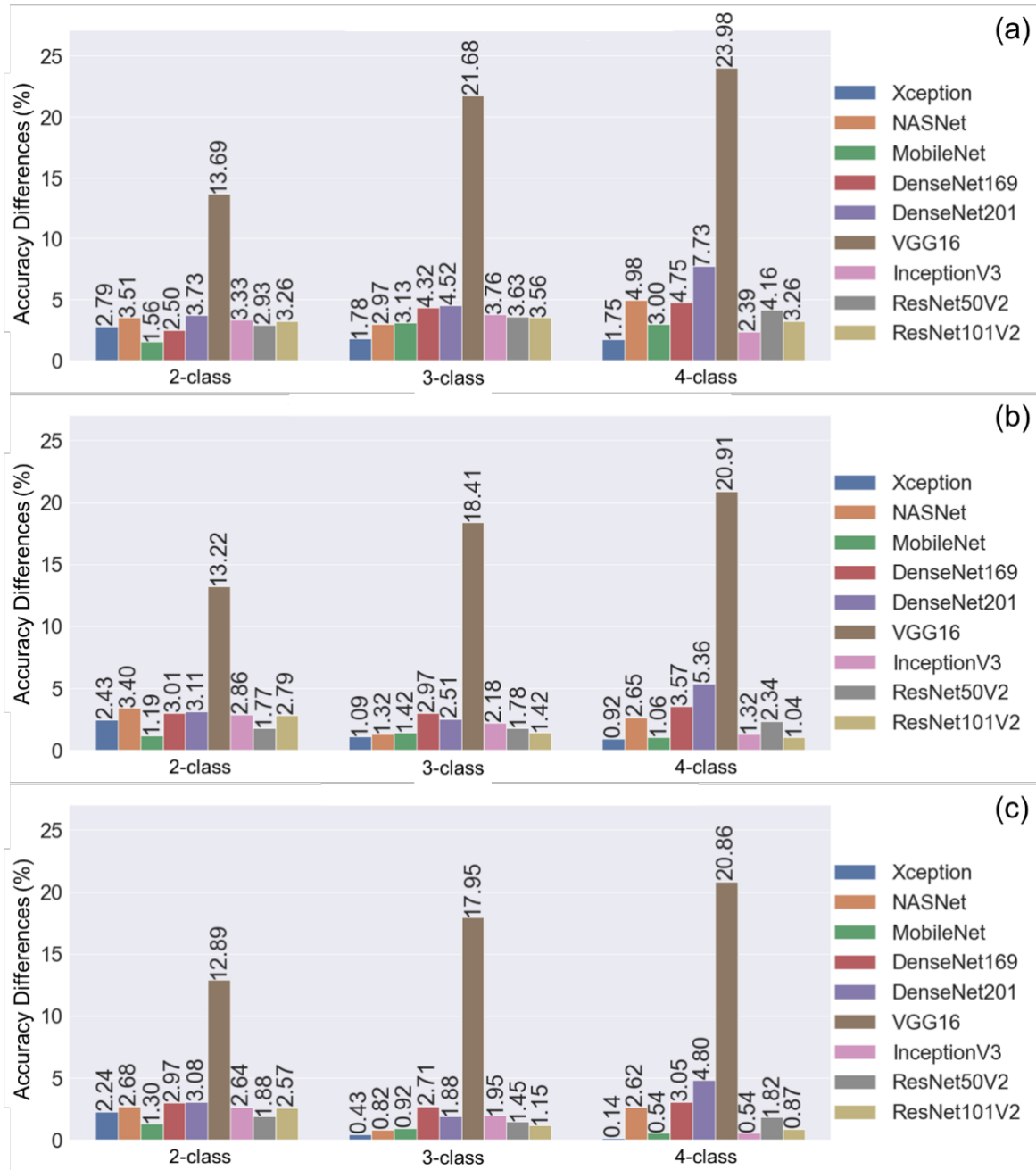


**Figure 4.** Amount of improvement in test accuracies of TL models grouped by number of classes.

Figure 5 (a, b, and c) shows the confusion matrices for the applications with four, three and two classes, respectively, where the highest accuracy values are obtained for the test dataset. In the proposed DeepFeat-E hybrid model, the highest accuracy values were obtained with the DenseNet201 TL model's deep features (DenseNet201F) and Stacking ensemble learning method.

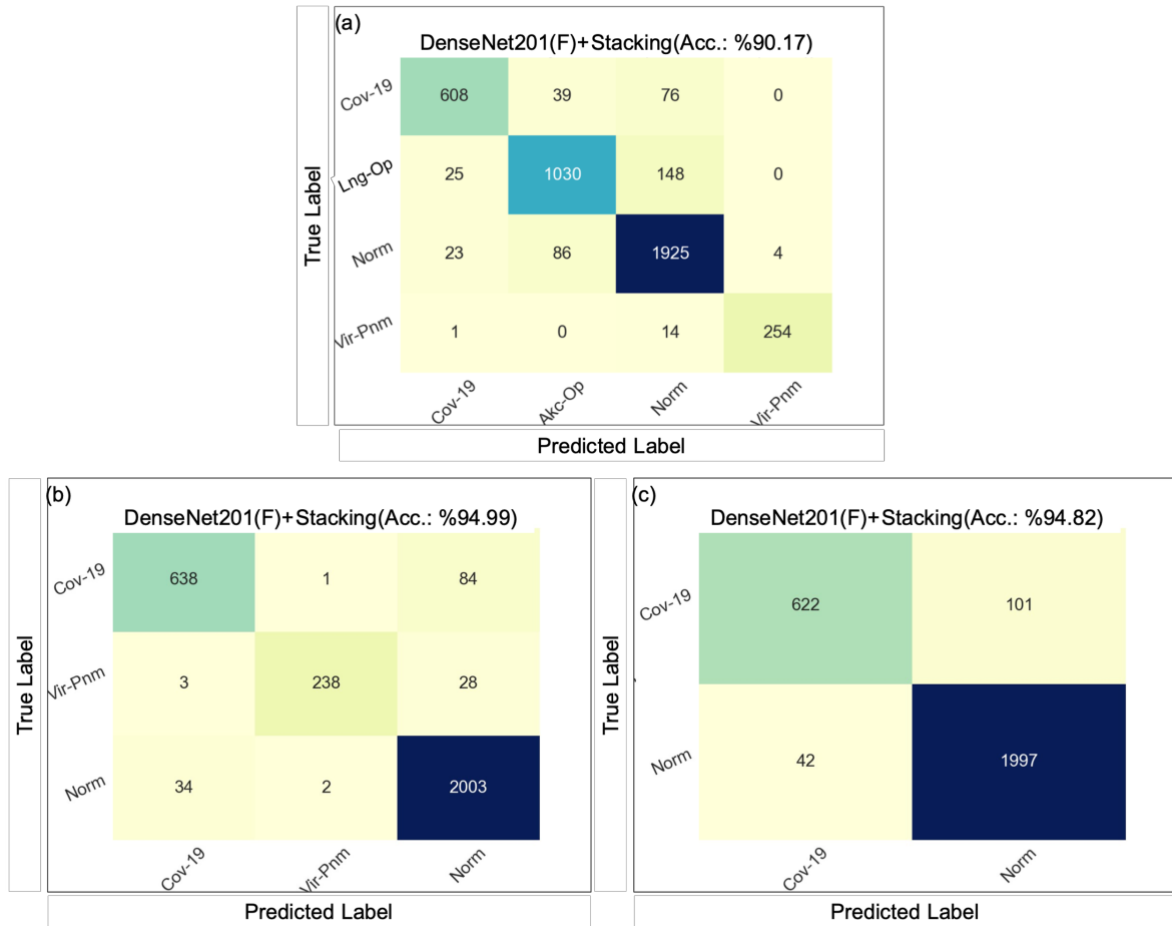


Figure 5. Best test accuracy confusion-matrixes for four-class (a), three-class (b) and two-class (c) applications.

## 5. Discussion

In this study, we propose a hybrid artificial intelligence system, DeepFeat-E, based on deep features extracted from X-Ray images using pre-trained TL models and an ensemble learning structure in which these features are processed by five selected best classical ML models. Although there are many artificial intelligence systems based on deep networks for COVID-19 diagnosis in the literature, this study differs from them since it is based on ensemble learning methods [6,15,25–29]. On the other hand, although there are similar studies using ensemble classifiers in the literature, it is seen that there are various studies in which snapshots of the same convolutional neural network or TL model during the training process are used as separate classifiers in the ensemble classifier [19–24]. However, in the system proposed in this study, deep features are extracted from pre-trained TL models and these features are classified in ensemble learning methods using classical ML methods. In the proposed system, there is only training in ensemble learning methods. In addition, other aspects that make the study valuable are the size of the dataset, the number of classes, the variety of the used TL models and the way in which the deep features are obtained and processed.

For comparison purposes, the performances of the hybrid model proposed in this study and other similar studies in the literature are listed in Table 7. The table shows the deep learning method used in the studies on X-Ray images, whether they are ensemble learning or not, the number of examples and classes in the datasets, and the accuracy values obtained as percentages. The table shows that the success rates vary according to the number of categorical classes of the images and the datasets used.

**Table 7.** Comparison of studies diagnosing COVID-19 from X-Ray images.

Author	Method	Ensemble	Number of Samples	# Class	Acc. (%)
Karim et al. [21]	DeepCOVIDExplainer	Yes	COVID-19: 358, Pneumonia: 5538, Normal: 8066	3	96.10
Mahmud et al. [20]	CovXNet	Yes	COVID-19: 305, Pneumonia-Bact.: 305, Pneumonia-Vir.: 305, Normal: 305	4 3 2	90.3 89.6 97.4
Chowdhur et al. [19]	ECOVNet	Yes	COVID-19: 589, Pneumonia: 6053, Normal: 8851	3	97.00
Apostolopoulos and Mpesiana [25]	VGG19	No	COVID-19: 224, Pneumonia-Bact.: 700, Normal: 504	3 2	93.48 98.75
Wang et al. [6]	COVID-Net	No	COVID-19: 358, Pneumonia: 5538, Normal: 8066	3	93.30
Ozturk et al. [26]	DarkCovidNet	No	COVID-19: 125, Pneumonia: 500, No-Findings: 500	3 2	87.02 98.08
Khan et al. [27]	CoroNet	No	COVID-19: 284, Pneumonia-Bact.: 330, Pneumonia-Vir.: 327, Normal: 310	4 3 2	89.65 94.59 99.00
Ahamed et al. [15]	Modified ResNet50V2	No	COVID-19: 1143, Pneumonia-Vir.: 1150, Pneumonia-Bact.: 1150, Normal: 1150	4 3 2	96.45 97.24 99.35
Tang et al. [22]	EDL-COVID	Yes	COVID-19: 573, Pneumonia: 6053, Normal: 8851	3	95.00
Huang and Liao [28]	LightEfficientNetV2	No	COVID-19: 600, Pneumonia: 600, Normal: 600	3	98.33
Islam et al. [29]	Cov-RADNet	No	COVID-19: 3616, Lung-Opacity: 6012, Pneumonia-Vir.: 1345, Normal: 10192	4 3 2	97.00 99.50 99.72
Banerjee et al. [23]	DenseNet-201+BlendingwRF	Yes	COVID-19: 568, Pneumonia: 6052, Normal: 8851	3	94.55
Banerjee et al. [23]	DenseNet-201+Blending(RF)	Yes	COVID-19: 219, Pneumonia: 1345, Normal: 1341	3	94.13
Gour and Jain [24]	Stack CNN	Yes	COVID-19: 546, Pneumonia: 1355, Normal: 1139	3	97.27
<b>This work</b>	DeepFeat-E	Yes	COVID-19: 3616, Lung-Opacity: 6012, Pneumonia-Vir.: 1345, Normal: 10192	4 3 2	<b>90.17</b> <b>94.99</b> <b>94.82</b>

In the proposed system in this study, the highest accuracy values were obtained by using the deep features of the DenseNet201 TL model and the Stacking transfer learning method. It is seen that the accuracy values of %82.45, %90.47 and %91.09 are obtained in four, three and two class test datasets, respectively, in the applications where the CT model is used directly (Table 4). On the other hand, the proposed hybrid system improves the test accuracies to %90.17 (+7.73 points), %94.99 (+4.52 points) and %94.82 (+3.73 points) for four, three and two class datasets, respectively (Table 5 and Table 6). Therefore, it is understood that the proposed hybrid approach improves the success performance in all the applications performed in this study and has an acceptable accuracy. Accordingly, it is understood that in all four, three and two-class data sets, at least 9 out of 10 samples could be

correctly diagnosed. Compared to other studies in the literature, there are studies with higher accuracy than the present study (Table 7). However, the fact that the data set used in this study is much larger and different data sets are used are thought to be the main reasons underlying this difference in success. Using the same dataset, Islam et al. [29] obtained more successful results in their study (Table 7). However, in their study, they performed balanced analyses by equalizing the number of class-based instances of this dataset, which contains different instances for each class. On the contrary, in this study, the number of class-based instances in the dataset was not equalized and the analyses were performed using an unbalanced number of class instances.

In addition, it has been observed that the proposed DeepFeat-E hybrid model is more successful and increases the diagnostic accuracy compared to the performances obtained when the TL models are used directly. Accordingly, for the four-class test dataset, the highest accuracy was %85.09 with MobileNet when using the TL models directly, and when the proposed hybrid system was used for the same model, the accuracy increased to %88.09 (+3 points) with the Stacking ensemble learning method. Likewise, when TL models are used directly for three and two-class test data sets, the highest accuracy was obtained with the MobileNet TL model as %90.53 and %91.53, respectively. Here too, the accuracy increases to %93.99 (+2.46 points) and %93.67 (+3.13 points) with the Stacking ensemble learning method when the proposed hybrid system is used. As seen in Table 5 and Table 6, all of the ensemble classifiers have higher accuracy values than the TL models, so it can be said that the proposed hybrid system significantly increases the success. As a result, it is seen that the proposed hybrid model is more successful than TL models in diagnosing COVID-19 and other lower respiratory tract infections and has an acceptable level of success with accuracy values of over %90 when compared to other studies in the literature.

## 6. Conclusion

Reducing the impact of both human health and economic damages caused by the COVID-19 pandemic is directly related to the rapid and accurate diagnosis of the disease. Therefore, rapid diagnosis, identification, treatment and isolation of COVID-19 are of utmost importance. Methods used in the diagnosis of the disease, such as PCR testing or manual interpretation of CT or X-Ray images, are known traditional methods. However, since they are faster and safer methods, medical image-based artificial intelligence systems and especially deep learning methods are successfully applied in the diagnosis of COVID-19.

Although there are similar artificial intelligence studies on COVID-19 diagnosis using ensemble learning methods in the literature, it is seen that snapshots obtained in the same training process are used as ensemble classifiers in these studies. With the hybrid diagnostic system named DeepFeat-E proposed in this study, it is attempted to diagnose COVID-19 from X-Ray images using deep features obtained from pre-trained TL models and classifiers consisting of classical machine learning methods. It was observed that the proposed system achieved the highest success with the deep features of DenseNet201 TL models and the Stacking ensemble learning method. Accordingly, the test accuracy was 90.17%, 94.99% and 94.82% for four, three and two class applications, respectively. It was also observed that the system increased the accuracy values obtained in all TL models by varying amounts (Table 6). The fact that the proposed system uses pre-trained TL models has significant advantages such as eliminating the need for big data for training the models and reducing resource and time costs. Therefore, the results obtained in this study show that the proposed DeepFeat-E hybrid system can be used quickly and reliably in the diagnosis of COVID-19 and lower respiratory tract infections.

## References

- [1] Kumari S, Ranjith E, Gujjar A, Narasimman S, Zeelani HSAS. Comparative analysis of deep learning models for COVID-19 detection. *Global Transitions Proceedings* 2021;2:559–65.
- [2] Pang L, Liu S, Zhang X, Tian T, Zhao Z. Transmission dynamics and control strategies of COVID-19 in Wuhan, China. *J Biol Syst* 2020;28:543–60.
- [3] Abir FF, Alyafei K, Chowdhury MEH, Khandakar A, Ahmed R, Hossain MM, et al. PCovNet: A presymptomatic COVID-19 detection framework using deep learning model using wearables data. *Comput Biol Med* 2022;147:105682.
- [4] Lewnard JA, Lo NC. Scientific and ethical basis for social-distancing interventions against COVID-19. *Lancet Infect Dis* 2020;20:631–3.
- [5] Makris A, Kontopoulos I, Tserpes K. COVID-19 detection from chest X-Ray images using Deep Learning and Convolutional Neural Networks. *11th hellenic conference on artificial intelligence*, 2020, p. 60–6.
- [6] Wang Y, Kang H, Liu X, Tong Z. Combination of RT-qPCR testing and clinical features for diagnosis of COVID-19 facilitates management of SARS-CoV-2 outbreak. *J Med Virol* 2020.

- [7] Verma SS, Prasad A, Kumar A. CovXmlc: High performance COVID-19 detection on X-ray images using Multi-Model classification. *Biomed Signal Process Control* 2022;71:103272.
- [8] Tung H, Tekin R. New Feature Extraction Approaches Based on Spatial Points for Visual-Only Lip-Reading. *Traitement Du Signal* 2022;39.
- [9] Noyan T, Kuncan F, Tekin R, Kaya Y. A new content-free approach to identification of document language: Angle patterns. *Journal of the Faculty of Engineering and Architecture of Gazi University* 2022;37:1277–92.
- [10] Kuncan F, Kaya Y, Tekin R, Kuncan M. A new approach for physical human activity recognition based on co-occurrence matrices. *J Supercomput* 2022;78:1048–70.
- [11] Kaya Y, Tekin R. A Novel Feature Extraction Method for Classification of Epileptic EEG Signals. *Journal of Natural & Applied Sciences* 2018.
- [12] Kaya Y, Kuncan F, Tekin R. A New Approach for Congestive Heart Failure and Arrhythmia Classification Using Angle Transformation with LSTM. *Arab J Sci Eng* 2022:1–17.
- [13] Sobahi N, Atila O, Deniz E, Sengur A, Acharya UR. Explainable COVID-19 detection using fractal dimension and vision transformer with Grad-CAM on cough sounds. *Biocybern Biomed Eng* 2022;42:1066–80.
- [14] Ren Z, Chang Y, Bartl-Pokorny KD, Pokorny FB, Schuller BW. The acoustic dissection of cough: diving into machine listening-based COVID-19 analysis and detection. *MedRxiv* 2022.
- [15] Ahamed KU, Islam M, Uddin A, Akhter A, Paul BK, Yousuf MA, et al. A deep learning approach using effective preprocessing techniques to detect COVID-19 from chest CT-scan and X-ray images. *Comput Biol Med* 2021;139:105014.
- [16] Ozcan T. A new composite approach for COVID-19 detection in X-ray images using deep features. *Appl Soft Comput* 2021;111:107669.
- [17] Gilanie G, Bajwa UI, Waraich MM, Asghar M, Kousar R, Kashif A, et al. Coronavirus (COVID-19) detection from chest radiology images using convolutional neural networks. *Biomed Signal Process Control* 2021;66:102490.
- [18] Basu A, Sheikh KH, Cuevas E, Sarkar R. COVID-19 detection from CT scans using a two-stage framework. *Expert Syst Appl* 2022;193:116377.
- [19] Chowdhury MEH, Rahman T, Khandakar A, Mazhar R, Kadir MA, Mahbub Z bin, et al. Can AI help in screening viral and COVID-19 pneumonia? *IEEE Access* 2020;8:132665–76.
- [20] Mahmud T, Rahman MA, Fattah SA. CovXNet: A multi-dilation convolutional neural network for automatic COVID-19 and other pneumonia detection from chest X-ray images with transferable multi-receptive feature optimization. *Comput Biol Med* 2020;122:103869.
- [21] Karim MR, Döhmen T, Cochez M, Beyan O, Rebholz-Schuhmann D, Decker S. Deepcovidexplainer: explainable COVID-19 diagnosis from chest X-ray images. 2020 IEEE International Conference on Bioinformatics and Biomedicine (BIBM), IEEE; 2020, p. 1034–7.
- [22] Tang S, Wang C, Nie J, Kumar N, Zhang Y, Xiong Z, et al. EDL-COVID: Ensemble deep learning for COVID-19 case detection from chest X-ray images. *IEEE Trans Industr Inform* 2021;17:6539–49.
- [23] Banerjee A, Sarkar A, Roy S, Singh PK, Sarkar R. COVID-19 chest X-ray detection through blending ensemble of CNN snapshots. *Biomed Signal Process Control* 2022;78:104000.
- [24] Gour M, Jain S. Automated COVID-19 detection from X-ray and CT images with stacked ensemble convolutional neural network. *Biocybern Biomed Eng* 2022;42:27–41.
- [25] Apostolopoulos ID, Mpesiana TA. Covid-19: automatic detection from x-ray images utilizing transfer learning with convolutional neural networks. *Phys Eng Sci Med* 2020;43:635–40.
- [26] Ozturk T, Talo M, Yildirim EA, Baloglu UB, Yildirim O, Acharya UR. Automated detection of COVID-19 cases using deep neural networks with X-ray images. *Comput Biol Med* 2020;121:103792.
- [27] Khan AI, Shah JL, Bhat MM. CoroNet: A deep neural network for detection and diagnosis of COVID-19 from chest x-ray images. *Comput Methods Programs Biomed* 2020;196:105581.
- [28] Huang M-L, Liao Y-C. A lightweight CNN-based network on COVID-19 detection using X-ray and CT images. *Comput Biol Med* 2022:105604.
- [29] Islam MK, Habiba SU, Khan TA, Tasnim F. COV-RadNet: A Deep Convolutional Neural Network for Automatic Detection of COVID-19 from Chest X-Rays and CT Scans. *Computer Methods and Programs in Biomedicine Update* 2022;2:100064.
- [30] Rahman T, Khandakar A, Qiblawey Y, Tahir A, Kiranyaz S, Kashem SBA, et al. Exploring the effect of image enhancement techniques on COVID-19 detection using chest X-ray images. *Comput Biol Med* 2021;132:104319.
- [31] Chollet F. Xception: Deep learning with depthwise separable convolutions. *Proceedings of the IEEE conference on computer vision and pattern recognition*, 2017, p. 1251–8.
- [32] Zoph B, Vasudevan V, Shlens J, Le Q v. Learning transferable architectures for scalable image recognition. *Proceedings of the IEEE conference on computer vision and pattern recognition*, 2018, p. 8697–710.

- [33] Howard AG, Zhu M, Chen B, Kalenichenko D, Wang W, Weyand T, et al. Mobilenets: Efficient convolutional neural networks for mobile vision applications. ArXiv Preprint ArXiv:170404861 2017.
- [34] Huang G, Liu Z, van der Maaten L, Weinberger KQ. Densely connected convolutional networks. Proceedings of the IEEE conference on computer vision and pattern recognition, 2017, p. 4700–8.
- [35] Simonyan K, Zisserman A. Very deep convolutional networks for large-scale image recognition. ArXiv Preprint ArXiv:14091556 2014.
- [36] Szegedy C, Vanhoucke V, Ioffe S, Shlens J, Wojna Z. Rethinking the inception architecture for computer vision. Proceedings of the IEEE conference on computer vision and pattern recognition, 2016, p. 2818–26.
- [37] He K, Zhang X, Ren S, Sun J. Identity mappings in deep residual networks. European conference on computer vision, Springer; 2016, p. 630–45.
- [38] Sarkar D, Bali R, Ghosh T. Hands-On Transfer Learning with Python: Implement advanced deep learning and neural network models using TensorFlow and Keras. Packt Publishing Ltd; 2018.
- [39] Zhou K, Greenspan H, Shen D. Deep learning for medical image analysis. Academic Press; 2017.
- [40] Geurts P, Ernst D, Wehenkel L. Extremely randomized trees. Mach Learn 2006;63:3–42.
- [41] Li J, Cheng K, Wang S, Morstatter F, Trevino RP, Tang J, et al. Feature selection: A data perspective. ACM Computing Surveys (CSUR) 2017;50:1–45.
- [42] Zhou Z-H. Ensemble methods: foundations and algorithms. CRC press; 2012.
- [43] Wolpert DH. Stacked generalization. Neural Networks 1992;5:241–59.
- [44] Bohmrah MK, Kaur H. Classification of Covid-19 patients using efficient fine-tuned deep learning DenseNet model. Global Transitions Proceedings 2021;2:476–83.



## The Effect of The Number of Reference Points and Distribution on Coordinate Transformation in Underground Mining Measurements

Levent TAŞÇI<sup>1</sup>, Hacı Sait ARSLAN<sup>2</sup>

<sup>1</sup> Department of Civil Engineering, Faculty of Engineering, Fırat University, Elazığ, Turkey

<sup>2</sup> ETI Chrome Company, Elazığ, Turkey

<sup>1</sup> ltasci@firat.edu.tr, <sup>2</sup> Hacı Sait.ARSLAN@etikrom.com

(Geliş/Received: 24/01/2023;

Kabul/Accepted: 25/02/2023)

**Abstract:** This article focuses on examining the effect of the number and distribution of reference points on coordinate transformations in underground mining measurements using a handheld laser scanner. The points inside the mine were measured as reference using a Total Station. The same point cloud data was subjected to coordinate transformation with different numbers and elevations of reference points. It was observed that the homogeneous distribution of reference points used in the transformation increases precision in the horizontal and vertical directions. Both homogeneous and excessive use of transformation points result in the same good results in the horizontal, but in the vertical, it improves further. Using a large number of transformation points and using them at different elevations results in the same good results in the horizontal, but in the vertical, it increases precision even more. The article concludes that a sufficient number of homogeneously and heterogeneously distributed reference points are necessary for accurate coordinate transformation.

**Keywords:** Laser Scanner, Point Cloud, 3D Transformation, Geodetic Coordinate,

### Yeraltı Madencilik Ölçümlerinde Referans Noktası Sayısı ve Dağılımının Koordinat Dönüşümüne Etkisi

**Özet:** Bu makale, el tipi lazer tarayıcı kullanılarak yer altı maden ölçümlerinde referans noktalarının sayısı ile dağılımının koordinat dönüşümlerinin etkisini incelemeye odaklanmıştır. Maden içindeki noktalar, Total Station kullanılarak referans olarak ölçülmüştür. Aynı nokta bulutu verileri farklı sayıda ve yükseklikteki referans noktalarının dağılımı ile koordinat dönüştürme işlemine tabii tutulmuştur. Dönüşümde kullanılan referans noktalarının homojen dağılımının yatay ve dikey yönde hassasiyeti artırdığı gözlemlenmiştir. Hem homojen hem de aşırı sayıda dönüşüm noktasının kullanımı yatayda aynı iyi sonuçları verir, ancak dikeyde daha da geliştirir. Büyük sayıda dönüşüm noktasının ve bunları farklı yüksekliklerde kullanmanın, yatayda aynı iyi sonuçları verdiği, ancak dikeyde hassasiyeti daha da artırdığı gözlemlenmiştir. Makale, doğru koordinat dönüşümü için yeterli sayıda homojen ve heterojen şekilde dağıtılmış referans noktalarının kullanılmasının gerekli olduğu sonucuna varmaktadır.

**Anahtar kelimeler:** Lazer Tarayıcı, Nokta Bulutu, 3D Dönüşüm, Jeodezik Koordinat

#### 1. Introduction

Underground mining surveying is the process of measuring and mapping the underground mines to determine the location, shape and size of mining operations. This is a critical step in the mining process as it allows mining companies to safely and efficiently extract resources while minimizing the potential for accidents and damage to the environment. The main objective of underground mining surveying is to create a detailed map of the mine, including information on the location of the ore body, the shape and size of the mining area and the location of any underground infrastructure such as ventilation shafts and tunnels. This information is then used to plan and execute mining operations, such as drilling and blasting, as well as to monitor and control the mining process to ensure safety and efficiency. One of the key challenges in underground mining surveying is the need to accurately measure and map the mine in a three-dimensional environment. This requires the use of specialized surveying equipment and techniques, such as laser scanning and underground GNSS, which can accurately measure the position and orientation of underground features. Another challenge in underground mining surveying is the need to transform coordinates between different reference systems. This is necessary because different mining operations may use different coordinate systems and the data collected by surveying equipment may also be in different formats. Coordinate transformation is the process of converting coordinates from one reference system to another and it is critical for ensuring that the data collected by the surveying equipment is accurate and can be used effectively in the mining process. In conclusion, underground mining surveying is a critical step in the mining process that allows mining companies to safely and efficiently extract resources while minimizing the potential

for accidents and damage to the environment. The challenges of measuring and mapping in a three-dimensional environment and transforming coordinates between different reference systems require the use of specialized surveying equipment and techniques, as well as careful coordination and data management.

The laser scanning method was first introduced in Poland in 2003 and has since been extensively researched by cartographers and other experts. Prior to this, the only way to measure inaccessible places was through photogrammetric methods. However, advancements in technology have made it possible for the concept of point clouds to be used in geodesy and underground mining measurements [1-2]. The laser scanning technique involves -measuring the time it takes for a laser beam emitted from a scanning device to strike an object surface, reflect and return, which is then converted into a distance measurement and compared to photos taken. This measurement method has reduced the need for GNSS, Total Station and other geodetic measurement devices, as it requires less personnel, can be completed faster and can produce millions of point clouds representing a structure. Laser scanning technologies are also used in situations where traditional measurement methods are unable to generate enough points [3]. In his 2011 study, Dumalski [2] highlighted the potential applications of laser scanning and conducted practical tests on the use of laser scanners in vertical displacement analysis. In 2010, Yue and colleagues [4] used the laser scanner measurement method to measure slope deformations and found that the slope displacement trend was stable and the degree of landslide risk was low. In 2013, El-Tokhey and colleagues [5] conducted an experimental study to compare the results of measuring 9 points on a slope using both the total station technique and laser scanning and to evaluate the accuracy of the laser scanning data. They found that polynomial transformation was the best approach for converting from laser data to total station data and that it improved the accuracy of the results. In 2012, Gonzalez and colleagues [6] presented a new technique for determining the real accuracy that can be obtained using surface fitting techniques and found that the RIEGL laser scanner system could detect small deformations and could be used for monitoring deformations of engineering structures. In their 2009 study, Yıldız and Altuntaş [3] found that the number and distribution of reference points used for converting point clouds obtained by terrestrial laser scanning into the Geodetic Coordinate System have an impact on the accuracy of the conversion. They observed that as the number of Ground Control Points increases, errors in monitoring points decrease.

## **2. The aim of this study**

This study aimed to use a hand-held laser scanner (Zebrevu by GeoSLAM) to measure and analyze an underground chrome mine in Elazığ, Turkey. The coordinates were transformed using total station measurements taken at various points within the mine gallery, which were distributed in different ways (heterogeneously and homogeneously) and at different heights. The goal of the study was to understand the impact of the distribution, number and height of the reference points on the transformation process within the mine gallery.

## **3. Laser scanner coordinate system**

Geodetic coordinate measurement of an object is done in 3 different ways, depending on the size, location and characteristics of the scanner. These are: direct geodetic coordinate measurement, indirect geodetic coordinate measurement and data-based geodetic coordinate measurement [7].

Indirect geodetic coordinate measurement is done by converting the point cloud produced by the laser scanner into geodetic coordinates using known control points. At least three control points are used to calculate the transformation parameters between coordinate systems [8-9]. The control points can be marked in the measurement area with special markers (such as paper targets or sphere and cylinder targets) before the laser scanning process, or any detail point that can be selected on the model can also be used as a control point. In this method, the geodetic coordinates of the control points must be measured by terrestrial methods. The geodetic coordinates of the points used in the transformation can be measured with a total station or GNSS receivers. Direct geodetic coordinate measurement is applied in different ways depending on the characteristics of the laser scanner. It can be done by setting a theodolite on the scanner and setting the scanner on a known coordinate point, by mounting a GNSS receiver and compass on the scanner, or by mounting 2 GNSS receivers on the scanner. Data-based coordinate measurement is applied by combining laser scanning measurements with previously converted laser scanning measurements or other data in a geodetic coordinate system. This combination can be done using any point cloud merging method or image processing techniques [7].

#### 4. Coordinate transformation

In laser scanners with GNSS, the resulting point cloud is obtained in the desired coordinate system. In systems without GNSS, point clouds are obtained locally and, if desired, are transformed into the desired geodetic coordinate system using a transformation method based on known coordinates. Coordinate transformation is a common practice in geodesy. Coordinate transformation is done to fully establish the relationship between point coordinates produced in different coordinate systems and to ensure datum unity. If it is desired to create local coordinate information obtained from laser scanner measurements in the country's coordinate system, it is necessary to connect the scanner coordinate system to a geodetic network with at least 3 control points. As a result of this connection, a three-dimensional coordinate transformation is carried out and the transformation is made to the desired coordinate system. The size measured by terrestrial laser scanners and the scanner coordinate system is shown in Figure 1.

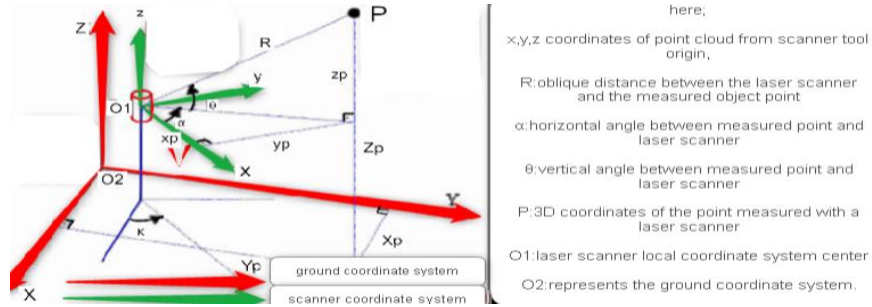


**Figure 1.** Terrestrial laser scanner measurements, scanner coordinate system and earth coordinate system

In this study, coordinate transformations were performed using the "3D Surface Matching Method with Least Squares" found in the Leica Cyclone 3DR software. This method is the process of matching inclined surfaces with the least squares method. The 7 transformation parameters between surfaces are calculated with a 3D similarity transformation. If the surface elements of a single object are selected as the reference window,  $f(x, y, z)$  and the research window,  $g(x, y, z)$  in two different point clouds, the problem that arises is to find the best match between the reference window elements and the research window elements in terms of position, orientation and shape similarity. A random error value,  $e(x, y, z)$  is added to this and the following connection is obtained [10].

$$f(x, y, z) + e(x, y, z) = g(x, y, z) \quad (1)$$

To express the relationship between conjugate surfaces, the 7-parameter 3D similarity transformation given in equation 2 is used. (Yıldız ve et al., 2008)

$$[X \ Y \ Z]^T = m R_{(\omega, \phi, \kappa)} [x \ y \ z]^T + [t_x \ t_y \ t_z]^T \quad (2)$$

$[X \ Y \ Z]^T$ : 2. system coordinates

$R_{(\omega, \phi, \kappa)}$ : orthogonal transformation matrix elements

$[t_x \ t_y \ t_z]^T$ : translation vector

$[x \ y \ z]^T$ : 1. system coordinates

$m$ : is the scale coefficient

The study was carried out in the underground chrome mine of Eti Chrome Company located within the boundaries of Incebayır village, Alacakaya district in Elazığ province. The underground chrome mine located within the boundaries of Incebayır village is 80 km away from the city center of Elazığ province and 15.4 km away from the Alacakaya district of Elazığ province. The satellite image of the location of the underground chrome mine within the boundaries of Elazığ is shown in Figure 2.

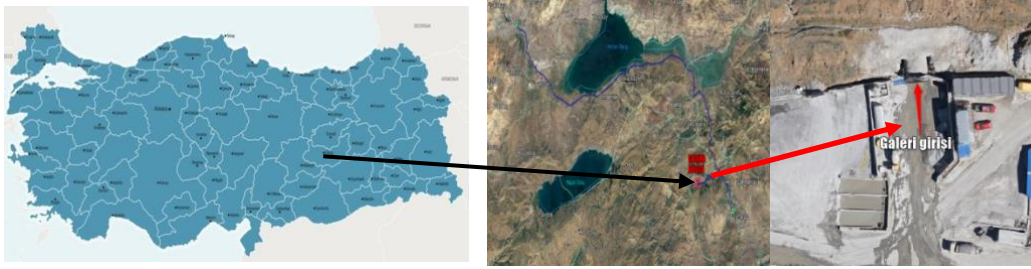


**Figure 2.** Satellite image of the study area within the borders of İncebayır Village, Alacakaya district of Elazığ Province

## 5. Application

The study was carried out in an underground chrome mine, using a Zeb-Revo handheld laser scanner in an area with a 250 m inclined distance and a 20 m elevation difference. The device weighs 665 g and is easy to carry, making the measurement process easier. According to the manufacturer, it works with a closing technique and the accuracy of the measurement points is evaluated as  $5 \text{ mm} + 1 \text{ mm} / \text{m}$ . The image and technical features of the device are shown in Figure 3.

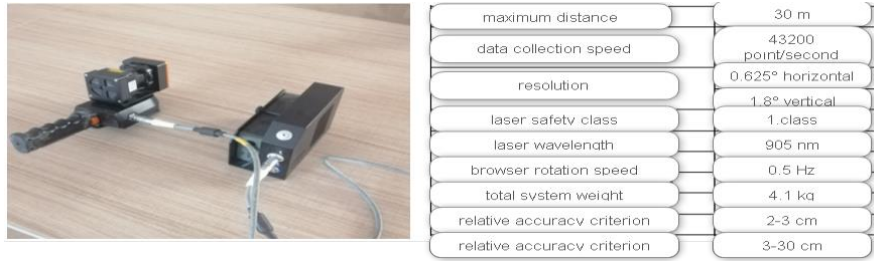


**Figure 3.** Geo Slam Zebreo laser scanner image and technical features

The laser scanner measurement was transformed into the geodetic network in four different ways. The accuracy of the transformations was studied based on total station measurement. Conical objects with distinguishable geometry and identifiable iron bars on the gallery ceiling were used for coordinate system transformation in the laser scanner measurement. The image of the conical objects used for the transformation in the gallery is shown in Figure 4.



**Figure 4.** Conical object used in the transformation of the point cloud obtained from laser scanning.

The gallery side walls were measured using the classical measurement device, the total station, using the backsight method. The total station measurement was accepted as the reference for the comparison of the transformations. The ED-50 coordinate system values were given to the endpoints of the conical objects and the identifiable iron points on the ceiling using the Leica brand total station. For the coordinate transformation, three points were placed close to the starting point of the measurement (approximately 5m.), one point approximately in the middle of the measurement area, 1 point at the end of the measurement area and two iron rods with

identifiable geometry on the ceiling. In addition, 1 control cone was placed to compare the transformation results that will not be used in the coordinate transformation. As a result of the values given in the ED-50 coordinate system, the point cloud obtained from the measurement was connected to the geodetic network from the scanner's coordinate system by making four different transformations. The measurement geometry is shown in Figure 5.

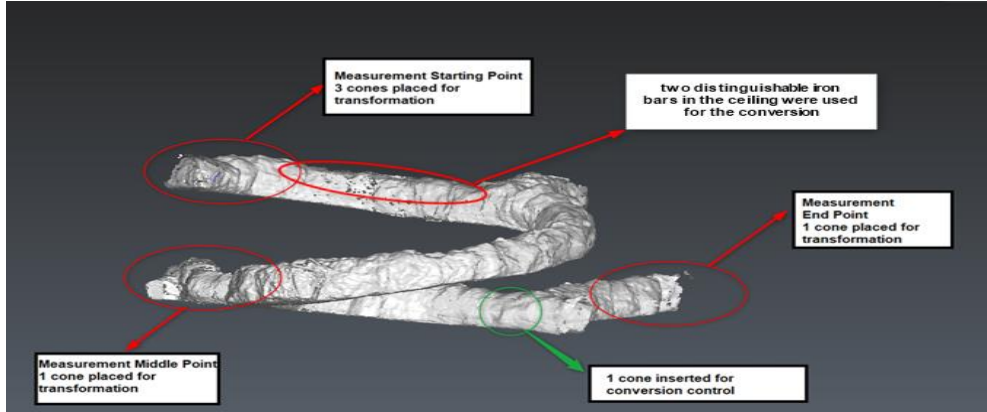


**Figure 5.** The underground mine measurement and measurement geometry were conducted using the laser scanner.

To connect the point cloud data in the scanner coordinate system obtained from measurement to the geodetic network, four different transformations were used. In the first transformation, three closely located cones were used at the starting point. In the second transformation, three cones, one at the starting point, one at the middle of the measurement and one at the end of the measurement, were used. In the third transformation, five cones left in the measurement area for reference were used. In the fourth transformation, two distinguishable iron objects on the ceiling were added to the three cones in the second transformation and a total of five reference points were used, the same as in the fourth transformation. The transformation points in the first transformation were evaluated as heterogeneous and in the second transformation, as homogeneously distributed. In the third transformation, the number of transformation points was increased differently from the first and second transformations and in the fourth transformation, the reference point number was the same as in the third transformation (five transformation points) but evaluated differently by using distinguishable iron on the ceiling instead of 2 cone objects on the ground.

A laser scanner called Zebrevu was used to produce two compressed files with the extensions bag and params. The data was processed using the GeoSlam Hub program, resulting in a point cloud file with the extension LAS. The point cloud processing program Leica Cyclone was then used to convert this file. In Leica Cyclone, the three-dimensional point cloud file was opened and noisy points around the cones and iron rods were removed. The cones and iron rods' coordinates in the Ed-50 coordinate system were added to the program as an a. txt file and 3-dimensional transformations were performed using 3 coordinates from 3 cones in the first and second transformations, 5 coordinates from 5 cones in the third transformation and 3 coordinates from 3 cones in the fourth transformation, as well as the coordinates of 2 iron rods from the ceiling.

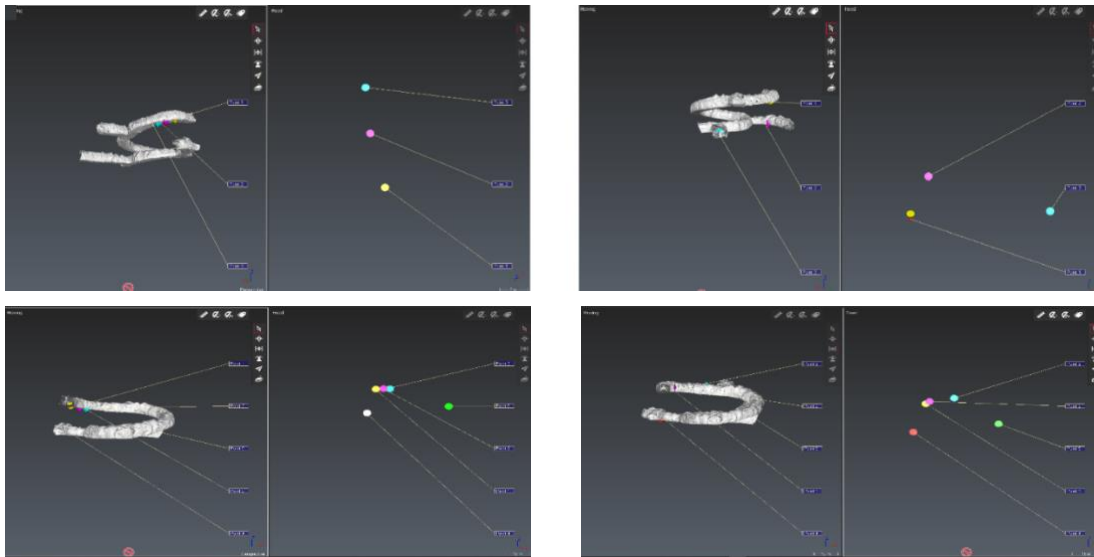


**Figure 6.** The first, second, third and fourth transformation processes in the Leica Cyclone program.

## 6. Results

In the first and second transformations, only the starting point's transformation cone was used in common, so it was observed that the measurement data at the starting point of the two transformations were consistent with each other. However, it was observed that there were significant differences in the horizontal and vertical directions between the point clouds obtained from the two transformations throughout the entire measurement area, excluding the starting point. When the total station gallery measurement, which is considered as a reference, is taken into account, it was determined that the second transformation (transformation in which the transformation cones are distributed homogeneously) is precise and the first transformation (transformation in which the transformation cones are distributed heterogeneously) is inaccurate in the horizontal and vertical directions. The situation in which the first transformation point cloud, the second transformation point cloud and the total station measurement are compared horizontally and vertically is shown in Figure 7.

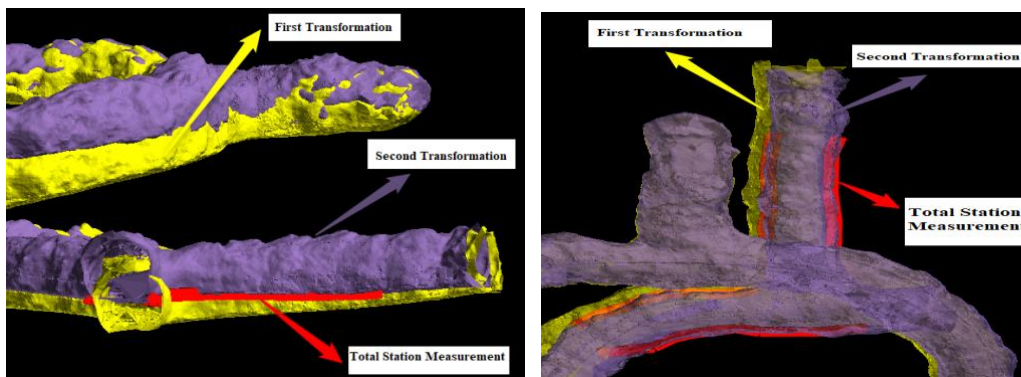


**Figure 7.** Horizontal, vertical comparison of first transformation and second transformation point cloud and total station measurement

In the third transformation, a total of five cones were used for the transformation using two other cones at the starting point in addition to the second transformation. It was observed that the precision did not change much on the horizontal, but increased significantly on the vertical. In the fourth transformation, the number of transformation points is the same as in the third transformation, but two iron rods located on the gallery ceiling were used instead of two cones on the ground. It was observed that the precision of the four different transformation

is not much different from that of the third transformation, but the vertical precision increased slightly. To compare the transformation results with numerical values, a control cone was placed at the end of the measurement area. When the coordinate value of the control cone was read from the point cloud generated by the four transformations and compared with the coordinate value taken by the total station, the deviations in the Y and X directions are given in Table 1.

**Table 1.** Horizontal and vertical numerical comparison of measurements and conversions using a control cone

	Y (m)	X(m)	Z (m)	$\Delta Y$ (cm)	$\Delta X$ (cm)	$\Delta Z$ (cm)
<b>Total Station</b>	<b>566077.477</b>	<b>4262431.940</b>	<b>1086.150</b>	---	---	---
<b>1. Transformation (3 Cone objects Heterogene)</b>	<b>566077.087</b>	<b>4262431.990</b>	<b>1083.970</b>	<b>139.0</b>	<b>-105.0</b>	<b>-218.0</b>
<b>2. Transformation (3 Cone objects Homegene)</b>	<b>566077.511</b>	<b>4262431.928</b>	<b>1086.084</b>	<b>-3.4</b>	<b>1.2</b>	<b>-6.6</b>
<b>3. Transformation (5 Cone objects Homegene)</b>	<b>566077.508</b>	<b>4262431.923</b>	<b>1086.102</b>	<b>-3.1</b>	<b>1.7</b>	<b>-4.8</b>
<b>4. Transformation (3 Cone objects+ 2 Iron Rod on the Ceiling Homegene)</b>	<b>566077.504</b>	<b>4262431.921</b>	<b>1086.123</b>	<b>-2.7</b>	<b>1.9</b>	<b>-2.7</b>

## 7. Conclusion

In this study, four different transformations were compared. In the first and second transformations, the transformation cones were placed in the measurement area homogeneously and heterogeneously. It was found that the transformation was precise when the cones were placed homogeneously and not precise when the cones were placed heterogeneously. In the third transformation, the number of points used in the transformation was increased compared to the second transformation and it was observed that the precision did not change much in the horizontal but increased significantly in the vertical. In the fourth transformation, the number of points used in the transformation is the same as in the third transformation, but the iron rods located on the gallery ceiling were used instead of the two cones on the ground. It was also observed that the precision of the fourth transformation is not much different from that of the third transformation, but the vertical precision increased slightly. In conclusion, it was observed that the homogeneous distribution of reference points used in the transformation increases precision in the horizontal and vertical directions, both homogeneous and excessive use of transformation points result in the same good results in the horizontal, but in the vertical, it improves further, using a large number of transformation points and using them at different elevations results in the same good results in the horizontal, but in the vertical, it increases precision even more.

## References

- [1] Schmitz B, Holst C, Medic T, Licht DD, Kuhlmann H. How to Efficiently Determine the Range Precision of 3D Terrestrial Laser Scanners. *Sensors* 2019; 19, 1466.
- [2] Dumalski A. Evaluation of the possible application of terrestrial laser scanner-station in vertical displacement measurements. *Technical Sciences/University of Warmia and Mazury in Olsztyn*, 2011; 33-43.
- [3] Yıldız F, Altuntaş C. Yersel Lazer Tarayıcı Nokta Bulutlarının Jeodezik Koordinat Sistemine Dönüştürülmesi, *Harita Dergisi* 2009; Sayı:142.
- [4] Yue D, Wang J, Zhou J, Chen X, Ren H. Monitoring slope deformation using a 3-D laser image scanning system: a case study. *Min Sci Technol (China)* 2010; 20(6), 898-903.
- [5] El-Tokhey M, Abdel-Gawad AK, M Yasser, El-Maghraby AM. Accuracy assessment of laser scanner in measuring and monitoring deformations of structures 2012; 26. 144-151.
- [6] Gonzalez H, Solla M, Armesto J, Arias P, Range, Close & Sensing, Remote & Group, Photogrammetry. Novel method to determine laser scanner accuracy for applications in civil engineering. *Optica Applicata* 2012; 42.
- [7] Altuntaş C. Yersel Lazer Tarayıcı Nokta Bulutlarının Birleştirilmesi ve Jeodezik Koordinat Sistemine Dönüştürülmesi: Literatür Araştırması, *Selçuk-Teknik Dergisi* 2017; Cilt:16, Sayı:1-2017, Konya.

- [8] Scaioni M, Forlani G. Independent model triangulations of terrestrial laser scanner data, In proc. of Vision Techniques for Digital Architectural and Archaeological Archives, Portonovo - Ancona , Italy, ISPRS Archives 2003; Vol.XXXIV-5/W12, 308-313.
- [9] Elkharchy I, Neimeier W. Optimization and strength aspects for georeferencing data with terrestrial laser scanner systems, 3D IAG712th FIG symposium, Baden, Austria,2006; p.10 pages, May 22-24.
- [10] Zeybek M. El-tipi LiDAR ölçme sistemleri ve 3B veri işleme. Türkiye Lidar Dergisi 2019; 1(1), 10-15.



## Electroencephalogram-Based Major Depressive Disorder Classification Using Convolutional Neural Network and Transfer Learning

Şüheda KAYA<sup>1</sup>, Burak TAŞCI<sup>2\*</sup>

<sup>1</sup> Elazığ Mental Health Hospital, Elazığ 23200, Turkey

<sup>2</sup> Vocational School of Technical Sciences, Firat University, Elazığ 23119, Turkey

<sup>1</sup> suheda\_sener@hotmail.com, <sup>2\*</sup> btasci@firat.edu.tr

(Geliş/Received: 26/01/2023;

Kabul/Accepted: 02/03/2023)

**Abstract:** Major Depressive Disorder (MDD) is a worldwide common disease with a high risk of becoming chronic, suicidal, and recurrence, with serious consequences such as loss of workforce. Objective tests such as EEG, EKG, brain MRI, and Doppler USG are used to aid diagnosis in MDD detection. With advances in artificial intelligence and sample data from objective testing for depression, an early depression detection system can be developed as a way to reduce the number of individuals affected by MDD. In this study, MDD was tried to be diagnosed automatically with a deep learning-based approach using EEG signals. In the study, 3-channel modma dataset was used as a dataset. Modma dataset consists of EEG signals of 29 controls and 26 MDD patients. ResNet18 convolutional neural network was used for feature extraction. The ReliefF algorithm is used for feature selection. In the classification phase, kNN was preferred. The accuracy was yielded 95.65% for Channel 1, 87.00% for Channel 2, and 86.94% for Channel 3.

**Key words:** Major Depressive Disorder; EEG; ReliefF; Knn

### Konvölüsyonel Sinir Ağı ve Transfer Öğrenme Kullanılarak Elektroensefalogram Tabanlı Majör Depresif Bozukluk Sınıflandırması

**Öz:** Majör Depresif Bozukluk (MDB), yüksek oranda kronikleşme, intihar ve yineleme riski taşıyan, iş gücü kaybı gibi ciddi sonuçları olan ve dünya çapında yaygın olan bir hastalıktır. MDB tespitinde EEG, EKG, beyin MR, doppler USG gibi objektif testler tanıya yardımcı olarak kullanılmaktadır. Yapay zeka alanındaki gelişmeler ve depresyonla ilgili objektif testlerden elde edilen örnek verilerin ile, MDB'den etkilenen bireylerin sayısını azaltmanın bir yolu olarak erken depresyon teşhis sistemi geliştirilebilir. Bu çalışmada EEG sinyallerini kullanarak derin öğrenme tabanlı bir yaklaşımla MDB otomatik teşhis edilmeye çalışılmıştır. Çalışmada veri seti olarak 3 kanallı modma veri seti kullanılmıştır. Modma veri setinde 29 kontrol ve 26 MDB hastasının EEG sinyalinden oluşmaktadır. ResNet18 evrişimli sinir ağı öz nitelik çıkarmak için kullanılmıştır. Öz nitelik seçimi için ReliefF algoritması kullanılmıştır. Sınıflandırma aşamasında ise k-EYK tercih edilmiştir. kanal 1 için %95.65, kanal 2 için %87.00 ve kanal 3 için 86.94 doğruluk elde edilmiştir.

**Anahtar kelimeler:** Majör Depresif Bozukluk; EEG; ReliefF; k-EYK

### 1. Introduction

Major Depressive Disorder (MDD) is a mental illness that presents with symptoms such as not enjoying life, loss of interest and desire, distress, irritability, cognitive disorders, deterioration in thought processes, negative thoughts such as worthlessness, thoughts of guilt, hopelessness, hypochondriac preoccupation, and suicidal thoughts. In the fifth edition of the diagnostic and statistical manual of mental disorders (DSM-5), the criteria for the diagnosis of MDD are either a depressed mood or a lack of pleasure for at least two weeks [1]. MDD was found in 2.0-4.0% of the significant population sample and is a prevalent public health problem. Less than half of people with MDD seek treatment; if not treated, the depression period of people can last up to 6-12 months and become chronic. Diagnosis of the disease is based on subjective methods such as a one-on-one interview with a psychiatrist or psychologist and psychometric scales. The absence of a known biomarker makes the diagnosis difficult due to the patient's subjectivity in responding to psychological assessment scales and heterogeneous symptoms such as sleep, appetite, and attention level. Factors such as the patient's statements at the time of the interview, the variety of symptoms, and the experience of the specialist significantly affect the diagnosis, the chosen treatment, and the healing process. For these reasons, developing an objective diagnostic method for early and accurate diagnosis and appropriate and effective treatment is important. Recently, automatic recognition of mental states and mental disorders has attracted significant interest from the computer vision and artificial intelligence community. Neural activity and mental disorders in the brain affect the bioelectrical activity of the brain. Previous work has mostly been on functional magnetic resonance imaging (fMRI) [2]. Non-invasive sensor-

\* Corresponding author: btasci@firat.edu.tr, ORCID Number of authors: <sup>1</sup> 0000-0002-0853-5777, <sup>2</sup> 0000-0002-4490-0946

based devices such as electroencephalogram (EEG) have been widely used in the literature in recent years. With the help of electrodes placed on the scalp with the EEG device, the electrical activity between nerve cells is recorded as oscillations [3]. The processing of EEG signals to be recorded from this device plays an important role in detecting different diseases such as MDD, bipolar disorder, anxiety, schizophrenia, and sleep disorders [4].

In particular, in MDD, the release of cortisol in the body increases, which affects the production and communication of neurons, and as a result, slows down the functionality of some parts of the brain and changes electrical activity patterns. Measuring voltage changes caused by ionic current flows within the brain's neurons with the non-invasive method, EEG, may help diagnose MDD objectively [5]. Detection of these irregularities in brain physiology plays an important role in the early diagnosis of the depression process. Electrophysiological differences were found in literature studies examining depression patients and healthy controls in terms of EEG signals [6]. In this context, many computer-assisted different studies have been developed. In our country, Mumtaz et al., EEG signal energy and interhemispheric asymmetry in the frontal, temporal, parietal, and occipital lobes were found to be significant in the diagnosis of depression [7].

Some studies in the literature for MDD detection with EEG signals are given below.

Sharma et al.[8] used EEG signals from 21 drug-free depressed and 24 normal patients. It achieved 99.10% accuracy with LSTM-CNN. Seal et al.[9] classified depression with the 18-layer CNN network. It had achieved 99.37% accuracy. Saaedi et al.[10] detected MDD using the EEG signals of 30 healthy and 34 MDDs. They achieved  $95.283\% \pm 2.109$  accuracy with CNN 1D,  $96.226\% \pm 1.208$  with CNN 2D,  $89.057\% \pm 1.849$  with LSTM,  $99.245\% \pm 1.152$  with CNN 1D-LSTM and  $96.415\% \pm 3.422$  with CNN 2D-LSTM. Ćukić et al.[11] detected depression using 23 depression and 20 normal EEG signals. HFD achieved 97.56% accuracy with the SampEn method and Naive Bayes classifier. Mumtaz et al. [12] detected depression using 33 depression and 30 normal EEG signals. He achieved 98.20% accuracy, 99.78% specificity, and 98.34% sensitivity with CNN-LSTM. Uyulan et al.[13] detected 46 healthy and 46 MDD EEG signals as MDD using deep learning architectures. With MobileNet, it achieved 92.66% accuracy. Khan et al.[14] obtained 100% accuracy of EEG signals of 30 MDD and 30 healthy controls with 3D-CNN. Tasci et al.[15] had classified MDD using the modma dataset. In the method they proposed, Twin Pascal's Triangles Lattice Pattern was used. The feature was selected with NCA. It achieved 100% accuracy of 128-channel EEG signals with 10 fold CV. Wang et al.[16], had classified MDD using the odma dataset. ALEXNet was used in their proposed method. 13, 17, 28, 40, 46, 66 and 69 channels were found to be associated with depression.

In this study, MDD was tried to be diagnosed automatically using EEG signals. For this, EEG signals were first converted into spectrogram images. These images were trained on the ResNet-18 deep learning model, and their features were extracted. The extracted features were selected by the Relieff algorithm. These features were classified using the kNN algorithm.

## 2. Material and Method

### 2.1. Dataset

In this study, the multi-modal open dataset for mental-disorder analysis: 3-channel EEG datasets of MODMA were used [17]. Lanzhou University's UAIS laboratory published this EEG dataset in 2020. The sampling frequency of the EEG signals in the MODMA 3 channel dataset is 250Hz. It contains the EEG signal of 3 channels in total. Psychiatric disorders have a strong relationship with the prefrontal lobe. Therefore, EEG signals were collected from Fp1, Fpz, and Fp2 electrodes. The connection of the electrodes is shown in Figure 1.

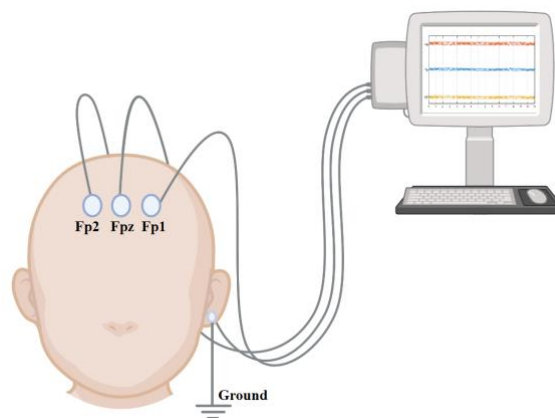


Figure 1. Electrode placement for the 3-Channel EEG dataset

Table 1. Properties of MODMA 3 channel dataset

Class	MDD		Control	
	Female(n=11)	Male(n=15)	Female(n=10)	Male(n=19)
Age+sd	27.09±8.34	33.33±11.94	28.5±7.32	31.94±8.84
Max Age	45	56	41	43
Min Age	18	16	22	19
Education(years)	15.54±1.96	11.73±3.65	17.4±2.36	16.26±1.52
PHQ-9	18.27±5.79	17.4±4.25	2.1±2.37	2.47±1.64
CTQ-SF	46.90±12.06	52.66±11.70	43.7±10.19	39.78±4.79
LES	-61.63±76.67	-35.26±50.82	0±19.04	8.78±34.79
SSRS	34.36±8.24	31.86±9.21	42.3±5.53	42.31±6.87
GAD-7	13.27±6.58	12.86±4.58	1.2±1.68	1.84±2.00
PSQI	12±4.17	12±6	2.6±2.17	3.84±2.14

\* CTQ-SF, Childhood Trauma Questionnaire; GAD-7, Generalized Anxiety Disorder; LES, Life Event Scale; PHQ-9, Patient Health Questionnaire; PSQI, Pittsburgh Sleep Quality Index; SSRS, Social Support Research Scale.

EEG signals obtained from each individual were divided into 15-second dimensions. As a result, 2348 15-second MDD EEG signals and 2108 15-second healthy control EEG signals were obtained from the dataset.

**2.2. Method**

In this study, MDD detection was made from EEG signals of health and MDD cases. The 3-channel EEG signals of the MODMA dataset were used in the study. EEG signals are divided into 15-second segments. One spectrogram image was obtained from each 15-second signal segment. Then the obtained images were resized (224x224) according to the input of the ResNet-18 network. The Resnet-18 network is trained using the images obtained from the first channel. One thousand features were obtained from the fc1000 layer of the trained network. Five hundred of the obtained features were selected with the help of relieff feature selection algorithm. Then, 500 selected features were classified with the help of kNN classifier. A graphical summary of the proposed method is given in figure 2.

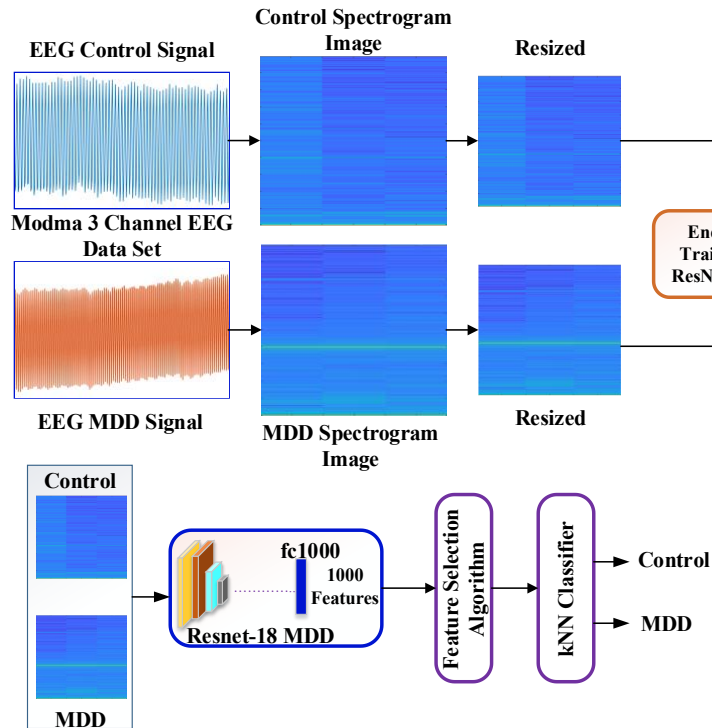


Figure 2. Graphical representation of the proposed method

**2.2.1. Creation of spectrogram images**

The Fourier Transform can describe all the frequency components included in the stationary signal. However, not all signals are stationary. Short-Time Fourier Transform (STFT) provides simultaneous frequency and time analysis of the signal. [18]. STFT is obtained by multiplying the Fourier transform function of a signal by the window function. Displaying a 2-D function of a signal, time, and frequency is called a spectrogram. [19].

**2.2.2. Resnet 18**

Resnet-18 is a convolutional neural network with 72 layers, 18 in-depth, 44MB in size, and 11.7 million parameters. The image input size is 224x224. Resnet network model has 2-D convolution, batch normalization, ReLU, 2-D Global average pooling, fully connected, addition, and softmax layers [20]. The general structure of the Resnet 18 architecture is given in figure 3.

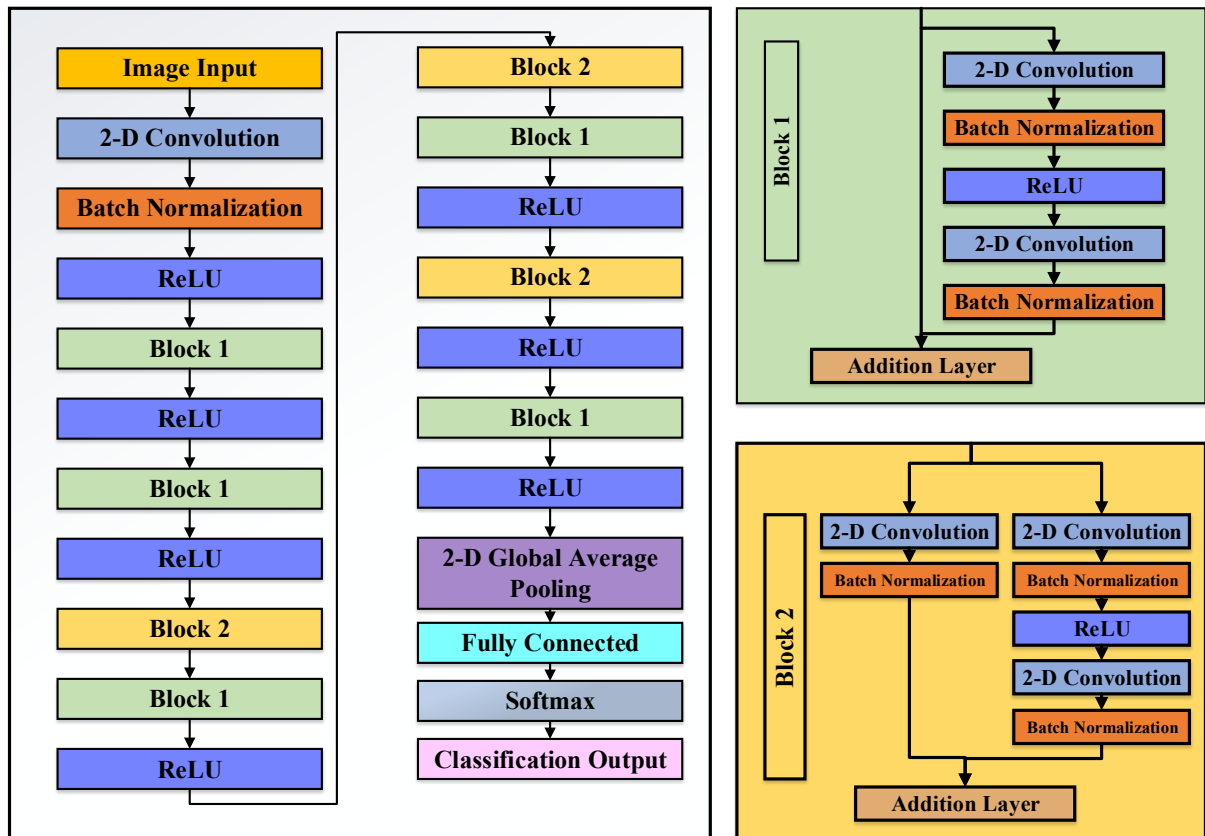


Figure 3. General structure of the ResNet18 architecture

**2.2.3. ReliefF Algorithm**

Relief algorithm is a feature selection method developed by Kira et al. in 1992. The main purpose of this method is to weigh the features according to their correlation [21]. Relief algorithm gives successful results on the data of two classes. However, it did not give successful results for datasets containing more than two classes. To eliminate this problem, Kononenko developed the ReliefF algorithm in 1994, which works on datasets with more than two classes [22].

**2.2.4 kNN Classifier**

kNN is a classification method used in data mining. The k-Nearest Neighbor classifier is one of the easiest and most frequently used classification algorithms that classifies data based on the closest training data in the feature space. This method performs the classification process according to the class of the nearest neighbor as much as the k value given. The k-NN algorithm classifies a vector using vectors of known class. In the k-NN method, the distance of the test data to the training data is calculated by the Euclidean method as specified. The k-training data, which is closest to the test data, belongs to the same class with the highest ratio [23].

### 3. Experimental Results

All coding in the study was carried out in the MATLAB 2010a simulation program installed on a desktop computer with an 11th Generation Intel brand i9-11900 processor, 2.500Ghz, 64GB DDR4 memory, and 1024GB SD storage capacity. As the first step in coding, EEG signals were converted to spectrogram images. The ResNet18 network was trained using the spectrogram images obtained from the first channel. Loss and accuracy graphs are given in Figure 4. The weights of the fully connected layer named fc1000 of the ResNet 18 model trained for feature extraction were used. There are 1000 nodes in this layer. Therefore, 1000 features were extracted. Five hundred features were selected using the ReliefF algorithm. The classification accuracies obtained with these classifiers are tabulated in Table 2. A 10-fold cross-validation technique was used for all classifiers. As can be seen in Table 2, the best classification accuracy was obtained with the 95.60% kNN classifier, while the worst classification accuracy was obtained with the fine-tree classifier.

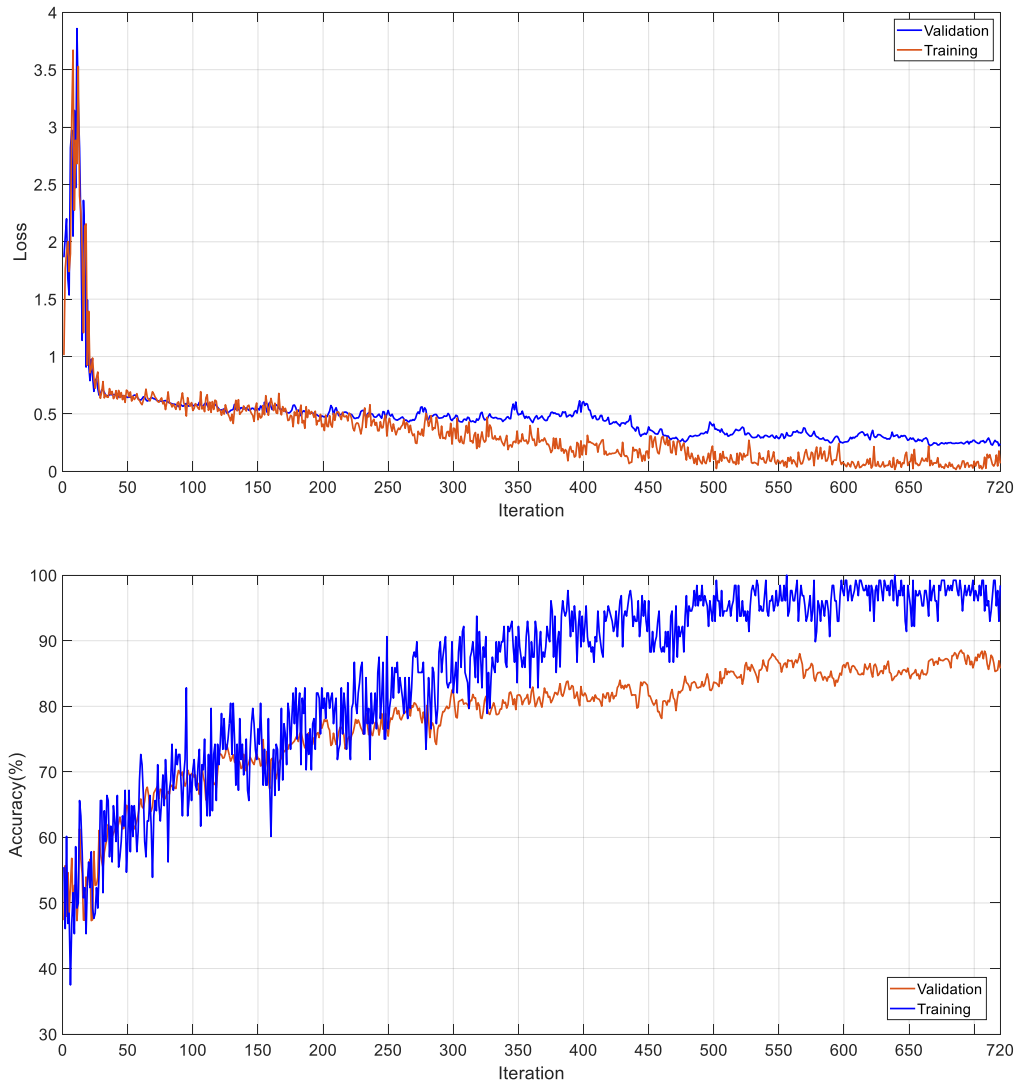


Figure 4. Training and validation curves of the ResNet 18

The complexity matrix for the kNN classifier with the best performance is given in Figure 5. Sensitivity, specificity, precision, and F-score performance metrics were calculated using true positive, true negative, false positive, and false negative values in the complexity matrix. These values are given in Table 3.

Table 2. Accuracy results of channel-1 according to classifiers

Classifier	Accuracy(%)
kNN[23]	<b>95.6</b>
SVM[24]	94.5
Naive Bayes[25]	93.3
ANN[26]	93.2
Logistic Regression[27]	91.6
Fine Tree[28]	90.8

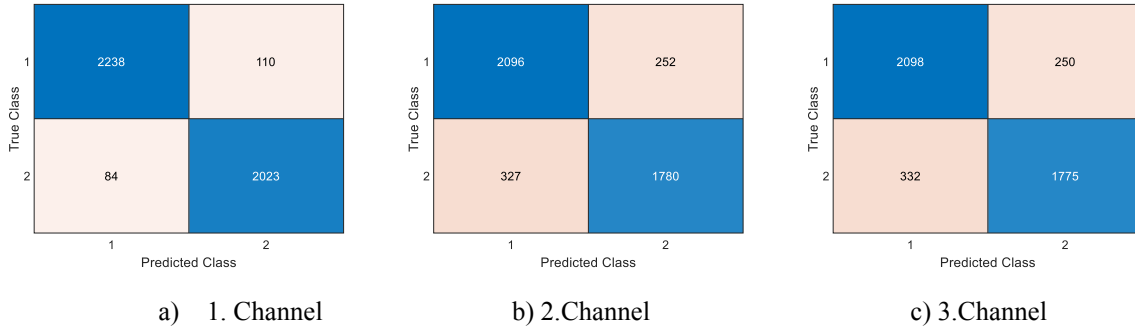


Figure 5. Confusion matrix results: 1: MDD, 2: Healthy

Table 3. Results of other performance metrics

	Class	Accuracy(%)	Precision(%)	Recall(%)	Sensitivity(%)	Specificity(%)
Channel 1	MDD	95.65	96.38	95.32	95.32	96.01
	Healthy		94.84	96.01	96.01	95.32
Channel 2	MDD	87.00	86.50	89.27	95.32	96.01
	Healthy		87.60	84.48	96.01	95.32
Channel 3	MDD	86.94	86.34	89.35	95.32	96.01
	Healthy		87.65	84.24	96.01	95.32

Using the same dataset in Table 4, Soni et al. [29], used Euclidean distance and Node2vec methods. With this method, 82.30% classification accuracy was obtained.

Table 4. Comparison with the method using the same dataset

Reference	Method	Split Ratio	Results
Soni et al.[29]	Euclidean distance, Node2vec	10-fold CV	Accuracy:82.30; Precision: 78.90; Recall: 71.80;
Proposed Model	Spectrogram, ResNet18, ReliefF, kNN	10-fold CV	<u>Channel 1</u> Accuracy:95.65; Precision: 96.38; Recall: 95.32;
			<u>Channel 2</u> Accuracy:87.00; Precision: 86.50; Recall: 89.27;
			<u>Channel 3</u> Accuracy:86.94; Precision: 86.34; Recall: 89.35;

## 5. Conclusion

In this study, a deep learning-based approach was used to detect MDD from EEG signals. In this approach, spectrogram images were created to obtain strong 2D representations. These representations are used in the ResNet 18 model. One thousand features were extracted from this model. Five hundred of the extracted features were selected by Relieff algorithm. The best classification performance for the selected features was obtained in the kNN classifier with 95.65%. The proposed approach was developed based on the performance of another method using the same dataset. The classification accuracy has been increased by approximately 13.35%. However, the result obtained is not at a sufficient level of performance to be used in decision support application. For this, the size of the dataset needs to be increased. In addition, performance can be increased with CNN models created from scratch with a larger dataset.

## References

- [1] American Psychiatric Association A, Association AP. Diagnostic and statistical manual of mental disorders: DSM-5: Washington, DC: American psychiatric association; 2013.
- [2] Han K-M, De Berardis D, Fornaro M, Kim Y-K. Differentiating between bipolar and unipolar depression in functional and structural MRI studies. *Prog Neuro-Psychopharmacol Biol Psychiatry* 2019; 91:20-7.
- [3] Mumtaz W, Malik AS, Yasin MAM, Xia L. Review on EEG and ERP predictive biomarkers for major depressive disorder. *Biomed Signal Process Control* 2015; 22:85-98.
- [4] Acharya UR, Sudarshan VK, Adeli H, Santhosh J, Koh JE, Adeli A. Computer-aided diagnosis of depression using EEG signals *Eur Neurol* 2015; 73:329-36.
- [5] Mahato S, Paul S. Electroencephalogram (EEG) signal analysis for diagnosis of major depressive disorder (MDD): a review. *Nanoelectronics, Circuits and Communication Systems*. 2019; 323-35.
- [6] Liao S-C, Wu C-T, Huang H-C, Cheng W-T, Liu Y-H. Major depression detection from EEG signals using kernel eigen-filter-bank common spatial patterns. *Sensors (Basel)* 2017; 17:1385.
- [7] Mumtaz W, Xia L, Ali SSA, Yasin MAM, Hussain M, Malik AS. Electroencephalogram (EEG)-based computer-aided technique to diagnose major depressive disorder (MDD). *Biomed Signal Process Control* 2017; 31:108-15.
- [8] Sharma G, Parashar A, Joshi AM. DepHNN: a novel hybrid neural network for electroencephalogram (EEG)-based screening of depression. *Biomed Signal Process Control* 2021; 66:102393.
- [9] Seal A, Bajpai R, Agnihotri J, Yazidi A, Herrera-Viedma E, Krejcar O. DeprNet: A deep convolution neural network framework for detecting depression using EEG. *IEEE Trans Instrum Meas* 2021; 70:1-13.
- [10] Saeedi A, Saeedi M, Maghsoudi A, Shalhaf A. Major depressive disorder diagnosis based on effective connectivity in EEG signals: A convolutional neural network and long short-term memory approach. *Cognit Neurodyn* 2021; 15:239-52.
- [11] Ćukić M, Stokić M, Simić S, Pokrajac D. The successful discrimination of depression from EEG could be attributed to proper feature extraction and not to a particular classification method. *Cognit Neurodyn* 2020; 14:443-55.
- [12] Mumtaz W, Qayyum A. A deep learning framework for automatic diagnosis of unipolar depression.. *Int J Med Inf* 2019; 132:103983.
- [13] Uyulan C, Ergüzel TT, Unubol H, Cebi M, Sayar GH, Nezhad Asad M, et al. Major depressive disorder classification based on different convolutional neural network models: Deep learning approach. *Clin EEG Neurosci* 2021; 52:38-51.
- [14] Khan DM, Yahya N, Kamel N, Faye I. Automated diagnosis of major depressive disorder using brain effective connectivity and 3D convolutional neural network. *IEEE Access*. 2021; 9:8835-46.
- [15] Tasci G, Loh HW, Barua PD, Baygin M, Tasci B, Dogan S, et al. Automated accurate detection of depression using twin Pascal's triangles lattice pattern with EEG Signals. *Knowl Based Syst* 2023; 260:110190.
- [16] Wang B, Kang Y, Huo D, Chen D, Song W, Zhang F. Depression signal correlation identification from different EEG channels based on CNN feature extraction. *Psychiatry Res Neuroimaging* 2023; 328:111582.
- [17] Cai H, Gao Y, Sun S, Li N, Tian F, Xiao H, et al. Modma dataset: a multi-modal open dataset for mental-disorder analysis. *arXiv preprint arXiv:200209283*. 2020.
- [18] De Ryck T, De Vos M, Bertrand A. Change point detection in time series data using autoencoders with a time-invariant representation. *IEEE Trans Signal Process* 2021; 69:3513-24.
- [19] Mustafa M, Taib MN, Murat ZH, Sulaiman N, Aris SAM. The analysis of eeg spectrogram image for brainwave balancing application using ann. 2011 *UkSim 13th International Conference on Computer Modelling and Simulation: IEEE*; 2011. 64-8.
- [20] He K, Zhang X, Ren S, Sun J. Deep residual learning for image recognition. *Proceedings of the IEEE conference on computer vision and pattern recognition* 2016; 770-8.
- [21] Kira K, Rendell LA. A practical approach to feature selection. *Machine learning proceedings* 1992: Elsevier; 1992. 249-56.
- [22] Kononenko I. Estimating attributes: Analysis and extensions of RELIEF. *European conference on machine learning: Springer*; 1994; 171-82.

- [23] Peterson LE. K-nearest neighbor. Scholarpedia 2009; 4:1883.
- [24] Vapnik V. The support vector method of function estimation. Nonlinear modeling: Springer; 1998; p. 55-85.
- [25] Rish I. An empirical study of the naive Bayes classifier. IJCAI 2001 workshop on empirical methods in artificial intelligence 2001; 41-6.
- [26] Yegnanarayana B. Artificial neural networks: PHI Learning Pvt. Ltd.; 2009.
- [27] Kleinbaum DG, Dietz K, Gail M, Klein M, Klein M. Logistic regression: Springer; 2002.
- [28] Safavian SR, Landgrebe D. A survey of decision tree classifier methodology. IEEE Trans Syst Man Cybern 1991; 21:660-74.
- [29] Soni S, Seal A, Yazidi A, Krejcar O. Graphical representation learning-based approach for automatic classification of electroencephalogram signals in depression. Comput Biol Med 2022; 145:105420.



## BP19: An Accurate Audio Violence Detection Model Based On One-Dimensional Binary Pattern

Arif Metehan YILDIZ<sup>1\*</sup>, Tugce KELEŞ<sup>2</sup>, Kubra YILDIRIM<sup>3</sup>, Sengul DOĞAN<sup>4</sup>, Turker TUNCER<sup>5</sup>

<sup>1,2,3,4,5</sup> Department of Digital Forensics Engineering, College of Technology, Firat University, Elazığ, Turkey

\*<sup>1</sup> a.metehanyildiz@gmail.com, <sup>2</sup> tkeles@firat.edu.tr, <sup>3</sup> kubra.yildirim@firat.edu.tr, <sup>4</sup> sdogan@firat.edu.tr, <sup>5</sup> turkertuncer@firat.edu.tr

(Geliş/Received: 31/01/2023;

Kabul/Accepted: 01/03/2023)

**Abstract:** Audio violence detection (AVD) is a hot-topic research area for sound forensics but there are limited AVD researches in the literature. Our primary objective is to contribute to sound forensics. Therefore, we collected a new audio dataset and proposed a binary pattern-based classification algorithm.

**Materials and method:** In the first stage, a new AVD dataset was collected. This dataset contains 301 sounds with two classes and these classes are violence and nonviolence. We have used this dataset as a test-bed. A feature engineering model has been presented in this research. One-dimensional binary pattern (BP) has been considered to extract features. Moreover, we have applied tunable q-factor wavelet transform (TQWT) to generate features at both frequency and space domains. In the feature selection phase, we have applied to iterative neighborhood component analysis (INCA) and the selected features have been classified by deploying the optimized support vector machine (SVM) classifier.

**Results:** Our model achieved 97.01% classification accuracy on the used dataset with 10-fold cross-validation.

**Conclusions:** The calculated results clearly demonstrated that feature engineering is the success solution for violence detection using audios.

**Key words:** Audio violence detection, feature engineering, machine learning, sound forensics

## BP19: Tek Boyutlu İkili Modele Dayalı Doğru Bir Sesli Şiddet Tespit Modeli

**Özet:** Sesten şiddet tespiti (AVD), ses adli bilişimi için oldukça taze bir araştırma alanıdır, ancak literatürde sınırlı AVD araştırmaları vardır. Öncelikli hedefimiz ses adli bilişimine katkıda bulunmaktır. Bu nedenle, yeni bir ses veri seti topladık ve ikili örüntü tabanlı bir sınıflandırma algoritması önerdik.

**Gereç ve yöntem:** İlk aşamada yeni bir AVD veri seti toplandı. Bu veri seti iki sınıflı 301 ses içerir ve bu sınıflar şiddet ve şiddetsizliktir. Bu veri setini test ortamı olarak kullandık. Bu araştırmada bir özellik mühendisliği modeli sunulmuştur. Öznitelikleri çıkarmak için tek boyutlu ikili model (BP) düşünülmüştür. Ayrıca, hem frekans hem de uzay alanlarında özellikler oluşturmak için ayarlanabilir q-faktörü dalgacık dönüşümü (TQWT) uyguladık. Öznitelik seçimi aşamasında yinelemeli komşuluk bileşen analizi (INCA) uygulanmış ve seçilen öznitelikler optimize edilmiş destek vektör makinesi (SVM) sınıflandırıcı kullanılarak sınıflandırılmıştır.

**Bulgular:** Modelimiz, kullanılan veri setinde 10 kat çapraz doğrulama ile %97.01 sınıflandırma doğruluğu elde etti.

**Sonuçlar:** Hesaplanan sonuçlar, özellik mühendisliğinin ses kullanarak şiddet tespiti için başarılı bir çözüm olduğunu açıkça göstermiştir.

**Anahtar kelimeler:** Sesli şiddet tespiti, özellik mühendisliği, makine öğrenimi, ses adli bilişimi

### 1. Introduction

Speech is defined as the verbal transmission or expression of thoughts. On the other hand, communication is the exchange of thoughts, behaviors and information in which there is a sender-receiver relationship between any individual or group of individuals. When the relationship between these two concepts is examined, a multidimensional situation naturally emerges. First of all, making sense of how this relationship between individuals is established poses a difficult problem for machine learning methods. For example, with the combination of understanding a speech, communication patterns, the environment in which the communication is established and the surrounding context, a subjective situation that can naturally differ from individual to

\* Corresponding author: a.metehanyildiz@gmail.com. ORCID Number of authors: <sup>1</sup> 0000-0003-0451-8600, <sup>2</sup> 0000-0003-0131-2826, <sup>3</sup> 0000-0002-4738-2777, <sup>4</sup> 0000-0001-9677-5684, <sup>5</sup> 0000-0002-1425-4664

individual arises. Because each individual is triggered differently by different factors in his own particular, and this situation is then called as different character structure. Therefore, there is a need to use many more models at the same time [1]. This environment becomes more complex when a different language or violent speech content is involved.

As a result, violent behaviors can harm other people in the environment and the individual. The emotional and instinctive states of the individuals who engage in these behaviors in the communication environment, together with the degree of violence, can determine whether or not there is any aggression. On the other hand, it examines the relationship between aggression and behavior and the relationships between subjective feelings and objective actions [2].

When various studies in the literature are examined, it is seen that some intimate-partner (lovely) relationships carry out a process that can cause serious injuries and even death, both psychologically and physically [3]. This environment, which takes place with the thought of keeping the partner under power and control in these relationships, creates a potential context for excessive emotions and conflicts [4]. On the other hand, some researchers have had difficulty recognizing emotions accurately due to personal emotions' ambiguity and multifaceted nature [5, 6]. Researchers have attempted to recognize and detect emotions using speech recognition [7, 8], violence analysis from images [9-11], and Natural Language Processing (NLP), which are generally applied to large datasets created using social media. In order to understand the emotion of interactions, applications such as Instagram, Facebook, Twitter, and Youtube were used [12-15].

NLP forms a fundamental link in the field of artificial intelligence and computer science. NLP studies include theory and methods that enable effective communication between humans and computers in natural language [16]. For these reasons, it is seen that it is frequently used to interpret, decode and make sense of human languages in a meaningful way. These features can help determine the relationship between individuals, conflict of emotions and level of violence. In recent years, many studies have been carried out to detect negative emotions such as abusive use of language and cyberbullying in online conversations. However, it is relatively difficult in real-life ritual to obtain a live recording of any setting [17, 18]. For example, when fully focused on the speech content, other details in the environment (intensity of sound, frequency of sound, physical characteristics of the environment, size of the environment, distance, etc.) are ignored. If we look at this event from the point of view of forensic information, it is necessary to evaluate the conversations and the environment in which the conversation takes place as a whole. In addition to these, one of the important points in determining the intensity is the entropy criterion. This process, which is based on sudden changes in the energy level of the audio signal, is used as an auxiliary argument in determining the intensity [19].

Collecting accurate and unmodified audio data is also a difficult process for forensic experts. Otherwise, obtaining erroneous results casts a shadow over a judicial review. Therefore, it is very important to be able to detect violence in terms of sound forensics. Based on the existing literature, it is seen that although audio is a very useful source of information, can be processed more simply than videos, and can be self-sufficient in terms of expressing violence most of the time, it is often overlooked.

A new sound classification model has been proposed using lightweight methods to detect intensity over sound, which is a difficult process in this research area. This model will be simply applied to solve sound classification problems with high success rate. With this proposed method, it is desired to solve the important problems in the literature.

### 1.1. Motivation and contributions

Sound forensics is one of the main branches of digital forensics. Therefore, it is a very important research area for gathering digital evidence but the incident response/digital forensics experts have extracted digital evidence manually and it is a time-consuming and difficult process[20]. Therefore, digital forensics professionals need an intelligent assistant to extract more digital evidence. Thus, we collected a new AVD dataset by using public sound sources. In order to get high classification performance on the collected audio dataset, we have recommended a feature engineering model by mimicking a deep learning structure since we have presented a multileveled feature extraction method. Furthermore, the presented model is a lightweight sound classification model since it uses lightweight methods to get classification results.

The contributions of our proposal are:

- A new AVD dataset was collected.
- A simple model has been presented and this model has got high classification performance.
- This model is an accurate model and can easily be applied to solve other sound classification problems

## 2. Dataset

We collected an AVD dataset from YouTube. This dataset has two classes and these classes are (i) violence and (ii) nonviolence. We only collected the sounds from the videos and we segmented these sounds. The length of the created each segment is about 2/3 seconds. The violence class has 154 sound observations and there are 147 sounds in the nonviolence class. The sample sounds have been demonstrated in Figure 1.

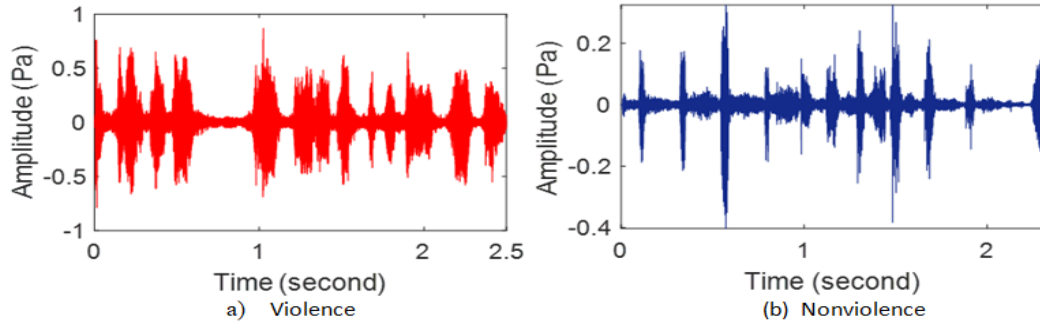


Figure 1. The sample sounds of the gathered dataset.

## 3. Our Proposal

The essential objective of the proposed model is to get high classification performance with a simple and lightweight feature engineering model. Our model uses TQWT and the one-dimensional BP to get features [21, 22]. The top of these features have been selected by deploying INCA [23] selector and the optimized SVM has been used to get the prediction vector. The schema of our proposal is demonstrated in Figure 2.

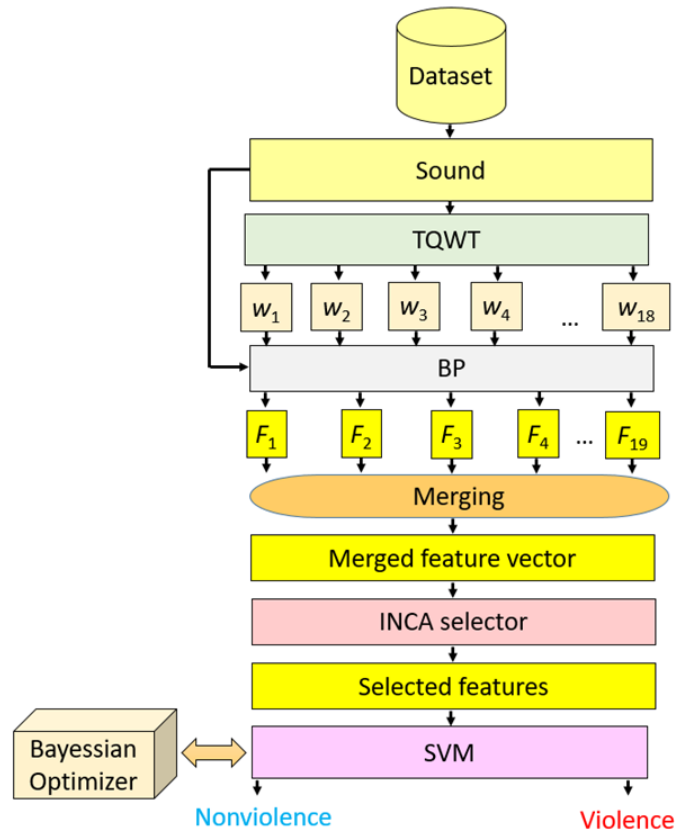


Figure 2. Schema of the proposed model. Herein,  $w$ : TQWT bands,  $F$ : feature vector.

The steps of our proposal are also given below for better explanation.

Step 0: Load the collected AVD dataset.

Step 1: Apply TQWT to the sound signal to generate 18 wavelet bands. Herein, the used parameters of the TQWT are 2,3 and 17. The given three parameters are named q-factor (q), redundancy value (r) and the number of levels (L) and TQWT-generated L+1 wavelet bands.

Step 2: Apply BP to the raw sound and the wavelet bands generated. The used feature extractor (BP) has been clarified below. In this step, 19 (by deploying 18 wavelet bands + 1 raw sound signal) feature vectors have been created and the length of each feature vector is equal to 256.

Step 2.1: Create overlapping blocks and the length of each block is nine.

Step 2.2: Generate binary features by deploying the center value and other values of each block.

Step 2.3: Transform/convert binary features to a decimal value and create a feature map signal.

Step 2.4: Extract the histogram of the feature map signal and obtain a feature vector with a length of 256.

The graphical denotation of the one-dimensional BP is depicted in Figure 3.

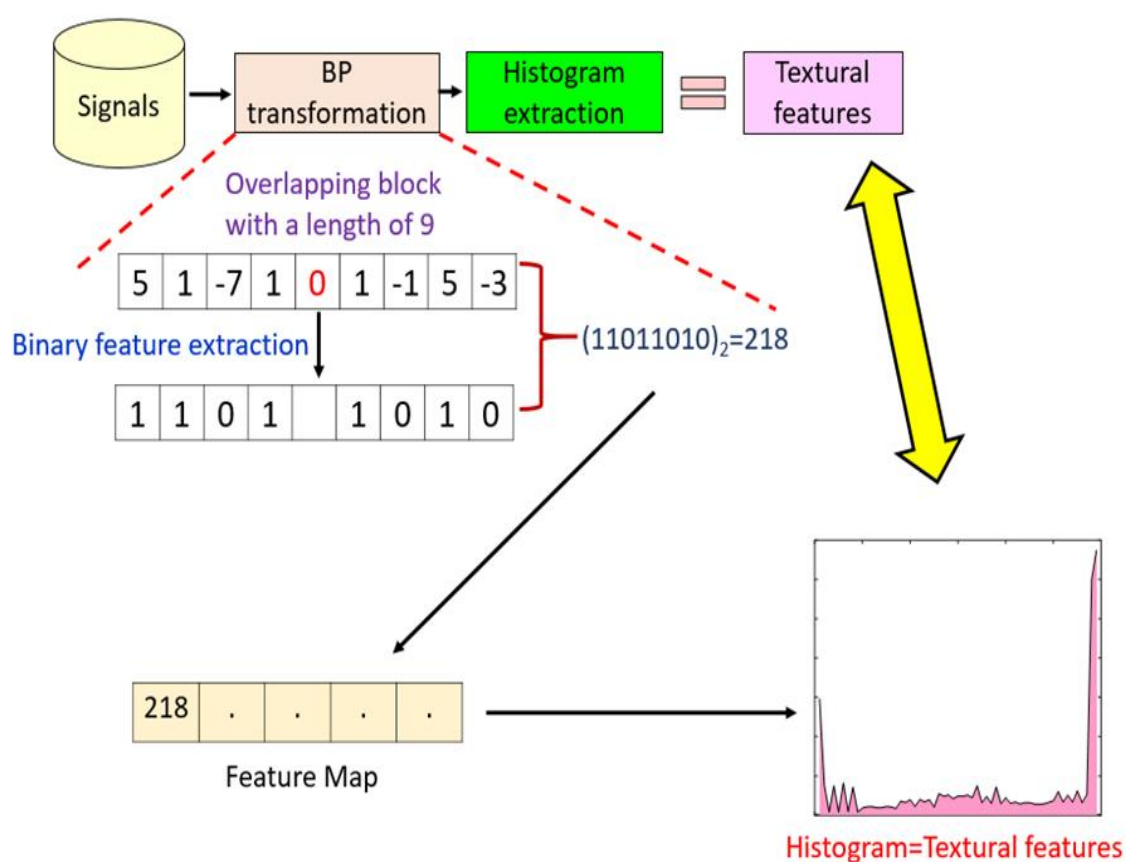


Figure 3. Graphical explanation of the BP feature extractor.

Step 3: Merge the generated 19 feature vectors and create the final feature vector with a length of 4864 ( $=256 \times 19$ ).

Step 4: Apply iterative INCA and choose the top 966 features from the created 4864 features.

Step 5: Classify these features by deploying the optimized SVM.

The given five steps above have been explained in our proposal.

#### 4. Performance Evaluation

In this research, we have used a TQWT and BP-based model. BP generates features from 19 signals. Hence, this model is named BP19, like VGG19 or DarkNet19. However, this model is a lightweight model. We used MATLAB (2022a) programming environment to implement this model. We did not use any graphical processing

unit or parallel programming technique to get classification results. Furthermore, BP19 is a parametric classification model. The parameters used to create BP19 are listed in Table 1.

**Table 1.** The parameters used to create BP19

Method	Parameters	Output
TQWT [21]	q:2, r:3, J:17	18 wavelet bands
BP [22]	Length of overlapping block: 9, kernel: signum	256 features
Our feature extraction method	19 input (18 wavelet bands + 1 raw sound)	4864 features
INCA [23]	Loop range: [100-1000], Classifier: kNN	966 features
SVM [24]	Kernel: Gaussian, kernel scale: 86.94, Box constraint: 17.83, validation: 10-fold cross-validation	Results
Bayesian optimizer [25]	Fitness function: Maximizing accuracy, number of iterations: 1000	The optimized parameters of the SVM

The proposed BP19 has been created by deploying these parameters which are listed in Table 1. This problem is a binary classification problem [26]. Therefore, we have used accuracy, sensitivity, specificity and geometric mean performance metrics. In order to calculate these performance metrics, we have given the computed confusion matrix as below (see Figure 4).



**Figure 4.** The calculated confusion matrix. 1: Violence, 2: Control.

The evaluation metrics are mathematically defined below[27].

$$Accuracy = \frac{TN + TP}{TN + FN + FP + TP} \tag{1}$$

$$Sensitivity = \frac{TP}{TP + FN} \tag{2}$$

$$Specificity = \frac{TN}{TN + FP} \tag{3}$$

$$\text{Geometric Mean} = \sqrt{\left(\frac{TP}{TP + FN}\right)\left(\frac{TN}{TN + FP}\right)} \quad (4)$$

The calculated performance values per Figure 4 are listed in Table 2.

**Table 2.** The calculated performance results (%) by deploying our proposed BP19.

Performance metric	Result(s)
Accuracy	97.01
Sensitivity	97.40
Specificity	96.60
Geometric mean	97

Table 2 demonstrated that our model reached over 96% classification performance per the used all performance metrics.

## 5. Ablation

In this section, our primary goal is to demonstrate the superiority of BP19. Therefore, we have applied BP to the audio signals, and the calculated results are given in this section. Therefore, we have created two cases and these cases are defined below.

Case 1: By applying BP for features extraction and the generated features are fed to the SVM classifier.

Case 2: By applying BP for features extraction and the top features have been selected by deploying INCA. The selected features are classified by deploying INCA.

The ablation results are shown in Figure 5.

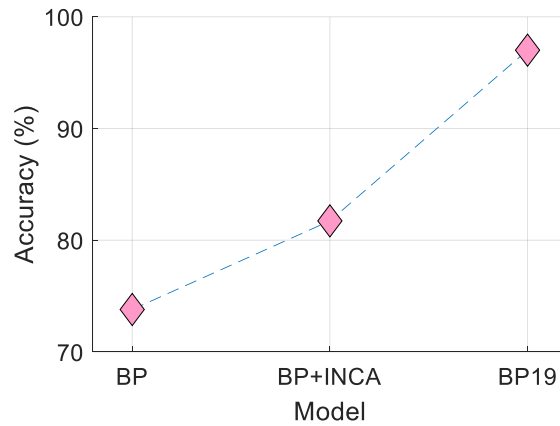


**Figure 5.** Accuracies of the models. BP: Case 1, BP+INCA: Case 2, BP19: Our model.

## 6. Feature Analysis

In the proposed BP19, we have used 19 signals. In order to detect the classification contribution of the generated 19 one-dimensional signals, we counted the selected features per the used signal and the feature analysis results have been depicted in Figure 6.

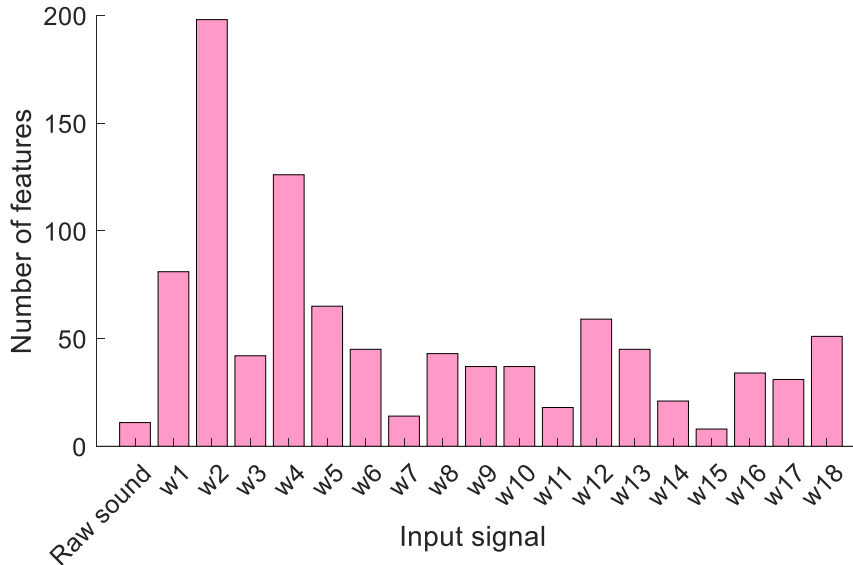


**Figure 6.** The number of selected features from the used input signals.

Figure 6 demonstrated that the 198 out of the generated 256 features from w2 (the generated second wavelet band by TQWT) are selected as top feature by INCA. Thus, the most valuable signal is w2. Only 11 features from the raw sound/audio signal. Per the number of feature, the worst band is w15 since INCA selected only 8 features from this signal.

## 7. Conclusions

We presented the BP19 model, and this model got results from the collected AVD dataset. Our collected dataset has 301 audios and these are categorized into (i) violence and (ii) control. The proposed BP19 creates 19 signals and generates features from these signals by deploying BP function. INCA selected the most informative 966 features, which have been classified by employing an optimized SVM with 10-fold cross-validation. Our model attained 97.01% classification accuracy and 97% geometric mean. Furthermore, we analyzed features per the generated signals and gave ablation results to show the superiority of our model. Finally, we investigated the classification ability of a feature engineering model. Results and findings demonstrate that high classification performance was attained with a simple model of the violence audio.

In the near future, we are planning to collect a big AVD dataset and propose self-organized feature engineering models. By using these models, automated AVD applications can be presented.

## Acknowledgement

I would like to thanks all the authors who contributed to science by working in the field of Digital forensic while writing this article, and my advisor Turker Tuncer and head of our department Sengul Dogan who contributed to the creation of the article.

## References

- [1] Anwar A, Kanjo E, Anderz DO. DeepSafety: Multi-level Audio-Text Feature Extraction and Fusion Approach for Violence Detection in Conversations. arXiv e-prints 2022; arXiv:2206.11822.
- [2] Baumeister RF, Bushman BJ. Emotions and aggressiveness, International handbook of violence research. Heitmeyer W, Hagan J, editors. Springer Dordrecht, 2003; 479–493.
- [3] Allen T, Novak SA, Bench LL. Patterns of injuries: accident or abuse. *Violence Against Wom* 2007;13(8):802–16.
- [4] Bulut M, Aslan R, Arslantaş H. Kabul Edilmemesi Gereken Toplumsal Bir Gerçek: Yakın Partner Şiddeti. *Sakarya Tıp Dergisi* 2020; 10(2):334–347.
- [5] Davidson T, Warmesley D, Macy M, Weber I. Automated hate speech detection and the problem of offensive language. In: Proceedings of the international AAAI conference on web and social media; 15-18 May 2017; Montreal, Quebec, Canada. pp. 512–515.

- [6] Bhavan A, Chauhan P, Shah RR, others. Bagged support vector machines for emotion recognition from speech. *Knowl-Based Syst* 2019; 184:104886.
- [7] Atmaja BT, Akagi M. Speech emotion recognition based on speech segment using LSTM with attention model. In: 2019 IEEE International Conference on Signals and Systems (ICSigSys); 16 – 18 July 2019; Bandung, Indonesia. pp. 40–44.
- [8] Li Y, Zhao T, Kawahara T, others. Improved End-to-End Speech Emotion Recognition Using Self Attention Mechanism and Multitask Learning. In: *Interspeech*. 15-19 September 2019; Graz, Austria. pp. 2803–2807.
- [9] Hajarolasvadi N, Demirel H. Deep facial emotion recognition in video using eigenframes. *IET Image Process* 2020; 14(14):3536–3546.
- [10] Hu M, Wang H, Wang X, Yang J, Wang R. Video facial emotion recognition based on local enhanced motion history image and CNN-CTSLSTM networks. *J Vis Commun Image R* 2019; 59:176–185.
- [11] Du Z, Wu S, Huang D, Li W, Wang Y. Spatio-temporal encoder-decoder fully convolutional network for video-based dimensional emotion recognition. *IEEE T Affect Comput* 2019; 12(3):565–578.
- [12] Plaza-del-Arco FM, Martín-Valdivia MT, Urena-Lopez LA, Mitkov R. Improved emotion recognition in Spanish social media through incorporation of lexical knowledge. *Future Gener Comp Sy* 2020; 110:1000–1008.
- [13] Yang CT, Chen YL. Dacnn: Dynamic weighted attention with multi-channel convolutional neural network for emotion recognition. In: 2020 21st IEEE international conference on mobile data management (MDM); 30 June - 3 July 2020; Versailles, France. pp. 316–321.
- [14] Batbaatar E, Li M, Ryu KH. Semantic-emotion neural network for emotion recognition from text. *IEEE access* 2019; 7:111866–111878.
- [15] Abdullah NSD, Zolkepli IA. Sentiment analysis of online crowd input towards brand provocation in Facebook, Twitter, and Instagram. In: *Proceedings of the International Conference on Big Data and Internet of Thing*; 20 - 22 December 2017; London, United Kingdom. pp. 67–74.
- [16] Kang Y, Cai Z, Tan CW, Huang Q, Liu H. Natural language processing (NLP) in management research: A literature review. *Journal of Management Analytics* 2020; 7(2):139–172.
- [17] Sharma HK, Kshitiz K, others. Nlp and machine learning techniques for detecting insulting comments on social networking platforms. In: 2018 International Conference on Advances in Computing and Communication Engineering (ICACCE); 22-23 June 2018; Paris, France. pp. 265–272.
- [18] Mossie Z, Wang JH. Vulnerable community identification using hate speech detection on social media. *Inf Process Manag* 2020; 57(3):102087.
- [19] T. Giannakopoulos, D. Kosmopoulos, A. Aristidou, and S. Theodoridis, Violence content classification using audio features, in *Advances in Artificial Intelligence: 4th Hellenic Conference on AI, SETN 2006*; 18-20 May 2006; Heraklion, Crete, Greece. pp. 502-507.
- [20] Khanafseh M, Qatawneh M, Almobaideen W. A survey of various frameworks and solutions in all branches of digital forensics with a focus on cloud forensics. *Int J Adv Comput Sci Appl* 2019; 10(8).
- [21] Subasi A, Tuncer T, Dogan S, Tanko D. Local binary pattern based feature extraction and machine learning for epileptic seizure prediction and detection. *Modelling and Analysis of Active Biopotential Signals in Healthcare Volume 2*, Bristol, UK : IOP Publishing, 2020; pp. 6-1 to 6-31.
- [22] Zeng W, Yuan J, Yuan C, Wang Q, Liu F, Wang Y. A new approach for the detection of abnormal heart sound signals using TQWT, VMD and neural networks. *Artif Intell Rev* 2021; 54(3):1613–47.
- [23] Tuncer T, Ertam F. Neighborhood component analysis and reliefF based survival recognition methods for Hepatocellular carcinoma. *Physica A: Statistical Mechanics and its Applications* 2020; 540:123143.
- [24] Keerthi SS, Shevade SK, Bhattacharyya C, Murthy KRK. A fast iterative nearest point algorithm for support vector machine classifier design. *IEEE T Neural Networ* 2000; 11(1):124–36.
- [25] Wu J, Chen XY, Zhang H, Xiong LD, Lei H, Deng SH. Hyperparameter Optimization for Machine Learning Models Based on Bayesian Optimization. *Journal of Electronic Science and Technology*. 2019; 17(1):26–40.
- [26] Primus P, Haunschmid V, Praher P, Widmer G. Anomalous Sound Detection as a Simple Binary Classification Problem with Careful Selection of Proxy Outlier Examples. In: *Proceedings of the Detection and Classification of Acoustic Scenes and Events 2020 Workshop (DCASE2020)*; 2–3 November 2020; Tokyo, Japan. pp. 170-174.
- [27] Dogan S, Barua PD, Kutlu H, Baygin M, Fujita H, Tuncer T, et al. Automated accurate fire detection system using ensemble pretrained residual network. *Expert Syst Appl* 2022; 203:117407.



## Effect on Thermal and Structural Properties of Element Content in CuAlBe Shape Memory Alloys Irradiated with a Constant Gamma Radiation Dose

Ş. Nevin BALO<sup>1\*</sup>, Abdulvahap ORHAN<sup>2</sup>

<sup>1,2</sup> Department of Physics, Science Faculty, Firat University, Elazig, TURKIYE

\*<sup>1</sup> nbalo@firat.edu.tr, <sup>2</sup> vahaporhan@gmail.com

(Geliş/Received: 01/02/2023;

Kabul/Accepted: 11/03/2023)

**Abstract:** Since gamma radiation is a type of radiation that can change the structural properties of materials, CuAlBe shape memory alloy with two different weight percentages was used in this study. CuAlBe shape memory alloys were irradiated with a constant gamma radiation dose of 40 kGy, and the resulting thermal and structural changes in the alloys were investigated. Changes in enthalpy and in the transformation temperature of the alloys were determined by differential scanning calorimetry (DSC), and thermodynamic parameters of alloy samples were calculated. Microstructural changes were determined by X-ray analysis. Microstructural changes were verified by metallographic observations, and microhardness measurements were taken. The study investigated to what extent the physical parameters of CuAlBe shape memory alloys changed depending on the alloying elements when subjected to a constant irradiation dose.

**Key words:** CuAlBe shape memory alloy, gamma radiation, microhardness.

### Sabit Gama Radyasyon Dozu ile Işınlanan CuAlBe Şekil Hatırlamalı Alaşımlarda Element İçeriğinin Termal ve Yapısal Özellikleri Üzerine Etkisi

**Öz:** Gama radyasyonu malzemelerin yapısal özelliklerini değiştirebilecek nitelikte bir radyasyon çeşidi olduğu için, bu çalışmada iki farklı ağırlık yüzdesine sahip CuAlBe şekil hatırlamalı alaşımı kullanıldı. CuAlBe şekil hatırlamalı alaşımları, 40 kGy sabit gama radyasyon dozu ile ışınlanmış ve bunun sonucunda alaşımlarda meydana gelen termal ve yapısal değişiklikler incelenmiştir. Alaşımların entalpi ve dönüşüm sıcaklığındaki değişimler, diferansiyel taramalı kalorimetri (DSC) ile belirlendi ve alaşım numunelerinin termodinamik parametreleri hesaplandı. Mikroyapısal değişiklikler, X-ışını analizi ile belirlendi. Mikroyapısal değişiklikler metalografik gözlemlerle doğrulandı ve mikrosertlik ölçümleri alındı. Çalışmada CuAlBe şekil hatırlamalı alaşımların sabit ışınlama dozuna maruz bırakıldığında alaşım elementlerine bağlı olarak fiziksel parametrelerinin ne ölçüde değiştiği araştırılmıştır.

**Anahtar kelimeler:** CuAlBe şekil hatırlamalı alaşım, gama radyasyonu, mikrosertlik.

#### 1. Giriş

One of the most obvious effects of irradiation on metals and alloys is the displacement of the atoms that make up the structural components. The materials used in reactor systems are predominantly crystalline alloys. Radiation is simply a form of energy that exists in motion. The types of radiation that can change structural materials are ionizing radiation. By ionizing radiation is meant rays of very small wavelengths or very high frequency and energy sources of radiation. Ionizing radiations consist of neutrons, ions, electrons, and gamma rays. All these forms of radiation have the ability to displace atoms from their lattice regions, which drives changes in metals and alloys [1,2].

In addition, two types of high-energy radiation or beam sources are used on the basis of advanced, innovative, evolutionary nuclear industrial applications. One of them is radioactive isotopes such as Co-60 and Cs-137 that emit gamma radiation, and the other is electron beam accelerators where high-energy electrons are produced. The substance irradiated with these two types of ionizing radiation device or ionizing radiation source, which are completely different from each other, does not turn into radioactive material, radioisotope sources, and radiation sources [3,4].

It is important to have a clear understanding of the effect of radiation on materials in order to take into account the effects of irradiation in material design and to develop materials that are more resistant to radiation. The application of shape memory material technology in the nuclear industry offers new opportunities for safety in this

\* Corresponding author: [nbalo@firat.edu.tr](mailto:nbalo@firat.edu.tr). ORCID Number of authors: <sup>1</sup> 0000-0001-5632-9559, <sup>2</sup> 0000-0001-6190-9179

industrial sector, such as reducing personal exposure, life cycle cost reduction, and performance improvement [1,5].

Shape memory alloys have the ability to undergo reversible thermoelastic phase transformations from main phase austenite to product phase martensite and from product phase martensite to main phase austenite. This particular behavior accounts for their two main functional properties: superelasticity and the shape memory effect. Shape memory alloys are often used as miscellaneous materials in many applications due to these unique properties and behaviors. With these materials, extraordinary solutions to important engineering problems are made possible, thanks to their unique properties. The fields of application are very diverse and are being expanded continuously. Some include space technology, medicine, robotics and energy engineering among others [6-9].

Among shape memory alloys, Cu-based shape memory alloys, which are used as an alternative to NiTi shape memory alloys, are preferred because of their high electrical and thermal conductivity, good damping and vibration resistance, high transformation temperature properties, and their low cost and ease of manufacture. The Cu-based shape memory alloys can transform from the ordered DO<sub>3</sub> structure to a long-period stacking structure known as 18R. Also, they can achieve shape recovery in the crystallization range known as the  $\beta$ -phase, which contains an irregular body-centered cubic (BCC) structure and can be observed at high temperature during the heating process [10-13].

These properties make Cu-based alloys useful for high temperature applications. In particular, Cu-Al-Ni shape memory alloys exhibit shape memory features around 200 °C. The addition of alloying elements, heat treatment and numerous irradiation types with different parameters can be applied to partially affect the transformation temperatures, phase sequences and morphologies, which improve the performance of the alloy. Gamma irradiation is considered to be the most vital type of exposure because it can pass through protective layers and penetrate materials. Nevertheless, details on the effects of gamma ( $\gamma$ ) irradiation on shape memory alloys are very useful for practical applications in the field of irradiated environments [10].

CuAlBe system has been developed as a shape memory alloy. CuAlBe shape memory alloys are of interest for medium and low-temperature applications. By adding the element beryllium (Be) to the eutectoid CuAl-system, the austenite and martensite phase transformation temperatures decrease without changing the concentration of the eutectoid point. Minute changes in the amount of Be in the CuAlBe shape memory alloys alter the transformation temperatures drastically. Therefore, it enables alloys to be designed over a wide transformation temperature range. Also, it becomes easier to obtain pseudoelastic behavior at room temperature with decreasing conversion temperature. These alloys have a lot of potential for use as passive seismic energy dampers in building structural frames or bridges. [14-16].

In a study by Balo and Eskil, it was observed that a non-monotonic changes in characteristic transformation temperatures with increasing radiation dose in CuAlBe alloy irradiated with different radiation dose, as well as a decrease in crystal size and an increase in microhardness value. The increase in microhardness, ie radiation hardening, is a result of the formation of point defects in the metal structure. Some changes in sample properties were noted with increasing radiation dose [17].

The application of SM material technology in the nuclear industry may offer new opportunities. SMA's have been used as active elements in mechanical devices for monitoring nuclear facilities [18]. SMA technology can be designed to identify specific irradiation areas where applications are practical. Setting critical temperatures has become an important field of study for the use of alloys in targeted technological applications. Adjusting these temperatures to the required values can be accomplished by changing the alloying elements or their composition. It is hoped that the results of our study will shed light on technological applications.

In this study, we focused on the effects on transformation temperatures, thermodynamic parameters, microstructure, and microhardness of CuAlBe shape memory alloys with different weight percentages irradiated with 60 Co gamma radiation source. The study was planned in two phases to observe the effects of irradiation. (1) pre-irradiation measurements and (2) post-irradiation measurements.

In the literature, no study investigating the effect of alloying elements on the physical behavior of Cu-based shape memory alloys irradiated with gamma radiation has been found.

## 2. Experimental

CuAlBe alloys of different weight percentages were obtained from the Tréfinmétaux Research Center in France. Table 1 summarises the compositions of the alloy samples. The parts cut from the alloys were exposed to heat treatment at a temperature in the  $\beta$  phase region. This region was determined from the equilibrium diagrams of CuAlBe. Details of the heat treatment have been provided in previous studies [14,19,20]. In Saraykoy Nuclear Research and Training Center (SANAM), Turkey Atomic Energy Agency was irradiated with 40 kGy dose gamma

radiation some of the heat-treated (homogenous) samples. The rate of the irradiation dose was set at 1273 Gy/hr. The irradiation duration was 31.42 hours, and the irradiation dose was controlled automatically by the irradiation system. Using Perkin Elmer 8000 Differential Scanning Calorimetry (DSC), the transformation temperatures of the unirradiated and irradiated samples were determined. DSC measurements of the unirradiated alloy samples were carried out at a scanning speed heating/cooling of 10°C/min under atmospheric pressure in the appropriate temperature range. X-ray diffraction patterns of the samples were measured with a Bruker AXS D8 Advance Model XRD meter in the range of 30° to 90°. X-ray analyses of the alloy samples were performed using CuK $\alpha$  radiation at room temperature. The wavelength of the X-rays was 1.54060 Å. Optical microscope observations were made following polishing and chemical etching processes that were applied to the alloy samples. Microhardness measurements were then recorded.

**Table 1.** Composition (wt%) of the investigated CuAlBe alloys.

Alloy	Al (wt%)	Be (wt%)
CAB1	11.8	0.47
CAB2	11.6	0.42

### 3. Results and Discussions

#### 3.1. Differential scanning calorimetry measurements

Differential scanning calorimetry (DSC) was used to determine the endothermic and exothermic transformation enthalpies and transformation temperatures of the alloy samples that were unirradiated and irradiated with a constant gamma irradiation dose. The transformation temperatures of the alloys used in this study are given in Table 2. The transformation temperatures of the alloy samples,  $A_s$ ,  $A_f$ ,  $M_s$  and  $M_f$  were determined using the tangent method. Here, the subindexes A austenite, M martensite, s, and f indicate the starting and ending temperatures [21,22]. The samples put in the DSC for calorimetric analysis were obtained at a 10°C/min heating–cooling rate in under atmospheric pressure atmosphere. The DSC curves for the CAB1 alloy samples were obtained by increasing the temperature from –40°C to 30°C and back to –40°C over a certain period of time. The DSC curves for the CAB2 alloy samples were obtained by increasing the temperature from 30°C to 110°C and back to 30°C over a certain period of time. Considering the results obtained, it was observed that phase transformation temperatures can change depending on the 40 kGy constant irradiation dose level applied to the alloy samples. An increase in transformation temperatures was observed of the samples irradiated with constant 40 kGy gamma irradiation.

The DSC curves of the unirradiated and irradiated samples of the CAB1 and CAB2 alloys are given in Fig. 1 and Fig. 2, respectively. As seen in Table 1, when the Al weight percent was decreased from 11.8% to 11.6% and the Be percent was decreased from 0.57 to 0.47 in the CAB2 alloy, the transformation temperatures increased. Transformation temperatures were observed to increase to positive temperature values. The thermodynamic parameters of the alloys used in this study are given in Table 3. The decrease in Al and Be percentages also increased the equilibrium temperature,  $T_0$ .

The equilibrium temperature,  $T_0$ , is defined as the critical temperature at which the Gibbs free energies of the austenite and martensite phases are equal. It is used to calculate the entropy values,  $\Delta S_{M \rightarrow A}$  in reverse transformations. The area under the endothermic and exothermic peaks in the DSC curves gives the enthalpy values,  $\Delta H_{M \rightarrow A}$  and  $\Delta H_{A \rightarrow M}$ . To compute the values of  $T_0$  parameter the following relations were used [20,23-27].

$$\Delta S_{M \rightarrow A} = \Delta H_{M \rightarrow A} / T_0 \quad (1)$$

$$T_0 = (A_f + M_s) / 2 \quad (2)$$

The supercooling  $T_0 - M_s$  represents the hysteresis in the transformation, which is characterized by the driving force for the nucleation of martensite,  $\Delta G^{A \rightarrow M}$  as,

$$\Delta G^{A \rightarrow M}(M_s) = \Delta G^{M \rightarrow A}(T_0) - \Delta G^{M \rightarrow A}(M_s) = -(T_0 - M_s) \Delta S^{M \rightarrow A} \quad (3)$$

The elastic energy  $G_E$  stored in the self-accommodated martensitic variations is related to the difference  $M_f - M_s$  by

$$\Delta G_E = \Delta G^{A \rightarrow M}(M_s) - \Delta G^{A \rightarrow M}(M_f) = (M_s - M_f)\Delta S^{M \rightarrow A} \quad (4)$$

Entropy is the state of disorder. In martensite  $\rightarrow$  austenite ( $M \rightarrow A$ ) transformations of the unirradiated and irradiated alloy samples were changed entropy values. The variation of irregularity (entropy) in the unirradiated and irradiated alloy samples showed that the alloys did not remain stable. Entropy increased in the irradiated CAB1 alloy and decreased in the CAB2 alloy. At the same time, the entropy of the irradiated CAB2 sample is smaller than the entropy values of the unirradiated CAB1, irradiated CAB1, and unirradiated CAB2 samples. In other words, the irradiated CAB2 sample has a more stable structure. Similar changes are also observed in the elastic energy. The elastic energy of the alloy sample with a small entropy is also small. Elastic energy varies inversely with Gibbs free energy.

**Table 2.** Characteristic transformation temperatures unirradiated and irradiated CuAlBe shape memory alloy samples at a 10°C/min heating-cooling rate.

Dose (kGy)	Alloys	$M_s$ (°C)	$M_f$ (°C)	$A_s$ (°C)	$A_f$ (°C)
0	CAB1	-16.02	-20.79	-12.88	-1.73
40	CAB1	-15.92	-24.91	-13.59	-2.73
0	CAB2	65.66	57.23	74.28	91.23
40	CAB2	68.34	62.63	73.49	93.39

**Table 3.** Thermodynamic parameters of unirradiated and irradiated CuAlBe shape memory alloy samples at a 10°C/min heating-cooling rate.

Dose (kGy)	Alloys	$T_0$ (K)	$\Delta H_{M \rightarrow A}$ (J/kg)	$\Delta H_{A \rightarrow M}$ (J/kg)	$\Delta S_{M \rightarrow A}$ (J/kgK)	$\Delta G_{A \rightarrow M}$ (J/kg)	$\Delta G_E$ (J/kg)
0	CAB1	264.12	4464.7	-2411.1	16.90	-120.66	80.61
40	CAB1	263.67	5656.3	-4190.5	21.45	-141.35	192.83
0	CAB2	351.45	7871.4	-4549.7	22.39	-286.36	188.74
40	CAB2	353.86	4708.7	-3791.7	13.30	-166.51	75.94

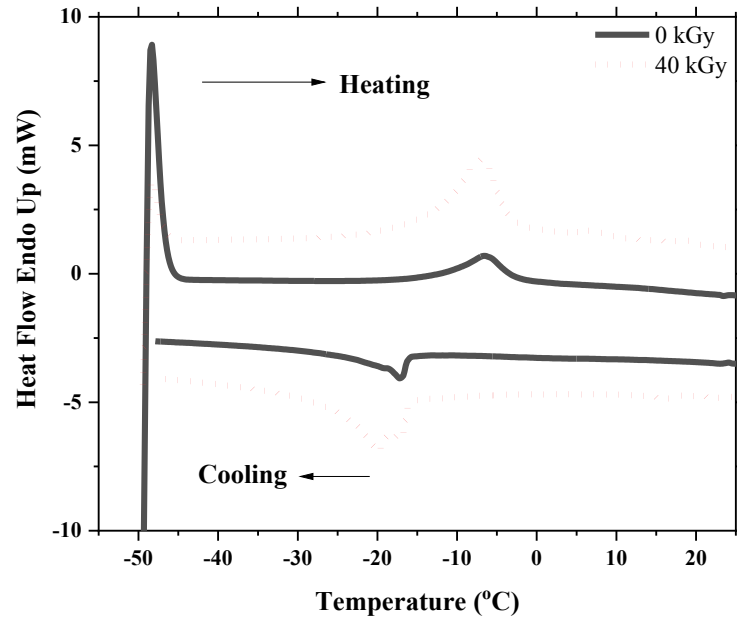


**Fig. 1.** DSC curves of the CAB1 alloy sample at a) unirradiated and b) irradiated.

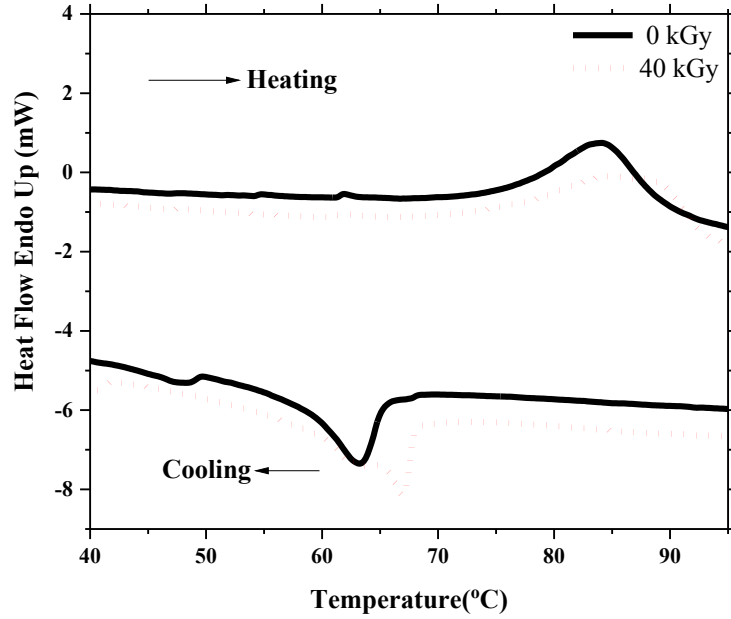


Fig. 2. DSC curves of the CAB2 alloy sample at a) unirradiated and b) irradiated.

### 3.2. X-ray diffraction (XRD) results

X-ray patterns were used to analyze the structures of samples unirradiated and irradiated with 40 kGy gamma radiation. X-ray analyses of CuAlBe shape memory alloy samples were performed at room temperature with CuK $\alpha$  radiation. The XRD patterns of the CAB1 alloy samples that were unirradiated and irradiated with 40 kGy radiation dose are given in Fig. 3a and 3b. In Fig. 3a, the basic peak (220) and (400) (331) peaks of the austenite structure were observed. The peak (220) is at maximum intensity. In addition, the peaks of the martensite structure (122) and very weakly, (320) were observed. In Fig. 3b, the  $\beta$  peak (331) and (511) are very weak, and  $\beta'$  peak at maximum intensity (320) is observed. Diffraction patterns of the CAB2 alloy samples are given in Fig. 4a and 4b. They only show the peaks belonging to the martensite structure. Peak intensities changed with the application of the irradiation at 40 kGy [28-30]. Unirradiated CAB1 alloy exhibited peaks of the martensite phase as well as austenite phase, depending on the cooling rate. According to the phase diagram given in the literature, the CuAl alloy of near eutectoid composition (Cu-11.6-11.8wt. %Al) tends to form an austenite phase above 560°C [15,28].

The crystallite size for the alloy samples were calculated using the Debye Scherrer equation [31-33]:

$$D = \frac{0.9\lambda}{FWHM \cos\theta} \quad (3)$$

where D is crystallite size,  $\lambda$  is the X-ray wavelength, *FWHM* is the full width at half the maximum peak and  $\theta$  is the Bragg angle.

Crystallite sizes for the alloy samples are given in Table 4. As seen from this table, the crystallite size increased when irradiation was applied at the dose of 40 kGy to the CAB1 alloy. The CAB2 alloy shrank following the 40 Gy irradiation dose and produced the smallest crystallite size.

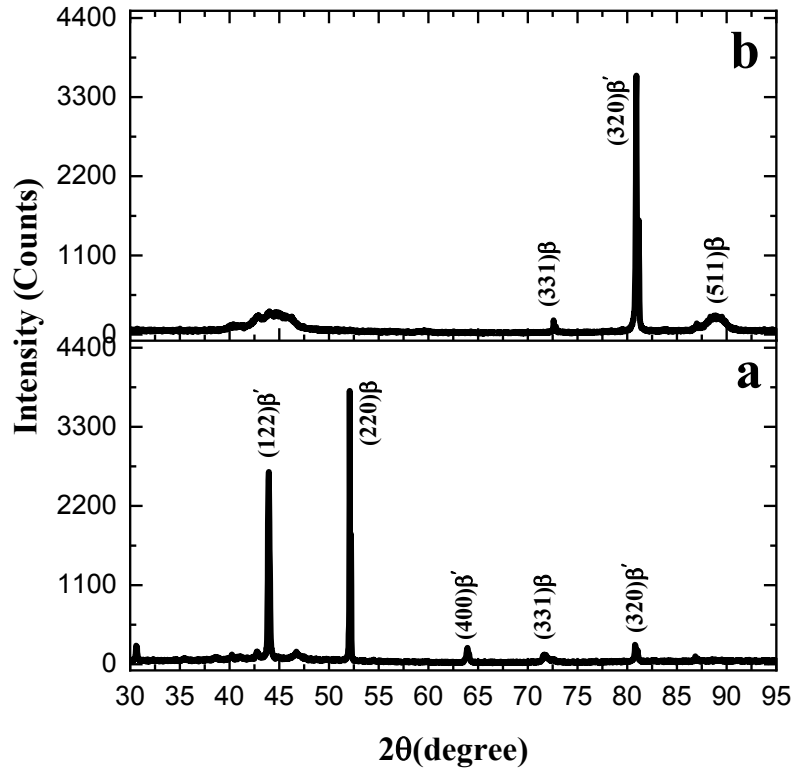


Fig. 3. X-ray diffraction patterns of CAB1 alloy sample a) unirradiated b) irradiated.

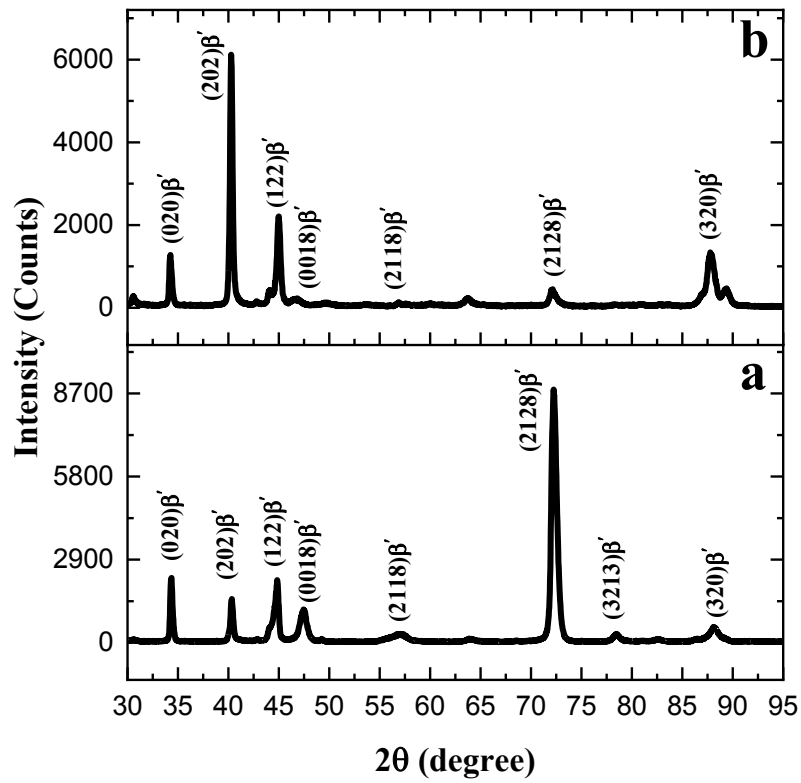


Fig. 4. X-ray diffraction patterns of CAB2 alloy sample a) unirradiated b) irradiated.

### 3.3. Metallographic observations and microhardness results

Optical images of the CAB1 alloy sample are given in Fig. 5a and 5b. As can be seen from the images, the alloy has a polycrystalline structure. Although the alloy seems to exhibit austenite structure at room temperature, there are still untransformed martensite areas [34,35]. More grains are seen in the surface photograph of the sample irradiated with 40 kGy radiation dose at the same magnification and the amount of martensite has increased.

As can be seen from the optical images of the CAB2 alloy sample, the structure turned into a martensite structure with the decrease of Al and Be elements in the alloy. The grain boundaries are distinct within the structure, and the sizes of the grains are different from each other. The structure is dominated by V-type and zigzag-like martensites (Fig. 6a) [36]. With the irradiation dose of 40 kGy, the grains seem to have grown. Fewer grain boundaries were observed. V-type and needle-like martensites are present in the structure (Fig. 6b).

The Cu-based alloy samples were subjected to a 300-gram force (gf) load for 10 seconds to measure their microhardness. Average microhardness values are given in Table 4. Comparing the microhardness values of CAB1 alloy sample when it was heat-treated and treated with 40 kGy irradiation, the microhardness of the sample treated with radiation was observed to be lower. The microhardness value of the CAB2 alloy sample a very small decreased with irradiation at the dose of 40 kGy.

The results showed that small changes in the weight percentages of alloying elements and the irradiation dose affected the structure, grain size, and microhardness values.

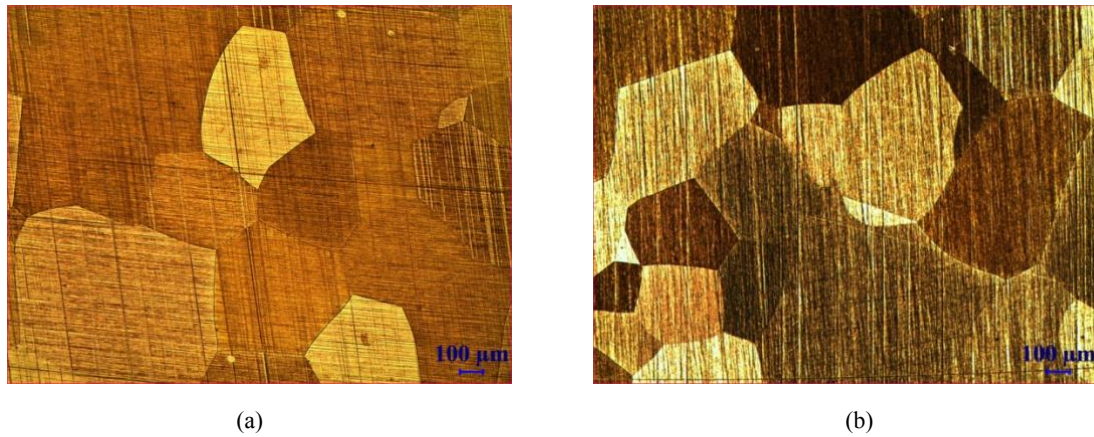


**Fig. 5.** Optical images of CAB1 alloy sample a) unirradiated b) irradiated.

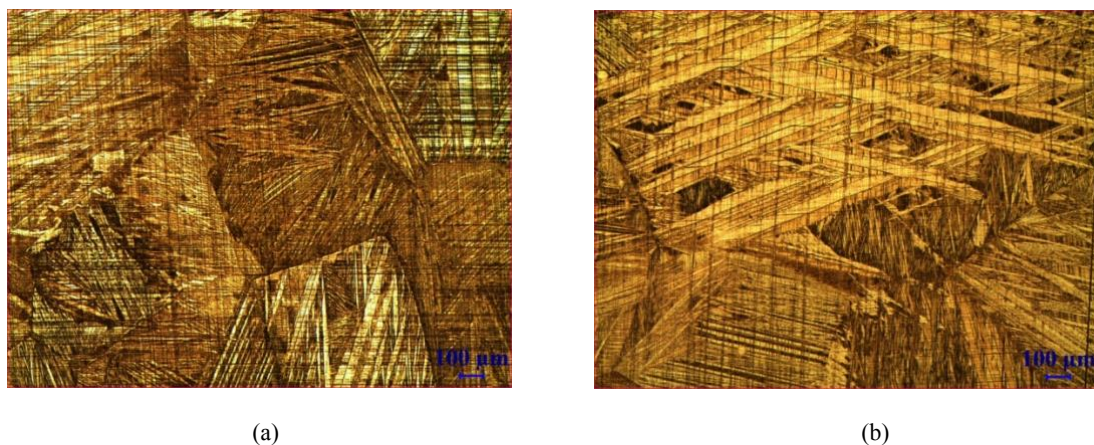


**Fig. 6.** Optical images of CAB2 alloy sample a) unirradiated b) irradiated.

**Table 4.** Average Vickers hardness and crystal size of CuAlBe shape memory alloys.

Dose (kGy)	Alloys	Average HV <sub>0.3</sub> Measurements	Crystallite Size (nm)
0	CAB1	265.4	94.4710
40	CAB1	246.8	111.5525
0	CAB2	201.6	64.0801
40	CAB2	199.6	30.0718

#### 4. Conclusions

Cu-based shape memory alloys are highly sensitive to alloying elements. In the CuAlBe shape memory alloys, the transformation temperatures ( $A_s$ ,  $A_f$ ,  $M_s$ , and  $M_f$ ), increased with the decrease of Be and Al content. In the CuAlBe alloys used in this study, the structure was completely transformed into martensite at room temperature by decreasing the Be content to 0.42. This result was verified by, the austenite→martensite and the martensite→austenite transformation temperatures obtained from DSC measurements of the alloy sample. X-ray diffraction measurements and optical microscope observations also support this result [37,38]. Comparing the DSC analysis of CuAlBe shape memory alloy samples treated with an irradiation dose of 40 kGy, the transformation temperatures changed and the temperature difference  $A_f-M_s$  decreased. It was also observed that the thermodynamic parameters  $\Delta H_{M\rightarrow A}$  and  $\Delta H_{A\rightarrow M}$ ,  $\Delta S_{M\rightarrow A}$  changed. With entropy, the elastic energy and average stiffness of samples can be controlled. As the entropy increases, the elastic energy of the sample increases, and the average microhardness decreases.

From the XRD analysis results, the shape memory alloy CAB1 has a two-phase structure (austenite, martensite), while the CAB2 shape memory alloy has only the martensite phase structure. Although it looks like there is only austenite at a first glance in the optical image of the CAB1 alloy sample, needle-like martensites are also present in the structure.

The crystallite size calculated according to the XRD analysis results of unirradiated CuAlBe alloys decreased with the decrease in Al and Be contents. The crystallite size of the unirradiated CAB1 alloy sample was 94.4710 nm, while the crystallite size of the unirradiated CAB2 alloy sample was 64.0801 nm. While the crystallite size of the CAB1 alloy irradiated with a radiation dose of 40 kGy increased, a very small decrease in the crystallite size of the CAB2 alloy was observed.

Microhardness is inversely proportional to the grain size, decreasing with an increase in grain size. Of the alloy samples irradiated with a 40 kGy dose, the microhardness values of the CAB1 alloy decreased, while the microhardness of the CAB2 alloy a small decreased.

In conclusion, we have evaluated that in CuAlBe shape memory alloys, both the weight percentages of the elements and atomic effects due to the irradiation affected transformation temperatures, thermodynamic parameters, and the microstructure.

#### Acknowledgments

The study carried out was supported by Firat University Scientific Research Projects Unit (FÜBAP) under project number FF.19.09.

#### References

- [1] Was GS. Fundamentals of radiation materials science: Metals and Alloys, Springer-Verlag Berlin Heidelberg 2007.
- [2] Sun Y, Chmielewski AG. Applications of ionizing radiation in materials. Vol.1 Institute of Nuclear Chemistry and Technology Warszawa 2017.
- [3] Mansur LK, Bloom EE. Radiation effects in reactor structural alloys. J Met 1982; 23-31.
- [4] Chernov IP, Mamontov AP, Botaki AA, Cherdantsev PA, Chakhlov BV, Sharov SR. Anomalous effects of small doses of ionizing radiation in metals and alloys. Plenum Publishing Corporation 1985; 497-499. (Translated from Atomnaya Energiya, 1984; 57: 56-58.
- [5] Butler D. Nuclear power's new dawn, Nature 2004; 429: 238–240.
- [6] Oliveria JP, Zeng Z, Berveiller S, Bouscaud D, Braz Fernandes FM, Miranda RM, Zhou N. Laser welding of Cu-Al-Be shape memory alloys: Microstructure and mechanical properties. Mater Des 2018; 148: 145-152.
- [7] Shelyakov AV, Sitnikov NN, Sheyfer DV, Borodako KA, Menushenkov AP, Fominski VY. The formation of the two-way shape memory effect in rapidly quenched TiNiCu alloy under laser radiation. Smart Mater Struct 2015; 24 (11): 1-7.
- [8] Aversa R, Tamburrino F, Petrescu RV, Petrescu FI, Artur M, Chen G, Apicella A. Biomechanically inspired shape memory effect machines driven by muscle like acting NiTi alloys. Am J of Appl Sci 2016; 13: 1264-1271.



- [9] Guniputi NN, Murigendrappa SM. Influence of Gd on the microstructure, mechanical and shape memory properties of Cu-Al-Be polycrystalline shape memory alloy. *Mat Sci Eng A* 2018; 737: 245-252.
- [10] Saud SN, Hamzah E, Abubakar TA, Refaei A, Hosseinian R. The influence of  $\gamma$ -irradiation on the structure and properties of the Cu-11.5 wt. % Al- 4 wt. % Ni shape memory alloys. *Adv Mater Res* 2014; 845: 128-132.
- [11] Wang ZG, Zu XT, Wu JH, Liu LJ, Mo HQ, Huo Y. Electron irradiation-induced evolution of the martensitic transformation characteristics in a CuZnAl shape memory alloy. *J Alloys Compd* 2004; 364: 171-175.
- [12] Castro ML, Romero R. Isothermal decomposition of the Cu-22.72 Al-3.55 Be at.% alloy. *Mat Sci Eng A* 2000; 287: 66-71.
- [13] Silva RAG, Adorno AT, Magdalena AG, Carvalho TM, Stipcich M, Cuniberti A, Castro ML. Thermal behavior of the Cu-22.55 at.% Al alloy with small Ag additions. *J Therm Anal Calorim* 2011;103: 459-63.
- [14] Balo ŞN, & Ceylan M. Effects of Be content on some characteristics of Cu-Al-Be shape memory alloys. *J Mater Process Technol* 2002;124: 200-208.
- [15] Montecinos S, Simison SN. Study of the corrosion products formed on multiphase CuAlBe alloy in a sodium chloride solution by micro-Raman and in situ AFM measurements. *Appl Surf Sci* 2011; 257: 7732-7738.
- [16] Montecinos S, Cuniberti A, Castro ML, Boeri R. Phase transformations during continuous cooling of polycrystalline  $\beta$ -CuAlBe alloys. *J Alloys Compd* 2009; 467: 278-283.
- [17] Balo ŞN, Eskil M. Thermodynamic and crystallographic properties of gamma radiated shape memory Cu-Al-Be alloy. *Appl Phys A* 2021; 127(8): 1-10.
- [18] Giurgiutiu V, Zagrai A. The use of smart materials technologies in radiation environment and nuclear industry. SPIE's 7th International Symposium on Smart Structures and Materials and 5th International Symposium on Nondestructive Evaluation and Health Monitoring of Aging Infrastructure; 5-9 March 2000; Newport Beach, CA. 3985-103.
- [19] Zuniga-Flores H, Belkahla S, Lovey FC, Guenin G. The two way effect of Cu-Al-Be Alloys: General characteristics and aging. *ICOMAT,92* Proceedings of the International Conference on Martensitic Transformations, Monterey, California, USA 1992; 1053-1058.
- [20] Balo ŞN, Ceylan M, Aksoy M. Effects of deformation on the microstructure of Cu-Al-Be shape memory alloy. *Mater Sci Eng A* 2001; 311: 151-156.
- [21] Lagoudas DC. (Ed.), *Shape memory alloys: Modeling and engineering applications*, Springer Science & Business Media 2008.
- [22] Lecce L. *Shape memory alloy engineering: For aerospace, structural and biomedical applications*, Elsevier 2014.
- [23] Wayman C, Tong H. On the equilibrium temperature in thermoelastic martensitic transformations. *Scr Metall* 1977; 11(5): 341-343.
- [24] Canbay CA, Karaduman O, Özkul I, Ünlü N. Modifying thermal and structural characteristics of CuAlFeMn shape memory alloy and a hypothetical analysis to optimize surface-diffusion annealing temperature. *JMEPEG* 2020; 29: 7993-8005.
- [25] Tong H, Wayman C. Characteristic temperatures and other properties of thermoelastic martensites. *Acta Metall* 1974; 22: 887-896.
- [26] Canbay CA, Karaduman O, Ünlü N, Özkul I. An exploratory research of calorimetric and structural shape memory effect characteristics of Cu-Al-Sn alloy. *Physica B: Condensed Matter* 2020; 580: 411932.
- [27] Romero R, Pelegrina JL. Change of entropy in the martensitic transformation and its dependence in Cu-based shape memory alloys. *Mater Sci Eng A* 2003; 354: 243-250.
- [28] Ergen S, Uzun O, Yilmaz F, Kiliçaslan MF. Shape memory properties and microstructural evolution of rapidly solidified CuAlBe alloys. *Mater Charact* 2013; 80: 92-97.
- [29] Mallik US, Sampath V. Influence of quaternary alloying additions on transformation temperatures and shape memory properties of Cu-Al-Mn shape memory alloy. *J Alloys Compd* 2009; 469(1-2): 156-163.
- [30] Karaduman O, Özkul I, Canbay C.A. Shape memory effect characterization of a ternary CuAlNi high temperature SMA ribbons produced by melt spinning method. *Adv Eng Sci* 2021; 1: 26-33.
- [31] Canbay CA, Karaduman O, Ünlü N, Özkul I. Study on basic characteristics of CuAlBe shape memory alloy. *Brazilian J Phys* 2021; 51: 13-18.
- [32] Cullity BD. *Elements of X-ray diffraction*, Addison-Wesley Publishing Company, Massachusetts, 1978.
- [33] Balo ŞN, Yakuphanoglu F. The effects of Cr on isothermal oxidation behavior of Fe-30Mn-6Si alloy, *Thermochim Acta* 2013; 560: 43-46.
- [34] Sánchez-Arévalo FM, Pulos G. Use of digital image correlation to determine the mechanical behavior of materials. *Mater Charact* 2008; 59(11): 1572-1579.
- [35] Araya R, Marivil M, Mir C, Moroni O, Sepulveda A. Temperature and grain size effects on the behavior of CuAlBe SMA wires under cyclic loading. *Mater Sci Eng A* 2008; 496(1-2): 209-213.
- [36] Montecinos S, Cuniberti A. Effects of grain size on plastic deformation in a  $\beta$  CuAlBe shape memory alloy. *Mater Sci Eng A* 2014; 600: 176-180.
- [37] Albuquerque VHC de, Melo TADA, Gomes RM, Lima SJG de, Tavares JMR. Grain size and temperature influence on the toughness of a CuAlBe shape memory alloy. *Mater Sci Eng A* 2010; 528(1): 459-466.
- [38] Dunne D, Morin M, Gonzalez C, Guenin G. The effect of quenching treatment on the reversible martensitic transformation in CuAlBe alloys. *Mater Sci Eng A* 2004; 378(1-2): 257-262.



## Predicting the Height of Individuals with Machine Learning Methods by Considering Non-Genetic Factors

Osman ALTAY<sup>1\*</sup>, Tuğba ÇELİKTEN<sup>1</sup>, Tuba AKBAŞ<sup>1</sup>, Hüseyin Yasin DÖNMEZ<sup>1</sup>

<sup>1</sup> Yazılım Mühendisliği, Hasan Ferdi Turgutlu Teknoloji Fakültesi, Celal Bayar Üniversitesi, Manisa, Türkiye

\*<sup>1</sup> osman.altay@cbu.edu.tr, <sup>1</sup> tugba.celikten@cbu.edu.tr, <sup>1</sup> tubakbas1@gmail.com, <sup>1</sup> hyasindonmez@gmail.com

(Geliş/Received: 06/02/2023;

Kabul/Accepted: 13/03/2023)

**Abstract:** As many parents want to know how many centimeters their child will be in the future, many people in their developmental years want to know how many centimeters their future height will be. In addition, the development of children in terms of height and weight is medically controlled from the moment they are born. As a result, height development is important for both individuals and medical professionals. In this study, it is aimed to predict the height of individuals using personal and family information and factors affecting height. In the study, the 10 most known characteristics among the factors affecting height were selected. These attributes, mother's height, father's height, economic status, jumping and weight sports status, gender, information about the child's age, history of chronic illness in the individual, the longest living region, and the individual's height were taken as input values in machine learning methods. Using these input values, the length of the individual was predicted using Linear Regression (LR) and Artificial Neural Network (ANN) from machine learning methods. In addition, three error measurement methods were used to evaluate the success of the model: mean absolute error (MAE), mean square error (MSE) and R-Square ( $R^2$ ). In the  $R^2$  evaluation metric, the method was 84.48% in LR and 81.74% in ANN.

**Key words:** Height of individuals, machine learning algorithms, artificial neural network, linear regression.

## Genetik Olmayan Faktörler Ele Alınarak Bireylerin Boyunun Makine Öğrenmesi Yöntemleri ile Tahmini

**Öz:** Pek çok ebeveyn doğmuş veya doğacak olan çocuğunun gelecekte kaç santimetre boya sahip olacağını bilmek istediği gibi birçok gelişim çağındaki birey de ilerdeki boylarının kaç santimetre olacağını bilmek ister. Ayrıca tıbbi olarak çocukların gelişimleri boy ve kilo olarak ilk doğdukları andan itibaren kontrol edilmektedir. Bu yüzden boy gelişimi hem bireyler için hem de tıbbi olarak önemlidir. Bu çalışmada ise bireylerin kişisel ve aile bilgilerinden yararlanılarak ve boy uzunluğuna etki eden etmenler kullanılarak boylarının tahmin edilmesi amaçlanmıştır. Yapılan çalışmada boy uzunluğuna etki eden etmenler arasından en bilinen 10 nitelik seçilmiştir. Bu nitelikler, anne boy uzunluğu, baba boy uzunluğu, ekonomik durum, sıçrayış ve ağırlık sporları yapma durumu, cinsiyet, kaçınıcı çocuk olduğu bilgisi, bireyde geçirilen kronik rahatsızlık öyküsü, en uzun yaşanan bölge ve bireyin boyu makine öğrenmesi yöntemlerinde giriş değerleri olarak alınmıştır. Bu giriş değerleri kullanılarak bireyin boyu makine öğrenmesi yöntemlerinden Lineer Regresyon (LR) ve Yapay Sinir Ağı (YSA) kullanılarak tahmin edilmiştir. Ayrıca modelin başarısını değerlendirmek için ortalama mutlak hata (OMH), ortalama kare hata (OKH) ve R-Kare ( $R^2$ ) olmak üzere üç hata ölçüm yöntemi kullanılmıştır.  $R^2$  değerlendirme metrinde LR yöntemi %84.48 ve YSA ise %81.74 başarımla elde edilmiştir.

**Anahtar kelimeler:** Bireylerin boyu, makine öğrenmesi algoritmaları, yapay sinir ağları, lineer regresyon.

\* Corresponding Author: osman.altay@cbu.edu.tr. ORCID Numbers of Authors: 0000-0003-3989-2432, 0000-0001-7480-4026, 0000-0002-6431-7520, 0000-0002-5583-8375

## 1. Introduction

Along with the development of technology throughout history, the factors affecting the development of human beings are also being investigated. It has emerged as a result of research that the environment, heredity, and hormones have an effect on human development and health [1]. The development of an individual occurs as a result of the complex interaction of environment and heredity in two directions. The environment is the natural environment that includes the factors affecting living things and the living things themselves. Heredity is the ability or trait that is passed on from parents to their children through genetic pathways. Genes passed down through the generations in the family consist of deoxyribonucleic acid (DNA). Individuals are separate and special from each other as a result of the environment in which they live and the genes that come from their family. As a result, the development of each individual may be different from that of other individuals [1]. Hereditary traits and diseases are passed on to future generations through DNA. Hereditary diseases occur due to chromosomal or gene defect inherited from parents to the individual. Some of these diseases are down syndrome, albino, hemophilia, fish scale etc. are diseases. Some of the hereditary features can be counted as many features, such as the individual's height, eye color, blood group, skin color, facial features, the shape of our fingers, and the shape of their hair. Environmental factors, on the other hand, can be given as examples of parents' parenting style, nutrition, unrest in the family, the mother's age, the geographical region, the number of siblings, and the parents' education level. It has been shown in the literature that hormones also have an effect on development. For example, an imbalance in the endocrine glands affects the development of the organism [1].

Artificial intelligence is a broad discipline with roots in philosophy, mathematics, and computer science that aims to understand and develop systems that demonstrate the characteristics of intelligence. The development of artificial intelligence still continues today and is used in many areas. Many areas, such as health services, education, banking, agriculture, the economy, and the military, can be given as examples. Some of the artificial intelligence applications used in healthcare diagnosis and prediction include applications such as prediction of hospitalization for heart disease, cardiovascular risk estimation, diagnosis of pneumonia from a lung x-ray, and identification of benign and malignant tumors [3]. Between 2000 and 2006, many researches and studies were carried out in the field of artificial intelligence. As a result of these studies, artificial intelligence has become an indispensable part of daily life and for the first time, a vacuum cleaner called Roomba and a product that uses artificial intelligence has managed to enter our homes. After 2006, companies such as Twitter, Facebook, Amazon, and Google realized the power of artificial intelligence, and many companies gave more importance to the studies in the field. These studies have succeeded in making artificial intelligence technologies more popular and have contributed to the development of artificial intelligence by further increasing the acceleration of artificial intelligence [4]. Although artificial intelligence is a basic science field, it includes machine learning and deep learning sub-branches.

Machine learning (ML) is a sub-science of artificial intelligence that aims to create a mathematical model by processing the data given to it by machines [5]. Machine learning strategies are grouped under three main headings. These include supervised, unsupervised, and reinforced learning. Supervised learning is the most widely used algorithm among machine learning algorithms. After the data is labeled, the model is trained, and predictions are made with the data that the model does not see. Regression and classification techniques are used in supervised learning. Unsupervised learning is another branch of machine learning. There is no labeled data here. The algorithm makes inferences by taking unlabeled data as input. Clustering techniques are used in unsupervised learning. In clustering algorithms, data are grouped according to their similarity [6]. Using clustering algorithms, applications are being developed on topics such as voice and image processing, keyword searching, call center records, speech recognition, and grouping customer purchasing behavior [7]. Reinforcement learning is a machine learning algorithm that automatically evaluates the most appropriate behavior in a given context or environment to increase the efficiency of software tools and machines. This type of learning is based on reward or punishment. It is a tool used to train artificial intelligence models that can help increase automation or optimize the efficiency of complex systems such as robotics, autonomous driving, and supply chain logistics [8].

As a result, in this study, height prediction was made using the machine learning algorithms ANN and LR. The results of the study showed that the height of people, which shows their development and is followed from birth, can be predicted by machine learning methods. The general organization of the study is as follows: In the second section, "Materials and Methods," the creation of the data set, the statistical distribution of the attributes of the data set, and the machine learning methods are explained in detail. In the third section, the results obtained from machine learning methods are given and examined. Finally, the article is completed with conclusions and recommendations.

## 2. Materials and Methods

### 2.1. Data Acquisition

281 samples of data were collected from individuals aged 18 and over living in different regions of our country. In the data set, values less than 150 centimeters for the mother's height, values less than 160 centimeters for the father's height, and values greater than 6 for the number of children in the family were not taken. Meaningless data were also cleaned from the data set and analyzed with a 254-sample data set.

In the data set, mean maternal height is 161 centimeters, median is 161 centimeters, variance is 30, standard deviation is 5.5, shortest height is 150 centimeters, longest is 178 centimeters, range is 28, and the most repeated value is 160 centimeters. The mean father's height was 173 centimeters, the median was 173 centimeters, the variance was 40, the standard deviation was 6.3, the shortest height was 160 centimeters, the longest was 190 centimeters, the interval was 30, and the most repeated value was 170 centimeters. The average height of the individuals was 170 centimeters; the median was 170 centimeters; the variance was 91; the standard deviation was 9.5; the shortest height was 150 centimeters; the longest was 197 centimeters; the interval was 47; and the most repeated value was 170 centimeters. There are 145 female and 109 male individuals in the data set. There are three different economic situations. The general economic situation of the families is moderate. In the data set, these levels and examples are Bad (19), Average (206), and Good (29). The data set includes 7 geographical regions in total, and the Aegean Region is the largest sample in the data set from these regions. There are 27 samples of data from the Mediterranean Region, 16 from the Eastern Anatolia Region, 111 from the Aegean Region, 15 from the Southeast Anatolian Region, 24 from the Central Anatolia Region, 9 from the Black Sea Region, and 52 from the Marmara Region. Detailed information is given in Table 1.

**Table 1.** Statistical analysis of the data set

Attributes	Standard Deviation	Mean	Median	Variance	Minimum	Maximum	Range	Mod
Mother's height	5.532	161.618	161.0	30.608	150	178	28	160
Father's height	6.392	173.393	173.0	40.864	160	190	30	170
Individual's chronic discomfort	0.375	0.169	0.0	0.141	0	1	1	0
gender	0.495	0.570	1.0	0.245	0	1	1	1
General economic status of the family	0.433	1.039	1.0	0.188	0	2	2	1
jumping sports status	0.472	0.334	0.0	0.223	0	1	1	0
Status of doing weight sports	0.392	0.188	0.0	0.153	0	1	1	0
Region where individual has lived the longest	1.930	2.897	2.0	3.728	0	6	6	2
Which child of the family	1.075	1.972	2.0	1.157	1	6	5	1
Height of individuals	9.556	170.122	170.0	91.324	150	197	47	170

Height distributions of mothers, fathers and individuals in the data set are shown in Figure 1.

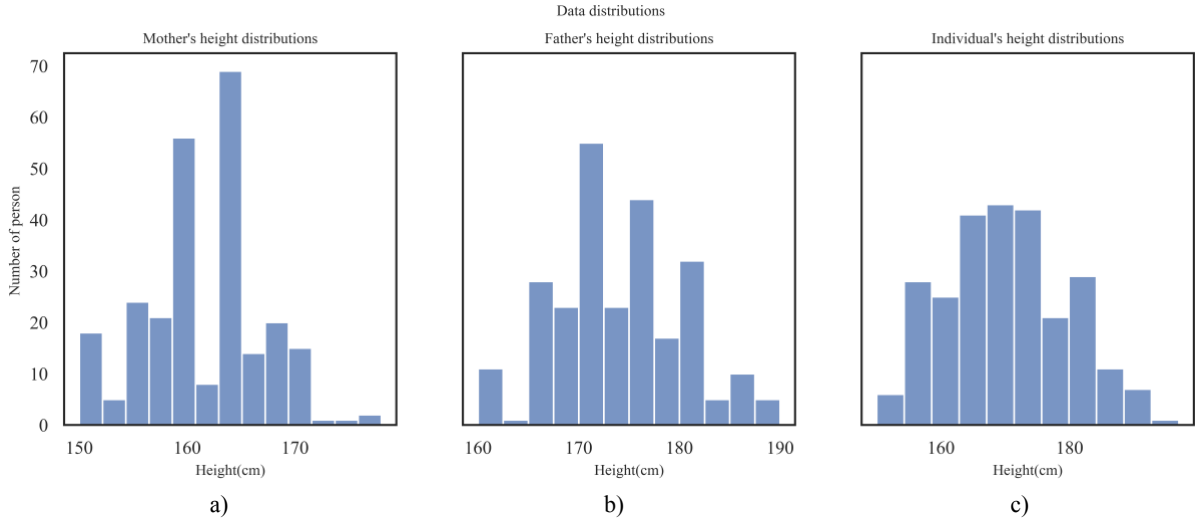


**Fig. 1.** Data distribution of heights, a) Mother’s height distribution b) Father’s height distributions c) Individual’s height distributions

The economic situation, gender and region distributions are shown in Figure 2.

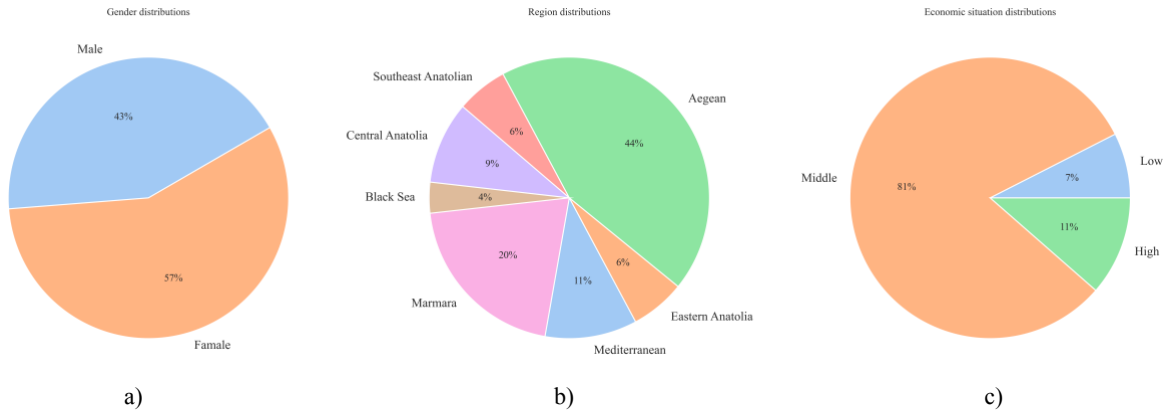


**Fig. 2.** The economic situation, gender and region distributions a) Gender distributions b) Region distributions c) Economic situation distributions

## 2.2. Machine Learning Algorithms

### 2.2.1. Artificial Neural Networks

The first practical use of neural networks was made when the perceptron network was released in the late 1950s. Neural networks based on brain structure originally developed in the 1940s [9]. Modeling nonlinear functions has been accomplished with the use of artificial neural networks (ANNs). They are capable of making predictions about various nonlinear functions that are accurate enough or almost so. Because they can anticipate nonlinear functions with such ease, neural networks are very useful for processing data [10].

Artificial neurons (ANN) have been patterned after their natural counterparts in the human brain and nervous system. Weighted connections link neurons together. The network consists of layers, or groups of neurons, with each layer's output feeding into the next. In this way, ANNs may be trained to solve regression issues and make predictions about their results [10]. In general, an ANN model has been made up of an activation function, weights, the sum of computed weights, input and output neurons, and a learning function. Weights indicate the connection strength of  $w_{ij}$  neurons. The  $b$  value indicates the deviation value. Net  $n_i$  represents the input neurons. The following equation has been used to calculate a rudimentary neural network model:

$$(n)_j = \sum_{i=1}^n w_{ij}x_i + b \tag{1}$$

All neurons in feedforward networks are independent of one another and are only linked to one another via the neurons in the layer below them. The input of one layer becomes the output of the next layer. The connection between the layers takes place using weights. A feedforward ANN consists of data nodes that act as input neurons in the input layer, spreading the data to the hidden layer(s) and output layer via weights [10].

The input and output layers can have more than one neuron, depending on the result. The number of hidden layers or neurons that will provide the best results cannot be determined with certainty. Therefore, constructing an ANN architecture and making the optimal adjustment for the given problem requires experience and experimentation [11].

The activation function that the ANN utilizes for the model structure greatly influences the capability and effectiveness of finding a beneficial solution to a specific issue. The network's speed is greatly influenced by the activation function selection. Depending on the task at hand, several activation functions may be used in ANN models [12] and many different activation functions can be used. ReLU was employed as the activation function in this investigation, while the linear function was used in the bottom layer. Equation 2 specifies the linear activation function used in this research, and Equation 3 describes the ReLU activation function applied in this research:

$$f(n)_j = (n)_j \quad (2)$$

$$f(n)_j = \begin{cases} 0, & (n)_j < 0 \\ (n)_j, & (n)_j \geq 0 \end{cases} \quad (3)$$

One of the most well-known ANNs used to solve engineering challenges is the multilayer perceptron, which has successfully been shown to anticipate nonlinear correlations in a variety of applications [10]. To make a forecast, the ANN model must be trained. There are many different ways to train neural networks, and the way they work depends on the data set. Back propagation is a common and effective algorithm used to train multilayer sensor networks [13]. Backpropagation ANN sends the weight values of all the neurons in each layer to Equation 1, then moves on to the next layer. Then, the error for each layer is passed back to the layer below it. This is called the process of training or learning. During the training process, the network is shown a pair of templates that match the inputs and the outputs that are wanted. ANN uses weights and model thresholds to figure out the real outputs. By sending the error back over the network, the actual output is matched to what the network predicted. The weight values in each layer are changed to reduce the error in the output layer. The main goal of this process is to reduce the difference between the predicted output and the actual output [14]. ANNs need a large number of test cases in the training data set to be very accurate [15].

### 2.2.2 Linear Regression

LR includes a response variable  $y$  and a single predictive variable  $x$ . This is the simplest form of regression, and  $y$  is used as a linear function of  $x$ . It has been stated as Equation (4) [16]:

$$y = b + wx \quad (4)$$

It is assumed that the  $y$ -difference is constant and that  $b$  and  $w'$  are regression coefficients that determine the  $y$ -intercept and slope, respectively. Therefore, the regression coefficients  $b$  and  $w'$  can be weighted as follows [16]:

$$y = w_0 + w_1x \quad (5)$$

The least squares approach, which calculates the best suited straight line with the smallest difference between the actual data and the line's predict, may be used to solve these coefficients. Variable  $D$  is the set of values for some population,  $x$  is the response variable, and  $y$  is the set of values associated with the response variable  $x$ . The training set contains  $(x_1, y_1), (x_2, y_2), \dots, (x_D, y_D)$ , data points. The regression coefficients can be predicted using equations (6) and (7) [16].

$$\frac{\sum_{i=1}^D (x_i - \bar{x})(y_i - \bar{y})}{\sum_{i=1}^D (x_i - \bar{x})^2} \quad (6)$$

$$w_0 = \bar{y} - w_1\bar{x} \quad (7)$$

Here  $x_1, x_2, \dots, x_D$  is the mean of  $\bar{x}$  and  $y_1, y_2, \dots, y_D$  is the mean of  $\bar{y}$ . The coefficients  $w_0$  and  $w_1$  generally provide good approximations to complex regression equations.

### 3. Results and Discussion

In the study, two different machine learning methods were used to predict height using 10 different features. These are the ANN and LR methods. In the evaluation of the designed models, the data set consisting of 254 samples was randomly divided into training and test data. Training data consists of 203 samples (80%) and test data consists of 51 samples (20%). The activation functions of the ANN layers were determined as ReLU and Linear, respectively. For the training of the created ANN, Adam was determined as the optimizer parameter, and MSE was determined for the loss parameter. For the training of the model, the epoch number is set to 150 and the batch size value is set to 16. All coding was done in Python using NumPy, Keras, Pandas, TensorFlow, Sklearn, Seaborn and Matplotlib libraries. In the study,  $R^2$ , Mean Absolute Error (MAE) and Mean Square Errors (MSE) were used in the performance evaluation of ANN and LR.  $R^2$  is the coefficient that decides the accuracy of the model, so it is expected to give high results. It is expected to yield low results since MAE and MSE are the error criteria used for continuous variables [17]. MAE is calculated by taking the absolute value of the difference between the true value and the predicted value. It is expressed in MAE Equation 8, with  $y_i$  being the actual value and  $\hat{y}_i$  being the predictive value [18], [19].

$$MAE = \frac{1}{n} \sum_{i=1}^n |y_i - \hat{y}_i| \tag{8}$$

MSE is expressed as the difference between the predicted and actual value. It provides a value indicating how close the fit line is to the data points. To return negative values to positive values, the value is squared. The smaller the MSE value, the better the performance of the model. It is calculated by taking the difference and averaging the squared value. The MSE is expressed in Equation 9 [20].

$$MSE = \frac{1}{n} \sum_{i=1}^n (y_i - \hat{y}_i)^2 \tag{9}$$

$R^2$  is using for evaluate how well the model is performing. It is expressed as the square of the correlation coefficient containing the actual and predicted values.  $R^2$  value close to 1 indicates that the model has achieved good performance.  $R^2$  is expressed in Equation 10 [21].

$$R^2 = 1 - \frac{\sum(y_i - \hat{y}_i)^2}{\sum(y_i - \bar{y})^2} \tag{10}$$

The MAE value was found to be 2.720 for ANN and 2.780 for LR. The MSE value was found to be 12,754 for ANN and 10,857 for LR. With  $R^2$  values, a success rate of 81.74% and 84.48% was obtained in ANN and LR, respectively. According to these measurement results, it was seen that the model designed with LR was more successful than the model designed with ANN. Measurement methods and results for ANN and LR are shown in Table 2.

**Table 2.** Results of machine learning algorithms

Evaluation Metrics	Algorithms	
	ANN	LR
MAE	2.720	2.780
MSE	12.754	10.857
$R^2$	0.817	0.844

The relationship between the predicted height value and the actual height value for ANN and LR has been shown in Figure 3 and Figure 4, respectively, with a line graph.





**Fig. 3.** Predicted height value and actual height value (ANN)



**Fig. 4.** Predicted height value and actual height value (LR)

The scatter plots between the predicted height value and the actual height value for ANN and LR have been shown in Figure 5.

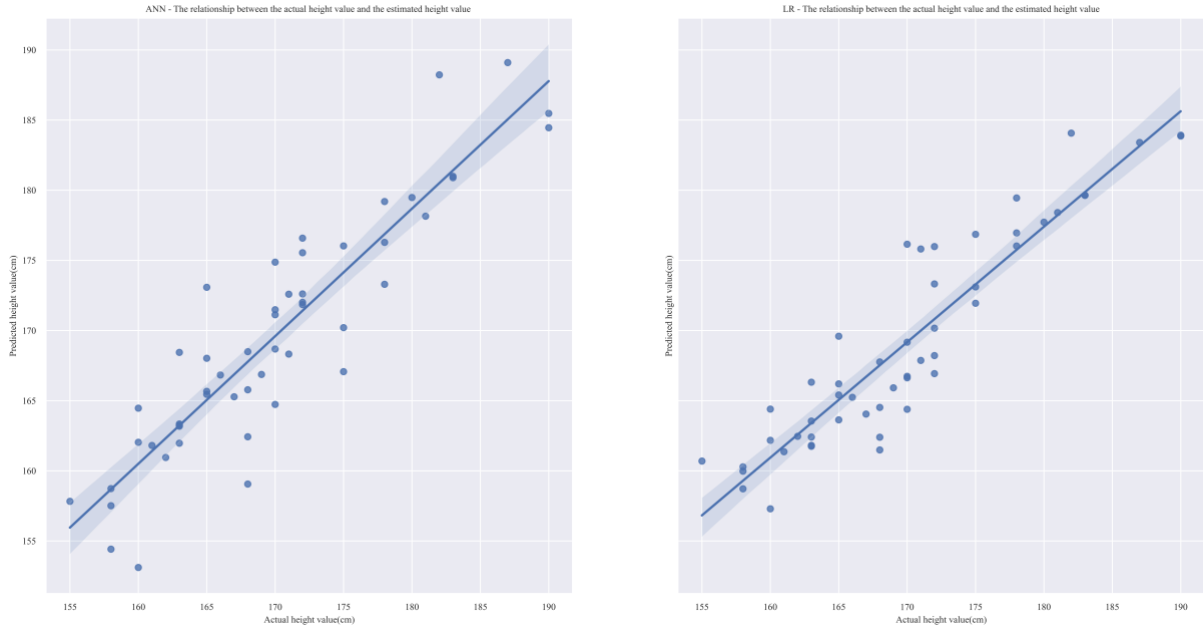


Fig. 5. Scatter plots of ANN and LR

#### 4. Conclusion

The height of individuals was predicted by machine learning methods using 10 different non-genetic features. For this purpose, data were collected through questionnaires and made suitable for machine learning methods. Among the machine learning methods, the LR and ANN methods, which are the most frequently used in the literature, were preferred. It has been observed that the LR method can predict the height of individuals. As a result of the study, the LR method was able to perform approximately 3.3 percent better than ANN at  $R^2$  value. Thus, it has been shown that the height of people, which has been tracked since the day they were born, can be predicted by machine learning methods in terms of how many centimeters it will be in adulthood. It is thought that the study will be beneficial for individuals and health centers. In future studies, performance can be improved with different methods by expanding the data set.

#### References

- [1] Ummanel A, Dilek A. Gelişim ve öğrenme. Öğr İlke ve Yönt; (2016): 35-52.
- [2] Uzun S. Yaşlılarda, kadınlarda ve adölesanlarda kişilik algısı değişimi ve nedenleri. J Humanit Soc Sci 2020; 3 (1): 431-449.
- [3] Panch T, Szolovits P, Atun R. Artificial intelligence, machine learning and health systems. J Glob Health 2018; 8(2).
- [4] Coşkun F, Gülleroğlu HD. Yapay zekânın tarih içindeki gelişimi ve eğitimde kullanılması. Ankara Univ J of Fac of Educ Sci (JFES) 2021; 54(3): 947-966.
- [5] Ersöz F, Çınar Y. Veri madenciliği ve makine öğrenimi yaklaşımlarının karşılaştırılması: Tekstil sektöründe bir uygulama. Avrupa Bilim ve Teknoloji Dergisi 2021; (29): 397-414.
- [6] Aytakin HT. Makine öğreniminin araştırmacıların veri analizi bağlamında potansiyel önemi. Ufuk Üniversitesi Sosyal Bilimler Enstitü Dergisi 10(19): 85-106.
- [7] Atalay M, Çelik E. Büyük veri analizinde yapay zekâ ve makine öğrenmesi uygulamaları-artificial intelligence and machine learning applications in big data analysis. Mehmet Akif Ersoy Üniversitesi Sosyal Bilimler Enstitü Dergisi 2017; 9(22): 155-172.
- [8] Sarker IH. Machine learning: Algorithms, real-world applications and research directions. SN Comput Sci 2021; 2(3): 160.
- [9] Esfe MH, Ahangar MRH, Rejvani M, Toghraie D, Hajmohammad MH. Designing an artificial neural network to predict dynamic viscosity of aqueous nanofluid of TiO<sub>2</sub> using experimental data. Int Commun Heat Mass Transfer 2016; 75: 192-196.

- [10] Ulas M, Altay O, Gurgenc T, Özel C. A new approach for prediction of the wear loss of PTA surface coatings using artificial neural network and basic, kernel-based, and weighted extreme learning machine. *Friction* 2020; 8: 1102-1116.
- [11] Mukherjee A, Biswas SN. Artificial neural networks in prediction of mechanical behavior of concrete at high temperature. *Nucl Eng Des* 1997; 178(1): 1-11.
- [12] Yu X, Ye C, Xiang L. Application of artificial neural network in the diagnostic system of osteoporosis. *Neurocomputing* 2016; 214: 376-381.
- [13] Simpson PK. *Artificial neural systems: foundations, paradigms, applications, and implementations*. McGraw-Hill, Inc., 1991.
- [14] Momeni E, Armaghani DJ, Hajihassani M, Amin MFM. Prediction of uniaxial compressive strength of rock samples using hybrid particle swarm optimization-based artificial neural networks. *Measurement* 2015; 60: 50-63.
- [15] Dreyfus G. *Neural networks: methodology and applications*. Springer Science & Business Media 2005.
- [16] Altay O, Gurgenc T, Ulas M, Özel C. Prediction of wear loss quantities of ferro-alloy coating using different machine learning algorithm. *Friction* 2020; 8: 107-114.
- [17] Gültepe Y. Makine öğrenmesi algoritmaları ile hava kirliliği tahmini üzerine karşılaştırmalı bir değerlendirme. *Avrupa Bilim ve Teknoloji Dergisi* 2019; (16): 8-15.
- [18] Iqbal N, Khan AN, Rizwan A, Ahmad R, Kim BW, Kim K, Kim DH. Groundwater level prediction model using correlation and difference mechanisms based on boreholes data for sustainable hydraulic resource management. *IEEE Access* 2021; 9: 96092-96113.
- [19] Altay O, Varol Altay E. A novel hybrid multilayer perceptron neural network with improved grey wolf optimizer. *Neural Comput Appl* 2023; 35(1): 529-556.
- [20] Gurgenc T, Altay O. St37 çeliğinin tornalanmasında yüzey pürüzlülüğünün destek vektör regresyonu kullanılarak tahmini. *Firat Univ J of Eng Sci* 2022; 34(2).
- [21] Gurgenc T, Altay O. Surface roughness prediction of wire electric discharge machining (WEDM)-machined AZ91D magnesium alloy using multilayer perceptron, ensemble neural network, and evolving product-unit neural network. *Mater Test* 2022; 64(3): 350-362.



## A Hierarchical Reinforcement Learning Framework for UAV Path Planning in Tactical Environments

Mahmut Nedim ALPDEMİR<sup>1\*</sup>

<sup>1</sup> BİLGEM, TÜBİTAK, Ankara, Türkiye

\*<sup>1</sup> nedim.alpdemir@tubitak.gov.tr

(Geliş/Received: 16/12/2022;

Kabul/Accepted: 21/03/2023)

**Abstract:** Tactical UAV path planning under radar threat using reinforcement learning involves particular challenges ranging from modeling related difficulties to sparse feedback problem. Learning goal-directed behavior with sparse feedback from complex environments is a fundamental challenge for reinforcement learning algorithms. In this paper we extend our previous work in this area to provide a solution to the problem setting stated above, using Hierarchical Reinforcement Learning (HRL) in a novel way that involves a meta controller for higher level goal assignment and a controller that determines the lower-level actions of the agent. Our meta controller is based on a regression model trained using a state transition scheme that defines the evolution of goal designation, whereas our lower-level controller is based on a Deep Q Network (DQN) and is trained via reinforcement learning iterations. This two-layer framework ensures that an optimal plan for a complex path, organized as multiple goals, is achieved gradually, through piecewise assignment of sub-goals, and thus as a result of a staged, efficient and rigorous procedure.

**Keywords:** Hierarchical reinforcement learning, tactical UAV path planning, machine learning, path optimization.

### Taktik Ortamlarda İHA Güzergahı Planlama Amaçlı Hiyerarşik Pekiştirmeli Öğrenmeye Dayalı bir Çerçeve

**Öz:** Pekiştirmeli öğrenme ile radar tehdidi altındaki İHA'ların güzergah planlamasının yapılması, modelleme ile ilintili zorluklardan başlayıp seyrek geri-besleme (sparse feedback) problemine uzanan bir dizi zorluklar içerir. Esasen, amaca yönelik davranışların seyrek geri beslemenin söz konusu olduğu karmaşık ortamlarda öğrenilmesi hususu pekiştirmeli öğrenme algoritmaları açısından temel bir problemdir. Bu makalede, daha önce bu alanda yaptığımız bir çalışmanın genişletilmesi suretiyle, bahse konu bu probleme, hiyerarşik pekiştirmeli öğrenme yöntemine dayalı özgün bir çözüm önerilmektedir. Bu çözüm, aktörlere üst seviye hedeflerin atanmasını yöneten bir meta-denetleyici ile aktörün alt seviye eylemlerini yöneten bir alt-denetleyicinin hiyerarşik bir şekilde çalışması prensibine dayanmaktadır. Çözümümüzdeki meta-denetleyici, yüksek-seviye hedeflerin atanması sürecini tanımlayan bir durum geçiş düzeneği kullanılarak eğitilen bir regresyon modeline, alt-düzyen denetleyici ise pekiştirmeli öğrenme ile eğitilen bir DQN'e dayanmaktadır. Bu iki katmanlı çerçeve, birden fazla hedef şeklinde organize edilmiş karmaşık bir güzergah için en iyi planın, hedeflerin aşamalı olarak atanması suretiyle ilerleyen; kademeli, etkin ve sıkı bir yöntem ile tedricen başarılmasını sağlamaktadır.

**Anahtar kelimeler:** Hiyerarşik pekiştirmeli öğrenme, taktik İHA güzergah planlama, makine öğrenmesi, güzergah optimizasyonu.

### 1. Introduction

The problem of Tactical UAV (TUAV) path optimization under radar threat includes several constraints which make it different from other path planning problems. Perhaps the most important of these constraints is the requirement to evade the detection and tracking of radars capable of undermining the survivability of the UAV. In [37] we have illustrated the integrated use of RL methods and a transfer learning approach in a single framework to solve the UAV path optimization problems in a tactical environment. As stated in [37] there are a number of peculiarities in comparison to more conventional problem settings, regarding UAV path optimization and the problem of Tactical UAV path planning under hostile radar tracking threat. To recap, these can be summarized as follows:

1. Radar coverage areas exhibit different properties from a penetration point of view, since depending on the performance parameters of the radars, those 3D regions would translate into different threat levels for a potential target. Moreover, those regions may be overlapping as opposed to conventional physical obstacles.
2. In a tactical context, some radars have an associated response period and a missile impact-to-kill time, leading to legitimate penetration periods without impairing the survivability of the target.

\* Corresponding author: nedim.alpdemir@tubitak.gov.tr. ORCID Number of author: <sup>1</sup> 0000-0001-6411-1453

3. Target detection is achieved via the interaction of the propagating radar EM waves with the Radar Cross Section (RCS) of the target which is a function of multiple parameters such as the radar operating frequency, the shape of the UAV and more importantly the engagement geometry between the radar and the UAV. The engagement geometry, in particular, implies that multiple angles (such as the bank angle, the aspect angle and elevation angle) would change as a result of the maneuvers performed by the UAV. So, even if the slant range (i.e., direct distance) to the radar is relatively stable, its detectability can still fluctuate dramatically.

4. The operating environments tend to be larger compared to in-door or small-sized urban areas, which implies that the feedback signals leading the agent towards the goal(s) may be delayed. This induces a well-known complication termed as *sparse reward problem*.

In fact, learning a task in a complex environment where sparse-feedback is an issue, is a significant challenge for artificial intelligence as noted in [16]. In such environments, the learning process should either incorporate a structured and effective way of representing the knowledge at multiple levels of spatio-temporal abstractions, or otherwise it should make sure that the reward signals provide sufficient and timely feedback to direct the agent effectively towards the goal. In practice, a variant of the general path planning problem may emerge when there are a set of well-defined sub-tasks during the course of the total mission flight time. The interim tasks can be as simple as passing along a pre-defined fixed location, or they may require more complex logic which may involve a set of constraints that must be satisfied at multiple levels. In reinforcement learning terms this translates into a *hierarchical learning process* guided via a multiple goal structure, leading to the concept of *Hierarchical Reinforcement Learning (HRL)*. As such, HRL inherently caters for sparse reward problem and conveniently accommodates a class of problems involving multiple tasks with a well-defined arrangement.

However, HRL is a specific form of the general problem with non-trivial implications and therefore induces some adjustments to the underlying formal model (i.e., Markov Decision Process (MDP)) as well as to the architecture of the framework providing the solution to the problem. In particular, from a theoretical point of view, the fact that actions of the agent may now be organized with regard to a set of temporal and/or logical abstractions, breaks the Markov Principle which states that the transition from current (present) state ( $S_t$ ) to the next state ( $S_{t+1}$ ) is entirely independent of the past (i.e. the previous states). In other words, Markov Property entails that the actions of the agent must be atomic in time and the current state already captures the information of the past states. Relaxation of this principle leads to a variant of MDP known as *Semi-Markov Decision Process (SMDP)* [39], [40]. From an implementation point of view, on the other hand, the framework providing the solution should include a layered architecture where higher level(s) would deal with assignment and learning of more abstract tasks, and lower level(s) would handle optimum action selection for the agent towards achieving a particular (sub)task.

In this paper we extend our previous work reported in [37] to provide a solution to the problem setting stated above, using hierarchical reinforcement learning in a novel way that involves a meta controller for higher level goal assignment and a controller that determines the lower-level actions of the agent. Our meta controller is based on a regression model trained using a state transition scheme that defines the evolution of goal designation, whereas our lower-level controller is based on a Deep Q Network (DQN) [25] and is trained via reinforcement learning iterations. This two-layer framework ensures that an optimal plan for a complex path, organized as multiple goals, is achieved gradually, through piecewise assignment of sub-goals, and thus as a result of a staged, efficient and rigorous procedure.

The rest of the paper is organized as follows: Section 2 provides some background and related work and introduces the details of the environment modeling; Section 3 sketches the theoretical framework of Reinforcement Learning, Section 4 introduces the specific RL formulation of the TUAV path optimization problem, Section 5 presents the experiments, results and discussions, and finally Section 6 provides the concluding remarks.

## 2. Background And Environment Modeling

TUAV path optimization under radar tracking threat has been explored by a number of researchers in non-RL settings [33, 21, 36, 17, 35, 12, 11]. The methods proposed by these researchers include Nonlinear Trajectory Generation (NTG) algorithm [11], Label Setting Algorithm (LSA) [33],  $A^*$  algorithm [21, 35], numerical optimization procedure for a minimax optimal control, with moving average functional [12]. Among the non-RL based solutions the one presented in [12] is utilized in our work since it integrates the model of the aircraft, a probabilistic model of a radar, and a behavioral approximation of missile subsystems based on the decision process for launching a SAM and the requirement to maintain tracking during missile flyout. Two of the components, namely radar and RCS models, however, are extended to incorporate pulse integration capability of a radar and to

account for the impact of target fluctuation via the Swerling type, which can have a significant effect for airborne platforms with a certain agility.

To put the path optimization problem in perspective with respect to RL, it is important to note that RL can be thought as a form of simulation-based, approximate dynamic programming, and as stated in [8], it provides a viable solution to such optimization problems. In fact, the ability of RL to tackle control and optimization problems is well-appreciated in the literature [27, 2, 24]. As such, more and more research work are being reported which involve RL based solutions. In a recent survey, AlMahamid and Grolinger [37] provide a systematic review of 159 recent works reported between 2016 and 2021, that use RL as a solution to UAV navigation and path planning problems. We note that none of the covered papers in this comprehensive review proposes a HRL-based solution to tactical UAV path optimization problem under radar threat. Incidentally, use of HRL in UAV path planning problems, in general, has been on the agenda only very recently. One of the quite recent works that resort to HRL as a solution in the UAV path planning context is that of Cheng Y. et.al [44] who aim to model cooperative formation of swarm UAVs. They combine a variant of MAXQ approach and simulated annealing to accomplish grid method-based path planning for multi-UAV collaborative formation. They report quicker astringence, lower volatility, better learning effect, less time consumed and optimized searched route compared to non-hierarchical RL methods. Their problem setting is different to ours, in that their main objective is to achieve collaborative formation of multiple UAVs and that they do not consider evading lethal threats in tactical environments. Another recent work that proposes an HRL-based solution to missile guidance problem with threat-region (i.e., circular no-fly zones) avoidance is that of Bohao et.al. [46], who use an improved version of hierarchical deep deterministic policy gradient (DDPG) algorithm. From a problem-context point of view their objective has some similarities to ours since it involves navigation to a target (although using UAVs) and threat avoidance. However, from a methodological point of view, there are important differences. Their purpose of employing hierarchical learning is to weaken acceleration chattering rather than constructing a temporal abstraction for staged navigation. They achieve this by employing a somewhat shallow hierarchy of two DDPG value networks sharing the same policy network. Being a DDPG based solution, their approach uses a continuous action space, a policy-gradient learning method and an actor-critic architecture in each of the DDPG component. Our solution is based on a strictly layered architecture, uses discrete action space and is based on learning directly the optimum Q-Values (rather than the optimum policy). The last research work we would like to compare is that of Qin et.al. [50] who propose to solve the trajectory design problem of rechargeable UAVs in continuous data collection tasks using a hierarchical DQN (H-DQN) architecture based on SMDP. Their problem setting is significantly different to ours in that higher level tasks (called options in their paper akin to the options formalism of Sutton et.al,[47]) pertain to pre-defined UAV behaviors such as data collection, returning to base for re-charge etc. Whereas in our work, higher level tasks are interim sub-goals inspired by navigational targets. From an algorithmic point of view their method has similarities in particular in the way low level tasks are learned, which involves training a DQN network with experience replay using epsilon greedy exploration. The main methodological difference is that our framework is more akin to Hierarchies of Abstract Machines (HAMs) of Parr [39] and our learning scheme is based on Feudal RL (more on this in Section 3 and Section 4.)

In the following subsections we provide the details of the modeling aspects that are important for understanding the underlying logic of the environment state generation in our framework.

## 2.1 Modeling of the RL Environment

The modeling related aspects of our RL environment were developed in [37], here we include a concise summary of the mathematical model that underpins the overall response of the environment with respect to the interactions of the agent. For details that cannot be found in this paper we refer the reader to the aforementioned publication.

### 2.1.1 A Probabilistic Model of Radar for detection, tracking and destruction of a target

From a probabilistic point of view, based on the SNR values and a choice of false alarm rate ( $P_{fa}$ ) it is possible to compute a *probability of detection* for a combination of pulse integration capability of the radar and the type of the target behavior. [18] states that for a single pulse (no pulse integration) radar and non-fluctuating target the following approximation gives the solution:

$$P_d \approx 0.5 \times \operatorname{erfc} \left( \sqrt{-\ln(P_{fa}) - \sqrt{\operatorname{SNR} + 0.5}} \right) \quad (1)$$

In the context of tactical UAV survivability, target *tracking* is more important than target *detection*, since for a successful engagement, a track lock has to be acquired and maintained on the target for a certain period of time. Therefore, the *probability of track* has to be included in the model. [34] states that given a  $P_d$  value and a probabilistic account of the track loss, the probability of track of a radar can be calculated in a recursive way using the following Equation:

$$\begin{aligned} z[n+1] &= (1 - z[n-l])P_d \times (1 - P_m)^l + z[n] \\ P_{track} &= 1 - z[k]; \quad n > l, \quad \text{and} \quad P_m = 1 - P_d \end{aligned} \quad (2)$$

where a track loss is set to occur only after  $l$  number of consecutive misses in a  $k$  number of such observations, subject to  $k > l$ . However, for an effective and convenient computational model of radar-target engagement, a direct relationship between critical parameters of the engagement is required. [12] proposes a concise formulation where the relationship between the target range, the RCS of the target and the probability of track is established and parameterized by a combination of performance and operational characteristics of the radar.

$$P(R, \sigma) = \frac{1}{1 + \left(c_2 \times \frac{R^4}{\sigma}\right)^{c_1}} \quad (3)$$

The function  $P(R, \sigma)$  given above in Equation (3), is a direct function of range ( $R$ ) and RCS ( $\sigma$ ) where  $c_1$  and  $c_2$  are constants and can be determined using the operational parameters and some required performance characteristics of a radar. To account for cases where a number of radars are installed to form a tactical network, the aggregate probability of being tracked by a number of those radars has to be computed. Under the assumption that tracking logic of the participating radars is not shared among them the aggregate probability can be evaluated as follows;

$$P_{tr} = 1 - (1 - P_{tr_1})(1 - P_{tr_2}) \dots (1 - P_{tr_n}) \quad (4)$$

Where  $P_{tr_1}$  denotes the probability of the UAV being tracked by a first radar,  $P_{tr_2}$  denotes the probability of the UAV being tracked by a second radar and so on, and  $P_{tr}$  is the probability of the event that the UAV is tracked by an overall integrated air defense network consisting of all radars in a given mission area.

The last element of our probabilistic engagement model, is the probability of the TUAV to be hit by a missile after it has been detected and a track lock is acquired on it. In this respect, two primary factors have to be considered: 1 - system response time,  $T_r$  (i.e., the time interval in which the radar system concludes that a missile must be fired and actually fires it), 2 - missile flyout time,  $T_f$  (the time interval in which a missile travels to physically hit or explode in proximity to the aircraft). For an aircraft to be destroyed at time  $t$ , the radar system must have tracked it during the continuous interval  $[t - (T_r + T_f), t]$ . If  $\Delta T = T_r + T_f$  is defined to be the threat window, then probability of kill is defined as:

$$P_k(t) \approx \frac{1}{\Delta T} \int_{t-\Delta T}^t P_t(\tau) d\tau \quad (5)$$



### 2.1.2 A Kinematic Bank-to-Turn Model of the UAV

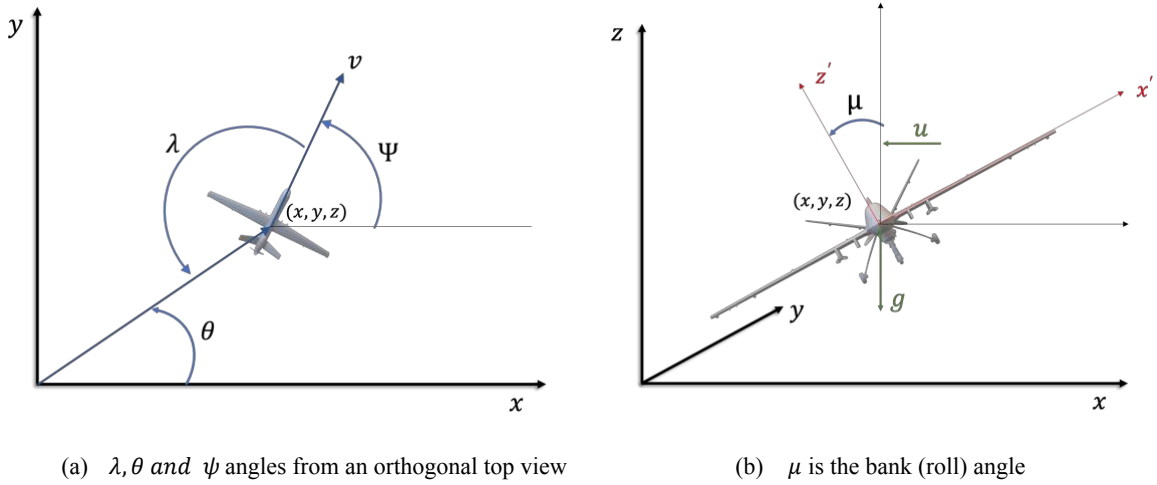


Figure 1 A Visual representation of UAV model parameters

The UAV is represented using a kinematic model given in [12] and also adopted in [36], which account for the coupling between the RCS and aircraft dynamics. To be more specific, the turn rate of the aircraft is determined by its bank angle which in turn is determined by a steering input represented by  $u$ . Hence, the RCS and dynamics of the aircraft are coupled through the aspect and bank angles.

Figure 1 (a) shows an orthogonal top view to indicate the relationship between  $\lambda, \theta$  and  $\psi$  angles.

Figure 1 (b) shows a tilted 3D view of a UAV to illustrate the relationship between  $\mu$  (the bank (roll) angle)  $u$  and  $g$ . According to this model, the bank-to-turn aircraft is assumed to move in a horizontal plane at a constant altitude governed by the equations:

$$\dot{x} = v \cos \psi, \quad (6)$$

$$\dot{y} = v \sin \psi, \quad (7)$$

$$\dot{\psi} = u/v \quad (8)$$

Where,  $x$  and  $y$  are Cartesian coordinates of the UAV,  $\psi$  is the heading angle,  $v$  is the constant speed,  $u$  is the input signal which is the acceleration, normal to the flight path vector. Further, to define the position and posture of the aircraft with respect to a given  $i_{th}$  radar the following equations are defined [1]:

$$\theta = \arctan\left(\frac{y-y_i}{x-x_i}\right), \quad (9)$$

$$\lambda = \theta - \psi + \pi \quad (10)$$

$$\phi = \arctan\left(\frac{z}{\sqrt{(x-x_i)^2+(y-y_i)^2}}\right), \quad (11)$$

$$\mu = \arctan(u/g) \quad (12)$$

$$R_i = \sqrt{(x-x_i)^2+(y-y_i)^2+z^2} \quad (13)$$

Where,  $\theta, \lambda, \phi, \mu$  are the azimuth, aspect, elevation and bank (or roll) angles, respectively,  $z$  is the aircraft altitude,  $x_i, y_i$  are the coordinates of the  $i_{th}$  radar on the  $x-y$  plane (note that  $z=0$  for any radar),  $g$  is the acceleration of gravity and  $R_i$  is the range of the  $i_{th}$  radar to the aircraft. To ensure a certain degree of faithfulness to the actual RCS of the aircraft rather than rely on a simple isotropic RCS, we adopt the optical region approximations using a 3D Elliptical RCS model, which is one of the suggested approximations in the literature [18]. Based on Equations (9), (10), (11) and (12), the RCS of the aircraft can be modeled as a function of the aspect angle  $\lambda$ , the elevation angle  $\phi$ , and the bank angle  $\mu$ , (as suggested in [12]) such that;

$$\sigma(\lambda, \phi, \mu) = \frac{\pi a^2 b^2 c^2}{(a^2 \sin^2 \lambda_e \cos^2 \mu_e + b^2 \sin^2 \lambda_e \sin^2 \mu_e + c^2 \cos^2 \lambda_e)^2} \quad (14)$$

$$\lambda_e = \arccos\left(\frac{\cos \phi}{\cos \lambda}\right) \quad (15)$$

$$\mu_e = \mu - \arctan\left(\frac{\tan \phi}{\sin \lambda}\right) \quad (16)$$

### 3. Theoretical Background On Hierarchical Reinforcement Learning

Reinforcement Learning (RL) can, informally, be defined as learning from incrementally gained experience via interactions with an environment to achieve a pre-defined goal. As such, it is a computational paradigm where an *agent* learns a policy of optimal *actions* by seeking to maximize the cumulative *rewards* obtained as a result of its interactions with an environment along a task horizon, in conjunction with a set of state that evolves during these interactions. The primary formal framework used for the specification of the above definition is the Markov Decision Process (MDP) [28, 7]. In a set theoretical setting, an MDP is formally defined (see, for instance, [31]) as a tuple of five elements  $\langle S, A, T, R, \gamma \rangle$  where  $S$  is a finite set of states defining a discrete state space,  $A$  is a finite set of actions defining a discrete action space,  $T$  a transition function defined as  $T: S \times A \times S \rightarrow [0,1]$ ,  $R$  is a reward function defined as  $R: S \times A \times S \rightarrow R$  and  $\gamma \in (0,1)$  denotes a discount factor. The transition function  $T$  and the reward function  $R$  together define the model of the MDP. Given an MDP, a policy is a computable function that outputs for each state  $s \in S$  an action  $a \in A$  (or  $a \in A(s)$ ). Formally, a deterministic policy  $\pi$  is a function defined as  $\pi: S \rightarrow A$ . It is also possible to define a stochastic policy as  $\pi: S \times A \rightarrow [0,1]$  such that for each state  $s \in S$ , it holds that  $\pi(s, a) \geq 0$  and  $\sum a \in \pi(s, a) = 1$ .

It has been argued that RL as a computational paradigm faces some important challenges such as sampling and exploration inefficiency, sparse reward problem in long horizon tasks, low interpretability, inherent difficulties with transfer of learned skills (of the agent), complexity of reward function design process etc. (see for instance [41],[42],[43] for more discussion). HRL extends the capabilities of RL by introducing an approach where complex tasks are abstracted into smaller sub-tasks which can also be re-used for other similar complex tasks. More specifically, HRL increases exploration efficiency via temporally extended exploration (due to temporal correlation of higher level tasks), alleviates the sparse reward problem by utilizing various forms of intrinsic motivation in order to provide additional denser reward signals for individual abstractions, addresses sample inefficiency through efficient use of temporal and state abstractions, facilitate transfer learning and increase interpretability using various forms of abstractions.

HRL is formalized on the basis of the theory of Semi-Markov Decision Process (SMDP) [39], [40]. It is stated in [[39], [40] that an SMDP is a stochastic control process comparable to an MDP, but it differs from MDP in that it incorporates the concept of time for which an action is executed after it has been chosen. In the context of HRL, the actions which are not atomic (i.e., span a certain amount of time) are the subtasks. Starting from a state  $s_t \in S$ , assume that an agent chooses a subtask  $\omega_t \in \Omega$ , where  $\Omega$  is the set of subtasks (or the subtask space). The reward obtained as a result of performing the subtask  $\omega_t$  starting from state  $s_t$  is denoted as  $R(s_t, \omega_t)$ , calculated as follows,

$$R(s_t, \omega_t) = \mathbb{E}_{a \sim \pi_{\omega_t}(s)} \left[ \sum_{i=0}^{c_{\omega_t}-1} \gamma^i r(s_{t+i}, a_{t+i}) \mid s_t, a_t = \pi_{\omega_t}(s_t) \right]. \quad (17)$$

Equation (17) indicates that the reward  $R(s_t, \omega_t)$  is equal to the expected cumulative reward obtained while following the subtask policy  $\pi_{\omega_t}$  from time  $t$  until the termination of  $\omega_t$  after  $c_{\omega_t}$  timesteps. Now, an optimal task policy would be the one that leads to the following desired maximum Q-value:

$$Q(s_t, \omega_t) = R(s_t, \omega_t) + \sum_{s_{t+c_{\omega_t}}, c_{\omega_t}} \gamma^{c_{\omega_t}} P(s_{t+c_{\omega_t}}, c_{\omega_t} \mid s_t, \omega_t) \max_{\omega_{t+\omega_t}} Q(s_{t+c_{\omega_t}}, \omega_{t+c_{\omega_t}}), \quad (18)$$

Where,  $\forall s \in S$  and  $\forall \omega \in \Omega$ . It should be noted that the Q-value in Equation (18) also depends on  $R(s_t, \omega_t)$  and  $P(s_{t+c_{\omega_t}}, c_{\omega_t} | s_t, \omega_t)$ . These two quantities are determined by the execution of  $\omega_t$  using its policy  $\pi_{\omega_t}$ . Therefore, an agent actually needs to learn multiple policies at different levels of a task decomposition hierarchy.

As noted in [41], earlier HRL methods, were mostly based on three main approaches: the options formalism of Sutton et.al,[47] the Hierarchies of Abstract Machines (HAMs) of Parr [39] and Parr and Russell [40], and the MAXQ framework of Dietterich [48], which share many common elements and more importantly rely on SMDP as the underlying theory. Further research has resulted in many variants and improvements as detailed in recent comprehensive surveys such as [42] and [43]. One such relatively recent approach listed in the larger taxonomy of approaches is called Feudal Reinforcement Learning (Feudal RL) [49]. Feudal RL involves a hierarchy, in which the action space of a higher-level policy consists of subgoals corresponding to various subtasks. A subgoal chosen by the higher-level policy is taken as input by a universal policy at the lower level. The objective of this lower-level universal policy is to achieve the input subgoal. The universal policy at each level can be treated as a sub-agent (as part of the HRL agent) that can perform all the possible subtasks at that level. This leads to the feudal concept of a “manager” sub-agent (higher-level policy) directing a “worker” sub-agent (lower-level policy). This method is particularly relevant to our work, since we adopt the main framework proposed in it.

### 3.1 Methodological Details of Our Framework Based on HRL

In this work we adopt a two-layered architecture consisting of a controller and a meta-controller. We adopt a Feudal RL approach which is briefly described as follows: a higher-level manager selects a subtask that is to be fulfilled by a worker at a lower-level. The manager assigns the subtask to the worker via a sub-goal. The objective of the worker is to achieve the designated sub-goal. The cumulative rewards produced by a task are visible only to the manager at the highest level while the workers at other levels learn using the rewards for reaching the subgoals. In this setting, we use a multinomial logistic regression model [51] to implement a meta controller for the manager which is then trained using a state transition graph that models the selection of the appropriate high-level goal based on a meta state depicting the status of the higher-level learning process. Since this meta state is a categorical description of the higher-level tasks and the confidence in the learning level of those tasks, we use an encoding scheme similar to one-hot encoding to model the relevant state data.

For the worker, we implement a lower-level controller, using one of the most popular model-free, Q-Learning-based RL algorithms, namely Deep Q Network (DQN) which was developed by [20]. DQN relies on a neural network for approximating the behavior of the Q-function in a non-linear manner. In fact, a DQN is a multi-layered (deep) neural network which takes a vector of observations,  $\omega_t \in \Omega$ , as its input, and assigns likelihood values to a vector of action values  $Q(\omega_t, \cdot; \theta)$  in its output, where  $\theta$  are the parameters of the network. Standard Q-learning algorithms were plagued with instability until [20] introduced two mechanisms that address this deficiency. The first of these mechanisms is the *experience replay* which involves accumulating a customizable window of observation sequence and randomizing over the data in this sequence to remove correlations in the observation history and to smooth over changes in the data distribution. During the training of the DQN, experiences are first accumulated in the experience replay buffer using  $\epsilon$ -greedy policies. The second of these mechanisms is called a *target network* and relies on the use a separate neural network (architecturally identical to the *value network*), with parameters  $\theta^-$ . During the training, the parameters of the value network are copied over to the target network every  $k$  steps, so that then  $\theta_t^- = \theta_t$ , and kept fixed on all other steps.

In its original form, experience replay buffer is sampled uniformly. A more effective variant was introduced by [25] called *prioritized experience replay*. The motivation here is to increase the impact of surprising and/or task-relevant transitions within the experiences during the learning process. More specifically, this technique, uses the magnitude of the temporal-difference (TD) error pertaining to transitions, and tends to favor (i.e., prioritize) those with high expected learning progress. Such selective prioritization may result in a loss of diversity and can introduce bias, but these are reconciled with stochastic prioritization and importance sampling respectively.

## 4. Casting the Problem into A Reinforcement Learning Context

RL assumes a specific framework in which an agent interacts with its environment conforming to a relatively simple but a well-defined pattern. Hierarchical RL, on the other hand, adds a further meta-layer for the assignment and management of tasks that may consist of an arbitrary hierarchy. The structural (or data-model centric) aspects of this interaction scheme and its associated management layer can be specified via an agent observation space, a meta-layer observation space and an action and task space. The algorithmic (or behavioral) aspects, on the other

hand, can be specified via the reward function. In this section we first provide the details of those structural and behavioral aspects, and then we proceed by introducing our algorithm that implements the actual hierarchical learning scheme based on the specified aspects.

#### 4.1 Agent Observation Space

An observation for the lower-level controller agent,  $\rho_t \in \Omega$ , is the observable part of the environment state by the agent at time step  $t$ .  $\omega_t$  is defined as a tuple as below:

$$R_g = \sqrt{(x_g - x)^2 + (y_g - y)^2}, \quad (19)$$

$$\alpha = \arctan\left(\frac{y_g - y}{x_g - x}\right), \quad (20)$$

$$\beta = |\psi - \alpha|, \quad (21)$$

$$\rho_t = \langle \|\ x \ \|, \|\ y \ \|, \|\ R_g \ \|, P_{tr}, P_k, \alpha, \psi, \mu, \beta, \|\ RCS_1 \ \|, \dots, \|\ RCS_n \ \|, MS_g \rangle \quad (22)$$

where  $P_{tr}$  is the aggregate probability of track at a certain time step, as defined earlier in Equation (4),  $P_k(t)$  is the probability of kill as defined earlier in Equation (5),  $x_g, y_g$  are the coordinates of the center of the goal area in x-y plane,  $x, y$  are the coordinates of the UAV in x-y plane,  $\alpha$  is the angle between the x-axis and the line connecting the current UAV position to the center of the goal area (i.e. the goal angle),  $\beta$  is the difference between the UAV direction angle (i.e.  $\psi$  as defined in Equation (8)) and the goal angle,  $\mu$  is the UAV bank (or roll) angle as defined in Equation (12), and  $RCS_i$  is the RCS of the UAV with respect to the  $i^{th}$  radar in the mission area,  $n$  being the total number of radars deployed in the mission area.  $MS_g$  is the one hot encoded sub-goal achievement meta state that describes the current state of the agent with regard to achieving the set of all sub-goals. The  $\|\ \cdot \ \|$  symbol denotes normalization.

#### 4.2 Meta-Level Observation Space

The observation space for higher level meta controller,  $\sigma_t$ , is an n-tuple representing the task (or goal) meta state, encoded similar to one-hot encoding defined as follows;

$$\sigma_t = \langle x_1, \dots, x_n, m \rangle; \ n = \text{number of subgoals}$$

$$x_i = 1_M(u_i) = \begin{cases} 1 & \text{when } u_i \in G_t \\ 0 & \text{when } u_i \notin G_t \end{cases}$$

$$m = \begin{cases} 1 & \text{when } x_i \text{ is learned successfully} \\ 0 & \text{when } x_i \text{ is NOT learned} \end{cases}$$

$$G_t = \{g_{1_t}, \dots, g_{k_t}\}; \ k \leq n; \ k_t = \text{number of subgoals achieved by the agent at time } t$$

where  $1_M(u_i)$  is an indicator function that determines whether a specific element of the tuple  $\sigma_t$  is 1 or 0 depending on the sub-goal number being encoded;  $m$  is a binary code that indicates whether the encoded goal is learned successfully or not, and  $G_t$  is the set of sub-goals achieved (or visited) by the agent at time  $t$  including the final goal.  $G_t$  grows as the agent achieves more goals. Note that with this encoding scheme our framework supports categorical states, so it is inherently suitable for extension to other contexts, involving more liberal task definitions such as non-navigational behaviors (e.g., hover along a circle for reconnaissance).

#### 4.3 Action And Task Space

For the lower-level controller, the actions in our problem setting are defined in terms of steering input,  $u$ , to the UAV navigation system, as specified in Equation (8). We adopt a discrete action space which is defined as follows:

$$A = \{u_1, \dots, u_7\}, \quad u_i \in [-15, 15] \quad (23)$$

$$u_i = u_{i-1} + 5, \quad (24)$$

where  $A$  is a finite set that defines all the available actions containing 7 elements. The elements range from -15 to 15 with an increment of 5. Positive values cause the aircraft to perform a right-turn maneuver, whereas negative values cause the aircraft to perform a left-turn maneuver.

For the higher-level meta controller, the task space consists of a single integer representing the task (i.e., sub-goal) number to be assigned to the lower-level worker as the target.

#### 4.4 Reward Function

Our reward function is designed to provide direction and range feedback with respect to the designated (active) goal, as early as possible. The overall cumulative reward signal,  $R_t$ , is composed of a number of sub-components as defined below:

$$RW_{gr} = \|1 - R_g\|$$

$$PN_{ptk} = \begin{cases} 0, & \text{if } P_{tr} < \xi \\ 2(P_{tr}(t) + P_k(t)), & \text{otherwise} \end{cases}$$

$$FB_{dir} = \begin{cases} 5(1 - \|\beta\|), & \text{if } \beta < 10 \\ -2\|\beta\|, & \text{otherwise} \end{cases}$$

$$R_t = \begin{cases} -50, & \text{if } (P_k(t) > \zeta) \vee (\text{UAV out of area}) \\ \alpha RW_{sg}, & \text{if UAV in goal area} \\ RW_{gr} + FB_{dir} - PN_{ptk}, & \text{otherwise} \end{cases}$$

where  $P_{tr}$  is the aggregate probability of track at a certain time step, as defined in Equation (4),  $P_k(t)$  is the probability of kill which was defined in Equation (5),  $\xi$  is the tracking probability threshold (the probability value at which a track lock is initiated),  $\zeta$  is the kill probability threshold (i.e. the value of  $P_k(t)$  for which a UAV-kill event is set to happen),  $R_g$  and  $\beta$  are defined in Equations (19) and (21) respectively,  $PN_{ptk}$  is the penalty for being tracked or killed,  $RW_{gr}$  is the reward for getting nearer to the goal,  $FB_{dir}$  is the direction feedback which increases as the heading of the UAV aligns better towards the goal,  $RW_{sg}$  is a specific numeric reward for reaching a certain sub-goal weighted with a coefficient  $\alpha$ . Here  $\alpha$  takes greater values as the target sub-goal is closer to the final goal.

A 2D visualization scheme, as depicted in Figure 2, is employed to represent the output of the reward function, where reward values are used to generate a color-coded image map. The figure illustrates a rectangular mission area containing 2 radars installed in various locations, and some interim goal areas placed in different locations within the mission area. Radar coverage areas are indicated via opaque circular regions. As it would be expected, those circular areas are discouraged by the reward function, so blue color signifies negative reward values (i.e., punishment), darker shades indicating more dramatic penalty levels. Positive reward values are indicated by a red color, signifying direction-wise and range-wise proximity of the agent to active (i.e., currently assigned) goals. In this respect, Figure 2 (a) depicts a case where an agent with a direction angle of 0 (i.e.,  $\psi = 0$ ) obtains increasingly higher positive rewarded values as it moves towards the goal along a straight line. Note that the central line of the

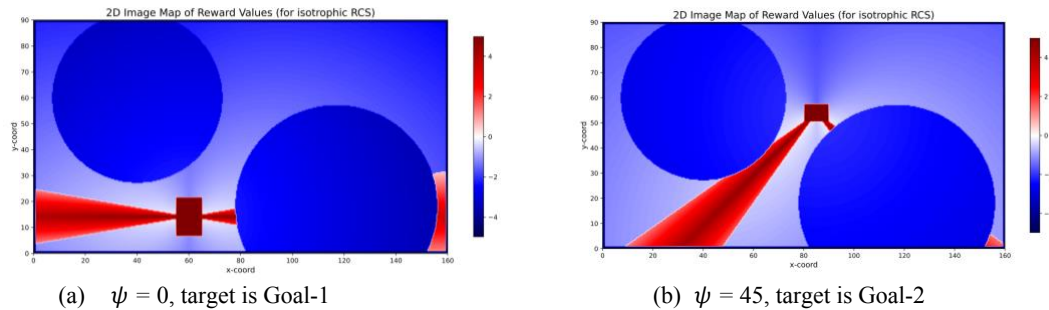


Figure 2 Color-coded representation of reward function returns for different UAV direction angle ( $\psi$ ) values. ( $\psi$  equals 0 and the target is Goal-1 on the left.  $\psi$  equals +45 and the target is Goal-2 on the right)

path exhibits highest positive rewards (indicated by a darker red color), since it minimizes the difference between the goal angle and UAV’s direction. Figure 2 (b) illustrates a case where an agent with a direction angle of 45 (i.e.,  $\psi = 45$ ) gets increasingly higher positive reward values as it approaches towards the goal along a diagonal line with a 45 degrees angle with the center line of the goal area etc. Note that the illustrations are only valid for scenarios employing an isotropic RCS for the UAV. Cases involving non-isotropic RCS, would result in dramatic changes (in fact fluctuations) in the probability of detection values, depending on the maneuvers of the UAV, due to changes in the three engagement angles. This would make the reward signals much harder to map in a comprehensive way.

#### 4.5 The Hierarchical RL Algorithm

We now describe the algorithm that implements the HRL solution. The procedure given in Algorithm 1 starts with the initialization of the meta controller using the set of goals and a multinomial logistic regression model. Then there is a pre-training step (in line 6) in which the meta controller is trained using a set of meta state transitions and corresponding next states for each meta state tuple in this set. Note that the state tuples are n-tuples encoded using a scheme similar to one-hot encoding and the next states are task (or goal) numbers denoting the next task (goal) to be targeted. For instance, the following examples illustrate three cases where in the first one, the first goal was visited but wasn’t learned (so the last member of the tuple, i.e., the confidence bit  $m$ , is still 0) therefore the next meta state (goal) is 1, suggesting that the agent should still target this goal until it confidently learns it. In the second one, the meta state indicates that the first goal is visited and learned, so the next task is targeting goal number 2. In the third example, the first goal and the second goal are visited and the last goal (i.e. goal number 2) is also learned, so the next goal is goal number 3, etc. Note that these examples are valid for a 3-goal scenario. Note also that, contrary to strict one-hot encoding, meta state tuple can contain multiple “1” values.

(1,0,0,0) → 1  
 (1,0,0,1) → 2  
 (1,1,0,1) → 3

Following the training of the meta controller the environment is reset and low-level training of the controller starts as a conventional RL training loop, except that the outer loop uses the *pre-trained meta controller* to assign high level goals each time a specific goal is achieved and learned successfully. This is indicated in line 12 of the algorithm. The loop starting with line number 14 handles the training of lower level controller, which involves asking the controller to predict the next low level action (line 15), forwarding the environment state one step using the new action (line 16), calling the optimization step to perform training of the Q-Function which is implemented as a DQN in our case (line 18), checking if a goal was reached and making sure the active goal (i.e. the goal that was assigned to the agent currently) was learned successfully (lines 19 to 29). Note that this procedure is a two-stage training process where the first stage is an off-line pretraining phase (for the meta controller). Note also that this framework does not allow for dynamic goal discovery, the meta level goal structure has to be predefined.

Algorithm 1 Procedure for training the hierarchical DQN agent

```

1 Procedure HRL ( $X, Y, G, F_{lr}, env$ )
2 //X is a set of meta state tuples, Y is the next state vector (for a given
3 meta state)
4   initialize meta_controller( $G, F_{lr}$ ) //  $F_{lr}$  is a sklearn logistic regression model
5   // G is a set of goals
6   meta_controller.train(X, Y) //train the logit model using X and Y
7   obs = env.reset()
8   R = 0; t = 0
9   While t < max_steps
10    goal_state = obs.get_metastate()
11    //get next task (goal) from the meta controller
12    new_goal = meta_controller.get_next_goal(goal_state)
13    env.set_target_goal(new_goal)
14    While True
15      act = contoller.act(obs) //get next action from the controller

```

```

16     obs, rew, done = env.step(act)
17     R += rew; t += 1
18     contoller.train(obs, rew, done)
19     if goal_reached
20         if is_active_goal_learned()
21             env.designate_next_goal()
22         else:
23             success_ratio = evaluate_success(new_goal)
24             if success_ratio >= 0.7
25                 learned_current_goal = True
26                 env.set_confidence(new_goal,1)
27             else:
28                 learned_current_goal = False
29                 obs = env.reset()
30     if done or reset or learned_current_goal
31         break
32     End While
33 End While
34 End Procedure

```

## 5. Experiments and Results

The experiments are carried out in a simulated tactical area where two radars are installed. The x and y dimensions of the area is 160 km by 90 km. The radars have different performance specifications characterized by the parameters given in Table 1, where  $P_{tx}$  refers to peak transmit power,  $f$  is the operating frequency,  $F_n$  refers to the noise figure,  $pw$  is the pulse width,  $P_{fa}$  is the probability of false alarm,  $SNR_{min}$  is the minimum required SNR,  $t_{resp}$  is the response time of the radar and  $v_m$  is the speed of the Surface to Air (SAM) missile. Both radars have the ability to perform non-coherent pulse integration,  $k$  and  $l$  parameters given in Equation (2) are taken to be  $k = 30, l = 4$ . Three scenarios are experimented:

1. In the first one only one goal exists in the environment which is located far from the entry point to the mission area. In this environment a standard DQN algorithm is used to illustrate the results of using plain RL in such long horizon tasks.
2. In the second scenario a two-goal environment is used and the agent is trained using HRL approach.
3. In the third scenario one more sub-goal is added to the environment and the performance of the HRL agent is demonstrated.

Table 1 Important parameters of two different radar types

Radar Type	$P_{tx}(dBW)$	$f(GHz)$	$F_n(dB)$	$pw(\mu s)$	$P_{fa}$	$SNR_{min}(dB)$	$t_{resp}(s)$	$v_m(m/s)$
Type-1	54.47	8	0.4	8	$10^{-6}$	10	22	1200
Type-2	55.18	7	0.4	5.19	$10^{-6}$	13	20	1300

In all of the scenarios above;

1. The UAV is assumed to cruise at a constant altitude of 9000m, at a constant speed of 170m/s (0.49Mach). In other words, take-off, climbing, descending and landing phases are not considered.
2. The target fluctuation category of the UAV is assumed to be swerling-1 as defined in [29].
3. At each time step in the simulation, the aggregate probability of track (obtained using Equation (4)) is calculated and checked against a *tracking probability threshold* of value 0.9. If the aggregate prob. of track is greater than that value, then for each of the contributing radars, a track sequence is triggered at that time step.
4. If a track sequence is initiated for a particular radar, then missile hit time,  $t_{hit} = R_t/v_m$  is calculated for that radar and at each consecutive time step the probability of track is checked against a *track loss threshold*. If the probability of track continues to remain above the track loss threshold for a time window equal to  $t_{resp} +$

$t_{hit}$  of that radar, then the UAV is considered to be lost. Note that it is assumed that  $t_{hit}$  stays constant during the threat window.

5. To model the difficulty of breaking a track lock via maneuvers once it is acquired, the track loss threshold is set to 0.6, indicating that the track lock remains unbroken until the probability of track goes below 0.6.

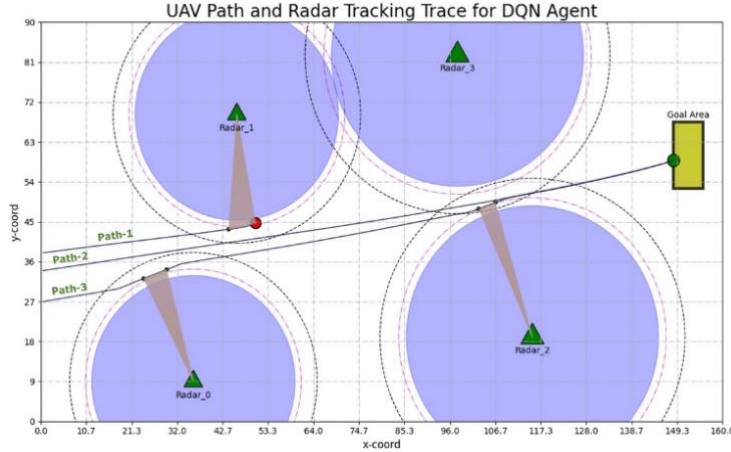


Figure 3 An example post mission trace graph

During the experiments, the flight path of the aircraft and the track history of the radar are logged and plotted to provide a visual performance evaluation scheme. An example graph is given in Figure 3. Here, opaque circular areas delineate the region where probability of track is greater than 0.9 for an isotropic RCS of  $1.2m^2$ . The dotted circles at the outer perimeter indicate the points at which the probability of track is equal to 0.54. Maximum detection range based on the minimum SNR value of each radar is also calculated and illustrated using red dotted circles in between of those two. Some example flight trajectories are included in the figure, where Path-1 denotes a scenario where the UAV was destroyed by Radar-1 following a track period (track initiation point and kill point are denoted by a small black dot and relatively larger red dot respectively), Path-2 illustrates a fully successful trial and Path-3 illustrates two tracking events initiated by Radar\_0 and Radar\_2, neither of them being able to destroy the target. This layout and notational convention are used throughout the experiments.

For all scenarios, to model the lower-level controller we use a DQN with input size of 15 (equal to the size of the observation vector), an output size of 7 (equal to the size of the discrete action space) and 2 hidden layers of 400 channels each. We use ADAM [14] algorithm for the optimization of the neural network. The experience replay buffer has a start size of 256, and is sampled using a batch size of 128. The exploration policy is managed via a decaying  $\epsilon$ -greedy explorer epsilon values ranging in the interval [1.0, 0.1].

## 5.1 Presentation of The Results and Discussions

In all of the experiments we performed the evaluation process at 10 episode intervals, averaging cumulative reward obtained from 5 evaluation runs. During evaluation runs the agent does not take any exploratory actions, it fully exploits the current learning level of the DQN. As illustrated in , in the first scenario the agent was unable to learn to reach the target goal area although the experiment was extended to last for nearly 700 episodes (around 1 million steps). Note that the training curve seem to stabilize around a particular cumulative reward value (around 7000), but evaluation curve swings along a large interval. This is because the DQN agent struggles to converge to a successful policy given the delayed feedback conditions in this long horizon setting.



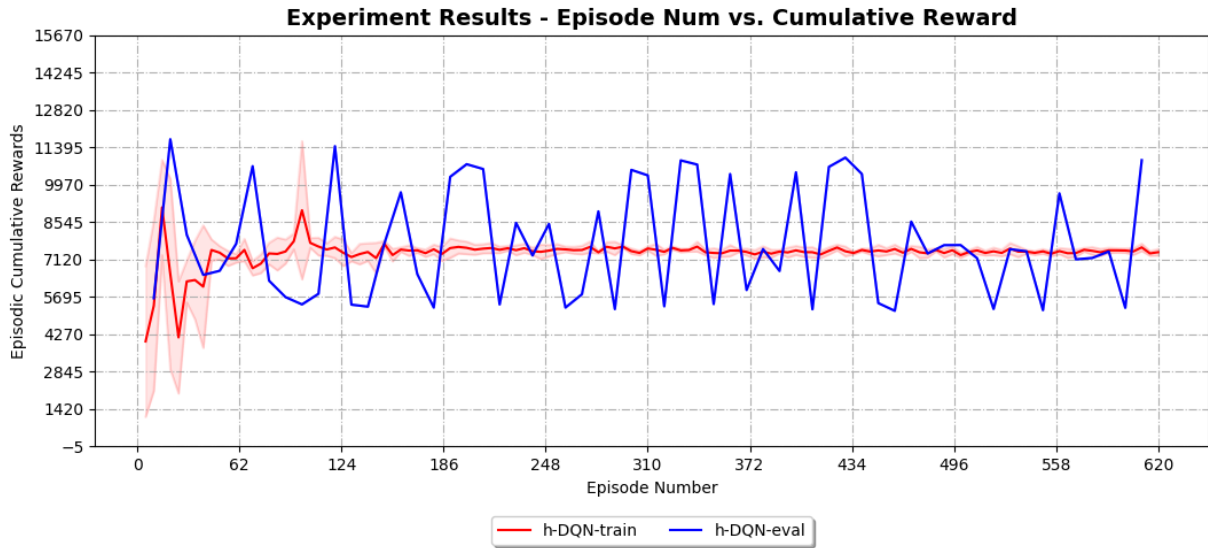


Figure 4 Training statistics and evaluation results for the first scenario

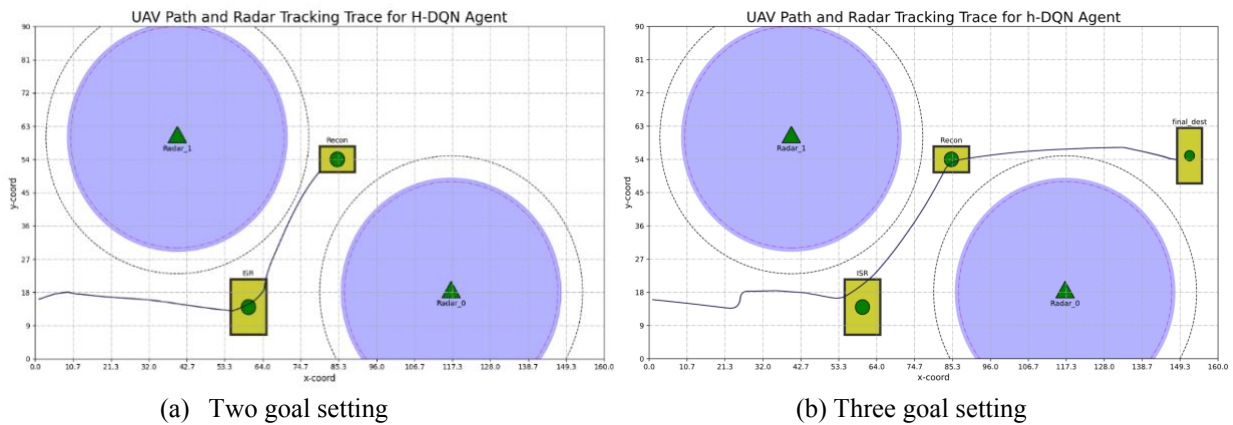


Figure 5 Illustration of navigation paths for the second and the third scenario

Figure 5 on the other hand illustrates the path of the UAV learned via the HRL algorithm, in two-goal (a) and three-goal (b) settings. The labels attached to the goal areas stand for Intelligence Surveillance and Reconnaissance (ISR) and Reconnaissance (RECON) to indicate that interim goals may serve different purposes in the mission planning.

Figure 6 provides the training statistics and evaluation results for the second scenario (i.e. two-goal setting). Note that small green circles that appear on the evaluation curve denote the point where the agent successfully learns the actively assigned goal. So, for instance, for the two-goal setting the first goal is learned at the end of 10th episode, whereas the second (and final) goal was achieved at the end of episode number 100.

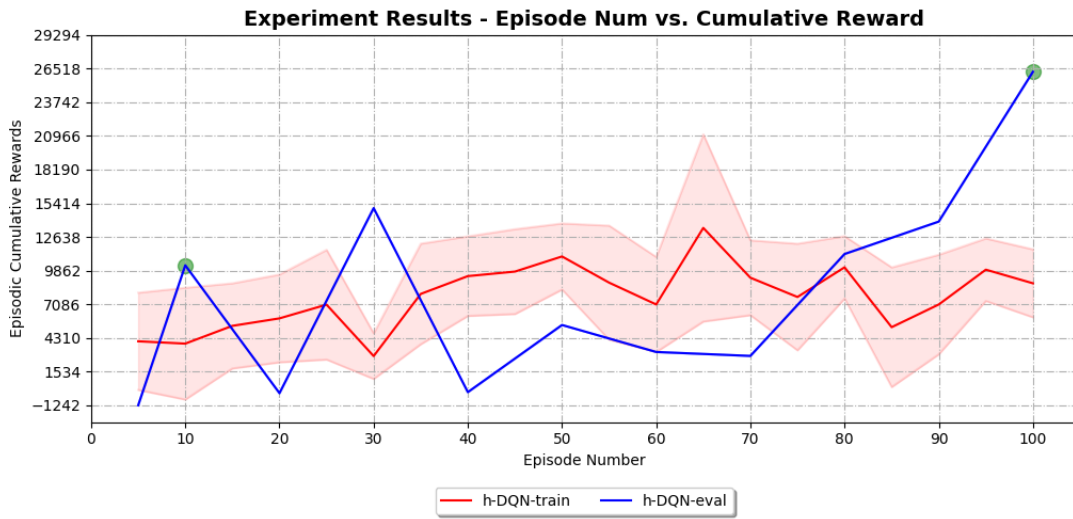


Figure 6 Training statistics and evaluation results for two-goal scenario

Similarly, Figure 7 provides the training statistics and evaluation results for the third scenario (i.e. three-goal setting). Note that this time the first goal is achieved in episode number 13, the second goal is achieved in episode number 250, and the third goal is achieved around episode number 290. Note that in this three-goal scenario the second goal is learned much later compared to the two-goal scenario. Although we use fixed seed to initialize random number generators used in the framework, as we pointed out earlier, we use perturbation of the UAV entry point to the mission area, which introduces a certain degree of randomness to the process. So this behavior is something we would expect.

The results indicate that our HRL framework ensures that the agent learns the complex navigation arrangements in a reasonable amount of time, and via a well-defined procedure.

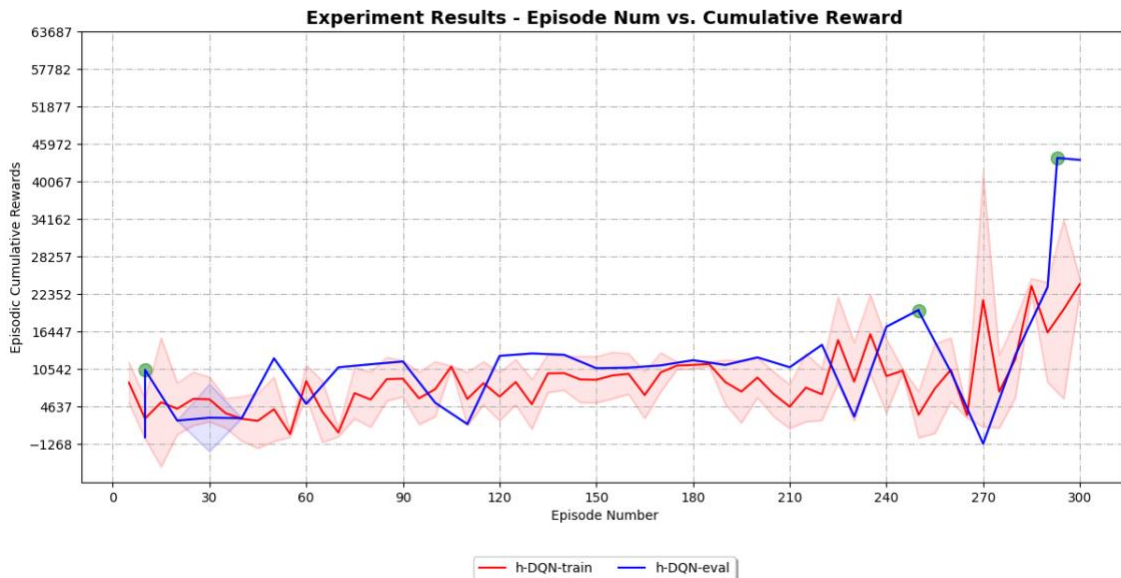


Figure 7 Training statistics and evaluation results for three-goal scenario

## 6. Conclusion

In this paper we have implemented an HRL based framework to provide a solution to sparse reward problem surfacing in complex, long-horizon path planning settings. Our proposed framework combines a meta controller for higher level goal assignment and a controller that determines the lower-level actions of the agent in a novel way, and thus constitutes one of the first examples of such a hierarchical learning scheme put into the use for UAV path planning in tactical environments. Several concluding remarks are worth noting:

1. The experiment results are a clear manifestation of the fact that hierarchical learning schemes do indeed lead to considerable improvement of the performance of the RL agent in path planning scenarios.
2. This two-layer framework ensures that an optimal plan for a complex path, organized as multiple goals, is achieved gradually, through piecewise assignment of sub-goals, and thus as a result of a staged, efficient and rigorous procedure.
3. The fact that our meta layer is pre-trained using a set of pre-defined state transitions that prescribe the evolution of goal assignment based on well-defined goal achievement state, makes the higher-level logic deterministic. This brings about performance and more robustness to the training process but limits the applicability of the solution to relatively more conservative settings. This implies that the more liberal problem settings such as those that require dynamic goal discovery are not readily addressed.
4. Our framework supports categorical states at the meta-level, so the proposed encoding scheme combined with a variable reward function selection mechanism is inherently suitable for extension to other similar contexts, involving more liberal task definitions such as non-navigational behaviors (e.g., hover along a circle for reconnaissance).

## Acknowledgements

The work presented in this paper has been partially supported by TÜBİTAK BİLGEM. We are grateful for that support. All of the theoretical and practical work including authorship of the paper is performed by the single author.

## References

- [1] Abell DC, Caraway III WD. A method for the determination of target aspect angle with respect to a radar, July, 1998.
- [2] Bertsekas DP. Reinforcement Learning and Optimal Control. Athena Scientific, Belmont, Massachusetts.
- [3] Bouhamed O, Ghazzai H, Besbes H, Massoud Y. Autonomous uav navigation: A ddpq-based deep reinforcement learning approach, 2020.
- [4] Brockman G, Cheung V, Pettersson L, Schneider J, Schulman J, Tang J, Zaremba W. Openai gym. arXiv preprint arXiv:1606.01540, 2016.
- [5] Challita U, Saad W, Bettstetter C. Deep reinforcement learning for interference-aware path planning of cellular-connected uavs. In 2018 IEEE International Conference on Communications (ICC), 2018, pp. 1–7.
- [6] Fujita Y, Nagarajan P, Kataoka T, Ishikawa T. Chainerrl: A deep reinforcement learning library. Journal of Machine Learning Research 2021; 22(77): 1–14.
- [7] Garcia F, Rachelson E. Markov Decision Processes, pp. 1–38. John Wiley and Sons, Ltd, 2013.
- [8] Gosavi A. Control Optimization with Reinforcement Learning pp. 197–268. Springer US, Boston, MA, 2015.
- [9] Hare J. Dealing with sparse rewards in reinforcement learning. CoRR, abs/1910.09281, 2019.
- [10] Hester T, Vecerik M, Pietquin O, Lanctot M, Schaul T, Piot B, Sendonaris A, Dulac-Arnold G, Osband I, Agapiou JP, Leibo JZ, Gruslys A. Learning from demonstrations for real world reinforcement learning. CoRR, abs/1704.03732, 2017.
- [11] Inanc T, Muezzinoglu MK, Misovec K, Murray RM. Framework for low-observable trajectory generation in presence of multiple radars. Journal of Guidance Control and Dynamics 2008; 31(6):1740–1749.
- [12] Pierre T, Kabamba, Semyon M, Meerkov, Frederick H. Zeitz. Optimal path planning for unmanned combat aerial vehicles to defeat radar tracking. Journal of Guidance Control Dynamics 2006; 29(2):279–288.
- [13] Kang EW. Radar System Analysis, Design and Simulation. ARTECH HOUSE, INC. 2008.
- [14] Kingma DP, Ba J. Adam: A method for stochastic optimization, 2017.
- [15] Aristotelis L, Anestis F, Ioannis V. Deep reinforcement learning: A state-of-the-art walkthrough. The Journal of Artificial Intelligence Research 2020; 69: 1421–1471.

- [16] Le TP, Vien NA, Chung T. A deep hierarchical reinforcement learning algorithm in partially observable markov decision processes. *IEEE Access* 2018; 6:49089–49102.
- [17] Jeong-Won L, Bruce W, Kelly C. Path Planning of Unmanned Aerial Vehicles in a Dynamic Environment.
- [18] Mahafza BR. Radar Systems Analysis and Design Using Matlab. CRC Press, third edition, 2013.
- [19] Mes MRK, Rivera AP. Approximate Dynamic Programming by Practical Examples, Springer International Publishing, Cham. pp. 63–101.
- [20] Mnih V, Kavukcuoglu K, Silver D, Rusu AA, Veness J, Bellemare MG, Graves A, Riedmiller M, Fidjeland AK, Ostrovski G, Petersen S, Beattie C, Sadik A, Antonoglou I, King H, Kumaran D, Wierstra D, Legg S, Hassabis D. Human-level control through deep reinforcement learning. *Nature* 2015; 518(7540): 529–533.
- [21] Pelosi M, Kopp C, Brown M. Range-limited uav trajectory using terrain masking under radar detection risk. *Appl Artif Intell* 2012; 26(8): 743–759.
- [22] Pham HX, La HM, Feil-Seifer D, Nguyen LV. Autonomous UAV navigation using reinforcement learning. *CoRR*, abs/1801.05086, 2018.
- [23] Qu C, Gai W, Zhong M, Zhang J. A novel reinforcement learning based grey wolf optimizer algorithm for unmanned aerial vehicles (uavs) path planning. *Applied Soft Computing* 2020; 89: 106099.
- [24] Benjamin R. A tour of reinforcement learning: The view from continuous control, *Annu Rev Control Robot Auton Syst* 2019; 2(1): 253–279.
- [25] Tom Schaul, John Quan, Ioannis Antonoglou, and David Silver. Prioritized experience replay, 2015. *cite arxiv:1511.05952Comment: Published at ICLR 2016.*
- [26] Skolnik MI. Radar Handbook. McGraw-Hill, second edition, 1990.
- [27] Sutton RS, Barto AG, Williams R J. Reinforcement learning is direct adaptive optimal control. *IEEE Control Systems Magazine* 1992;12(2):19–22.
- [28] Sutton RS, Barto AG. Reinforcement Learning: An Introduction. A Bradford Book, Cambridge, MA, USA, 2018.
- [29] Swerling P. Probability of Detection for Fluctuating Targets. RAND Corporation, Santa Monica, CA, 1954.
- [30] Mirco T, Harald B, Richard N, David G, Marco C. Uav path planning using global and local map information with deep reinforcement learning, 2020.
- [31] Martijn van Otterlo and Marco Wiering. Reinforcement Learning and Markov Decision Processes, chapter 1, pages 3–42. Springer Berlin Heidelberg, Berlin, Heidelberg, 2012.
- [32] Chao Y, Xiaojia X, Chang W. Towards real-time path planning through deep reinforcement learning for a uav in dynamic environments. *J Intell Robot Syst* 2020; 98(2): 297–309.
- [33] Michael Z, Stan U, Robert M. Aircraft routing under the risk of detection. *Naval Research Logistics* 2006; 53(8):728–747.
- [34] Frederick H. Zeitz. Ucav path planning in the pesence of radar-guided surface-to-air missile threats, Phd thesis, University of Michigan, 2005.
- [35] Weiwei Z, Wei W, Nengcheng C, Chao W. Efficient uav path planning with multiconstraints in a 3d large battle field environment. *Math Probl Eng* 2014:597092.
- [36] Zhe Z, Jian W, Jiyang D, Cheng H. Rapid penetration path planning method for stealth uav in complex environment with bb threats *Int J Aerosp Eng* 2020:8896357.
- [37] Alpdemir MN. Tactical UAV path optimization under radar threat using deep reinforcement learning. *Neural Comput Applic* 2022; 34: 5649–5664.
- [38] AlMahamid F, Grolinger K. Autonomous Unmanned Aerial Vehicle navigation using Reinforcement Learning: A systematic review *Eng Appl Artif Intell* 2022; 115: 105321
- [39] Parr R. Hierarchical control and learning for Markov decision processes, Ph.D. Thesis, University of California at Berkeley, 1998.
- [40] Parr R, Russell. Reinforcement learning with hierarchies of machines, in: *Advances in Neural Information Processing Systems* 10, MIT Press, Cambridge, MA, 1998, pp. 1043–1049.
- [41] Barto AG, Mahadevan S. Recent Advances in Hierarchical Reinforcement Learning *Discrete Event Dyn Syst* 2003; 13: 341–379.
- [42] Hutsebaut-Buyse M, Mets K, Latré S. Hierarchical Reinforcement Learning: A Survey and Open Research Challenges, *Mach Learn Knowl Extr* 2022; 4(1): 172-221.
- [43] Pateria S, Subagdja B, Tan A, Quek C. Hierarchical Reinforcement Learning: A Comprehensive Survey. *ACM Comput Surv* 2022; 54(5):35.
- [44] Cheng Y, Li D, Wong WE, Zhao M, Mo D. Multi-UAV Collaborative Path Planning using Hierarchical Reinforcement Learning and Simulated Annealing *J Int J Performability Eng* 2022;18(7): 463-474.
- [45] Qin Z, Zhang X, Zhang X, Lu B, Liu Z, Guo L. The UAV Trajectory Optimization for Data Collection from Time-Constrained IoT Devices: A Hierarchical Deep Q-Network Approach. *Applied Sciences*. 2022; 12(5): 2546.
- [46] Li B, Wu Y, Li G. Hierarchical reinforcement learning guidance with threat avoidance, *Journal of Systems Engineering and Electronics* 2022; 33(5): 1173-1185.
- [47] Sutton RS, Precup D, Singh S. Between MDPs and semi-MDPs: A framework for temporal abstraction in reinforcement learning. *Artif Intell* 1992; 112: 181–211.

- [48] Dietterich TG. Hierarchical reinforcement learning with the MaxQ value function decomposition. *J Artif Intell Res* 2000; 13: 227–303.
- [49] Dayan P, Hinton GE. Feudal reinforcement learning. *Advances in Neural Information Processing Systems*. Morgan-Kaufmann 1993; 5: 271–278.
- [50] Qin Z, Zhang X, Zhang X, Lu B, Liu Z, Guo L. The UAV Trajectory Optimization for Data Collection from Time-Constrained IoT Devices: A Hierarchical Deep Q-Network Approach. *Applied Sciences* 2022; 12(5):2546.
- [51] Hosmer DW, Lemeshow S. *Applied Logistic Regression*, John Wiley & Sons, Inc., Second Edition, 2000.

## CDIEA: Chaos and DNA Based Image Encryption Algorithm

Ali ARI<sup>1\*</sup>,

<sup>1</sup> Scientific and Technological Research Center, İnönü University, Malatya, Türkiye

\*<sup>1</sup> ali.ari@inonu.edu.tr

(Geliş/Received: 16/02/2023;

Kabul/Accepted: 21/03/2023)

**Abstract:** A proposal for an image encryption algorithm called Chaos and DNA Based Image Encryption Algorithm (CDIEA) has been put forward. CDIEA is a combination of block cipher algorithms, permutations, chaotic keys, and DNA operations. It leverages the strong structures of modern cryptography and the properties of chaotic systems, rather than relying solely on chaos. The permutations used in CDIEA are constructed using a strategy called the wide trail design, which makes it resilient to many forms of cryptanalysis. CDIEA operates as a byte-oriented SP-network and has been confirmed to have high security for practical image encryption through both theoretical analysis and computer experiments.

**Key words:** Image encryption; Chaos; DNA; Cryptography

## CDIEA: Kaos ve DNA Tabanlı Görüntü Şifreleme Algoritması

**Öz:** Kaos ve DNA Tabanlı Görüntü Şifreleme Algoritması (CDIEA) adı verilen bir görüntü şifreleme algoritması önerisi ortaya atılmıştır. CDIEA, blok şifreleme algoritmaları, permütasyonlar, kaotik anahtarlar ve DNA işlemlerinin bir kombinasyonudur. Yalnızca kaosa güvenmek yerine, modern kriptografinin güçlü yapılarından ve kaotik sistemlerin özelliklerinden yararlanır. CDIEA'da kullanılan permütasyonlar, onu birçok kriptanalize dayanıklı hale getiren geniş iz tasarımı adı verilen bir strateji kullanılarak oluşturulmuştur. CDIEA, bayt yönelimli bir SP ağı olarak çalışır ve hem teorik analiz hem de bilgisayar deneyleri yoluyla pratik görüntü şifreleme için yüksek güvenliğe sahip olduğu onaylanmıştır.

**Anahtar kelimeler:** Görüntü şifreleme, Kaos, DNA, Kriptoloji

### 1. Introduction

The importance of communication security arises with the rapid developments in computer and communication technologies. Many mathematicians, computer scientists and electrical engineers that are professional in their fields focused on the subject of cryptology to provide the security of millions of users who process in electronic environments. Researchers have been proposed several cryptographic algorithm and protocol using abstract algebra, number theory, and coding theory [1, 2]. Cryptology experts are constantly working to develop more powerful, faster, robust, and reliable encryption systems. Chaos based cryptology is one of the new methods introduced to carry out this goal [3-6]. Utilization of chaotic systems in the process of designing cryptographic structures is theoretically feasible since the characteristics of chaotic systems overlap with those of the cryptographic characteristics [3, 4]. Many studies have been done for design and analysis of chaos based encryption systems over the last 20 years. One of the most common subjects studied in this field is chaos based image encryption [7-13]. Nevertheless, the cryptanalysis of these algorithms has shown several significant weaknesses [14-20]. The performed analysis studies have shown that the encryption systems determined by weak transformations are not secure. One specific type of attack against chaos-based encryption targets the chaotic aspect of the cryptography. The encryption process is transformed into an alternate form where the chaotic

\* Corresponding author: ali.ari@inonu.edu.tr ORCID Number of author: <sup>1</sup> 0000-0002-5071-6790

components are replaced by secret mapping or variables. This exposes any algebraic vulnerabilities in the remaining parts of the algorithm [5, 14, 15]. In this research, a novel image encryption algorithm called CDIEA has been proposed. It merges the robust structures of modern cryptography with the principles of chaos and DNA operations. CDIEA was created as a solution to the inadequacy of traditional text encryption methods in protecting image data due to its unique properties. The algorithm is an iterated block cipher based on permutations, chaotic keys with uniform distribution, and DNA operations, and operates as a byte-oriented SP-network. The encryption scheme's transformations were modeled after those of the AES block cipher, leading to exceptional confusion and diffusion capabilities.

The paper is structured as follows. The CDIEA method is explained in detail in Section 2, where its unique features and design rationale are outlined. Section 3 showcases the early results of our security analysis of CDIEA. Finally, the paper concludes in Section 4.

## 2. Structure of CDIEA construction

Main modules of CDIEA are illustrated in Figure 1. CDIEA consist of four main modules. These modules are DNA operations module, chaotic key generation module, encryption module, and chaotic bit block permutation module. The algorithm's operation is given step-by-step below.

- Step 1.** Plain image is converted into a one-dimensional bit array.
- Step 2.** The one-dimensional bit array  $M$  split into 512-bit blocks  $m_1, m_2, \dots, m_l$ ,
- Step 3.** DNA operations are applied for each bit block. In Section 2.1, DNA operations are described in detail.
- Step 4.** Chaotic key generator module produces a 512-bit secret key for each block. In Section 2.2, chaotic key generator module is described in detail.
- Step 5.** The encryption component transforms two inputs, each consisting of 512 bits, into an output of 512 bits. The first input is the chaotic key input and the second is the bit block. The details of the encryption module can be found in Section 2.3.
- Step 6.** Ciphred bit blocks are permuted using chaotic permutation module. In Section 2.4, this module is described.
- Step 7.** Steps 3-6 are performed 10 times for each 512-bit block.

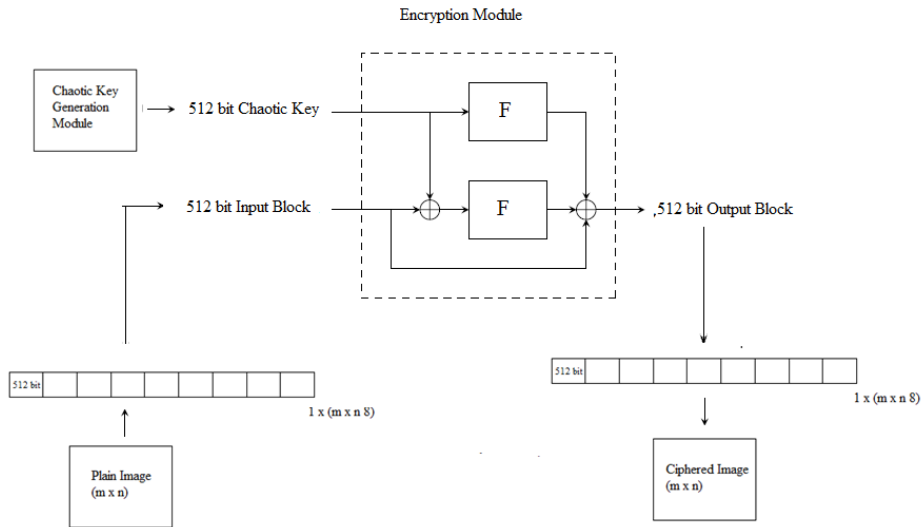


**Figure 1.** Main modules of CDIEA

**2.1. DNA operations module**

DNA computing is a novel approach to computing that employs DNA instead of conventional methods. It is a multidisciplinary field that is rapidly advancing and has yielded a number of biological and algebraic operations based on DNA sequences [23-25]. A DNA sequence consists of four base pairs, namely A, C, G, and T, where A and T are complementary to each other, as well as C and G. Information is represented by DNA sequences in DNA computing, and binary numbers are used to represent the four bases. Each base is represented by two bits of binary information. In the binary system, 0 and 1 are complementary, and similarly, the combinations 00 and 11, as well as 01 and 10, are also complementary. The four bases can be expressed by 00, 01, 10, and 11, resulting in 24 possible coding combinations. However, due to the complementary relationship between DNA bases, only eight coding combinations that satisfy this principle exist. Table 1 lists these eight encoding rules. For instance, the binary pixel value of an image is [10010011], which corresponds to the DNA sequence [GCAT] based on the first encoding rule. Similarly, the decoding sequence can be determined as [00111001] according to the sixth decoding rule.

**Table 1.** DNA coding rules

Combination	Coding Rule
Rule Combination 1	A: 00 C: 01 G: 10 T: 11
Rule Combination 2	A: 00 G: 01 C: 10 T: 11
Rule Combination 3	C: 00 A: 01 T: 10 G: 11
Rule Combination 4	C: 00 T: 01 A: 10 G: 11
Rule Combination 5	G: 00 A: 01 T: 10 C: 11
Rule Combination 6	G: 00 T: 01 A: 10 C: 11
Rule Combination 7	T: 00 C: 01 G: 10 A: 11
Rule Combination 8	T: 00 G: 01 C: 10 A: 11



In the DNA operation module, 512-bit output block are obtained by applying the following operations for each 512-bit input blocks.

- DNA encoding rule selected by using  $key_1$  ( $key_1$  is part of the secret key.  $key_1 \in [1,8]$ ) and get DNA sequence matrixes  $D_1$ .
- DNA encoding rule selected by using  $key_2$  ( $key_2$  is part of the secret key.  $key_2 \in [1,8]$  and  $key_1 \neq key_2$ ) and get DNA sequence matrixes  $D_2$ .
- Carry out DNA addition operation DNA sequence matrixes. DNA addition and subtraction rules are given Table 2.
- DNA decoding rule selected by using  $key_3$  ( $key_3$  is part of the secret key.  $key_3 \in [1,8]$ ) and get binary bit sequence.

**Table 2.** DNA addition and subtraction rules

+/-	A	T	C	G
G	C	A	G	G
C	A	T	C	T
T	G	C	T	A
A	T	G	A	C

## 2.2. Chaotic Key Generation Module

Chaotic systems are highly influenced by their starting conditions and control parameters. The path of chaotic signals exhibit unpredictability and random-like behavior. Mathematically, chaos is the randomness in a straightforward deterministic dynamic system [26]. Chaos-generated random numbers have also been employed as secret keys [27-30]. The utilization of chaotic numbers is backed by their uncertainty, wide-spectrum characteristics, non-repeating, intricate time-based behavior, and ergodic qualities. This module is used to generate round keys. Algorithm is explained in detail below.

Step 1: Choose a chaotic system to serve as the source of randomness.

Step 2: Determine the state variables based on the selected initial conditions and control parameters.

Step 3: Using Eq. (1), generate pseudorandom numbers using the selected state variable.

$$\text{ChaoticKey}(i) = (1000 * (x(i) + \text{abs}(x(i)))) \% 1 \tag{1}$$

System equations, initial conditions, and control parameters of some chaotic systems are given in Table 3 [26].

**Table 3.** Examples of chaotic systems

Chaotic Systems	Equation	Initial Values	Control Parameters
Chen system	$\begin{cases} \dot{x} = a(y - x) \\ \dot{y} = (c - a)x - xz + cy \\ \dot{z} = xy - bz \end{cases}$	$(x_0, y_0, z_0)$ $= (-3, 2, 20)$	$a = 35, b = 3,$ and $c = 28$
Chua circuit	$\frac{dV_{C1}}{dt} = \frac{1}{C_1 R} (V_{C2} - V_{C1}) - f(V_{C1})$ $\frac{dV_{C2}}{dt} = \frac{1}{C_2 R} (V_{C1} - V_{C2}) - i_L$ $\frac{di_L}{dt} = -\frac{V_{C2}}{L}$	$1/L = 25.58$	$1/C_1 R = 15.6,$ $1/C_2 R = 1,$ $a = -5/7$ and $b = -8/7$
Lorenz system	$\frac{dx}{dt} = a(y - x)$ $\frac{dy}{dt} = (bx - y - xz)$ $\frac{dz}{dt} = (xy - cz)$	$-20 \leq x \leq 20,$ $50 \leq y \leq 50,$ $50 \leq z \leq 50$	$a=10, b=28$ and $c=8/3$
Van der Pol oscillator	$dx = y$ $dy = a * (1 - x^2) * y - x^3 + b * \cos(c * z)$ $dz = 1$	$x = 0$ $y_0 = 0$ $z_0 = 0$	$a=0.2, b=5.8$ and $c=3$

### 2.3. Encryption Module

The structure of encryption module is illustrated in Figure 2. Encryption module uses a permutation. Three transformations are defined for each permutation. Transformations are illustrated in Figure 3. These are

substitution, shift, and mix transformations. The transformations operate on a state, which is represented as a matrix  $A$  of bytes (of 8 bits each). The matrix has 8 rows and 8 columns.

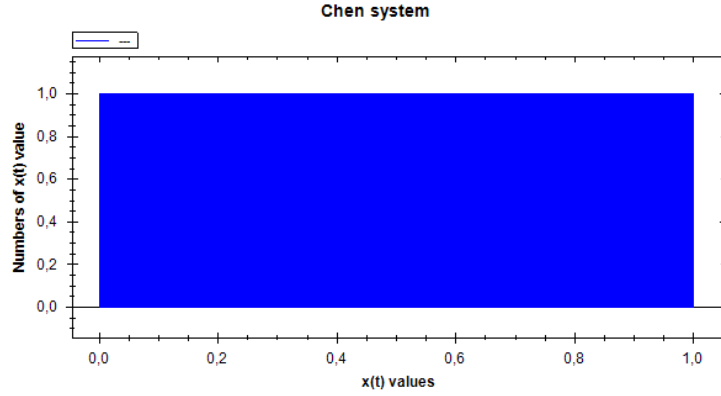


**Figure 2.** Distribution diagram analysis for Chen system

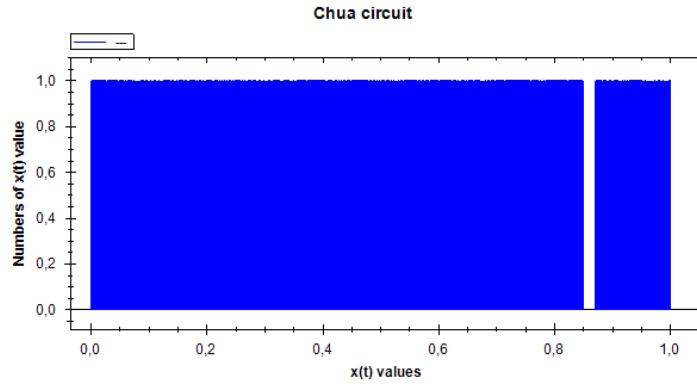


**Figure 3.** Distribution diagram analysis for Chua circuit

The substitution transformation substitutes each byte in the state matrix by another value, taken from the s-box. This s-box is the same as the one used in AES. If  $a_{i,j}$  is the element in row  $i$  and column  $j$  of  $A$ , then substitution performs the Eq. (2).

$$a_{i,j} \leftarrow S(a_{i,j}) \tag{2}$$

Shift transformation cyclically shifts the bytes within a row to the left by a number of positions. The shift transformation is illustrated in Figure 4.

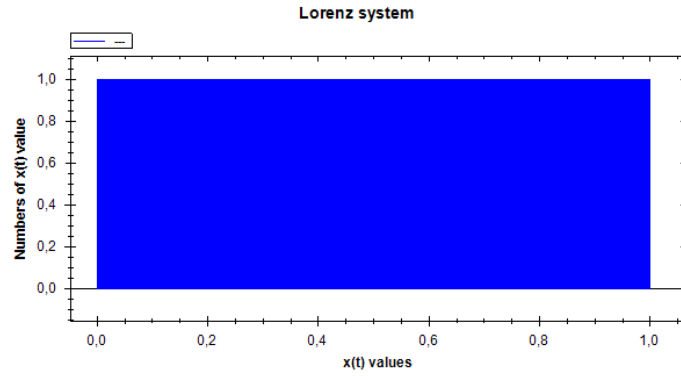


**Figure 4.** Distribution diagram analysis for Lorenz system

The mix transformation operates on each column of the matrix independently. The elements of the state matrix  $A$  are considered to be bytes in F256. This transformation involves multiplying each column of  $A$  by a constant 8x8 matrix  $B$  in F256. The overall transformation of the matrix  $A$  can be represented by Eq. (3).

$$A \leftarrow B \times A \quad (3)$$

The matrix  $B$  is specified via the irreducible polynomial  $x^8 \oplus x^4 \oplus x^3 + x + 1$  over  $F_2$ .  $B$  can be written as Eq. (4).

$$B = \begin{bmatrix} 02 & 02 & 03 & 04 & 05 & 03 & 05 & 07 \\ 07 & 02 & 02 & 03 & 04 & 05 & 03 & 05 \\ 05 & 07 & 02 & 02 & 03 & 04 & 05 & 03 \\ 03 & 05 & 07 & 02 & 02 & 03 & 04 & 05 \\ 05 & 03 & 05 & 07 & 02 & 02 & 03 & 04 \\ 04 & 05 & 03 & 05 & 07 & 02 & 02 & 03 \\ 03 & 04 & 05 & 03 & 05 & 07 & 02 & 02 \\ 02 & 03 & 04 & 05 & 03 & 05 & 07 & 02 \end{bmatrix} \quad (4)$$

## 2.4. Chaotic Permutation Module

CDIEA is a block encryption algorithm with 512-bit block size. A grey-level image  $P(m, n)$ , where  $m, n$  are the image dimensionalities of rows and columns, has contain  $l = (m \times n \times 8) / 512$  blocks. Permutation matrix is generated using the following algorithm.

- Step 1: Choose a chaotic system as the source of randomness.
- Step 2: Obtain the state variables based on selected initial conditions and control parameters.
- Step 3: Collect samples of the selected state variable at regular intervals equal to (number of data /  $l$ ).
- Step 4: Assign numerical codes to each sample starting from 0 to  $l$ .

Step 5: Create a permutation matrix using the codes assigned to the samples, with the code of the smallest output being placed in the first cell.

Step 6: Apply the permutation matrix to the ciphered blocks to replace them.

In order to illustrate how permutation matrix is generated with an example a simple system orbit is given in Figure 5. By taking 16 samples on the orbit a 1x16 permutation matrix is generated. Output values, the corresponding code value for each sample taken on the orbit, and the formed permutation matrix are given in Table 4. (For details see [31])

**Table 4.** Example of chaotic permutation

Sampling Order	No 1	No 2	No 3	No 4	No 5	No 6	No 7	No 8	No 9	No 10	No 11	No 12	No 13	No 14	no 15	No 16
Output Value	30.2	8.9	1.7	3.4	14.2	0.01	5,6	19,6	28.2	16.9	23.7	32.4	25.2	6.01	9,6	7
First Codes	0	1	2	3	4	5	6	7	8	9	10	11	12	13	14	15
Permutation Matrix	5	2	3	6	13	15	1	14	4	9	7	10	12	8	0	11

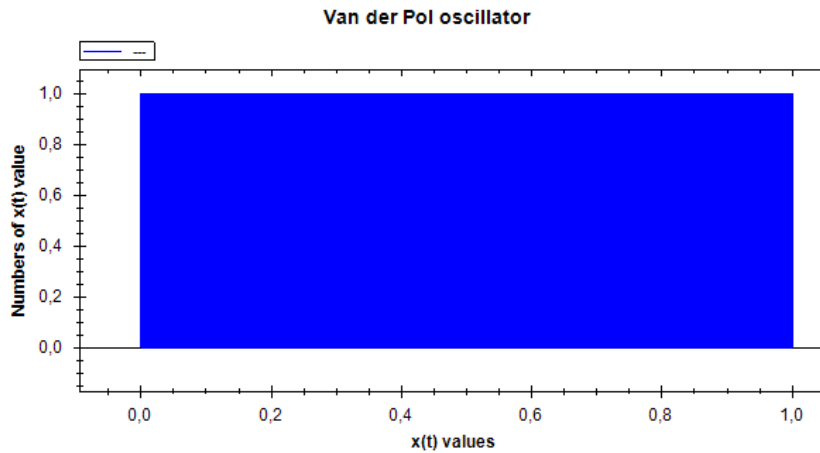


**Figure 5.** Distribution diagram analysis for Van der Pol oscillator

### 3. Security Analysis

The protection of a cryptographic system is of utmost importance. A secure encryption scheme should be able to defend against various forms of attacks, including cryptanalytic attacks, such as statistical attacks, brute-force attacks, attacks based solely on ciphertext, and attacks with access to known plaintext, among others [32-35]. In this section, the results of a security analysis of CDIEA will be explored.

### 3.1. Differential cryptanalysis

The permutation process in CDIEA is designed to have diffusion properties, meaning it helps to scramble the data and make it more difficult for an attacker to reverse the encryption. This is due to the combination of the mix transformation having nine branches and the shift transformation being optimized to move the data in each column to eight different columns. As a result, CDIEA is expected to have at least 81 active s-boxes in any four-round differential trail. This, in combination with the s-box having a maximum difference propagation probability of  $2^{-6}$ , means that the probability of any differential trail being successful over four rounds is estimated to be at most  $2^{-486}$ . So, in a classical differential attack scenario where an attacker tries to find a specific pattern in every round, it is highly unlikely they will succeed in breaking CDIEA's encryption.

### 3.2. Linear cryptanalysis

The propagation of linear and differential trails is quite alike [35]. As the mix transformation has a linear branch number of 9, it is guaranteed that in any four-round linear trail, CDIEA will have at least 81 active s-boxes [22, Theorem 9.5.1]. Given that the s-box has a maximum correlation of  $2^{-3}$ , the highest correlation for a four-round linear trail is estimated to be  $2^{-3 * 81} = 2^{-243}$ .

### 3.3. Algebraic cryptanalysis

It is well established that 40 quadratic equations can be established from the input and output bits of the AES s-box [21, 22]. These equations, along with one additional equation with a probability of 255/256, also apply to the s-box used in CDIEA. Using these equations, it has been demonstrated that a single AES encryption can produce a set of 8000 quadratic equations in 1600 variables, which can then be used to determine the secret key. Although the time complexity of solving this system of equations for AES is currently unknown, it is believed that it would take longer than an exhaustive search for the key. In comparison, the encryption function of CDIEA utilizes 1280 s-box applications, making it less vulnerable to algebraic attacks than AES. However, if an efficient attack method is discovered for CDIEA that exploits the quadratic s-box equations, it is likely that a similar attack would also be successful for AES.

### 3.4. Security analysis of chaotic key generation module

The performance of pseudo-random number generators (PRNGs) must be statistically indistinguishable from truly random sequences. Evaluating the quality of PRNGs requires statistical analysis of their output sequences by using statistical randomness tests. These tests are designed to test a null hypothesis ( $H_0$ ), which states that the input sequence is random. The test takes a binary sequence as an input and decides to either accept or reject the hypothesis. Statistical tests have a probabilistic nature and there are two possible types of errors. A type I error

occurs when the data is random but the null hypothesis is rejected. A type II error occurs when the data is non-random but the null hypothesis is accepted. The probability of a type I error is referred to as the level of significance of the test, represented by alpha ( $\alpha$ ). A statistical test produces a p-value between 0 and 1, where if the p-value is greater than alpha, the null hypothesis is accepted; otherwise, it is rejected.

A test suite is a compilation of statistical randomness tests that aim to assess the randomness qualities of sequences. There are a number of test suites in the literature, including:

- The first set of randomness tests by Knuth, which was introduced in his well-known book [36].
- CRYPT-X, developed at the Queensland University of Technology [37].
- The DIEHARD Test Suite, created by Marsaglia and released in 1995 on CDROM [38].
- TESTU01, a newly designed test suite which categorizes tests into those for real numbers in (0, 1) and those for bits [39].
- The NIST Test Suite, which initially consisted of 15 tests [40].

NIST Test Suite has been used in this study to assess randomness. The obtained results are shown in Table 5. The names of the NIST tests listed in Table 5 are Test 1: Monobit Test, Test 2: Frequency Within Block Test, Test 3: Runs Test, Test 4: Longest Run Ones in a Block Test, Test 5: Binary Matrix Rank Test, Test 6: Discrete Fourier Transform Test, Test 7: Non Overlapping Template Matching, Test 8: Overlapping Template Matching, Test 9: Maurers Universal Test, Test 10: Linear Complexity Test, Test 11: Serial test, Test 12: Approximate Entropy Test, Test 13: Cumulative Sums Test, Test 14: Random Excursion Test, and Test 15: Random excursion variant test, respectively.

**Table 5.** Results of SP 800-22 test

Test Name	Chen system	Chua circuit	Lorenz system	Van der Pol oscillator
Test 1:	√	√	√	√
Test 2:	√	√	√	√
Test 3:	√	√	√	√
Test 4:	√	√	√	√
Test 5:	√	√	√	√
Test 6:	√	√	√	√
Test 7:	√	√	√	√
Test 8:	√	√	√	√
Test 9:	√	√	√	√
Test 10:	√	√	√	√
Test 11:	√	√	√	√
Test 12:	√	√	√	√
Test 13:	√	√	√	√
Test 14:	√	√	√	√
Test 15:	√	√	√	√

#### 4. Conclusion

A new image encryption method called CDIEA has been introduced. It uses chaos and DNA encoding to create permutations, which are based on parts of the AES block cipher, providing CDIEA with superior diffusion and confusion characteristics. The design of CDIEA is straightforward, making it a robust image encryption algorithm that can be easily implemented on various platforms.

#### References

- [1] Katz J, Lindell Y. Introduction to modern cryptography: principles and protocols, Chapman & Hall, 2008.
- [2] Paar C, Pelzl J. Understanding Cryptography a Textbook for Student and Practitioners, Springer, 2010.
- [3] Amigo JM, Kocarev L, Szczapanski J. Theory and practice of chaotic cryptography, Phys Lett A 2007; 366: 211-216.
- [4] Alvarez G, Li S. Some basic cryptographic requirements for chaos-based cryptosystems. Int J Bifurcat Chaos 2006;16 (8): 2129–2151.
- [5] Solak E. Cryptanalysis of Chaotic Ciphers, in: L. Kocarev, S. Lian (Eds.), Chaos Based Cryptography Theory Algorithms and Applications, Springer-Verlag 2011; 227-256.



- [6] Alvarez G, Amigo JM, Arroyo D, Li S. Lessons Learnt from the Cryptanalysis of Chaos-Based Ciphers, in: L. Kocarev, S. Lian (Eds.), *Chaos Based Cryptography Theory Algorithms and Applications*, Springer-Verlag 2011; 257-295.
- [7] Fridrich J. Symmetric ciphers based on two-dimensional chaotic maps, *Int J Bifurcat Chaos* 1998; 8(6): 1259–1284.
- [8] Patidar V, Pareek NK, Sud KK. A new substitution-diffusion based image cipher using chaotic standard and logistic maps. *Commun Nonlinear Sci Numer Simul* 2009; 14(7): 3056–3075.
- [9] Zhu C. A novel image encryption scheme based on improved hyperchaotic sequences, *Opt Commun* 2012; 285(1): 29-37.
- [10] El-Latif A, Li L, Wang N, Han Q, Niu X. A new approach to chaotic image encryption based on quantum chaotic system, exploiting color spaces, *Signal Processing*, 2013; 93(11): 2986-3000.
- [11] Zhang Q, Guo L, Wei X. Image encryption using DNA addition combining with chaotic maps, *Math Comput Model* 2010; 52: 2028-2035.
- [12] Bigdeli N, Farid Y, Afshar K. A robust hybrid method for image encryption based on Hopfield neural network, *Computers and Electrical Engineering* 2012; 38: 356–369.
- [13] Liu L, Zhang Q, Wei X. A RGB image encryption algorithm based on DNA encoding and chaos map, *Computers & Electrical Engineering* 2012; 38(5):1240-1248.
- [14] Arroyo D, Diaz J, Rodriguez FB. Cryptanalysis of a one round chaos-based Substitution Permutation Network, *Signal Processing* 2013; 93(5): 1358-1364.
- [15] Özkaynak F, Özer AB, Yavuz S. Cryptanalysis of a novel image encryption scheme based on improved hyperchaotic sequences, *Opt Commun* 2012; 285: 4946–4948.
- [16] Özkaynak F, Özer AB, Yavuz S. Cryptanalysis of Bigdeli algorithm using Çokal and Solak attack, *International Journal of Information Security Science* 2012; 1(3): 79-81.
- [17] Özkaynak F, Özer AB, Yavuz S. Analysis of Chaotic Methods for Compression and Encryption Processes in Data Communication, 20th IEEE Signal Processing and Communications Applications Conference 2012.
- [18] Özkaynak F, Özer AB, Yavuz S. Security Analysis of an Image Encryption Algorithm Based on Chaos and DNA Encoding, 21th IEEE Signal Processing and Communications Applications Conference 2013.
- [19] Solak E, Çokal C, Yildiz OT, Biyikoglu T. Cryptanalysis of fridrich’s chaotic image encryption. *Int J Bifurcat Chaos* 2010; 20(5): 1405–1413.
- [20] Rhouma R, Solak E, Belghith S. Cryptanalysis of a new substitution–diffusion based image cipher, *Commun Nonlinear Sci Numer Simul* 2010; 15(7) : 1887-1892.
- [21] Knudsen L, Robshaw M. *The Block Cipher Companion*, Springer, 2011.
- [22] Daemen J, Rijmen V. AES Proposal: Rijndael, First Advanced Encryption Conference, California, 1998.
- [23] Gaborit P, King OD. Linear constructions for DNA codes, *Theor Comput Sci* 2005; 334: 99–113.
- [24] Xiao GZ, Lu MX, Qin L, Lai XJ. New field of cryptography: DNA cryptography, *Chin Sci Bull* 2006; 51(12): 1413–1420.
- [25] Gehani A, LaBean TH, Reif JH. DNA-based cryptography. DIMACS series in discrete mathematics, *Theor Comput Sci* 2000; 54: 233–249.
- [26] Sprott J. *Elegant Chaos Algebraically Simple Chaotic Flows*. World Scientific, 2010.
- [27] Stojanovski T, Kocarev L. Chaos-based random number generators – Part I: Analysis, *IEEE Transactions on Circuits and Systems I: Fundamental Theory and Applications* 2001; 48: 281-288.
- [28] Kocarev L, Jakimoski G. Pseudorandom bits generated by chaotic maps, *IEEE Transactions on Circuits and Systems I: Fundamental Theory and Applications* 2003; 50: 123-126.
- [29] Barash L, Shchur LN. Periodic orbits of the ensemble of Sinai-Arnold cat maps and pseudorandom number generation, *Phys Rev E* 2006; 73: 036701.
- [30] Barash LY, Shchur LN. RINGSSELIB: Program library for random number generation, SSE2 realization, *Comput Phys Commun* 2011; 182(7):1518-1527.
- [31] Özkaynak F, Özer AB. A method for designing strong S-Boxes based on chaotic Lorenz system. *Phys Lett A* 2010; 374: 3733–3738.
- [32] Bard GV. *Algebraic Cryptanalysis*, Springer, 2009.

- [33] Joux A. Algorithmic cryptanalysis, Chapman & Hall, 2009.
- [34] Biham E, Shamir A. Differential Cryptanalysis of DES-like Cryptosystems, *Journal of Cryptology* 4 1991; 3-72.
- [35] Matsui M. Linear Cryptanalysis Method for DES Cipher, *Advances in Cryptology - Eurocrypt '93*, *Lecture Notes in Computer Science* 1994; 765: 386-397.
- [36] Knuth DE. *Seminumerical Algorithms*, volume 2 of *The Art of Computer Programming*, Addison-Wesley, 1981.
- [37] Caelli W, Dawson E, Nielsen L, Gustafson H. *CRYPT-X statistical package manual*, measuring the strength of stream and block ciphers, 1992.
- [38] Marsaglia G. *The Marsaglia random number CDROM including the DIEHARD battery of tests of randomness*, 1996.
- [39] L'Ecuyer P, Simard R. Testu01: A c library for empirical testing of random number generators. *ACM Trans Math Softw* 2007; 33(4): 22.
- [40] Rukhin A, Soto J, Nechvatal J, Smid M, Barker E, Leigh S, Levenson M, Vangel M, Banks D, Heckert A, Dray J, Vo S. *A statistical test suite for random and pseudorandom number generators for cryptographic applications*, 2001.



## Deep Transfer Learning-Based Broken Rotor Fault Diagnosis For Induction Motors

Fırat DİŞLİ<sup>1\*</sup>, Mehmet GEDİKPİNAR<sup>2</sup>, Abdulkadir ŞENGÜR<sup>3</sup>

<sup>1,2,3</sup> Electrical and Electronics Engineering Department, Technology Faculty, Firat University, Elâziğ, Turkey  
<sup>\*1</sup> dislifirat@gmail.com, <sup>2</sup> mgedikpinar@gmail.com, <sup>3</sup> ksengur@gmail.com

(Geliş/Received: 08/03/2023;

Kabul/Accepted:21/03/2023)

**Abstract:** Due to their starting and running torque needs as well as their four-quadrant operation, modern industrial drives utilise induction motors (IM). Failures in the rotor bars of the motor can be found using the voltages and currents of each of the three phases as well as the acceleration and velocity signals. For the diagnosis of the quantity of broken rotor bars for a failed IM, conventional signal processing-based feature extraction techniques and machine learning algorithms have been applied in the past. The number of broken rotor bars is determined in this study by looking into a novel technique. For the aforementioned aims, specifically, the deep learning methodologies are studied. In order to do this, convolutional neural network (CNN) transfer learning algorithms are described. Initially, a bandpass filter is used for denoising, and then the signals are transformed using the continuous wavelet transform to create time-frequency pictures (CWT). The collected images are used for deep feature extraction and classification using the support vector machine (SVM) classifier, as well as for fine-tuning the pre-trained ResNet18 model. Metrics for performance evaluation employ categorization accuracy. Additionally, the results demonstrate that the deep features that are recovered from the mechanical vibration signal and current signal yield the greatest accuracy score of 100%. Nonetheless, a performance comparison with the publicly available techniques is also done. The comparisons also demonstrate that the proposed strategy outperforms the compared methods in terms of accuracy scores.

**Key words:** Broken Rotor Bars, Deep Learning, Continuous Wavelet Transform, Convolutional Neural Network, Induction Motor, Support Vector Machine.

### Asenkron Motor Kırık Rotor Çubuğu Arızasının Derin Transfer Öğrenme Tabanlı Teşhis

**Öz:** Modern endüstriyel sürücüler, başlatma ve çalıştırma torku gereksinimleri ve dört bölge çalışabilmesi nedeniyle asenkron motorlarını kullanırlar. Üç fazın her birinin gerilimleri ve akımları ile titreşim sinyalleri, motorun rotor çubuklarındaki arızaları belirlemek için kullanılabilir. Literatürde, arızalı bir asenkron motorun kırık rotor çubuklarının sayısını teşhis etmek için geleneksel sinyal işleme tabanlı özellik çıkarma yaklaşımları ve makine öğrenimi algoritmaları kullanılmaktadır. Bu çalışmada, kırık rotor çubuklarının sayısının belirlenmesi için yeni bir algoritma önerilmiştir. Spesifik olarak, belirtilen amaçlar için derin öğrenme yaklaşımları incelenmiştir. Bu amaçla, evrişimli sinir ağı (CNN) üzerinde transfer öğrenme yaklaşımı sunulmaktadır. Arıza teşhisi için motorun titreşim sinyali ve bir faz akım sinyali kullanılmıştır. Gürültü giderme için, başlangıçta bir bant geçiren filtre kullanılmış ve daha sonra sürekli dalgacık dönüşümü (CWT) kullanılarak sinyaller zaman-frekans görüntülerine dönüştürülmüştür. Elde edilen görüntüler ile önceden eğitilmiş ResNet18 modelinin ince ayarı kullanılarak derin öznetelik çıkarımı yapılmış ve destek vektör makinesi (SVM) sınıflandırıcısı ile de arıza sınıflandırması yapılmıştır. Sınıflandırma doğruluğu, performans değerlendirme ölçütleri için kullanılmış ve yapılan deneyler ile mekanik titreşim sinyali ve akım sinyalinden çıkarılan derin öznetelikler ile en yüksek doğruluk puanının %100 ile elde edildiğini göstermektedir. Öte yandan, yayınlanan yaklaşımlarla bir performans karşılaştırması da yapılmaktadır. Son olarak, karşılaştırmalar, önerilen yöntemin karşılaştırılan yöntemlerden daha iyi doğruluk puanları ürettiğini göstermektedir.

**Anahtar kelimeler:** Asenkron Motor, Derin Öğrenme, Destek Vektör Makinesi, Evrişimli Sinir Ağı, Kırık Rotor Çubuğu

#### 1. Introduction

Induction motors (IMs) are frequently used in modern industry because of their high efficiency, low cost, and high starting torque [1]. Since IMs are the main movement providers in many fields such as mining, transportation, and textile, the working conditions of IMs affect the whole work process [2]. For this reason, condition monitoring and condition-based maintenance are required in IMs. Although IMs are robust machines, faults inevitably occur in these motors. Common fault types in these motors are bearing, broken rotor bars, and winding faults. According to the studies in the literature, rotor bar failure accounts for 9% of total failures. While the rotor bars start to fail as small cracks, they become completely broken over time. With these failures, the motors start to work with vibration and noise, and thus, a decrease in efficiency takes place. In progressive failure levels, the motors become inoperable and undesirable situations emerge in the system [1-4].

\* Corresponding author: dislifirat@gmail.com. ORCID Number of authors: <sup>1</sup> 0000-0003-0016-3558, <sup>2</sup> 0000-0002-1045-7384, <sup>3</sup> 0000-0003-1614-2639

Using stator current or monitoring motor vibration signals is at the forefront in detecting rotor bar failure which is common in IMs. In addition, current and vibration signals are analyzed by using signal processing techniques such as FFT (fast fourier transform) and DWT (discrete wavelet transform). Recently, with the increase in the computational capabilities of computers, fault detection and diagnosis has gained importance by using artificial neural network, machine learning, and deep learning algorithms as well as signal processing techniques [2,28-31].

Kumar et al. proposed dilated CNN-based method for bearing and broken rotor bar failure diagnosis. They converted the vibration signals obtained from the IM into images using wavelet decomposition and then they classified them with dilated CNN. They reached an accuracy of 99.5% in their study [1]. Taher et al. created a defective motor model using FEM (finite element method) and Matlab. They first applied notch filter and then DWT to the current signals obtained from the model. Using the 6th and 7th levels of the detail coefficients obtained as a result of the DWT, they stated that these two levels could be used in the diagnosis of rotor bar failure [2]. Mustafa et al. applied Park transform to the current and voltage signals of the failed motor to diagnose the broken rotor bar failure and created a Fault Diagram using the Set Membership Identification method from the  $I_q$  and  $V_q$  components [3]. Heider et al. proposed an EPFA-based algorithm for rotor failure diagnosis. In their study, both synthetically produced and stator current signals obtained from FEM were used [4]. Shi et al. have run their method for diagnosing the magnitude of rotor bar failure in a 3-phase IM on a dynamic model of the motor and tested it on a real motor. The main idea of their work was to generate a fault index by using an arithmetic mean and standard deviation and these values were obtained from WT-applied stator current [5]. Aydin et al., applied Hilbert transform and MCSA (motor current signature analysis) techniques to the stator current signal to determine the number of broken rotor bars [6]. Sabir et al., using DWT and ETSA (electrical time synchronous averaging) from the current signals obtained from the rotor failure experiment set they created, found the rotor failure frequency range and classified the failure with Fuzzy Logic [7]. Bessam et al. created a broken rotor bar failure test set and performed tests at different loads in order to determine the number of broken rotor bars. By applying the Hilbert transform and FFT to the stator current, harmonics were obtained. They classified the number of broken rotor bars with the NN (neural network) they created using the position and amplitude of these harmonics [8]. Singh et al. created an experimental set with a half-broken rotor bar for the detection of broken rotor bars in an IM at the initial stages. They diagnosed the rotor failure at the initial stages by using the current signals obtained from the experimental set, using MCSA and MUSIC (multiple signal classification) [9]. Ameid et al. have attempted a sensorless diagnostic based on FOC (field oriented control) for rotor failure of a vector-controlled IM. For this purpose, a Matlab model and experimental set of the failed IM were created. By applying DWT to the current signal, they detected the fault with the energy levels of the sidebands of the signal. In addition, they used a driver to compensate for the effect of the fault on the speed during operation [10]. Quiroz et al. performed rotor failure diagnosis in the LS-PMSM (line start permanent magnet synchronous motor) transient state. Although MCSA is difficult in the transient state of the motor, this analysis was performed in the transient state since current flows through the rotor bars in the LS-PMSMs in the transient state. The 13 most important features of the stator current signals obtained from healthy and faulty motors were extracted with Statical Time Domain Features and classified with the help of the Random Forest algorithm. In the second case, they re-run their models with 2 of the most important features (Features Importance) and classified them. They asserted that they achieved success by 98.8% when they used 13 features and 98.4% with 2 features [11].

Gandhi et al. generated abnormal gear teeth and broken rotor bar failure both experimentally and in simulation software (Matlab/Simulink). They developed two models based on PSO (particle swarm optimization) and MPSO (modified PSO) and tested these models in their simulation and experimental systems. In their study, they concluded that the increase in fault density became noticeable from the frequency characteristic [12]. On the other hand, Rangel-Magdaleno et al. used 3mm 5mm 7mm and 10mm drilled rotors to diagnose different levels of broken rotor failure. They calculated the Kurtosis value after using the current signal EMD (empirical mode decompose) of a healthy and damaged motor at different levels and applying Hilbert transform to each of its IMFs (intrinsic mode functions). Afterwards, they showed that it was possible to detect the fault status of the motor with the Kurtosis value they obtained [13].

Differently, Malek et al. constructed a Matlab model of the motor to determine the exact location of the broken rotor bar. The stator currents were obtained by starting the motor both directly and with the help of an inverter. Then, they applied Hilbert Transform to the stator currents and determined the exact position of the broken rotor bar with the algorithm they developed [14]. Furthermore, Halder et al. have diagnosed the broken rotor failure by doing the transient analysis of the IM. Firstly, they used both FEM and open-source IM data. Secondly, they analyzed the stator current by applying STFT (short time fourier transform) and Inverse Thresholding techniques [15]. Similarly, Liu et al. created a 2-bar broken dynamic model of the motor using the

multi-loop equivalent circuit of the rotor in Matlab. They analyzed the stator current obtained from the model with both the Compressive Sensing method and MCSA and deduced the fault characteristics of the motor. In their study, they asserted that fault diagnosis could be made quickly with the Compressive Sensing technique [16]. Georgulas et al. applied PCA (Principle Component Analysis) to the stator current for broken rotor failure in a 3-phase IM and classified the obtained components with HMM (Hidden Markov Models). According to them, the combination of PCA and HMM was successful in fault diagnosis [17]. Lastly, Khater et al. determined the number of broken bars in the rotor depending on the rotor resistance change. Since the rotor resistance could not be measured directly, the data obtained with the torque meter and angular speedometer was successfully determined with the help of some formulas [18].

This study uses a brand-new method for identifying damaged rotor bars. For the aforementioned aims, specifically, deep learning methodologies are studied. The illustration of the proposed method is given in Figure. 1. To do this, convolutional neural network (CNN) transfer learning algorithms are described. Utilized are the radial mechanical vibration speeds on the driven side signal and the current signal.

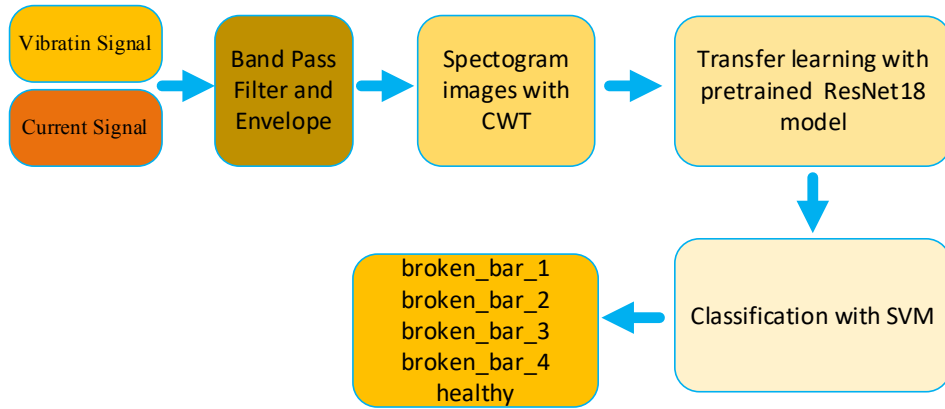


Figure. 1 Proposed methodology

First, a bandpass filter is used to denoise the signals, and then a continuous wavelet transform is used to turn the data into time-frequency pictures (CWT). The collected pictures are used for the support vector machine (SVM) classifier's deep feature extraction and classification as well as for fine-tuning the pretrained ResNet18 model. The performance evaluation metric is classification accuracy. The results of the trials demonstrate that the deep features derived from the mechanical vibration signal and current signal yield the greatest accuracy score of 100%. There is also a performance comparison with the methods that have been published. The comparisons indicate that the suggested technique outperforms the competing methods regarding accuracy scores.

## 2. Theoretical Background

### 2.1. Broken Rotor Bar

By observing the distinctive harmonic components ( $f_{BRB}$ ) in the stator line-current and vibration signal, it is possible to detect induction motor broken-rotor-bars (BRB) in steady-state [10]. These frequencies in the current signal are defined as follows,

$$f_{BRB} = f_s(1 \pm 2ks) \quad (1)$$

Where  $k$  is  $1, 2, 3, \dots, n$ ,  $f_s$  is frequency of the magnetic field and  $s$  is the rotor slip and it is calculated as:

$$s = \frac{n_s - n}{n_s} \quad (2)$$

Where  $n_s$  is synchronous speed and  $n$  is the rotor speed.

## 2.2. Continuous Wavelet Transform

In this section, principles related to CWT (continuous wavelet transform) are presented. Wavelet transform, abbreviated as WT, is considered an effective technique for machine diagnostics using sound, vibration and current signals, as it can be used to analyse both stationary and transient signals [19]. According to the studies, WT has certain advantages in characterizing the signal at different levels in the time and frequency domain. The principle of CWT which is a different approach to WT, can be defined as follows [20].

$$C_\psi = \int_{-\infty}^{\infty} \frac{|\hat{\psi}(f)|^2}{|f|} df < \infty \quad (3)$$

A wavelet  $\psi(t)$  is a function of the zero average.

$$\int_{-\infty}^{\infty} \psi(t) dt = 0 \quad (4)$$

$\psi(t)$  is a wavelet function and  $L_2(\mathbb{R})$  is the space of square-integrable functions. The corresponding wavelet family consists of a series of wavelets produced by dilation and translation from the main wavelet  $\psi(t)$ , this is given in equation 5.

$$\psi_{x,y} = \frac{1}{\sqrt{x}} \psi\left(\frac{t-y}{x}\right) \quad (5)$$

Here, the scale factor  $x$ , the time position  $y$ , and the energy conservation factor  $1/x$  are all present. When  $x$  is little, it is possible to study higher frequency components; conversely, when  $x$  is large, it is possible to analyze lower frequency components. The basis function can be moved by  $y$  in the direction that time moves when  $y$  is a fixed value. The inner product of the  $L_2$  norm in Hilbert space can be used to organize the CWT of the  $u(t)$  signal as in equation 6.

$$W_y(x) = \langle \psi_{x,y}(t), u(t) \rangle = \frac{1}{\sqrt{x}} \int u(t) \psi_{x,y}^* dt \quad (6)$$

The complex conjugate symbol here is  $*$ . Both the temporal location  $y$  and the scaling factor  $x$  are dynamic. This can be explained as the dot product  $\psi_{x,y}(t)$  of a set of wavelet functions and the signal  $u(t)$ . Wavelet coefficients, which are scale and time position functions of  $W_y(x)$ , are used to express CWT. This describes the relationship between the CWT and the signal's wavelet function. The wavelet function and the original signal are more comparable the higher the wavelet coefficient. This technique is computationally challenging since the scaling factor  $x$  and shift factor  $y$  in CWT are always changing. By digitizing either or both of the scale factor  $x$  or the shift factor  $y$ , complexity can be decreased. As a result, various wavelet transform types are created. A binary wavelet transform is what is used, for instance, when the scale factor is binary discrete but the shift factor is continuous [20].

For a discrete array  $u_m$ ,  $t = m\delta t$  and  $y = n\delta t$ , where  $m, n=0,1,2,\dots, N-1$ ,  $N$  is the sampling point and  $\delta t$  is the sampling interval. The CWT of  $u_m$  is defined as follows,

$$W_n(x_j) = \sum_{m=0}^{N-1} u_m \psi^* \left[ \frac{(m-n)\delta t}{x_j} \right] \quad (7)$$

By varying the index  $j$  and  $n$  corresponding to the  $x$  scale factor and  $y$  duration, respectively, a picture of both the scale versus amplitude of any feature and how that amplitude changes over time can be constructed. Thus,  $W_x(x_j)$ , where the  $u_m$  function is performed by a CWT, can be viewed as an arbitrary time-frequency domain of the original signal [20].

### 2.3. ResNet

Residual Networks (ResNet) are convolutional networks developed to deal with vanishing and exploding gradient problems. For a more superficial model, layers added to its deeper counterpart are called identity mapping. ResNet implements a residual module, as shown in Figure. 2, which allows each stacked layer to learn a residual mapping [21].

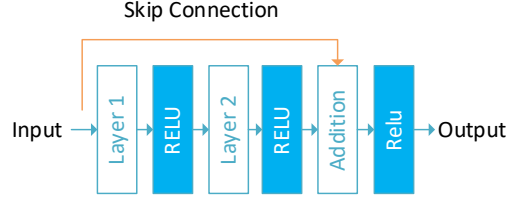


Figure 2. Schematic of a ResNet module

The final result, known as the underlying mapping, can be written as  $H(x)$ , where  $x$  stands for the first entries in the stacked layers. Instead of enabling stacked layers to approximate to  $H(x)$ , the deep residual learning module permits fit mapping to  $F(x) = H(x) x$ . As a result, the original mapping is transformed into  $F(x)+x$ , which the residual module can execute as a short cut in the neural network. There are no additional parameters or computational overhead introduced by the shortcut connections  $F(x) + x$  in the Residual module. Because to its simplicity in adapting to the underlying mapping, ResNet is appealing in practice [22].

Identity mapping is done by the Residual module, and the outputs of the shortcut links are combined with the outputs of the stack layers. The module can now be specified mathematically as in equation 8.

$$y = F(x, \{W_i\}) + h(x) \tag{8}$$

Here,  $h(x)$  stands for the initial input vector and  $y$  for the output vector. The residual mapping function  $F(x, \{W_i\})$  is fitted by stack layers. For instance,  $F = \sigma W1$  if  $F$  only contains one layer and one activation layer (ReLU).

In some circumstances,  $h(x)$  and  $y$  have distinct dimensions. To match dimensions, a square matrix or linear projection  $W_s$  can be conducted as described in equation 9.

$$y = F(x, \{W_i\}) + W_s h(x) \tag{9}$$

Convolutional layers (CL) are the basis of ResNet and aim to reduce the number of model parameters. In CLs, the inputs evolve with multiple convolution cores and then output features are produced by the activation unit. The formula expression of these operations can be given by equation 10 [23].

$$y_j^{l+1} = f(\sum_i x_i^l * w_{ij}^l + b_j^{l+1}) \tag{10}$$

Here  $l$  represents the number of network layers,  $j$  the index of the output feature map, and  $i$  the index of the input feature map. The  $*$  represents the convolution operation used for the  $i$ . feature maps  $x_i^l$  and the  $j$ . kernel  $w_{ij}^l$  in layer  $l$ . The  $b_j^{l+1}$  bias is then added to the  $j$ . feature maps in the  $l + 1$  layer. Finally,  $f$  denotes the nonlinear activation function. ReLU is commonly used as an activation function and can be expressed as in equation 11.

$$y = \max(0, x) \tag{11}$$

Pooling is another important operation, often used to reduce the size of the feature matrix. There are various methods such as max-pooling and average-pooling to implement this process. The equations for max-pooling and average-pooling operations are given as follows, respectively.

$$z_{ij}^k = \max x_{pq}^k (p, q \in R_{ij}) \tag{10}$$

$$z_{ij}^k = \frac{1}{|R_{ij}|} \sum x_{pq}^k (p, q \in R_{ij}) \tag{11}$$



Here  $z_{ij}^k$  represents the output from the  $k$ . feature map of the pooling operation,  $x_{pq}^k$  represents the value of the  $R_{ij}$  neuron in the pooling region.

## 2.4. Support Vector Machine

The SVM (support vector machine) classifier is a continuous multiple nonlinear classifier. The linear classifier, which is the original format of SVM, works with the logic of separating two sample groups that can be linearly classified in two-dimensional space with a straight line. Instances in high-dimensional space can be separated by a hyper-plane. Instead of separating using a hyper-plane, simpler decomposition can be made by mapping data in low-dimensional space to high-dimensional space. With this principle, a kernel function is used to make the samples linearly separable. In addition, the soft margin of the SVM strengthens the generalization performance. Thus, they can be used effectively for regression and classification problems. Let  $x_i$  be an input vector,  $y_i$  the corresponding outputs, so that the training set is  $\{(x_1, y_1), (x_2, y_2), \dots, (x_n, y_n)\}$ . Here  $n$  is the total number of samples in the training set. The purpose of SVM is to find the hyper-plane that divides it into two different  $y(y=1, y=-1)$  in the training set. Hyper-plane can be considered as a linear plane and expressed as in equation 14 [24].

$$f(x) = w^T x + b \quad (14)$$

Here  $w$  and  $x$  are the vectors of a column with the same dimensions. For optimal classification, the hyper-plane must be defined. A common definition is that the optimum hyper-plane takes the greatest geometry distance  $\gamma$  between the hyper-plane and two different clusters, as shown in Figure. 3. Hyper-plane calculation is as in equation 15.

$$y_i(w x_i + b) \geq 1 \quad (15)$$

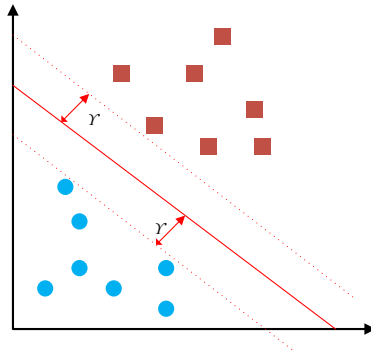


Figure 3. Geometric distance in training set

Considering the generalization performance, misclassification in SVM can be expressed by  $\xi_i$ .

$$\xi_i = \max(0, 1 - y_i (w x_i + b)) \quad (16)$$

An example of a soft variable in the classification problem is given in Figure. 4. By adding a soft variable, the optimization problem changes from equation 15 to the situation in equation 17.

$$y_i (w x_i + b) \geq 1 - \zeta_i \quad (17)$$

The kernel function is used to convert linear SVM to nonlinear. The whole problem is looking for  $w$  which is correct.  $w$  can be expressed as linear combinations.

$$w = a_1 y_1 x_1 + a_2 y_2 x_2 + \dots + a_n y_n x_n \quad (18)$$

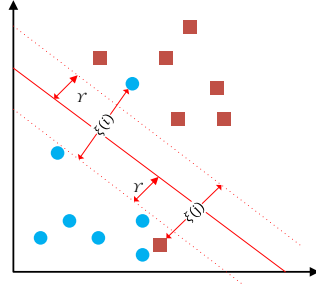


Figure 4. Soft variable of the optimization problem

In equation 18  $a_i$  is the natural number, it is called the Lagrange Multiplier. Most of the time the Lagrange Multiplier is 0, only for minority samples, the classification determines the hyper-plane [24]. Thus, the function  $f(x) = \langle w, x \rangle + b$  can be written as,

$$f(x) = \sum_{i=1}^n a_i y_i \langle x_i, x \rangle + b \quad (19)$$

## 2.5. Transfer Learning

Transfer learning (TF), a common and effective approach in deep learning models, is to use a pre-trained network. A pre-trained network is a neural network trained on a large dataset, typically for a large-scale classification task. Fine-tuning and Feature Extraction are common methods of using a pre-trained network. Feature Extraction is the use of representations learned by a previous network to extract meaningful features from new samples. A new classifier to be trained from scratch is added on top of the previously trained model so that the previously learned feature maps for the dataset can be reused. Fine Tuning is the training of some of the upper layers of a frozen model base with the newly added classifier after thawing. Thus, it makes the more abstract representations of the model to be reused more suitable for the problem [25].

## 3. Dataset

A publicly available broken rotor bar dataset has been used in our experiments. Electrical and mechanical signals from tests on three-phase IMs have been included in the dataset. Different mechanical stresses on the IM axis and various degrees of broken bar defects in the motor rotor have been tested along with data on the rotor without defects. The characteristics of the IM used in the study are 3-phase, 1-hp, 220/380V, 4 poles and a nominal speed of 1785 rpm. The dataset contains electrical and mechanical signals from experiments on three-phase IMs. The dataset contains four fault classes and one healthy class. For all classes, the dataset has been constructed with 0.5, 1.0, 1.5, 2.0, 2.5, 3.0, 3.5, and 4.0 Nm torques as the load condition. Ten experiments have been performed for each combination of healthy and loading conditions for dataset construction. The experiments were performed for the mechanical vibration speeds radial on the driven side (Vib\_acpi) and the first-phase current signal (Ia) for each combination of healthy and loading conditions. The sampling frequency of vibration signals is 7600 Hz and the sampling frequency of electrical signals is 50 kHz [26].

## 4. Experimental Works and Results

A computer with having i7 intel microprocessor with 64 GB ram was used in experimental works. Besides, an Nvidia M4000 GPU with 8 GB ram was used for deep learning applications. All coding has been carried out with MATLAB. From the power spectrum of one of the vibration signals, Vib\_acpi, observe that there are frequency components of interest in the [900 1300] Hz region. Thus, a bandpass filter was used for filtering the Vib\_acpi and Ia signals, respectively. The envelope of signals after band-pass filtering was calculated. The length of signals in the dataset is 18 seconds and a non-overlapping window of length 1 second was used in 11-15 time intervals for the sampling of the envelopes of the Vib\_acpi and Ia signals. Thus, a total of 2000 signal samples for each Vib\_acpi and Ia signal were constructed and used in the experimental works. Figure. 5 shows the sample of the envelope of Vib\_acpi signals for all classes. Besides, in Figure. 6, the envelope of the Ia current signal for all classes was given.

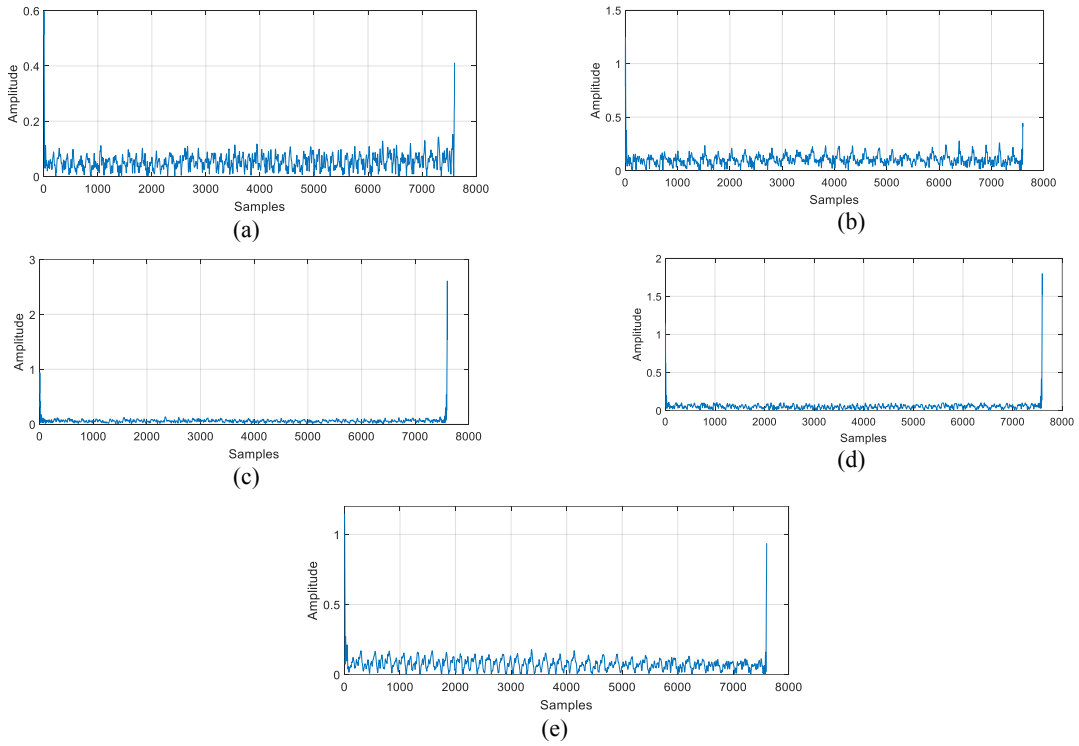


**Figure 5.** The envelope of the Vib\_apci signals for all classes for 0.5 Nm load a) Healthy, b) One broken bar, c) Two broken bars, d) Three broken bars and e) Four broken bars

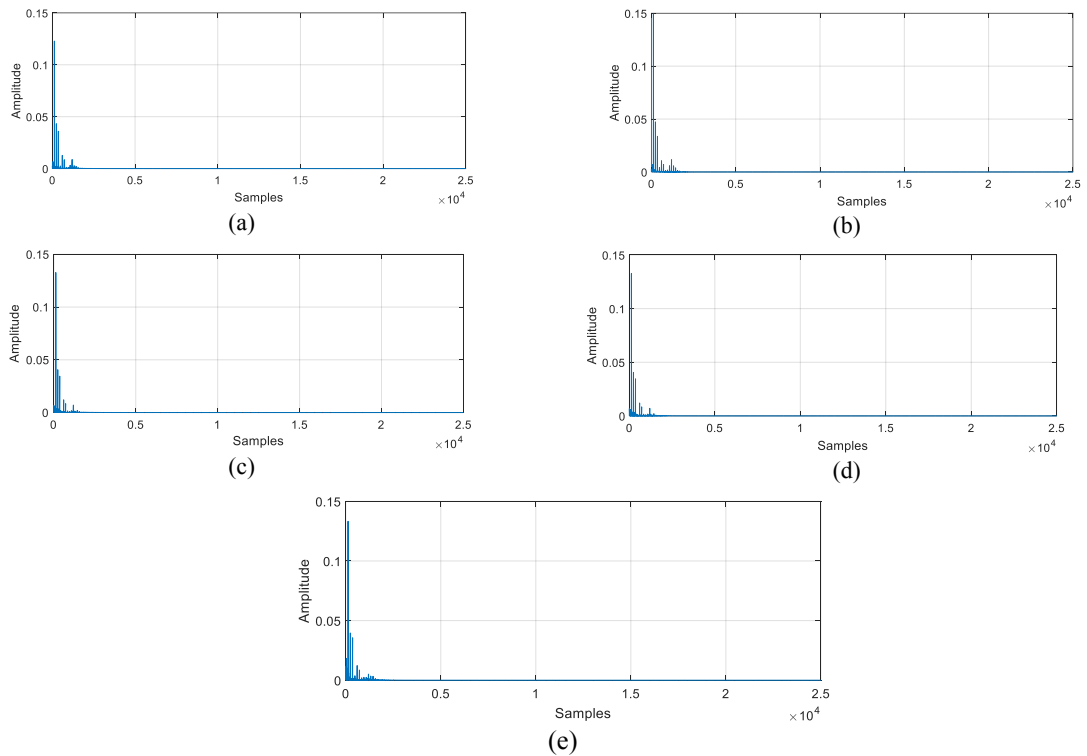


**FIGURE 6.** The envelope of the Ia signals for all classes for 0.5 Nm load a) Healthy, b) One broken bar, c) Two broken bars, d) Three broken bars and e) Four broken bars

Besides, Figures 7 and 8 show the time-frequency representations of the signals that were given in Figs. 2 and 3 by using the CWT. The ‘viridis’ color mapping was used in the representation of the time-frequency images.

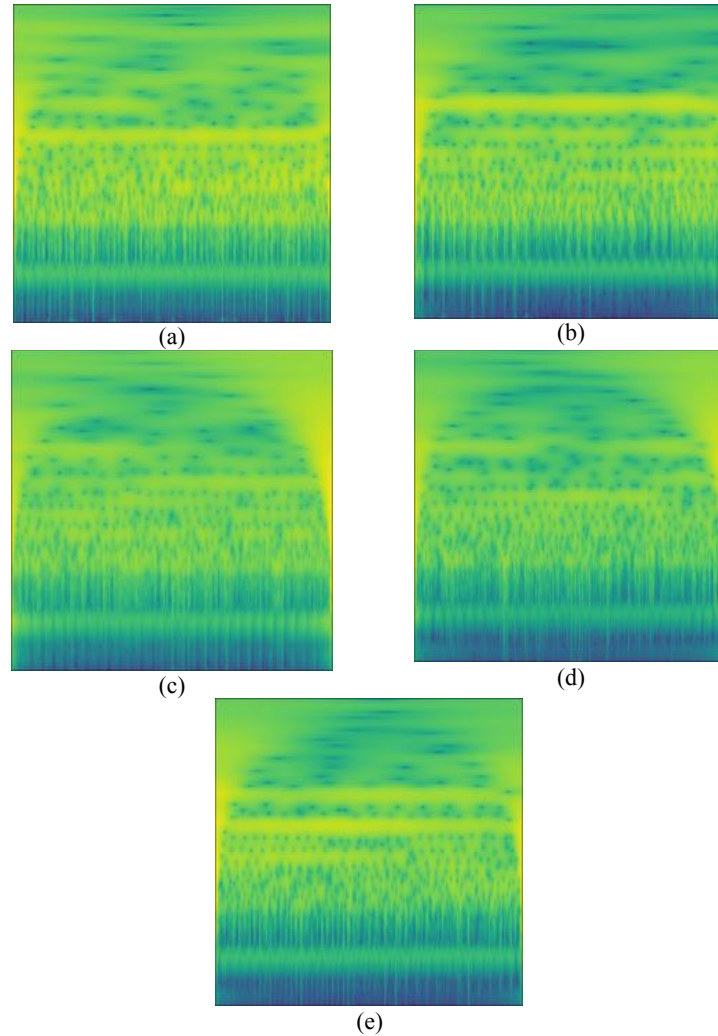


**Figure 7.** The time-frequency representation of the Vib\_acpi signals for all classes for 0.5 Nm load a) Healthy, b) One broken bar, c) Two broken bars, d) Three broken bars and e) Four broken bars

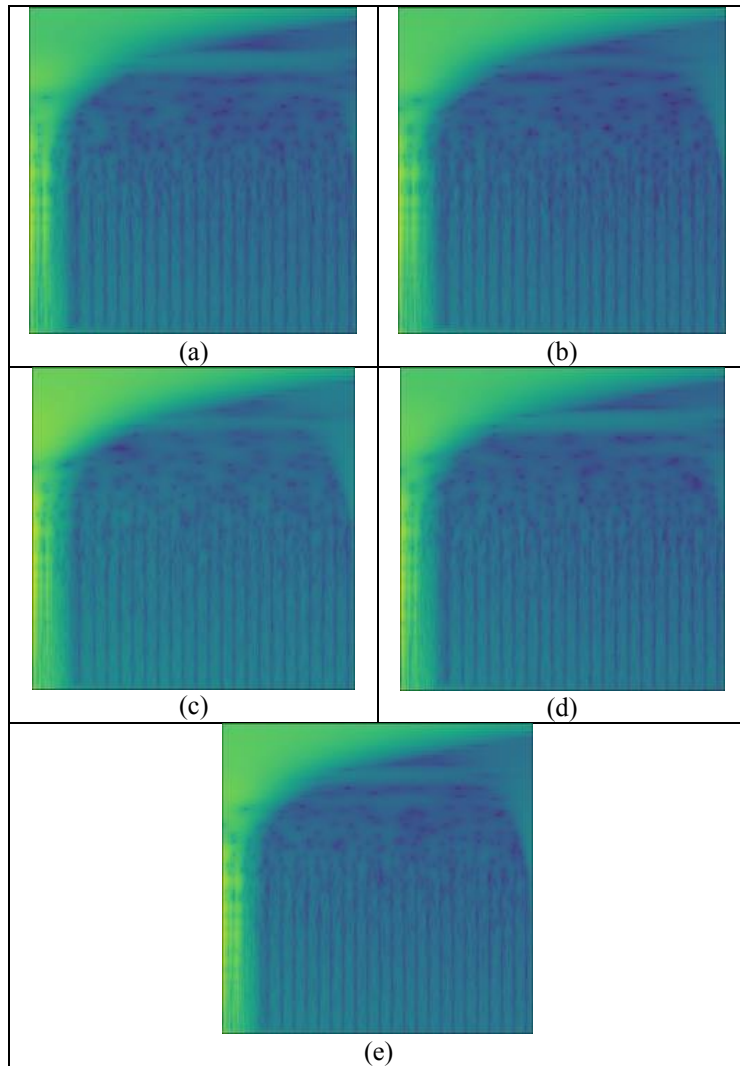


**Figure 8** The time-frequency representation of the Ia signals for all classes for 0.5 Nm load a) Healthy, b) One broken bar, c) Two broken bars, d) Three broken bars and e) Four broken bars

As we investigated the achievements of the transfer learning approaches on the broken rotor bar classification problem, both deep feature extraction from the ResNet model and fine-tuning of the ResNet model was carried out. ResNet18 model was considered in experimental works due to its shallow architecture against the ResNet 50 and ResNet 101 models [22]. In deep feature extraction, the '*res3b\_relu*' layer of the ResNet18 model was used and for fine-tuning, the ResNet18 model, the fully connected and classification layers were adjusted according to our mentioned problem.

The fine-tuning process was carried out with the 'sgdm' optimizer in all experiments. Figure. 9 shows the training progress of the fine-tuning of the ResNet18 model. As seen in Figure. 9, the training and validation accuracies were around 90% at the 10<sup>th</sup> epoch. And the accuracies were increased until the end of the 20<sup>th</sup> epoch. Between the 30<sup>th</sup> and 50<sup>th</sup> epochs, a bit of overfitting was observed, and the final validation accuracy was 98.00%. In Figure 10, the confusion matrix was given. In the confusion matrix, the x-axis shows the predicted classes and the y-axis shows the true classes, respectively.

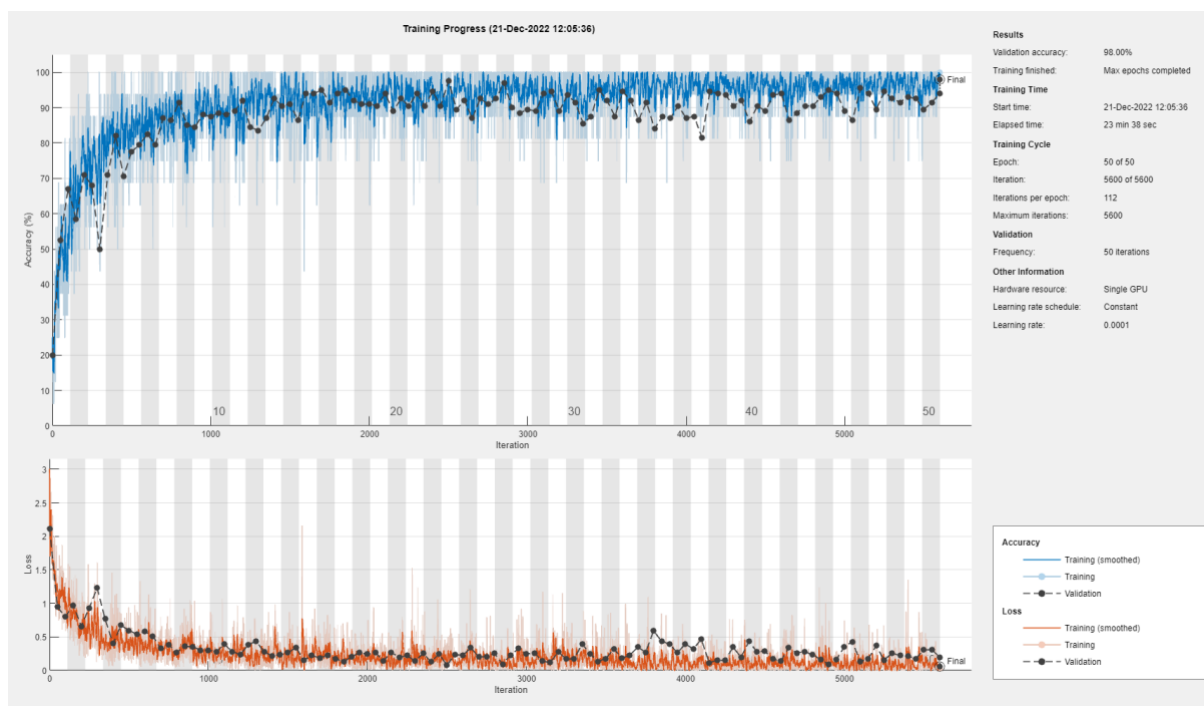


**Figure 9.** Result of the training progress for fine-tuning of the ResNet18 model for Ia.

As seen in Figure 10, for broken\_bar\_1, broken\_bar\_3 and healthy classes, all samples were correctly classified. For the broken\_bar\_2 class, only one sample was wrongly classified as broken\_bar\_3. Similarly, three samples from the broken\_bar\_4 class were classified as broken\_bar\_3. From this confusion matrix, it is observed that the broken\_bar\_3 class was confused with the broken\_bar\_2 and broken\_bar\_4 classes.

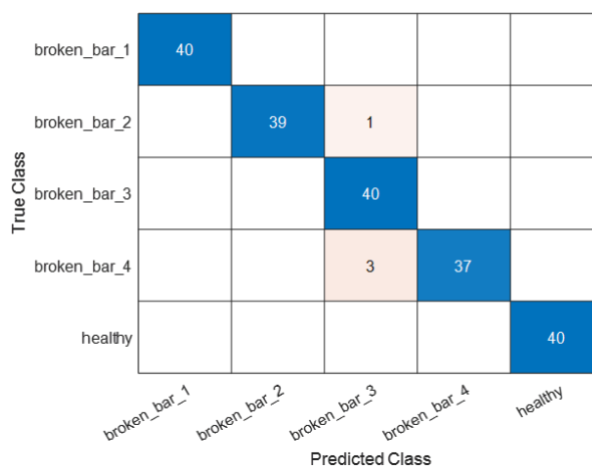


**Figure 10.** Confusion matrix for classification process for Ia

Figure 11 shows the training progress of the fine-tuning of the ResNet18 model for Vib\_acpi. As seen in Figure 11, the training and validation accuracies were over 95% at the 10th epoch.

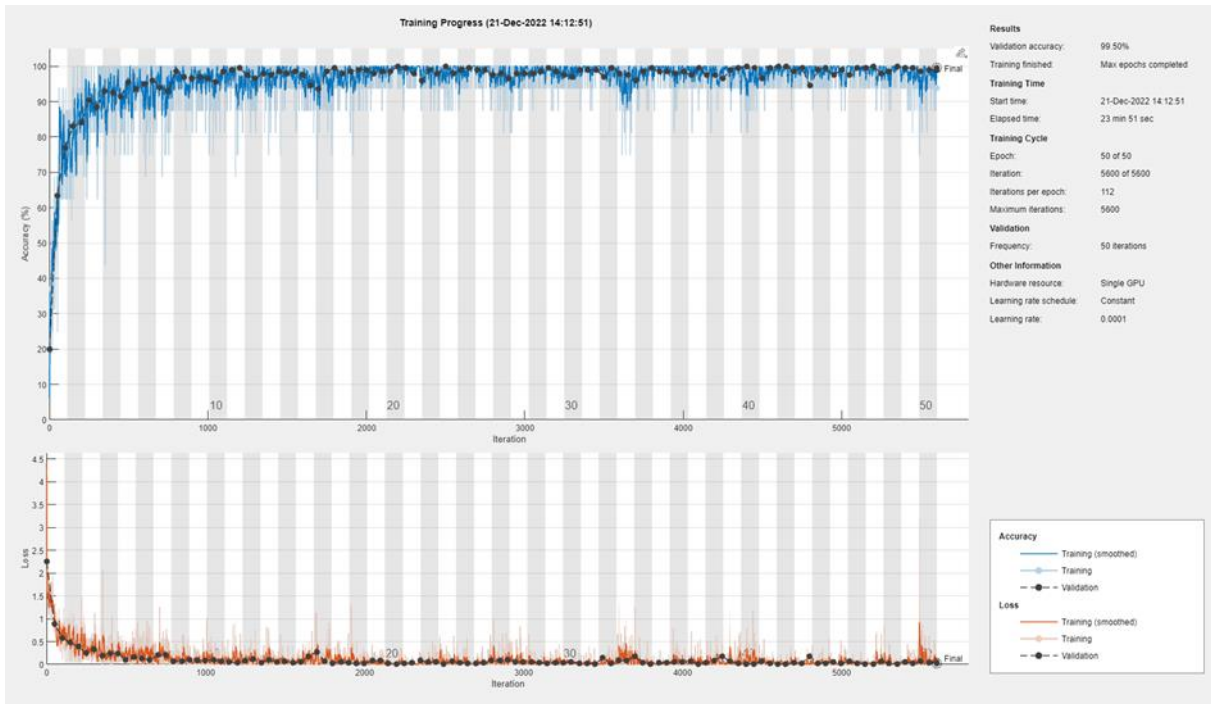


Figure 11. Result of the training progress for fine-tuning of the ResNet18 model for Vib\_acpi.

And the accuracies were stable until the end of the 50<sup>th</sup> epoch. At the 15<sup>th</sup> and 33<sup>rd</sup> epochs, there have been instantaneous drops in the accuracy but in the final epoch, the accuracy was 99.50%. In Figure 12, the confusion matrix was given. As seen in Figure 12, only one sample from the healthy class was wrongly classified as broken\_bar\_3. And other classes were all classified with 100% accuracy scores.

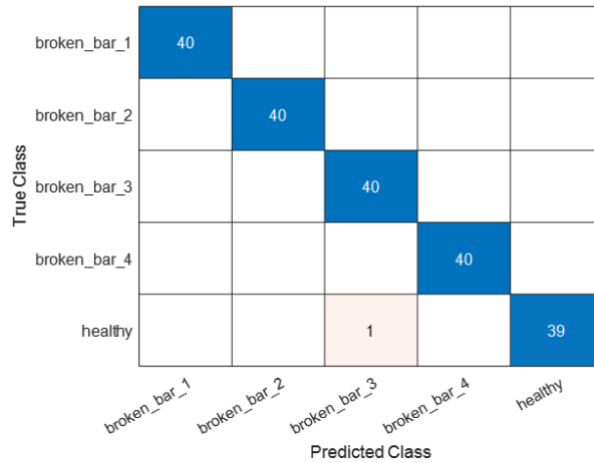
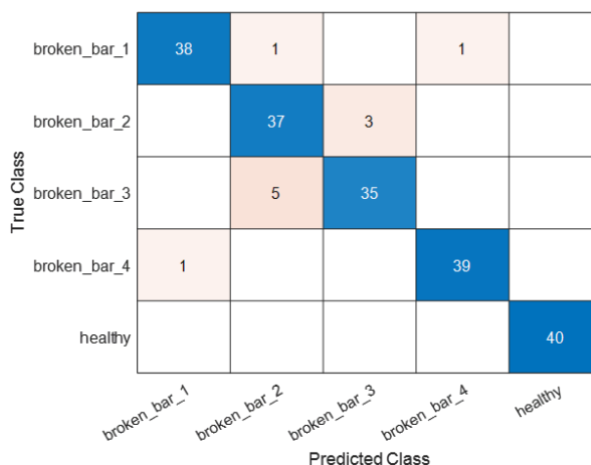


Figure 12. Confusion matrix for classification process for Vib\_acpi

After fine-tuning the ResNet18 model, another experiment was carried out where deep features were extracted from the 'res3b\_relu' layer and an SVM classifier was used in classification. Figure. 13 shows the obtained confusion matrix for the mentioned experiment on the Ia. As observed in Figure. 13, the overall accuracy score was 94.5%. And when this result was compared with the result that was obtained from the fine-tuning of ResNet18, a performance decrease was seen. There was a 3.5% performance decrease between these two experiments. Only the healthy class was classified with a 100% accuracy score and 2, 3, 5 and 1 samples were wrongly classified for the broken\_bar\_1, broken\_bar\_2, broken\_bar\_3 and broken\_bar\_4 classes, respectively.



**Figure 13.** Confusion matrix for deep features+ SVM classification process for Ia

In Figure 14, the achievement of the deep feature extraction and SVM classification process for Vib\_acpi was shown. The calculated overall accuracy score was 99% where a total of two samples from the broken\_bar\_3 and broken\_bar\_4 classes were wrongly classified. Besides, the broken\_bar\_1, broken\_bar\_2 and healthy classes were 100% correctly classified.

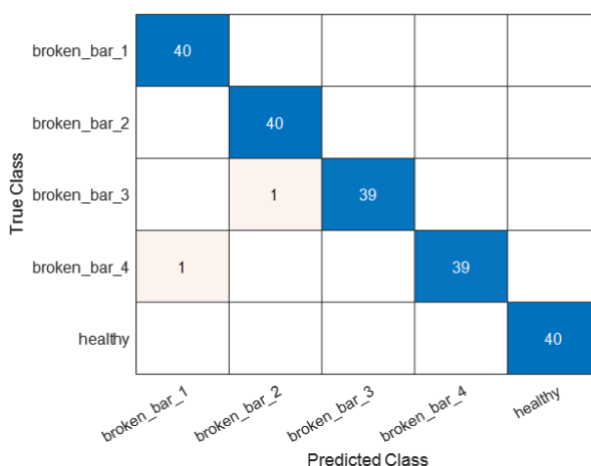


**Figure 14.** Confusion matrix for deep features+ SVM classification process for Vib\_acpi

Lastly, a final experiment was conducted where the deep features from Vib\_acpi and Ia were concatenated to form a new feature vector and the SVM classifier was used in the classification of this new feature vector. The obtained result for this experiment was shown in Figure. 15. As seen in Figure. 11, the overall classification accuracy was 100%. This accuracy score was the highest among all experiments that have been conducted in this study.



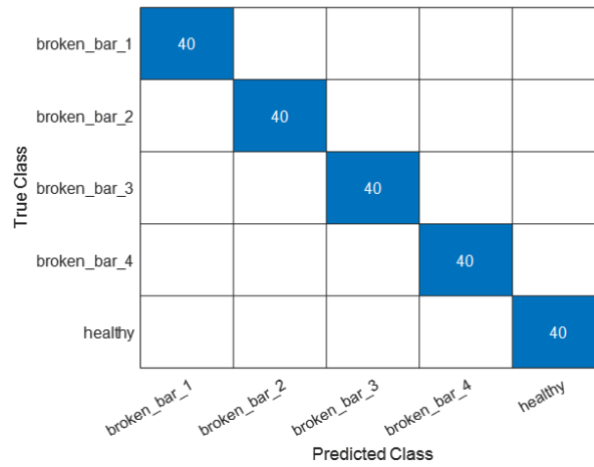


**Figure 15.** Confusion matrix for deep features+ SVM classification process for Vib\_acpi+Ia

The comparison of the obtained results with the existing results were given in Table 1. In the compared method, time domain statistical features, and various frequency domain features were extracted and concatenated from the Vib\_acpi signal. Then, one way ANOVA method was used for ranking the features for a potential feature selection operation and the first 10 to 15 features were selected and decision tree (DT) and k nearest neighbour (kNN) classifiers were used for the classification of the selected features. The identical feature extraction mechanism was also applied to the Ia signal.

**Table 1.** Performance comparison of the proposed method with some of the published results

	Features	Classifier	Accuracy (%)
Reference [27]	Statistical and frequency-based features by using Vib_acpi and Ia.	DT	93.8
Reference [27]	Statistical and frequency-based features by using Vib_acpi and Ia.	kNN	98.8
This study	Fine-tuning of ResNet18 on Vib_acpi	CNN	99.5
This study	Fine-tuning of ResNet18 on Ia	CNN	95.0
This study	Deep feature extraction from Vib_acpi	SVM	99.0
This study	Deep feature extraction from Ia	SVM	94.5
This study	Deep feature extraction and concatenation on Vib_acpi and Ia	SVM	100.0

As seen in Table 1, while the statistical and frequency domain features with the kNN classifier produced a 98.8% accuracy score, a 93.8% accuracy score was obtained with the identical features and DT classifier. The best accuracy score of 100% has been produced with the concatenation of the deep features and SVM classifier.

### 5. Conclusions

In this paper, deep transfer learning approaches are proposed for an accurate determination of the number of broken rotor bars for IMs. In the past, the general trend on such a prediction used to be based on statistical feature extraction and using a traditional machine learning approach. However, nowadays, the development of deep

learning and deep transfer learning approaches are used for the prediction of the number of broken rotor bars for IMs. Using both fine-tuning and deep feature extraction methods has been an advantage. The obtained results show that the deep learning approaches are quite efficient in the detection of the number of broken rotor bars. Especially, using the deep features, which are extracted from vibration signal and current of phase, produced the highest accuracy score that has been obtained so far.

### References

- [1] Kumar P, Hati AS. Dilated convolutional neural network-based model for bearing faults and broken rotor bar detection in squirrel cage induction motors. *Expert Syst Appl* 2022;191.
- [2] Taher SA, Malekpour M, Farshadnia M. Diagnosis of broken rotor bars in induction motors based on harmonic analysis of fault components using modified adaptive notch filter and discrete wavelet transform, *Simul Model Pract Theory* 2014; 44: 26–41.
- [3] Mustafa MO, Nikolakopoulos G, Gustafsson T, Kominiak D. A fault detection scheme based on minimum identified uncertainty bounds violation for broken rotor bars in induction motors. *Control Eng Pract* 2016; 48: 63–77.
- [4] Halder S, Dora BK, Bhat S. An Enhanced Pathfinder Algorithm-based MCSA for rotor breakage detection of induction motor, *J Comput Sci* 2022;64.
- [5] Shi P, Chen Z, Vagapov Y, Zouaoui Z. A new diagnosis of broken rotor bar fault extent in three-phase squirrel cage induction motor, *Mech Syst Signal Process* 2014; 42(1–2): 388–403.
- [6] Aydin I, Karakose M, Akin E. A new method for early fault detection and diagnosis of broken rotor bars. *Energy Convers Manag* 2011; 52(4): 1790–1799.
- [7] Sabir H, Ouassaid M, Ngote N. An experimental method for diagnostic of incipient broken rotor bar fault in induction machines. *Heliyon* 2022; 8(3).
- [8] Bessam B, Menacer A, Boumehraz M, Cherif H. Detection of broken rotor bar faults in induction motor at low load using neural network. *ISA Transactions* 2016; 64: 241–246.
- [9] Singh G, Naikan VNA. Detection of half broken rotor bar fault in VFD driven induction motor drive using motor square current MUSIC analysis, *Mech Syst Signal Process* 2018; 110: 333–348.
- [10] Ameid T, Menacer A, Talhaoui H, Azzoug Y. Discrete wavelet transform and energy eigen value for rotor bars fault detection in variable speed field-oriented control of induction motor drive. *ISA Transactions* 2018; 79: 217–231.
- [11] Quiroz JC, Mariun N, Mehrjou MR, Izadi M, Misron N, Mohd Radzi MA. Fault detection of broken rotor bar in LS-PMSM using random forests. *Measurement: Journal of the International Measurement Confederation* 2018; 116: 273–280.
- [12] Gandhi P, Turk DN, Dahiya DR. Health monitoring of induction motors through embedded systems-simulation of broken rotor bar fault and abnormal gear teeth fault, *Microprocess Microsyst* 2020; 76.
- [13] Rangel-Magdaleno J, Peregrina-Barreto H, Ramirez-Cortes J, Cruz-Vega I. Hilbert spectrum analysis of induction motors for the detection of incipient broken rotor bars. *Measurement: Journal of the International Measurement Confederation* 2017; 109: 247–255.
- [14] Abd-el-Malek M, Abdelsalam AK, Hassan OE. Induction motor broken rotor bar fault location detection through envelope analysis of start-up current using Hilbert transform, *Mech Syst Signal Process* 2017; 93: 332–350.
- [15] Halder S, Bhat S, Dora BK. Inverse thresholding to spectrogram for the detection of broken rotor bar in induction motor. *Measurement: Journal of the International Measurement Confederation* 2022;198.
- [16] Liu D, Lu D. Off-the-grid compressive sensing for broken-rotor-bar fault detection in squirrel-cage induction motors. *IFAC-PapersOnLine* 2015; 28(21): 1451–1456.
- [17] Georgoulas G, Mustafa MO, Tsoumas IP, Antonino-Daviu JA, Climente-Alarcon V, Stylios CD, Nikolakopoulos G. Principal Component Analysis of the start-up transient and Hidden Markov Modeling for broken rotor bar fault diagnosis in asynchronous machines, *Expert Syst Appl* 2013; 40(17): 7024–7033.
- [18] Khater FMH, Abu El-Sebah MI, Osama M, Sakkoury KS. Proposed fault diagnostics of a broken rotor bar induction motor fed from PWM inverter. *Journal of Electrical Systems and Information Technology* 2016; 3(3): 387–397.
- [19] Meng L, Su Y, Kong X, Xu T, Lan X, Li Y. Intelligent fault diagnosis of gearbox based on differential continuous wavelet transform-parallel multi-block fusion residual network. *Measurement: Journal of the International Measurement Confederation* 2023; 206.
- [20] Wu J da, Chen JC. Continuous wavelet transform technique for fault signal diagnosis of internal combustion engines. *NDT and E International* 2006; 39(4): 304–311.

- [21] Liang P, Wang W, Yuan X, Liu S, Zhang L, Cheng Y. Intelligent fault diagnosis of rolling bearing based on wavelet transform and improved ResNet under noisy labels and environment. *Eng Appl Artif Intell* 2022;115.
- [22] He K, Zhang X, Ren S, Sun J. Deep Residual Learning for Image Recognition, 2015, <http://arxiv.org/abs/1512.03385>.
- [23] Kumar A, Vashishtha G, Gandhi CP, Tang H, Xiang J. Tacho-less sparse CNN to detect defects in rotor-bearing systems at varying speed, *Eng Appl Artif Intell* 2021;104.
- [24] Kang H, Zong X, Wang J, Chen H. Binary gravity search algorithm and support vector machine for forecasting and trading stock indices, *International Review of Economics and Finance* 2023; 84: 507–526.
- [25] Lyu F, Zhou H, Liu J, Zhou J, Tao B, Wang D. A buried hill fault detection method based on 3D U-SegNet and transfer learning, *J Pet Sci Eng* 2022; 218.
- [26] Aline ET, Rogério AF, Marcelo S, Narco ARM. Experimental database for detecting and diagnosing rotor broken bar in a three-phase induction motor, *IEEE Dataport* 2020.
- [27] Mathworks Online Available <https://www.mathworks.com/help/predmaint/ug/broken-rotor-fault-detection-in-ac-induction-motors-using-vibration-and-electrical-signals.html>. Access Date: 12 Nov 2022.
- [28] Turkoglu M, Aslan M, Ari A, Alçin ZM, Hanbay D. A multi-division convolutional neural network-based plant identification system, *Peer J Comput Sci* 2021; 7: p. e572.
- [29] Ari A. Multipath feature fusion for hyperspectral image classification based on hybrid 3D/2D CNN and squeeze-excitation network, *Earth Sci Informatics* 2023; 16: 1–17.
- [30] Donuk K, Ari A, Hanbay D. A CNN based real-time eye tracker for web mining applications, *Multimed Tools Appl* 2022; 81: 1–18.
- [31] Demir F, Sengur A, Ari A, Siddique K, Alswaitti M. Feature Mapping and Deep Long Short Term Memory Network-Based Efficient Approach for Parkinson’s Disease Diagnosis,” *IEEE Access*, 2021; 9: 149456–149464.



# COPYRIGHT RELEASE FORM

## TURKISH JOURNAL OF SCIENCE AND TECHNOLOGY (TJST) Published by Firat University

Firat University, Fen Bilimleri Enstitüsü Müdürlüğü  
Turkish Journal of Science & Technology Editörlüğü  
Elazığ-TURKEY,  
Manuscript title: .....

Full names of all authors (in order to appear on manuscript): .....

Name, address etc. of corresponding author: .....

ID Number: ..... Telephone: .....

E-mail: ..... Mobile phone: .....

The author(s) warrant(s) that:

- a) the manuscript submitted is his/her/their own original work;
- b) all authors participated in the work in a substantive way and are prepared to take public responsibility for the work;
- c) all authors have seen and approved the manuscript as submitted;
- d) the manuscript has not been published and is not being submitted or considered for publication elsewhere;
- e) the text, illustrations, and any other materials included in the manuscript do not infringe upon any existing copyright or other rights of anyone. Notwithstanding the above, the Contributor(s) or, if applicable the Contributor's Employer, retain(s) all proprietary rights other than copyright, such as

- a) patent rights;
- b) to use, free of charge, all parts of this article for the author's future works in books, lectures, classroom teaching or oral presentations;
- c) the right to reproduce the article for their own purposes provided the copies are not offered for sale.

However, reproduction, posting, transmission or other distribution or use of the article or any material contained therein, in any medium as permitted hereunder, requires a citation to the Journal and appropriate credit to Firat University as publisher, suitable in form and content as follows:

Title of article, author(s), journal title and volume/issue, Copyright© year.

All materials related to manuscripts, accepted or rejected, including photographs, original figures etc., will be kept by Turkish Journal of Science and Technology editority for one year following the editor's decision. These materials will then be destroyed. I/We indemnify Firat University and the Editors of the Journals, and hold them harmless from any loss, expense or damage occasioned by a claim or suit by a third party for copyright infringement, or any suit arising out of any breach of the foregoing warranties as a result of publication of my/our article. I/We also warrant that the article contains no libelous or unlawful statements and does not contain material or instructions that might cause harm or injury.

This copyright form must be signed by all authors. Separate copies of the form (completed in full) may be submitted by authors located at different institutions; however, all signatures must be original.

ID number: ..... ID number: .....

Full name (block letters) ..... Full name (block letters) .....

Signature ..... Date ..... Signature ..... Date .....

ID number: ..... ID number: .....

Full name (block letters) ..... Full name (block letters) .....

Signature ..... Date ..... Signature ..... Date .....

ID number: ..... ID number: .....

Turkish authors must supply their ID card number; foreign authors must supply their passport number (if possible)